UNIVERSITAT POLITÈCNICA DE CATALUNYA BARCELONATECH

Coastal risk forecast system: fostering proactive management at the Catalan coast

Manuel García-León

UNIVERSITAT POLITÈCNICA DE CATALUNYA

BARCELONA TECH

Escola Tècnica Superior d'Enginyers de Camins, Canals i Ports de Barcelona

Laboratori d'Enginyeria Marítima (LIM/UPC)

Programa de Doctorat en Enginyeria Civil

Coastal Risk Forecast System

Fostering proactive management at the Catalan Coast

PhD Thesis presented by

Manuel GARCÍA-LEÓN

for the degree of DOCTOR OF PHILOSOPHY IN CIVIL ENGINEERING

Barcelona, June 2018

Laboratori d'Enginyeria Marítima

UNIVERSITAT POLITÈCNICA DE CATALUNYA

Supervisors

Dr. Vicente Gràcia Garcia

Prof. Agustín Sánchez-Arcilla

Contents

List of Figures

List of Tables

Symbol Index

Abbreviatures

AIC	Akaike's Information Criterion
BIC	Bayesian Information Criterion
BSS	Brier Skill Score
CAP	Common Alerting Protocol
CBRDM	Community Based Disaster Risk Methodologies
COE	Coefficient of Efficiency (-)
CSI	Coastal State Indicators
DSS	Decision Support System
EA	East Atlantic Oscillation
ECMWF	European Centre for Medium-Range Weather Forecasts
EEA	European Environmental Agency
EMMA	European Multi-Purpose Meteorological Awareness Programme
ESA	European Space Agency
GAMLSS	Generalized Additive Models for Location, Shape and Scale
GDP	Gross Domestic Product
GEAS	Global Environmental Alert Service
GFS	Global Forecasting Service
GHG	Greenhouse Gases
GIS	Geographic Information System
GLM	Generalized Linear Models
GMSL	Global Mean Sea-Level
HDPE	High Density Polyethylene
IBI-MFC	Iberia-Biscay-Ireland Monitoring and Forecasting Centre

ICGC	Institut Cartogràfic i Geològic de Catalunya (Catalan Cartographic and Geological Institute)
IGN	Instituto Geográfico Nacional (Spanish National Geographic Institute)
IIASA	International Institute for Applied Systems Analysis
ITeC	The Catalonia Institute of Construction Technology
LIDAR	Laser Imaging Detection and Ranging
MWL	Mean Water Level [m]
NAO	North Atlantic Oscillation
NBS	Nature-Based Solutions
NEMO-OPA	Nucleus for European Modelling of the Ocean - Ocean Dynamics Core
NRMSE	Normalized root mean square error
OGC	Open Geospatial Consortium
PdE	Puertos del Estado monitoring network
QAM	Quick Adaptation Measures
QDM	Quick Defence Measures
REDCOS	Puertos del Estado - Coastal buoy network
REDEXT	Puertos del Estado - Deep water buoy network
REDMAR	Puertos del Estado - Tide gauge monitoring network
RSLR	Relative Sea Level Rise
RSS	Real Simple Syndication
SAR	Synthetic Aperture Radar
SC	Scandinavian (Atmospheric) Pattern
SLR	Sea Level Rise
SST	Sea-surface temperatures
SWAN	Simulating WAves Nearshore
UNEP	United Nations Environment Programme
WRF	Weather Research and Forecasting model
XIOM	Xarxa d'Instrumentació Oceanogràfica i Meteorològica

XML	Extensible Markup Language

Wave storm identifiers

D-08	December 2008 (26/12/2008 - 30/12/2008)
D-16	December 2016 (17/12/2016 - 23/12/2016)
F-16	February 2016 (26/12/2008 - 30/12/2008)
J-16	January 2016 (10/01/2016 - 12/01/2016)
J-17	January 2017 (16/01/2017 - 24/01/2017)
N-15	November 2015 (01/11/2015 - 04/11/2015)
O-15	October 2015 (29/09/2015 - 01/10/2015)

Symbol Index (Latin)

A	Action Wave Density $[J/s\,m^2]$
A_{dean}	Dean parameter [-]
A_{gen}	Wave generation linear term at SWAN model $[W/m^2]$
B_{gen}	Wave generation exponential term at SWAN model $[W/m^2]$
Brm_{bch}	Berm height [m]
$buil_{\%}$	Percentage of building area at the backshore [%]
C_{eq}	Depth-averaged equilibrium concentration of sediment $[m^3/m^3]$
$c_{p,mt}$	The specific heat of dry air at constant pressure (meteorological module) $[J\,kg^{-1}\,K^{-1}]$
$c_{v,mt}$	The specific heat of dry air at constant volume (meteorological module) $[J\,kg^{-1}\,K^{-1}]$
c_w	Ocean wave celerity [m/s]
D_{storm}	Storm duration $[h]$
D_w	Wave breaking energy dissipation [W/m^2]
E_w	Total wave energy [W/m^2]
ero_{rate}	Beach erosion rate [m/yr]
f_{Ts}	Sediment transport depth factor [m/s]
$F_{w,x}$	Cross-shore Wave Forcing (morphodynamic module) $[N/m^2]$
$F_{w,y}$	Longshore Wave Forcing (morphodynamic module) $[N/m^2]$

$H_{s,peak}$	Significant wave height at the storm peak [m]
H_s	Significant wave height [m]
H_w	Wave height [m]
K_s	Shoaling coefficient [-]
k_w	Wavenumber [rad/m]
L_{bch}	Beach alongshore length [m]
L_w	Wavelength [m]
$m_{x,mt}$	Map factor in x-direction (meteorological module) [-]
$m_{y,mt}$	Map factor in y-direction (meteorological module) [-]
n_{Rvk}	Constant of the exponent in Roelvink's dissipation model (morphodynamic module) [-]
$p_{0,mt}$	Reference pressure (meteorological module) [N/m^2]
$p_{dh,mt}$	Hydrostatic component of the pressure (meteorological module) [N/m^2]
$p_{dhs,mt}$	Pressure values along the surface (meteorological module) [N/m^2]
$p_{dht,mt}$	Pressure values along the top boundaries (meteorological module) [N/m^2]
p_h	Hydrostatic pressure [N/m^2]
p_{mt}	Atmospheric pressure field (meteorological module) [N/m^2]
q_b	Non-hydrostatic bottom pressure [N/m^2]
$Q_{m,mt}$	Generic coupled moisture variable (meteorological module) [-]
$R_{d,mt}$	Gas constant for dry air (meteorological module) [287 $J\,kg^{-1}\,K^{-1}$]
S_{tot}	Summation of source/sink terms of wave energy [W/m^2]
S_w	Wave energy at each directional sector [N m/m^2]
slp_{em}	Emerged beach slope [-]
t	Time [s]
T_{m02}	Mean wave period [s]
$T_{p,peak}$	Peak period at the storm peak [m]
T_r	Return period (years)
T_s	Adaptation time for the sediment concentration (morphodynamic simulation) [s]

u^E	Eulerian velocity field in X-direction [m/s]
u^L	Lagrangian velocity field in X-direction [m/s]
U_{mt}	Coupled horizontal velocity in x-direction (meteorological module) [m/s]
v^E	Eulerian velocity field in Y-direction [m/s]
v^L	Eulerian velocity field in Y-direction [m/s]
V_{mt}	Coupled horizontal velocity in y-direction (meteorological module) [m/s]
W_{bch}	Beach width [m]
w_b	Vertical velocity at the bottom $[m/s]$
W_{mt}	Coupled vertical velocity (meteorological module) [m/s]
w_{sed}	Sediment fall velocity (morphodynamic module) [m/s]
w_s	Vertical velocity at the free surface $[m/s]$
g	Gravity acceleration [9.81 m^2/s]

Symbol Index (Greek)

$\alpha_{(H_s,\mu_{\varepsilon_r})}$	Wave directional coefficient for the erosion cost marginal distribution at the Risk module [-]
$\alpha_{(H_s,\mu_{\varphi_r})}$	Wave directional coefficient for the flood cost marginal distribution at the Risk module [-]
$\alpha_{d,mt}$	Inverse density of the dry air (meteorological module) [m^3/kg]
χ	Cost function [-]
η	Free-surface elevation [m]
η_{mt}	Terrain-following hydrostatic-pressure vertical coordinate (meteorological module) [m]
γ_{br}	Wave breaking threshold (morphodynamic module) [-]
μ_{ε_r}	Location parameter for the erosion marginal distribution at the Risk module [-]
μ_{φ_r}	Location parameter for the flooding cost marginal distribution at the Risk module [-]
$\mu_{d,mt}$	Mass of the dry air within the column (meteorological module) [kg]
Ω	Dean Parameter - Dimensionless sediment fall velocity [-]

Ω_{mt}	Coupled coordinate velocity (meteorological module) [m/s]
ϕ_{mt}	Geopotential (meteorological module) [m^3/s]
σ_{ε_r}	Scale parameter for the erosion marginal distribution at the Risk module [-]
σ_{φ_r}	Scale parameter for the flooding cost marginal distribution at the Risk module [-]
τ_{bx}^E	Bottom shear stress in X-direction [N/m^2]
τ_{by}^E	Bottom shear stress in Y-direction [N/m^2]
τ_K	Kendall's dependence metric [-]
τ_{sx}	Wind shear stress in X-direction [N/m^2]
τ_{sy}	Wind shear stress in Y-direction [N/m^2]
θ_{cp}	Association parameter of the copula [-]
$\theta_{m,mt}$	Moist temperature potential (meteorological module) [K]
Θ_{mt}	Coupled potential temperature (meteorological module) [K]
θ_w	Ocean wave direction [rad]
ε_r	Eroded volume divided by surface at the Risk module [m^3/m^2]
φ_r	Flood cost divided by surface at the Risk module [$euros/m^2$]

Abstract

Coastal Risk Forecast System

Fostering proactive management at the Catalan Coast

PhD Candidate: Manuel García León

PhD Advisors: Dr. Vicente Gracia; Prof. Agustín Sánchez-Arcilla

The action of sea storms is one of the most complex littoral processes with deep management implications. Along the Catalan shoreline which is about 700 km long, 190 km are subject to erosion and/or flooding. Around one million people live in areas potentially affected. Sea Level Rise could exacerbate this problem in the near future. Reactive interventions have been the norm in coastal engineering and management. This dissertation proposes a pre-storm strategy that foster cost-effective eco-compatible measures, termed Quick Defence Measures (QDM). Pre-storm intervention requires to forecast the future post-storm state. Hence, the main objective of this thesis is to assess present coastal risk through a Coastal Early Warning System (CEWS), termed LIM-COPAS, that forecasts the more relevant episodic coastal hazards at the area.

LIM-COPAS consists of four modules: (i) meteorological model; (ii) wave generation/propagation code; (iii) coupled morpho-hydrodynamic model and (iv) risk module via non-stationary multivariate probabilistic models. The performance of this suite of models has been tested with (i) a set of hindcast events and (ii) synthetic storm conditions. The hindcasted events have been: December 2008 (D-08); October-2015 (O-15); November 2015 (N-15); January 2016 (J-16); February 2016 (F-16); December 2016 (D-16) and January 2017 (J-17).

In D-08, errors in nearshore spectral wave parameters have been about twice than those in the offshore area. The error was around 20% in hydrodynamics and 50% in morphodynamics. The post-storm response has been acceptably reproduced, with a Brier Skill Score near 0.4.

LIM-COPAS has shown good accuracy with high return period events (i.e. $T_{r,waves} \geq 10\,yrs$, D-16 and J-17), but lower agreement was found for milder storms (i.e. O-15 and F-16).

The meteorological module provided wind fields that were systematically overestimated. The integrated Mean Bias (MB) was $-1.52 \pm 0.78\ m/s$. Tarragona (Coefficient of Efficiency, $COE = 0.27 \pm 0.13$) and Begur ($COE = 0.29 \pm 0.17$) had metrics above the average value ($COE = 0.24 \pm 0.14$); but lower agreement was found at Mahón ($COE = 0.13 \pm 0.16$) and Dragonera.

Wave metrics were more accurate than for the wind fields. The integrated H_s COE was 0.52±0.12 and T_{m02} COE was 0.36±0.14. At the central coast, H_s has presented good metrics: low MB ($-0.06 \pm 0.08\ m$) and high COE (0.58 ± 0.11). The northern coast metrics were the most stable.

The newly developed risk module has been implemented at 79 beaches. Erosion has been estimated as a bounded cost, whereas flooding as a high upside cost. Dissipative beaches tend to exhibit higher costs than reflective beaches under high sea levels. $T_{r,waves} \leq 10\ yrs$ events joint with storm-surges can lead to significant damage costs. The estimated losses for the N-15 event ($2510 \cdot 10^3 euros$) do not differ excessively from J-17 ($3200 \cdot 10^3$ euros).

Two types of QDM have been numerically tested: (i) sand dunes and (ii) geotextile detached breakwaters. The benefits from maintaining the sand volumes outperform the flooding cost reduction. In general terms, the detached breakwater can be a suitable option for beaches in an intermediate morphodynamic state against low to moderate sea levels and high wave return periods. At dissipative beaches, dunes are the best option, but they require a minimum beach width (around $30\ m$) that ensures their lifetime.

QDM functionality can be enhanced with compatible long-term actions (nourishments, sand bypasses, submerged vegetation, etc.). A healthy beach state is paramount for the QDM effectiveness. A higher sustainable management under present and future climate can be reached with the joint combination of (i) CEWS as a short-term forecasting tool; (ii) QDM that mitigate storm impacts and (iii) long-term interventions that improves the beach health.

Key words: coastal risk, storm impact, littoral management, coastal early warning system, WRF, SWAN, XBEACH, non-stationary copula

Sistema de predicción para el riesgo costero

Fomentando la gestión proactiva de la Costa Catalana

Doctorando: Manuel García León

Directores de la tesis: Dr. Vicente Gracia; Prof. Agustín Sánchez-Arcilla

La acción de los temporales de mar es uno de los procesos litorales más complejos, con profundas implicaciones en la gestión del litoral. A lo largo de la línea de costa catalana, 190 km están sometidos a erosión y/o inundación. Cerca de un millón de personas viven en áreas potencialmente afectadas. La tradición en ingeniería y gestión costera han sido intervenciones reactivas. Esta tesis propone una estrategia pre-tormenta que fomente una serie de medidas eco-compatibles, denominadas Medidas de Acción Rápida (MAR). Las intervenciones pre-tormenta requieren predecir el estado post-temporal de la costa. Por tanto, el principal objetivo de esta tesis es evaluar el riesgo costero episódico mediante un Sistema de Alarma Temprana Costero (CEWS), denominado LIM-COPAS, que predice las peligrosidades costeras más relevantes en dicho área.

LIM-COPAS consiste de cuatro módulos: (i) modelo meteorológico; (ii) código de generación/propagación del oleaje; (iii) modelo acoplado morfo-hidrodinámico y (iv) un módulo de riesgo vía modelos probabilísticos multivariantes y no-estacionarios. El comportamiento de estos módulos ha sido analizado mediante (i) una serie de eventos pasados y (ii) temporales sintéticos. Los eventos pasados han sido: Diciembre 2008 (D-08); Octubre 2015 (O-15); Noviembre 2015 (N-15); Enero 2016 (J-16); Febrero 2016 (F-16); Diciembre 2016 (D-16) y Enero 2017 (J-17).

En D-08, los errores en los parámetros espectrales de oleaje costero han sido casi el doble que en mar abierto. El error ha sido del 20 % en la hidrodinámica y del 50 % en la morfodinámica. La respuesta post-temporal ha sido reproducida aceptablemente, con Brier Skill Score cercanos a 0.4.

LIM-COPAS ha demostrado buena precisión con tormentas de alto período de retorno (i.e. $T_{r,waves} \geq 10\,yrs$, D-16 y J-17), pero menor concordancia fue encontrada para las tormentas moderadas (i.e. O-15 y F-16).

El módulo meteorológico estimó campos de viento que fueron sistemáticamente sobreestimados. El Sesgo Medio (MB) integrado fue de $-1{,}52 \pm 0{,}78\ m/s$. Tarragona (Coeficiente de Eficiencia, $COE = 0{,}27 \pm 0{,}13$) y Begur ($COE = 0{,}29 \pm 0{,}17$) tuvieron métricas por encima de la media ($COE = 0{,}24 \pm 0{,}14$); no obstante, peor ajuste se encontró en Mahón ($COE = 0{,}13 \pm 0{,}16$) y Dragonera.

Las métricas de oleaje fueron más precisas que las del viento. H_s COE integrada fue $0{,}52 \pm 0{,}12$ y T_{m02} COE fue $0{,}36 \pm 0{,}14$. En la costa central, H_s presentó buenas métricas: bajo MB ($-0{,}06 \pm 0{,}08\ m$) y alto COE ($0{,}58 \pm 0{,}11$). Las métricas en la costa norte fueron las más estables.

El módulo de riesgo ha sido implementado en 79 playas. La erosión se ha estimado como un coste acotado, mientras que la inundación como un coste con alta cota superior. Las playas disipativas tienden a exhibir mayores costes que las playas reflejantes bajo altos niveles del mar. Episodios con $T_{r,waves} \leq 10 yrs$, concomitantes a

mareas meteorológicas pueden conllevar costes significantes. Las pérdidas estimadas para N-15 ($2510 \cdot 10^3 euros$) no difieren en exceso de J-17 ($3200 \cdot 10^3$ euros).

Dos tipos de MAR han sido testeadas numéricamente: (i) dunas y (ii) diques exentos constituídos por geotextiles llenos de arena. Los beneficios de mantener estables los volúmenes de arena superan la reducción de los costes por inundación. En términos generales, los diques exentos pueden ser una opción adecuada para playas de estado morfodinámico intermedio frente a oleaje de alto período de retorno y niveles del mar bajos a moderados. En playas disipativas, las dunas son la mejor opción, pero requieren un ancho mínimo de playa (cerca de $30\,m$) que garantice su vida útil.

La funcionalidad de las MAR puede mejorarse mediante acciones compatibles a largo-plazo (alimentaciones, bypass de arena, vegetación submergida, etc.). Un estado de playa saludable es esencial para la efectividad de las MAR. Una gestión más sostenible bajo clima presente y futuro puede ser alcanzada mediante (i) CEWS como herramienta de predicción a corto plazo; (ii) MAR que mitiguen los impactos de los temporales y (iii) intervenciones a largo-plazo que mejoren la salud de la costa.

Palabras clave: riesgo costero, impacto de temporales, gestión del litoral, sistema de alarma temprana costero, WRF, SWAN, XBEACH, cópula no-estacionaria

Acknowledgements

The support of **Organismo Público Puertos del Estado (Spain)** has been crucial to made this dissertation possible. Without their willingness to kindly share their observational network (REDCOS, REDEXT and REDMAR) joint with their model outputs, this dissertation would not have been possible. In the same regard, I would like to acknowledge the **Institut Cartogràfic i Geològic de Catalunya** (**ICGC**), **XIOM** network, **IFREMER** (altimeter data), European Centre for Medium-Range Weather Forecasts (**ECMWF**) and the **Copernicus Marine Environment Monitoring Service**.

I would also like to show my gratitude towards the **WRF**, **SWAN**, **XBEACH** and **The R Project** communities. Without their openness to share their codes as open-source, it would have been impossible to realise this thesis.

The PhD candidate acknowledges the PhD scholarship from the Government of Catalonia *(DGR-FI-AGAUR-14)*. He also duly acknowledges the received funding from the DG-ECHO iCOAST project *(ECHO/SUB/2013/661009)*; the European Union's H2020 project *(H2020-EO-2016-730030-CEASELESS)*; the European Union's FP7 project RISES-AM *(FP7-ENV-603396)* and the Spanish national projects COBALTO *(CTM2017-88036-R)* and PLAN-WAVE *(CTM2013-45141-R)*.

I would like to show my gratitude towards my dissertation committee, and the international external reviewers who have enriched this work.

Manuel García León

Laboratori d'Enginyeria Marítima (LIM/UPC)

Universitat Politècnica de Catalunya - Campus Nord

D-1 Building, Office 103C

Barcelona, 13th May of 2018

These lines conclude: (i) a good challenge, (ii) intense hard-working years and (iii) a part of my incomplete path towards maturity. In these tasks, I have not been alone. In these lines, I would like to express my most sincere gratitude to all the people that directly/indirectly have contributed in this quest.

First and foremost, it is a honour to acknowledge the outstanding work made by my supervisors: **Dr. Vicenç Gràcia** and **Prof. Agustín Sánchez-Arcilla**.

Thank you very much, Vicenç. I have been working closely with you for almost eight years. And it has been a pleasure. Despite that the external framework have not been favourable at all times; you have done beyond your best for setting up the close team that we are. We have endured together rejection, but we have also enjoyed acceptance.

Thank you very much, Agustín. In previous dissertations, almost anything possible has been said about you: a ceaseless idea generator, a calm and wise man. I can only validate such statements. Your advice and involvement have been essential throughout these years. You have known what to do in really hard moments.

I have had a strong influence from my seniors at Laboratori d'Enginyeria Marítima. Thank you, Mr. Joaquim Sospedra, Dr. Xavier Gironella, Dr. Manuel Espino, Prof. Joan Pau Sierra, Dr. César Mösso, Dr. Marc Mestres, Prof. José Jiménez and Dr. Daniel González. It has been a pleasure to learn from you.

Thank you very much, as well, to our wonderful administrative staff: Ms. Genoveva Comas, Ms. Alba Serra, Ms. Marisol Esplandiu, Ms. Emilia Baños and Ms. Carme García. And last, but not least important, to my colleagues, be it present or former LIM/CIIRC staff: Dr. Anna Mujal, Dr. Corrado Altomare, Dr. Manel Grifoll, Dr. Pablo Cerralbo, Dr. Elena Pallarès, Mr. Joan Puigdefabregas, Mr. Jordi Cateura, Dr. Jaime López, Mr. Jesús Gómez, Mr. Óscar Galego, Mr. Ricardo Torres, Dr. Herminia Valdemoro, Ms. Laura Ràfols, Dr. Andrea Marzeddu and Dr. Iván Cáceres.

The Civil Engineering School at Barcelona has had a huge impact on my personality. I sincerely thank the professors and colleagues that have taught me so much in these 13 years. But, surely, apart from the LIM/UPC, the Group of Probability and Statistics (COSDA-UPC) deserves special attention. They have really helped me to structure my mind and to start asking the appropriate questions. Additionally, their unquestionable human value is even more appreciated. Thank you so much to Dr. Maribel Ortego, Prof. Eusebi Jarauta, Dr. Raimon Tolosana and Prof. J.J. Egozcue. Special thanks, as well, to Prof. J.M. Redondo who managed to boost my interest in Physical Oceanography at my early university years.

Alongside with the dissertation and the projects, teaching has been another opportunity that I sincerely appreciate to my group. Thank you very much, students from ETSECCPB and from University of Barcelona (BsC in Marine Sciences). I hope that I have taught you something useful. But, probably, you have taught me more than I did. Special thanks to Mr. Agustín Sánchez-Arcilla Jr., Mr. Albert Grases, Mr. David Teruel and Mr. Víctor Martínez. I wish all of you success and a healthy happy life.

From July to October 2016, Jue and me had the chance to visit the international research centre GeoEcoMar (Romania). Fruitful collaboration emerged from those three months. I would like to thank Dr. Adrian Stanica for kindly hosting us in your institution. We felt like at home. Much of this success is due to Dr. Irina Dinu, who did an outstanding work as a host. Additionally, their expertise helped us to clarify vital points in our (Jue and me) research. I deeply appreciate the time and the energy devoted to make such a wonderful visit. Thank you very much.

Special thanks to the ICGC team (Dr. Marta González, Mr. Jordi Pinyol and Mr. Pere Oller). I am proud of the work that the we did together in the iCoast project and in the coastal hazard mapping project. It has been a truly pleasure to collaborate with you.

As exposed in the previous Subsection, this thesis has received funding from the iCoast, RISES-AM- and CEASELESS EU projects. It has been an immense pleasure to collaborate with all of the people and institutions involved in these projects. I have learnt so much from you. Thank you very much to Dr. Rodolfo Bolaños, Dr. Jeremy Gault, Prof. Robert Devoy, Prof. Piero Lionello, Dr. Judith Wolf, Dr. Svetlana Jevrejeva, Dr. Elena Cristofori, Dr. Alessandro Demarchi, Dr. Cathal O'Mahony, Prof. Jens Kappenberg, Dr. Carles Ibáñez, Dr. Nuno Caiola, Dr. Paolo Scussolini, Dr. Phillip Ward, Prof. Robert Nicholls, Dr. Sally Brown, Dr. Tom Bucx, Dr. Joost Stornkhorst, Dr. Jan Mulder, Prof. Luigi Cavaleri, Dr. Joanna Staneva, Dr. Jean Bidlot, Dr. Xiaoli Guo Larsén, Prof. John W. Day, and so many more. Apologies if I forgot someone, please do not feel excluded.

In a more personal background, I want to thank Mr. Mao Yanxin for his sincere friendship. At the end, as we promised, we will finish our dissertations (almost) at the same time. I apologize for my delay. I want also to acknowledge Ramón and Isabel who patiently taught me how to accept my inner nature. Thank you.

I am indebted to Santi Zuloaga and his life partner, Bea. Thank you for your sincere friendship and for mentor me to become a Civil Engineer. Joint with my family, you are one of the main contributors that I have reached this goal. You taught me how to be a good engineer and a better man. Thank you.

Thank you very much, García Lin family (mother, father, Roser, Jiji, grandparents, ancestors and family-in-law). Deeply special thanks to my parents, Rosario and Manuel. I am lucky to have the best parents that a child could wish. I just hope that someday I will be as good father as you are. Thank you, Roser. I think that herein is a good place to say that I am proud of being your brother. Same goes for you, Jiji. I am also grateful to my family-in-law for raising up such two wonderful girls. I wish all of you a happy life.

Finally, I am deeply grateful to Dr. Jue Lin Ye. We met really young. We have grown up together. We have shared hopes and pain. I know that things have not been easy; but we have endured them together. We have become a family. I am so proud of being your husband.

All of you made possible this humble contribution.

1. Introduction

Action of sea storms at the Catalan coast poses a present complex challenge for the **territory management**. In the **1994-2008** period were identified 297 storms, in which 147 were weak, 82 moderate, 59 significant, 8 severe and 1 extreme (November 2001) (Mendoza et al., 2011). This last storm, lead to one casualty and economic losses up to 13 millions of euros. Unfortunately, in the last 20 years, extreme storms have been responsible for at least 50 casualties in the NW Spanish Mediterranean coast.

The coastline has an estimate length of **700 km**, in which **192 km** suffers an erosive trend and/or flooding (enclosing around **123 km^2** in urban and industrial areas, plus **217 km^2** as high ecological value), affecting the residential area of around 1 million people (Guillén, 2008). Catalonia is one of the regions with more **tourism** in Europe, concentrating the 85% at the littoral zone. The losses in the tourist sector due to coastal erosion are proportional to the importance of the sector in the economy of the region (around 11% of the GDP, Duro and Rodríguez (2011)). However, this phenomena is repeated along the whole **European Union**: there are more than **15.000 km** of shoreline affected by erosion, leading to area losses of around 15 $km^2/year$ (EUROSION, 2004). These trends could be exacerbated progressively due to **climate change consequences,** specially due to Sea Level Rise (Abadie et al., 2017; Hinkel et al., 2014; Sierra and Casas-Prat, 2014).

Reactive interventions (i.e. post-storm action) have been the norm in the Spanish Coastal Management strategy. Only in the Catalan region, more than 50 million euros have been invested for the development and maintenance of coastal protection works and promenades (CEDEX, 2013). More than 10 millions m^3 of sand has been spent in beach nourishment alone (Gràcia et al., 2013c). Moreover, some of these solutions demand hard engineering (i.e. revetments, groins, breakwaters) that imposes a steady constraint against natural fluxes. At some cases, these blockages can even exacerbate coastal hazards, such as erosion.

However, these kind of interventions are not feasible in the current slow-growth paradigm. Then, this **dissertation proposes a pro-active management** (i.e. pre-storm action), in order to promote cost-effective measures, that are more eco-compatible with the existing coastal uses. This compatibility would avoid to reach tipping points and regime shifts, that once surpassed, can be cost-prohibitive to revert back.

Pre-storm intervention requires to foresee the future post-storm coastal state. Hence, **this dissertation proposes** a Coastal Early Warning Systems, termed LIM-COPAS, **as a forecast system for assessing episodic coastal risk**. CEWS particularly

aims to short-range forecasts (time scale of 3-6 days) at local scales (littoral cell scale), with high resolution models (Baart et al., 2016, 2009).

A higher sustainable management can be reached with the joint combination of (i) CEWS as a short-term forecasting tool; (ii) pro-active interventions that mitigate storm impacts and (iii) long-term interventions that improves the beach health (Morris et al., 2018). My proposed justification for this statement is embodied in this dissertation.

These first Sections addresses the **Motivation** for this work (Sec. 1.1), the **Objectives** and steps (Sec. 1.2) and the **Outline** of this document (Sec. 1.3).

1.1. Motivation

This motivation has a double aim: (i) to introduce the different topics that will be addressed in this dissertation; (ii) to establish a common framework that links these concepts.

The coastal zone produces an important part of the global GDP (Turner et al., 1996; Nordhaus, 2006). Hence, its optimum functionality and management (protection, natural, socio-economic) is a catalyst for societal growth. According to Martínez et al. (2007), around 41% of the world population (2.5 billion people in 2003) lives within 100 km of the coastline. Projections for coastal population show more increase than at the other areas, specially at Africa and Asia (Merkens et al., 2016; Neumann et al., 2015).

Several activities need to co-exist in a limited area. The uncertainties are remarkable, not only in the physical processes but also in the socio-economic. Urban growth at some areas has grown exponentially in a matter of decades. Such a complex puzzle is difficult to be tackled.

Coastal hazards can be found at different spatial and temporal scales, but the most important are erosion, flooding and accumulation. The dynamics of each hazard is different: flooding is a transient phenomena, accumulation and erosion are associated to sediment dynamics that span different scales: from hours-days (e.g. storm scale) to centuries (e.g. long-term regression due to sea level rise). However, these hazards have something in common: they are dynamic and they enter with conflict with the compatibility of uses at the coastal fringe.

The Catalan Coast is a particular fragile environment in these respects, especially non-cohesive areas (beaches). During the second half of the 20th century, urban growth led to the unplanned construction of several infrastructures, boosted by the prospects of economic growth due to tourism. Hard structures, such as groins, revetments, detached breakwaters and beach nourishment were the answers to that coastal occupation. The rigidisation of the coastline enhanced the problems and led to the current landscape: storm-induced damages at the Catalan coast increased at an approximate rate of 40% per decade (Jiménez et al., 2012). But such vulnerability does not rise due to a change of the drivers: SLR is around several mm/year

(Jevrejeva et al., 2014), wave-storm components and storminess have not changed significantly (Lin-Ye et al., 2017) and storm-surges remain similar (Conte and Lionello, 2013).

This vulnerability raising is due to the alarming urbanisation rate. More than 50 million euros have been invested in Catalonia for the development and maintenance of coastal protection works and promenades (CEDEX, 2013), in which more than 10 millions m^3 has been spent in beach nourishment alone (Gràcia et al., 2013c).

The common solution for storm impacts has been a **reactive strategy** (i.e. post-storm intervention). In the present economic situation (slow growth paradigm), this kind of investments are not feasible. These coastal interventions are not sustainable in the next decades. A way to diminish the losses is to forecast the future state of the coast prior to an episodic hazard, and then, to **foster cost-effective actions** that compatibilises the coastal uses.

However, episodic hazards are difficult to be forecasted. Not only because the drivers are complex to be forecasted, but also because the spatial scale of the coastal hazards is usually local (of the order of tenths of meters). Such local features are not known with the required detail. The physical processes are complex to be modelled (overtopping, undertow currents, wave breaking) and local in nature.

Coastal Early Warning Systems (CEWS) **aim to forecast a future coastal hazard for bounding risk under certain extreme forcings** (i.e. storms). They particularly aim to short-range forecasts (time scale of 3-6 days) at local scales (littoral cell scale), with high resolution models (Baart et al., 2009, 2016). To know the morphodynamic state of a coastal tract with a forecast horizon of 72 hours provides a valuable time window for the decision making. With such time buffer, **preventive and mitigation measures** against storm impact can be deployed.

The main advantages of CEWS are:

- They provide reliable information that foster proactive interventions, that may be substantially more cost-effective than reactive interventions. Once made the forecast, the responsible tries to adapt its local constraints in a way that reduces/mitigates the storm impact. Most interventions aims to reduce the fluxes.
- CEWS are a layer of applicability of the existing oceanographic operational systems. They may be built on existing oceanographic forecasting services such as NOAA, CMEMS, national circulation (IBI-MFC, Sotillo et al. (2015)) and waves forecasting (Gómez and Carretero, 2005), etc.
- Coastal forecasting may have further (multiple uses) applicabilities beyond coastal hazards (erosion, flooding). They can provide an estimate of the coastal state, that can serve for improving the initial conditions (bathymetry and coastline position) for other oceanographic applications, such as harbour management, oil-spills and water quality preservation.

As a mild drawback, however, it can be said:

- An important body of knowledge in the particular area is needed. Hence,

long-term monitoring is highly recommendable.

- The models need to be updated and validated with the new constraints. Hence, the development of a CEWS is cyclical and requires a maintenance to ensure the consistency of the conditions (initial and boundary conditions).

Extreme events are rare in magnitude and timing. Meteo-oceanographic marine events can be driven by a intense climate anomaly, or they can be driven by a combination of regional and local factor that unleashes instabilities in the atmosphere. Additionally, Climate change may lead to changes in extremes (Trenberth and Shepherd, 2015; Trenberth, 2007).

Understanding the physical processes and the availability of models that allows to test several what-if scenarios is paramount for avoiding unexpected responses (Lin and Emanuel, 2016). Process-based models that do not overparametrise processes and coupling are essential. These models, though, generate a vast quantity of information that requires to be processed through methodologies which do not oversimplify the existing spatiotemporal patterns. Proper validation and error metrics (Hernández et al., 2015) are essential to avoid overparametrization or reaching to simplistic conclusions that can provide a model that can be unuseful or having low skill in the near future.

It has to be considered that some models that are not useful today, maybe they will be in the future, because they consider regime shiftings in some physical processes that we have overparametrized in the present version of our forecasting systems.

Despite that short-term forecasting has a limited forecast horizon (3 to 5 days), this time buffer is invaluable for triggering mitigation actions. The challenge is complex, because forecasting involves several spatial and temporal scales. Then, depending on the variable, the degree of accuracy varies significantly: for instance, wave forecasting shows better skill than circulation. The consistency and coherence at the different scales of the forecast is fundamental. For instance, Lin-Ye et al. (2017) found relationship of large-scale climate indices (such as NAO or the Scandinavian Pattern) with wave-storm components, such as the significant wave height and the peak period.

The lack of observations at the marine side further harnesses proper forecasting. It is needed, as well, to monitor several components at once, in order to stablish interactions and dependence structures among the variables. From a forecasting point of view, sudden regime shifting of all meteo-oceanographic variables is rare. For instance, some early symptoms such as anomalies in sea level pressure, local rainfall and moisture can be good proxy indicators that a marine extreme event would happen (see Ch. 5). Threshold levels and the boundaries of regime shifting needs to be assessed with different physical magnitudes and at several points in the space.

Uncertainty reduction is the main aim of forecasting. This extra time for planning, though, requires to add more models and observations into the complex forecasting chain. In the case of individual models, coupling is not perfect and not all information can be embedded into the higher resolution one. Information exchange

between models, via one-way or two-way coupling is not straightforward. Hypothesis among models may differ and inconsistencies may appear. As will be highlighted in Ch. 4, perturbations in the higher hierarchical levels (such as the meteorological model) add an error than tends to be additive with the errors of the models.

This uncertainty can be tackled with several ways: through ensembles, with data assimilation, via improving the physical processes,etc. Deterministic forecasting with process-based models provides high resolution information, but usually, the computational resources are limited to a single node of a forecast. In this dissertation, uncertainty has been tried to be partially bounded with a probabilistic risk module at the end of the forecasting system (risk module, see Ch. 6). Despite that the physics are overly simplified, compared with the proposed morphodynamic module, it provides a quick-scan forecast of the coastal state, with low computational demands. Because the models depend on non-stationary multivariate probability distribution functions, a first approximation of the risk uncertainty can be estimated.

This initiative benefit from process-based models, then reinforcing the need for the whole forecasting chain. The risk module requires wave and sea level information for building a multivariate probability distribution function, unique for each model. The order of magnitude of this risk module coincides with the investments made for coastal protection enhancement. However, the veracity of the risk forecast is tightly dependent on the overall quality of the whole forecasting system.

The probabilities also provide some relief for the forecaster. Deterministic forecasting tends to be evaluated as a **shadeless prognosis**; however probabilistic forecasting incorporates the concept of bounding a range of plausible values. Additionally, probability and risk are the lingua franca of investors. Adapting the outputs from physical forecasts into the technicalities of investment management provides a **seamless product** that will be more applicable to end-users.

In a **driven-by-complexity era**, featured by **slow-growth** and **natural resources scarcity**, proper choice and optimization will be key issues on prosperity and sustainability. Operational forecasting provides valuable time for thinking, analysing, readapting existing plans and addressing the current challenges of our society. Going one step aside (i.e. pro-active action) provides time for rational decision making. An example of direct applicability of the CEWS forecasts are Quick Defence Measures (QDM, Ch. 7). These interventions aims to enhance the coastal protection function against episodic hazards via low-cost, local and timely interventions. Transient dunes, reshaping of the emerged beach profile, sand bags as defences against floodings, etc. constitute an alternative against traditional hard coastal structures. Note that the word "timely" implies complex planning and detailed forecasts. In this regard, **climate change** will imply new scenarios in which extreme events can have more incidence, specially due to Sea Level Rise (Sánchez-Arcilla et al., 2016b).

Proactive Interventions can help to dampen the consequences of extreme events. High sustainability pathways (green curve in Fig. 1.1) not only aim to change the trend (note the increment of resistance from the green to the red function), but also needs to address specific extreme events. Long-term oriented interventions cannot

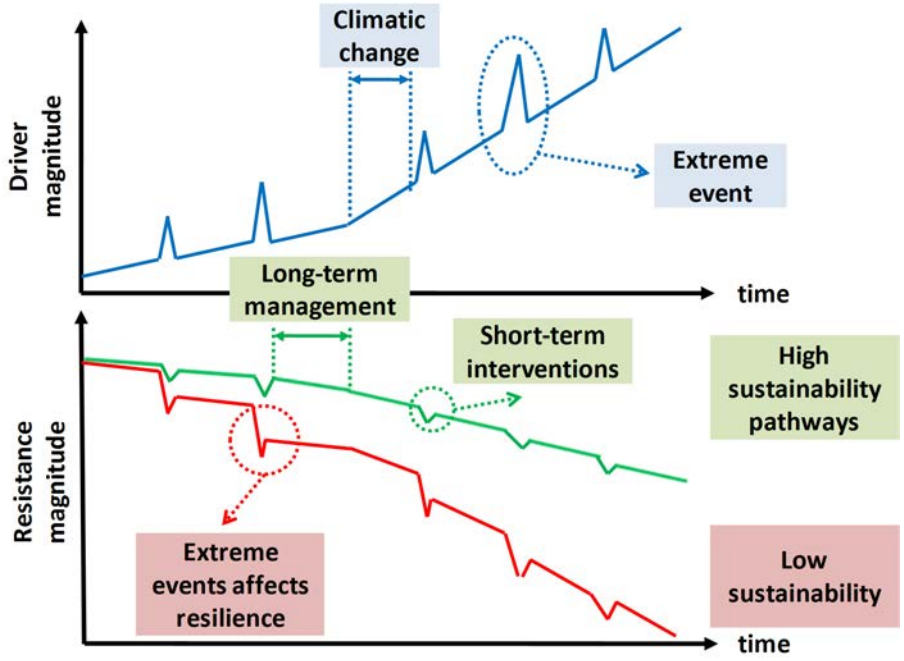

Figure 1.1.: Schematic layout of the evolution of **drivers** (**blue**) and resistance magnitude at the coastal zone with **high sustainability** (**green**) and **low sustainability** pathways (**red**).

cope with certain extreme events thresholds, because they will require restrictive conditions that would be economical infeasible. Hence, the combination of short-term actions (such as QDM), joint with long-term strategies (such as Nature Based Solutions, as submerged biota) can provide an affordable pathway.

In short, Coastal Early Warning Systems, such as the proposed LIM-COPAS, will rise adaptation and mitigation capabilities against present and future episodic coastal hazards.

1.2. Objectives

The aim of this thesis is to **assess present coastal risk** at the **Catalan Coast** through **a Coastal Early Warning System (CEWS), LIM-COPAS (LIM-COastal Processes Assessment System)**, that forecasts the more relevant episodic coastal hazards at the area. With this aim, this dissertation makes strong emphasis on the **simulation and analysis of the coastal response in terms of flooding/erosion against storm impacts** (i.e. the time interval in which there exists a higher morphodynamic variability).

The main objective of this thesis can be classified into the following three areas: *(i) Conceptualization of the problem; (ii) Architecture of the system (design of the solution); (iii) Performance of the system with hindcasted scenarios.*

The following steps has been proposed to achieve the main goal:

1. **Conceptualization of the problem**
   a) To identify the main coastal hazards at a set of pilot sites for implementing the system.
2. **Architecture of the system. Design of the solution.**
   a) To propose the modelling chain of a coastal forecast system that spans from the mesoscale (meteorological module) to the local scale (beach).
   b) To set-up the different modules: at individual scale and their couplings.
   c) To conceptualize and develop a risk module that would translate physical forecasts (drivers and coastal hazards) into risk.
   d) To propose a set of metrics for estimating the skill capabilities (models vs observations).
   e) To design a set of proactive interventions for diminishing coastal risks (such as transient dunes and detached breakwaters, see Ch. 7) that can benefit from coastal forecasting.
   f) To select a set of scenarios (hindcast events (Ch. 4 - 6), synthetic storms in Ch. 6 - 7) that would provide a good indication of the overall performance of the system.
3. **Performance of the system with hindcasted events and synthetic scenarios (Ch. 4 - 7)**
   a) To test the different modules with the hindcasted events and storm scenarios proposed in Objective 2.f.
   b) To compare hindcast storms with in-situ and remote observations.
   c) To propose and test different configurations of the modelling chain.
   d) To identify the sensibility to the inputs.
   e) To identify sources of uncertainty in the modelling chain.
   f) To quantify the limits of the forecasting with the proposed tools.
   g) To determine the feasibility of proactive interventions for diminishing coastal risk (see Ch. 7).

Note that the Chapters may have different objectives and/or can be overlapped. For instance, the evaluation of the wave module has been done both in Ch. 4 and 5. In Ch. 4 was presented a first iteration of the system (Sánchez-Arcilla et al., 2014). A posteriori of these results, it was decided try to generate better wind forcings and to use high resolution circulation fields from IBI-MFC.

1.3. Outline of the thesis

The objectives and macro-topics of the dissertation can be matched via a set of boxes (see Fig. 1.2). Chapters 2 and 3 embed the general structure of the dissertation. Chapters 4 to 7 address the specific modules of the Coastal Forecasting System.

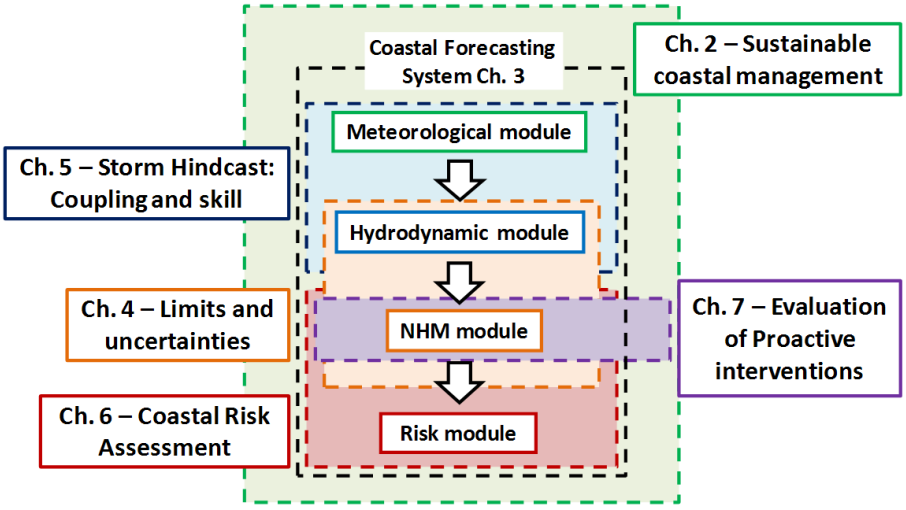

Figure 1.2.: Chapter structure of this dissertation and its overlapping with the different modules of the proposed Coastal Forecasting System. **Legend:** NHM (Morphodynamic module).

Chapter 1 introduces the existing problem that will be addressed in this dissertation (episodic coastal hazards) and the proposed solution. The objectives and steps of the thesis are listed, joint with an outline of this dissertation.

Chapter 2 bounds episodic coastal hazards to the specific study area (the Catalan Coast) and relates it with a sustainable coastal management pathways. Coastal hazards are described, joint with the present and future landscape of the study area. Finally, Coastal Early Warning Systems are presented, describing some recent initiatives such as the MICORE project.

Chapter 3 presents the theoretical background of LIM-COPAS. The general forecasting strategy, the hypothesis beneath each specific module and the error metrics are summarised.

Chapter 4 addresses the limits and uncertainties that have the hydrodynamic and the morphodynamic model. The morphodynamic module will be calibrated with post-storm LIDAR information.

Chapter 5 shows the performance of the meteorological and hydrodynamic module under six recent storm hindcasts.

In **Chapter 6**, a risk module based on multivariate probability distribution functions is proposed. The module will be developed and validated with the same hindcast storms from Ch. 5.

Chapter 7 highlights an applicability for the forecasts outputs via proactive actions, termed Quick Defence Measures (QDM). The efficiency of these interventions are numerically assessed at two beaches (Sant Sebastià and Gavà, both at Barcelona).

Summary and Conclusions summarises and concludes this dissertation.

Appendix A shows detailed maps of the Catalan Coast (Northern and Central

parts).

Appendix B presents the morphological features of the beaches that will be considered in this dissertation. It will also include the main statistics from that summarise the calibration dataset for the risk module (Ch. 6).

Appendix C contains the time series (in-situ observations vs. model) for the same hindcast storms in Ch. 5.

Finally, **Appendix D** displays the wave boundary conditions for the risk module (Ch. 6), that will be obtained from the Ch. 5.

2. Sustainable coastal management with Forecast Systems

2.1. Introduction

Note: This Chapter addresses concepts that appeared in (Sánchez-Arcilla et al., 2016a).

The aim of this thesis is to assess present episodic coastal risk at the Coastal Coast through a forecasting system. But the coastal zone problems are not just limited to episodic erosion and flooding. This chapter aims to provide an **overall vision** of the **present** and **future landscape** of the NW Mediterranean coast. Prior to entering into the details and results of the CEWS, it has been considered to bound the big-picture of the coastal zone management with this introductory chapter.

This Chapter is structured as follows: Sec. 2.2 defines the Risk and Hazard terminology that will be addressed throughout the dissertation. Sec. 2.3 presents the usual coastal hazards at the different spatio-temporal scales. Sec. 2.4 describes the Catalan coast in terms of its meteo-oceanographic drivers and morphodynamical features. In the same section can also be found the following future projections: physical (sea level rise and waves) and population. Examples of reactive and proactive management strategies are highlighted. This proactive management requires Coastal Early Warning Systems (CEWS), that are defined in Sec. 2.5. Finally, it is proposed, in broad terms, a sustainable roadmap with CEWS (Sec. 2.6).

2.2. Risk terminology

There exists a wide range of definitions for the terms hazard, vulnerability and risk. This dissertation will reference the ones derived from the European project FLOODSite (2005):

- **Hazard:** A physical event, phenomenon or human activity with the **potential capacity of damaging**. A hazard does not lead necessarily to damage.
- **Vulnerability:** System characteristics that describe its **potential to be damaged**, i.e. combination of the propensity of a system for experiencing damages (susceptibility) and its value.
- **Risk:** Function that depends on (i) the type and its probability of occurrence, (ii) the exposition degree of the receiver, (iii) the sensitivity of the receiver to

this damage (for example, it is not the same ocean waves impacting at a cliff rather than a sandy coast) and (iv) the value of the receiver (for any archetype). Hence, the process risk can be expressed as (Eq. 2.2.1):

$$Risk = Hazard\ Probability \times Consequence \tag{2.2.1}$$

The units in which the risk is measured, depends on how the probability and the consequences are evaluated. The probability can be expressed as an uncertainty measure of a phenomenon, or as a frequency (number of observations / number of cases). At both cases, the probability refers to a certain limited **time period**. For instance, the probability of exceedance in 1 year, during the useful life or as a function of the return period. Consequences are usually expressed as monetary terms when referred to infrastructure and belongings.

2.3. Coastal hazards

In this section will be defined the main coastal hazards (*Erosion* (Sec. 2.3.1), *Accumulation* (Sec. 2.3.2) and *Flooding* (Sec. 2.3.3)) with specific examples from the Study Area.

2.3.1. Erosion

The most frequent hazard at the Catalan coast is **erosion** (Gràcia et al., 2013c; Jiménez et al., 2012). This process is defined as the **shoreline retreat**, exhibiting a **land loss** at the emerged part. This physical macroprocess can be classified into different temporal and spatial scales, each associated to a driver that unleash these negative beach volume gradient. Below will be described in a more specific manner the different subcategories, focusing on **storm events**, due to its relationship with the LIM-COPAS system.

2.3.1.1. Episodic scale

Erosion on **episodic scale** is the result of the shoreline retreat due to the impact of an **extreme condition** or storm. A wave storm is the result from a combination of the wind regime with the atmospheric pressure that induces high sea waves. The morphodynamic response uses to be a shoreline retreat where the sediment is mobilised offshorewards, thus creating a sandbar that displaces offshoreward the wave breaking zone[1]. The quantification of the event can be expressed as the magnitude of the associated retreat to a determined storm (i.e. in m/T_r terms, where T_r is the return period associated to the evaluated storm).

[1]If it is considered that the relationship between dissipation area and energy remains constant.

Hazard	Sub-Category	Parameter	Graphic	Spatial Scale		Magnitude
Erosion	Episodic	Coastal retreat	Symbol	Beach	Homogeneous Tract	m/(storm T_r)
	Medium-term			Beach	Homogeneous Tract	m/year
	(*) Rotation					Qualitative High-Low
	Long-term			Comarcal	Supra Comarcal	m / IPCC projection
	(*) Breaching			Singular case of the Trabucador Bar		

Table 2.1.: List of the main features in **Erosion** induced hazards. **Legend:** *Sub-Category* corresponds to the problem classification due to erosion. *Parameter* determines whether such a threat exists. *Graphic* as an option for representing such hazard in a CEWS. *Spatial scale* as the specific spatial subpartition scale for each category and *magnitude* as the quantifying unit for the threat. The asterisk (*) means that these sub-categories are special cases of episodic erosion.

The magnitude of this variable can be estimated through process-based models, such as SBEACH (Larson et al., 1990), DELFT-3D (Lesser et al., 2004) or XBEACH (Roelvink et al., 2009). The inconvenience of this approximation is the fact that it is not an inferred measurement, thus the uncertainty may vary in function of the selected methodology. Another possibility for determining the hazard magnitude is by **historical records** of the shoreline position (Jiménez et al., 2012). For this aim, it is required to identify anomalies in the historical retreat database and associate them with a storm within an specific time interval. The lack of long enough time series is the main constraint for the use of such alternative methodology. **Rotation** and **breaching** are specific cases of erosion.

2.3.1.1.1. Rotation Rotation is a special case of beach erosion that usually happens at episodic scale, but also may happen in mid-term. Beach rotation is the result of **wave direction regime shift**, not necessarily required as extreme waves, that incides at a beach and produces sediment transport towards a lateral boundary of the littoral cell. It is a process that may exhibit at pocket beaches or coastal tracts (note that the dimension of the zones used to be around an order of magnitude near hundreds of meters) located between groins with high retention capacity. The result of this process is the **transient loss of emerged land area** in a determined beach tract by sediment accumulation in the opposed side. This situation can be compensated with the posterior wave incidence that induces transport in the opposite side.

2.3.1.1.2. Breaching Breaching of a barrier beach happens under inundation regime within Sallenger (2000) scale. The Trabucador Bar is the only case at the Catalan coastal fringe. This phenomenon is characterized by the action of wave storms joint with an extreme sea level. These drivers generate breaches and small channels along the barrier beach, thus connecting the open sea with the inner bay. Gràcia et al. (2013b) analysed the breaching of the Trabucador Bar with the same solver than has been implemented in the morphodynamic module of this dissertation (see Ch. 3).

2.3.1.2. Mid-term erosion

Mid-term erosion, at a **decadal scale**, is the result of the sediment budget within a cell or tract (i.e. the inflow-outflow rates of sediment that enters through the inshore, offshore and lateral boundaries).

In mid-term, the offshore side that is determined by the active depth (i.e. concept that expresses the depth until the bed changes) is not important. Therefore, in this boundary, there is no net sediment budget at this time scale. At the inshore side, the actual configuration of the Catalan coast, with the existence of sea promenades, highways, urban areas, etc. induces that in some tracts there is not considered a significant sediment exchange. In addition, the strong regulation and hardening of rivers and streams, has lead to a decrease of nearshore sediment load. Consequently, the uses of the sediment budget are affected by the shoreline variations. The morphological effect of a negative balance (i.e. sediment volume loss at the tract) is the shoreline retreat.

2.3.1.3. Long-term erosion

In case the temporal scale is expanded to an order of **hundreds of years**, sea level rise associates a **shoreline retreat** (Bruun, 1962; Hinkel et al., 2013). The quantification is hard and complex, specially due to the lack of time series superior to 100 years and the uncertainty of the forcings. Therefore, this process is frequently evaluated through theoretical models in which the sediment transport and the morphological response are parametrized in function of the oscillations of the sea level and the sediment size. However, the level of uncertainty of such results is large, due to the difficulties in obtaining representative data and for the intrinsic simplicity that lies beneath these models, that can hardly be calibrated or validated.

Moreover, the sea level rise is relative to the continent. Consequently, it is strongly required to have subsidence levels (Ibáñez et al., 2010, 2014) along the coastal fringe, because the same sea level rise can imply different effects in function of the local subsidence. Finally, mean sea level forecast is hardly complex (Jevrejeva et al., 2014; Grinsted et al., 2015), despite being accepted the projections made by the Intergovernmental Panel for Climate Change (IPCC), being continuously updated, finding the AR5 scenarios (see Sec.2.4.3).

2.3.2. Accumulation

Accumulation can be defined as the **shoreline advance**, as a consequence of sediment surplus within a littoral area. Though this phenomenon can be considered as a neutral process (or even a positive one), it can also threaten the development of socio-economic and natural activities. For instance, the solid material inside the harbour mouth can hamper its functionality; the submerged land-loss in bays or river mouth can unleash authoctonous biodiversity losses; or the sand accumulation in the backshore can obstruct sewer outfalls during urban floods.

At the specific case of the Catalan Coast, a relevant fraction of the accumulation zones comes from changes in the littoral drift (CIIRC, 2010), that implies a dominant **southward longshore sediment transport**. The magnitude of this transport comes from the intensity of the marine drivers (waves and sea level) and the morphological features (coastline orientation, sediment size and availability of material). The disruption of the littoral drift due to anthropogenic obstacles (i.e. harbours and groins) has led to significant upstream sand accumulations and downstream erosive gradients by the ceaseless decrease of sand budget (Tab. 2.1).

Harbours block solid discharge and such blocking leads to direct problems. When a breakwater is filled (i.e. the maximum retention is achieved), the sand is advected due to wave-induced currents (i.e. following the littoral drift), being accumulated at the offshore side of the breakwater. Once the sand reaches the harbour mouth, **wave diffraction** at the breakwater head shifts the direction of the sand transport, and waves tend to enter inside the marina. In this zone, the hydrodynamic action is lower (due to the infrastructure sheltering) and the sediment is distributed at the bottom. This phenomenon, named **siltation**, diminished the dimensions (width and water depth) of the main access channel to the harbour, hence requiring periodical dredging.

Siltation is also common in sand spits as the Fangar and Alfacs bay in the Ebro Delta (Guillén, 1992). In this case, the evolution of sand spits from the joint action of diffraction and overtopping leads to a sand spit progradation by sand accumulation. These local accumulations can close the bay access.

The discontinuities produced by rivers and streams in the beach can also be siltated. An example of this behaviour is the Tordera river mouth (see Fig. A.2). This flash-flood regime river usually has its mouth closed during summer, due to the accumulated sand advected by the littoral drift. The potential risk, then, happens under flood regime; because in case that the river mouth is partially or fully siltated, then flooding can be exacerbated upstream.

Another possible threat is the **sand accumulation in the backshore**, combining the joint action of waves and sea level. It uses to be more frequent in **coarse sand** beaches because the natural slope is steeper, thus run-up is higher. The sand accumulation in the backshore is the result of wave overtopping on the beach and the generation of a difference between the magnitude of the up-rush transport and the return flow.

The **existence** of accumulation is usually more useful than its magnitude. Hence, it can be classified as an unlikely/likely probable event.

Hazard	Sub-Category	Parameter	Graphic	Spatial scale	Frequency
Accumulation	Harbour mouth Bays River Mouth Backshore	Existence	Symbol	Local	Likely / unlikely probable

Table 2.2.: List of the main features in **Accumulation** induced hazards. **Legend:** *Sub-Category* corresponds to the problem classification due to sand accumulation. *Parameter* determines whether such a threat exists. *Graphic* as an option for representing such hazard in a CEWS. *Spatial scale* as the specific spatial subpartition scale for each category and *frequency* as the category for the threat.

2.3.3. Flooding

Coastal flooding can be defined as the emerged area affected by a marine floodplain. Hence, flooding is characterized by the joint action of **run-up** and **overtopping** plus **extreme water levels**. Flooding is associated with an episodic scale that depends on the joint action of duration, wave height and mean sea level (Table 2.3).

This hazard is relatively frequent at the Catalan coast due to its own intrinsic features (squeezed backshore, with a lack of space for damping the floodplain) and the storm impact. Chapters 4 and 6 analyse different recent episodes, such as December 2008, that lead to important overtopping fluxes in Blanes, Tossa de Mar and Llançà.

Two approaches can be used for characterizing flooding: (i) to evaluate the **storm impact level** with **measurements** (*a posteriori analysis*, Jiménez et al. (2012)) or (ii) to **estimate** the **storm impact** through **numerical modelling** (with the clear advantage of achieving an *a priori* approximation of the response, Sánchez-Arcilla et al. (2013)). **Measurements on the storm impact level are scarce** or even non-recorded. Hence, it is recommended flooding assessment through the run-up evaluation, as to whether field data or numerical models that can reproduce the backshore physics (i.e. those ones with **dry/wet algorithms**).

Run-up can be estimated with semi-empiric equations, computational fast that simplifies the physical processes (Sancho-García et al., 2012; Stockdon et al., 2006). Overtopping can be assessed with two different strategies: (i) **to determine the frequency** (return periods of 10, 50 or 100 years) in which a coastal tract would be overtopped, or (ii) to **evaluate the existence of this hazard** and its characterization in time. Nevertheless, the evaluation of flooding through numerical

models provides a more detailed overview of the phenomena; then defining an affectation line at the beach. The latter approach would be addressed both in the Morphodynamic and the Risk module of this dissertation (see Ch. 4,6 and 7).

It must be remarked that **sea level rise** would lead to a gradient of backshore flooding. The same proposal of a delimitation line (see Tab. 2.3) for the different proposed scenarios by the IPCC-AR5 (Stocker et al., 2013), adapted for the Catalan coast (including the local subsidence) in a temporal horizon that spans the end of the 21st century (see Sec. 2.4.3).

Hazard	Sub-Category	Parameter	Graphic	Spatial scale	Frequency
Flooding	Episodic - waves	Elevation	Line	Local	$T_r = 10, 50, 100$
	Long-term MWL			Regional	2100 IPCC

Table 2.3.: List of the main features in **Flooding** induced hazards. **Legend:** *Sub-Category* corresponds to the problem classification due to flooding. *Parameter* determines whether such a threat exists. *Graphic* as an option for representing such hazard in a CEWS. *Spatial scale* as the specific spatial subpartition scale for each category and *frequency* as the hydrodynamic scenarios and timepoints for the threat assessment.

2.4. Study Area (The Catalan Coast)

Starting from a geographical vision, the Catalan coastal fringe (NW Mediterranean Sea) ranges from Portbou Cape (L'Alt Empordà) to the Sènia river mouth. The latter constitutes a natural frontier between the autonomous regions of Catalonia and Valencian Community (see Fig. 2.1). The overall coastal length differs among the different Urbanistic Management Plans, but it is usually adopted 700 km, following DPTOP (2005). 43% of the overall length are sandy beaches (250 km), in which more than the half can be considered as urbanised (i.e. presence of sea promenades, highways, buildings, etc.).

The coastal area represents **7%** of the overall **Catalan territory**, despite it concentrates almost **half of the total population** (IDESCAT, 2018). The averaged population density in the coastal fringe is about 510 $people/km^2$, whilst the same index in the autonomous region is 235 $people/km^2$. Main socio-economic activities at this area comprise commerce, industry, agriculture and residential developments, being tourism the dominant one (Sardà et al., 2005).

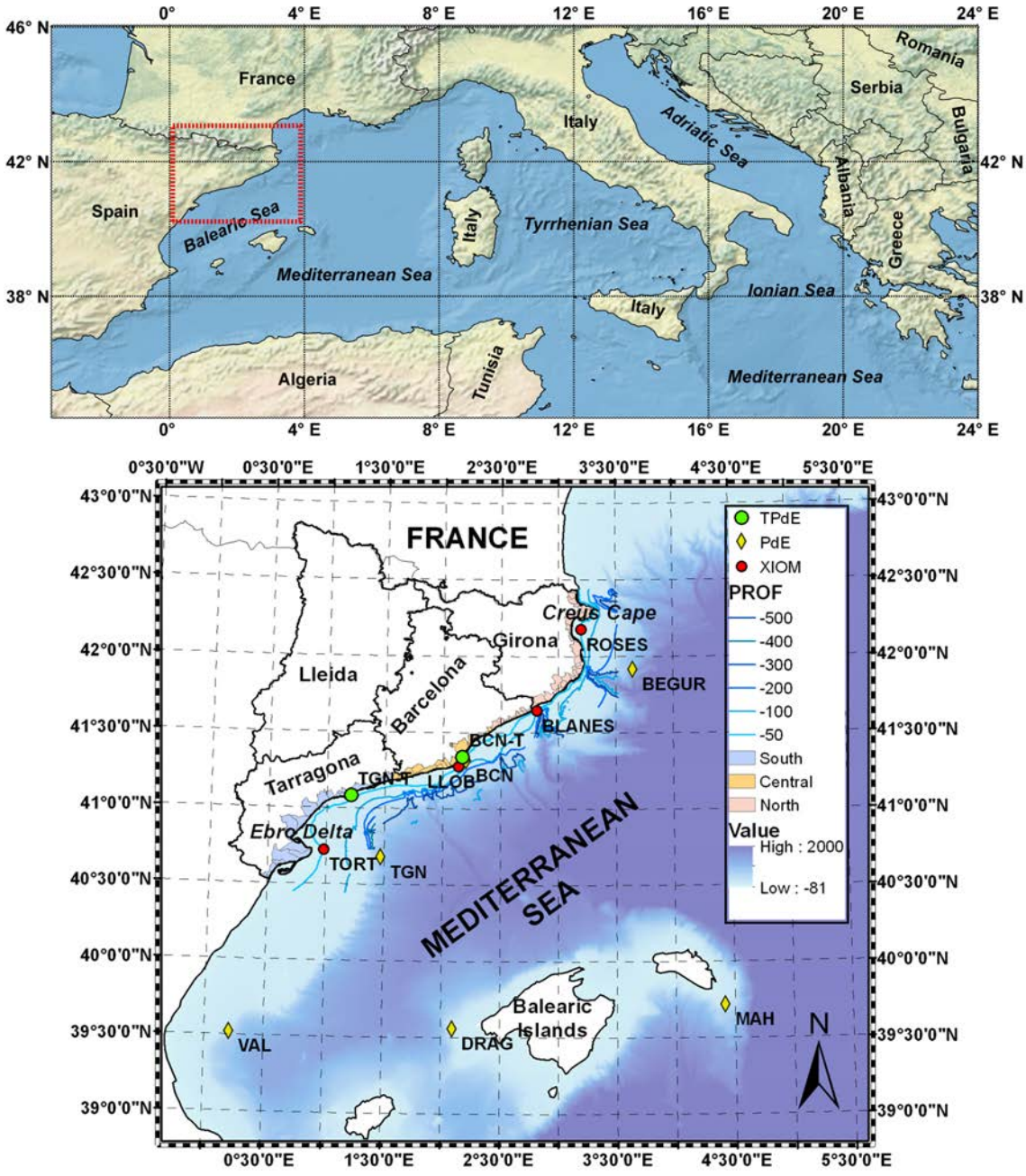

Figure 2.1.: Geographical and administrative situation of the Catalan Coast, located at the NW Mediterranean Sea. The contour areas show the bathymetry. Yellow diamonds denote the position of the buoys of the PdE network (see Sec. 3.2.2). In red dots, it can be found the XIOM dataset. In green dots, the tidal gauges at Barcelona and Tarragona harbour.

2.4.1. Hydrodynamic regime and coastal archetypes

The NW Mediterranean Sea is a **micro-tidal** and **fetch limited** environment. The astronomical tidal range is less than 0.4 m although during storms the associated surge can reach values near to 1 m (Fig. 2.2). The mean offshore significant wave height for the area is 0.7m with an associated wave period of 7 s. The directional distribution of waves at the Northern and Southern parts of the coast show a predominance of NW and N components, whereas at the central part the East and South directions are dominant.

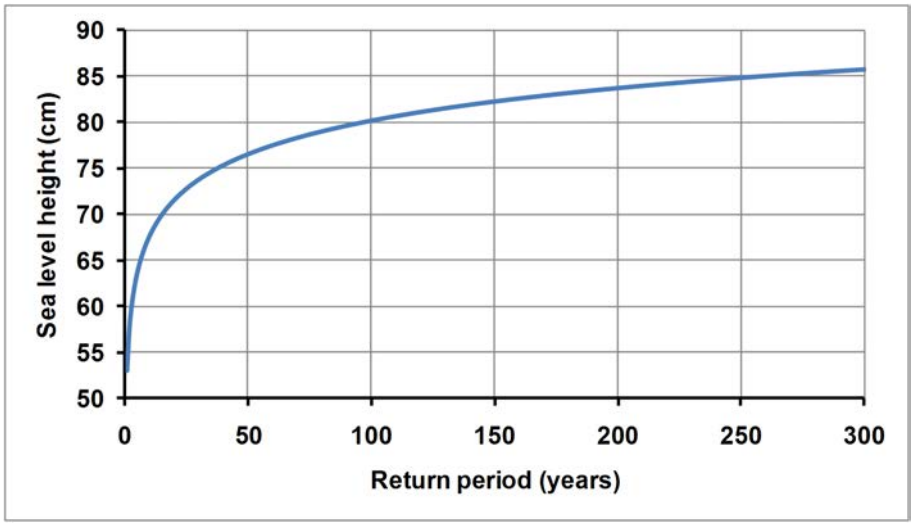

Figure 2.2.: Extreme sea level height (cm) versus return period (years) at the **tidal gauge** of the **Barcelona harbour**. The sea level is referenced to the IGN Datum.

However, wave heights more than 6 times the mean value can be reached during storm conditions, in a matter of few hours. There are two main meteorological patterns for wave storminess (Bolaños et al., 2009): (i) an intense high-pressure centre on the British islands which induces strong North-Eastern and Eastern winds and (ii) a Mediterranean cyclogenesis in front of the Catalan coast that generates Eastern winds. The maximum recorded H_s is about 6 m (with H_{max} up to 10 m) and peak periods of about 14 s. Fig. 2.3 shows the wave directional diagrams at different locations along the coast obtained from the existing wave buoys for the period 1984 to 2007. As it can be seen north-eastern and Eastern components feature the highest waves whereas the southern component, although present, has typically lower values.

The wave climate is controlled by (i) short fetches, (ii) shadow effect for waves from the south and east due to the Balearic islands; (iii) complex bathymetry with deep canyons close to the coast, (iv) high spatiotemporal wind field variability, (v) calm waves during the summer and energetic storms from October to May (storm season),

(vi) the presence of wind jets channelized by river valleys and (vii) bimodal spectra derived from sea and swell waves combinations.

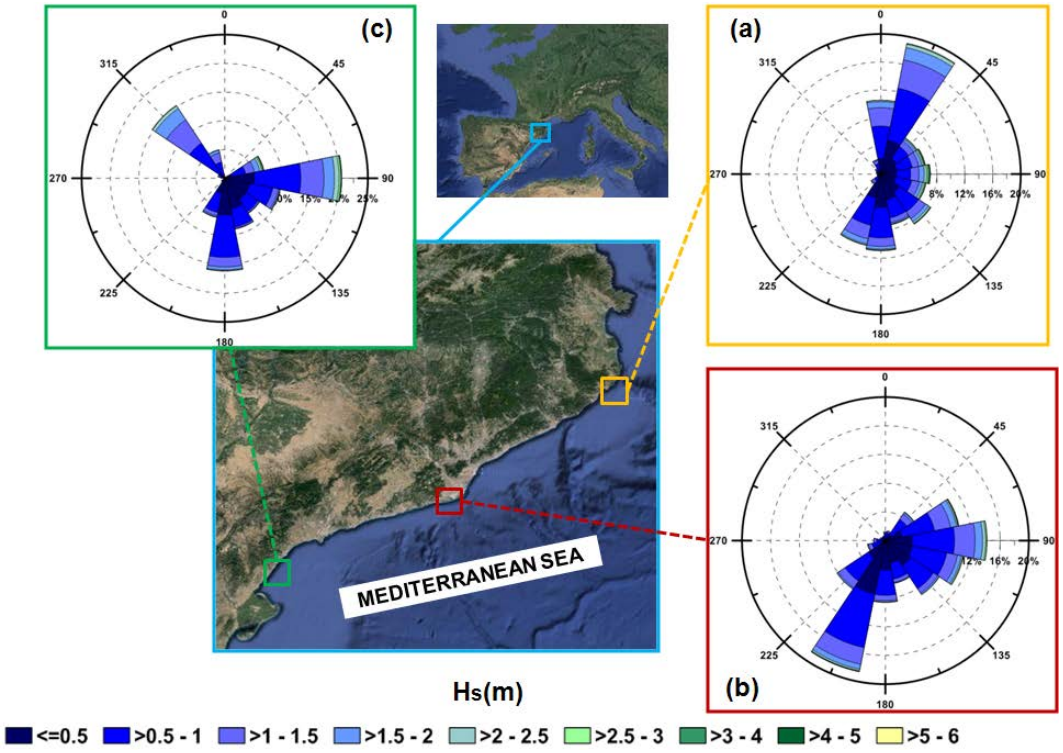

Figure 2.3.: Wave roses in the **Catalan Coast**. In *(a) Blanes Buoy wave climate (Northern)*; *(b) Llobregat buoy (Central)*; *(c) Cap Tortosa buoy (South)*. The legend shows the significant wave height H_s in meters.

The correlation between wave storms and surges is complex (see Ch. 4-5), meaning that storms can be found in wave records, with and without an associated mean water level surge. When wave storms and storm surges are superposed with an inadequate infrastructure planning (a relevant part were designed ignoring the wave action), the diagnosis is a **highly vulnerable coast**. The main damages at the Catalan coast are: (i) damage on coastal defences; (ii) beach erosion; (iii) inland sand deposits; (iv) damage on minor facilities and (v) flooding.

The Catalan coast presents almost all type of littoral environments (see Fig. 2.5). The **northern sector** (Costa Brava) is composed by the presence of cliffs (about 280 km of the total length) and prominent headlands delimiting pocket beaches that span a vast range of dimensions and are typically of coarse sediment (see Fig. A.1). The **southern part** (Costa Daurada and Ebro Delta) is typically represented by low lying beaches of fine sediments. The central part (Maresme, Barcelona and Costa del Garraf) is under the influence of the metropolitan area of Barcelona and concentrates most of the marinas and urban settlements. This heavy urbanisation level has led to a segmented coastal landscape due to an important need for coastal

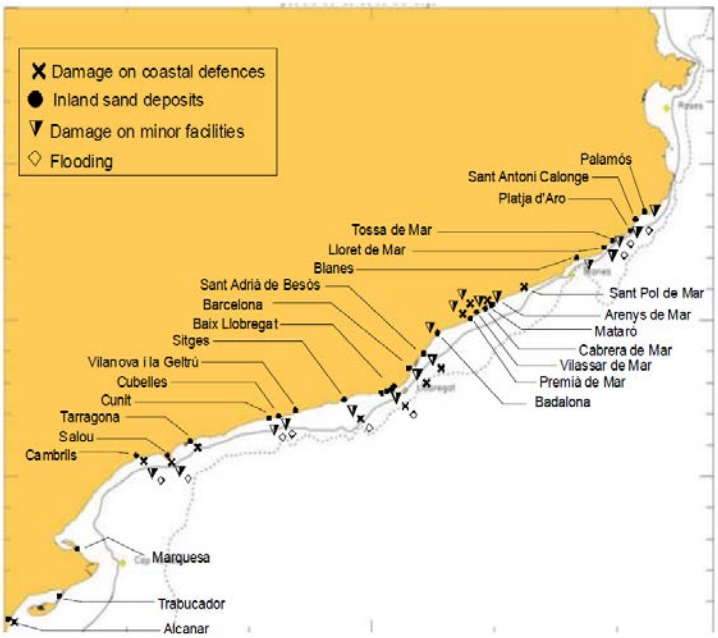

Figure 2.4.: Study area showing the main coastal municipalities and the recorded damages by marine hydrodynamic action. **Source:** Sánchez-Arcilla et al. (2012).

protection (see Figs. A.2,A.3). The main morphological features are the Ebro delta unit at the south (a 50 km sandy fringe), the straight segmented and relatively coarse sand beaches at the centre (represented by the Barcelona–Maresme system) and the Tordera delta and Costa Brava pocket beaches and cliffs at the North tract.

Natural and artificial barriers modulate sediment dynamics and divide the coast into **22 littoral cells** (CIIRC, 2010). The average beach has a **width** of about **37 m**, with a **mean sand size** from **0.2** to **1.8 mm** (median value of about 0.7 mm) and a foreshore slope steeper than 1/10. The spatial distribution of sediment along the coast reflects the differences in river basins, which have historically provided solid discharges to the coast, later reworked by wave action. Beaches located close to the mouth of the main rivers present finer sediment than for the beaches fed by ephemeral stream flows. This **general pattern** has been **modified** in the last decades by the **supply** of allocthonus **sediments** (of marine and terrestrial origin) in a considerable number of beach nourishment operations that have created an artificial morphodynamic signature in most of the beaches. As an example of this alteration, only in the central part of the Catalan coast, **more than $10 \cdot 10^6$ m^3 of sand** have been supplied in different beach nourishment operations during the **last 20 years** (Gràcia et al., 2013c).

Urban sandy beaches are typically bounded in their backside by a seafront promenade and infrastructures like streets, roads, railways and houses. In the last years, the **maintenance** and **development** of **promenades** has been one of the major investments undertaken by the Spanish government, with more than **50 M euros**

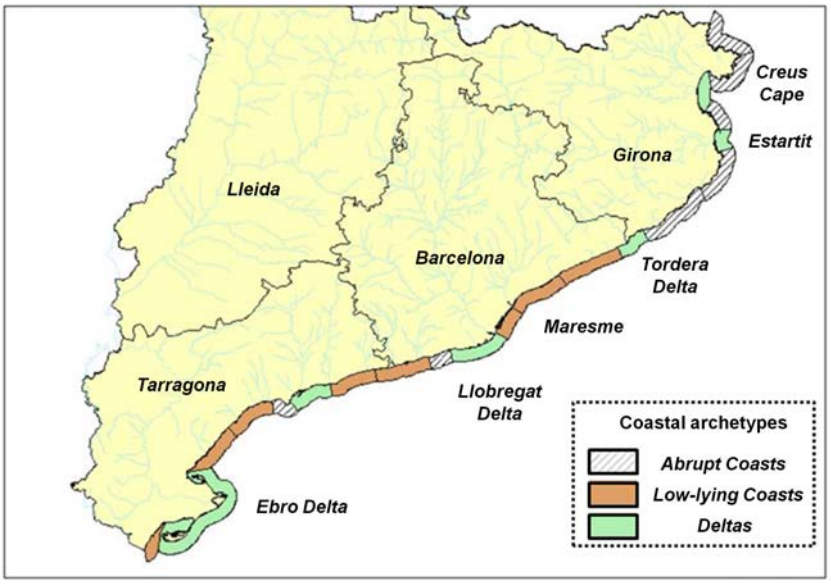

Figure 2.5.: Map of coastal archetypes in Catalonia classified with geomorphological criteria. **Source:** Adapted from ACA (2006).

only in Catalonia during the last two decades (CEDEX, 2013; Hamm et al., 2002).

The shoreline changes for the period 1995–2004 show a **general retreat**, facing erosion at more than **70**% of the Catalan beaches (CIIRC, 2010), with average rates of about $-2.1\ m/yr$ and of about $-3.3\ m/yr$ when the Ebro delta is considered. Only 24% of the beaches have experienced accretion with an average rate of about $+1.5\ m/yr$. These mainly correspond to areas located at the end of coastal cells which bank up the sediment from the upstream part of the cell or, in the particular case of the Ebro delta, from its ending spits.

In this dissertation, it has been set-up the morphodynamic module for **54 beaches** (see Ch. 6). They are comprised in the Northern and Central part of the coast. The morphodynamic features of these beaches can be found in Tab. B.1 (Calibration beaches in Ch. 6, i.e. those ones that have simulations with the Morphodynamic module) and Tab. B.3 (Validation beaches in Ch. 6). This sample summarises the main coastal archetypes that can be found in the area: (i) urban beaches with coastal protection infrastructure, (ii) open beaches and (iii) pocket beaches.

2.4.2. General atmospheric pattern

2.4.2.1. Temperature

The general **temperature pattern** at Catalonia presents a **Mediterranean climate** with relatively elevated annual average temperatures that ranges from $0°C$ to the coldest zones at the Pyrenees, to $17°C$ at the coastal sector. The greatest variability of the annual thermal amplitude is localised in the interior plains, within

an interval of 18-21°C, and the coastal zone presents an oscillation between 13-15°C (Figure 2.6). Consequently, in the littoral areas the **summer** is **fresh** and the **snow** events are **rare**.

The pattern and the temperature distribution are the result of an elevated number of factors, highlighting the **thermal regulation** by the **sea**. In general, it is distinguished by **two** great **air masses**: (i) the **maritime tropical**, that it is characterised by an anticyclone that comes from the African continent; and in the other side, (ii) the so-called **polar marine**, constituted by a cold and dry mass of air that comes from the Northern Atlantic, showing up in the cold months of the year.

2.4.2.2. Wind

In this dissertation, strong emphasis will be done to Eastern (**Llevant**) storms, because they drive coastal hazards at the Northern and Central parts of the Catalan Coast (see Ch. 4-6). However, there are other wind regimes that are more frequent, such as **Tramontana** and **Mistral**. These two wind regimes, despite that they do not generate waves that hit directly at the most part of the Catalan coast, are relevant in magnitude and frequency and they may have an important role in wind-induced circulation. The Tramontana are wind fields that comes Northward or NE, turbulent, dry and wet, plus they are specially present during the **cold months** (i.e. November to March). It can reach peak values of 200 km/h and can maintain high magnitudes during days.

The **Mistral**, that comes from the **NW** sector, shares the same properties (cold, turbulent and dry), channelised by the Occidental Pyrenees and the Ebro valley, reaching 200 km/h. It is the dominant regime between the Salou Cape and the Ebro Delta.

Ponent wind (W sector) is less frequent, but it can reach strongly the Catalan coast through the Iberian peninsula. It uses to be associated to the depressions at the Northern Europe. **Garbí** (SW sector) is a wind with thermal origin, that drives heavy seas at the central and southern coast, being reinforced with Atlantic fronts. Mitjorn (South), Xaloc (SE) and Llevant (E) are **moist winds** associated to **warm fronts**. The synoptic situation that generates them is a North African depression joint with an anticyclone in the Northern Europe.

2.4.2.3. Precipitation

The orographic differences in the Catalan region induce a great spatial variability in the precipitation regime. Then, annual precipitation values above **1200 mm** can be reached in the high mountain range area and below **300 mm** in the occidental plains (Fig. 2.6). The **700 mm-isohyet** is used as a **delimitation line** of the **wet** and **dry** zone, then classifying the littoral zone as dry. However, some nearshore zones are rainier than others, due to the mountain ranges that store the moist air from the Mediterranean. The mountains also act as a natural barrier against the penetration

of precipitation fields that penetrates into the interior part of the region. For the coastal fringe case, the higher rain intensity season is in autumn, specially during the September and October months. Minimum precipitation is usually recorded during **July**, with averaged values similar to the ones in **January** and **February**.

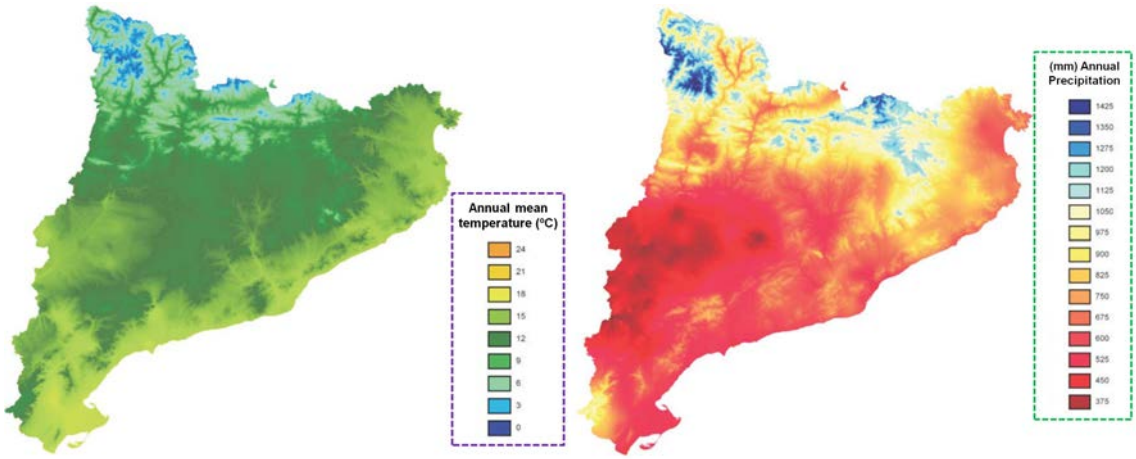

Figure 2.6.: Mean annual temperature *(Left)* and **precipitation** *(Right)* map in Catalonia. (Left) Celsius degrees scale (C) and in mm (Right). **Source:** Ninyerola et al. (2003).

2.4.3. Future changes in Climate and human change factors

Present conditions present a fragile balance between coastal resilience and extreme meteoceanographic drivers. But the future can be even more complicated. Changes in mean sea level, storminess and wave regimes may drive significant changes to the present coastal state.

Direct human impacts (urbanization, structures, river regulation) condition coastal vulnerability and are the primary factors for the evolution of developed coasts (Cooper and Pilkey, 2012). Climatic change, linked to global warming of the Atmosphere–Ocean (A–O) system, results in thermal expansion of ocean water (steric effect) and the addition of land-based ice meltwater. This causes most of the observed Sea Level Rise (SLR) (Church et al., 2013; Devoy, 1987, 2015).

Recent past observations show global mean sea-level changes (GMSL) since the 1880s of circa 0.2 m (0.19m, 1901–2013) at averaged rates of 1.7–1.8 mm/year, though with strong temporal (decadal scale) and regional variations (EEA, 2014; Jevrejeva et al., 2014; Menéndez and Woodworth, 2010). During this interval, mean global sea-surface temperatures (SST) have also risen by circa 0.8 °C , altering storminess in many ocean regions (Stocker et al., 2013; EEA, 2014).

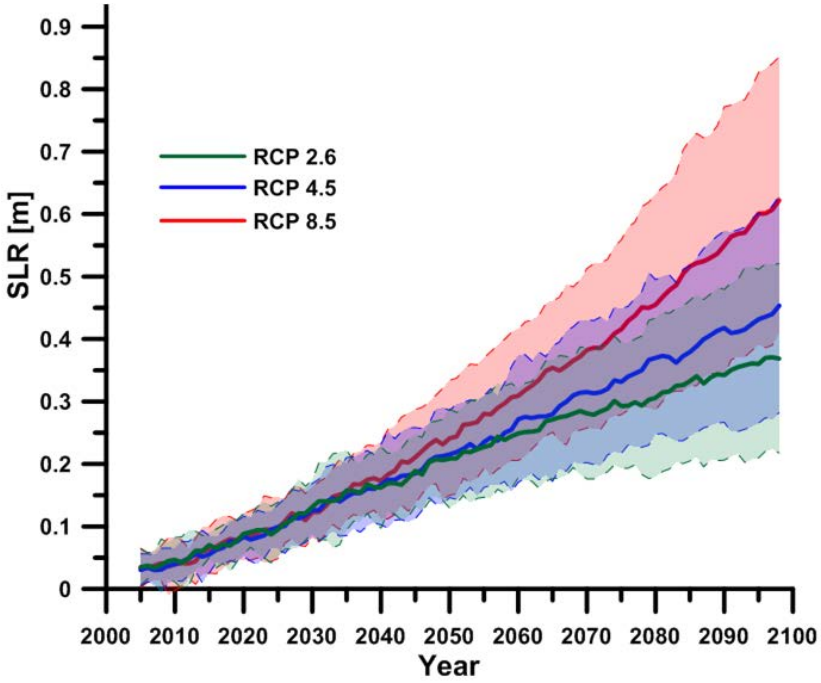

Figure 2.7.: Projected **regional Sea Level Rise** up to 2100 at the NW Mediterranean Sea (Stocker et al., 2013) for the RCP 2.6 (green), 4.5 (blue) and 8.5 (red) scenarios. At each case, the solid line represents the mean value, whereas the coloured bands are the 90% confidence interval.

Future climate projections for **European coasts**, based on model ensembles, show **SLR rates similar to global values** (Lowe et al., 2010; Church et al., 2013). For low greenhouse gas (GHG) emission scenarios (SRES B2-A1B; RCP 2.6) mean SLR is likely to be in the range of 0.26–0.54 m above 1990 levels by 2080–2100. For higher emissions (SRES A1F; RCP 8.5) mean SLR will be in the range $0.45-0.81\ m$ and continuing to rise between 1–3 m by 2300 (EEA, 2014), depending on levels of continued GHG emissions.

Current satellite altimetric observations of SLR rates for European waters, also supported by tide gauge data, commonly show values above **3.2–3.4 mm/yr** (EEA, 2014), except for regions of significant geotectonic subsidence (e.g., deltas and seismically active plate margins) or affected by continuing postglacial isostatic uplift. These rates **are likely to accelerate** beyond **4–5 mm/year** by the **mid 21st century**.

Model projections indicate anomalies in wind fields whose average intensity tend to a **poleward shift** in **Northern Europe** (Lionello et al., 2008; Nissen et al., 2014). However, at the Mediterranean basin there is a less definite trend. These wind anomalies may imply **changes** in wind wave patterns, affecting **wave directionality** and mean significant **wave height** (Casas-Prat and Sierra, 2013). The same authors, through outputs from **AR4** scenarios and for the 2071–2100 period at the NW Mediterranean Sea, presented a **significant wave height** variation around

$\pm$**10**% whereas the same variable for a **50 year return period** varied within a $\pm$**20**% **interval**.

Recently, Lin-Ye et al. (2017) have characterized the **future extreme wave climate** at the same area, for the **1950-2100** period, under a **RCP 8.5** scenario. It has been found that wave-storm components are related with large-scale indices such as the North Atlantic Oscillation (NAO), the East Atlantic Oscillation (EA) and the Scandinavian Pattern (SC). The **storminess increases with negative values of NAO**. The **location - parameters** (that are strongly related with the mean value)[2] of wave height at the storm peak, peak wave period, total storm energy and storm duration (D_{storm}) **decrease with time**; except for the latter one (D_{storm}) at the northern part of the Catalan Coast. These same parameters present relationship with EA, SC and its dynamics.

Similar evolution trends apply to **storm surges** although in all cases due attention should be paid to the different behaviour of mean trend and variance characterizing storms (Lowe et al., 2010). For instance, Conte and Lionello (2013) presented **variations up** to $\pm$**5**% for both positive and negative surges in the Mediterranean Sea.

The downscaling for semi enclosed basins (e.g. the Mediterranean Sea) is complex, becoming more difficult for smaller sub-basins (e.g. the Black Sea and Danube Delta, see Stanica and Panin (2009)). Coastal processes and SLR at such local scales are driven by regional steric (temperature) effects, precipitation–evaporation balance, river inflows and other oscillations at various frequencies (e.g. water exchanges between the Mediterranean and North Atlantic) (Tsimplis et al., 2004; Dan et al., 2009; Valchev et al., 2012).

Sea levels in the **Western Mediterranean** have **risen** by **2.5 mm/yr** since the **1990s**, with current satellite records showing an acceleration of SLR commensurate with the wider European and global patterns of SLR curves (EEA, 2014). Although downscaled A–O GCM experiments are not well developed for the Mediterranean region, model projections show the continuation of this SLR trend up to 2100, coupled with regional rises in temperature (Church et al., 2013).

In Fig. 2.7, SLR projections for the RCP 2.6, 4.5 and 8.5 scenarios are presented at the nearest node of the NW Mediterranean Sea (Sánchez-Arcilla et al., 2016a). At the end of this century, the projections highlight a mean projected SLR of 60 cm at RCP 8.5 scenario and circa 35 cm for the RCP 2.6. The 90% confidence interval shows more deviation at RCP 8.5 than the milder scenarios.

[2]The definition of location parameter in a GAMLSS can be found in this dissertation (see Sec. 3.3.4) and in the probabilistic risk module in Ch. 6.

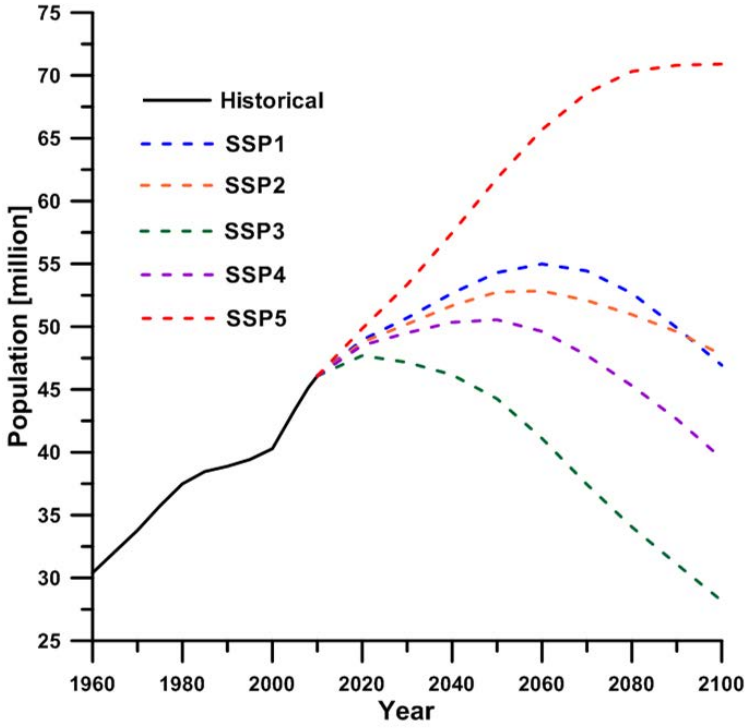

Figure 2.8.: Projected population from **2010 to 2100** at **Spain** (IIASA (2012)). Black solid line is the historical. The dotted lines represent each SSP.

Note also that the mean trends of RCPs tend to diverge in the second part of the twenty-first century. This behaviour can, thus, convey a misleading message at the beginning of this century and can even justify postponing response decisions, since the larger part of the uncertainty (and impacts) will start to happen by 2040–2050. The reason beneath the mean trends of the RCPs seem to match at the forthcoming decades (2020-2050), is due to the strong relationship between near future SLR projections and present/recent past GHG emissions. Hence, in order to start noticing a decrease of the SLR rate by 2050s, it is imperative to cut anthropogenic emissions in the next years.

The likely future increase in coastal area population (Neumann et al., 2015; Merkens et al., 2016), associated to industrialization, urban growth and expanding tourism, will bring the numbers of people living in the littoral closer to the levels elsewhere in Europe. This means more than 25% of Europe's current population living at the coast (IPCC, 2014). Continuation of the established upward trend in this **population growth will increase the coastal vulnerability** to the impacts of future SLR and storminess under climate warming.

In Fig. 2.8 the population growth projections are presented (from 1960 to 2010, the historical data is from World Bank country database) based on the IIASA (2012) database. Each projection belongs to a SSP family (O Neill et al., 2014), covering the following pathways: **SSP1** *(sustainability)*, **SSP2** *(middle of the road)*, **SSP3**

(regional rivalry), **SSP4** *(inequality)* and **SSP5** *(rapid growth)*.
Lower population is expected in the **SSP3** narrative, because its represents a future in which the countries are almost self-sufficient with minor trades and exports. However, **SSP5** represents a rapid growth with expenditure for mitigation strategies. Note that the **SSP5** follow the same population gradient than the last decade (2000 onwards) in which both have experienced a rapid growth. Nevertheless, the **common trend** in **Spain** is towards **stabilization** (except in SSP5 and SSP3).

2.4.4. Sustainability practices

Once described the main physical and geographical features of the Study Area, it is needed to bound pros and cons of the coastal zone management policies. The next Section briefly summarises a subset of Low Sustainable interventions and High Sustainable interventions.

2.4.4.1. Low sustainability practices

Urban development at the Catalan coastal started in the **70s** under **low regulatory conditions** (Malvarez et al., 2000). The lack of a general management strategy followed by the construction of coastal promenades, secondary houses (fed by tourism requirements) and existing **urban growth** pressure jointly with the **regulation of river basins** have led to the present sediment starvation, then needing **coastal protection**.
The urban development has resulted in **high population density** along the coastal fringe (6.000–7.000 users/km of coast when permanent residents plus tourists are considered, Gràcia et al. (2013c)). This squeezing requires a minimum beach width to support coastal functions and also to defend the hinterland (infrastructures and territory). At the second half of the 1980s and early 1990s, **beach nourishment** was the common solution to **fight against erosion**, with more than 10 Mm^3 in about 10 years of which only a small fraction remains in place. This situation has been pointed out by some recent research (EUROSION, 2004; Marchand et al., 2011).
The **lack** of a general **coastal master plan** to **fight** against **erosion** (i), the difficulty to obtain suitable volumes of sediment with enough quality (ii) plus the present economic situation (iii) has led to the present **reactive management strategy**. In such strategy, **actions** are taken **after the impact**. This reactive management also includes the "no active intervention" policy, resulting often in a **degenerative beach state**.
The **Central part** of the Catalan coast (excluding the Ebro system), that is the **Barcelona–Maresme** coastal stretch, is an example of such situation. The area is the longer tract with eroding beaches and also where most of the locally accretive beaches are found. This behaviour is basically due to the **net littoral drift**, from north to south, and the existence of numerous marinas interrupting the alongshore

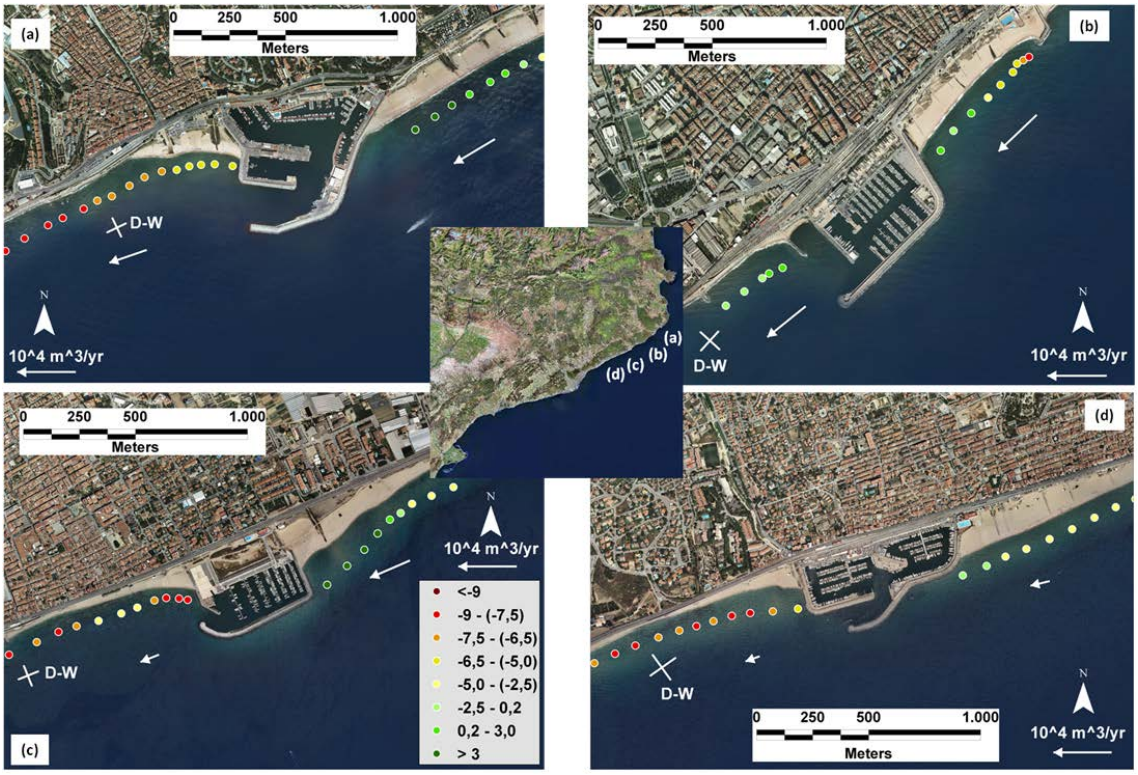

Figure 2.9.: Mid-term erosion trends at the Catalan harbours. (a) Arenys de Mar; (b) Mataró; (c) Premià de Mar; (d) Masnou. The D-W denote the divergence points. The coloured points shows the shoreline retreat/accretion in m/yr. The vectors show the annual longshore sand transport in module (in $1 \cdot 10^4$ m^3/yr) and direction. The scale of these vector can be found below the North.

dynamics. This restriction creates a local shoreline retreat at the beaches in the north of the cells and a lower accretion at the southern part of the cells, linked to the downstream barrier.

The area is directly exposed to the most energetic wave events (Eastern component) and has a backside limit due to an almost fully occupied territory (settlements and infrastructures). This situation blocks the natural onshore dynamics typically observed during high energy episodes. **Coastal segmentation** has created a sediment redistribution pattern which is **incompatible** with the **socio-economic demand** of a **minimum** homogeneous emerged **beach width** along the sector. The alongshore sediment blockage generated by the construction of structures and the near total **decrease** of **river sediment supply** (large enough in size to be stable for the emerged beach) has resulted in a sediment budget imbalance at most littoral cells.

The existence of these artificial obstacles has also created a divergence in alongshore sediment transport, generating local erosional hot spots at the south of the barriers which lead to important local losses of emerged beach (see Fig. 2.9). The **periodic beach nourishment** of those areas or/and the construction of **small groins**

that constrain sediment mobility have been **common strategies** for maintaining beach width. However, **high erosion rates** and the **scarcity** of suitable sediment cast some doubts on the sustainability of such an approach, normally interrupted whenever the economic or environmental situations make this solution unacceptable. This has led to the construction of alongshore riprap revetments to defend certain sectors.

The deployment of **groins** to increase the **residence time** of the sediment within the cell has also proved to be **fruitless** (CEDEX, 2013; Jiménez et al., 2011). Two main processes can explain such behaviour: (i) the creation of **offshore currents** that **transport sediment** out of the cell **towards deeper regions** and (ii) the **re-orientation** of the **shoreline** parallel to the most **energetic wave trains**. In the first case, although the sediment does not leave the domain, it is deposited in an area where only high wave conditions can return it to the coast, leading to a growing deficit of emerged sand volume. The shoreline re-orientation is highly sensitive to the incident wave direction. In these beaches, waves act very obliquely to the shoreline due to the low periods. Man-made obstacles can only retain a limited sand volume, with sediment rapidly reaching the head of the groins and by-passing it towards the down drift sector (Jiménez et al., 2011; Sánchez-Arcilla et al., 2014, 2015a).

The complexity of these morphodynamic processes has led to two main management strategies: (i) a **discontinuous maintenance** and armouring of the coast and (ii) the **small partitioning into smaller coastal cells** that will next be subject to an almost complete closure with submerged breakwaters (e.g. Barcelona urban beaches). However, neither option has allowed the maintenance of a homogeneous beach width. Two **main processes** can explain such **non-desired dynamics**: (i) the **segmentation** creates a subset of **diffraction points** that form **logarithmic shaped bays** with less width at the centre and wider areas at the borders and (ii) the **natural cyclic onshore-offshore** coastal dynamics which **favours** an **offshore transport** of **finer sediments**, reducing the width of the emerged beach. This has resulted in low sustainability for a narrow coastal fringe that presents a high level of vulnerability under present and future climates.

2.4.4.2. High sustainability practices

Due to the **scarcity of sediment** for many sectors in the Catalan coast, the actions undertaken in the last 20 years (also extensive for the rest of the Spanish territory) have been **unsuccessful** to **maintain** a **sandy belt** as required by tourism and hinterland protection. New coastal strategies that incorporate the whole river catchment basin and targeting medium to long term scales, shifting from protection to a more **pro-active policy** will increase the overall coastal sustainability. The Spanish Ministry of Environment is preparing such a plan under the principles that coastal management **should consider sediment availability** and **climate change** plus a commitment to integration regarding scales and uses. However, there has not yet been a general implementation of the plan and in many cases coastal manage-

ment continues along the old track. Because of that, **municipalities** are starting to play a **more active role** demanding not only economic resources but also making **proposals** for maintaining a minimum beach width to ensure beach functions (see Ch.7).

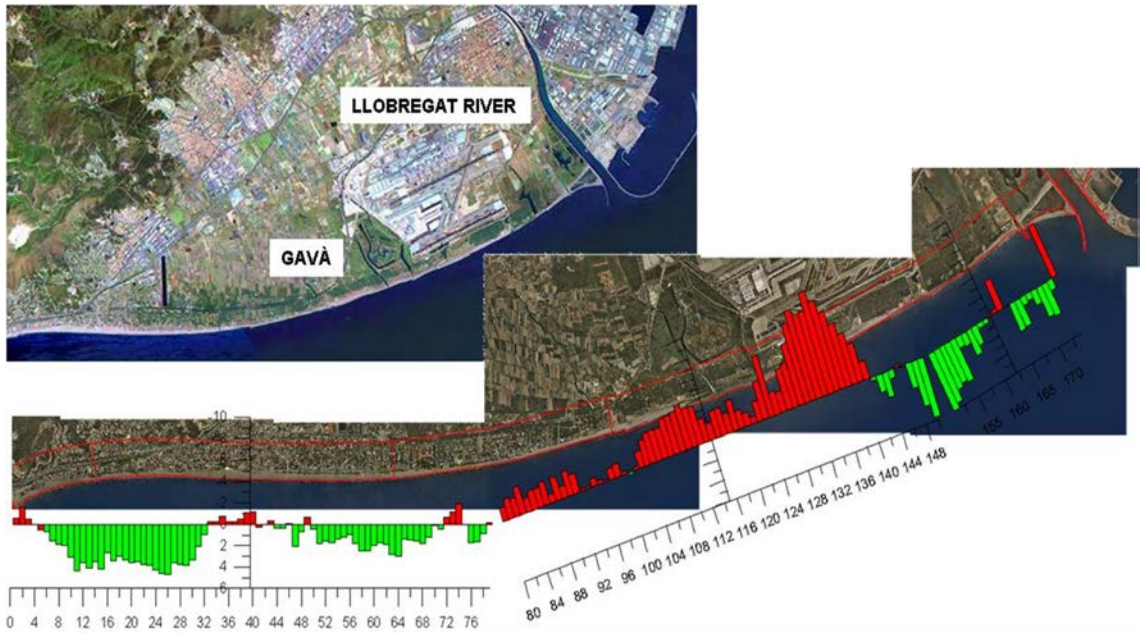

Figure 2.10.: Shoreline changes in south Barcelona harbour during the period 2004 - 2010.

Strong emphasis on sustainability is currently addressed at the Ebro Delta, located 200 km south of Barcelona. Flooding and erosion are considered as the most important risks by stakeholders (Rovira et al., 2014). This is due to the scarcity of sediment arriving from the regulated river catchment basin. Providing additional sediment volumes for offsetting subsidence and horizontal erosion would be an illustration of working with natural processes to increase resilience. This could be achieved by **regulated floods** from **riverine** and **marine origins** (Ibáñez et al., 2014; Sánchez-Arcilla et al., 2015b).

Another case of such practices comes from the southern Barcelona coast, showing the feasibility of **sustainable shoreline retreat** (Fig. 2.10). The observed **erosion** is the result of combined **human** and **natural factors**, making it difficult to establish a main culprit. The expansion of Barcelona harbour with the construction of a long jetty (down to 8 m water depth) in the Llobregat River (Fig. 2.10) has shortened the supply of sediment from the North. A small marina (Port Ginesta) closes the cell at the South. The sequence of southern and northern storm waves is no longer able to produce alongshore sediment fluxes in the two shore parallel directions. The barrier effect **enhances cross shore transport** (losses) and prevents river discharges to supply sediment to the active coastal profile.

The coastal management plan for the area consists of **periodic nourishments** that **back-pass sand** from the **southern end** of the littoral cell to the **northern** border. However, after almost one million cubic meters of sand nourished in the last 6 years, the desired effects have not been achieved and at present some of the beaches exhibit an alarming reduction of emerged width. This is due to the difficulty of finding suitable sediment sizes, since the expected alongshore winnowing results in a grain size classification providing only the finer fractions at the end of the unit (the more frequent source areas).

Taking all those aspects into consideration, the **Gavà** municipality has considered a maintenance plan where the main target is to **safeguard** a **minimum emerged width**. Based on this, an initial nourishment has been designed taking the sediment from the emerged and shallow neighbouring beaches instead of looking for sources outside the littoral cell. Sediment placement has also been designed to have a **smooth coastline shape**, in order to **reduce longshore** sediment transport **gradients** (LIM/UPC, 2014). Besides, at the back beach an ephemeral small dune of 1.5 m has been proposed to protect infrastructures from storm events of 15 years return period. The **dune** acts also as a **sediment buffer** which will naturally feed the area, thus enhancing the presence of an emerged beach. Fig. 2.11 shows the dune/beach profile response at different locations selected for testing the design using a modified XBEACH model (Roelvink et al., 2009). The parameters of the model have been calibrated with similar dissipative beaches in the surrounding areas (Gràcia et al., 2013b).

The main morphodynamic changes are found between the **−0.5** and **2 m** isobaths. Several dune layouts were tested showing **similar morphodynamic simulations**: **erosion** at the **emerged** part and sand **accumulation** in the **submerged** part. This general behaviour can be explained by the **relatively steady offshore wave climate** for return periods from 2 to 15 years (meteo and fetch controlled).

The simulated behaviour shows an increase in sand transport under storms. This leads to erosion at the emerged part of the profile and accumulation in the submerged part. For extreme wave conditions and under high mean sea levels, the beach response is a **scarp** that enhances **erosion**. After a cumulative set of storms, the natural beach recovery is reduced and requires higher energy swells (uncommon in the area) or artificial means.

The averaged loss of sand with the transient dune during storms (spanning from 5 to 15 years return periods) is around **15,000 m^3**. Water depths **from 0 to 2 m** present an accretive behaviour (around **7,000 m^3**). Longshore currents play an important role (around **0.4 m/s** in average), with the littoral drift mobilising significant sand volumes southwards.

The emerged zone flattens when the dune collapses. Note that at Fig. 2.11, the dune starts to fail not under a collision regime (erosion at the offshore side), but because of **overtopping** volumes from the storm peak. The **dune** can withstand **increases** of **40 cm** in mean sea levels that would correspond to a **present storm surge** or a **future climatic rise**. Beyond that point, the dune entirely collapses

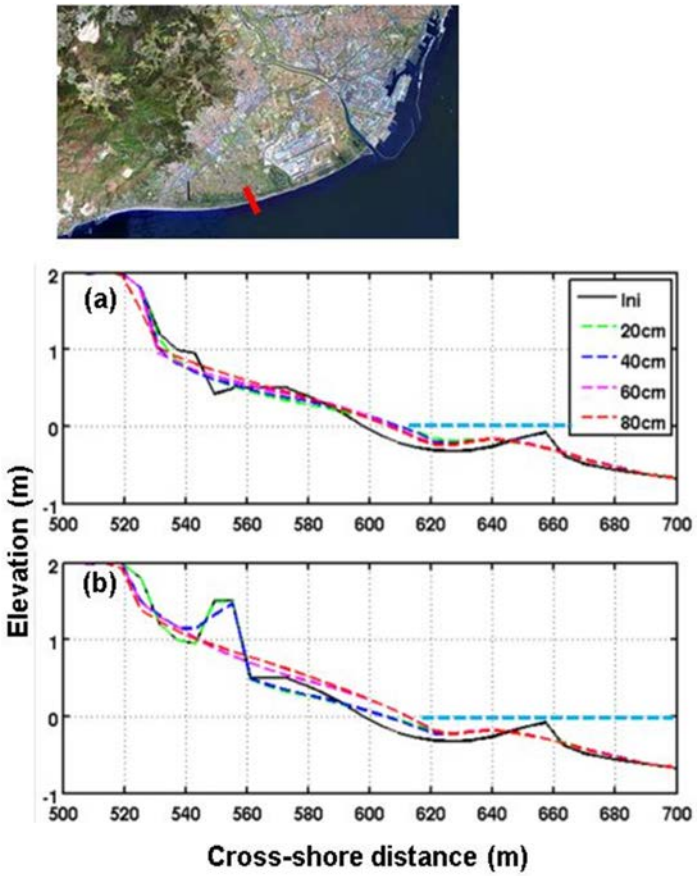

Figure 2.11.: Transient dune alternatives and storm response at Gavà beach (NW Mediterranean).

and sea level has a more prominent effect in the morphodynamic signature. This is because as waves increase, more sediment can be advected onshorewards, reaching a maximum for elevations between 1.5 and 2 m.

In Ch. 7, a deeper analysis of this dune system will be done. However, it has been considered to explain the general concept behind Quick Defence Measures (QDM) at this point, in order to illustrate to the reader that exist alternatives to reactive management strategies.

Permanent monitoring of beach evolution and the main driving factors (waves and mean water level) have been proposed to support objective decisions and an ephemeral set of QDM. The concept behind these interventions is linked to the difficulty of guaranteeing **permanent protection** and accepting a permanent maintenance of the beach. The idea of ephemeral defences has been taken into consideration in other European regions (Harley and Ciavola, 2013) and assessed numerically for some nearby beaches (García-León et al. (2015), see Ch. 7). Such transient measures must work together with a forecasting (Early Warning) system that supports dynamic interventions or maintenance of the beach.

2.5. Coastal Early Warning Systems

High sustainability practices involve **proactive** action. But timing is essential in proactive action, specially under extreme events. Time is scarce and interventions require (i) resources to be allocated and (ii) decisions to be taken. **Forecasting** the future state of the coast, then, becomes one of the best ways to **increase the time buffer**. Early Warning Systems (EWS) are a suitable choice for this task. In this Section, it will be defined what is an Early Warning System (Sec. 2.5.1) and its sub-branch (Coastal Early Warning Systems, Sec. 2.5.2) for addressing coastal hazards. Recent CEWS pilot initiatives such as the MICORE project will also be described (Sec. 2.5.2.1).

2.5.1. Early Warning Systems

2.5.1.1. EWS components

In accordance with UNISDR (2010), an Early Warning System (EWS) is defined as the set of adequate and effective information sources, communicated from specialized institutions, with the aim of avoiding or reducing a risk, then preparing agents (individuals or communities) exposed against a hazard. Hence, an EWS can be defined as the set of necessary skills for generating and conveniently disseminating early alerts for allowing threatened individuals, communities and organizations by a certain hazard with the aim of **reducing the probability of human losses**. This definition does not include a time scale reference in which the alarm must be transmitted to the stakeholders.

The architecture of a complete and effective EWS must include at least the following four elements. If **one** of these modules **fails**, that implies the **whole system failure**:

1. **Risk awareness:** The risk evaluation provides essential information for defining mitigation priorities, prevention strategies and EWS design.
2. **Monitoring and alarm service:** System with capacity for forecasting and data gathering, that provides in a systematic basis, estimations of the potential risk that have to withstand the communities, the economy and the environment.
3. **Dissemination and communication**: The communication systems must be **accurate** for the alarm message distribution to the potentially affected municipalities, as well as the governmental agencies at local and regional scale. The messages need to be understood by the general public and the authorities. Hence, this information must be **reliable**, **synthetic** and **simple.**
4. **Response capacity:** The key issues for effective early warnings are coordination, good governance and appropriated intervention plans. Additionally, **education** and **public awareness** are critical aspects for disaster mitigation.

When it is analysed who executes the monitoring and forecasting, there can be found two trends: **centralized systems** where a national agency acts as a provider; or **decentralized systems**, where these tasks are conducted by a subset of agencies, municipality-level workers and volunteers at a local scale.

The development of EWS and Community Based Disaster Risk Methodologies (CBRDM) has notably advanced from the 2004 Tsunami at the Indian Ocean (Thomalla and Larsen, 2010). However, in the early stages, the development was focused on the technological implementation; thus relegating human factors such hazard awareness, disaster preparation, conciliation priorities in the context of multiple agendas (although one zone can be partitioned due to political criteria or natural hazards that do not follow the same patterns), in addition to motivation and support for synergistic CBDRM activities within the EWS. This trend is presently shifting by **intensifying the participation of the stakeholders in the design phase** (Voinov and Bousquet, 2010).

By the same token, it has been published the results of a global questionnaire in which the main attributes and hindrances are highlighted (UNISDR, 2010). The report concludes:

1. **Different hazards require different early warnings systems:** For instance, the alarm requirements for a tsunami strongly differs from a drought.
2. **There exist a considerable number of systems that can provide warnings for an elevated number of natural hazards:** Nevertheless, there exists usual conflict with the link between the technical skills for sending the alarm and the public capacity for effective action. A common weak point is the incapacity of the alarm for conducting the proper response by the emergency management bodies, community-based organizations and the general public.
3. **The effectiveness of an EWS depends on considering both hazards and vulnerabilities within a reduction risk paradigm.** This measure requires a reinforcement of the inter-institutional efficiency, the efficiency of the actions at an individual and joint level, plus the public preparedness.

In order to fulfil such criteria, The Catalan Government (Generalitat de Catalunya) created the PROCICAT (2013) plan, establishing the following specific hazards: *(i) precipitation; (ii) flooding; (iii) snowfall and frost; (iv) storms; (v) droughts; (vi) earthquakes; (vii) landslides*. Each of this hazards have the following attributes: *(i) Risk name; (ii) Associated Plan; (iii) Information sources; (iv) Decision making organizations; (v) Hazard scenarios; (vi) Thresholds for triggering the specific emergency plans; (vii) Communication protocols for each scenario.*

2.5.1.2. GEAS

GEAS (Global Environmental Alert Service, Grasso and Singh (2007)) is a multiscale system for the identification, selection and communication of EWS, focused on new methodologies for the decision making aid, within the UNEP **action framework**. GEAS analyses the state-of-the-art of the scientific knowledge plus the avail-

able observations, with the aim of producing **wide distributed alerts**. GEAS resources are concentrated in accessible near-real-time environmental policies, sciences and hazards. This proposal is big-community based, specially in **developing countries** that have an **elevated threat of natural hazards** but **without** EWS.

Internet is the proposed communication channel within a **bottom-up** scheme (i.e. manage resources in the individual parts of a system, for a posteriori coupling within a complex component, Jakeman et al. (2006)). This message will be composed with the following technologies:

- Remote sensing and data-acquisition networks (i.e. buoy networks, meteorological stations).
- Geographic Information Systems (GIS) and digital cartography.
- Telecommunications, with strong emphasis on the connectivity that Internet offers.

With this scheme, UNEP, via GEAS, will provide local level information to a global public (i.e. globalization of the local information). Additionally, though a *top-down* process, product of the joint management of the UNEP with an elevated number of local agents, the information will flow from global sources to other higher resolution scales (regional, national and local). Hence, it will be fostered their transparency, embedding the global information. The potential users of this scheme would be clustered as:

1. UNEP Administration Council, constituted by environmental ministries.
2. UNEP Regional Offices, that coordinate the intra-regional environmental activities and maintain links with the national environmental and civil society ministries.
3. Environmental agreement.
4. Public information structures, with the aim of publishing and disseminating the information to the political managers, the mass media and the civil society.

The architecture of GEAS consists of two components:

1. **Near-real-time natural hazards** alarms.
2. **Environmental hotspots** alerts.

This dissertation is based on the EWS, and these can be found in the first point. Hence, it will be thoroughly described below:

Starting with a number of **regional nodes**, this subsystem consists on the implementation of a **global multi-hazard EWS**. This concept is not based on a single centralized system, as to whether in a **coordinated network of national systems**. Its inputs will comprise: (i) a monitoring network, (ii) alarm centres, (iii) numerical modelling and forecasting, (iv) telecommunications networks, plus (v) preparedness and response capacity. This would allow to identify more efficiently the hazard occurrence, with the aim of having enough response time under a crisis.

This subsystem can be divided into the following parts:

1. Resources

a) Data identification and data sources.
b) Automatic data transmission from reliable sources though the use of international protocols and regulations.

2. Analysis
   a) Detection and data filtering from multiple information sources.
   b) Integration, synthesis and compilation.
   c) Creation of an alert database.
   d) Database of alert detection.
3. Output
   a) Distribution of real time graphical information.
   b) Web services.
   c) E-mail and SMS notification.

The data sources for the GEAS database generation must be reliable and with a standard format (i.e. Open Geospatial Consortium (OGC), Common Alerting Protocol (CAP), Real Simple Syndication (RSS), Extensible Markup Language (XML), Botts et al. (2008)). This requirement is fulfilled by a set of institutions listed below:

- **Global Disasters Alert and Coordination Systems (GDACS):** it has an e-mail service, SMS and fax for the users. The notification service is focused on humanitarian organizations, rescue teams or aid agencies.
- **United States Geological Survey (USGS):** the only specific alert realised by this agency deals with earthquakes via e-mail.
- **Humanitarian Early Warning Systems (HEWS):** This agency publishes the information on web-sites (RSS), plus a service of e-mail and mobile phone.
- **AlertNet (alert information service provided by the Reuters agency) and ReliefWeb:** They have web services, e-mail, SMS and reports.

A database and a near-real-time map can be built from these information sources. The map shows the position and the event type at a global scale. Through the **KML** (Keyhole Markup Language) protocol, this information will be exportable to software based on massive infrastructure such as Google Maps and Google Earth.

2.5.1.3. EMMA

Despite GEAS (see Sec. 2.5.1.2) was planned as a generic EWS, the EMMA programme (European Multi-Purpose Meteorological Awareness Programme, WMO (2010)) has as an objective to develop a Geographical Information System (GIS) accessible for the general public with the forecasting of possible **meteorological threats**, **at least 24-hours before** the event.

This system can act as a complement for the present national Early Warning Systems, providing a simple method for boosting people awareness about meteorological

hazards, so as to transmit meteorological data (with strong emphasis on those associated to extreme events) among the different European forecasting centres.

The main features of this web service system are:

1. **Codified regions** with a chromatic index associated to the incidence level of the forecasted meteorological action.
2. A core of **extreme** meteorological phenomena at **continental scale**. Hence, the web service can show this core as an homogeneous set, as well as local scale (heterogeneous), in case that the action level differs excessively between spatial scales.
3. With the aim of fostering public awareness, there co-exist **different complementary information levels**, that can be accessed interactively.
4. **Multilingual support** in the official European languages, at least with the data from the higher hierarchical levels (i.e. national level).

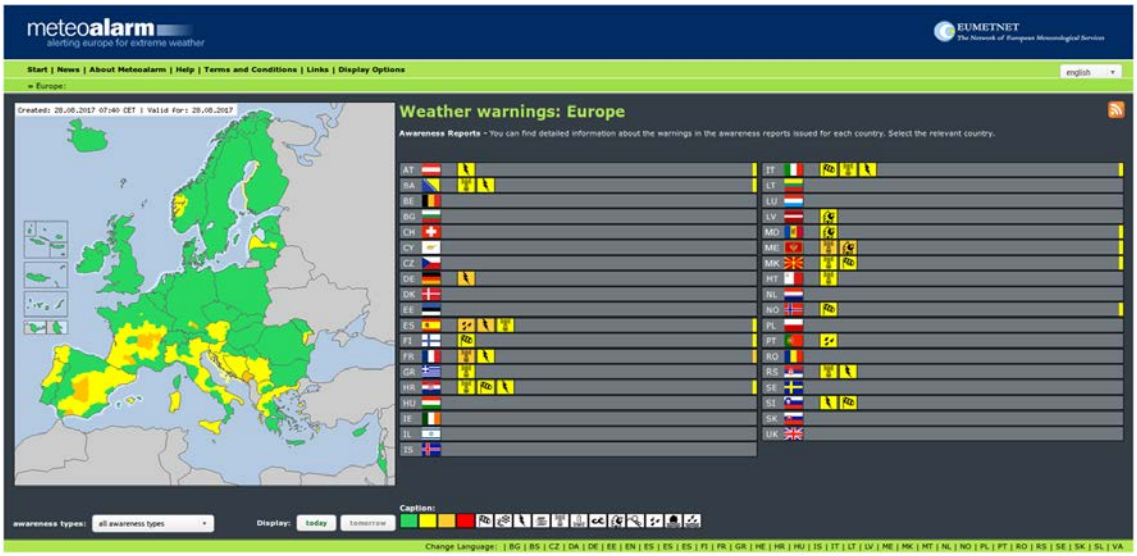

Figure 2.12.: Meteorological hazard forecast in Europe at 28th August 2017. Note the coloured risk scale: *green (no-hazard), yellow (potentially hazardous), orange (hazardous situation), red (extreme hazardous).* **Source:**`http://www.meteoalarm.eu/` *(**Last visit:** 28th August 2017).*

This service can be accessed via the website `http://www.meteoalarm.eu/`. As an example, in Figure 2.12 can be found the forecast for the 28th August 2017.

2.5.2. Coastal Early Warning Systems

Once described the early warning systems with strong emphasis on the meteorological hazards, the remaining subdivision are those EWS devoted to **mitigate coastal hazards** (see Sec. 2.3), Coastal Early Warning Systems (CEWS). CEWS aims to

mitigate the consequences of the coastal hazards at different spatio-temporal scales, providing forecasting for processes such as overtopping, overwashing, beach and dune erosion, dune breaching and flooding.

Society needs an efficient management of the available resources. The main constraints at the coastal fringe are economic restrictions and the increase of the coastal vulnerability (due to the storm impact, the anthropogenic footprint, sea level rise or changes in incident wave direction). Haerens et al. (2012) defended that such factors have been the responsible for the recent CEWS development with the following architecture:

1. **Monitoring module:** Data gathering and compilation of meteorological data, waves, sea level and morphology features.
2. **Forecasting module:** Taking as boundary conditions the results obtained in the previous module, it has been obtained forecasts of the hydro-morphodynamic variation of the coast through coupled nested numerical models (Sánchez-Arcilla et al., 2012; Gràcia et al., 2014). These models, can be calibrated and validated with monitoring, and the forecast skill can be improved with continuous **data assimilation** (Evensen, 2001).
3. **Decision support module:** Ranging from the model results, these are interpreted in simpler elements; usual in the littoral management as a decision support tool. Noteworthy are indicators such as **Coastal State Indicators** (van Koningsveld et al., 2005) or the **Storm Impact Scale** (Sallenger, 2000).
4. **Visualization module:** The potential threat is addressed in a multilayer scheme, i.e. the direct emergency managers will be informed with a lower threshold of risk than the general public, and such information will be more technical. Each user profile needs an output and interpretation methodology.

A relevant part of the pilot European CEWS derives from the outcomes of the EU-funded **MICORE** project (see Sec. 2.5.2.1). The main features would be described below.

2.5.2.1. MICORE EU-funded project

The MICORE project van Dongeren et al. (2009) (2008-2011) had as one of its main goals the validation of a morphodynamic model (XBEACH, Roelvink et al. (2009)) for forecasting a set of pilot cases in Europe, plus implementing CEWS at such sites. With that aim, a subset of beaches were selected, then modelled with XBEACH and compared with other local models such as LITPROF (DHI, 2017) or SBEACH (Larson et al., 1990). Due to the geographical and climate variety, the algorithm should allow a wide variety of results. As a quality metric of the results (benchmarking) with the other models, it was used the Brier Skill Score (BSS, see Eq. 3.4.10 at Sec. 3.4). The study areas are briefly described in the Tab. 2.4. At an individual level, it can be remarked the following outcomes:

From **July 2008**, it was obtained the coastal erosion forecast at **Egmond (The Netherlands)** every 6 hours (during 12 hours, with a daily frequency). At The

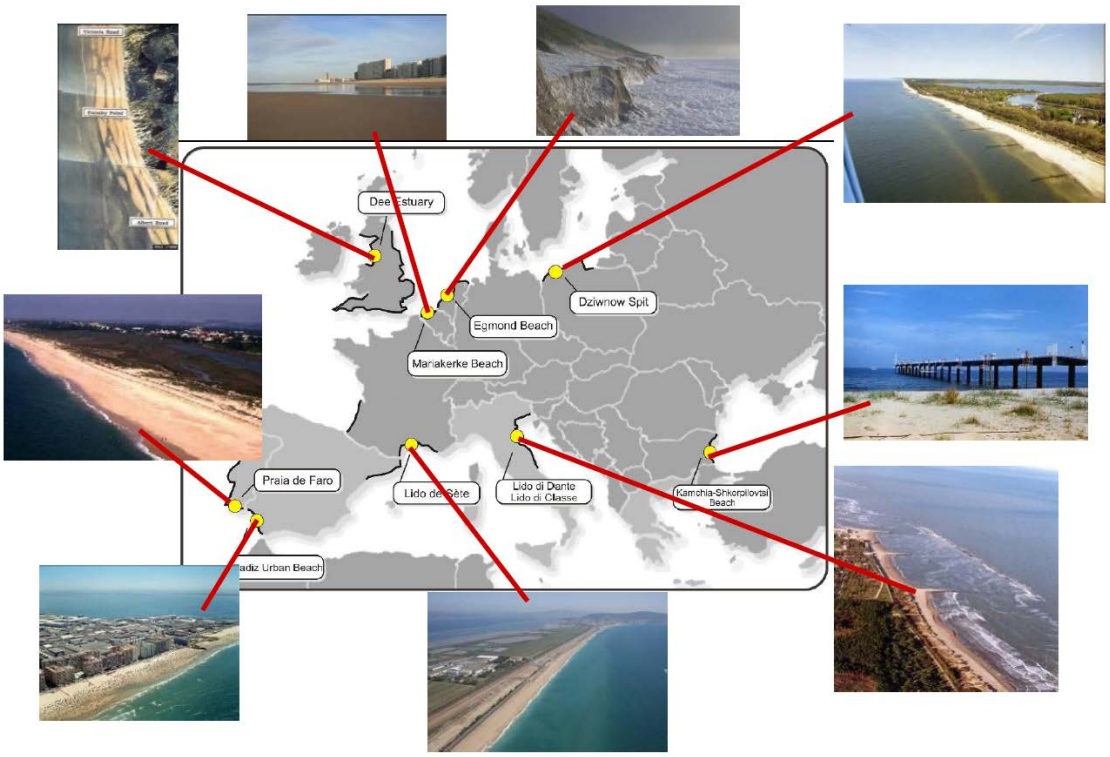

Figure 2.13.: European beaches that constituted the MICORE project: Egmond (Netherlands), Lido de Dante (Italy), Praia de Faro (Portugal), Urban beach of Cádiz (Spain), Lido di Sète (France), Mariakerke beach (Belgium), Dee Estuary (United Kingdom), Dziwnow Spit (Poland) and Kamchia-Shkorpilovtsi Beach (Bulgaria). **Source:** van Dongeren and de Vries (2011).

Netherlands, the MICORE project was mainly focused on validating the morphodynamic model with the generated database. Through an **Argus** system (Holman and Stanley, 2007) plus the application of **BeachWizard** (van Dongeren et al., 2008), it was obtained time series that described not only extreme events, but also moderate conditions. The latter would serve for expanding XBEACH applicability (the model is still under active development, and the main objective is that it can reproduce the state of the coast under extreme and moderate conditions). This pilot zone was aimed to be the reference for other Dutch sites.

The **Lido de Dante beach (Italy)** is a mix between an urban and natural beach. It can be found three detached offshore breakwaters, distributed alongshore. The physics of these structures required a 2DH model. In 1D-simulations, spurious inshoreward mass fluxes (piling-up) appeared at the rear of the structure. Two events were studied: December 2008 and March 2010. In this case, the XBEACH provided better fitness than the SBeach model. Such better skill was due to a better representation of the frontal erosion of the dunes.

The **Praia de Faro case (Portugal)** is a reflective beach that was evaluated with

three profiles under extreme conditions. Though sensibility studies, it was remarked the concept that even at the same study area the optimal parameters can be different among the three profiles. These discrepancies arise from the **overestimation of the berm erosion** and the intense formation of an **avalanching mechanism/beach scarping**. Additionally, the model did not reproduce an expected **submerged bar growth**. It was recommended to adapt the model formulation for addressing the storm effects in steep and reflective beach slopes. Nevertheless, with a proper calibration were achieved **BSS** ranging from 0.2 - 0.7, that were notably superior to the ones obtained with **LITPROF**.

The Spanish case study was the **Urban Beach of Cádiz**, that was evaluated with the XBEACH and PETRA (SMC) (IH-Cantabria, 2009) models. Three 1-D profiles were tested with a mild storm. The BSS values were superior in SMC, because the berm erosion was more accurate; though both codes provide similar values at other partitions. The mismatch was justified due to the absence of the long wave effects in the run-up computation; joint with the sediment transport processes at SMC that are relegated to a minor role due to the mild wave conditions (but the same processes would be prominent with more energetic events).

However, the modelled run-up values matched with the field campaign, denoting that the sediment transport gradient was not conditioned by overestimations of the hydrodynamic module, but for transport modelling limitations at the swash zone.

Field campaign results did not matched with simulations at **Lido di Sète (France)**. The December 2008[3] event does not match properly either with the local model (Marsouin), neither XBEACH. In one hand, the local model mismatches due to the lack of integrated processes: it does not account cross-shore processes, neither wave asymmetry, infragravity waves, run-up computation or offshore sand deposition. In the other hand, XBEACH does not have incorporated routines for the **sand bar migration under mild storms**, which is the main observed process in this event.

At **Ostende beach** and **Mariakerke** (Belgium), the 1D version of the XBEACH exhibited good results: the erosion profile at low water depths and the emerged zone is well reproduced. The average BSS with the local model (DUROSTA) was 0.45, while XBEACH skill was 0.53. However, DUROSTA provides slightly better results in profiles with "hard structures" (i.e. breakwaters). Such discrepancy happens because the XBEACH could not model short-wave reflection, hence underestimating the local scouring surrounding the breakwater, both for the real episode and another synthetic one with a 1000 years return period. Noteworthy, 2DH simulations produced better results than the 1D case, specially in cases where the breakwaters and the beach are oblique.

The **Sefton Coast** (United Kingdom) case remarked that any change of the model parameters has to be conducted systematically, without forgetting their physical meaning. The 31 March 2010 storm was used as calibration scenario; and **moderated BSS** were obtained for that event and other ones from the 2002-2008 period.

[3]Please refer to Ch. 4 for the hydrodynamic modelling and coastal impact analysis of the same storm (December 2008) at the Catalan Coast.

It was requested to revise the formulations and their possible effects under high return period events.

However, the same group showed good model agreement at **River Alt** (United Kingdom), specially on reproducing marine flooding at the hinterland. It was remarked their feasibility for delineating flooding evacuation routes. The authors reported that other models with more advanced discretization algorithms (i.e. flexible meshes) should provide "a priori" better results, but they do not. The better skill of XBEACH was justified by the implementation of littoral dynamics processes.

At **Dziwnow Spit** (Poland), the domain is represented by three profiles. The profile that did not have hard structures exhibited the best BSS results. The model was able to reproduce the erosion of the dune and beach. However, at the submerged part of the profiles, specially where a sandbar is located, the bar growth was insufficient. The deviations degenerated in a maximum BSS of 0.39.

Finally, at **Kamchia-Shkorpilovtsi Beach** (Bulgaria), another 1D model (IO-BASMM) was compared against XBEACH, leading both unsatisfactory results (null or even negative BSS values), because the first model underestimated the berm erosion whilst XBEACH overestimated it. Fortunately, as happened with the Belgian case, the 2DH approach improved the forecast: both the berm erosion and the computed run-ups matched with the post-storm measurements, despite the submerged bar was not properly modelled. Further studies and 1D analyses shown that the bidimensional processes were determinant.

2.6. A sustainable roadmap with CEWS

The interventions described in Sec. 2.4.4 span a representative vision of present and near future coastal interventions in the Study Area. The spatial scales and lifetime differ among them, but **some commonalities** can be extracted towards the design of a shared roadmap. Two complementary paradigms are proposed for that: (i) the benefits of long-term planning, based on top-down strategies and (ii) the efficiency of short-term interventions, driven by bottom-up strategies.

Identifying flexibilities and **rigidities** constitutes the first step for designing a pro-active pathway to sustainability. An adaptive plan needs to have some solid foundations (rigidities) but with enough flexibility to ensure that it will be applicable for the changing demands from climate, society or other factors. Three layers can be envisioned for developing this plan: (i) coastal archetype representing the physical substratum, (ii) climate factors incorporating climatic and event scales and (iii) social factors providing policy criteria and access to funding. The archetypes are the layer in which more rigidity exists; because it is based on the geology, sediment budget and the constraints generated by existing or planned infrastructures.

Table 2.4.: Main features of the case studies from the MICORE project

Country	Study areas	Main features	Km	D_{50}(mm)	Storm event database
Italy	*Lido di Dante - Lido di Classe*	Natural with dunes, river mouth - defended coastline, infrastructures, high touristic value, microtidal	8	0.02	Storm classification: T1, T10, 100 maximum level.
Portugal	*Praia de Faro*	Barrier islands, dunes, overwash, inlets, high touristic value, infrastructures, microtidal	8	0.5	Morphodynamic changes, impacts, hazard maps
Spain	*La Victoria - Sancti Petri*	Urban beach, high touristic value, defended coastline, infrastructures - natural sand pits with dunes, overwash, river mouths, salt wedge, touristic value, mesotidal	10	0.2	NPA-DB online, historical database
France	*Lido of Sète to Marseillan*	Low barrier island, dunes, high touristic value, defended coastline, infrastructures, micro tidal	13	0.125-0.320	Intensive field campaigns, impact observations
United Kingdom	*Dee Estuary*	Estuary zone with high occupation and hard engineering, defended coastline, infrastructures, sand dunes, tidal flats, salt wedges, high touristic value, river mouth, macrotidal	10	0.25	Radar monitoring network, historical database
Holland	*Egmond*	Nourished beach, dunes, high touristic value, mesotidal	5	0.210	Compilation of end-users information
Belgium	*Mariakerke*	Urban dissipative beach periodically nourished, infrastructures, defended coastline, dunes, high touristic value, macro tidal	3	0.214	Protected against T=1000 years storms.
Poland	*Dziwnow Spit*	Sand spit with low dunes, defended coastline, nourishment for protecting infrastructure, high touristic value, tideless.	15	0.3	Statistical storm T=100 years.
Bulgaria	*Kamchia - Shkorpilovtsi*	Open beach at the Black Sea, river mouth, touristic value, tideless.	13	0.25	Database with 52 storms and post-storm field campaigns

The **Maresme strait** has cells with lengths smaller than 2 km and a **rigid backshore** partly occupied by a railway and motorway used daily by Barcelona commuters. The costs of substituting these infrastructures limit the fan of possible adaptation options.

As a consequence, the coastal protection function gains importance because of such valuable assets and this raises the vulnerability level. **Better infrastructure attracts population** and the coastal fringe **vulnerability increases** in a feedback loop that, unless broken, will take risk to an unacceptable level in the near future under climate change.

A **long-term plan** requires setting up a **reference baseline**. In the near future (until 2040), **SLR** projections present **similar values**. At the second half of this century, however, the SLR **gradient** becomes **sharper** for the high-end scenario (**RCP 8.5**). A high-end scenario is preferred as a baseline, because it is both plausible and **conservative**. Bereft of cheap energy and natural resources, the costs of adaptation and mitigation will increase throughout time and the transition towards a low-carbon society will be difficult (Brown et al., 2013; Hinkel et al., 2014). Available resources may be allocated to further economic growth (with the possibility of reaching a dead-end at the short-term) or to a **societal transition** combining **rigid** and **flexible elements**. Choosing the first option would only be justified for lower RCPs, lowering adaptation costs (with respect to higher RCPs) at the second part of the century and resulting in **savings** that could be used for **fostering economic growth**.

Monitoring networks should provide the quantitative data required for a continuous reassessment of impacts and the effect of responses. Dynamic pathways need such information for **forecasting** and **verification** (Haasnoot et al., 2012). This constitutes the basis for uncertainty reduction in the DPSIR chain, thus providing robustness in the decision making. **Long time series** such as the Puertos del Estado and XIOM networks **verify model** projections and **sharpen** the definition of the **pathways**, integrating processes and interactions that the models cannot reproduce. In Chapters 4 and 5, in-situ observations will be compared with the proposed forecasting system.

Probabilistic projections can cope with some of the models' limitations. They can be introduced through combinations of perturbations in boundary/initial conditions and through multi-ensemble simulations (Wang et al., 2015). This probabilistic approach can serve for defining upper limits (Jevrejeva et al., 2014) or bounding the uncertainty (Muis et al., 2015). Consistency among climatic co-factors and their dependencies also enhances robustness and it can be introduced with multivariate statistical methods such as Hierarchical Archimedean Copulae (Lin-Ye et al., 2016). An example of non-stationary multivariate risk model will be shown in Ch. 6.

Local interventions for coastal sustainability are here clustered into two groups: **working with nature** (overwash enhancement at Ebro Delta) and **Quick Defence**

Measures (QDM, see Ch. 7), such as the fuse dune system at Llobregat Delta. The QDM method consists of coastal protection based on specific actions that should be deployed **prior** to **extreme events**. The interest in these interventions will grow in a changing climate, because enhanced flooding and erosion due to SLR and increases in population will raise social and economic vulnerability (Sec. 2.4.3). QDM will become more competitive, because (i) they present lower costs and impacts than conventional engineering solutions and (ii) they offer added flexibility based on local resources (Sánchez-Arcilla et al., 2015a). Such an approach, however, requires the support of an Early Warning System to predict the storm impact with enough advance time to deploy the QDM at the more vulnerable coastal sectors.

Local interventions for urgent short term problems are often in conflict with long term sustainability criteria and cannot be easily implemented by lack of a legal framework for **fast track interventions** (Gault et al., 2011). The deployment of a QDM can be forecasted 72 h prior to an extreme event and it would require about 24 h to be built. Such short term decisions should always **provide** the **flexibility** needed to deal with coastal **uncertainties** and be shared with local stakeholders to facilitate the uptake of new solutions. This is now easier than a few years back, due to the advent of more sophisticated tools for diagnosis and forecasting coastal impacts and interactions (García-León et al., 2015; Gràcia et al., 2014). Early Warning Systems fed by observational networks can forecast extreme events and associated coastal hazards (Sánchez-Arcilla et al., 2014). These tools would provide local communities with **objective information** that ensures the timely deployment of QDM or longer term proactive interventions. This would result in **lower mitigation costs** and **carbon footprint** (compared to conventional engineering solutions).

The adaptation pathway should also include a **follow-up**, to assess the efficiency of the proposed interventions and establish critical or **tipping points** in the development (Haasnoot et al., 2012). It is an essential requirement for an adaptation plan since only this information will allow a critical assessment of the positive and negative impacts of the intervention which together with its initial and maintenance costs should permit a continuous assessment of the long term consequences. The pathway should thus include an **adjustment block**, consisting of all interventions that maximise the benefit or mitigate the negative impact of past interventions. This adjustment should also incorporate a **continuous monitoring,** such as for instance would be required by artificial nourishment or vegetation, in the sense that part of the adjustment is the maintenance of those activities (Sánchez-Arcilla et al., 2017). The pathway should finally include an **educational component**, to allow a **proper interpretation** of **costs** and **benefits** at the various **time scales** and thanks to that, provides a **structured input** from **stakeholders** and the users of that coastal system.

2.7. Conclusions

This Chapter has described the general landscape of the problem that will be tackled in this dissertation: episodic coastal risk. Risk has been defined, and the different kind of coastal hazards (erosion, accumulation and flooding) as well. Special emphasis has been done on the episodic scales (the storm scale), because both the forecasting system and the interventions will aim to this scale.

The Catalan Coast landscape has been described. The main features have been highlighted: hydrodynamics, atmospheric patterns (wind, temperature and precipitation), the effects that climate change may have on the hydrodynamics (sea level rise, waves, surges, etc.) and population trends. The problem has been bounded, identifying erosion and flooding as the most relevant hazards in the study area (i.e. more than 70% of the beaches are affected).

Reactive strategies (i.e. hard works) have been the norm in coastal management. These reactive actions would be infeasible in the near future, due to sand scarcity, economic constraints and the increases of hydrodynamic drivers (waves, storminess and sea level rise). New proactive strategies have been proposed: innovative nourishments, transient dunes and detached breakwaters. However, some of these strategies need to be timely implemented, hence, forecasting is paramount. Coastal Early Warning Systems are a suitable option for addressing these hazards. It has been described the different elements of an Early Warning System and examples of international iniciatives, such as GEAS, EMMA or MICORE.

Finally, it has been addressed the place that CEWS would have in a high sustainable roadmap: (i) enforce/boost local interventions; (ii) reinforce the need for long-term continuous meteo-oceanographic monitoring by creating new services that fed from these data networks; (iii) foster the educational component about disaster risk reduction. Some challenges are also highlighted as: (i) the identification of the long-term trend of these hazards; (ii) the establishment of a follow-up plan that includes tipping points (regime shifting); (iii) a transition from deterministic to probabilistic risk forecasts, in order to bound uncertainty under such ever-changing conditions. In short, the joint contribution of long-term planning (top-down strategies) and short-term interventions (bottom-up strategies) can provide a dynamic equilibrium for the coastal zone.

3. Coastal Forecasting System: LIM-COPAS

This Chapter describes the **theoretical background** of the **Coastal Forecasting System**, termed LIM-COPAS (LIM - COastal Processes Assessment System) and its modules. Sec. 3.1 summarises the System Strategy (a broad description of the different modules and their connections); Sec. 3.2 describes the input data *(ERA-INTERIM, IBI-MFC)* and the observational networks *(Puertos del Estado, XIOM, and LIDAR)* for assessing the veracity of the different modules. Sec. 3.3 presents the different modules: Meteorological (Sec. 3.3.1); Hydrodynamic (Sec. 3.3.2); Morphodynamic (Sec. 3.3.3) and Risk (Sec. 3.3.4). Finally, the error metrics (observations vs. model outputs) and fitting criteria are enumerated in Sec. 3.4.

3.1. General System Strategy

LIM-COPAS (Fig. 3.1) is structured in four modules: (i) a meteorological unit that provides wind field forecasts that becomes the boundary conditions for a (ii) wave generation and propagation unit that reproduces ocean waves physics; such waves are the forcings for a (iii) coupled hydromorphodynamic code that models the coastal state against storm impacts. Prior and after the last module, a (iv) risk assessment module estimates the probability distribution function of monetary losses due to flooding and erosion.

The **meteorological** data derives from a downscaling performed with the **WRF** model (Skamarock et al., 2005). The ERA-INTERIM global reanalysis performed by ECMWF (see Sec. 3.2.1) is used as boundary conditions. WRF runs three two-way nested domains that span the area marked in Fig. 3.2. This discretization strategy ensures that the spatial scale among different meshes does not differ excessively. The large-scale meteorological phenomena can be well captured with the Europe domain (orange), with a spatial resolution of 27×27 km, but some local constraints (i.e. orography and pressure anomalies) need a finer discretization. Such limitation can be overcome with the other two domains, NW Mediterranean Grid (brown, 9×9 km) and Balearic Sea Grid (red, 3×3 km). The time step at the last nesting is of the order $\Delta t_{WRF} \approx 10\ s$.

Wind forecasts at 10 meters are used as input information for the **SWAN wave model** (Booij et al., 1999), a third-generation spectral model that generates and propagates ocean waves. Wind information is updated each 20 minutes. Two meshes

are proposed for the analysis held in Ch. 5: (i) a regional one that spans the NW Mediterranean Sea (discontinuous purple line in Fig. 3.2) with a spatial resolution of 5×5 km; (ii) a nested one that covers the Balearic Sea, with a resolution of 2×2 km (green line). The first mesh deals with wave generation and deep-water propagation, whereas the second one models the wave fields from the deep-waters to the continental shelf. Wave-current interaction can lead to changes in wave refraction, frequency shifting and wave dissipation (Jordá et al., 2007) at the continental shelf. The IBI-MFC (see Sec. 3.2.3) currents and sea level fields are used as input in the local domain with hourly updating. The wave model is run as non-stationary with a time step of $\Delta t_{SWN} \approx 10\ min$, in order to avoid numerical instabilities and diffusion.

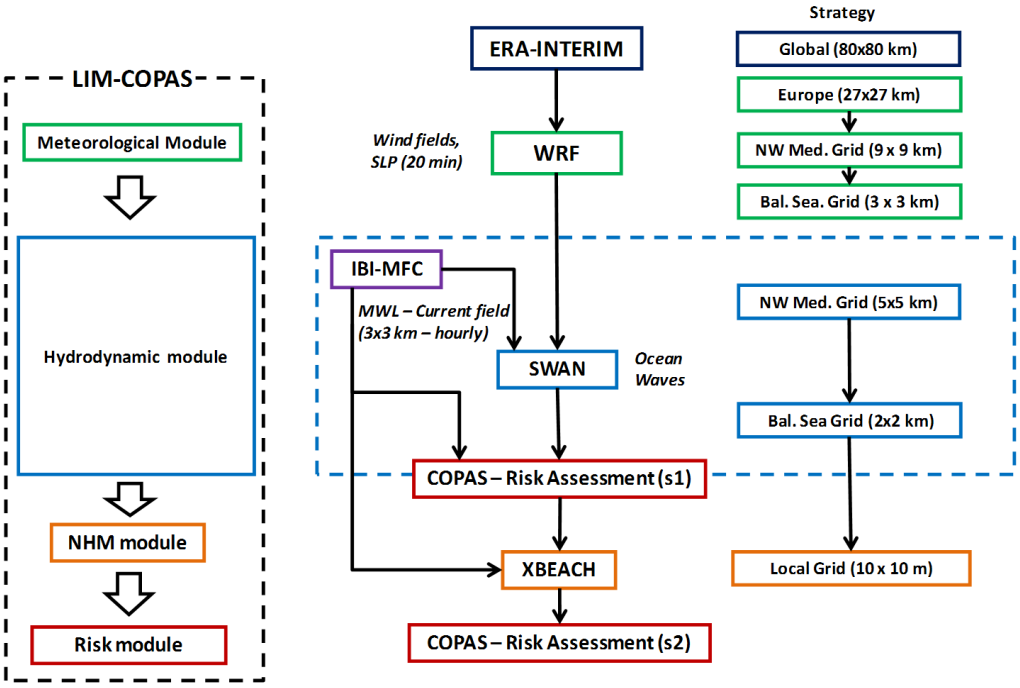

Figure 3.1.: Flowchart of **LIM-COPAS** and its different modules. At the left, the simplified hierarchical scheme. At the center, the different numerical models and dataset involved. At the right, the proposed nesting strategy. **Legend:** green (meteorological), blue (hydrodynamic), orange (morphodynamic) and red (risk module).

SWAN provides bidimensional wave spectrum and statistics every 20 mins. 2D Wave spectrum (frequency-direction) and IBI-MFC sea level fields constitutes the boundary conditions for the **morphodynamic module** (**XBEACH**, Roelvink et al. (2009)). XBEACH is a 2DH code that can reproduce short and long wave propagation, nearshore circulation and sediment transport (Sec. 3.3.3). The spatial resolution is specific to each case study, but the general setting is as follows: (i) the computational meshes are irregular (different gridsizes at the cross-shore dimension

(C-S)) and curvilinear; (ii) from the emerged to the surf zone, the cross-shore resolution is 5 m; (iii) from the surf zone to the offshore boundary it gradually varies from 5 to 20 meters; (iv) the alongshore dimension is kept as constant (computational domains with alongshore boundaries lower than 1 km have gridsizes of around 10-20 m; whereas those ones longer than 1 km have an approximate resolution of 20-30 m).

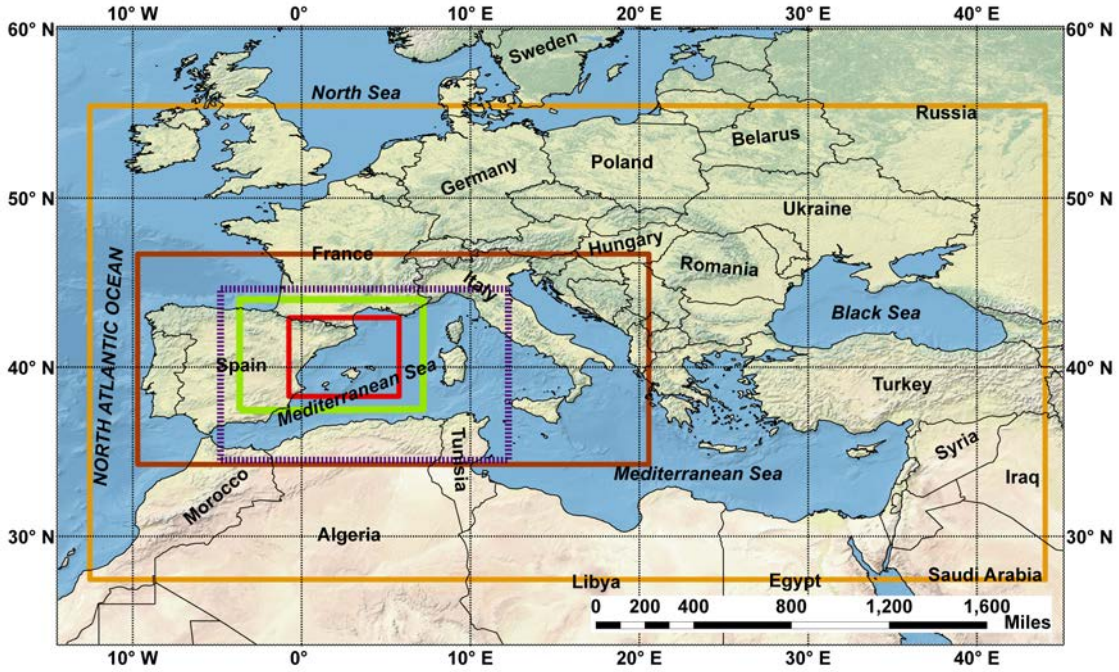

Figure 3.2.: Nesting strategy for the wave and meteorological model that will be implemented in Chapter 5. For the meteorological model (WRF), a two-way nesting has been used with three levels: (1) European grid (marked in orange) with a spatial resolution of 27×27 km; (2) Western Mediterranean grid (marked in brown), with a resolution of 9×9 km and a (3) NW Mediterranean grid (3×3 km). The last grid level for almost all simulations has been the the domain marked in red, except for the January 2017 episode that has been the green one. For the wave model (SWAN), a one-way nesting has been used at two levels: (1) Western Mediterranean grid (discontinuous purple line) with (5×5 km); (2) NW Mediterranean grid (2×2 km), marked in red.

Despite that the morphodynamic module can provide accurate forecasts, the main limitation is the required computational time, that can be excessive for relatively reduced areas. The computational time can be between 30-90 mins with parallel computing (SIMO, 2015), becoming an important bottleneck in the forecasting chain. Then, with the aim of fast scanning wider area, a probabilistic risk module is used (Sec. 3.3.4). Coastal risk is estimated in a simplified approach that considers

non-stationary multivariate dependence and requires low computational cost. Note that the training dataset comes from XBEACH model outputs (see Ch. 6).

All these modules provide highly detailed descriptions (at spatio-temporal scale) of the different processes. However, their direct application for coastal management requires a post-analysis (Risk assessment - s2) that integrates these forecasts into parameters that decision makers can translate into action. For instance, **probability** and/or uncertainty that a **cost** will **surpass** a **certain monetary quantity**.

This **information** has to be **communicated** to a set of **institutions**. Hence, the institutions proposed in this dissertation for the **dissemination, communication and response capacity** (elements **3** and **4** of an **EWS**, as exposed in the proposed definition in the Sec. 2.5.1.1) are: *(i) Direcció General de Protecció Civil; (ii) Direcció General de Prevenció, Extinció d'Incendis i Salvaments; (iii) Sistema de Emergencias Médicas (SEM); (iv) Policia de la Generalitat (Mossos d'Esquadra); (v) Agencia Catalana de l'Aigua; (vi) Federació de Municipis de Catalunya; (vii) Associació Catalana de Municipis; (viii) Diputación de Barcelona, Girona y Tarragona; (ix) Federación Catalana de Salvamento y Socorrismo; (x) Asociación de Empresas Catalanas de Salvamento Acuático; (xi) Cruz Roja de Cataluña.*

The connection among the different elements and this dissertation can be checked at Fig. 1.2.

3.2. Datasets

3.2.1. ERA-INTERIM

Testing a CEWS requires to verify how the system would provide alarms to previous events. Hindcast and reanalysis datasets are necessary for reproducing accurate weather conditions at a particular past time. **ERA-INTERIM** (Berrisford et al., 2011) is a **global reanalysis dataset** produced by the European Consortium for Medium Range Weather Forecasting (ECMWF). The temporal coverage ranges from **1979** to the **present day**. The dataset is based on model outputs that are consistent with assimilated observations via a 2006 release of the Integrated Forecast System (IFS - Cy31r2). The system includes a 4-D variational analysis (4D-Var) with a 12-hour analysis window (Dee et al. (2011)). The horizontal resolution is approximately 80 km (T255 spectral) with 60 vertical levels from the surface up to 0.1 hPa.

Analyses are available every **6 h** (00:00, 06:00, 12:00 and 18:00 h UTC) with outputs for **surface** and **pressure level** parameters (velocity, temperature, pressure fields). ERA-INTERIM has been used extensively in the Mediterranean Sea for analysing climatic patterns, climate processes and meteoceanographic related products.

3.2.2. Meteoceanographic observations: Puertos del Estado and XIOM networks

Puertos del Estado (PdE) (1992 - present day) network is a meteo - oceanographic network that spans the whole Spanish coast. Three sub-networks have been used in this dissertation (Ch. 5-7): (i) REDEXT that consists of wave buoys deployed at deep waters; (ii) REDCOS whose aim is to complement REDEXT at places that have special importance for the development of harbour activities and / or for the validation of wave models; and (iii) REDMAR that uses tide gauges for measuring the sea level within the marinas.

The position of the selected observational points from the PdE network can be checked in Fig.2.1: Barcelona coastal buoy (BCN-REDCOS), located at 68m water depth; Tarragona deep water buoy (TGN-REDEXT), at 688m water depth; Begur Cape (BEGUR-REDEXT), at 1200m water depth; Mahon (MAH-REDEXT), at 300m water depth; Valencia (VAL-REDEXT), at 260m water depth; Dragonera (DRAG-REDEXT), at 135m water depth; Barcelona harbour tidal gauge (BCN-T,REDMAR) and Tarragona harbour tidal gauge (TGN-T,REDMAR). The sampling time for the buoys is 1 hour, whereas for the tidal gauge the frequency is 5 minutes. The wave buoys provide the main meteorological (u_{10}) and wave statistics ($H_s, T_p, WDIR$) for validating the meteorological and hydrodynamic module, respectively. The tidal gauges provides the total sea level time series and their decomposition as tidal constituents and storm surge.

XIOM (Xarxa d'Instrumentació Oceanogràfica i Meteorològica, 1984 - 2013) was a network for oceanographic and coastal meteorological measurements owned by the Catalan Government. The network consisted in the following list of equipment deployed at the NW Mediterranean Sea: four wave buoys (Cap Tortosa (TORT), Delta Llobregat (LLOB), Blanes (BLANES) and Roses (ROSES) in Fig.2.1), two sea level gauges (Sant Carles Harbour and Deltebre, at the Ebro Delta) and three meteorological stations (Ampolla Harbour, Sant Carles Harbour and Deltebre; all three at the Ebro Delta).

Apart from the monitoring equipment, extensive data quality control and interpretation was also carried out by the XIOM staff. A review of its main features and applications can be found in (Bolaños et al., 2009). Observations from this network has been used in Ch. 4, in particular the following buoys: Cape Tortosa buoy, located at 60m water depth; Delta Llobregat buoy, at 45m water depth and Blanes buoy, at 65m water depth. All three have a sampling of 20 minutes every 1 hour. Wave statistics ($H_s, T_p, WDIR$) constitute the main statistics that are used for validating the hydrodynamic module. Note that XIOM buoy network was deployed at intermediate waters. Hence, these observations were valuable due to its representativeness of the local physical processes that cannot be measured with deep water buoys. This oceanographic network complemented the PdE network, because they provided information in places where PdE did not have coverage.

Table 3.1.: Water depth (in meters) of the meteo-oceanographic buoys used in this dissertation. ***Legend:*** *PdE (Puertos del Estado network) and XIOM (Xarxa d'Instrumentació Oceanogràfica i Meteorològica).*

Buoy	Depth (m)
Barcelona (PdE)	68
Tarragona (PdE)	688
Begur (PdE)	1200
Dragonera (PdE)	135
Mahón (PdE)	300
Valencia (PdE)	260
Blanes (XIOM)	65
Llobregat (XIOM)	45
Cape Tortosa (XIOM)	60

3.2.3. IBI-MFC

Wave-current interaction can have a role during extreme conditions at local scales, specially in the continental shelf (Jordá et al., 2007; Grifoll et al., 2016). The CEWS presented in this dissertation does not have a circulation and sea level model, but the last nested mesh of the wave model (Balearic Sea) uses circulation fields and sea levels as input. The Copernicus IBI-MFC (Iberia-Biscay-Ireland Monitoring and Forecasting Centre, Sotillo et al. (2015)) uses a 3D baroclinic hydrodynamic model based on the Nucleus for European Modelling of the Ocean - Ocean Dynamics Core (NEMO, Madec (2008)). It assumes hydrostatic equilibrium and Boussinesq approximation, and uses a non-linear split explicit free surface to simulate fast external gravity waves such as tidal motions.

This modelling framework includes high-frequency processes required to characterize regional-scale marine processes. The horizontal resolution is 1/36° (circa 2-3 km) that leads to solve a significant part of the internal wave spectrum and the sub-mesoscale-regimes. The time frequency of the outputs is hourly. The forcings are 3-hourly atmospheric fields (10-m wind, surface pressure, 2-m air temperature, relative humidity, precipitations, shortwave and longwave radiative fluxes) from the ECMWF. Lateral open boundary data (temperature, salinity, velocities and sea level) are interpolated from the outputs of the Copernicus GLOBAL eddy resolving system, plus an explicit representation of the main tidal harmonics. A data-assimilation module SAM2 (Lellouche et al., 2013), based on a reduced-order

Kalman filter, allows the model to be constrained in a multivariate way with sea temperature, salinity measurements and sea level anomalies.

3.2.4. LIDAR and bathymetry

LIDAR (Light Detection and Ranging) is a remote-sensing optical technology that measures the distance from a sender point towards an object or surface through a pulse laser. The distance to the object/surface can be computed with the time lag from the laser light emission until its reflection. This system can obtain a terrain elevation cloud via an airborne scanner laser. This scanning requires the combination of two movements: (i) a longitudinal movement from the airplane trajectory and (ii) a transversal one with a mobile mirror that deviates the light emitted by the scanner.

The Institut Cartogràfic i Geològic de Catalunya (ICGC) gathers periodically LIDAR data via an airbone scanner laser. The coastal fringe is one of the main addressed areas due to its dynamic nature. ICGC also filters the raw data, analyses it and create a set of subproducts such as high resolution Digital Elevation Models (DEMs).

In this dissertation, the **emerged part** of all domains at the Morphodynamic module (see Figs. A.1,A.2 and A.3) comes from LIDAR data. The emerged part at domains from 1 to 4 were derived directly from LIDAR observations (see Tab. B.1), whereas the rest were extracted by 2×2 m subproduct grids that were generated by ICGC.

The calibration of a domain in the Morphodynamic module requires to hindcast storms and to compare the post-storm predicted versus observations. LIDAR becomes a cost-effective solution for such calibration, specially in those cases that there exist pre and post-storm information. Pre-post storm information was available for a limited subset of beaches during the December 2008 storm. This information is used as reference for calibrating and assessing the module performance in Ch. 4.

The bathymetry for the wave model comes from the GEBCO (GEB-2008) dataset which has a resolution of circa 1 km. This resolution was not enough for the Morphodynamic module. Hence, recent bathymetric charts were digitized and adapted to the LIDAR observations for the sake of consistency.

3.3. Modules description

3.3.1. Meteorological module

ERA-INTERIM re-analysis are delivered at a spatial and temporal resolution that it is not enough to capture properly the local features of a storm at the Catalan Coast. As explained at the Study Area (Sec. 2.4), the Catalan Coast is constrained by a set of mountain chains that channels wind fluxes in a limited directional range (Bolaños et al., 2009; Grifoll et al., 2015). ERA-INTERIM current resolution does

not solve these constraints and can lead to smooth forecasts. Hence, downscaling is required. The mesoscale WRF model (Skamarock et al., 2005) has been used for downscaling the ERA-INTERIM hindcasts. This solver integrates the **compressible, nonhydrostatic Euler equations**. Four basic conservation principles form a coupled set of relations:

1. Conservation of **mass** (Eq. 3.3.14).
2. Conservation of **heat** (Eq. 3.3.20).
3. Conservation of **motion** (Eqs. 3.3.15,3.3.16,3.3.17).
4. Conservation of **water**, **other gaseous** and aerosol materials (Eq. 3.3.22).

The WRF-ARW equations are formulated using a terrain-following hydrostatic-pressure vertical coordinate denoted by η_{mt} (Eq. 3.3.1):

$$\eta_{mt} = \left(p_{dh,mt} - p_{dht,mt}\right)/\mu_{d,mt} \tag{3.3.1}$$

Where $\mu_{d,mt}$ (Eq. 3.3.2) represents the mass of the dry air in the column:

$$\mu_{d,mt} = p_{dhs,mt} - p_{dht,mt} \tag{3.3.2}$$

And $p_{dh,mt}$, $p_{dhs,mt}$, $p_{dht,mt}$ represent the hydrostatic pressure of the dry atmosphere and the hydrostatic pressure at the surface and the top of the dry atmosphere, respectively. $\mu_{d,mt}\,(x,y)$ represents the mass per unit area within the column in the model domain at (x,y), the appropriate flux form variables are (Eq. 3.3.3,3.3.4,3.3.5,3.3.6,3.3.7):

$$U_{mt} = \mu_{d,mt} u_{mt}/m_{y,mt} \tag{3.3.3}$$

$$V_{mt} = \mu_{d,mt} v_{mt}/m_{x,mt} \tag{3.3.4}$$

$$W_{mt} = \mu_{d,mt} w_{mt}/m_{y,mt} \tag{3.3.5}$$

$$\Omega_{mt} = \mu_{d,mt} \eta_{mt}/m_{y,mt} \tag{3.3.6}$$

$$\Theta_{mt} = \mu_{d,mt} \theta_{mt} \tag{3.3.7}$$

$$Q_{m,mt} = \mu_{d,mt} q_{m,mt} \tag{3.3.8}$$

Where map scale factors $m_{x.mt}$ and $m_{y,mt}$ (Eq. 3.3.9) are defined as the ratio of the distance in computational space to the corresponding distance on the earth's surface:

$$(m_{x,mt}, m_{y,mt}) = \frac{(\Delta x, \Delta y)}{distance\ on\ the\ earth} \tag{3.3.9}$$

Where p_{mt} is the atmospheric pressure field, ϕ_{mt} is the geopotential ($\phi_{mt} = gz$) and $\alpha_{d,mt}$ is the inverse density of the dry air ($\alpha_{d,mt} = 1/\rho_{d,mt}$). These three terms can be decomposed in two parts:$\overline{(\cdot)}\,(\overline{z})$ is the mean operator and $(\cdot)^{'}$ is the instantaneous (Eqs. 3.3.10,3.3.11 ,3.3.12 and 3.3.13).

$$p_{mt} = \overline{p}_{mt}\,(\overline{z}) + p^{'}_{mt} \tag{3.3.10}$$

$$\phi_{mt} = \overline{\phi}_{amt}\,(\overline{z}) + \phi^{'}_{mt} \tag{3.3.11}$$

$$\alpha_{d,mt} = \overline{\alpha}_{d,mt}\,(\overline{z}) + \alpha^{'}_{d,mt} \tag{3.3.12}$$

$$\mu_{d,mt} = \overline{\mu}_{d,mt}\,(\overline{z}) + \mu^{'}_{d,mt} \tag{3.3.13}$$

Once defined these variables, the moist Euler equations can be expressed as Eq.3.3.14 for **mass conservation** and Eqs.3.3.15,3.3.16,3.3.17 for the **flux-form Euler momentum equations** at **x**, **y** and **z** respectively:

$$\partial_t \mu^{'}_{d,mt} + m_{x,mt} m_{y,mt} \left[\partial_x U_{mt} + \partial_y V_{mt}\right] + m_{y,mt} \partial_{\eta_{mt}} \Omega_{mt} = 0 \tag{3.3.14}$$

$$\begin{gathered} \partial_t U_{mt} + m_{x,mt} \left[\partial_x \left(U_{mt} u_{mt}\right) + \partial_y \left(V_{mt} u_{mt}\right)\right] \\ + \partial_{\eta_a} \left(\Omega_{mt} u_{mt}\right) + \left(m_{x,mt}/m_{y,mt}\right) \left(\alpha_{mt}/\alpha_{d,mt}\right) \\ \left[\mu_{d,mt} \left(\partial_x \phi^{'}_{mt} + \alpha_{d,mt} \partial_x p^{'}_{mt} + \alpha^{'}_{d,mt} \partial_x \overline{p}_{mt}\right) + \partial_x \phi_{mt} \left(\partial_{\eta_{mt}} p^{'}_{mt} - \mu^{'}_{d,mt}\right)\right] \\ = F_{U,mt} \end{gathered} \tag{3.3.15}$$

$$\begin{gathered} \partial_t V_{mt} + m_{y,mt} \left[\partial_x \left(U_{mt} v_{mt}\right) + \partial_y \left(V_{mt} v_{mt}\right)\right] \\ + \left(m_{y,mt}/m_{x,mt}\right) \partial_{\eta_{mt}} \left(\Omega_{mt} v_{mt}\right) + \left(m_{y,mt}/m_{x,mt}\right) \left(\alpha_{mt}/\alpha_{d,mt}\right) \\ \left[\mu_{d,mt} \left(\partial_y \phi^{'}_{mt} + \alpha_{d,mt} \partial_y p^{'}_{mt} + \alpha^{'}_{d,mt} \partial_y \overline{p}_{mt}\right) + \partial_y \phi_{mt} \left(\partial_{\eta_a} p^{'}_{mt} - \mu^{'}_{d,mt}\right)\right] \\ = F_{V,mt} \end{gathered} \tag{3.3.16}$$

$$\begin{gathered} \partial_t W_{mt} + \left(m_{x,mt} m_{y,mt}/m_{y,mt}\right) \left[\partial_x \left(U_{mt} w_{mt}\right) + \partial_y \left(V_{mt} w_{mt}\right)\right] \\ + \partial_{\eta_{mt}} \left(\Omega_{mt} w_{mt}\right) - m^{-1}_{y,mt} g \left(\alpha_{mt}/\alpha_{d,mt}\right) \\ \left[\partial_{\eta_{mt}} p^{'}_{mt} - \overline{\mu}_{d,mt} \left(q_{v,mt} + q_{c,mt} + q_{r,mt}\right)\right] + m^{-1}_{y,mt} \mu^{'}_{d,mt} g = F_{W,mt} \end{gathered} \tag{3.3.17}$$

The right-hand-side (RHS) terms $F_{U,mt}$,$F_{V,mt}$, $F_{W,mt}$,$F_{\theta,mt}$and $F_{Q_m,mt}$ represent forcing terms arising from model physics, turbulent mixing, projections and the earth's rotation. The inverse density of air, α_{mt} (Eq.3.3.18), requires the q_* mixing ratios (mass per mass of dry air) such as water vapour ($q_{v,mt}$), cloud ($q_{c,mt}$), rain ($q_{r,mt}$), ice($q_{i,mt}$), etc.

$$\alpha_{mt} = \alpha_{d,mt} \left(1 + q_{v,mt} + q_{c,mt} + q_{r,mt} + q_{i,mt} + ...\right)^{-1} \tag{3.3.18}$$

The **geopotential equation** (Eq.3.3.19) is used instead of prognostic pressure equation, because geopotential is a conserved variable. Additionally, the pressure equation together with the conservation equation for the potential temperature are linearly dependent:

$$\begin{gathered} \partial_t \phi'_{mt} + \mu^{-1}_{d,mt} \\ \left[m_{x,mt} m_{y,mt} \left(U_{mt} \partial_x \phi_{mt} + V_{mt} \partial_y \phi_{mt}\right) + m_{y,mt} \Omega_{mt} \partial_{\eta_{mt}} \phi_{mt} - m_{y,mt} g W_{mt}\right] = 0 \end{gathered} \tag{3.3.19}$$

The **potential temperature** can be modelled through a conservation equation (Eq.3.3.20):

$$\begin{gathered} \partial_t \Theta_{mt} + m_{x,mt} m_{y,mt} \left[\partial_x \left(U_{mt} \theta_{mt}\right) + \partial_y \left(V_{mt} \theta_{mt}\right)\right] \\ + m_{y,mt} \partial_{\eta_{mt}} \left(\Omega_{mt} \theta_{mt}\right) = F_{\theta,mt} \end{gathered} \tag{3.3.20}$$

Where $\theta_{m,mt}$ is the moist temperature potential, that can be approximated with Eq.3.3.21:

$$\theta_{m,mt} = \theta_{mt} \left(1 + \left(R_{v,mt}/R_{d,mt}\right) q_{v,mt}\right) \approx \theta_{mt} \left(1 + 1.61 q_{v,mt}\right) \tag{3.3.21}$$

The other included conservation equations deals with scalars such as **water**, other **gaseous and aerosol materials** (Eq.3.3.22):

$$\begin{gathered} \partial_t Q_{m,mt} + m_{x,mt} m_{y,mt} \left[\partial_x \left(U_{mt} q_{m,mt}\right) + \partial_y \left(V_{mt} q_{m,mt}\right)\right] \\ + m_{y,mt} \partial_{\eta_{mt}} \left(\Omega_{mt} q_{m,mt}\right) = F_{Q_m,mt} \end{gathered} \tag{3.3.22}$$

Where $Q_{m,mt}$ can be any scalar. Water must be solved with three equations (one per state: solid, liquid and vapour mass of water to the mass of air in the same volume). Despite the resolution of the water conservation equations are analogous to other scalars equations, in literature they are usually treated as different ones. The source-sink terms ($F_{Q_m,mt}$) for the water have more importance in mesoscale models, and tend to be more complex.

The hydrostatic balance (Eq.3.3.23) assumes that the influence of the rotation of the Earth on the vertical acceleration is inconsequential for any reasonable velocity:

$$\partial_{\eta,mt} \phi'_{mt} \;=\; -\overline{\mu}_{d,mt} \alpha'_{d,mt} - \alpha_{d,mt} \mu'_{d,mt} \tag{3.3.23}$$

Finally, the equation of state is needed for closure (Eq.3.3.24) (diagnostic relation for the full pressure, vapour plus dry air):

$$p_{mt} = p_{0,mt} \left(R_{d,mt} \theta_{m,mt} / p_{0,mt} \alpha_{d,mt} \right)^{\gamma_{mt}} \tag{3.3.24}$$

Where $R_{d,mt}$ is the gas constant for dry air and $p_{0,mt}$ is a reference pressure (usually 10^5 Pascals). The remaining physical constants are: (i) $\gamma_{mt} = c_{p,mt}/c_{v,mt}$ as the ratio of the heat capacities for dry air; (ii) the specific heat of dry air at constant pressure, $c_{p,mt} = 7 \times R_{d,mt}/2$ and (iii) the specific heat of dry air at constant volume, $c_{v,mt} = c_{p,mt} - R_{d,mt}$.

The outputs of the model span a wide range of meteorological variables. The proposed CEWS (Fig.3.1) uses the **wind fields** at 10-m from the sea surface (u_{10}).

3.3.2. Hydrodynamic module

The **SWAN** model is a third-generation numerical model whose aim is to obtain realistic estimations of the nearshore wave parameters due to **wind**, **currents** and **bathymetry**. The model solves the action balance equation with the associated source and sink terms, without a priori *no restriction* with the wave spectra. The energy spectrum or spectral energy $E(\sigma, \theta)$ contains all the information about the frequency (σ) and propagation direction (θ) distribution.

The energy balance equation (Eq.3.3.25) assumes that the spectral energy evolution is equal to the sum of energy sources and sinks (S_{tot}). In case a current field is included as boundary condition, the spectral energy is non-conservative, thus this magnitude has to be substituted by the action density $A = E/\sigma$ concept (Holthuijsen et al., 1993). Therefore, the evolution of action density A can be described through the four components at the left of the balance (Eq.3.3.25), that establish the variation of A in the four domains of definition (from left-to-right): the **time component**, the **space**, the **frequency shift** and the **wave propagation direction**.

$$\underbrace{\frac{\partial A}{\partial t}}_{time} + \underbrace{\nabla_{\vec{x}} \cdot \left[\left(\vec{c_g} + \vec{U} \right) A \right]}_{space} + \underbrace{\frac{\partial c_\sigma A}{\partial \sigma}}_{frequency} + \underbrace{\frac{\partial c_{\theta_w} A}{\partial \theta_w}}_{direction} = \underbrace{\frac{S_{tot}}{\sigma}}_{source-sink} \tag{3.3.25}$$

In the other hand, the sources and sink include the physical processes of wave generation, wave dissipation and non-linear wave interactions. In the SWAN model, these processes are parametrized in a set of different formulations that the user can choose.

The **wave generation** is the phenomena that transfers the wind momentum to the waves. In SWAN, such process is parameterized with two mechanics: (i) linear resonance mechanism (Phillips, 1957) and (ii) exponential feedback mechanism (Miles, 1957). Consequently, the wave generation can be defined through the sum of the

linear and exponential term (Eq. 3.3.26):

$$S_{in}(\sigma, \theta_w) = A_{gen} + B_{gen} E(\sigma, \theta_w) \tag{3.3.26}$$

Where A_{gen} and B_{gen} depend on the wave frequency and direction, plus the wind magnitude and direction. The SWAN model computes the A_{gen} term with Cavaleri and Malanotte-Rizzoli (1981) expression. In this dissertation, it has been considered $A_{gen} = 0$ because this term does not exhibit significant performance in the estimation of the integrated wave parameters, as detailed in Alomar (2012). For the B_{gen} term, it is possible to use two formulations. The first one is the Komen et al. (1984) expression, that considers the **velocity friction induced by wind**. The second one is the Janssen (1991) formula that takes into account explicitly the wind-wave interaction by considering the physical processes in the planetary boundary layer and the length of roughness at the free-surface. In this dissertation it has been used the **Janssen's expression**, because the wave integrated parameters exhibit **fewer subpredictions** (Alomar, 2012; Pallarés et al., 2014). In the same publications, it can also be found the local model adjustments.

The **wave dissipation energy** can be modelled with three formulations: the **whitecapping dissipation**, the **bottom friction** and the **wave depth-induced breaking**. The whitecapping is controlled basically by the wave steepness. The SWAN model uses the formulated based on the pulse model developed by Hasselmann (1974), where the coefficients are estimated with the fully developed wave energy balance closure. That implies that the whitecapping dissipation depends on the selected formula for wave generation.

The interaction between the waves and the water depth can be defined as **bottom friction** phenomena that can be parameterized in SWAN with: (i) the empirical JONSWAP model (Hasselmann et al., 1973), (ii) drag force formulation (Collins, 1972) and the (iii) viscosity model (Madsen et al., 1988). The **depth-induced wave breaking** is parameterized with the Battjes and Janssen (1978) expression. In the SWAN computational domain of this dissertation, waves are not propagated towards its breaking, therefore, it is not required to consider this expression.

Finally, the non-linear interactions describe the phenomena where the wave trains interact and exchange energy, thus redistributing around the spectra. In deep and intermediate waters, the linear interactions of 4-wave groups (quadruplets) are predominant, whereas in shallow waters, the 3-wave groups (triads) are more important. In SWAN, the quadruplets are approximated with the **Discrete Interaction Approximation (DIA)** (Hasselmann et al., 1985) and the triads with the **Lumped Triad Approximation (LTA)** (Eldeberky and Battjes, 1995).

The numerical scheme in SWAN is based in implicit methods that exhibit robustness while requiring relatively long time steps for high resolution simulations.

3.3.3. Morphodynamic module

The **XBEACH** model (Roelvink et al., 2009) comprises a complex numerical model that encloses the coastal processes that happen under extreme conditions, specially between the wave breaking zone and the emerged part of the beach, thus reproducing the processes in a 2DH domain (depth-averaged bidimensional flux). The system is divided into two coupled blocks: the **hydrodynamic** and the **morphodynamic block** (Figure 3.3).

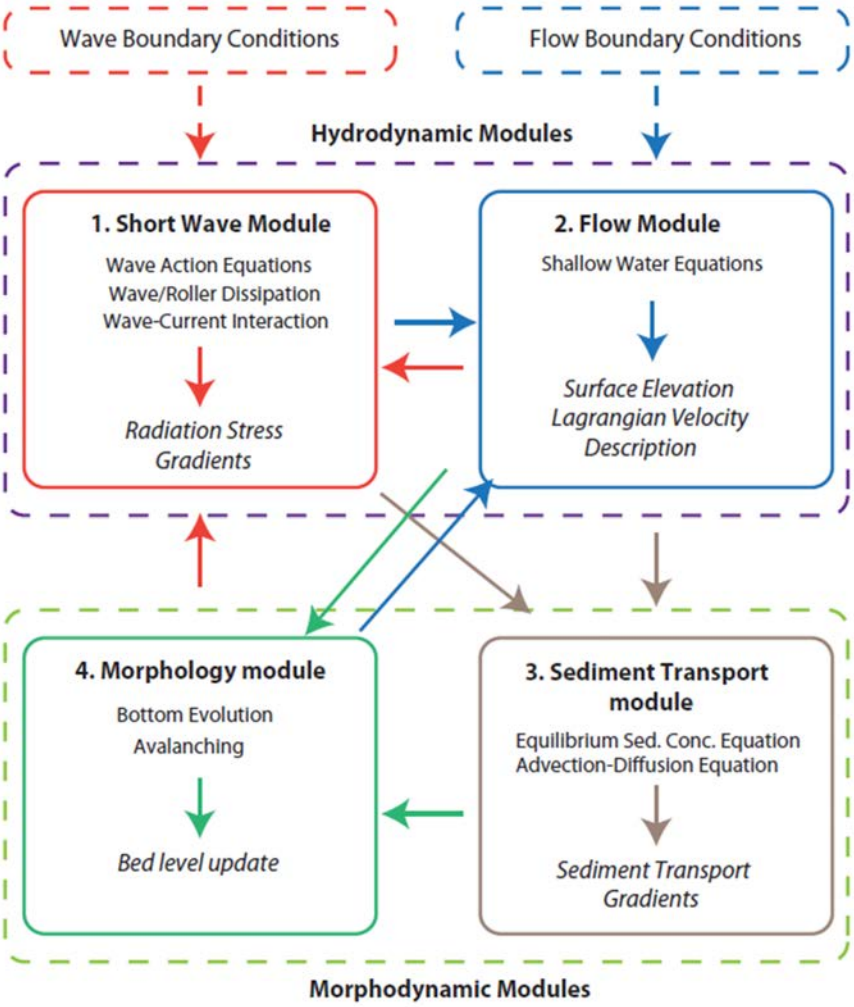

Figure 3.3.: Flowchart of the different internal modules of the XBEACH model.

First, the short waves are computed with the wave action balance (Holthuijsen et al., 1993) at a wave group time scale (propagation). Given a threshold, the effect of the waves breaking at shallow water conditions is computed with a roller equation balance (Stive and Dingemans, 1984).

The obtained wave forces, which varies at a wave group scale, act as a source term in the non-linear shallow water equations. The wave mass flux contributes to the long wave movements. **Mean offshore fluxes** (undertow) are also taken into account.

Once the hydrodynamic fields are obtained, the morphodynamic module starts. For this dissertation, this is based on van Rijn (2007) formulation for the equilibrium of the sediment concentration, then acting on the source term for the advection-diffusion equations (Galapatti, 1983).

Finally, the bed-update is computed through **sediment transport gradients**. Therefore, the new bathymetry has an effect on wave action, currents and littoral current for the next time step, as a consequence of the feedback of the algorithm.

3.3.3.1. Wave action module

The XBEACH (Roelvink et al., 2009) model solves the wave action balance (Eq.3.3.27) at a wave group time scale. Short wave action is considered, despite the frequency distribution is reduced to a **representative peak frequency**.

$$\frac{\partial A}{\partial t} + \frac{\partial c_x A}{\partial x} + \frac{\partial c_y A}{\partial y} + \frac{\partial c_{\theta_w} A}{\partial \theta_w} = -\frac{D_{waves}}{\sigma} \tag{3.3.27}$$

Considering $A(x, y, t, \theta)$ (Eq.3.3.28) as the wave action density:

$$A(x, y, t, \theta_w) = \frac{S_w(x, y, t, \theta_w)}{\sigma(x, y, t)} \tag{3.3.28}$$

Where θ represents the wave incidence angle with respect the x-axis. S_w represents the wave energy density for each directional sector and σ is the intrinsic wave frequency. The wave propagation velocities are c_x and c_y , respectively. The group celerity c_g is obtained through linear wave theory. In the other hand, c_θ corresponds to the propagation velocity at the θ space.

The threshold which determines whether a wave group is breaking and its associated breaking mode, it is modelled with specific wave breaking formulations. In this dissertation, it has been used a modified version of the Roelvink's **wave breaking** model(Roelvink, 1993):

$$D_b = \frac{\alpha}{4}\rho_w g f_m \frac{H_{rms}^3}{h} \tag{3.3.29}$$

$$\overline{D_{waves}} = P_b D_b = \left(1 - exp\left(-\left(\frac{H_{rms}}{\gamma_{br} h}\right)^{n_{Rvk}}\right)\right)\frac{\alpha}{4}\rho_w g f_m \frac{H_{rms}^3}{h} \tag{3.3.30}$$

Where, ρ is the water density. The variables are $\alpha = \mathcal{O}(1)$,γ and the exponent n are calibration parameters.
The total wave dissipation $\bar{D}_w$ is proportionally distributed along the wave directions. The source term of Eq.3.3.27 is determined from the Eq. 3.3.31:

$$D_{waves}(x,y,\theta) = \frac{S_w(x,y,\theta)}{E_w(x,y)} \bar{D}_{waves}(x,y,t) \tag{3.3.31}$$

Bottom friction dissipation can be modelled with the Eq.3.3.32:

$$D_f = \frac{2}{3}\rho\pi f_w \left(\frac{\pi H}{T_{rep} sin(kh)}\right)^3 \tag{3.3.32}$$

Where f_w is a calibration parameter that has null value as a default, but in this dissertation it is used as a tuning parameter.
Once obtained the wave action spatial distribution (wave energy), the radiation stresses are obtained through linear wave theory:

$$\begin{cases} S_{xx,waves}(x,y,t) = \int \left(\frac{c_g}{c}(1+cos^2\theta_w) - \frac{1}{2}\right) S_w d\theta_w \\ S_{xy,waves}(x,y,t) = S_{yx,w} = \int sin\theta_w cos\theta_w \left(\frac{c_g}{c} S_w\right) d\theta_w \\ S_{yy,waves}(x,y,t) = \int \left(\frac{c_g}{c}(1+sin^2\theta_w) - \frac{1}{2}\right) S_w d\theta_w \end{cases} \tag{3.3.33}$$

XBEACH includes a **roller energy balance** with the aim of **redistribute the energy once the waves onset breaking**. Analogous to Eq.3.3.27, the directional distribution of the wave action density is considered, but the frequency distribution is limited to a representative peak frequency. Energy dissipation D_{roller} is used as a source term.

$$\frac{\partial S_r}{\partial t} + \frac{\partial c_x S_r}{\partial x} + \frac{\partial c_y S_r}{\partial y} + \frac{\partial c_{\theta_w} S_r}{\partial \theta_w} = -D_{roller} \tag{3.3.34}$$

Where the roller energy for each directional sector is represented by $S_r(x,y,t,\theta_w)$. The total roller dissipation $\left(\overline{D_{roller}}\right)$ is parametrized using Reniers et al. (2004b) formula (Eq.3.3.35):

$$\overline{D_{roller}} = \frac{2gsin(\beta_{roller}) E_{roller}}{c_w} \tag{3.3.35}$$

Then, applying a similar concept to the wave action balance, the total energy dissi-

pation $\overline{D_r}$ is proportional distribution spanning all the wave directions (Eq.3.3.36):

$$D_{roller}\left(x,y,t,\theta_w\right)=\frac{S_r\left(x,y,t,\theta_w\right)}{E_r\left(x,y,t\right)}\overline{D_{roller}}\left(x,y,t\right) \tag{3.3.36}$$

Roller contribution in the radiation stress tensor is determined by Eq.3.3.37:

$$\begin{cases} S_{xx,roller}\left(x,y,t\right)=\int\cos^2\theta_w S_r d\theta_w \\ S_{xy,roller}\left(x,y,t\right)=S_{yx,r}\left(x,y,t\right)=\int\sin\theta_w\cos\theta_w S_r d\theta_w \\ S_{yy,roller}\left(x,y,t\right)=\int\sin^2\theta_w S_r d\theta_w \end{cases} \tag{3.3.37}$$

Finally, the components of the radiation stress tensor, $F_x\left(x,y,t\right)$ and $F_y\left(x,y,t\right)$are obtained. These will transmit the short wave contribution to the shallow water equations (Eqs.3.3.39,3.3.40 and 3.3.41).

$$\begin{cases} F_{w,x}\left(x,y,t\right)=-\left(\frac{\partial S_{xx,waves}+S_{xx,r}}{\partial x}+\frac{\partial S_{xy,w}+S_{xy,r}}{\partial y}\right) \\ F_{w,y}\left(x,y,t\right)=-\left(\frac{\partial S_{xy,waves}+S_{xy,roller}}{\partial x}+\frac{\partial S_{yy,w}+S_{yy,r}}{\partial y}\right) \end{cases} \tag{3.3.38}$$

3.3.3.2. Flow module

The equations that consider the variation of the water surface and momentum, thus including long waves (infragravity waves) and non-stationary currents are the **depth-averaged nonlinear shallow water equations** (Eqs.3.3.39, 3.3.40 and 3.3.41).

$$\frac{\partial u^L}{\partial t}+u^L\frac{\partial u^L}{\partial x}+v^L\frac{\partial u^L}{\partial y}-fv^L-v_h\left(\frac{\partial^2 u^L}{\partial x^2}+\frac{\partial^2 u^L}{\partial y^2}\right)=\frac{\tau_{sx}}{\rho h}-\frac{\tau_{bx}^E}{\rho h}-g\frac{\partial\eta}{\partial x}+\frac{F_{w,x}}{\rho h} \tag{3.3.39}$$

$$\frac{\partial v^L}{\partial t}+u^L\frac{\partial v^L}{\partial x}+v^L\frac{\partial v^L}{\partial y}-fu^L-v_h\left(\frac{\partial^2 v^L}{\partial x^2}+\frac{\partial^2 v^L}{\partial y^2}\right)=\frac{\tau_{sy}}{\rho h}-\frac{\tau_{by}^E}{\rho h}-g\frac{\partial\eta}{\partial x}+\frac{F_{w,y}}{\rho h} \tag{3.3.40}$$

$$\frac{\partial\eta}{\partial t}+\frac{\partial hu^L}{\partial x}+\frac{\partial hv^L}{\partial y}=0 \tag{3.3.41}$$

Where f is the Coriolis coefficient. The horizontal viscosity is associated with lateral mixing ν_h and the turbulent terms due to wave breaking (Battjes, 1975). Wave contributions $F_{w,x}\left(x,y,t\right)$ and $F_{w,y}\left(x,y,t\right)$ are computed with Eq.3.3.38.

3.3.3.3. Sediment transport module

Sediment transport modelling is solved by the **advection-diffusion equation** (Galapatti, 1983):

$$\frac{\partial hC}{\partial t}+\frac{\partial hCu_{AV}}{\partial x}+\frac{\partial hCv_{AV}}{\partial y}+\frac{\partial}{\partial x}\left[D_h h\frac{\partial C}{\partial x}\right]+\frac{\partial}{\partial y}\left[D_h h\frac{\partial C}{\partial y}\right]=\frac{hC_{eq}-hC}{T_s} \quad (3.3.42)$$

Where C represents the bottom mean sediment concentration whose time scale variation is a wave group, u_{AV} and v_{AV} are the flux velocity related with the wave nonlinearity (**wave asymmetry**), whereas T_s is the temporal scale for the sediment concentration adaptation (then, for low T_s values, there are needed quasi-instantaneous transport variations).

In order to compute the equilibrium concentration, C_{eq}, the present dissertation has used the van Rijn (2007) formulation:

$$\begin{aligned} C_{eq} = {} & \tfrac{A_{sb}}{h}\left(\sqrt{(u^E)^2+0.64u_{rms,2}^2}-u_{cr}\right)^{1.5}+ \\ & \tfrac{A_{ss}}{h}\left(\sqrt{(u^E)^2+0.64u_{rms,2}^2}-u_{cr}\right)^{2.4}(1-\alpha_b m) \end{aligned} \quad (3.3.43)$$

This formula considers the **turbulence induced by wave breaking** (included in the near-bed orbital velocity ($u_{rms,2}$) Reniers et al. (2004a)). The other terms correspond to u_{cr}, which is the **critical shear velocity** for joint action of **waves** and **currents**; A_{ss} (Eq.3.3.44) and A_{sb} (Eq.3.3.45) are the suspended and bed load transport coefficients, respectively:

$$A_{ss}=\frac{0.012D_{50}\rho_s D_*^{-0.6}}{\left((s-1)\,gD_{50}\right)^{1.2}} \quad (3.3.44)$$

$$A_{sb}=\frac{0.015D_{50}\rho_s\left(D_{50}/h\right)^{1.2}}{\left((s-1)\,gD_{50}\right)^{0.75}} \quad (3.3.45)$$

Where ρ_s is the density of sediment, D_{50} is the mean grain size; s is the relative density ratio (ρ_s/ρ_w) and D_* the adimensional sediment grain size.

3.3.3.4. Morphological module

Finally, the morphological module uses the sediment transport gradients computed with Eq.3.3.42 for updating the bed elevation. Consequently, the following formu-

lation is used:

$$\frac{\partial z_b}{\partial t} + \frac{f_{mor}}{(1-p)}\left(\frac{\partial q_x}{\partial x} + \frac{\partial q_y}{\partial y}\right) = 0 \tag{3.3.46}$$

Where p is the bottom porosity and f_{mor} is the morphological acceleration factor. The **rates of sediment transport** q_x and q_y are obtained with:

$$\begin{aligned} q_x(x,y,t) &= hCu^E - D_s h\frac{\partial C}{\partial x} - f_{slope}\left|u^L\right| h\frac{\partial z_b}{\partial x} \\ q_y(x,y,t) &= hCv^E - D_s h\frac{\partial C}{\partial x} - f_{slope}\left|v^L\right| h\frac{\partial z_b}{\partial x} \end{aligned} \tag{3.3.47}$$

At the Eq. 3.3.47, f_{slope} is a slope corrector coefficient.

In order to simulate the sand volume moved during a storm event, an avalanching dune erosion model is implemented. This method considers bottom evolution, as well as mass transport from the emerged to the submerged zone. The sediment fluxes are triggered when a slope threshold surpasses m_{cr} , which can be user-defined for both emerged and submerged zones.

$$\begin{aligned} \left|\frac{\partial z_b}{\partial x}\right| &> m_{cr} \\ \left|\frac{\partial z_b}{\partial y}\right| &> m_{cr} \end{aligned} \tag{3.3.48}$$

In order to prevent shock-waves, the gradient of the elevation variation is limited to a maximum of **0.05 m/s**.

3.3.3.5. Non-hydrostatic module

The abovementioned description belongs to the usual phase-averaged configuration of the XBEACH model. However, some beaches exhibit local features such as detached breakwaters, cliffs and islands that affect the wave propagation. The phase-averaged assumption cannot deal with wave-by-wave processes such as wave diffraction or reflection and a phase-solving solver should be used. Some beaches of our calibration dataset (Barcelona, L'Estartit, Tossa de Mar, Premià de Mar) present some of these constraints. In those cases, XBEACH has been run in a **phase-solving mode** (non-hydrostatic assumption). This mode consists of computing directly the wave contributions $F_{w,x}(x,y,t)$ and $F_{w,y}(x,y,t)$ with the shallow water

equations and an additional non-hydrostatic term:

$$\frac{\partial u^L}{\partial t}+u^L\frac{\partial u^L}{\partial x}+v^L\frac{\partial u^L}{\partial y}+\frac{1}{h}\int_{-d}^{\zeta}\frac{\partial q}{\partial x}dz-fv^L-v_h\left(\frac{\partial^2 u^L}{\partial x^2}+\frac{\partial^2 u^L}{\partial y^2}\right)=\frac{\tau_{sx}}{\rho h}-\frac{\tau_{bx}^E}{\rho h}-g\frac{\partial \eta}{\partial x} \tag{3.3.49}$$

$$\frac{\partial v^L}{\partial t}+u^L\frac{\partial v^L}{\partial x}+v^L\frac{\partial v^L}{\partial y}+\frac{1}{h}\int_{-d}^{\zeta}\frac{\partial q}{\partial x}dz-fu^L-v_h\left(\frac{\partial^2 v^L}{\partial x^2}+\frac{\partial^2 v^L}{\partial y^2}\right)=\frac{\tau_{sy}}{\rho h}-\frac{\tau_{by}^E}{\rho h}-g\frac{\partial \eta}{\partial x} \tag{3.3.50}$$

$$\frac{\partial \eta}{\partial t}+\frac{\partial hu^L}{\partial x}+\frac{\partial hv^L}{\partial y}=0 \tag{3.3.51}$$

Where t is the time, the x and y axis form a parallel plane with the sea level, and the z-axis constitutes the vertical axis. The instantaneous water surface elevation is$\eta\left(x,y,t\right)$, $d\left(x,y\right)$ is the water depth and $h=\eta+d$ is the total depth. The depth-averaged velocities in the directions x and y are $u^L\left(x,y,t\right)$ and $v^L\left(x,y,t\right)$, respectively. The **non-hydrostatic pressure** (density-normalized) corresponds to the $q\left(x,y,z,t\right)$ term. The Coriolis coefficient f and the horizontal viscosity is associated with lateral mixing ν_h. The integral of the non-hydrostatic pressure gradient in the Eq.3.3.49 can be expressed through the Eq.3.3.52, according to Stelling and Zijlema (2003):

$$\int_{-d}^{\eta}\frac{\partial q}{\partial x}dz=\frac{1}{2}h\frac{\partial q_b}{\partial x}+\frac{1}{2}q_b\frac{\partial\left(\eta-d\right)}{\partial x} \tag{3.3.52}$$

Whereq_b is the non-hydrostatic bottom pressure. For the Eq.3.3.50, the same procedure can be used.

Due to the fact that q_b is included, it is required a set of extra equations. In order to obtain them, the **Keller-Box method** (Lam and Simpson, 1976) is applied, which notably enhances the frequency dispersion accuracy for short waves (Eq.3.3.53):

$$\frac{q\mid_{z=\eta}-q\mid_{z=-d}}{h}=-\frac{q_b}{h}=\frac{1}{2}\frac{\partial q}{\partial z}\mid_{z=\eta}+\frac{1}{2}\frac{\partial q}{\partial z}\mid_{z=-d} \tag{3.3.53}$$

The **vertical velocity** w_s at the **free surface** and the **bottom surface** w_b can be

computed with the expressions 3.3.54 and 3.3.55:

$$\frac{\partial w_s}{\partial t} + \frac{\partial q}{\partial z} \mid_{z=\eta} = 0 \tag{3.3.54}$$

$$\frac{\partial w_b}{\partial t} + \frac{\partial q}{\partial z} \mid_{z=-d} = 0 \tag{3.3.55}$$

Where the advective and diffusive terms have been neglected, thus considering them inferior in magnitude when they are compared with the vertical acceleration. Consequently, it is assumed that such acceleration is determined by the **non-hydrostatic pressure gradient**. The combination of the Eqs. 3.3.52, 3.3.54 and 3.3.55 leads to the expression 3.3.56:

$$\frac{\partial w_s}{\partial t} = \frac{2q_b}{h} - \frac{\partial w_b}{\partial t} \tag{3.3.56}$$

In the other hand, the **bottom vertical velocity**, w_b, can be computed though the following **kinematic condition** (Eq.3.3.57):

$$w_b = -u^L \frac{\partial d}{\partial x} - v^L \frac{\partial d}{\partial y} \tag{3.3.57}$$

Then, the **local mass conservation** (Eq.3.3.58) it is established as:

$$\frac{\partial u^L}{\partial x} + \frac{\partial v^L}{\partial y} + \frac{w_s - w_b}{h} = 0 \tag{3.3.58}$$

Hence, the wave action balance and the roller action balance equations are switched off. The rest of the procedure (sediment and morphodynamic modules, Sec. 3.3.3.3 and 3.3.3.4) are analogous to the phase-averaged approach.

3.3.4. Risk assessment module

In Chapter 6, a **probabilistic non-stationary multivariate model** will be built for coastal risk assessment. Hence, it is needed to define a set of random variables that will be modelled via probability density functions (PDFs). This thesis deals with episodic coastal hazard forecasting (flooding and erosion), then the PDFs needs to address **extremal properties**: positive skewness and excess kurtosis. A

widely used parametric extremal pdf is the Gumbel distribution (Gumbel (1935), Eq.3.3.59), that can address marginally both flooding and erosion.

$$f_m\left(y_m \mid \mu_m, \sigma_m\right) = \frac{1}{\sigma_m} \exp\left\{\left(\frac{y_m - \mu_m}{\sigma_m}\right) - \exp\left(\frac{y_m - \mu_m}{\sigma_m}\right)\right\} \tag{3.3.59}$$

Where the subscript m can take values 1 (flooding) and 2 (erosion). The support of $-\infty < y_m < \infty$ and the parameter ranges are $-\infty < \mu_m < \infty$ and $\sigma_m > 0$. However, at the coastal zone, such coastal hazards rarely are independent. Hence, the probabilistic model needs to consider the dependence structure between these variables. **Archimedean Copulas** can alleviate this issue. The next sections introduces the general features of Archimedean copulas (Sec. 3.3.4.1) and the proposed solution: upper-tail dependence with the Gumbel-Hougaard family (Sec. 3.3.4.1.1). Once defined the stationary version of the Copula, the non-stationary counterpart is addressed (Sec. 3.3.4.2).

3.3.4.1. Archimedean copulas

In this thesis, u_{rv} and v_{rv} are two random variables defined a priori by two marginal probability distribution functions (i.e. a Gumbel, but the theory presented herein is applicable to other pdfs).

Let $\mathbb{I} = [0, 1]$. A 2-copula is a bivariate function $\mathbf{C} : \mathbb{I} \times \mathbb{I} \to \mathbb{I}$ that:

1. The uniform marginals for all $u_{rv}, v_{rv} \in \mathbb{I}$ (Eq. 3.3.60),

$$\mathbf{C}\left(u_{rv}, 0\right) = 0, \quad \mathbf{C}\left(u_{rv}, 1\right) = u, \quad \mathbf{C}\left(0, v_{rv}\right) = 0, \quad \mathbf{C}\left(1, v_{rv}\right) = v_{rv} \tag{3.3.60}$$

2. The 2-increasing for all $u_{rv,1}, u_{rv,2}, v_{rv,1}, v_{rv,2} \in \mathbb{I}$ such that $u_{rv,1} \leq u_{rv,2}$ and $v_{rv,1} \leq v_{rv,2}$,

$$\mathbf{C}\left(u_{rv,2}, v_{rv,2}\right) - \mathbf{C}\left(u_{rv,2}, v_{rv,1}\right) - \mathbf{C}\left(u_{rv,1}, v_{rv,2}\right) + \mathbf{C}\left(u_{rv,1}, v_{rv,1}\right) \geq 0 \tag{3.3.61}$$

Following the Sklar (1959) theorem (2-dimensional case): Let F_{XY} be a joint distribution function with marginals F_X and F_Y. Then there exists a 2-copula $\mathbf{C}$ such that

$$F_{XY}\left(x, y\right) = \mathbf{C}\left(F_X\left(x\right), F_Y\left(y\right)\right) \tag{3.3.62}$$

For all reals x, y. If F_X and F_Y are continuous and$F_X^{[-1]}$,$F_Y^{[-1]}$ are their respective

quasi-inverses, then:

$$\mathbf{C}\left(u_{rv}, v_{rv}\right) = F_{XY}\left(F_X^{[-1]}\left(u_{rv}\right), F_Y^{[-1]}\left(v_{rv}\right)\right) \tag{3.3.63}$$

For any $(u_{rv}, v_{rv}) \in \mathbb{I}^2$.

In this thesis, we will focus on Archimedean copulas. This kind of copulas have a series of properties (symmetry, exchangeability, association, etc.) that eases the model building. However, for defining an Archimedean copula, first, we need to define the notion of generator γ_{cop}:

Let $\gamma_{cop} : \mathbb{I} \to [0, \infty]$ such that γ_{cop} is continuous and strictly decreasing, with $\gamma_{cop}(1) = 0$; also let γ_{cop}^{-1} denote the ordinary inverse function of γ_{cop}. The pseudo-inverse of γ_{cop} is the function $\gamma_{cop}^{[-1]} : [0, \infty] \to \mathbb{I}$ given by

$$\gamma_{cop}^{[-1]}(t) = \begin{cases} \gamma_{cop}^{-1}(t), & 0 \leq t \leq \gamma_{cop}(0) \\ 0, & \gamma_{cop}(0) \leq t \leq \infty \end{cases} \tag{3.3.64}$$

Note that $\gamma_{cop}^{[-1]}$ is continuous and non-increasing on $[0, \infty]$, and strictly decreasing on $[0, \gamma_{cop}(0)]$. Also, $\gamma_{cop}^{[-1]}(\gamma_{cop}(t)) = t$ on $\mathbb{I}$, and:

$$\gamma_{cop}\left(\gamma_{cop}^{[-1]}(t)\right) = min\left\{t, \gamma_{cop}(0)\right\} \tag{3.3.65}$$

If $\gamma_{cop}(0) = \infty$, then $\gamma_{cop}^{[-1]} = \gamma_{cop}^{-1}$. With this result (Eq. 3.3.65) an Archimedean copula can be defined as a 2-copula $\mathbf{C} : \mathbb{I} \times \mathbb{I} \to \mathbb{I}$:

$$\mathbf{C}\left(u_{rv}, v_{rv}\right) = \gamma_{cop}^{[-1]}\left(\gamma_{cop}(u) + \gamma_{cop}(v)\right) \tag{3.3.66}$$

If, and only if, γ_{cop} and $\gamma_{cop}^{[-1]}$are convex. This kind of copulas features:

1. $\mathbf{C}$ is symmetric, i.e., for all $u_{rv}, v_{rv} \in \mathbb{I}$,

$$\mathbf{C}\left(u_{rv}, v_{rv}\right) = \mathbf{C}\left(v_{rv}, u_{rv}\right) \tag{3.3.67}$$

2. $\mathbf{C}$ is associative, i.e., for all $u_{rv}, v_{rv}, w_{rv} \in \mathbb{I}$,

$$\mathbf{C}\left(\mathbf{C}\left(u_{rv}, v_{rv}\right), w_{rv}\right) = \mathbf{C}\left(u_{rv}, \mathbf{C}\left(v_{rv}, w_{rv}\right)\right) \tag{3.3.68}$$

3. If γ_{cop} generates $\mathbf{C}$, then also $\gamma'_{cop} = c\gamma_{cop}$ is a generator of $\mathbf{C}$, where c is a positive constant.

This thesis deals with extremes. Our extremes are dependent at the tails of the

marginal distribution. Then, it is necessary to define a metric for the tail dependence. Provided that the limits exists, let $Z = (X, Y)$. A random vector Z is upper tail dependent if:

$$\lambda_U = \lim_{t \to 1^-} \mathbb{P}\left\{X > F_X^{[-1]}(t) \mid Y > F_Y^{[-1]}(t)\right\} > 0 \tag{3.3.69}$$

Provided that the limits exists, the same vector is lower tail dependent if:

$$\lambda_L = \lim_{t \to 0^+} \mathbb{P}\left\{X > F_X^{[-1]}(t) \mid Y > F_Y^{[-1]}(t)\right\} > 0 \tag{3.3.70}$$

The value of the lower and upper tail coefficients λ_U and λ_L can be derived from the association parameter of the copula (see Section 3.3.4.1.1).

The dependence metric will be the Kendall's τ_K. One of its advantages relies on its support, that eases interpretation of the dependence, $\tau_K = [0, 1]$. $\tau_K = 0$ means independence and $\tau_K = 1$ means total dependence. The general definition is Eq.3.3.71:

$$\tau_K = \mathbb{P}\left\{(X_1 - X_2)(Y_1 - Y_2) > 0\right\} - \mathbb{P}\left\{(X_1 - X_2)(Y_1 - Y_2) < 0\right\} \tag{3.3.71}$$

In case that is assumed a dependence structure of X and Y via a copula $\mathbf{C}$:

$$\tau_K^{X,Y} = \tau_K^{\mathbf{C}} = Q(\mathbf{C}, \mathbf{C}) = 4 \int \int_{I^2} \mathbf{C}(u_{rv}, v_{rv})\, d\mathbf{C}(u_{rv}, v_{rv}) - 1 \tag{3.3.72}$$

If the copula is Archimedean (as in our case), then (Eq. 3.3.73):

$$\tau_K^{\mathbf{C}} = 1 + 4 \int_0^1 \frac{\gamma_{cop}(t)}{\gamma'_{cop}(t)} dt \tag{3.3.73}$$

3.3.4.1.1. Gumbel-Hougaard Family Gumbel-Hougaard Family (Eq.3.3.74) is an Archimedean copula suitable for the kind of coastal hazards that addresses the risk module, because the dependence is stressed in the **upper tail** of the marginal distributions.

$$\mathbf{C}_{\theta_{\mathbf{cp}}}(u_{rv}, v_{rv}) = exp\left[-\left\{(-log\ u_{rv})^{\theta_{cp}} + (-log\ v_{rv})^{\theta_{cp}}\right\}^{1/\theta_{cp}}\right] \tag{3.3.74}$$

Where $u_{rv}, v_{rv} \in \mathbb{I}$, and $\theta_{cp} \geq 1$ is a dependence parameter ($\theta_{cp} \in [1, \infty)$).

The following relationship exists between θ_{cp} and Kendall's τ_K:

$$\tau_K\left(\theta_{cp}\right) = \frac{\theta_{cp} - 1}{\theta_{cp}} \tag{3.3.75}$$

Note that the lower and upper tail dependence coefficients for the members of this family are given by, respectively, $\lambda_L = 0$ and $\lambda_U = 2 - 2^{1/\theta_{cp}}$.

3.3.4.2. Non-stationary Copula models with GAMLSS

One of the main constraints of fitting a probability distributions, is that sometimes the behaviour of a sample depends on a set of covariates (i.e. the distribution parameters are assumed as stationary, but they have relationship with other variables). Linear regression models are the most common ones, but the error distribution must be Gaussian. In this thesis, we are dealing with a sample that comes from extreme values and the Gaussian error assumption does not hold valid. Therefore, it is needed a flexible generalization of ordinary linear regression. Generalized Linear Models (GLM, Nelder and Wedderburn (1972)) can handle other error distribution, by allowing the linear model to be related with the response variable via a link function and by allowing the magnitude of the variance of each measurement to be a function of its predicted value.

In this dissertation, it will be used a further generalization: Generalized Additive Model for Location, Scale and Shape (GAMLSS, Rigby and Stasinopoulos (2005)). GAMLSS is a distribution based approach to (semiparametric) regression analysis that is more general than the GLM. In GAMLSS the distribution of the dependent variable is not just limited to the exponential family.

GAMLSS assumes independent observations $y_{obs,i}$ for $i = 1, 2, \ldots, n$ with probability (density) function $f\left(y_i \mid \mu_i, \sigma_i, \nu_i, \tau_i\right)$ conditional on $(\mu_i, \sigma_i, \nu_i, \tau_i)$ a vector of four distribution parameters, each of which can be a function to the explanatory variables. The first two population distribution parameters μ_i and σ_i are usually characterized as location and scale parameters, while the remaining parameter(s) are characterized as shape parameters, e.g. skewness and kurtosis.

$$\begin{aligned}
g_1\left(\boldsymbol{\mu}\right) &= \eta_1 = X_1\beta_1 + \sum_{j=1}^{J_1} h_{j1}\left(\mathbf{x}_{j1}\right) \\
g_2\left(\boldsymbol{\sigma}\right) &= \eta_2 = X_2\beta_2 + \sum_{j=1}^{J_2} h_{j2}\left(\mathbf{x}_{j2}\right) \\
g_3\left(\boldsymbol{\nu}\right) &= \eta_3 = X_3\beta_3 + \sum_{j=1}^{J_3} h_{j3}\left(\mathbf{x}_{j3}\right) \\
g_4\left(\boldsymbol{\tau}\right) &= \eta_4 = X_4\beta_4 + \sum_{j=1}^{J_4} h_{j4}\left(\mathbf{x}_{j4}\right)
\end{aligned} \tag{3.3.76}$$

Hence, a GAMLSS model for any four distribution parameter requires: (i) a random component $f\left(y_i \mid \mu_i, \sigma_i, \nu_i, \tau_i\right)$; (ii) a systematic component $\boldsymbol{\eta} = \boldsymbol{\beta}^T\mathbf{x}$ specifying the variation in a random variable Y accounted for by known covariates $\mathbf{x}$, and (iii) a link function $g_i\left(\mathring{\mathrm{u}}\right) = \boldsymbol{\beta}^T\mathbf{x}$ that ties the former two elements together. The vectors $\boldsymbol{\eta}$ and $\boldsymbol{\beta}$ refers to the additive predictors and the regression coefficients, respectively.

This approximation handles univariate PDFs, but the proposed risk module has to deal with episodic erosion and flooding hazards. These hazards are correlated, thus requiring a multivariate PDF. Copulas have been presented above as a flexible way to link marginal distribution functions. But the dependence parameter θ_{cp} also depends on a set of covariates. GAMLSS with copula theory can be merged (Klein et al., 2015; Sabeti et al., 2014) to obtain a **non-stationary multivariate distribution** (Eq. 3.3.77):

$$F\left(y_1, y_2 \mid \vartheta\right) = \mathbf{C}\left(F_1\left(y_1 \mid \mu_1, \sigma_1\right), F_2\left(y_2 \mid \mu_2, \sigma_2\right); \theta_{cp}\right) \tag{3.3.77}$$

Where $\vartheta = \left(\mu_1, \sigma_1, \mu_2, \sigma_2, \theta_{cp}\right)^T$,$F_1\left(y_1 \mid \mu_1, \sigma_1\right)$ and $F_2\left(y_2 \mid \mu_2, \sigma_2\right)$ are marginals cumulative density functions of Y_1 and Y_2 taking values in $(0, 1)$; μ_m,σ_m for $m = 1, 2$ are the location and scale parameters, respectively; $\mathbf{C}$ is the copula function with dependence coefficient θ_{cp}, and the parameters in ϑ are linked to $\mathbf{z}$ via additive predictors. Then, there are needed five additive predictors $\left(\eta_{\mu_1}, \eta_{\mu_2}, \eta_{\sigma_1}, \eta_{\sigma_2}, \eta_{\theta_{cp}}\right)$. A generic predictor η_i as a function of an intercept and smooth functions of sub-vectors of a generic covariate vector $\mathbf{z}_i$ can be defined as (Eq. 3.3.78):

$$\eta_i = \beta_{0i} + \sum_{k=1}^{K} s_k\left(\mathbf{z}_{ki}\right), \qquad i = 1, \ldots, n \tag{3.3.78}$$

Where $\beta_{0i} \in \mathbb{R}$ is an intercept coefficient, $\mathbf{z}_{ki}$ denotes the kth sub-vector of the complete covariate vector $\mathbf{z}_i$ (containing continuous *[wave height, sea level]* or categorical *[wave direction]* variables) and the K functions $s_k\left(\mathbf{z}_{ki}\right)$ represent generic effects that depends of the type of covariate. Each $s_k\left(\mathbf{z}_{ki}\right)$ can be approximated as a linear combination of J_K basis functions $b_{kj_k}\left(z_{ki}\right)$ and regression coefficients $\beta_{kj_k} \in \mathbb{R}$ (Eq. 3.3.79):

$$\sum_{j_k=1}^{J_k} \beta_{kj_k} b_{kj_k}\left(\mathbf{z}_{ki}\right) \tag{3.3.79}$$

The latter expression implies that Eq. 3.3.78 can be written as (Eq. 3.3.80):

$$\boldsymbol{\eta} = \boldsymbol{\beta_0} + \mathbf{Z}_1\boldsymbol{\beta}_1 + \ldots + \mathbf{Z}_K\boldsymbol{\beta}_K \tag{3.3.80}$$

Copula models for GAMLSS have been used for step 2 of the Risk Module. For obtaining the relationship between the betas and the beach parameters (step 3), GLM has been used instead. The methodology is analogous, but instead of requiring five link functions, it is only required one (i.e. $g(\mu)$).

3.4. Error Metrics

Data quality checking and standardization of any system requires **observations** (see Sec. 3.2.2,3.2.4) and a set of reliable **metrics** (Bennet et al., 2013). The veracity of a numerical model needs to be contrasted with observations. Such procedure can be performed with qualitative and quantitative methods. In this dissertation, both approaches has been tested at the different modules. This Section summarises the quantitative tools that will be used in the next Chapters.

3.4.1. Meteorological and Hydrodynamic module

The following metrics are used for the Meteorological and Hydrodynamic module, unless otherwise stated. In all cases, P_i and O_i refer to the computed and observed signals respectively, N is the number of data points and $\left(\overline{\circ}\right)$ is the mean operator.

The **mean bias** (MB) (Eq. 3.4.1) represents the integrated error between predicted and observed signal. A perfect model would provide $MB = 0$:

$$MB = \frac{1}{N}\sum_{i=1}^{N}(P_i - O_i) \tag{3.4.1}$$

The **Root Mean Squared Error** (RMSE) (Eq. 3.4.2) represents the sample standard deviation between predicted and observed signal. This metric is scale-dependent.

$$RMSE = \sqrt{\frac{\sum_{i=1}^{n}(P_i - O_i)^2}{N}} \tag{3.4.2}$$

The **Normalised Root mean Squared Error** (Eq. 3.4.3) eases the comparison between different datasets (as in Fig.4.5, in which each computational node has its particular time series), because it is scale-independent. It can be expressed as a

percentage, where lower values indicate less residual variance:

$$NRMSE = \sqrt{\frac{\sum_{i=1}^{n} (P_i - O_i)^2}{\sum_{i=1}^{N} O_i^2}} \tag{3.4.3}$$

The **Pearson correlation coefficient** (R, Eq. 3.4.4), is a measure of the linear correlation between two signals. It ranges between +1 and -1, where 1 is total positive linear correlation, 0 is no linear correlation, and -1 is total negative linear correlation.

$$R = \frac{\sum_{i=1}^{N} \left(\left(P_i - \overline{P} \right) \mathring{\mathrm{u}} \left(O_i - \overline{O} \right) \right)}{\sqrt{\sum_{i=1}^{N} \left(P_i - \overline{P} \right)^2} \mathring{\mathrm{u}} \sqrt{\sum_{i=1}^{N} \left(O_i - \overline{O} \right)^2}} \tag{3.4.4}$$

The **Coefficient of Efficiency** (COE) (Legates and McCabe, 1999, 2013) is a measure for model performance that is simple to interpret. A perfect model has a $COE = 1$. Despite COE has no lower bound, a value of $COE = 0.0$ implies that the model is no more able to predict the measured values than does the measured mean. Hence, the model has no predictive advantage, because the model can explain no more of the variation in the measured values than can the measured mean. Consequently, for negative COE values, the computed signal performs worse than the measured mean in predicting the variations in the observed signal.

$$COE = 1 - \frac{\sum_{i=1}^{N} |O_i - P_i|}{\sum_{i=1}^{N} \left| O_i - \overline{O} \right|} \tag{3.4.5}$$

The **cost function** (Holt et al., 2005) establishes a scale of model error to observed variance. If the cost, χ, is equal to zero, both the recorded and computed time series reach the same value. Increasing costs indicate lower similarity degree. Furthermore, the quadratic term ensures that large differences weigh heavily in the total χ value. Such a cost function can be written as (Eq. 3.4.6):

$$\chi = \sqrt{\frac{1}{N\sigma_O^2} \sum_{i=1}^{N} (P_i - O_i)^2} \tag{3.4.6}$$

Where σ_O^2 is the variance of the observations. This metric is used in Ch. 4 for the Hydrodynamic module.

A method for visually check and compare different models and metrics at the same time is via Taylor diagrams (Taylor, 2001). A Taylor diagram (please refer to Fig. 4.8 to see an example) consists of graphical representations of the correlation coefficient R, the standard deviation of each signal and the (centred) root mean square error. These three statistics are plotted in one (2D) graph benefiting from the Law of Cosines. The interpretation of this graphic relies on the distance between a reference signal (observations) and modelled signal. The shorter the distance, the better the correspondence.

3.4.1.1. Integrated parameters for the hydrodynamic module

SWAN is a spectral model based on the wave action balance (Sec. 3.3.2). Hence, each spatial grid point describes an energy spectrum $E(\sigma,\theta)$ in a particular time point. The spectrum can be summarised with a set of state of the art integrated parameters. The most usual are:

(i) The **Significant wave height** (H_s), in meters, that is related with the averaged wave energy of the spectrum (Eq. 3.4.7):

$$H_s = 4\sqrt{\int\int E(\omega,\theta)\,d\omega d\theta} \approx 4\sqrt{\int\int E(\sigma,\theta)\,d\sigma d\theta} \tag{3.4.7}$$

(ii) The **Peak wave period** (T_p), in seconds, that is the wave period that corresponds to the maximum energy of the spectrum.

(iii) The **Mean wave period** (T_{m02}), in seconds, that is related with the averaged wave period of the spectrum (Eq. 3.4.8):

$$T_{m02} = 2\pi\left(\frac{\int\int \omega^2 E(\omega,\theta)\,d\omega d\theta}{\int\int E(\omega,\theta)\,d\omega d\theta}\right)^{-1/2} = 2\pi\left(\frac{\int\int \omega^2 E(\sigma,\theta)\,d\sigma d\theta}{\int\int E(\sigma,\theta)\,d\sigma d\theta}\right)^{-1/2} \tag{3.4.8}$$

(iv) The **Mean wave direction** ($WDIR$), in degrees, that corresponds with the average wave direction of the spectrum (Eq. 3.4.9):

$$WDIR = \frac{180}{\pi} arctan\left[\frac{\int sin\theta E(\sigma,\theta)\,d\sigma d\theta}{\int cos\theta E(\sigma,\theta)\,d\sigma d\theta}\right] \tag{3.4.9}$$

These integrated parameters are used in Ch. 4-7.

3.4.2. Morphodynamic module

The performance of the Morphodynamic module (Ch. 4) has been evaluated through the Brier skill score (BSS) index (van Rijn et al. (2003), Eq. 3.4.10) :

$$BSS = 1 - \left[\frac{\left\langle \left(|z_{b,c} - z_{b,m}| \right)^2 \right\rangle}{\left\langle \left(|z_{b,0} - z_{b,m}| \right)^2 \right\rangle} \right] \tag{3.4.10}$$

where $z_{b,m}$ is the post-storm topography (in this dissertation, from LIDAR (Sec.3.2.4)), $z_{b,c}$ is the model output grid and $z_{b,0}$ is the pre-storm topography. A BSS value of **1** means that the simulations and measurements **fully agree**. As these two data sets diverge, the BSS gets smaller, even reaching negative values. The threshold value that indicates an **acceptable** reproduction is about **0.4**.

3.4.3. Risk module

Akaike Information Criterion (AIC, Akaike (1973)) and **Bayesian Information Criterion** (BIC, Schwarz (1978)) are two information metrics that are used for testing the goodness-of-fit of the sample with the risk module. For both cases, as lower the metric, the better. The definitions are Eq.3.4.11 and Eq.3.4.12, respectively:

$$AIC = -2\ell\left(\hat{\boldsymbol{\delta}}\right) + 2edf \tag{3.4.11}$$

$$BIC = -2\ell\left(\hat{\boldsymbol{\delta}}\right) + log\left(N\right) edf \tag{3.4.12}$$

Where edf are the effective degrees of freedom of the penalized model. The log-likelihood function for a copula model with continuous margins $\ell\left(\hat{\boldsymbol{\delta}}\right)$ can be defined as (Eq. 3.4.13,Kolev and Paiva (2009)):

$$\begin{aligned} \ell\left(\hat{\boldsymbol{\delta}}\right) = \sum_{i=1}^{n} \log\left\{c\left(F_1\left(y_{1i} \mid \mu_{1i}, \sigma_{1i}\right), F_2\left(y_{2i} \mid \mu_{2i}, \sigma_{2i}\right); \theta_i\right)\right\} \\ + \sum_{i=1}^{n}\sum_{m=1}^{2} \log\left\{f_m\left(y_{mi} \mid \mu_{mi}, \sigma_{mi}\right)\right\} \end{aligned} \tag{3.4.13}$$

The main difference between AIC and BIC is that the latter generally penalizes free parameters more strongly than AIC. Hence, BIC criteria prevails when trying to model a following the parsimony principle (i.e. building an useful model with the minimum number of parameters). Both metrics are general, so they can be used for GAMLSS and GLM.

4. From Hydrodynamics to Morphodynamics: Limits and uncertainties

Note: This Chapter is an expanded version of Sánchez-Arcilla et al. (2014).

Sánchez-Arcilla, A., García-León, M., Gràcia, V. (2014), Hydro-morphodynamic modelling in Mediterranean storms - errors and uncertainties under sharp gradients, Nat. Hazards Earth Syst. Sci., 2993-3004

Abstract

This paper deals with the limits in hydrodynamic and morphodynamic predictions for semi-enclosed coastal domains subject to sharp gradients (in bathymetry, topography, sediment transport and coastal damages). It starts with an overview of wave prediction limits (based on satellite images and buoy records) in a restricted domain, namely the Mediterranean basin, followed by an in-depth analysis of the Catalan coast, one of its land boundaries. The morphodynamic modelling for such regions is next discussed, based on the impact of a characteristic storm. The driving wave and surge conditions produce a morphodynamic response that is validated against the pre- and post-storm emerged beach state, recovered from two LIDAR images. The quality of the fit is discussed in terms of the physical processes and the suitability of the employed modelling suite. From here an assessment of errors and uncertainties is presented, with the aim of establishing the prediction limits for flooding and erosion analyses, key elements for coastal engineering decisions.

4.1. Introduction

Coastal regions are often characterized by sharp gradients in meteo-oceanographic drivers, sedimentary fluxes and socio-economic pressures. This happens under present climate conditions and would probably occur under future scenarios, which makes such coastal areas a challenging test case for predictions and projections alike. The study case is the Catalan coast in the NW Mediterranean (see Ch. 2, Fig. 4.1). This region is characterized by a complex coastal orography with the Pyrenees to the north as the main orographic feature running in an east-west direction. The coastal area is conditioned by the opening between the Pyrenees and the Alps in southern France and including the Rhone valley. The Catalan coast also features several abrupt mountain ranges parallel to the coast in a northeast-southwest direction.

During regional northern wind events, the orography favours wind channelling down the river valleys and through the openings in the coastal mountain range, which leads to jet-like wind patterns over the coastal area with a northwest direction. These land to sea winds from the northwest (Mestral in the local vernacular) are particularly intense and persistent, especially during the autumn and winter seasons. In winter and early spring, the eastern wind fields present the highest wind speeds and the longest fetch, resulting in the largest waves acting on this coast. They are associated to low pressure centres over the western Mediterranean, which often spend several days recirculating in this part of the basin and therefore generating wave storms with more than one peak. This turns out to be an effective mechanism for producing erosion, flooding and various types of damage along the coast.

The directional distribution of waves shows, in accordance with the presented wind features, a predominance of northwest and eastern waves, with some southern wave systems. Double peaked (bi-modal) wave spectra are often observed under strong local northwestern winds combined with offshore easterly or southerly winds in the offshore (Sánchez-Arcilla et al., 2008). This applies particularly to river valleys such as the Ebro delta region, where these bi-modal spectra can occur more than 50% of the time (Bolaños et al., 2009), with implications for the prediction of sediment transport and morphodynamic evolution. Along with the waves, mean sea levels also play a key role in coastal morphodynamics. Water levels in the area are dominated by storm surges which may reach up to 60 cm (Conte and Lionello, 2013). The astronomical tidal range, between 10 and 30 cm, is quantitatively less important, making the area a micro-tidal environment.

For this type of coastal domain, the sharp gradients (due to the topobathymetric features) in the spatial patterns of wind, wave and circulation fields impose a tough challenge for numerical simulations, demanding a fine gridsize to solve these variations. To prove this point, this Chapter will start by presenting wave simulations, the nesting strategy and how the computational results have been calibrated with available observations. This allows some boundaries to be established for a hindcasting evaluation (Sec. 4.2). This chapter continues with a **description of a significant wave storm** that has **recently affected the Catalan coast** and for which there are observational data (Sec. 4.3). It will be analysed the **wave propagation from deep to shallow water** depths, plus their resulting **errors**; then linking them to the controlling physical processes.

The morphodynamic response will be analysed next, based on pre/post-storm emerged LIDAR images and the simulated erosion and flooding (Sec. 4.4). This will allow the calculation of the errors (observations versus simulations) and the discussion of the underlying hydro-morphodynamic uncertainties (Sec. 4.5). Next, there will be a discussion on the limits of hydro-morphodynamic predictions and the implications for engineering design and management decisions (Sec. 4.6), followed by some conclusions (Sec. 4.7).

4.2. Regional wave assessment and modelling

Wave generation and propagation has been assessed with the SWAN model (see Sec. 3.3.2). Calculations are performed through a set of three nested domains that cover the Mediterranean Sea (Fig. 4.1). The first is the Mediterranean sea grid which has a resolution of $0.09° \times 0.09°$, comprising from -6 to 36.93° longitude and from 30 to 45.93° latitude. The second one is the Catalan sea domain, with a $0.025° \times 0.025°$ grid size, comprising from -0.5 to 4.0° longitude and from 33.5 to 38.5° latitude. The last one is a 1×1 km grid that represents the shelf domain off the Catalan coast, with a land boundary on the northwestern side and three open boundaries at the north, south and east of the domain. In all three cases, the bathymetry comes from the GEBCO (GEB-2008) dataset which has a resolution of 1 km approximately.

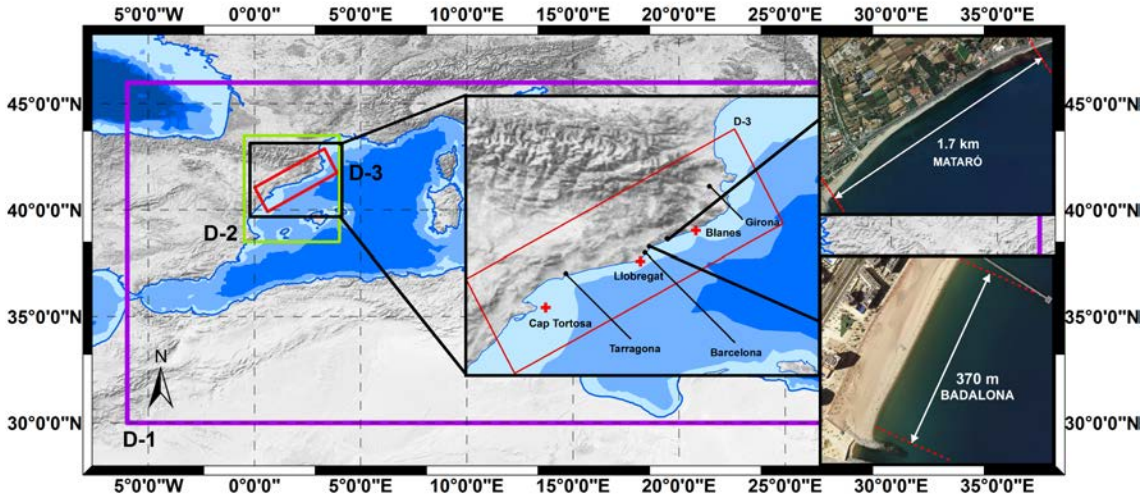

Figure 4.1.: Western Mediterranean Sea and the three domains employed in the numerical simulations of this Chapter. The purple one represents the western Mediterranean Sea (D-1), the green one the Balearic Sea (D-2) and the red one the Catalan Coast Shelf (D-3). The red crosses denote the XIOM buoy positions (see Fig. 4.2). The two insets (Mataró and Badalona municipalities) correspond to the areas selected for morphodynamic analysis.

Model boundary conditions are provided by offshore wind, mean sea level and current fields. Wind drivers are obtained from IFREMER blended wind fields (Bentamy et al., 2007) with a spatial grid resolution of $0.25° \times 0.25°$ [27×27 km] and 6 h time frequency. Data comprise operational ECMWF wind fields blended with remote sensing observations (QuikSCAT scatterometer and SSM/I radiometer) through optimal interpolation. The daily averaged sea level and water surface current fields are obtained from MyOcean reanalysis (Tonani et al., 2009). The latter have a horizontal grid resolution of 1/16° (ca. 6 - 7 km). Recently, Alomar et al. (2014) tested higher resolution wind models going down to a mesh size of 4 km and a wind input

every one hour. In all cases the differences between the input and dissipation terms were not relevant for such limited coastal domains.

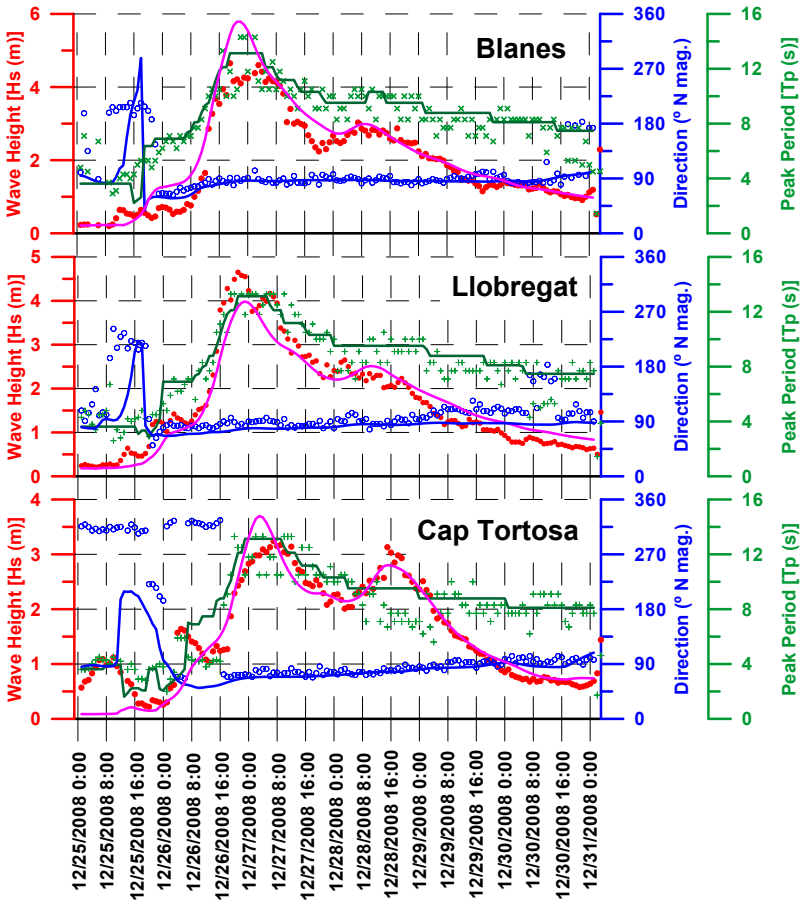

Figure 4.2.: Intercomparison of the recorded (XIOM network) and calculated wave parameters near the coast (Llobregat buoy, moored at 45 m; Blanes buoy, moored at 75 m and Cape Tortosa buoy, moored at 60 m). **Legend:** *Magenta solid line: computed wave height. Blue solid line: Computed direction. Green solid line: computed peak period. Red dots: XIOM wave height. Green crosses: XIOM peak period. Blue circles: XIOM wave direction.* **Time interval**: eight hours.

Simulations span 20-31 December 2008 (i.e. they are initiated six days prior to the storm peak on 26 December). This starting point guarantees enough time margin to avoid warm-up phenomena, excluding them as a possible uncertainty factor during the extreme event simulation. The model outputs are compared with different data sources ranging from altimeters (deep water) to buoy network data (intermediate water). Usually, a storm event is characterized by the storm duration and wave height, peak period and direction. Wave height records are available at both regional

and local scales, providing a natural integrator of meteorological parameters at the different spatial resolutions. The suitability of the models for the studied domain and some of the associated errors have also been analysed in Pallarés et al. (2014).

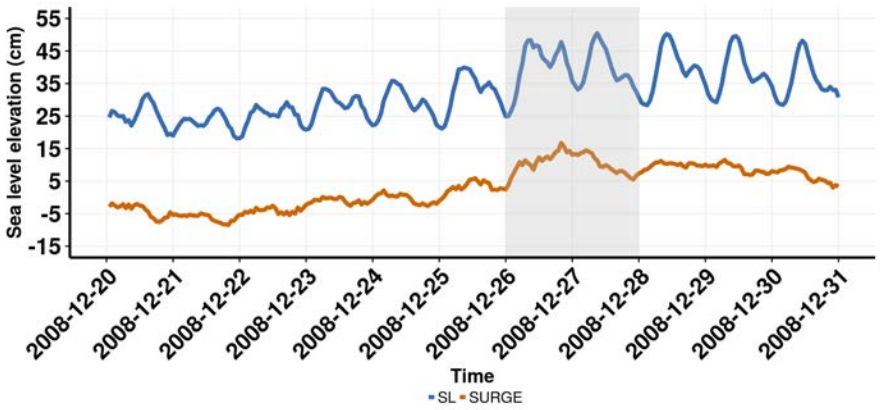

Figure 4.3.: Time series of the total sea level (in **blue**) and storm surge (in **orange**) at the **Barcelona harbour** for the **December 2008** storm. The shadowed area corresponds to the growth and decay time for the maximum wave height peak (please refer to Fig. 4.2). Time in days.

The first step in the error estimation is to compute the relation between **satellite** preprocessed **wave height data** (Queffeulou, 2004) and the **numerical output** at **deep waters**. Up to 14,000 data are within the considered regional area, derived from the combined tracks of four satellites: ERS-2 (21% of the total), ENVISAT (22%) , JASON-1 (27%) and JASON-2 (30%). The second step deals with **intermediate water** comparisons, based on the **XIOM** meteo-oceanographic network **observations**. In this case, hourly wave height, period and direction are recorded. Three directional buoys cover the three main Catalan coastal sectors (Fig.4.1): Barcelona (Llobregat buoy, deployed at 45 m depth), Girona (Tordera buoy, deployed at 75 m) and Tarragona (Cap Tortosa buoy, deployed at 60m). This observational network allows both average and extreme hydrodynamic patterns along the Catalan coast to be captured accurately (Bolaños et al., 2009). In the studied period, 22 - 31 December 2008, there were intervals of average and extreme wave energy levels. The error analysis begins two days after the simulation initial time. Based on previous results, it was known that when starting from a stationary state (pre-defined JONSWAP spectra), about 48 h is needed to reach an stabilization of the error.

4.3. Storm simulation and analysis

In the last two decades, up to 200 damaging wave storms have been reported at the Catalan coast. Although this zone could be considered as well monitored in terms of hydrodynamics (see Sec. 4.2), the lack of pre- and post-storm beach data introduces an important constraint in terms of storm impact assessment. However, for the selected storm (December-2008), pre- and post-storm sub-aerial profiles from a LIDAR campaign were available, offering an opportunity for improving morphodynamic response assessment under extreme conditions.

The selected event is a Mediterranean storm that affected the entire Catalan coast during almost 3 days (26 - 29 December 2008). A high pressure centre in northern Europe displaced a weak low pressure centre in front of the Catalan coast, which kept on growing due to the difference in air-water temperatures, generating strong eastern winds with speeds of about 50 $km \cdot h^{-1}$ and gusts of up to 85 $km \cdot h^{-1}$. As a consequence, an energetic storm centre, travelling from north to south, affected the Spanish northeast coastal zone for about 3 days, producing severe damage to many coastal infrastructures.

The highest waves recorded (XIOM network) appear in the central and northern coastal sectors with significant wave height (H_s) values up to 4.65m and peak periods up to 14.3 s (Fig. 4.2). In that area, H_s grew from 0.5m to 4.65 in about 12h as a result of the eastern strong winds, with maximum height values of about 8m. The southern buoys registered smaller wave heights and periods, up to 3.3m and 13.3s respectively. The storm duration (considering a threshold value of $H_s = 2m$) varies from 65 h at the northern part of the Catalan coast to 55 h at the central and southern parts. The wave direction had a clear eastern component throughout the whole event.

If only the wave height is considered, the storm had an associated return period of about 5 years. However, the long storm duration and the high integrated energy contents make the event more extreme. Hence, it belongs to the most damaging category that a storm can have in the Catalan coast (Sánchez-Arcilla et al., 2011c). The impact of this storm was significant **shoreline retreat**, with intense **overtopping** and flooding, especially at the **northern sector**, together with damage in many coastal and harbour structures. There were also **three casualties** and a generalized **social alarm**, which resulted in the closing of beaches and promenades. Further details of the storm characteristics and effects can be found in Sánchez-Arcilla et al. (2013) and Gràcia et al. (2013a).

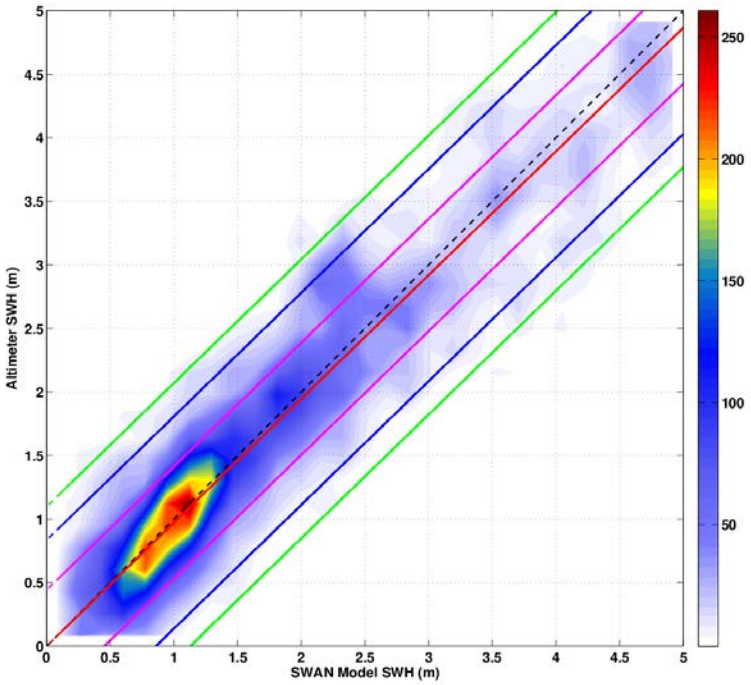

Figure 4.4.: Colour scale representing the **density** of **significant wave height** (SWH) points for the whole Mediterranean basin. The axes represent the **altimeter** wave height *(vertical axis)* vs. the **SWAN** wave height *(horizontal axis)*, both in metres. The red line corresponds to a linear fitting, the magenta, blue and green lines indicating the confidence of 70, 95 or 99 % respectively.

To evaluate the influence of the wave dissipation term in the action balance equation, a quadratic cost function (see Eq.3.4.6 in Sec.3.4) has been fitted. Only the white-capping component has been considered, since for deep to intermediate depths, the depth-induced breaking and bottom friction contributions are significantly smaller. The data set is the same as in Sec. 4.2, in which the source terms have been also evaluated.

The minimum χ cost (Eq. 3.4.6) obtained with altimeter wave height data is **0.37** with a rate of whitecapping dissipation of $2.25 \cdot 10^{-5}$. Costs between 0.4 and 1.0 may be interpreted as the range in which the variables are well-modelled and the predictive skill is **acceptable** (Holt et al., 2005). The dissipation parameter has been obtained with a sample that includes both moderate and extreme conditions (34% of the data records are above $H_s = 2m$) spanning the different storm stages (i.e. calm, growth and decay). Higher data densities are found in the interval of H_s 0.5 to 1.5 m, where model outputs vs. observations almost follow a linear trend (see red line in Fig. 4.4). The obtained fit tends to separate from the optimum ratio (dashed black line) at more energetic H_s values. Furthermore, when this linear trend is assumed, a forecasting error from 0.5m to 0.75m would be within a confidence interval from 70% (magenta lines) to 99% (green lines), respectively.

The spatial distribution of wave height differences has been analysed with a normalized root mean square error approach (NRMSE, Eq. 3.4.3). This statistical indicator is obtained by clustering the data subset within a $0.5° \times 0.5°$ grid and a time window of 20 min. In case of having more than one time point on the same grid node a mean NRMSE is obtained (Fig. 4.5):

This analysis has shown that wave heights are accurately reproduced with values ranging from **0.2** to **0.6**, at **deep waters** (i.e. with no obstacles such as islands, mountains and peninsulas that modify the meteo-oceanographic fields). However, sheltered nearshore areas such as the southern part of France, northern part of Adriatic Sea, Aegean Sea and the eastern part of Cyprus confirm the more limited model performance (NRMSE near 1.0) when using the coarse mesh. This error is partially alleviated by a suitable nesting strategy and by implementing more advanced nearshore physical parameterizations.

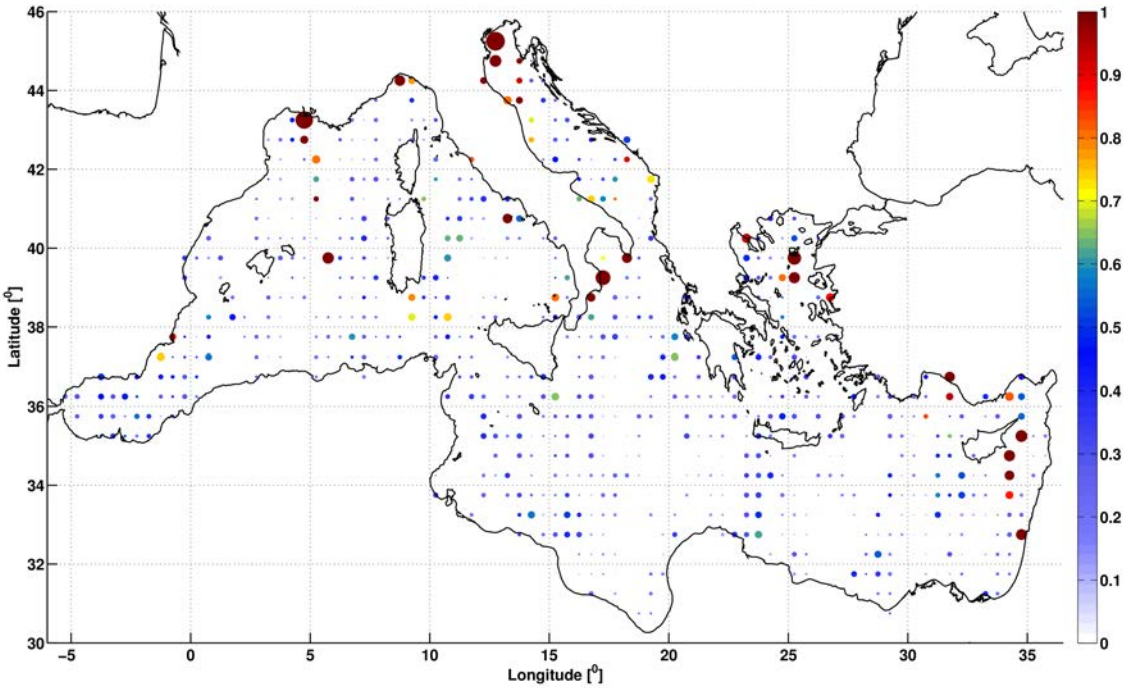

Figure 4.5.: Comparison between **simulations** and **altimeter data** for the wave height in the Mediterranean basin. The bubble size indicates the **wave height total error** in %. The colour scale represents the **NRMSE**.

At continental shelf scales, the XIOM buoy network has been compared with the finer mesh (1×1 km) checking the sharp gradients within the storm duration. As expected, wave height costs in intermediate waters indicate larger errors than for deep waters, with cost values of $\chi = 0.30$ at Llobregat and similar at Blanes ($\chi = 0.38$) and Cap Tortosa ($\chi = 0.40$) buoy positions. At Blanes, a 1.5m difference between predicted and measured wave height was obtained during the first storm peak, although the second peak presented a much better fit. In the southern part of the

coast, at the Cap Tortosa buoy, the first peak is overpredicted (3.14 m measured vs. 3.5 m modelled) while the second storm maximum is underpredicted. At the same place, it is observed that a 3 h lag exists for the predicted storm peak. **Llobregat** and **Cap Tortosa** points show a **smaller error than** the **Blanes** location (the Llobregat buoy for the first storm peak presented a discrepancy of 0.56m). The storm impact was lower in these central and southern coastal sectors. In all cases, the storm (wave height) growth and decay slopes were well hindcasted, capturing both the storm onset and peak pattern.

The peak period and average direction exhibit a similar behaviour, but with slightly higher cost levels (with a maximum value of $\chi = 0.55$), underlining that the model reproduces better the wave height pattern, particularly for the central coast (Llobregat buoy). The quality of the fit for peak periods depends on spectral shape and fetch geometry, thus complicating the hindcast. This makes the fit more complex, particularly when considering the directional veering and transient features typical of semi-enclosed domains with variable winds, where the growth rates may be larger than the commonly parameterized values (Alomar et al., 2014).

4.4. Nearshore hydro-morphodynamic impact - erosion and flooding

The main storm-induced **coastal impacts** (erosion and flooding) can be predicted from a coupled **nearshore model** driven by the waves generated in the previous section. For that purpose we have employed a 1×1 m digital elevation model (DEM) grid from LIDAR campaigns (see Sec. 3.2.4), reproducing the beach topography at two target locations, **Badalona** and **Mataró** beaches. Both are located at the central part of the Catalan coast (up-drift and down-drift of a harbour barrier) and suffered important damage during the storm event (Fig. 4.1). Bathymetry data from early 2008 was used for the submerged beach, as the best available characterization for the pre-storm profile.

The **Badalona** beach is a typical Mediterranean urban beach with a seafront promenade in its backshore between +5 and +6 m above MWL. The beach is characterized by coarse sediment, between 350 and $600\mu m$. It is a reflective beach (Wright and Short, 1984), with a Dean parameter (dimensionless sediment fall velocity) $\Omega < 1$ and a depth of closure of 6.35 m. The pre-storm bathymetry shows essentially parallel isobaths and a submerged slope of about 18H : 1V. The main storm impacts reported were severe shoreline retreat and flooding due to frequent run-up episodes.

The **Mataró** beach is located upstream of the Mataró port, in an accretive sector due to the barrier effect of the harbour. It features an alongshore revetment in its backside that protects a railway line from the impact of incoming waves. The beach width is variable, ranging from 10 m at the northernmost part up to 100 m at the southern end, supported by the harbour breakwater. In addition, the pre-storm isobaths show a steeper slope (26H : 1V) closer to the harbour barrier than at the

revetment zone (75H : 1V). The sediment is coarse, with median diameter of about $500\mu m$ (CIIRC, 2010). It is, thus, a reflective profile, with a depth of closure of about 6.9 m.

The main storm impacts reported were overtopping beyond the revetment and a reshaping of the upper part of the beach, which showed an important growth at the southern part due to the impoundments produced by the harbour breakwater.

The **differences** between **pre-** and **post-storm LIDAR** bathymetries have been calculated as a first assessment. In previous sections it has been shown that the December 2008 storm was a double peak event with a predominant eastern direction. Waves coming from the east led to cross-shore directed (undertow) fluxes and a longshore current from northwest to southwest due to oblique incidence. Cross-shore currents together with high run-ups (enhanced by the storm surge) were able to erode sub-aerial beach sediment. This material was transported onshorewards through overtopping or offshorewards driven by undertow currents. The longshore currents advected sand from northeast to southwest which was deposited at the southern part of the domain, impounded by the barrier presence. This barrier effect is due to the Badalona port in this case and to a non-permeable groyne in the Mataró case. In the accretive zone, the maximum shoreline advance was near 36 m at Mataró and 4 m at Badalona, whereas at the erosive zone the maximum shoreline retreat was 1.4 and 3.69 m, respectively.

The Badalona sector (Fig.4.6a) may be divided in **three transects**: from the northern part to the groin (B-North [B-N]), from the groin to the sewer outfall (B-Central [B-C]) and from the sewer outfall to the southern barrier (B-South [B-S]). There is a 2 km long, wide and open beach just outside the analysed domain (northern part) constituting a sediment source that is transported towards the Badalona sector by south-directed longshore currents. This material is retained by a groyne (see green line) located at about 100 m from the north border of the coastal stretch. In addition, cross-shore currents drive material towards the offshore part of the profile. From +5.0 to +2.5 m, erosion dominates and the sediment is relocated at the shoreface (i.e. from +2.0 to 0 m). On the contrary, deposition occurs at the central B-C zone where the sewer outfall acts as a sediment trap. Finally, the southern part acts as a sink zone, receiving sediment from longshore currents and the sewer outfall but remaining sheltered by the Badalona port.

The Mataró domain (Fig.4.7a) may be explained with only **two transects**: from the northern part to the stream [S point in magenta] (M-North [M-N]) and from the stream to the southern part (M-South [M-S]). At the north part a revetment (see green line) protects the railway from wave action. High run-up and surges enhance wave-induced eroding fluxes that take material from the sub-aerial beach towards the submerged beach, mainly by undertow currents. Such an offshore flux can be advected by longshore currents, which take it from the narrower northern sector (M-N) to the southern side (M-S), storing the sand next to the groyne. The stream mouth (see magenta line) shows a locally important accretion that should come from the river solid discharge, trapped by the low elevation zone present there.

There was a significant precipitation volume during the event, reaching daily mean values of 23.1 mm on 26 December and 16.6 mm on 27 December. Storm runoff contained fine material, making it difficult to distinguish between the inland or offshore origin of the sediments.

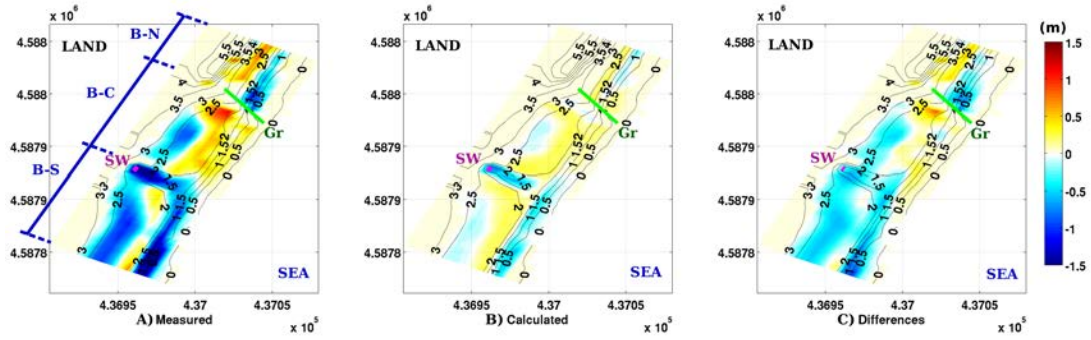

Figure 4.6.: Topography of the emerged beach for the **Badalona case**. Contour lines represent the initial state of the sedimentary deposit. Colour scale: **Blue** and **red** indicate **accretion** and **erosion**, respectively. **Green (Gr)** represents the groin position. **Magenta (SW)** represents the **sewer outfall** position. (a) Differences between the measured morphodynamic states (pre- minus post-storm conditions); (b) differences between the calculated morphodynamic states (pre- minus post-storm conditions); (c) differences between measures and calculated post-storm conditions. All values are in metres.

Nearshore hydro-morphodynamics have been computed with a locally adapted version of the XBEACH model (see Sec. 3.3.3). The two studied beaches (Badalona and Mataró) have been discretized with an irregular grid. The Badalona domain has a cross-shore distance of 500 m (maximum depth = 19.60 m) and an alongshore distance of 370 m. The mesh has a mean grid size of 6.2 m in the cross-shore and 4.56 m in the alongshore directions, with a total of 6724 nodes. The Mataró domain has a cross-shore distance of 1440 m (maximum depth = 11.24 m) and an alongshore distance of 1640 m, with 26,569 nodes. The mesh has a mean grid size of 8.9 m in the cross-shore and 10.12 m in the alongshore directions. The sediment is considered as uniform, both for Badalona beach ($D_{50} = 550\mu m$) and for Mataró beach ($D_{50} = 500\mu m$). The sediment equilibrium concentration has been evaluated with the van Rijn (2007) formulation, based on previous results from the Catalan coast (Sánchez-Arcilla et al., 2013).

For both beaches, the LIDAR campaign covered only the emerged part. Hence, the bathymetry has been digitized from the most updated available bathymetric information. Metrics have been calculated only where active grid points are present, disregarding non-erodible points that artificially increase BSS values. Previous work at the Catalan coast has resulted in BSS values around 0.44, which can be considered as acceptable (Gràcia et al., 2013b).

The offshore boundary conditions consist of: (i) directional spectra from the SWAN model output (see Sect.4.3) every 20 min, and (ii) sea level time series. These series are generated from blending Barcelona port sea level measurements (provided by Puertos del Estado) with assimilated local atmospheric pressure gauges, with a time sampling of 300 s. Storm surges did not influence significantly the sea level height, except on 26th and 27th December, when there was a daily averaged of 8 cm at both days (Fig. 4.3).

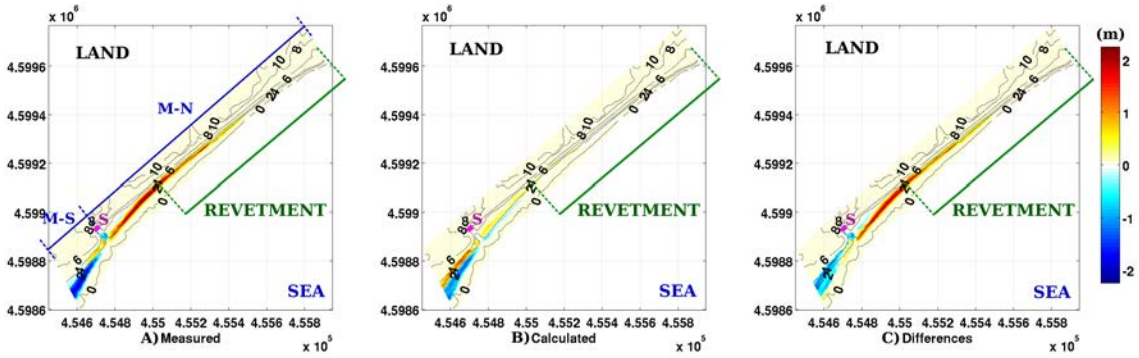

Figure 4.7.: Topography of the emerged beach for the **Mataró** case. Contour lines represent the initial state of the sedimentary diposit. Colour scale: **Blue** and **red** indicate **accretion** and **erosion**, respectively. **Green (Gr)** represents the revetment. **Magenta (S)** represents the **stream discharge** area. (a) Differences between the measured morphodynamic states (pre- minus post-storm conditions); (b) differences between the calculated morphodynamic states (pre- minus post-storm conditions); (c) differences between measures and calculated post-storm conditions. All units are in metres.

As noted in Figs. 4.6(b) and 4.7(b), the simulations have reproduced the observed erosion and accretion patterns. From a qualitative point of view, the model has even been able to capture the influence of local constraints such as the Badalona groin or the existing revetments. However, the sedimentary input from land, although observable, has not been taken into account due to the lack of reliable data.

With these settings a **BSS** of **0.36** has been obtained for **Badalona** beach, which can be considered as acceptable. However, the final offshore displacement of the run-up action point is 0.5 m (i.e. there is **no shoreline retreat** as the aerial photography suggested) whereas the **maximum simulated run-up is 2.3 m**.

Better results have been achieved at **Mataró** beach, although it is a larger area (**BSS = 0.38**). In this case, the emerged erosion/accretion patterns are well reproduced, showing a general **reflective** behaviour at the submerged part. Sediment from the depth of closure to the 2 m contour line goes onshorewards to the shoreline, leading to a steep and almost homogeneous submerged beach slope (4H : 1V).

The low BSS values stem from inaccuracies in the computed erosion/accretion magnitudes. Figures 4.6(c) and 4.7(c) show that the simulations underpredict the mea-

sured values, reaching **maximum error**s of **-0.8 m** in the Badalona case, and **1.5 m** in the Mataró case. The origin of these discrepancies will be addressed in the next section.

4.5. Errors and uncertainties

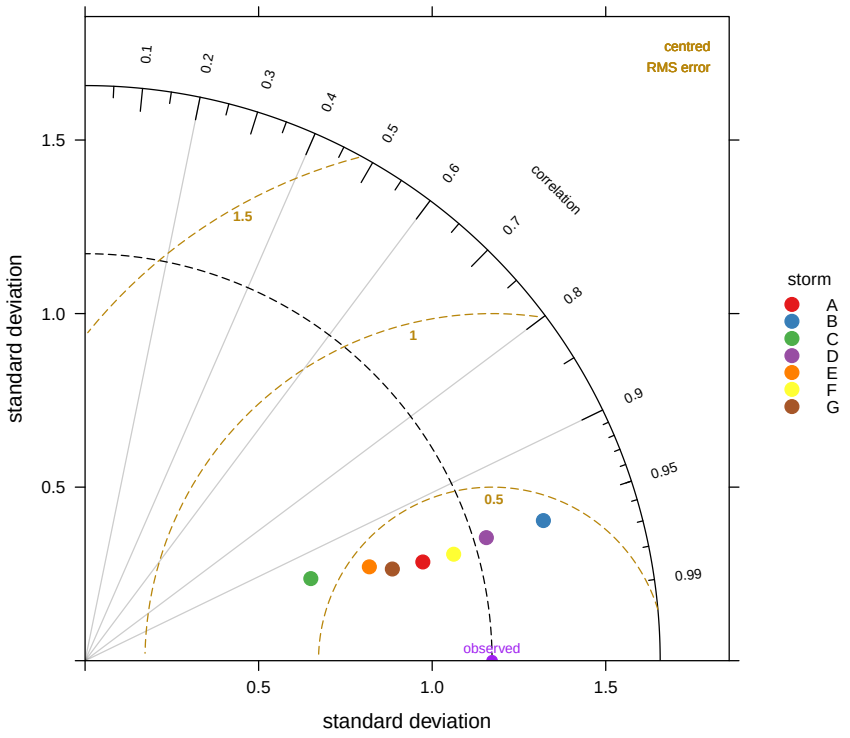

Figure 4.8.: Hydrodynamic sensitivity analysis (significant wave height, H_s) at the **Llobregat buoy** schematized in a Taylor diagram. Grey lines represent the correlation coefficient. Golden semicircles represent the CRMS error. **Point legend: A** (Original wind field), **B** (+20%), **C** (−20%), **D** (+10%), **E** (−10%), **F** (+5%) and **G** (−5%). All perturbations refer to wind driving (for base state, see text). Units en m.

Wave patterns have been reproduced with a **relative error level** of around **20** %. However, the resulting error in morphodynamics is around 1.0 m as maximum, leading to a relative error level beyond **50** %. The error is propagated in a non-linear sequential manner: from shelf meteo-oceanographic conditions, controlling regional hydrodynamics, to local (near-shore) hydro-morphodynamics and then to morphodynamic evolution. In Sec. 4.2, the wave dissipation term (characterizing wave energy levels as one of the main drivers) has been tuned considering the generation term as fixed. Therefore, we shall here consider dissipation as fixed and analyse

the sequential error propagation, with emphasis on the well-recognized wind field uncertainty (Cavaleri et al., 2010; Alomar et al., 2010).

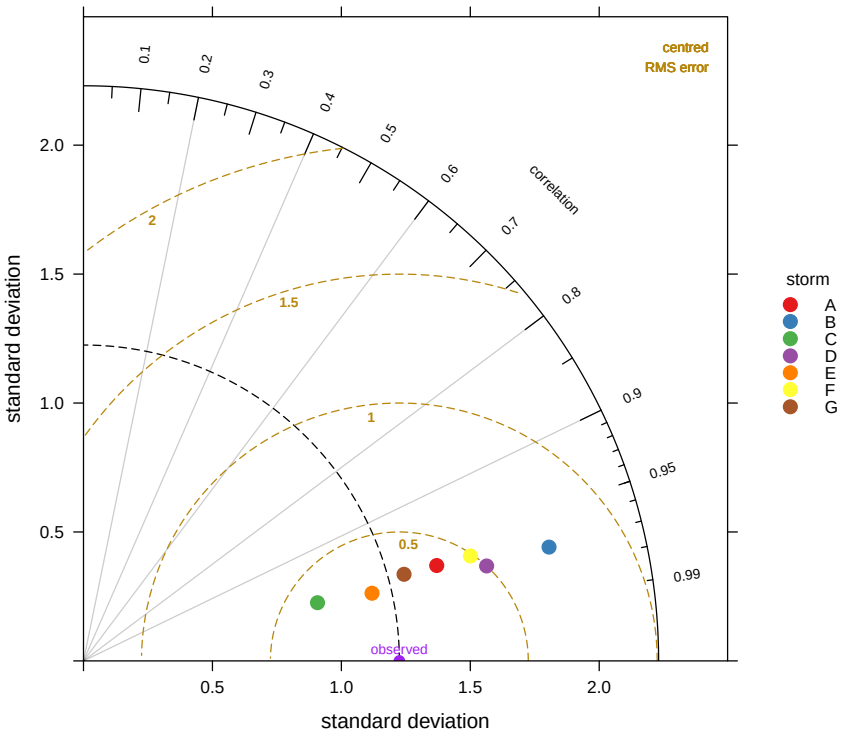

Figure 4.9.: Hydrodynamic sensitivity analysis (significant wave height, H_s) at the **Blanes buoy** schematized in a Taylor diagram. Grey lines represent the correlation coefficient. Golden semicircles represent the CRMS error. **Point legend: A** (Original wind field), **B** (+20%), **C** (−20%), **D** (+10%), **E** (−10%), **F** (+5%) and **G** (−5%). All perturbations refer to wind driving (for base state, see text). Units en m.

For this purpose a linear correlation between wind velocity measurements and simulations has been obtained, analogous to the one presented in Sec.4.2 (i.e. altimeter wind modulus vs. calculated wind field modulus). When the wind fields for this specific storm are **increased** by **10** %, the fitness improves at deep waters (i.e. D-1 domain, see Fig.4.1). This is in accordance with previous results (Bertotti and Cavaleri, 2011) and shows that a 15 % error in wind forecasting is not unusual, especially when sharp gradients occur. To perform an error assessment, the wind field modulus can be perturbed (Alomar et al., 2009, 2014) and quantify the consequences at nearshore scales. The following subset of cases has been selected, employing the same methodology described in Sects. 4.3 and 4.4: no perturbation (A); 20 % increase (B), 10 % increase (D) and 5 % increase (F); correspondingly 20 % (C), 10 % (E) and 5 % (G) decrements.

Wave height data from the XIOM buoy network will be compared with the SWAN

output from the D-3 domain (i.e. 1×1 km mesh). This diagram summarizes observations and model agreement, establishing a graphical relationship among standard deviation (scaled by the number of samples), centred root mean square error and the correlation coefficient. The model performance may be assessed from the distance between the observational reference point and the model points. Note that the reference point in the x axis is related to the standard deviation intrinsic to each buoy.

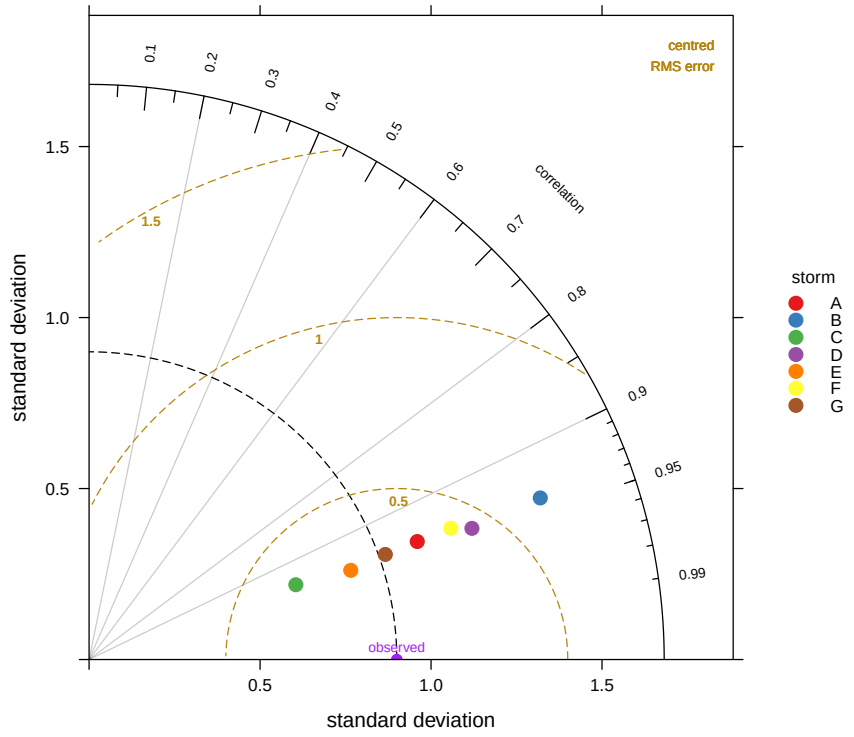

Figure 4.10.: Hydrodynamic sensitivity analysis (significant wave height, H_s) at the **Cape Tortosa buoy** schematized in a Taylor diagram. Grey lines represent the correlation coefficient. Golden semicircles represent the CRMS error. **Point legend: A** (Original wind field), **B** (+20%), **C** (−20%), **D** (+10%), **E** (−10%), **F** (+5%) and **G** (−5%). All perturbations refer to wind driving (for base state, see text). Units en m.

In all three buoys, the correlations are higher for the H_s than for the T_p. That is normal, because the H_s is the integrated energy across the two dimensions of the spectra, whereas T_p is representative of the peak bin. The matching among partitions of the spectra are harder to be modelled (Cavaleri, 2009).

Interestingly, each buoy presents distinctive trends but with commonalities that support the existence of a link between deep and intermediate water wave conditions (through the propagation physics). If the **wind modulus** field is **decreased**, **better** performance (smaller deviation) is found at **Blanes** (Tab. 4.2), while the **op-**

posite occurs at **Llobregat** (Tab.4.1). The performance of the model was worse for extreme cases: B and C did not show any improvement. On the same line, E(−10%) case at Blanes and F(+5%) case at Llobregat show smaller deviations than the base model. These results reinforce the concept that a perturbation ranging from 5 to 10% may provide wind fields that are more consistent with the waves.

The COE also confirms this trend: at Llobregat, the COE for H_s is slightly higher at case ***F*** (+5%) than the baseline, but the T_p shows worse values; at Blanes, the case ***G*** (−5%) has better COE and MB than the base scenario for both H_s and T_p; however, at **Cape Tortosa** (Tab.4.3), the base simulation is better than ***G*** (−5%), although the T_p is lower at the latter case.

The Taylor diagrams complement the former contents, but with slight differences: at Llobregat (Fig. 4.8), cases ***D*** (+10%) and ***F*** (+5%) have lower distance with the observations; but Blanes (Fig. 4.9) and Cape Tortosa (Fig. 4.13) coincide that cases ***E*** (−10%) and ***G*** (−5%) are more accurate. These differences may be attributed to that the Taylor aggregates three metrics (centred RMS, correlation and standard deviation), whilst the other metrics present in the Tables are individual.

Nevertheless, model and observations may be considered as well correlated, with mean coefficients near 0.95 at Llobregat and 0.97 at Blanes. Likewise, RMSE is higher at Blanes (mean value of 0.47) than at Llobregat (0.35). Moreover, distances among the different cases are greater at Blanes than at Llobregat, suggesting that Blanes is more sensitive to perturbations. This may be due to a **more exposed** to **eastern** wave storms at **Blanes** (more energetic, and thus more capable of producing morphodynamic impact) than the Llobregat buoy. Since higher waves were recorded and more variability exists at Blanes, the standard deviation is slightly larger.

Cap Tortosa results are similar to the ones from Blanes (Tab. 4.3): more agreement is found by decreasing the wind modulus by 10% (E case). Correlations are lower than the ones described above (0.94), but also in a positive way, with RMSE (0.36) and standard deviation (0.9) showing the lowest values. These metrics may be explained as the result of the **milder wave** conditions at the **south-central** (Tarragona) coastal sector for this event (see Fig.4.2), suggesting that simulations for moderate waves are better than for more extreme (high or low) ones.

Hydrodynamic drivers play a fundamental role in coastal evolution (Gràcia et al., 2013b), and a wider range of BSS values was expected when perturbing sea level and wave conditions. Directional wave spectra did alter the metrics but, surprisingly, sea level variations did not trigger any significant change in the response. This is attributed to the reserve beach berm level in some profiles and to the crest level of the promenade or revetment in others, suggesting a transient morphodynamic response.

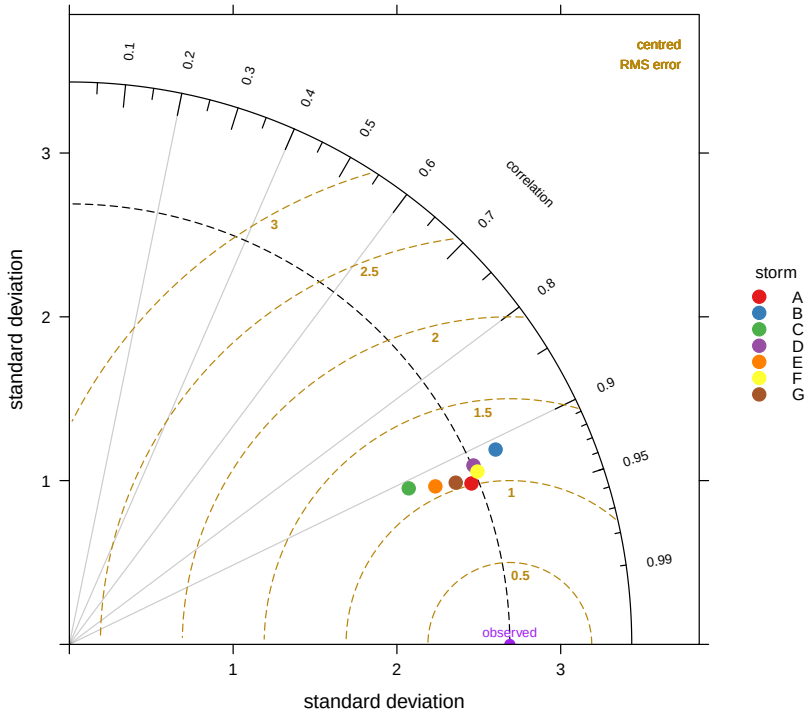

Figure 4.11.: Hydrodynamic sensitivity analysis (wave peak period, T_p) at the **Llobregat buoy** schematized in a Taylor diagram. Grey lines represent the correlation coefficient. Golden semicircles represent the CRMS error. **Point legend: A** (Original wind field), **B** (+20%), **C** (−20%), **D** (+10%), **E** (−10%), **F** (+5%) and **G** (−5%). All perturbations refer to wind driving (for base state, see text). Units en s.

Table 4.1.: Metrics for the significant wave height $H_s(m)$ and peak wave period $T_p(s)$ at the **Llobregat** buoy. ***Legend: MB*** *(Mean bias, in m);* ***RMSE*** *(Root Mean Square Error, in m);* ***r*** *(correlation coefficient);* ***COE*** *(Coefficient of Efficiency).*

Wind	**H_s**				**T_p**			
	MB	**RMSE**	**r**	**COE**	**MB**	**RMSE**	**r**	**COE**
A *(Base)*	0.04	0.35	0.96	0.68	-0.25	1.04	0.93	0.59
B (+20%)	-0.51	0.67	0.96	0.52	-1.23	1.71	0.91	0.37
C (−20%)	0.65	0.87	0.94	-0.12	1.18	1.64	0.91	0.22
D (+10%)	-0.21	0.41	0.96	0.66	-0.68	1.30	0.91	0.52
E (−10%)	0.38	0.58	0.95	0.46	0.53	1.19	0.92	0.48
F (+5%)	-0.11	0.34	0.96	0.69	-0.67	1.26	0.92	0.52
G (−5%)	0.20	0.44	0.96	0.60	-0.01	1.04	0.92	0.57

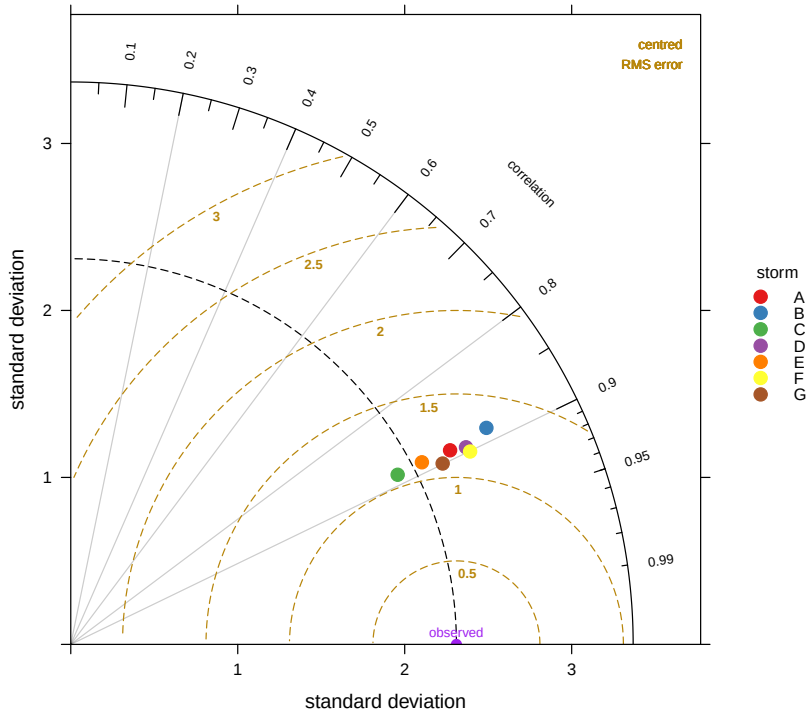

Figure 4.12.: Hydrodynamic sensitivity analysis (wave peak period, T_p) at the **Blanes buoy** schematized in a Taylor diagram. Grey lines represent the correlation coefficient. Golden semi-circles represent the CRMS error. **Point legend: A** (Original wind field), **B** (+20%), **C** (−20%), **D** (+10%), **E** (−10%), **F** (+5%) and **G** (−5%). All perturbations refer to wind driving (for base state, see text). Units en s.

Table 4.2.: Metrics for the significant wave height $H_s(m)$ and peak wave period $T_p(s)$ at the **Blanes** buoy. ***Legend:*** ***MB*** *(Mean bias, in m);* ***RMSE*** *(Root Mean Square Error, in m);* ***r*** *(correlation coefficient);* ***COE*** *(Coefficient of Efficiency).*

Wind	**H_s**				**T_p**			
	MB	**RMSE**	**r**	**COE**	**MB**	**RMSE**	**r**	**COE**
A *(Base)*	-0.25	0.47	0.97	0.74	-0.28	1.19	0.89	0.51
B (+20%)	-0.93	1.18	0.97	0.39	-1.28	1.83	0.89	0.27
C (−20%)	0.53	0.66	0.97	0.26	1.24	1.64	0.89	0.18
D (+10%)	-0.54	0.73	0.97	0.58	-0.70	1.37	0.89	0.45
E (−10%)	0.19	0.34	0.97	0.69	0.56	1.24	0.89	0.44
F (+5%)	-0.45	0.67	0.97	0.62	-0.66	1.33	0.90	0.49
G (−5%)	-0.05	0.34	0.97	0.76	0.00	1.08	0.90	0.55

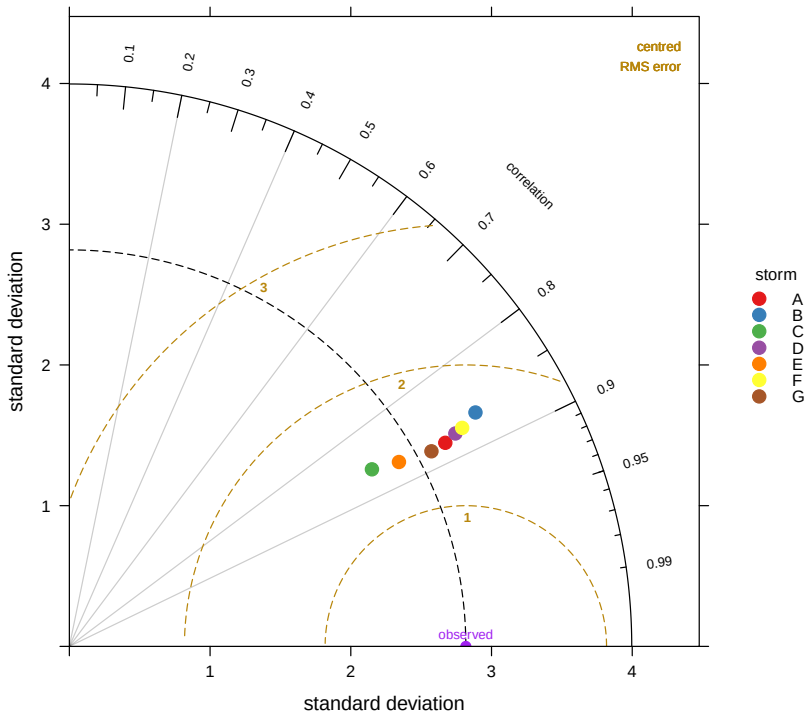

Figure 4.13.: Hydrodynamic sensitivity analysis (wave peak period, T_p) at the **Cape Tortosa buoy** schematized in a Taylor diagram. Grey lines represent the correlation coefficient. Golden semicircles represent the CRMS error. **Point legend: A** (Original wind field), **B** (+20%), **C** (−20%), **D** (+10%), **E** (−10%), **F** (+5%) and **G** (−5%). All perturbations refer to wind driving (for base state, see text). Units en s.

Table 4.3.: Metrics for the significant wave height $H_s(m)$ and peak wave period $T_p(s)$ at the **Cape Tortosa** buoy. ***Legend: MB*** *(Mean bias, in m);* ***RMSE*** *(Root Mean Square Error, in m);* ***r*** *(correlation coefficient);* ***COE*** *(Coefficient of Efficiency).*

Wind	**H_s**				**T_p**			
	MB	**RMSE**	**r**	**COE**	**MB**	**RMSE**	**r**	**COE**
A *(Base)*	0.07	0.36	0.94	0.73	-0.48	1.53	0.88	0.49
B (+20%)	-0.44	0.77	0.94	0.48	-1.52	2.25	0.87	0.30
C (−20%)	0.66	0.75	0.94	-0.15	1.16	1.83	0.86	0.22
D (+10%)	-0.13	0.46	0.95	0.65	-0.92	1.77	0.88	0.44
E (−10%)	0.41	0.51	0.95	0.42	0.37	1.44	0.87	0.43
F (+5%)	-0.08	0.42	0.94	0.68	-0.84	1.76	0.87	0.45
G (−5%)	0.22	0.38	0.94	0.67	-0.10	1.41	0.88	0.49

In Sec.4.3 it was noted that LIM-COPAS results were smoother than the observations (see Figs.4.6(c) and 4.7(c)), meaning that an increase of the drivers' magnitude would lead to sharper morphodynamic evolution. As an illustration, in Fig. 4.14 for the Mataró case (see purple line), a **moderate increase** of drivers (+5%, F case) **improves BSS** from 0.38 to **0.44**. This behaviour reinforces the critical role played by hydrodynamic forcing, whose best model skill is obtained by increasing the wind strength in a moderate way. However, there are still exceptions such as the **G case** (−5%), where a decrease of hydrodynamic action improves the sub-aerial beach accretion in Mataró south (see Fig. 4.7(b)), which goes from +6 to +4 m and results in more balanced metrics.

Therefore, whenever the wind strength is augmented, both correct and incorrect patterns tend to be amplified. A balanced fit quality is provided by the bias (see green line) and higher BSS values are, thus, not necessarily correlated with lower global mean error. For very energetic levels, e.g. B scenario (+20%), some simulations may even become morphodynamically unbounded and, thus, unstable.

Similar conclusions can be derived from the Badalona beach case (see red line), but in this case morphodynamic patterns are more complex due to local constraints. If the **wind** modulus is **decreased** by **5**% (G case), the balance between correct and incorrect patterns leads to **higher BSS** (from 0.36 to **0.40**). Note that this is another case where bias increases (see blue line) and BSS increases, indicating that the overall pattern reproduction is improved whereas the error level is not. This may be explained in terms of a balance between local variables and overall energetic level. For instance, when the wind input is reduced (−10 or −20% in E and C cases), the observed morphodynamic patterns (see Sect.4.3) are not properly developed, resulting in a BSS around 0.2. However, when the wind strength is decreased unrealistically, the sediment fluxes coming from the northern part of the domain start to bypass the groyne (see red line), reversing the behaviour in the central part [B-C], Fig. 4.6(a) and (c), from erosion to accretion.

4.6. Discussion

Uncertainty reduction, as seen in previous sections, depends critically on the **accuracy** of the **forcing fields** but is also influenced by all terms appearing in the governing equations. In this balance, the physics, the corresponding parameterizations and the numerical discretizations play important roles.

As shown in Sec.4.2, strong bursts of wind momentum transfer were captured by the wave model, albeit with large errors in areas near the land-ocean border (e.g. southern France, see Fig. 4.5). In the state-of-the-art, the implemented wave growth parameterizations are based on moderate wave conditions, because extreme event data for semi-enclosed domains are scarce. At intermediate waters, for this specific storm, the wave height gradients are well captured by the wave model, being steeper than the observed ones and leading to overestimation (i.e. at **Blanes** the **growth**

slope was $0.29mh^{-1}$ in the XIOM buoy, whilst $0.33mh^{-1}$ at the SWAN model) and milder when underestimating (i.e. at Llobregat was $0.22mh^{-1}$ at XIOM and $0.18mh^{-1}$ at the model). But at **Blanes**, the **error** at the **first storm peak** was near **1.5 m** (Sec. 4.3) whereas the discrepancy during wave growth was about 0.7 m. Despite model and observations have a similar growth slope, their offsets differ by about 1 m (Fig. 4.2). Note that the wave directional shift goes from 300 to 90° in less than 2 hours (from 17:00 to 19:00 on 26 December), with a fast veering at the northern part, more exposed than at the Central or southern parts. At Blanes, the wave action balance responds to that sudden shift with an unrealistic sharp increment of the wave height (0.6 m), leading to the abovementioned offset differences.

The time scale of hydrodynamics and morphodynamics may differ by one order of magnitude or more, introducing additional metric-related uncertainty (see Sects. 4.3 to 4.5). The Mataró domain (1700 m alongshore) is four times bigger than the Badalona one (370 m alongshore) and because of that (see Sec. 4.5), Badalona is more sensitive to wind input changes according to the employed metrics (see Fig.4.14). That **sensitivity** may be explained through the analysis of **run-up** and emerged **beach volume** time series. During the storm there are two run-up peaks. The first coincides with the storm peak and the second occurs at the growth phase of the second storm peak (30 h later approximately). When the wind modulus is increased, the run-up maxima show a direct proportionality. If the wind is reduced by 20%, the second run-up peak almost disappears, leading to total erosion volumes near zero at the emerged zone. However, if the wind fields are increased by 20%, the second run-up peak reaches 2 m and the first one 2.75 m, while in the unperturbed simulation the corresponding values are 1.3 and 2.3 m, respectively. Higher run-ups are correlated with **stronger undertow currents**, advecting sediment from the emerged to the submerged part of the beach and enhancing erosion.

As noted in Sec. 4.4, the final submerged beach slope tends to remain similar in all the simulations, being intrinsic to beach characteristics and parameterizations; the corresponding shorelines' positions are, however, different. Considering the final beach profile of the unperturbed simulations as reference, the -20 and -10% cases exhibit a **mean shoreline retreat difference** (onshore) of **30** and **18 m**, respectively. There is no difference in the final beach response between the base and the -5% simulation. However, same final beach profiles are found with the $+5$ and $+10\%$ increments, reporting a shoreline increase of 15 m. In these two cases, the mobility area begins further offshore (at about 5 m water depth) due to the wave action increase, whereas in the milder cases, all areas are displaced inshore. For more dissipative beaches (as in the Badalona case) we may find an opposite response, with shoreline retreat and offshore displacement associated to more energetic waves.

Adding **storm surges** to incident wave action (see Sec. 4.4) should have deep and significant morphodynamic consequences, although in some runs they may be numerically limited. A perturbation of $+0.1$ m in sea level due to surges or uncertainty provokes a markedly different beach response and flooding consequences. The

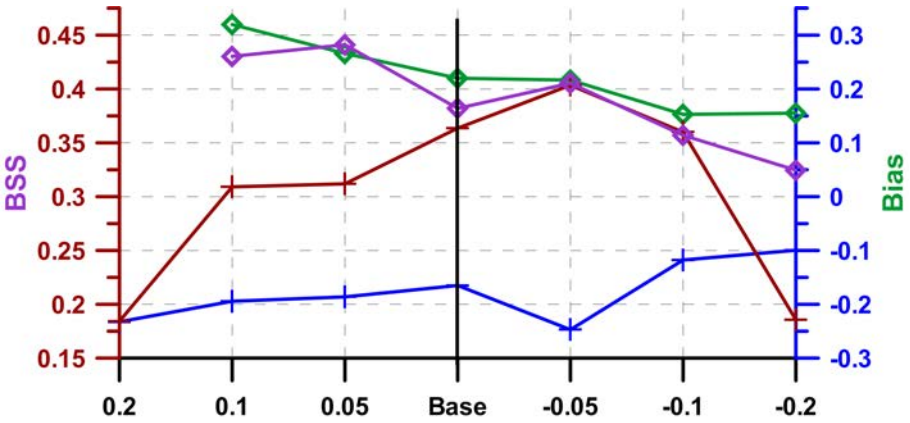

Figure 4.14.: Morphodynamic **sensitivity analysis**. *Left axis:* **Badalona** BSS appears in **red**; whereas the **Mataró** BSS is in purple. *Right axis:* Badalona bias is in **blue**; whilst the Mataró bias is in **green**. The x axis indicates the base simulation and the numerical results correspond to increments (or decrements) in the wind field input.

amount is a function of berm or structural crest levels (e.g. the promenade at the Badalona case and the revetment at the northern part of the Mataró case).

The simulated bottom and coastline evolution will depend on the overall sediment budget, which means considering the **land discharge** (in this case the sewer outfall at Badalona and the river stream at Mataró). They have not been included in the analysis, however, due to the **lack of quantitative observations**, but they are expected to have a significant (even if local) effect on the morphodynamic evolution under storm events, when **flash floods** in a few hours discharge most of the land-derived sediments expected in an average year (see Sec. 4.4, Figs. 4.6(a) and 4.7(a)).

In the presented cases, as usually happens in coastal studies, the emerged beach may be characterized (e.g. using LIDAR) in a more quantitative manner than the submerged part of the profiles, which had to be at least partly interpolated. This introduces another uncertainty in the computations, although in the presented cases the interpolated submerged beach behaved (qualitatively) as expected from previous knowledge (campaigns and simulations). The interpolation provides, in addition, the smooth bathymetry that is required to avoid instabilities in the simulations, which often requires artificial smoothing of surveyed isobaths to ensure numerical stability, particularly when sharp gradients are present. Because of that it cannot be stated, in general, that high-resolution bathymetry (with abrupt elevation changes) would significantly improve the results with respect to a smoothed geometry.

The connection between the emerged and submerged parts of the beach through the **swash zone** is another important hindrance in nearshore modelling. It depends on **non-linear processes** such as wave asymmetry, skewness and non-linear moments of bottom orbital velocity, including the turbulent component. As it has been noted in Sec. 4.4, van Rijn (2007) is one of the formulations that partially addressed some

of these complex physical processes. Some of these processes has been included in LIM-COPAS, but in a simplified form and without considering the new knowledge recently derived from **large-scale laboratory data** (Alsina and Cáceres, 2011; Sánchez-Arcilla et al., 2011a).

In addition to this land boundary condition, the **budget balance** will depend on the lateral sediment fluxes, which constitute another uncertainty source. These lateral conditions determine the real sand volume available in a littoral cell and, therefore, the amount that can be mobilized. The uncertainty can, however, be partially alleviated with **nested simulations** that move these poorly known sediment boundary fluxes far enough.

In all the above fluxes and boundary conditions there is also the question of multiple sediment sizes, which is the normal situation in real beaches but is seldom considered in simulations. Effects such as heterogeneous mixing and bottom armouring are still not considered in state-of-the-art models.

In summary, present models combine multiple limitations that, in addition to natural variability, result in **uncertainties** at **multiple scales** which are still **hard** to **quantify**, both **individually** and as part of a **joint assessment**.

4.7. Conclusions

Hydro-morphodynamic predictions in restricted domains show larger errors than simulations for open sea cases, where temporal and spatial scales show smaller gradients. Wave action is an important driver for morphodynamic evolution and the errors in spectral wave parameters near the coast are about twice what has been found in the middle of the Mediterranean basin. The spectral shape also has significant effects on sediment transport since, for instance, the existence of more than one spectral peak results in long waves or crossing wave trains, both of which may modify critically the associated morphological evolution. The appearance of time lags between predicted and simulated storm peaks is another type of error that, together with the under- and over-predictions mentioned in this Chapter, may lead to important differences when simulating erosion or flooding processes.

The spatial distribution of sediment fluxes introduces further uncertainties in the simulations, whose errors may go from 20% for hydrodynamics to more than 50% for the morphodynamics. This is due to the integrative nature of the calculated sea bed evolution (responding to wave and surge conditions plus the effects of sediment characteristics, the presence of barriers, etc.). The resulting evolution comes from mutually interacting longshore and cross-shore transports that must appear explicitly in the computations (e.g. the discussed offshore transport during storms that is then captured by the alongshore flux and leads to enhanced bypass around the tip of breakwaters or groins). The river and outfall solid discharges should also be considered in the analyses since their signature is apparent in some of the data. The lack of quantitative measurements, however, has precluded considering these

in the paper, adding another source of uncertainty. The morphodynamic computations also integrate the sediment fluxes at the lateral and shoreline boundaries, all of which are difficult to quantify. This explains the large discrepancies of simulations and observations (up to 1.5 in bed level in the worst cases) and justifies BSS values of around 0.30. The quality of simulated results decreases in the presence of structures (groins, revetments, etc.), where the modified sediment fluxes are even more uncertain (more complex hydrodynamics and morphodynamics, partial barrier effects, etc.).

The quality of the predictions may be improved by semi-empirical coefficients (e.g. a 10% increase in the driving wind velocity) or by improved physical formulations (swash zone parameterized fluxes for the shore boundary condition). For storm conditions, however, more energetic conditions may lead to larger errors if the input or boundary conditions are perturbed, but they may also converge more quickly towards the true state if these conditions correspond to the sought solution.

This illustrates the complex nature and propagation of errors in hydro - morphodynamic modelling suites and the need to combine measurements with high-resolution physics to improve the accuracy and robustness of the calculations. This would be the way to achieve better informed coastal decisions.

5. Storm Hindcast: coupling and skill

5.1. Introduction

Storm waves are the primary driver for episodic coastal hazards in the Catalan Coast, so the proposed forecasting system needs to provide reliable wave assessments. As exposed in Ch.2, the wave climate at the Catalan coast is characterized by: (i) short fetches, (ii) shadow effect for waves from the south and east due to the Balearic islands; (iii) complex bathymetry with deep canyons close to the coast, (iv) high spatiotemporal wind field variability, (v) calm waves during the summer and energetic storms from October to May (storm season), (vi) the presence of wind jets channelized by river valleys and (vii) bimodal spectra derived from sea and swell waves combinations. These features, some of them usual for a semi-enclosed basin, limit the reliability of wave predictions in the area.

Systematic **underestimation** (wave height and period) at the Catalan Coast under extreme regimes has been deeply analysed by several authors. Bolaños (2004) hypothesised that part of error was due to the **limited spatial** and **time scales** of the processes to be reproduced, around 10 km and 12 hours. The author increased wave accuracy by using an atmospheric model nested with enough resolution to reproduce the different phenomena.

Alomar (2012) proposed two ways to improve the wave forecasts. The first one was to **increase** the **spatial** and **temporal** resolution of the meteorological module to capture **wind** and **wave gradients** in the geographic dimensions. She proved that: (i) using a wind input with finer spatial resolution only improve the timing of the peaks, but not the magnitude; (ii) better temporal resolution leads to improve the maximum values for a storm event.

The second modification proposed in Alomar (2012) was adjusting the **wave growth rate**. It was confirmed that the observed rate of wave growth in the study region was faster than the simulations and faster than the rates derived for more homogeneous wind conditions.

Pallarés (2016) considered (i) the use of **unstructured grids** as an alternative of the regular nested grids; (ii) and **different coupling schemes** among the wave, circulation and atmospheric models for different situations. The results shown that two-way-coupling may improve accuracy when addressing sharp hydrodynamic gradients. She also obtained (iii) that the **mean wave period** could be **less underpredicted** with the **whitecapping** term **correction** proposed by Rogers et al. (2003). With this correction, that is dependent on the wave number and wave steep-

ness under young sea waves, it can be modelled increases of the energy spectra at lower frequencies.

The previous Ch. 4 shown the results of the hydrodynamic and morphodynamic modules under a specific storm event (D-08). Atmospheric conditions were hindcasted through wind fields blended with **remote sensing observations** (Bentamy et al., 2007). Hence, atmospheric module errors and limits were prescribed a priori. As highlighted in the same Chapter via a sensibility analysis, the accuracy of the wind fields influenced severely the whole forecasting chain. Hence, an improvement in the atmospheric data may increase the overall skill of the forecasting system. These conclusions lead to the design of the proposed LIM-COPAS architecture, as described in Ch. 3.

In this Chapter, two strategies have been tested for improving the accuracy of the wave forecasts: (i) an improvement of the wind input information by using an atmospheric model that would increase spatial ($3 \times 3\ km$) and temporal resolution (20 minutes), respect to Chapter 4; (ii) and an increase of the update frequency in the SWAN model for both the wind (every 20 mins) and the circulation (hourly) fields. These two improvements can be done via adding an atmospheric model (WRF) to the modelling chain proposed in Ch 4.

Hence, **the aim of this Chapter is to compare the Meteorological and Hydrodynamic modules in LIM-COPAS with in-situ observations for a subset of recent storms**.

Wind fields and integrated wave parameters are compared with **in-situ observations** from the **Puertos del Estado** network (PdE hereafter, see Sec. 3.2.2 for a description). **Six** recent **storms** will be analysed: October 2015 [O-15, hereafter] (29/09/2015 - 01/10/2015); November 2015 [N-15] (01/11/2015 - 04/11/2015); January 2016 [J-16] (10/01/2016 - 12/01/2016); February 2016 [F-16] (27/02/2016 - 28/02/2016); December 2016 [D-16] (17/12/2016 - 23/12/2016) and January 2017 [J-17] (16/01/2017 - 24/01/2017). These ones represent common synoptic scale anomalies in the study area.

The geographical position of the observational network elements can be found in Fig. 2.1 (see **yellow** diamonds). ERA-INTERIM reanalysis (see Sec. 3.2.1) is used as the boundary and initial conditions for the first parent grid (i.e. the orange one that spans the whole Southern Europe in Fig. 3.2). Due to its inherent reanalysis nature, ERA-INTERIM usually shows better skill than conventional operational forecasts. However, it has been considered that the first tests of the proposed coastal forecast system should be done with reanalysis data, in order to bound what would be the best skill that can be achieved with LIM-COPAS.

Note also that in this Chapter, the morphodynamic module will not be addressed. The reason comes from the lack of **post-storm LIDAR** data, thus harnessing to test the veracity of the modelled coastal response. Instead, the wave hindcasts derived from this Chapter will constitute the forcings for the Risk module (see Sec. 6.3.3.1), that will be tested in the next Ch. 6.

The Study Area and the Methodology have been already discussed in Ch. 2 and

Ch. 3, respectively. Hence, these two parts will not be described. The atmospheric module description can be found in Sec. 3.3.1, the hydrodynamic module in Sec. 3.3.2 and the description of the error metrics in Sec. 3.4. The Chapter is structured as follows: Sec. 5.2 describes the main features of the storm events, the results of the hindcast can be found in Sec. 5.3, discussed in Sec. 5.4 and concluded in Sec. 5.5.

In the Appendix C can be found the time series that show the model performance vs. observations. These series have not been included in the main text in order to ease readability.

5.2. Description of the storm events

The selection of the sample comprises the most recent events that have happened at the Catalan Coast (2015 - 2017 period), because storms previous to 2013 have been deeply analysed in the State of the Art (see Bolaños (2004); Alomar (2012); Pallarés (2016)). In this section can be found for each event, the synoptic, ocean circulation (from IBI-MFC, see Sec. 3.2.3), waves and water level (from PdE monitoring network, Sec. 3.2.2). This section uses local toponymy and the maps presented in the Appendix A are encouraged for the sake of interpretation.

5.2.1. October 2015 (O-15)

O-15 (29/09/2015 - 01/10/2015) was the first event of the 2015-2016 season. It was generated by a **low pressure area** that (i) came from Eastern Europe, (ii) crossed Catalonia between the 26-28 of September and (iii) remained within the Iberian Peninsula during the 29-30 of September, thus leading to an Eastern flux. **Heavy rains** happened at the Costa Brava (Northern Catalan coast), at Pre-Pyrenees and the Francoli river basin, with precipitations up to 100 mm.

The surface configuration was an **anticyclonic block** at Northern Europe, with a zonal (E-W direction) disposition, leading to a **Eastern flux**. In the mid- troposphere levels, a perturbation with cold-air in its centre (around -22°C) was located at the northern of Catalonia. Hence the **temperature vertical profile** was around -16/-18°C. Additionally, at 30/09/2015, a low-pressure area was placed at the Catalan littoral. The moist surface flux and relatively hot from the Mediterranean Sea, plus the cold temperature at the vertical profile were the main reasons that lead to the heavy precipitations that were recorded at the littoral and Pre-Pyrenees.

The absence of a **strong flux** at mid-levels at 29/09/2015 was the main reason for a relatively static rain. Hence, the quantity of precipitation was abundant (up to 100 mm) at different points of the Roses gulf (Creus Cape, see Fig. A.1). The highest record was 145.1 mm at Sant Pere Pescador, in which the precipitation was 140 mm, in just 5 hours.

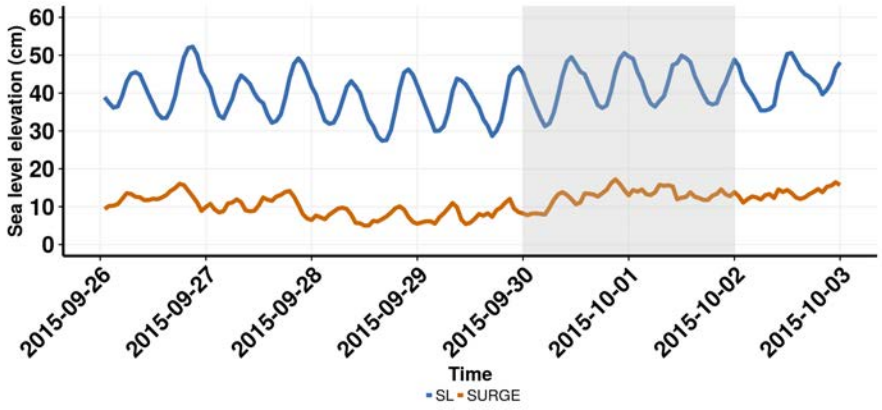

Figure 5.1.: Time series of the **total sea level** (in **blue**) and **storm surge** (in **orange**) at the **Barcelona harbour** tidal gauge for the **October 2015** storm. The shadowed area corresponds to the growth and decay time for the maximum wave height peak. PdE network. Time in days.

These Eastern fluxes lead to wind speeds of 16 m/s at the storm peak (30/09/2015 12:00 h) at Tarragona buoy (Fig. C.1). These winds lead to storm-peak H_s circa 3.5 m and $T_{m02} \approx 7.5$ s at Barcelona buoy (Fig. C.12); at Begur buoy were measured storm-peak $H_s \approx 4.3$ m and $T_{m02} \approx 7$ s (Fig. C.14); whereas at Tarragona the storm-peak H_s was circa 3.5 m and $T_{m02} \approx 7$ s (Fig. C.16). The **mean wave direction** for this episode was **East**.

The circulation fields from MFC-IBI showed a wide gyre that spans the Central part of the Catalan coast at the storm peak. The mean currents within the gyre are around 30 cm/s. Between the central part and the Ebro delta there exists a secondary gyre with similar current modulus.

The storm surge in this episode was **positive** with a **stable trend** (see orange time series below). The mean value reached around 14 cm for the whole episode at Barcelona (Fig. 5.1) and 13 cm at Tarragona (Fig. 5.2). At the storm peak (30/09/2015), the time series showed higher variance at Barcelona than at Tarragona.

5.2.2. November 2015 (N-15)

N-15 (01/11/2015 - 04/11/2015) was characterized by **important storm surges** in comparison with the waves. The origin of this episode was an isolated **low-pressure** at mid-altitudes joint with troposphere lows that came from the **Southern Iberian Peninsula**. The **SE surface flux** from the Mediterranean Sea, that was moist and relatively hot, plus the **cold air at medium levels** of the troposphere were the main drivers in the atmosphere instability.

This instability lead to wind and rainfall around Catalonia. The wind-speed was

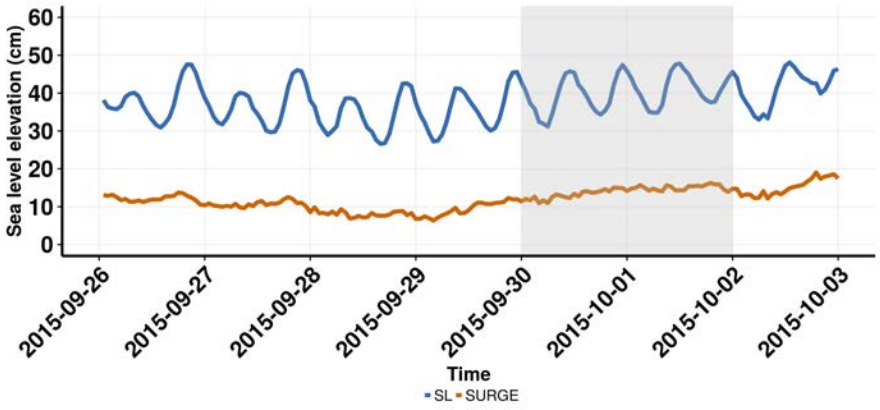

Figure 5.2.: Time series of the total sea level (in **blue**) and storm surge (in **orange**) at the **Tarragona harbour** tidal gauge for the **October 2015** storm. The shadowed area corresponds to the growth and decay time for the maximum wave height peak. PdE network. Time in days.

about 70-100 km/h at different Catalan Pre-littoral sectors, specially at the southern part. Winds up to 100 km/h were recorded at the Pyrenees and Pre-Pyrenees, and at Montseny peaks.

Rainfall coincided with the wave storm peak (02/11/2015). The intensities ranged from weak and moderate to heavy local rains, specially at the Southern part and pre-littoral area. More than 100 mm were measured at Pre-Littoral, Pyrenees and Pre-Pyrenees.

At the storm peak, the wind speeds reached $11\,m/s$ at Begur (Fig. C.2) and $14\,m/s$ at Tarragona (Fig. C.3). These conditions lead to waves with $H_s = 3.3\ m$ and $T_{m02} = 6.8\ s$ at Barcelona buoy (Fig. C.18); at Tarragona were measured storm-peak $H_s \approx 3.1\ m$ and $T_{m02} \approx 5.7\ s$ (Fig. C.20); whilst at Begur the storm-peak was $H_s \approx 4.1\ m$ and $T_{m02} = 6.5\ s$ (Fig. C.22). The mean wave direction for this event was East for the growth-phase and veered toward the South at the decay-phase.

The ocean currents from MFC-IBI exhibited a gyre at the Central part of the Catalan continental shelf whose modulus is around 35 cm/s. The local low pressure led to the highest storm surges (near 25 cm) for this list of events (see orange time series in Figs. 5.3 and 5.4). Two maximums were measured: (i) a first one at 28/10/2015; (ii) and a second one that matches with the wave storm at 02/11/2015. Note that there exists a lack of observations in Tarragona harbour (Fig. 5.4). These high sea levels, joint with moderate waves, would imply high costs (see Ch. 6).

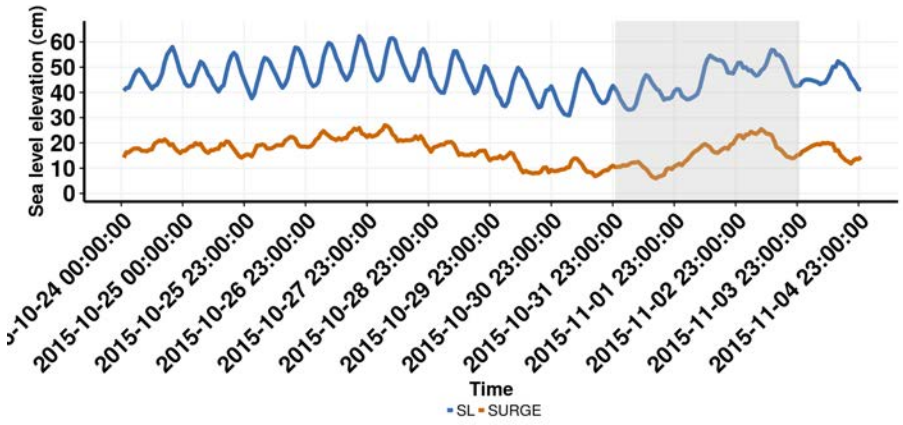

Figure 5.3.: Time series of the **total sea level** (in **blue**) and **storm surge** (in **orange**) at the **Barcelona harbour** tidal gauge for the **November 2015** storm. The shadowed area corresponds to the growth and decay time for the maximum wave height peak. PdE network. Time in days.

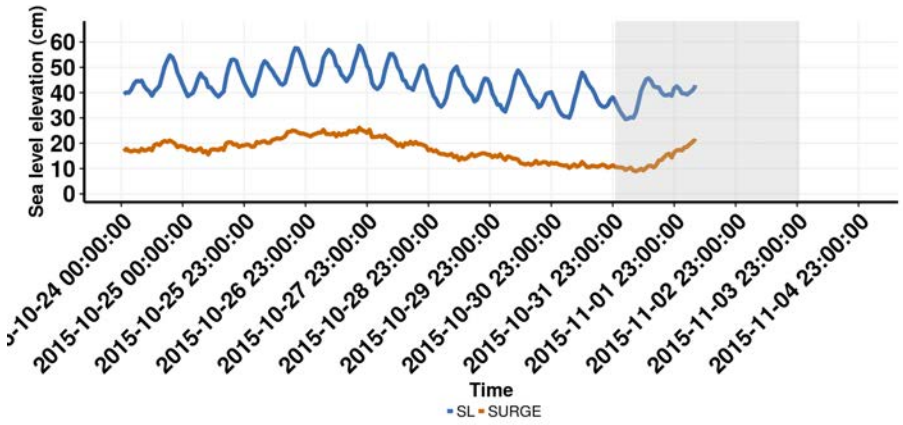

Figure 5.4.: Time series of the total sea level (in **blue**) and storm surge (in **orange**) at the **Tarragona harbour** tidal gauge for the **November 2015** storm. The shadowed area corresponds to the growth and decay time for the maximum wave height peak. Note that the last part of the series was missing data, hence, it could not be plotted. For the sake of comparison, the time axis share the same extension than in Fig. 5.3. PdE network. Time in days.

5.2.3. January 2016 (J-16)

J-16 (10/01/2016 - 12/01/2016) was featured by a **jet** current (**western** wind), as a consequence of a perturbation located at the **Western part** of the British Islands. This configuration led to snow and rainfall at the NW Catalonia. Additionally,

temperatures rose specially high at the Eastern Catalonia.

Weak rainfall happened from 08/01/2016 to 12/01/2016 at the northern area of the Pyrenees and locally isolated areas (Alt Empordà). Cumulative rain was low, but the snow level moved from 1000 to 800 m at the Northern area of the Pyrenees.

At the storm peak, the wind speeds reached $14\,m/s$ at Begur (Fig. C.2) and $15\,m/s$ at Tarragona (Fig. C.3). These conditions led to waves with $H_s \approx 2.75\ m$ and $T_{m02} \approx 6.5\ s$ at Barcelona buoy (Fig. C.24); at Tarragona were measured storm-peak $H_s \approx 3.4\ m$ and $T_{m02} \approx 5.4\ s$ (Fig. C.26); whilst at Begur the storm-peak was $H_s \approx 4.1\ m$ and $T_{m02} = 6.5\ s$ (Fig. C.28). The mean wave direction for this event was South-West.

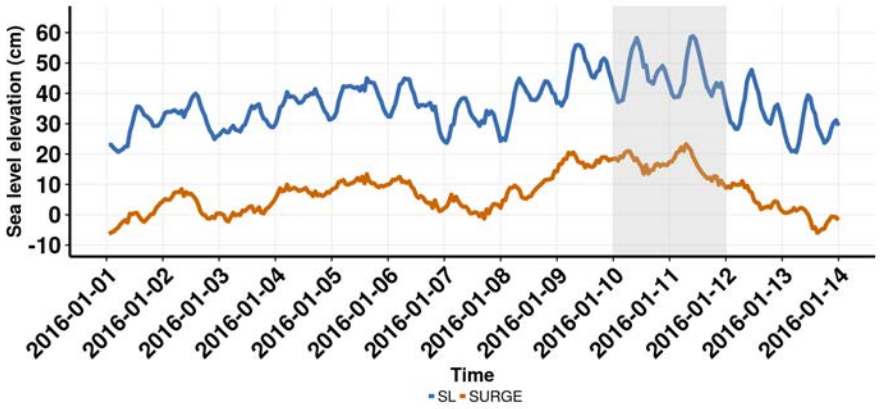

Figure 5.5.: Time series of the **total sea level** (in **blue**) and storm surge (in **orange**) at the **Barcelona harbour** tidal gauge for the **January 2016** storm. The shadowed area corresponds to the growth and decay time for the maximum wave height peak. PdE network. Time in days.

In this episode, the **wind** was channelled at the **Gibraltar strait**. Current induced by winds followed a similar path than the waves. The IBI-MFC outputs at the Central part of the Catalan coast were strongly eastwards ($50 cm/s$ at the continental shelf). At the Northern part, the modulus are somewhat lower ($30\ cm/s$). In this episode, the currents are the highest in the storm sample. The Gibraltar strait also exhibits Eastward currents up to $50\,cm/s$. The meridional component is lower than the zonal, except in Murcia and the Southern Valencian coast, in which modulus of around $55\,cm/s$ have been modelled.

The time series trend shows positive and negative surges. The trend highlights two positive surge periods: (i) 04/01/2016 - 07/01/2016; (ii) 08/01/2016 - 13/01/2016. At Barcelona tidal gauge, the storm surge reached peaks of 21 cm, with a mean value of 17 cm around the peak (Fig. 5.5). The storm surge peak reached 18 cm at Tarragona (Fig. 5.6) and shows **lower variance** than in **Barcelona**.

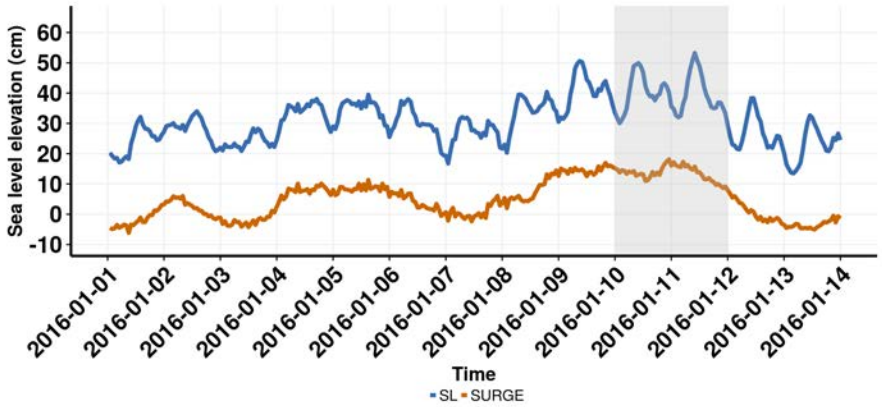

Figure 5.6.: Time series of the total sea level (in **blue**) and storm surge (in **orange**) at the **Tarragona harbour** tidal gauge for the **January 2016** storm. The shadowed area corresponds to the growth and decay time for the maximum wave height peak. PdE network. Time in days.

5.2.4. February 2016 (F-16)

F-16 (27/02/2016 - 28/02/2016) was characterized by a perturbation that affected Catalonia between the 26/02/2016 - 28/02/2016, then leading to a **temperature drop** and **snow** at **low-elevations**, specially at the West and the South. A low sea level pressure from the Atlantic Ocean moved to Catalonia during the 27/02 night. It remained there until the 28/02/2016 and it was displaced towards the Mediterranean Sea. General rainfall along Catalonia was between 20 - 50 mm.

At 27/02/16 12:00 h, the low-pressure centre reached 988 hPa. At this episode, the temperature was lower at the Southern and Western Catalonia (around -2 $°C$) than in the Pyrenees and the North-East, with values slightly positive at this level.

At the storm peak, the wind speeds reached 10 m/s at Begur (Fig. C.6) and 13 m/s at Tarragona (Fig. C.7). These conditions leads to waves with $H_s \approx 2.5\ m$ and $T_{m02} \approx 6.2\ s$ at Barcelona buoy (Fig. C.30); at Tarragona were measured storm-peak $H_s \approx 3.3\ m$ and $T_{m02} \approx 6.2\ s$ (Fig. C.32); whilst at Begur the storm-peak were $H_s \approx 3.1\ m$ and $T_{m02} = 6.3\ s$ (Fig. C.34). The mean wave direction for this event was Southern at the growth phase and an Eastward shift at the decay.

The IBI-MFC outputs shows (at the storm peak) moderate Eastern currents ($25 cm/s$) at the Central and Northern Coast. The meridional component is low except at the Begur Cape area in which the Southern current reaches 20 cm/s. The storm surge trend rises from negative surges to positive ones during the storm peak (see orange time series). Surges are not so low at the storm peak, though. At Tarragona 25 cm were reached (Fig. 5.7), whereas 20 cm in Barcelona (Fig. 5.8). The hydrodynamic conditions in this episode were the **mildest** in this dissertation. Then, the **predicted costs** will be the **lowest** (see Ch. 6).

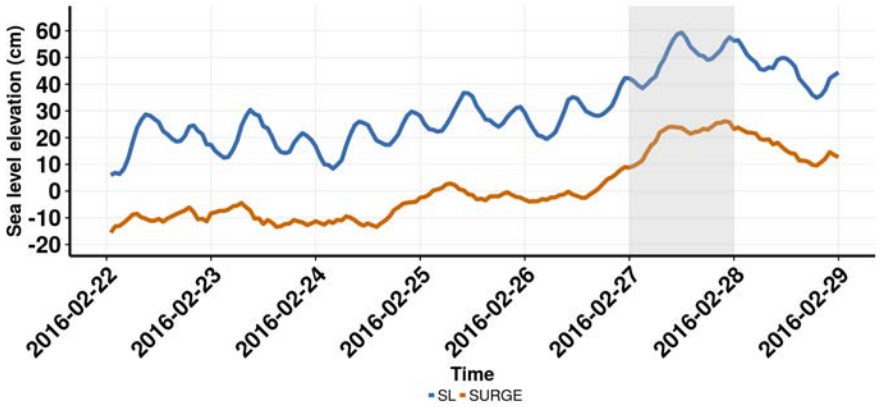

Figure 5.7.: Time series of the total sea level (in **blue**) and storm surge (in **orange**) at the **Barcelona harbour** tidal gauge for the **February 2016** storm. The shadowed area corresponds to the growth and decay time for the maximum wave height peak. PdE network. Time in days.

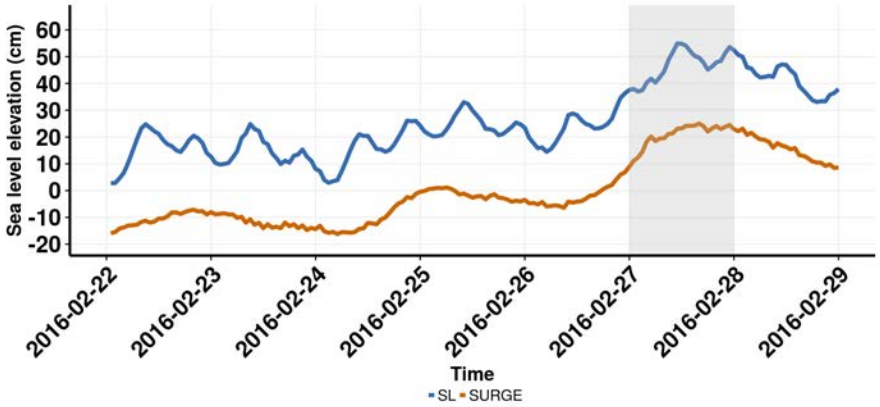

Figure 5.8.: Time series of the total sea level (in **blue**) and storm surge (in **orange**) at the **Tarragona harbour** tidal gauge for the **February 2016** storm. The shadowed area corresponds to the growth and decay time for the maximum wave height peak. PdE network. Time in days.

5.2.5. December 2016 (D-16)

D-16 (17/12/2016 - 23/12/2016) featured an Eastern flux driven by a perturbation located at the Mediterranean Sea. On 19/12/2016 and 20/12/2016, this flux triggered rainfall at the littoral and pre-littoral Catalan zone, but specially at the administrative units of Alt and Baix Empordà.

The event was due to (i) a **cold air mass** between the **mid** and **high levels** of the troposphere, that started to be disconnected from the general current, joint with (ii) the **generation** of an **extensive surface depression** located at the Western Mediterranean. This low pressure advected moist and relatively hot Eastern wind to the low levels of the atmosphere. These factors reinforced that the maximum rainfalls were at the Mediterranean fringe of the Iberian Peninsula.

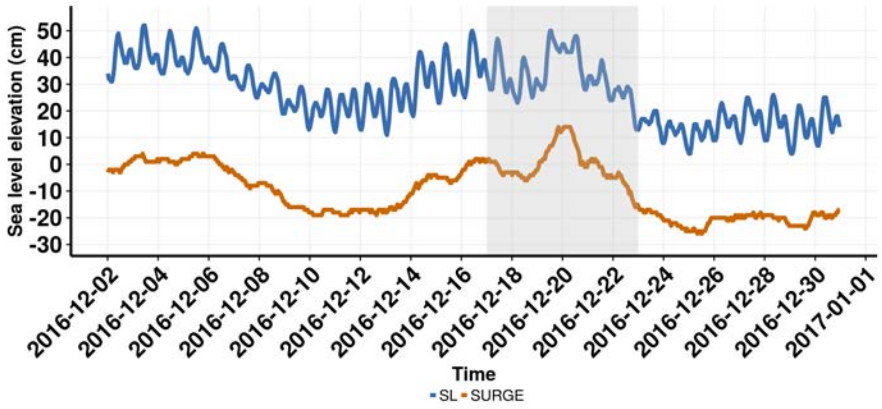

Figure 5.9.: Time series of the total sea level (in **blue**) and storm surge (in **orange**) at the **Barcelona harbour** tidal gauge for the **December 2016** storm. The shadowed area corresponds to the growth and decay time for the maximum wave height peak. PdE network. Time in days.

Precipitations were recorded at the littoral and pre-littoral on 19/12/2016; and from that evening at the rest of the North-East sector. **Precipitation** was generally **disperse** and had a **weak** intensity, whereas at local areas it reached moderate values. In general, low quantities were accumulated except from spikes at the Northern littoral. Until 20/12/2016 afternoon, rainfall was reported at the littoral and pre-littoral, local areas of the Central Catalonia and the North-East. Once reached that time, a **precipitation band** affected the abovementioned areas that ranged **weak** to **moderate intensities**.

At the storm peak, the wind speeds reached 17.5 m/s at Begur (Fig. C.8) and 15 m/s at Tarragona (Fig. C.9). These conditions leads to waves with $H_s \approx 4.2\ m$ and $T_{m02} \approx 9\ s$ at Barcelona buoy (Fig. C.36); at Tarragona were measured storm-peak $H_s \approx 4.3\ m$ and $T_{m02} \approx 7.5\ s$ (Fig. C.38); whilst at Begur the storm-peak $H_s \approx 6.7\ m$ and $T_{m02} = 8.3\ s$ (Fig. C.40). The mean wave direction for this event was East.

The IBI-MFC results presented a wind-induced circulation pattern that follows the same trend and direction than the winds and waves. The average circulation at the storm peak at the Northern part of the Catalan Coast (zonal 40 cm/s (to the west) and meridional 35 cm/s (to the south)). The sea level was lower than in other

events, though the surge at the peak remained positive (note that is negative at the beginning and at the end of the storm). In Barcelona, there was negative surge from 17th to the 19th; whereas at the storm peak the surge was positive (15 cm, see Fig. 5.9). At the decay phase (21/12/16), the surge dropped to negative (-15cm). At Tarragona the surge was positive throughout the storm (Fig. 5.10). Note that the surge at the storm peak was 10 cm higher than in Barcelona.

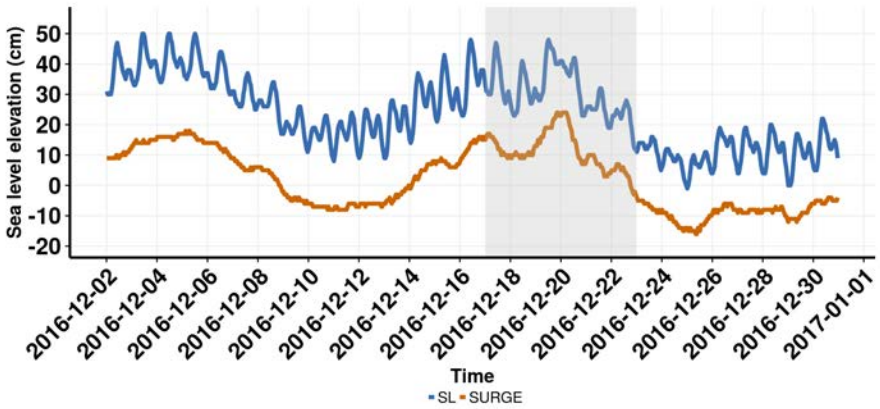

Figure 5.10.: Time series of the total sea level (in **blue**) and storm surge (in **orange**) at the **Tarragona harbour** tidal gauge for the **December 2016** storm. The shadowed area corresponds to the growth and decay time for the maximum wave height peak. PdE network. Time in days.

5.2.6. January 2017 (J-17)

J-17 (16/01/2017 - 24/01/2017) is the most extreme event that has been analysed in this dissertation. The synoptic conditions shared similarities with the D-16 storm. **Heavy rainfall** happened at the Northern and Southern Catalonia, snow at the Pre-Coastal range, high wind speeds at the whole coastal fringe plus an exceptional sea state. The **synoptic** situation was a **surface depression** that came from Northern Africa and was reinforced until being located at the southern part of the Balearic Islands. The **joint** action of **high pressure levels** at **Central Europe** led to a prominent **flux of maritime wind** (firstly Eastern and after North-Eastern).

The **Eastern** and **NE winds** were high at a wide part of the Coastal and Pre-Coastal area, specially on the early morning of 22^{nd} January, with speeds ranging from 70 to 90 km/h. If compared with the Northern winds at the Pyrenees that uses to surpass 100 km/h, these speeds may seem not so extraordinary. However, these values are quite unusual at the Barcelona metropolitan area and Maresme strait (see Figs. A.2 and A.3 for a geographical reference), that were heavily affected municipalities by this event.

At the coastal fringe, high waves were the most highlighting feature and led to

important infrastructure damage (see Ch. 6). On 21^{st} and 22^{nd} January, significant wave heights (H_s) ranging from 4 to 6 m were measured at almost the whole Catalan Coast. The storm was specially exceptional at the **Central** and **Southern** part, then becoming one of the **most important in the last decades**. Although waves were also high at the Northern part, there have been recent storms such as D-16 (see Sec. 5.2.5) that had similar magnitudes.

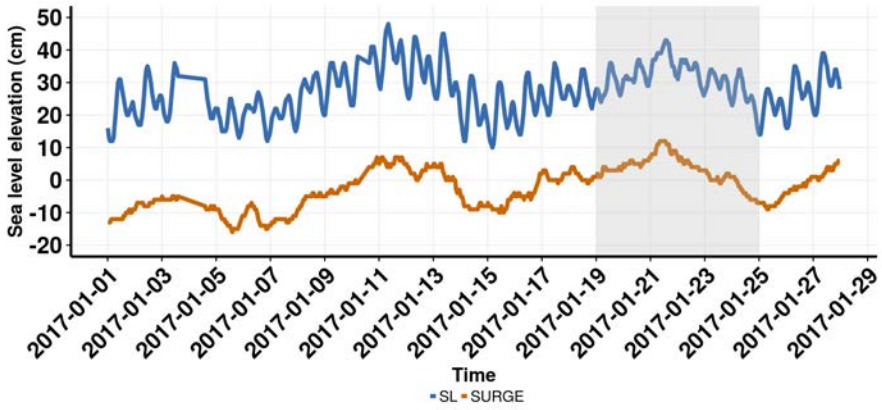

Figure 5.11.: Time series of the total sea level (in **blue**) and storm surge (in **orange**) at the **Barcelona harbour** tidal gauge for the **January 2017** storm. The shadowed area corresponds to the growth and decay time for the maximum wave height peak. PdE network. Time in days.

At the storm peak, the wind speeds reached $16 m/s$ at Tarragona (Fig. C.11). These conditions led to waves with $H_s \approx 4.8\ m$ and $T_{m02} \approx 8\ s$ at Barcelona buoy (Fig. C.42); at Tarragona were measured storm-peak $H_s \approx 6.2\ m$ and $T_{m02} \approx 8\ s$ (Fig. C.46); whilst at Begur the storm-peak was $H_s \approx 6.2\ m$ and $T_{m02} = 8.3\ s$ (Fig. C.44). The mean wave direction for this event was East.

The IBI-MFC outputs showed at the storm-peak a Northern wind-induced current (30 cm/s) from Creus Cape to l'Estartit (see Fig. A.1). Gyres are denoted at the Northern part of the coast, with a focused gyre (40 cm/s) at the Llobregat Delta-Garraf zone (see Fig. A.3 for a geographical reference). Despite waves were the most energetic in the sample, the MWL is the lowest (maximum around 42 cm). At the storm-peak, surges at Barcelona tidal gauge reaches 10 cm (see Fig. 5.11). Similarly to the D-16 event, though, the storm surge during the **storm peak** was **15 cm higher** at Tarragona (see Fig. 5.12) than in Barcelona.

These higher sea levels at Tarragona were a co-factor for the reported damaged at the Southern coast. An important part of this zone are dissipative beaches. As it will be shown in Ch. 6, low-lying dissipative beaches tend to be further damaged by high mean water levels.

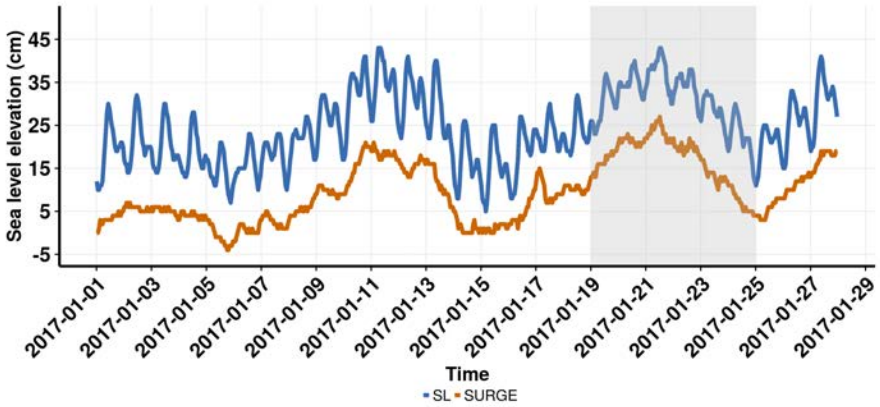

Figure 5.12.: Time series of the total sea level (in **blue**) and storm surge (in **orange**) at the **Tarragona harbour** tidal gauge for the **January 2017** storm. The shadowed area corresponds to the growth and decay time for the maximum wave height peak. PdE network. Time in days.

5.3. Hindcasted results

Once described the storm database, this Section will compare the modelled events vs in-situ observations via error metrics and Taylor diagrams (Taylor, 2001). The analysis will be divided into two Subsections: (i) Atmospheric module (Sec. 5.3.1) and (ii) Wave module (Sec. 5.3.2).

The analysis has been carried out via comparing the time series compiled in Appendix C and the metrics exposed in Sec. 3.4. In this regard, the joint interpretation of the **Mean Bias (MB)**, **Root Mean Square Error (RMSE)**, **correlation coefficient (r)** and the **Coefficient of Efficiency (COE)** can provide good insight on **how accurate** is the modelling chain.

The MB and the RMSE explains whether the model deviates too much from the measurements. The RMSE tends to penalize further deviations, though. When the trend of two time series diverges, the r coefficient is low. The COE shows the general agreement and indicates the overall performance.

The model skill has been assessed at a set of points at the Western Mediterranean Sea: Barcelona, Tarragona and Begur are comprised at the surroundings of the Study Area. However, it has been considered important to assess the model skill in Valencia buoy, Mahón and Dragonera. The reason has been to spot errors in the storm generation/propagation that otherwise could not have been possible to observe. Model skill has been analysed with the available data: some events present data gaps or no information at particular points.

5.3.1. Atmospheric module

This first module uses the WRF model (Sec. 3.3.1) using ERA-INTERIM reanalysis as boundary conditions for the first parent grid (see Sec. 3.2.1). WRF outputs are compared with offshore wind sea data from the Puertos del Estado network (see Sec. 3.2.2). The spatio-temporal output resolution in the last WRF nesting is $3 \times 3\ km$ and 20 mins, that ensures enough spatial accuracy for the **main orographic constraints** (Pyrenees, Ebro valley, Balearic islands, Lyon Gulf, etc.). The choice of 20 minutes was in order to update the SWAN wind fields at a sea-state time scale. As noted in the previous Ch. 4, sharp gradients may require timely update of the wind fields for avoiding problems in the computation of the wave generation terms.

In general terms, the proposed downscaling tends to overestimate the wind speed under extreme conditions (see time series in App. C). Maximum errors of the model coincide with the wave-storm peak at almost all simulations. At moderate and calm conditions, the error considerably diminishes.

The wind direction matches well with the measurements except from these cases in which the direction of the growth and decay phases of a storm do not coincide.

The **standard deviation** of the model is **systematically higher than** the **observed** one, at all points and for all events. Higher deviations of the standard deviation are found at the two most extreme events (D-16 and J-17). Note that N-15, J-16 and F-16 have **similar standard deviation**. The standard deviation of O-15 depends on the measurement point.

The standard deviation is similar for Tarragona and Begur buoys (around 2.3 m/s), whereas the modelled one can reach values up to 4 m/s for the **D-16** and **J-17**. At Dragonera and Mahón, the observed standard deviation is higher (around 3 m/s). As more severe is the storm, the standard deviation increases.

Note however, than D-16 and J-17 are the storms that present better skill. At **Tarragona** (Tab. 5.1), the episode that presents better skill is D-16 (COE=0.43). However, the one that presents lower skill is O-15 (COE=0.06). The MB is better at D-16 than J-17, but the opposite happens for the RMSE.

At **Dragonera** (Tab. 5.3) and **Mahón** (Tab. 5.4) similar conclusions arise: for the first one, at J-17 the skill is the best (COE=0.35), whereas O-15 is the lowest (COE=0.05); for the second one, J-17 has a COE=0.43, but a COE=-0.40 is estimated in O-15.

The J-17 event presents better skill at **Begur** (Tab. 5.2) and **Valencia** (Tab. 5.5), with COE=0.52 and COE=0.40, respectively. As in the other sites, O-15 is the event with the lowest skill (COE=-0.16) and (COE=0.40). These systematic trends will be analysed in the Discussion (Sec. 5.4).

Note that the same nesting strategy has been applied for all simulations except from the most recent one, **J-17**. For this event, the domain was extended to include part of the Iberian Peninsula (see Fig. 3.2). Such modification was hypothesised after a preliminary analysis of the database. The first results showed that the wind

fields tended to be overestimated with the previous nesting, specially under bimodal conditions.

Despite the global metrics has not improved significantly for the **J-17** storm (the correlation is near 0.8; the CRMS error is above 3 m/s and the standard deviation is close to $4-5$ m/s), the results at the storm peak are better than other storms (see time series in App. C.2.6).

5.3.2. Wave module results

In this section it will be discussed the following points: (i) the characterization in terms of the return period for each storm that will serve for linking the wave return period and the model performance; and (ii) the performance of the model for each storm event. As in the previous section, Taylor diagrams and error metrics will be used as reference.

According to the extreme wave climate present in the extreme wave climate reports from PdE and CIIRC (2010), the wave return periods were the following:

- The return period for **O-15** was about $T_r = 1-2$ yrs, at the Central and Northern part of Catalonia. At the Southern part, the return period was near $T_r = 1$ yrs.
- **N-15** had a $T_r = 1-2$ yrs, at the Northern and Central part.
- **J-16** had a $T_r = 1-2$ yrs at the Northern part. At the Barcelona buoy, the return period was somewhat lower than $T_r < 1$ yr. That is due to the sheltering effect. The wave direction (SSW) and the sheltering effect were the responsible that this storm did not affected the Northern part coastal zone. However, at deep waters (Begur buoy), the return period was near $T_r \approx 1$ yr ($H_s \approx$4 m).
- **F-16** had a return period lower than $T_r < 1$ yr at the Northern part, and $T_r = 1-2$ yrs at the Central part.
- **D-16** had a $T_r = 8-10$ yrs at the Central part; $T_r = 5-7$ yrs at the North. At the North, the wave return period was somewhat lower than in the Central area. At the Southern part $T_r = 2-4$ yrs.
- **J-17** had a $T_r = 10-12$ yrs at the Central part; $T_r = 5-7$ yrs at the North. At the Southern area, the T_r was $15-25$ $years$.

In the previous section, it was highlighted that the wind fields were overpredicted during the storm period. However, such overprediction provided the extra input for matching the wave-storm peak. Despite that in the state-of-the-art wave modelling the storm peaks tend to be underpredicted (Cavaleri, 2009; WISE Group, 2007; Pallarés et al., 2014), the **storms peak were well captured** and even **slightly overpredicted** at some areas.

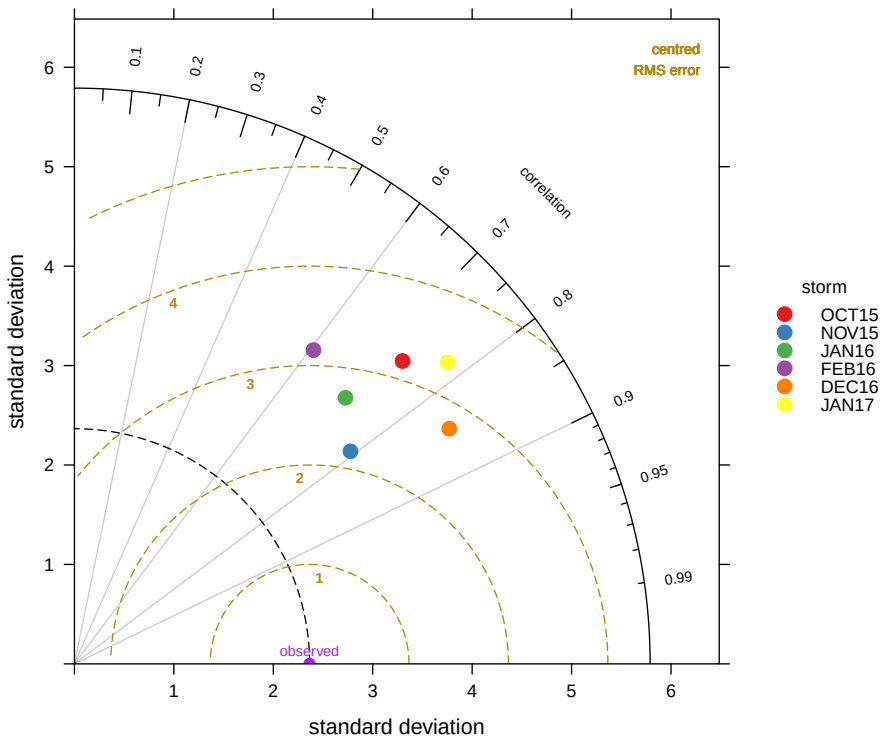

Figure 5.13.: Taylor diagram for the wind speed (m/s) at the **Tarragona** buoy. Grey lines represent the correlation coefficient. Golden semicircles represent the CRMS error. Each coloured dot represent a storm event.

Table 5.1.: Metrics for the wind speed (m/s) at the **Tarragona** buoy. ***Legend:*** ***MB*** *(Mean bias, in m/s);* ***RMSE*** *(Root Mean Square Error, in m/s);* ***r*** *(correlation coefficient);* ***COE*** *(Coefficient of Efficiency).*

Storm	MB	RMSE	r	COE
O-15	-2.98	4.36	0.73	0.06
N-15	-2.01	2.94	0.79	0.21
J-16	-0.64	2.78	0.71	0.31
F-16	-1.14	3.42	0.61	0.24
D-16	-1.28	2.73	0.85	0.43
J-17	-0.86	3.15	0.78	0.39

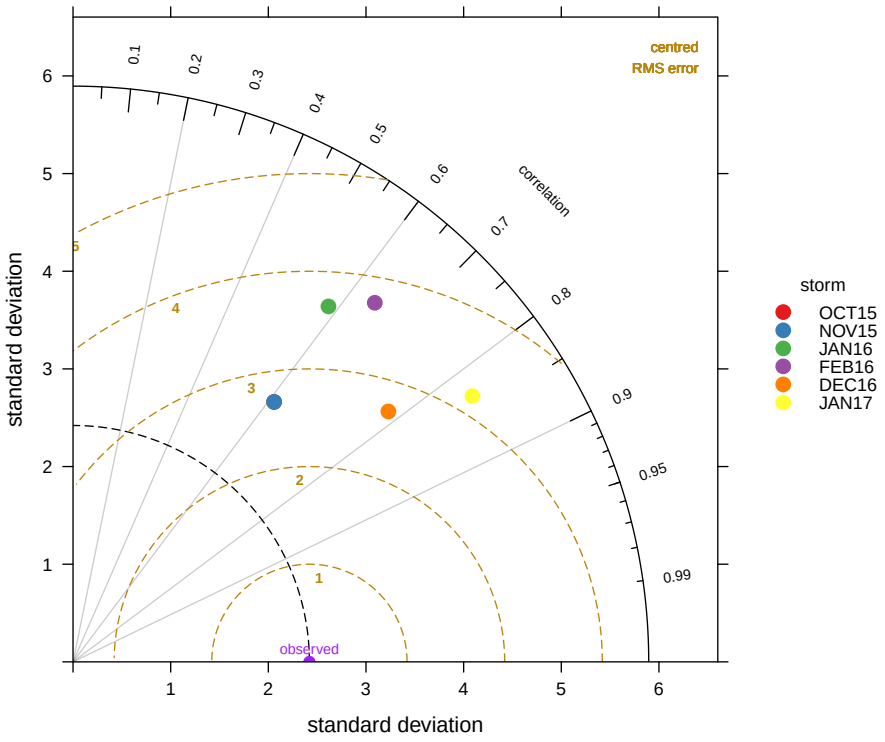

Figure 5.14.: Taylor diagram for the wind speed (m/s) at the **Begur** buoy. Grey lines represent the correlation coefficient. Golden semicircles represent the CRMS error. Each coloured dot represent a storm event.

Table 5.2.: Metrics for the wind speed (m/s) at the **Begur** buoy. ***Legend:*** ***MB*** *(Mean bias, in m/s);* ***RMSE*** *(Root Mean Square Error, in m/s);* ***r*** *(correlation coefficient);* ***COE*** *(Coefficient of Efficiency).*

Storm	MB	RMSE	r	COE
N-15	-2.42	3.61	0.61	**-0.16**
J-16	-2.03	4.31	0.58	0.17
F-16	-2.65	4.54	0.64	0.16
D-16	-1.18	2.84	0.78	0.32
J-17	-0.34	2.77	0.83	0.52

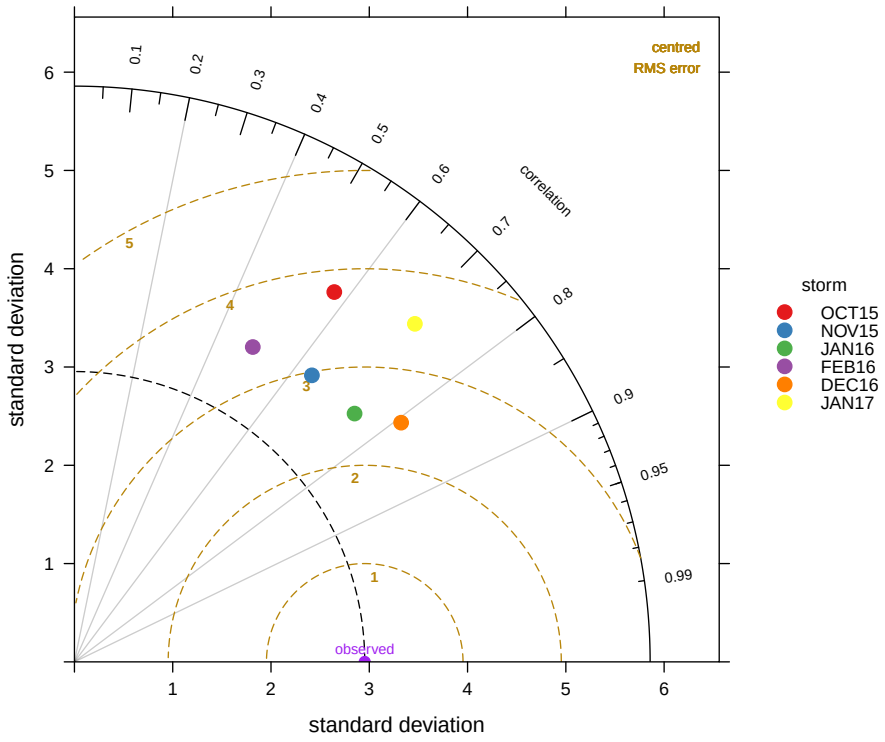

Figure 5.15.: Taylor diagram for the wind speed (m/s) at the **Dragonera** buoy. Grey lines represent the correlation coefficient. Golden semicircles represent the CRMS error. Each coloured dot represent a storm event.

Table 5.3.: Metrics for the wind speed (m/s) at the **Dragonera** buoy. ***Legend:*** ***MB*** *(Mean bias, in m/s);* ***RMSE*** *(Root Mean Square Error, in m/s);* ***r*** *(correlation coefficient);* ***COE*** *(Coefficient of Efficiency).*

Storm	MB	RMSE	r	COE
O-15	-2.04	4.28	0.57	0.05
N-15	-1.62	3.40	0.64	0.12
J-16	-1.33	2.91	0.75	0.28
F-16	-1.15	3.69	0.49	0.12
D-16	-1.67	2.96	0.81	0.35
J-17	-2.02	4.00	0.71	0.24

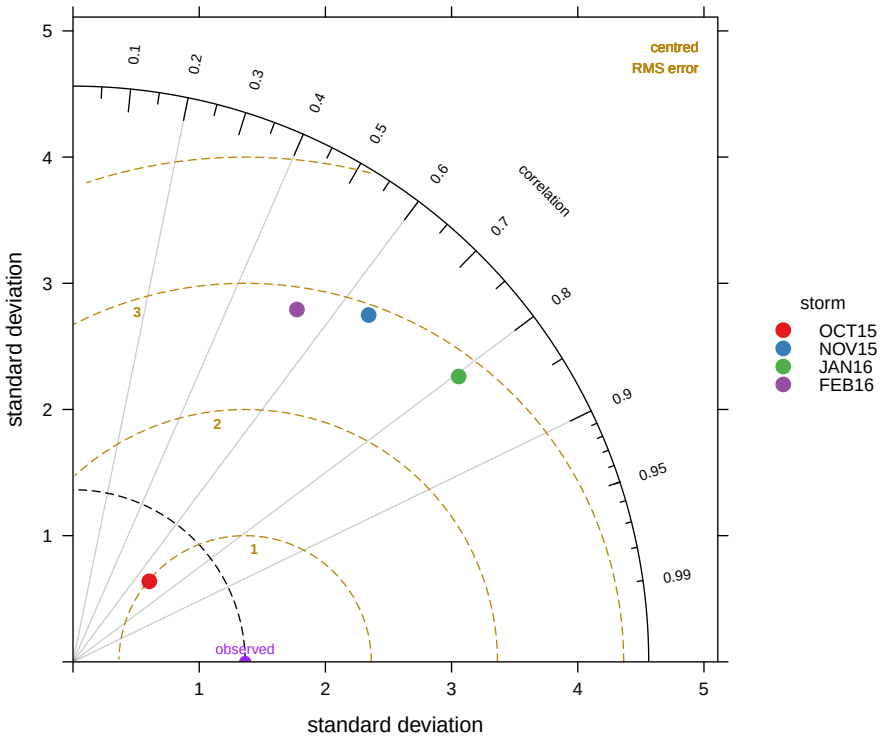

Figure 5.16.: Taylor diagram for the wind speed (m/s) at the **Mahón** buoy. Grey lines represent the correlation coefficient. Golden semicircles represent the CRMS error. Each coloured dot represent a storm event.

Table 5.4.: Metrics for the wind speed (m/s) at the **Mahón** buoy. ***Legend: MB*** *(Mean bias, in m/s);* ***RMSE*** *(Root Mean Square Error, in m/s);* ***r*** *(correlation coefficient);* ***COE*** *(Coefficient of Efficiency).*

Storm	MB	RMSE	r	COE
O-15	0.47	1.09	0.69	**-0.40**
N-15	-2.21	3.53	0.65	0.02
J-16	-1.57	2.75	0.80	0.31
F-16	-1.48	3.30	0.54	0.06

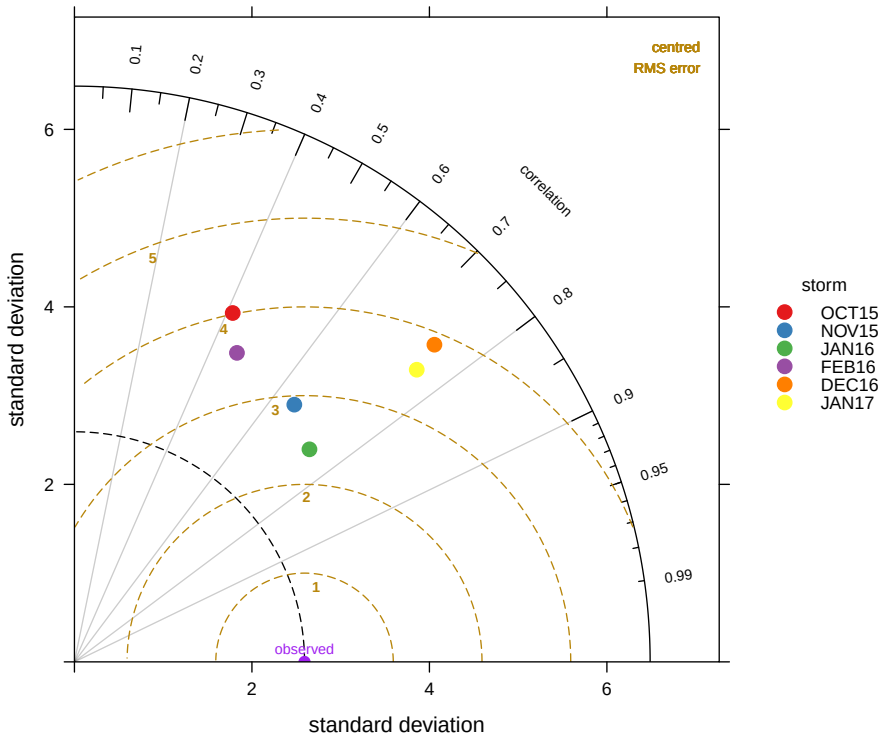

Figure 5.17.: Taylor diagram for the wind speed (m/s) at the **Valencia** buoy. Grey lines represent the correlation coefficient. Golden semicircles represent the CRMS error. Each coloured dot represent a storm event.

Table 5.5.: Metrics for the wind speed (m/s) at the **Valencia** buoy. ***Legend: MB*** *(Mean bias, in m/s);* ***RMSE*** *(Root Mean Square Error, in m/s);* ***r*** *(correlation coefficient);* ***COE*** *(Coefficient of Efficiency).*

Storm	MB	RMSE	r	COE
O-15	-1.47	4.26	0.41	**-0.01**
N-15	-2.43	3.89	0.65	**-0.01**
J-16	-1.09	2.72	0.74	0.28
F-16	-0.47	4.01	0.47	0.09
D-16	-2.39	4.30	0.75	0.32
J-17	-1.06	3.46	0.76	0.40

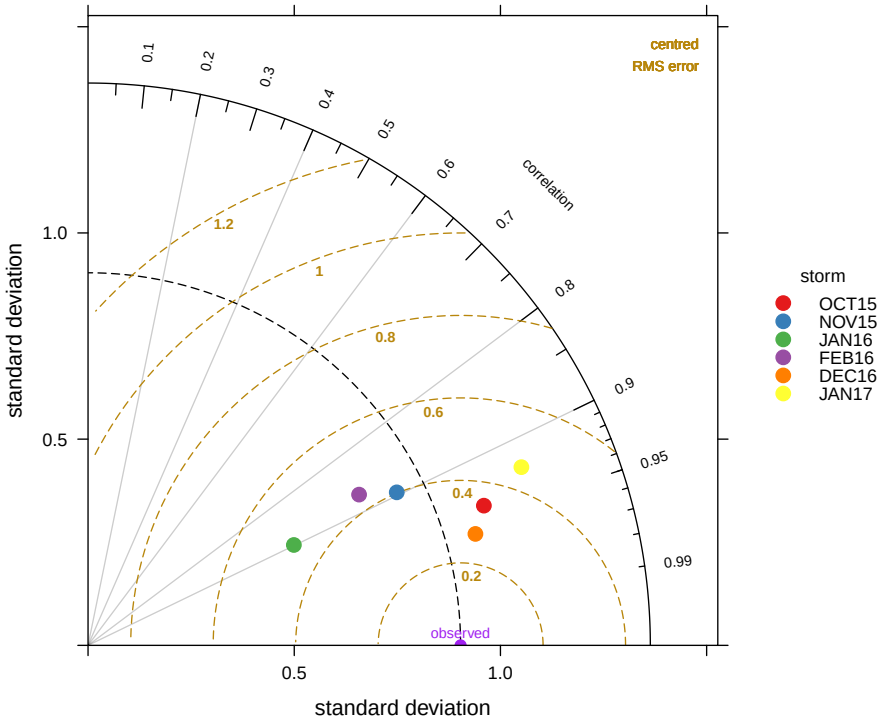

Figure 5.18.: Taylor diagram for the significant wave height $H_s(m)$ at the **Barcelona** buoy. Grey lines represent the correlation coefficient. Golden semi-circles represent the CRMS error. Each coloured dot represent a storm event.

Table 5.6.: Metrics for the significant wave height $H_s(m)$ and mean wave period $T_{m02}(s)$ at the **Barcelona** buoy. ***Legend:*** ***MB*** *(Mean bias, in m (or s));* ***RMSE*** *(Root Mean Square Error, in m (or s));* ***r*** *(correlation coefficient);* ***COE*** *(Coefficient of Efficiency).*

Storm	$\mathbf{H_s}$				$\mathbf{T_{m02}}$			
	MB	**RMSE**	**r**	**COE**	**MB**	**RMSE**	**r**	**COE**
O-15	-0.09	0.35	0.94	0.66	0.15	1.33	0.47	**-0.86**
N-15	-0.14	0.40	0.90	0.43	-0.39	1.08	0.73	0.28
J-16	0.08	0.26	0.90	0.50	0.19	0.85	0.74	0.30
F-16	-0.01	0.37	0.87	0.55	0.13	0.90	0.72	0.28
D-16	-0.09	0.30	0.96	0.73	-0.17	0.78	0.81	0.39
J-17	-0.11	0.48	0.92	0.60	-0.11	0.66	0.86	0.50

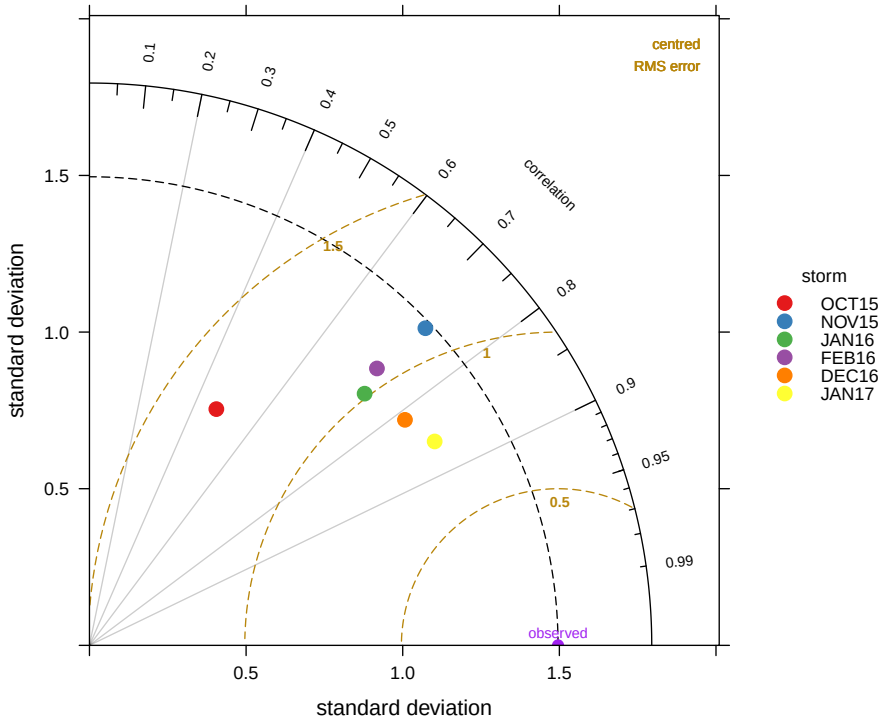

Figure 5.19.: Taylor diagram for the mean wave period $T_{m02}(s)$ at the **Barcelona** buoy. Grey lines represent the correlation coefficient. Golden semicircles represent the CRMS error. Each coloured dot represent a storm event.

At **Barcelona**, the D-16 and O-15 events are the ones that have the lowest distances at the H_s Taylor diagram (Fig. 5.18). J-16 is the one that shows the highest distance, because the modelled standard deviation was low compared with the other ones. Note however that the storm overall trend and storm peaks were well captured (Figs. C.24 and C.25). For the T_{m02} case (Fig. 5.19), the higher return periods storms, D-16 and J-17 are the ones with the lowest distance, partly because on the agreement with the modelled vs measured standard deviations.

The metrics confirm (Tab. 5.6) these behaviours: the episodes that present better skill are D-16 (in H_s, COE=0.73) and J-17 (in T_{m02}, COE=0.50). The ones that present lower skill are N-15 (in H_s, COE=0.43) and O-15 (in T_{m02}, COE=-0.86). The standard deviation (H_s) of the O-15, D-16 and J-17 simulations (Eastern storms) is higher than the measurements. This behaviour may be normal because there are no obstacles in that directional sector. The other storms show lower standard deviation than the observed.

The modelled mean wave period (T_{m02}) show lower variance than the observed. This behaviour may be due to the Barcelona harbour main breakwater that can be found near the Barcelona buoy. Important **wave reflection** occur at the zone that **may increase** the **standard deviation** of the measurements. SWAN is phase-averaged, then it cannot handle accurately reflection and the T_{m02} are smoothed.

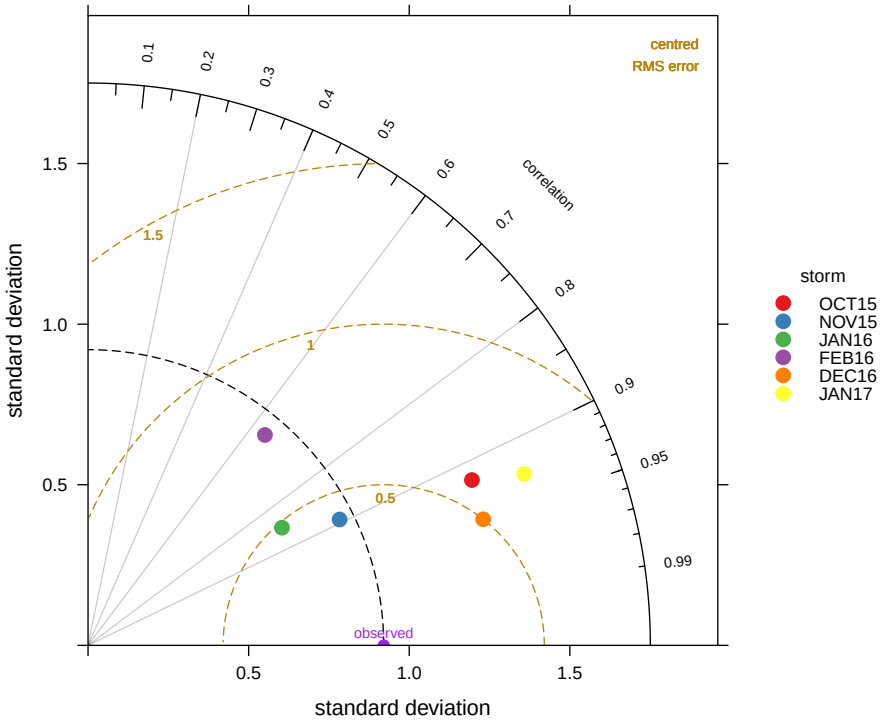

Figure 5.20.: Taylor diagram for the significant wave height $H_s(m)$ at the **Tarragona** buoy. Grey lines represent the correlation coefficient. Golden semicircles represent the CRMS error. Each coloured dot represent a storm event.

Table 5.7.: Metrics for the significant wave height $H_s(m)$ and mean wave period $T_{m02}(s)$ at the **Tarragona** buoy. ***Legend:*** ***MB*** *(Mean bias, in m (or s));* ***RMSE*** *(Root Mean Square Error, in m (or s));* ***r*** *(correlation coefficient);* ***COE*** *(Coefficient of Efficiency).*

Storm	**H_s**				**T_{m02}**			
	MB	**RMSE**	**r**	**COE**	**MB**	**RMSE**	**r**	**COE**
O-15	-0.35	0.68	0.92	0.52	-0.49	1.64	-0.03	**-1.08**
N-15	-0.29	0.49	0.89	0.43	-0.88	1.31	0.71	**-0.02**
J-16	0.16	0.40	0.85	0.38	-0.19	0.77	0.78	0.34
F-16	-0.01	0.66	0.64	0.27	-0.21	1.04	0.57	0.25
D-16	-0.18	0.52	0.95	0.68	-0.18	0.74	0.91	0.57
J-17	-0.12	0.56	0.93	0.64	-0.17	0.79	0.89	0.56

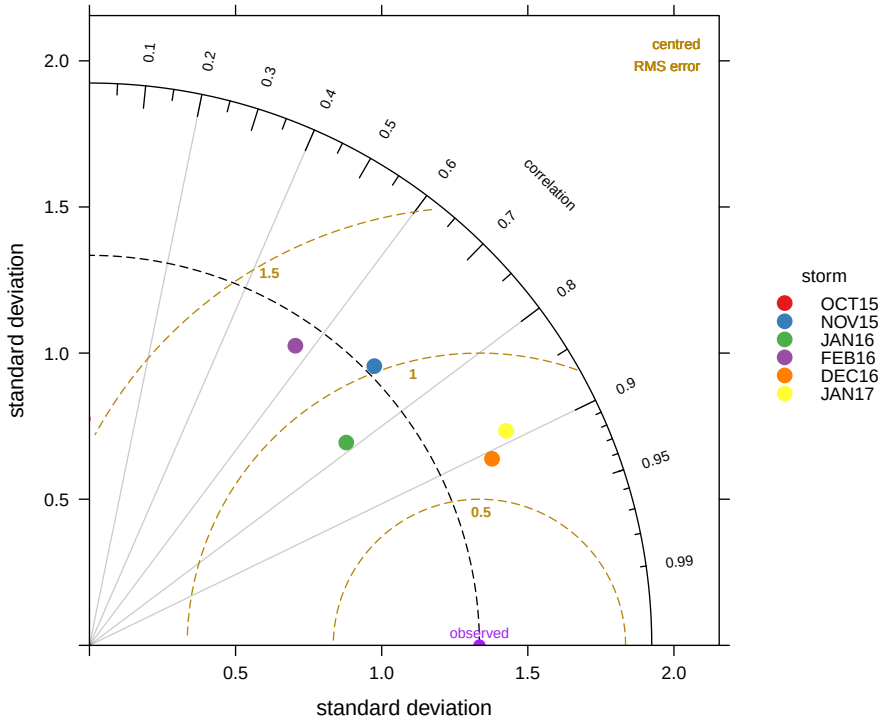

Figure 5.21.: Taylor diagram for the mean wave period $T_{m02}(s)$ at the **Tarragona** buoy. Grey lines represent the correlation coefficient. Golden semicircles represent the CRMS error. Each coloured dot represent a storm event.

At **Tarragona** (Tab. 5.7), the episode that presents better skill is D-16 (in H_s, COE=0.68; in T_{m02}, COE=0.57). The ones that present lower skill are F-16 (in H_s, COE=0.27) and O-15 (in T_{m02}, COE=-1.08). In general, the H_s COE values are lower than at Barcelona and Begur. As happened with the Barcelona buoy, the modelled Eastern storms (O-15, D-16 and J-17) have **higher standard deviation** than the **measurements**. Analogous behaviour is found for the T_{m02}.

The N-15 and J-16 events are the ones that present lower distance for the H_s (Fig. 5.20). Although the COE is higher for O-15, D-16 and J-17; the modelled standard deviation is higher than the observed. For the T_{m02}, the results coincide with the COE (Fig. 5.21): good agreement can be found for D-16 and J-17.

However, the T_{m02} performs poorly for the **O-15** case. At the beginning of the simulation are modelled almost 4 seconds in overestimations, whereas at the storm peak, there are underestimations of 1 sec. The first strong mismatch of 4 sec may be explained by an excess of energy at lower frequencies from the spectra.

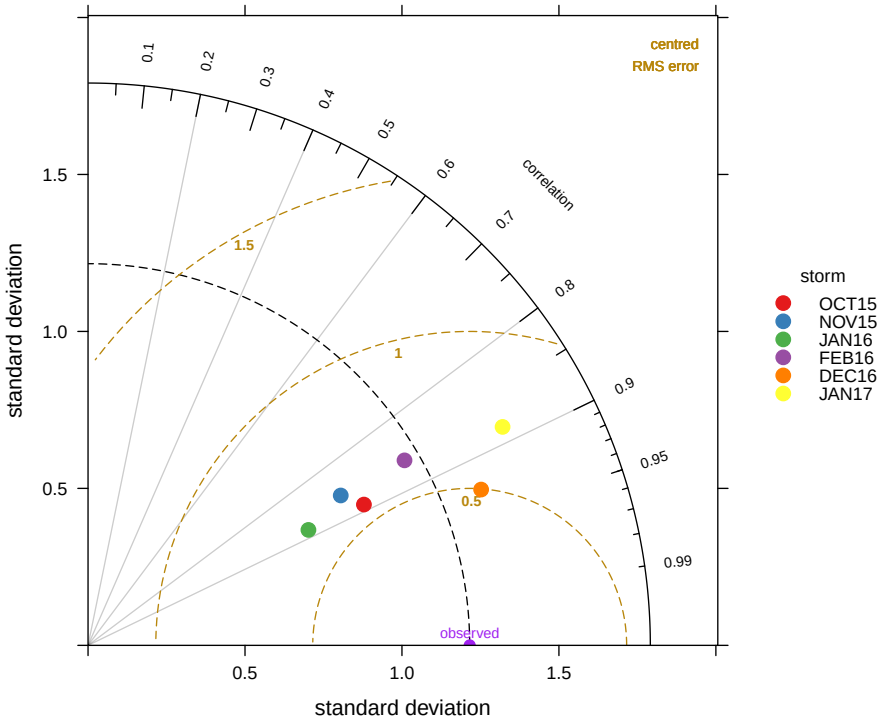

Figure 5.22.: Taylor diagram for the significant wave height $H_s(m)$ at the **Begur** buoy. Grey lines represent the correlation coefficient. Golden semicircles represent the CRMS error. Each coloured dot represent a storm event.

Table 5.8.: Metrics for the significant wave height $H_s(m)$ and mean wave period $T_{m02}(s)$ at the **Begur** buoy. ***Legend:*** ***MB*** *(Mean bias, in m (or s));* ***RMSE*** *(Root Mean Square Error, in m (or s));* ***r*** *(correlation coefficient);* ***COE*** *(Coefficient of Efficiency).*

Storm	**H_s**				**T_{m02}**			
	MB	**RMSE**	**r**	**COE**	**MB**	**RMSE**	**r**	**COE**
O-15	-0.08	0.57	0.89	0.51	-0.80	1.81	**-0.21**	**-1.00**
N-15	-0.17	0.51	0.86	0.51	-0.36	1.04	0.73	0.30
J-16	0.05	0.37	0.89	0.52	-0.12	0.76	0.81	0.33
F-16	-0.15	0.65	0.86	0.54	-0.16	0.91	0.87	0.39
D-16	-0.08	0.50	0.93	0.65	-0.18	0.77	0.84	0.42
J-17	0.04	0.70	0.88	0.53	-0.03	0.78	0.83	0.42

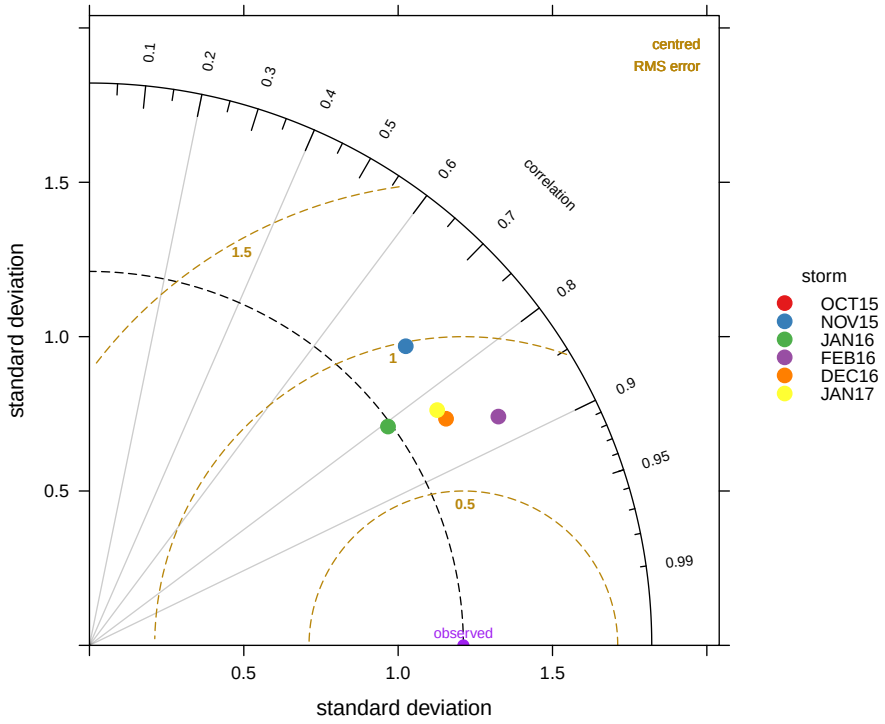

Figure 5.23.: Taylor diagram for the mean wave period $T_{m02}(s)$ at the **Begur** buoy. Grey lines represent the correlation coefficient. Golden semicircles represent the CRMS error. Each coloured dot represent a storm event.

At **Begur** (Tab. 5.8), the episode that presents better skill is D-16 (in H_s, COE=0.65; in T_{m02}, COE=0.42). The one that presents lower skill is O-15 (in H_s, COE=0.51; in T_{m02}, COE=-1.00). This buoy is located at deeper waters than Barcelona and Tarragona, and this zone is more active in terms of waves. The COE are not as high as in Barcelona, but they are better than in Tarragona. The RMSE are higher than in Barcelona, but the correlation coefficients are slightly lower.

The wave height H_s has higher standard deviation than the observed for the D-16 and J-17, but it is underestimated at the rest of events. The lowest distances are found with the D-16 and O-15 cases (Fig. 5.22).

The T_{m02} graphs matches with COE (Fig. 5.23): D-16 and J-17 have the lowest distances. The modelled values have higher standard deviation than the observations. The CRMS are centred in 0.75 for all events except N-15.

Note however, J-16 and F-16 have similar distances at the Taylor diagram: in J-16 the correlation is lower than F-16, whereas the latter has a higher RMSE and MB than J-16. It is a clear example that Taylor diagram distances, despite being identical, may signify different diagnostics.

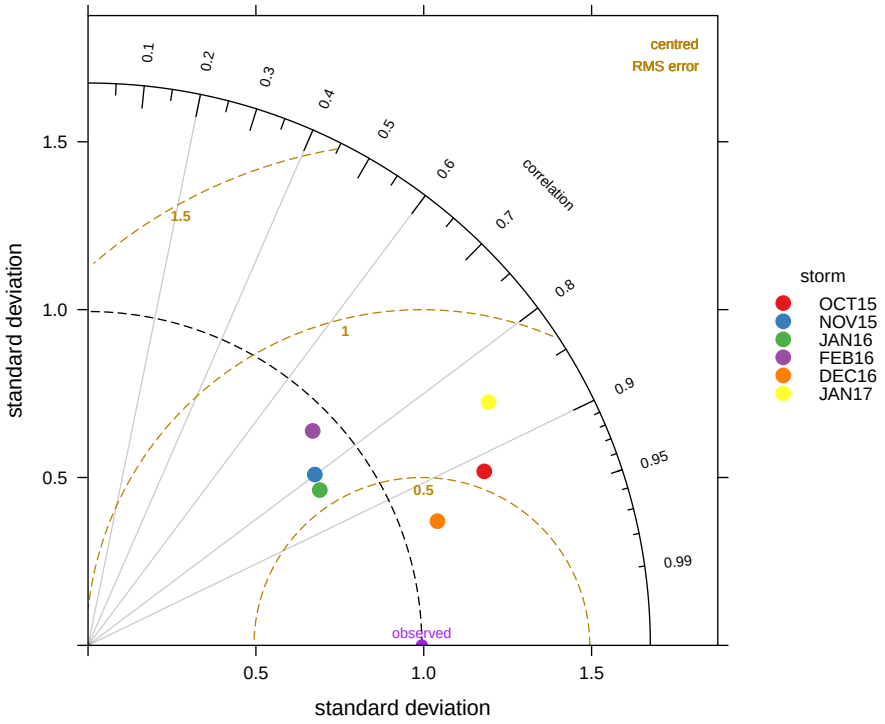

Figure 5.24.: Taylor diagram for the significant wave height $H_s(m)$ at the **Dragonera** buoy. Grey lines represent the correlation coefficient. Golden semicircles represent the CRMS error. Each coloured dot represent a storm event.

Table 5.9.: Metrics for the significant wave height $H_s(m)$ and mean wave period $T_{m02}(s)$ at the **Dragonera** buoy. ***Legend:*** ***MB*** *(Mean bias, in m (or s));* ***RMSE*** *(Root Mean Square Error, in m (or s));* ***r*** *(correlation coefficient);* ***COE*** *(Coefficient of Efficiency).*

Storm	$\mathbf{H_s}$				$\mathbf{T_{m02}}$			
	MB	**RMSE**	**r**	**COE**	**MB**	**RMSE**	**r**	**COE**
O-15	-0.11	0.56	0.92	0.54	-0.01	1.17	0.33	**-0.98**
N-15	-0.15	0.55	0.80	0.38	-0.25	0.85	0.68	0.29
J-16	0.23	0.52	0.83	0.38	0.15	0.66	0.78	0.40
F-16	-0.12	0.66	0.72	0.36	-0.38	0.95	0.70	0.21
D-16	-0.07	0.40	0.94	0.72	0.04	0.62	0.89	0.59
J-17	0.01	0.73	0.85	0.51	0.09	0.79	0.85	0.46

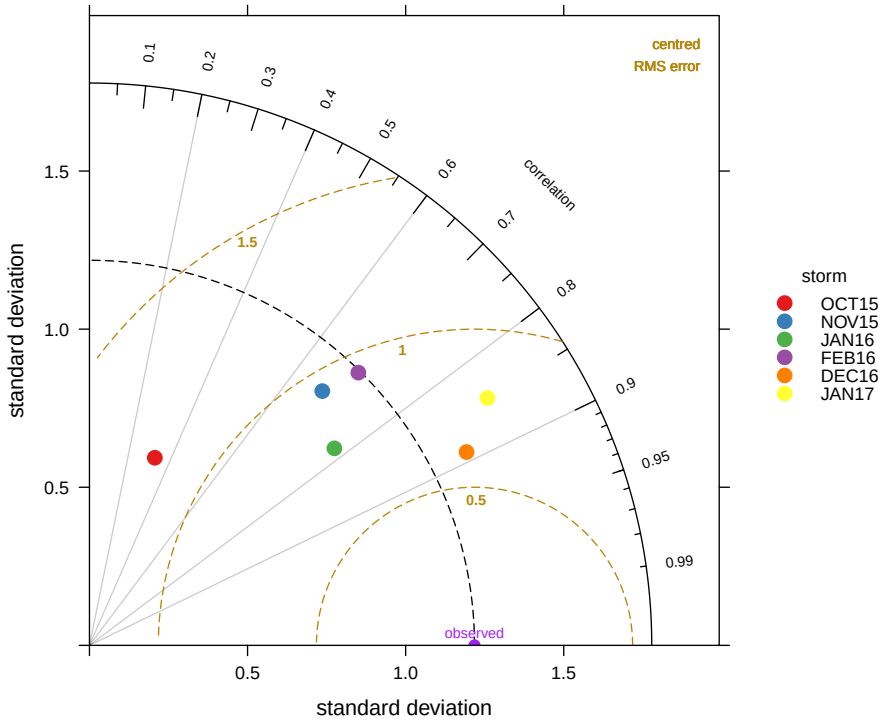

Figure 5.25.: Taylor diagram for the mean wave period $T_{m02}(s)$ at the **Dragonera** buoy. Grey lines represent the correlation coefficient. Golden semicircles represent the CRMS error. Each coloured dot represent a storm event.

At **Dragonera** (Tab. 5.9), the episode that presents better skill is D-16 (in H_s, COE=0.72; in T_{m02}, COE=0.59). Note that for D-16 event, this area shows better performance than all the other ones. Conversely, the event that presents lowest skill is F-16 (in H_s, COE=0.51; in T_{m02}, COE=-1.00), as in Tarragona.

As happened with other buoys, the H_s at the Eastern storms have higher standard deviation (O-15, D-16, J-17) than the measurements (Fig. 5.24). For these variables, the lowest distances are found for the D-16 and O-15 events.

Regarding the T_{m02}, the D-16 and J-17 storms have higher standard deviation than the observations (Fig. 5.25). D-16 shows lower distances and J-17 and J-16 have similar ones. In J-17, the higher CRMS error is compensated with the standard deviation.

As happened in **Tarragona**, the T_{m02} performs poorly for the **O-15** case. At the beginning of the simulation, the mean wave period was overestimated (errors of around 3 sec.); whereas at the storm peak there was an underestimation of 2 sec.

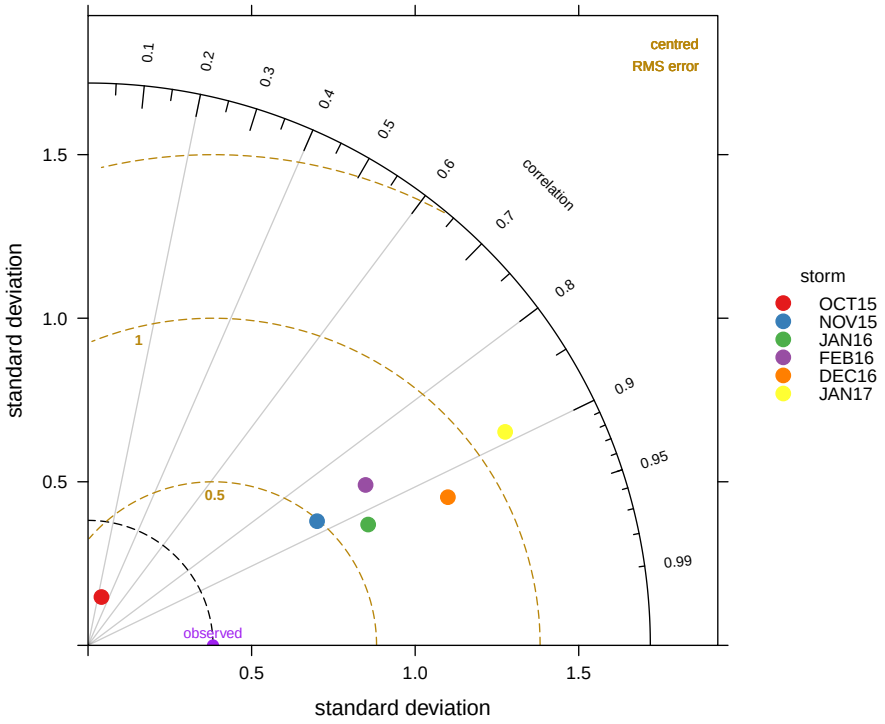

Figure 5.26.: Taylor diagram for the significant wave height $H_s(m)$ at the **Mahón** buoy. Grey lines represent the correlation coefficient. Golden semicircles represent the CRMS error. Each coloured dot represent a storm event.

Table 5.10.: Metrics for the significant wave height $H_s(m)$ and mean wave period $T_{m02}(s)$ at the **Mahón** buoy. ***Legend:*** ***MB*** *(Mean bias, in m (or s));* ***RMSE*** *(Root Mean Square Error, in m (or s));* ***r*** *(correlation coefficient);* ***COE*** *(Coefficient of Efficiency).*

Storm	**H_s**				**T_{m02}**			
	MB	**RMSE**	**r**	**COE**	**MB**	**RMSE**	**r**	**COE**
O-15	0.42	0.56	0.27	**-2.78**	-1.77	2.11	**-0.87**	**-2.05**
N-15	-0.16	0.42	0.88	0.44	-0.30	0.80	0.71	0.28
J-16	0.13	0.40	0.92	0.54	0.08	0.79	0.83	0.47
F-16	-0.07	0.50	0.87	0.46	-0.29	1.06	0.75	0.29
D-16	-0.09	0.47	0.92	0.68	0.07	0.84	0.86	0.46
J-17	0.21	0.69	0.89	0.53	0.22	0.93	0.84	0.43

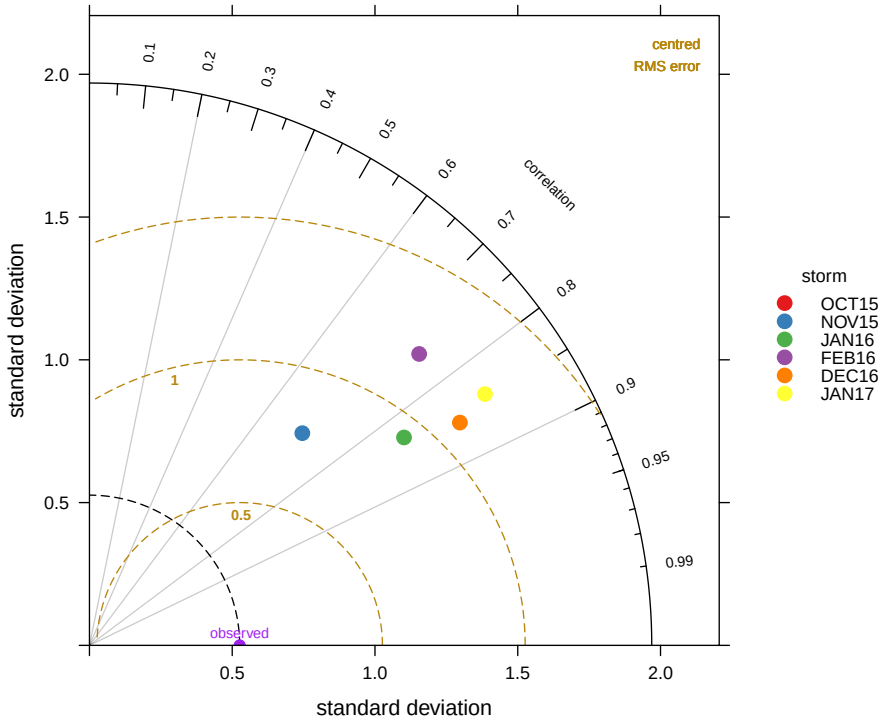

Figure 5.27.: Taylor diagram for the mean wave period $T_{m02}(s)$ at the **Mahón** buoy. Grey lines represent the correlation coefficient. Golden semicircles represent the CRMS error. Each coloured dot represent a storm event.

At **Mahón** (Tab. 5.10), the episode that presents better skill is D-16 (in H_s, COE=0.68; in T_{m02}, COE=0.46). Nevertheless, the one with lower skill is O-15 (in H_s, COE=-2.78; in T_{m02}, COE=-2.05). The results for the O-15 were not properly modelled, as the only simulation that shows negative correlation ($r = -0.87$).

In fact, for this specific event, there were no measurements for the storm. Only there were available measurements from 26^{th} to 27^{th} September, that coincides with the spin-up time of the model. Then, the error metrics can be considered as unreliable for this episode.

The modelled standard deviation is substantially higher than the observed, for all events except O-15. Lowest distances are found for N-15 and J-16 (Fig. 5.26). The high RMSE in D-16 and J-17 is the reason for exhibiting more distance than N-15 and J-16, despite that the first two ones have higher COE.

The T_{m02} Taylor diagram (Fig. 5.27) shows that the N-15 have lower distance than J-16, despite that the COEs differ significantly: N-15 (0.28) and J-16 (0.47). This is because the modelled standard deviation for the N-15 is substantially lower than in J-16. Despite that J-16 and D-16 have similar COE, the first one has lower CRMS and standard deviation.

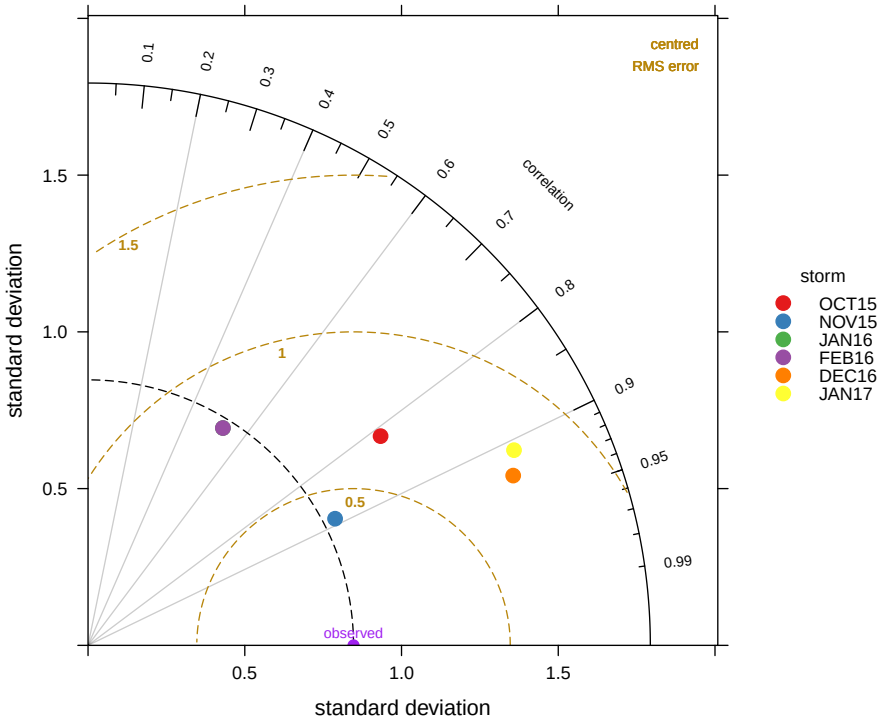

Figure 5.28.: Taylor diagram for the significant wave height $H_s(m)$ at the **Valencia** buoy. Grey lines represent the correlation coefficient. Golden semicircles represent the CRMS error. Each coloured dot represent a storm event.

Table 5.11.: Metrics for the significant wave height $H_s(m)$ and mean wave period $T_{m02}(s)$ at the **Valencia** buoy. ***Legend:*** ***MB*** *(Mean bias, in m (or s));* ***RMSE*** *(Root Mean Square Error, in m (or s));* ***r*** *(correlation coefficient);* ***COE*** *(Coefficient of Efficiency).*

Storm	$\mathbf{H_s}$				$\mathbf{T_{m02}}$			
	MB	**RMSE**	**r**	**COE**	**MB**	**RMSE**	**r**	**COE**
O-15	-0.12	0.68	0.81	0.43	0.61	1.62	0.20	**-2.05**
N-15	-0.27	0.49	0.89	0.45	-0.66	1.04	0.81	0.16
F-16	-0.03	0.70	0.53	0.26	-0.26	0.90	0.59	0.13
D-16	-0.32	0.68	0.93	0.65	-0.04	0.71	0.87	0.57
J-17	-0.11	0.63	0.91	0.65	-0.08	0.89	0.82	0.47

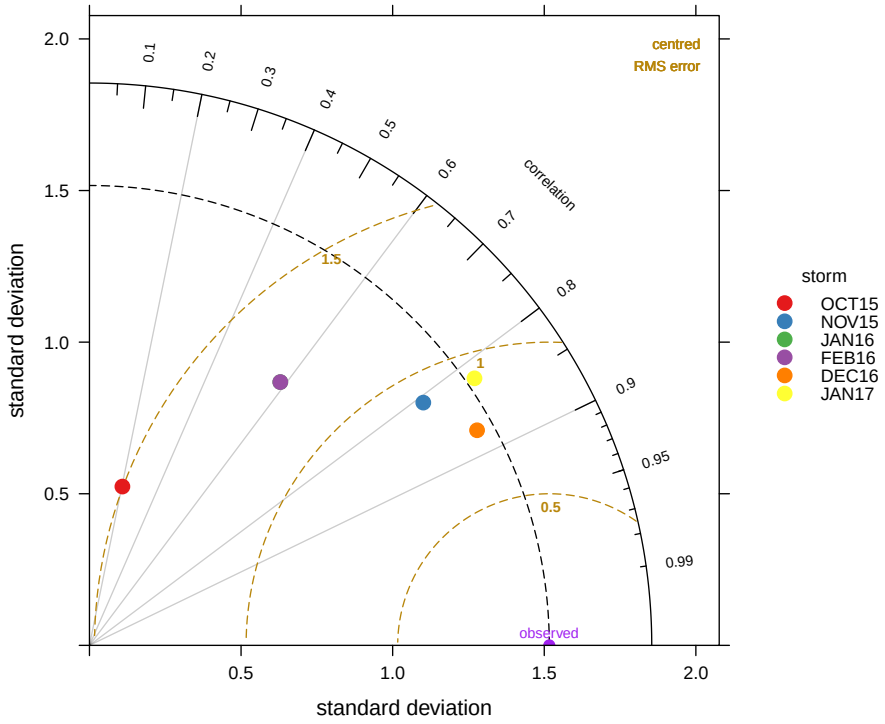

Figure 5.29.: Taylor diagram for the mean wave period $T_{m02}(s)$ at the **Valencia** buoy. Grey lines represent the correlation coefficient. Golden semicircles represent the CRMS error. Each coloured dot represent a storm event.

At **Valencia** (Tab. 5.11), the episode that presents better skill is D-16 (in H_s, COE=0.65; in T_{m02}, COE=0.57). However, the ones that present lower skill are F-16 (in H_s, COE=0.26) and O-15 (in T_{m02}, COE=-2.05). Note that T_{m02} for the O-15 has a low correlation ($r = 0.20$).

Similarly to the Dragonera and Tarragona, the mean wave period presents underestimation errors of 3 sec at the growth phase. The pressure anomaly is near the coast and should be offshoreward. At the beginning of the simulation, though, the overestimation errors are 1 sec.

Valencia H_s presents the same behaviour than the other buoys: Eastern storms (i.e. O-15, D-16, J-17) have higher modelled standard deviation than observed (Fig. 5.28). N-15 is the one that presents better metrics because the standard deviation and CRMS was the lowest. D-16 and J-16, though showing higher COE, have higher standard deviation and for that reason, they seem to mismatch.

Valencia T_{m02} has lower modelled standard deviation than observed (Fig. 5.29). In this case, Taylor diagrams and COE match: D-16 and J-17 both have the lowest distances and the highest COE.

5.4. Discussion

The Discussion of this Chapter deals with the following points: (i) specific details of the implementation (that are tightly related with the methodology, see Ch. 3); (ii) the individual analysis for each storm event; (iii) the general behaviour of the modelling chain; (iv) applicability and challenges for Coastal Forecasting, plus ways to overcome the present limitations.

5.4.1. Operational setting and parametrizations

Six recent storm **events** have been **modelled** and **compared** with **in-situ** observations. The main differences with the previous Ch. 4 are: (i) an increase of the wind spatial (from 25×25 km to 3×3 km) and temporal (from 6 h to 20 min) resolution; and (ii) the wave gradients are addressed with a more frequent update of the wave inputs (winds are updated every 20 minutes; whereas currents and sea level every 1 hour). This update interval aimed to properly capture the **strong bursts of wind momentum**, usual in the **growth phase of Mediterranean storms** (Cavaleri, 2009; Sánchez-Arcilla et al., 2008), specially those in which short-fetches are expected. The proposed nesting strategy aimed to capture the large-scale and mesoscale processes that can lead to adverse weather anomalies at the Catalan Coast.

The SWAN model has been deeply analysed in the Study Area at previous dissertations (Bolaños, 2004; Alomar, 2012; Pallarés, 2016) and at Ch. 4. Additionally, the parametrizations and physical processes in the wave model remain the same than at Ch. 4. Only the update frequency of the forcings differs. Thus, in this first part of the discussion, further attention will be paid to the atmospheric model.

In this module, the recommended parametrizations and discretization features for mesoscale processes have been adopted (Skamarock et al., 2005). Sensitivity analysis with different WRF formulations were carried out, but the results were not significantly affected. Only O-15 has shown discrepancies when changing the parametrizations for the surface processes, the microphysics or increasing the number of vertical levels. These results coincide with previous works in the same sea, such as Menéndez et al. (2014) who tested different WRF configurations and they did not experience important skill differences.

The computational time for running the atmospheric model using a 4 core conventional desktop computer is around 2 weeks for simulating a month. Using the same resources for the wave model it takes around 2 days for the first nested grid (Mediterranean Sea) and 1.5 days for the second grid (Catalan Coast). In the proposed operational strategy, the atmospheric model is one of the bottlenecks, because it is computationally expensive. It has to be remarked that low time steps ($\Delta t_{WRF} \approx 10$ s for the WRF model and $\Delta t_{SWN} \approx 10$ min for SWAN) have been used in the last nesting to avoid numerical instabilities and diffusion. In an operational setting, these time steps could be optimized, then reducing important

computational effort.

Once set-up the modelling chain, outputs were obtained and analysed. In the next paragraphs, it will be discussed the individual analysis of each storm event.

5.4.2. Individual analysis for each storm event

The events that presented **lower agreement** with the measurements were **O-15** and **F-16**. In the **O-15** case, the **pressure anomaly track** was not properly modelled, then the **spatial distribution** of the **wind** fields is not accurate. As exposed below, it seems that the **wave generation area** was probably **offshoreward** than the computed one. This track error lead to the following:

- At the wave storm peak, wind speed **overestimations** of about **10 m/s** were obtained at Tarragona and Valencia, whilst **6 m/s** at Dragonera.
- Despite the important wind speed error at the locations, the $\mathbf{H_s}$ is **accurate enough**. At Barcelona (COE=0.66 and $RMSE = 0.35\ m$) the metrics are only better in the D-16 storm; at Tarragona, the accuracy is lower than D-16 and J-17, but better than N-15, J-16 and F-16 (COE=0.52 and $RMSE = 0.68\ m$); whilst at Begur the accuracy was moderated (COE=0.51 and $RMSE = 0.57\ m$). The results indicate that the **total energy of the spectra was properly characterized** (i.e. the global magnitude of the episode), but the spatial distribution of the wind was not correct.
- The mean wave period ($\mathbf{T_{m02}}$) is **underestimated** at the storm. Despite that the total energy of the spectra matches well, the **high frequencies partitions** *(young wind-sea waves)* **have more energy than it should**.
- At **Valencia** buoy, the **growth phase** of the **wave storm** has sharper gradient than measured. That leads to a lag of the storm peak of almost 1 day. This fact reinforces the hypothesis that the most probable **generation area** was **offshorewards**.

The causes for this pressure anomaly mismatch may be due to: (i) the **surface winds** have **more dependence** on **surface fields** (temperature, moisture and/or pressure) than other events in the sample (D-16, J-17 and J-16); (ii) the **surface levels** were heavily **influenced** by **local coastal** phenomena; (iii) limitations of the model for addressing local phenomena, because most of them are based in parametrizations that cannot resolve the local scale (hundreds or even tens of metres). Note that this event was the only in which the pressure anomaly track changed remarkably under the abovementioned sensitivity analysis.

O-15 was a complex event to be modelled. Despite that the wind fields were moderated, the combination of a set of time-scale factors affected severely the hindcast. In a seasonal scale, **July** to **August** were particularly **hot months**. Actually, the temperature anomaly in July had not been **that high** since **2006** (almost $4°C$ in deviation from the climatic temperature and the monthly mean). On the contrary, **September** had a $-2°C$ temperature anomaly, the **lowest** since **2001**.

These anomalies may have driven **strong thermal contrast** between the Sea Surface Temperature (SST) and in-land surface temperature. Note also that ERA-INTERIM may have some mismatches between the SST and inland surface fields, specially under high spatial resolutions (circa 3 km, Hahmann et al. (2015)).

At 24/09/2015, an extended low-pressure area was located near Iceland. In 26/09, an extended high-pressure area was at the North Sea, between the British Islands and the Dutch-German coast. Note that this area is almost at the limits of the first grid of the atmospheric model. Hence, the reproduction of such high-pressure area has a coarse resolution at the North than in the South. As the event goes, this numerical problem exacerbates. The high-pressure area moves northwards (at 28/09/2015, the pressure centre is in the Baltic Sea, that is not solved within the WRF nesting) and the model partly consider it, via the lateral boundary conditions. But the pressure anomaly gradient cannot be properly reproduced. With such coarse spatial resolution, it seems plausible to have mismatches at (i) the intensity of the wind fields, plus (ii) an incorrect tracking of a low pressure system that appears on North Africa and moves to Corsica.

Hence, the surface and troposphere layers could be the main responsible for the mismatch between model and observations. Note that **local** and **daily scale** phenomena are even **harder to model**, such as the **heavy precipitation** that happened from 26/09/2015 to 30/09/2015. This local precipitation lead to increases in moisture that may lead to local instabilities. Precipitation is modelled with sub-grid scale parametrizations that depends on the temperature and the sea level pressure. **Slight inconsistencies among variables can drive further errors**. These inconsistencies may arise due to inaccurate surface physics or non-proper boundary conditions.

N-15 presents **better metrics** in wind speed and T_{m02} than O-15. The mean wave period at the storm-peak shows overestimations of 1.5 sec at Barcelona, Tarragona and Begur. At the same storm-interval, the wind speed has an overestimation of 6 m/s at Begur; whilst at Tarragona reaches 3 m/s. The H_s metrics are similar to the ones highlighted in O-15.

An important fact, in N-15, was the modelled discrepancies with the measured **wave direction shift** (from North-East to South-East). The wave outputs were essentially Eastern during the whole storm (see time series in Barcelona, Fig. C.19; and Tarragona, Fig. C.21). However, this directional **shifting** was **present** in the **WRF wind** fields (see Figs. C.2 and C.3). The **overestimation** of the wind speed during the **growth-phase**, though, could have lead to more persistent Eastern waves. Note also that important low sea-level pressure anomalies were located at the NW Mediterranean Sea (see storm surge contribution in Figs. 5.3 and 5.4), then indicating that **atmospheric low-level processes** had **important influence** in this episode.

In **J-16**, the wind speeds show good agreement at the Balearic island stations, Valencia and Tarragona. At Begur Cape, there exists **overprediction** from 8/01/16 to 9/01/16 (Fig.C.28). In this period, the **observations** change **abruptly** (both

in *intensity* and *direction*), whilst WRF represents a more stable behaviour. Such abrupt changes may be explained by **local instabilities** (driven by the reported temperature anomalies and moisture) that were responsible not only from this variability, but also from the measured rainfall (see Sec. 5.2.3).

This level of agreement verifies that the **orographic effects** at **Gibraltar strait** are well captured with the proposed spatial resolution. The sharp gradients of the SW jet current are properly modelled in intensity and direction. The **large-scale atmospheric processes** (synoptic and mesoscale) had a more prominent role than in O-15 or N-15. Despite the gradients, the H_s, T_{m02} and direction all presented good accuracy. The error was especially low at the growth, decay and peak of the storm (i.e. the most important parts of the event from a coastal hazard forecasting perspective). The high frequency of wind updating (20 minutes) and the current-coupling were factors that contributed to these results. Note in the time series (see Figs. C.26 and C.28) that even ephemeral H_s peaks were reproduced. In a sensibility analysis, in which the **current fields were not included**, the H_s **error** at the storm peak grew **30 cm**.

F-16, though being **moderate in intensity**, presents a combination of mesoscale and local processes than hampers modelling. It was the mildest event that has been considered in this dissertation, but the skill is somewhat comparable to O-15. The low sea level pressure comes from the North Atlantic and affected the whole Iberian Peninsula. The pressure centre was located at its Eastern side, though. From 26/02/2016 00:00 to 06:00 h, the sea level pressure at the centre experienced a sharp drop (around 10 hPa). This gradient was the reason for the **local sharp storm surge gradient** (15 cm in 12 hours in 27/02/16 (Fig. 5.8)). Note that February was a particularly **rainy month**, specially at the Barcelona area (130% from the climatic trend) and the Maresme strait (more than 190%). Hence, temperature and moisture levels were important at the low levels of the atmosphere. That would be an element that triggered this event.

The **wind speed COE** was **low** at all in-situ points, with the already reported overestimation. Modelled H_s and T_{m02} have the same magnitude than the measurements, except from Valencia that shows an overestimation of $H_s \approx 1\ m$ at the storm peak. However, all SWAN outputs present a **lag** of almost **1 day** at the storm peak. A possible cause for this behaviour may be a **mismatch** of the **pressure anomaly track**. That may explain not only the lag of the growth phase; but also the shifting of the wave direction (from South to East) at the decay phase. This shifting is well captured at Valencia and Barcelona (Fig. C.31), moderately at Tarragona (Fig. C.33) and poorly at Begur (Fig. C.35).

The best skills were found in the two most severe events of the database: **D-16** and **J-17**. The synoptic conditions for these two events were similar, with the only difference of the **lifetime of the pressure centre anomaly**: in J-17, the low pressure centre remained within the Mediterranean for 4 days; whereas in D-16 just lasted two days. Joint with a longer lifetime, the wind speed was also higher in J-17. The storm surge at the peak ranged about 10-15 cm at Barcelona and 20-25

cm at Tarragona. The wind fields presented good accuracy, with COEs near 0.4 in Tarragona; COE=0.52 in Begur (J-17) and COE=0.40 in Valencia. The correlation coefficients were higher than 0.75.

In D-16, the H_s storm-peak was overestimated 0.5 m in Barcelona and 1.5 m at Tarragona. Note that the order of magnitude matches with the same obtained in Ch. 4. The T_{m02} was underestimated at Barcelona, probably due to the **wave reflection** of the Barcelona breakwater. Tarragona and Begur wave periods (T_{m02}) exhibited overpredictions of 1 second at the storm-peak. A probable reason for this mismatch would be the systematic wind speed overestimation. At the same places, the modelled wave direction had a minor deviation towards the East.

In J-17, the modelled storm-peak variables (H_s,T_{m02} and direction) show even better agreement with the measurements. The storm-peak at Barcelona has 30 cm of error for the H_s (Fig. C.42); and an H_s error of less than 10 cm in Tarragona (Fig. C.46). Note that the waves were $H_{s,peak} = 5.3$ m at Barcelona, and $H_{s,peak} = 6.2$ m, at Tarragona. The reason for the better agreement at this storm interval can be partly explained for the **extension of the last nesting grid** in the meteorological model (see Fig. 3.2), that includes high resolution of the Northern Iberian Peninsula. The spatial wind distribution may be better represented, with the drawback that the computational cost of the J-17 grid is superior than for the rest of the sample.

Another factor for this better performance at the storm-peak was the wave-current coupling. As happened with J-16, wind-induced currents had relevant modulus that could dampen storm waves at both episodes. Hence, the sensibility analysis denoted a storm-peak H_s overestimation of about 40 cm when surface currents were not coupled.

5.4.3. General behaviour of the modelling chain

Once described the performance of the modelling chain at an individual storm scale, it is needed to synthesize the general behaviour of the tested modules of LIM-COPAS. With that aim, integrated metrics (i.e. the first and second moments of the whole sample of error metrics) for each buoy have been computed. The results are summarised in Tabs. 5.12, 5.13 and 5.14. Please note that O-15 metrics have not been included in this integrated value, because they tended to deviate the general interpretation of the system. Then, they can be considered as outlier due to their low performance. In general, the simulations presented a set of commonalities:

- There was a **systematic overestimation** of the wind fields (the $\mathbf{u_{10}}$ **MB** is negative). The modelled standard deviation is higher than the observed. Tarragona ($COE = 0.27 \pm 0.13$) and Begur ($COE = 0.29 \pm 0.17$) have metrics above the average value ($COE = 0.24 \pm 0.14$). The WRF model performed poorly at Mahón ($COE = 0.13 \pm 0.16$) and Dragonera. These two measurements points were near the land-sea boundary at the Balearic islands coastline, that is harder to be modelled than other deep water buoys (see below). Note that a similar trend under the Klaus storm (January 2009) was reported by

Bertotti et al. (2012). Additionally, WRF wind overestimation up to 50% at Eastern Mediterranean coastal areas has been highlighted in recent works (El-Samra et al., 2018), with a similar nesting scheme and parametrizations.

- The **wave metrics** were **higher** than for the **wind fields**. Significant wave height (H_s) reported better performance than T_{m02}. H_s is an integrated value of the bidimensional spectra and T_{m02} is harder to be captured in the area (Pallarés et al., 2014).
- **Begur** and **Barcelona** show good skill for the wave parameters (above the average value). At Barcelona, H_s presents good metrics: low MB ($-0.06 \pm 0.08\ m$), low RMSE ($0.36 \pm 0.08\ m$), high correlation (0.92 ± 0.03) and high COE (0.58 ± 0.11). This outcome is relevant, because **Barcelona buoy** shows the performance of the system at the Central part of the Catalan Coast. In Ch. 6, episodic coastal risk will be estimated at a set of beaches located in that area.
- The metrics of the wave parameters at **Begur** buoy were the most stable. The **standard deviation of the COE**, both for H_s and T_{m02} was the **lowest** (± 0.05). On the contrary, Valencia and Tarragona presented the lowest mean COE (both 0.49 for H_s and 0.33-0.34 for T_{m02}) and the highest standard deviation ($0.16 - 0.17$ for H_s and T_{m02}). Begur was located at deep waters (1200 m), whereas Tarragona and Valencia were at shallower waters (688 m and 260 m).
- The **wave metrics** from **high return period** events (D-16 and J-17) show **higher standard deviation** than the observed. The **moderate events** (F-16, N-15 and J-16) tend to present **lower standard deviation**.
- Wind fields tend to have higher skill and, consequently, more accurate wave parameters when the synoptic and mesoscale have a more prominent role (J-16, D-16 and J-17).
- The wave storm peak, except for the F-16 event, was properly reproduced in **timing** (i.e. no significant lag) and **intensity** (i.e. slight overpredictions). The wave growth and decay storm-phases are well captured. Using the hourly circulation fields as input, contributed to decrease the H_s overestimation trend (please note in Tab. 5.13 that the **MB are negative** at all points except Mahón).
- The mean COE highly depends on the variable: $u_{10}(0.24 \pm 0.14)$, $H_s(0.52 \pm 0.12)$ and T_{m02} (0.36 ± 0.14); but the standard deviation (st.dev) of the COE is similar, regardless of the variable. Among the different in-situ points, mean H_s COE can deviate six points, but seven points as st.dev; mean T_{m02} COE may vary three points, despite the st.dev. can deviate ten points; conversely, mean u_{10} COE can vary 10 points, but only 3 points in st.dev.
  The **mean COE** for the **wind** modulus is **site-dependent**, but the st.dev. shows robustness against different types of synoptic conditions; the **mean COE** for T_{m02} is more stable (i.e. the performance is similar at all in-situ points), but the performance is **dependent of the event**; the COE for H_s

has moderate fluctuations both in mean and st.dev. (i.e. the variable is moderately site-dependent and event-dependent). Hence, the behaviour of the wave model is not so site dependent as the meteorological model, but there may be particular events for any node in which the model may vary significantly.

Table 5.12.: Integrated metrics for the **wind speed** ($u_{10}(m/s)$) at each buoy and their buoy-averaged values. The first value is the mean value and the second one, the standard deviation. ***Legend: MB*** *(Mean bias, in m/s);* ***RMSE*** *(Root Mean Square Error, in m/s);* ***r*** *(correlation coefficient);* ***COE*** *(Coefficient of Efficiency).*

Buoy	$\mathbf{u_{10}(m/s)}$			
	MB	**RMSE**	**r**	**COE**
Tarragona	-1.49 ± 0.87	3.23 ± 0.61	0.75 ± 0.08	0.27 ± 0.13
Begur	-1.72 ± 0.95	3.61 ± 0.81	0.69 ± 0.11	0.29 ± 0.17
Dragonera	-1.64 ± 0.36	3.54 ± 0.55	0.66 ± 0.12	0.19 ± 0.11
Mahón	-1.20 ± 1.16	2.67 ± 1.10	0.67 ± 0.11	0.13 ± 0.16
Valencia	-1.49 ± 0.78	3.77 ± 0.60	0.63 ± 0.15	0.27 ± 0.13
Averaged	-1.52 ± 0.78	3.41 ± 0.76	0.68 ± 0.12	0.24 ± 0.14

Table 5.13.: Integrated metrics for the **significant wave height** ($H_s(m)$) at each buoy and their buoy-averaged values. The first value is the mean value and the second one, the standard deviation. ***Legend: MB*** *(Mean bias, in m);* ***RMSE*** *(Root Mean Square Error, in m);* ***r*** *(correlation coefficient);* ***COE*** *(Coefficient of Efficiency).*

Buoy	$\mathbf{H_s(m)}$			
	MB	**RMSE**	**r**	**COE**
Barcelona	-0.06 ± 0.08	0.36 ± 0.08	0.92 ± 0.03	0.58 ± 0.11
Tarragona	-0.13 ± 0.19	0.55 ± 0.11	0.86 ± 0.11	0.49 ± 0.16
Begur	-0.07 ± 0.09	0.55 ± 0.12	0.89 ± 0.03	0.54 ± 0.05
Dragonera	-0.04 ± 0.14	0.57 ± 0.11	0.84 ± 0.08	0.48 ± 0.14
Mahón	$+0.07 \pm 0.22$	0.51 ± 0.11	0.79 ± 0.26	0.53 ± 0.09
Valencia	-0.17 ± 0.12	0.64 ± 0.09	0.81 ± 0.17	0.49 ± 0.17
Averaged	-0.06 ± 0.16	0.53 ± 0.13	0.85 ± 0.13	0.52 ± 0.12

Table 5.14.: Integrated metrics for the **mean wave period** ($T_{m02}(s)$) at each buoy and their point-averaged values. The first value is the mean value and the second one, the standard deviation. ***Legend: MB*** *(Mean bias, in s);* ***RMSE*** *(Root Mean Square Error, in s);* ***r*** *(correlation coefficient);* ***COE*** *(Coefficient of Efficiency).*

Buoy	$\mathbf{T_{m02}(s)}$			
	MB	**RMSE**	**r**	**COE**
Barcelona	-0.03 ± 0.23	0.93 ± 0.24	0.72 ± 0.13	0.35 ± 0.10
Tarragona	-0.35 ± 0.29	1.05 ± 0.36	0.77 ± 0.14	0.34 ± 0.24
Begur	-0.28 ± 0.05	1.01 ± 0.28	0.82 ± 0.41	0.37 ± 0.05
Dragonera	-0.06 ± 0.21	0.84 ± 0.20	0.71 ± 0.20	0.39 ± 0.15
Mahón	-0.33 ± 0.74	1.09 ± 0.51	0.80 ± 0.06	0.39 ± 0.09
Valencia	-0.09 ± 0.46	1.03 ± 0.35	0.66 ± 0.28	0.33 ± 0.22
Averaged	-0.19 ± 0.40	0.99 ± 0.34	0.74 ± 0.16	0.36 ± 0.14

The modelling chain exhibits different skill depending on the synoptic conditions. The atmospheric conditions at the coastal zone are particular difficult to be handled due to the important strong land/sea contrasts (shortwave/longwave radiation, albedo, planetary boundary layer parametrizations, heat fluxes, etc.) and sea surface temperature (SST) gradients (that affects moisture and surface temperature). Some of these atmospheric processes depend on the wave fields (for instance, a rough water surface would have more roughness with the planetary boundary layer). Significant efforts have been done in this decade for a better understanding of these two-way interactions (Cavaleri et al., 2012; Sullivan and McWilliams, 2010). In the events presented in this Chapter, though, the meteorological and wave model errors are tightly related. Wind field quality affected severely the wave hindcasts.

In this Chapter, the main source of errors in WRF was **probably** the **inconsistency** among the interaction of the **atmospheric variables**. These mismatches led to instabilities driven by processes at lower spatial scales than the synoptic and the mesoscale ones. When these local processes have a prominent role (O-15, N-15 and F-16), the forecasts are hindered. Such inconsistency can be due to:

- Difficulties for achieving the same quality for all the forcings and partly inaccurate boundary conditions (for instance, the SST in ERA-INTERIM was not as accurate as land surface temperature).
- Lack of input-data for variables that may have impact under extremes regimes (i.e. run-off at certain rivers alters significantly SST and salinity in a flash-flood event).
- Model simplifications and hypothesis, such as sub-grid scale processes (precip-

itation, heat fluxes, pressure gradients) and local phenomena, such as land-sea breezes.

- Overparametrization of certain interactions among physical processes that should be considered as dynamic processes (for instance, the sea surface roughness due to waves, or the aerosols concentrations near the sea surface, etc.).
- Errors derived from the numerical scheme (i.e. artificial diffusion or smoothing at certain gradients).

It has been conducted extensive wind fields analysis at the abovementioned in-situ points. Assessing the error for other meteorological variables is out of the scope of this Chapter. The modelled systematic overestimation in the wind speed has boosted the following phenomena in the modelled waves:

- **Overestimation** of the **significant wave height** (H_s). Note however, that the wind speed and the H_s errors are not proportional. The significant wave height is an integrated value of the bi-dimensional wave spectra (Eq. 3.4.7), and is solved with a more relaxed time step.
- **Errors** in **wave period:** when overestimated winds are located at the coastal zone, the high-frequency partition of the wave spectra tends to be overestimated; however, when the winds are located at the offshore part, then the low-frequency partition may be overestimated. This behaviour has been described in the previous section when addressing O-15 and F-16 storms.
- **Errors** in **wave direction**, specially in cases in which the wind veers towards a different sector at the decay-phase. This phenomenon has been observed at N-15 and F-16.

Improving the quality of the wind fields in this Chapter is one of the cornerstones for improving the wave hindcasts. Re-addressing the hypothesis made in LIM-COPAS architecture can envisage a roadmap for improvement.

For instance, it was considered a one-way (offline) coupling between the meteorological and wave model (i.e. the coupling considers an exchange of energy from wind momentum to ocean waves; but there is no feedback to the atmospheric model). For calm conditions, this hypothesis it is often enough. Recent works at the same study area, such as the one in Grifoll et al. (2016), reinforce these statements.

However, this hypothesis is being questioned in recent works (Bruneau et al., 2018). Larsén et al. (2017) coupled WRF and SWAN with a momentum roughness length parametrization (Fan et al., 2012). This formulation tends to lower roughness under wind speeds up to 20 m/s than other formulations such as Beljaars (1995). Due to the fact that the main reason of the inaccuracies are the wind speed overestimation, it may be a suitable option to be tested.

Wave-current offline coupling was **relevant** for **high return periods** that coincide with strong wind-induced currents (D-16 and J-16). In other events, it was not so determinant. Nevertheless, using this information is more physically consistent that overparametrising or overfitting wave dissipation. The introduction of hourly current fields as input for the SWAN model dampens the significant wave

height at the coastal area.

Note that sea level and storm-surge was not modelled in LIM-COPAS, using IBI-MFC forcings instead. Note also that IBI surface currents and sea level was only added to the last SWAN nesting (the red domain in Fig. 3.2). The use of a circulation model, such as ROMS (Shchepetkin and McWilliams, 2005), coupled with waves or the atmospheric model, could provide better results, specially at coastal areas. A high resolution circulation model coupled with the atmospheric would provide updated SST fields, more consistent heat fluxes, moisture levels, etc. Wind fields and wind-induced currents at the continental shelf would be more consistent. This high resolution information would be essential to model land-sea processes.

Run-off processes and river discharges would also provide important local changes in sea salinity and temperature (Grifoll et al., 2014; Liste et al., 2014). The inclusion of the Ebro river discharge may affect the Tarragona buoy area and the Llobregat river, the one in Barcelona. These land-discharges reinforce the need for a regional circulation model.

Wave period forecasting can also be improved with better physics. For instance, the Barcelona buoy is located near the Barcelona harbour main breakwater. Underestimations of the mean wave period has been modelled in O-15 and D-16 during the storm-peak. Note also that the st.dev. of the COE is significant 0.35 ± 0.10 (Tab. 5.14). A reason may be that wave reflection can induce transfer to low frequencies of the wave spectra that are hard to reproduce with phase-averaged models. Parametrizations has been proposed in the literature (Van der Meer et al., 2005; Ardhuin and Roland, 2012), but another option would be the use of more computationally demanding phase-resolving models for coastal wave propagation.

The spatial resolution of the last WRF nesting ($3 \times 3\ km$) is enough for representing the synoptic and mesoscale processes plus the main orographic elements (such as the Alps or Pyrenees), but it may be coarse for local-scale phenomena. Important precipitation was reported in the Catalan coast during O-15, N-15 and F-16. Precipitation is solved in a sub-grid scale via parameterizations, but note that it may not prove accurate enough. This may lead to mismatches in the cloud fraction, the moisture levels, the heat fluxes, etc. It is out of the scope of this Chapter to analyse modelled vs. observed precipitation, but it cannot be ignored this source of uncertainty.

This local phenomena requires local detailed information. **Updated land-use maps** are essential for the surface microphysics. In this sense, remote sensing such as Landsat-7 or Sentinel-2 datasets may prove useful for updating and cross-checking this kind of information (Chen et al., 2016). At the Eastern Pyrenees (near the Study Area), Jiménez-Esteve et al. (2018) shown that the combination of updated land-use maps and high resolution can improve WRF performance.

Mahón and Dragonera buoys were the ones that shown worse performance in WRF. Balearic islands physics would probably need higher spatial resolution, or at least, input-data more consistent with these local features, specially at the land-sea boundary. Local ageostrophic circulations, related with the islands orography may be a

reason for the mismatch.

A way to increase the spatial resolution without increasing the computational demands would be via unstructured grids. These numerical schemes can be an alternative for avoiding several nestings, thus allowing an online exchange of information at different spatial scales. Pallarés et al. (2017) set-up an unstructured version of SWAN in the NW Mediterranean Sea and the metrics were comparable to the structured approach, but decreasing the computational time up to a half, specially when the boundary conditions are given in spectral form.

In the previous Ch. 4 a previous version of the modelling chain was tested for the **D-08**. In that case, winds comprise operational ECMWF winds blended with remote sensing observations (Bentamy et al., 2007). Wave parameters COE were better than the averaged ones from this Chapter (see Sec. 4.5): at Blanes, for the H_s was 0.74 and the T_p 0.51; at Llobregat, the same metrics were 0.68 and 0.59; and at Cape Tortosa, 0.73 and 0.49, respectively. However, when perturbing the wind fields (decreasing a 20% the reference wind modulus), the COEs drop dramatically to low levels: at Blanes, H_s COE was 0.26 and T_p COE was 0.18; at Llobregat, COE decreased to -0.12 and 0.22; and at Cape Tortosa to -0.15 and 0.22, respectively.

This fact reinforces the importance that wind field quality may have on the wave forecast. Note also that D-08 was an Eastern storm with similar features than D-16 and J-17. All three events share comparable agreement, despite that the wind fields for the two latter were not blended with observations.

In summary, the modelling chain has shown good performance at the area in which the morphodynamic (Ch. 4) and the risk module (Ch. 6) would be tested. In particular, the Risk module uses as covariates the significant wave height($H_{s,peak}$), and the wave direction ($\theta_{w,peak}$) at the storm-peak. As highlighted above, these variables have shown good agreement. Then, in the next Ch. 6, this wave hindcast will constitute the basis for estimating the erosion and flooding cost at the Northern and Central Catalan beaches.

5.4.4. Applicability and challenges for Coastal Forecasting

Once held the analysis of the LIM-COPAS under the proposed six recent storms, this subsection will address some general concerns about future challenges for the system and how to overcome these limitations.

This Chapter has shown that LIM-COPAS has good accuracy with high return period extreme events. Note, though, that the error metrics for the moderate events has been lower. They usually depend on the conjunction of large-scale and local scale processes that are harder to be forecasted. There exist a lack of observations for this wide range of possible cases. Cyclogenesis is one of the main processes in which more uncertainty exists. Additionally, an important fraction of these moderate events are driven by non-stationary cyclogenesis (Trigo et al., 2002; Campins et al., 2011), that diminishes forecast skill.

Ensemble meteo-oceanographic forecasting would be a way to bound the uncertainty in these cases. Note that there are already initiatives in the Mediterranean Sea (Milliff et al., 2011; Pinardi et al., 2011). Baroclinic disturbances, generation/translation of low-high pressure systems and local patterns (cloud fractions, precipitation, moisture, heat fluxes,etc.) would be benefited from this approach, because there exists an important uncertainty in these processes. Additionally, they have a significant impact on the two main hydrodynamic drivers at the study area: wind waves and storm surges.

Low return periods wave storms joint with storm-surges can induce additional **damage**. Despite that is out of the scope of this Chapter to study the co-existence of extreme surges and waves, it cannot be ignored the importance of extreme sea level forecasting in episodic coastal risk. For example, in F-16, the **storm-surge gradient was 20 cm in just 1 day**. Then, the forecasting of such sharp surge gradients can have a significant impact. Both N-15 and F-16 are clear examples. In the next Chapter, it will shown that LIM-COPAS estimated 2.5 M euros in losses for the N-15 (25 cm of storm surge, Fig. 5.3), despite the wave return period was moderate ($T_r = 1 - 2\ yrs$).

In this Chapter, IBI-MFC forcings has been used instead, but a complete CEWS would need to include a more specific circulation model, as the NIVMAR storm surge system (Álvarez-Fanjul et al., 2001). Plus, sea level pressure and wind fields are key atmospheric variables for modelling both wind waves and surges, then further justifying ensemble forecasting.

Another important source of uncertainty is that some processes are parametrized, in a way that assumes certain balances among meteo-oceanographic variables. However, this balance is non-stationary and the dependence structures need to be flexible. For instance, Lin-Ye et al. (2017, 2018) have shown that wave-storm components have a non-stationary relationship with large-scale indices. But note that even more relationships could be hidden at lower spatio-temporal scales. Meteorological and hydrodynamic models rely on a set of parameterizations that may lead to lower forecast skills in the next decades. Climate Change will probably affect extremes (Trenberth and Shepherd, 2015). In this regard, Emanuel (2017) alerted recently that incidence of hurricanes that intensify quickly just before landfall could increase substantially by the end of the century. He pointed out the need for (i) improving hurricane intensity forecast and (ii) preparing populations to respond to high-intensity landfalling hurricanes at short notice. In the NW Mediterranean Sea, Sea Level Rise joint with changes of wind gradients may increase coastal risk (Sierra and Casas-Prat, 2014; Sierra et al., 2015; Sánchez-Arcilla et al., 2016b).

Continuous monitoring of the meteo-oceanographic variables has to be **ensured** for **maintaining** and **improving CEWS**. Observations not only help to calibrate and validate the models, but they can also can increase forecast skill via data assimilation. At open sea, remote-sensing is a promising way to cover the current data gap, as in Yu et al. (2017). They assimilated Sentinel-1 Synthetic Aperture Radar (SAR) winds with the WRF 3DVAR for the Lionrock typhoon (August 2016). The

assimilation reduced track error (45 km lower than the non-assimilated simulation) and wind speed error (decrases around 2 m/s) at short-range forecasts (around 30 h).

Another important use of observations is to assess the **error distribution**. The same remote sensing network can be helpful for determining the spatial structure of the error, but the time error structure requires in-situ network. Time structure is fundamental for assessing the lags and the gradients (growth and the decay phases). Hence, a complete monitoring need to ensure both networks. The direct applicability would affect the accuracy of the forecast. For instance, in this Chapter, a plausible hypothesis for T_{m02} may be to assume a homogeneous (or weakly non-stationary) spatial error, but a non-stationary time error (because T_{m02} is time-dependent, see Sec. 5.4.3 above). Conversely, wind fields need to assume a non-stationary spatial error, but a homogeneous time error. Error characterization is invaluable for planning improvements in the forecasting chain, because it limits/bounds the areas and conditions to be addressed.

A good way for understanding how a dynamic system works is to have a representative sample of past extreme events. High resolution hindcasts and error distributions provide spatio-temporal gapless data on complex physical processes. When observations are not available, hindcasts can fill knowledge gaps about the past; until new evidence refuses the hypothesis embedded into our forecasting systems. They are benchmark scenarios for testing improvements in the forecasting chain, but they can also help to identify patterns. These patterns can become into rules. These rules can be adapted into tools that may serve for **complex decision making**.

5.5. Conclusions

In this Chapter, six recent storms (2015 - 2017 seasons) were hindcasted with LIM-COPAS (Ch. 3) and compared with Puertos del Estado observational network. ERA-INTERIM global reanalysis was used as boundary conditions for the meteorological module, that is composed by a two-way nested WRF model, with resolutions ranging from 27 to 3 km. The obtained wind fields, joint with IBI-MFC circulation and sea level, were used as input for a spectral wave model (SWAN). Waves were solved within two one-way nested grids: Western Mediterranean (5 km) and Balearic Sea (2 km).

Wind fields were systematically overestimated, with an integrated mean bias of $-1.52 \pm 0.78\ m/s$. The modelled standard deviation was higher than the observed. Tarragona ($COE = 0.27 \pm 0.13$) and Begur ($COE = 0.29 \pm 0.17$) had metrics above the average value ($COE = 0.24 \pm 0.14$). The worst performance was found at Mahón ($COE = 0.13 \pm 0.16$) and Dragonera ($COE = 0.13 \pm 0.16$). The reason may be that the physics at the land-sea boundary at the Balearic islands were harder to be modelled than other deep water buoys.

The spatial resolution of the last nesting ($3 \times 3\ km$) was enough to handling the

most important orographic features, but it may prove coarse for modelling local phenomena (cloud fraction, precipitation, moisture levels, heat fluxes, land-sea processes) and surface processes that are heavily parametrized.

As happened in the previous Ch. 4, errors in the meteorological model affected severely the quality of wave hindcasts. Wind overprediction was dampened in the SWAN model, that tends to underestimate wave peaks. Then, wave metrics were significantly higher. The integrated H_s COE was 0.52 ± 0.12 and T_{m02} COE was 0.36 ± 0.14. High return period events [D-16,J-17] ($T_{r,waves} \geq 10\, yrs$) had better skill than moderate ones (O-15, F-16 and N-15). The error metrics for the first two (D-16, J-17) were comparable to the ones presented in D-08 (see Ch. 4).

Wave directions were well captured, except in cases (N-15 and F-16) that the wind veers towards a different sector at the decay phase. Storm timing, growth and decay storm-phases were well captured. Only F-16 had a lag of almost 1 day. Poor performance events (O-15 and F-16) had probably a mismatch of the pressure anomaly track. Note also that heavy coastal rainfall coincided with the events, leading to complex local processes.

Offline coupling of ocean currents with waves increased the performance of the storm-peak modelling, specially in those cases in which strong wind-induced currents are within the inner shelf. In the presented database, wind-induced currents at J-16, D-16 and J-17 reached important modulus that dampened ocean waves. In these cases, offline coupling improved the performance between 20-50 cm the significant wave height at the storm-peaks. The inclusion of these consistent physical processes, instead of relying of overparametrization of wave dissipation mechanisms, proved to be essential to achieve better skills.

Barcelona and Begur had good skill for the wave parameters. At Barcelona, H_s presented low MB ($-0.06 \pm 0.08\, m$), low RMSE ($0.36 \pm 0.08\ m$) and high COE (0.58 ± 0.11). Begur parameters were the most stable. The standard deviation of the COE was the lowest (± 0.05), both for H_s and T_{m02}. Hence, it can be concluded that LIM-COPAS performed well at the Northern and Central Catalan Coast. This outcome is paramount for the next Chapter 6, because these wave hindcasts will be the hydrodynamic drivers for testing the Risk module.

6. Coastal Risk assessment

6.1. Introduction

Process-based morphodynamic forecasts provide high quality coastal hazard information, but they are computationally expensive. Hence, the **amount** of **coastal sites** and hydrodynamic **scenarios** that can be run in an **operational** system is **limited**. This limitation hampers: (i) the implementation of a CEWS at a regional level; (ii) the proper assessment of the uncertainty of the forecasts; (iii) timely updates of the forecasts that can benefit from near-real-time data assimilation from monitoring networks (as to in-situ or remote sensing based).

Coastal **risk forecasts** presents several layers of **uncertainty**. Process-based modelling may forecast hazardous levels at a time t, but a sudden update of the hydrodynamic drivers at the time step $t + 1$ may imply low risk. It is imperative to have a quick-scan response tool that addresses the uncertainty of the drivers. A CEWS has to address different hydroynamic scenarios at different hot-spots. A detailed, but unique wrong forecast in a single point would lead to a forecast skill of 0. It is better, then, to provide 50 forecasts at different points and be wrong at 25 out of 50, rather than just one prediction and be wrong.

A way to overcome this limitation is to use **statistical models** fitted with process-based outputs. Despite statistical models have simplified physics and they require expertise in how to build them, they are computationally **cheaper** and easy to be interpreted. The probabilistic definition of risk can be found in Sec.2.2. Coastal Engineering has rely on probabilistic models that consider stationarity and independence among variables. However, these assumptions rarely holds valid in real-world: (i) the response of correlated hazards such as episodic flooding and erosion demands a dependence structure (then, independence cannot be assumed), and (ii) the response would depend on the magnitude of the loads (thus, stationarity of the parameters cannot be assumed, as well).

Archimedean Copulas were introduced in Sec. 3.3.4.1 as a flexible way for defining a dependence structure between two univariate probability distribution functions. GAMLSS were presented in Sec. 3.3.4.2 as a general method for fitting non-stationary probability distribution functions. The combination of both concepts paves the way for **multivariate non-stationary statistical models**. Applications in Coastal Engineering can be found in (Lin-Ye et al., 2016, 2017). These models can alleviate the three abovementioned requirements: (i) computionally cheap forecasts at a wide range of hot-spots; (ii) methods for addressing uncertainty due to

its probabilistic nature and (iii) the possibility of near-real-time updates of the forecast merged with observations. These models, though, are complex to be built and requires expertise on both (i) the fitting dataset and (ii) the model building process.

The aim of this chapter is to **develop COPAS**, a **non-stationary multivariate statistical model** that can estimate the **flooding and erosion costs in microtidal beaches**. This model would act as a **quick-scan risk forecasting** module that would estimate the consequences of episodic coastal flooding and erosion at a wide range of beaches and hydrodynamic scenarios. This module will serve as a basis for optimize the computational cost of the Morphodynamic module. The module will be tested at a subset of **79 beaches** with the wave-storms that were modelled in Ch. 5. This Chapter is structured as follows: Sec. 6.2 states the four steps for building the non-stationary multivariate model. Results are listed in Sec. 6.3, discussed in Sec. 6.4 and concluded in Sec. 6.5.

6.2. Methodology

The **risk module** has been built following 4 steps (Figure 6.1):

1. **Generation of the sample** (Sec. 6.2.1)**:** A database (see Sec. B.1) that addresses two hazards (flooding and episodic erosion, see Sec. 2.3.3 and 2.3.1.1) has been built. Several wave storm conditions have been considered, in combination with different MWL scenarios. It has to be noted that some beaches (Barcelona, Gavà, Premià de Mar, Estartit) have more simulations than other ones due to the complexity of these specific domains.

2. **GAMLSS model building** for each beach (Sec. 6.2.2): Once built the database, each beach has been fitted with a non-stationary multivariate GAMLSS model. In these GAMLSS models, the response variables have been the flooding and erosion cost, whilst the co-variates have been the hydrodynamic forcings (storm-waves and MWL).

3. **Integration of the individual models into a risk formula** (Sec. 6.2.3): Each beach listed at Tab.B.1 has been fitted with an individual GAMLSS model. Each GAMLSS covariates have associated a set of coefficients. The **coefficients** of each individual model are **related** with its **morphodynamic features** (beach width, beach slope, berm height, etc.). Thus, the formula will allow building non-stationary multivariate probability distribution functions from the inputs described in Fig. 6.2.

4. **Application** (Sec. 6.2.4) of the risk formula at both the calibration (Tab. B.1) and validation beaches (Tab. B.3). The main outputs are (i) stress-curves, (ii) correlation-curves and (iii) forecast maps.

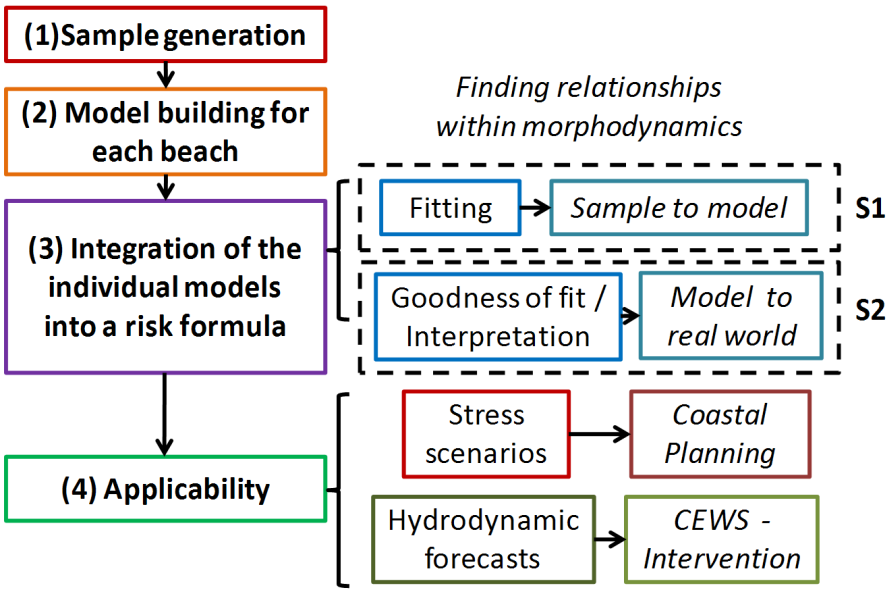

Figure 6.1.: General overview of the **proposed risk module**. **Legend:** S1 (sub-task 1) and S2 (sub-task 2).

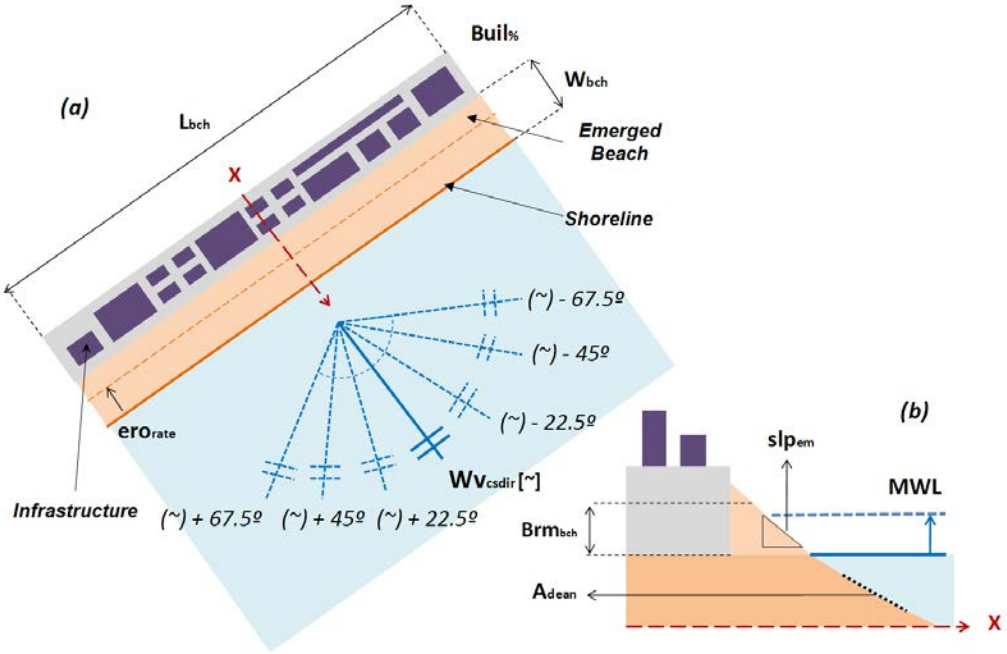

Figure 6.2.: Definition of the **main inputs** for the **risk formula**. (a) Planview of the littoral cell; (b) Cross-shore beach profile. The different elements will be described in Sec. 6.2.3.

Below it can be found a description of the different steps that have been covered in this analysis.

6.2.1. Step 1: Sample generation

In order to build a suitable formula, it is needed a sampling database that will contain a **representative sample** of the type of beaches (morphodynamic features such as the archetype (see Ch. 2) berm height, beach width, etc.) that we want to predict afterwards. It is also important that these beaches have been modelled under a certain range of scenarios, in order that the usual forecasted hydrodynamic conditions are within the ranges of the formulation.

The sample has been built as summarised at Figure 6.3: the first step is an **extreme wave climate** at deep waters, in order to obtain the boundary conditions for a **non-stationary SWAN** simulation (see Sec. 3.3.2). The extreme wave probabilistic functions have been extracted from Puertos del Estado buoy network and CIIRC (2010). In all cases, the simulation time has been a **storm duration of 24 hours** with equal growth and decay phases. This hypothesis can be considered valid according to the results of Lin-Ye et al. (2016). Once defined a synthetic time series of JONSWAP spectra as boundary conditions, the SWAN model has been run for a set of scalar return periods and directional sectors. As minimum, the storm sample covers return periods of 10, 50 and 100 years. When possible, additional return periods have been considered within the same interval (from 10 to 100 years).

From the SWAN model it has been obtained time series of 2D spectra that serve as offshore wave boundary conditions for the **XBEACH** model (see Sec. 3.3.3). Because this model is aimed for extreme events, in case that the storm peak at the offshore boundary is lower than 1.5 m, the simulation is not considered. With the same wave information, two types of simulations have been run: the first one with the sea level set to zero; and the second one with a stationary sea level. This stationary sea level can be considered as a transient storm surge (that lasts at least 24 h) or a certain sea level rise. The **same** scheme has been repeated for the **54 calibration beaches**.

Once the simulation has finished, a **postprocessing algorithm** computes the emerged sand beach erosion and the costs associated to flooding. The **sand erosion** is computed by **integrating** the **difference** between **pre-post** storm **emerged beach volumes**. These volumes are obtained directly from the model outputs.

The **flooding costs** require, for each simulation, the following steps:

1. **Determination of the floodplain:** if a computational node is flooded more than 15 min and surpasses a minimum threshold of 20 cm, then it is considered as a wet point. The maximum water depth at a single node is the maximum value reached throughout the simulation that has lasted at least 30 min.
2. **Overlapping of the floodplain with a building mask:** if the wet node coincides with a building (and its neighbouring nodes), then, the flood value is stored in a masked floodplain; otherwise, it is set to zero.
3. **Estimation of the flooding cost:** the masked floodplain serves as input for the empirical flood cost ($euros/m^2$) - water depth function for buildings by Velasco et al. (2016). The function holds valid for buildings and has been

extrapolated from flooding insurance studies at the Barcelona area. At areas outside Barcelona the housing costs may significantly differ. Hence, an empirical reduction is applied, according to the relative housing price. Once computed the costs for each building, the total flood cost is stored.

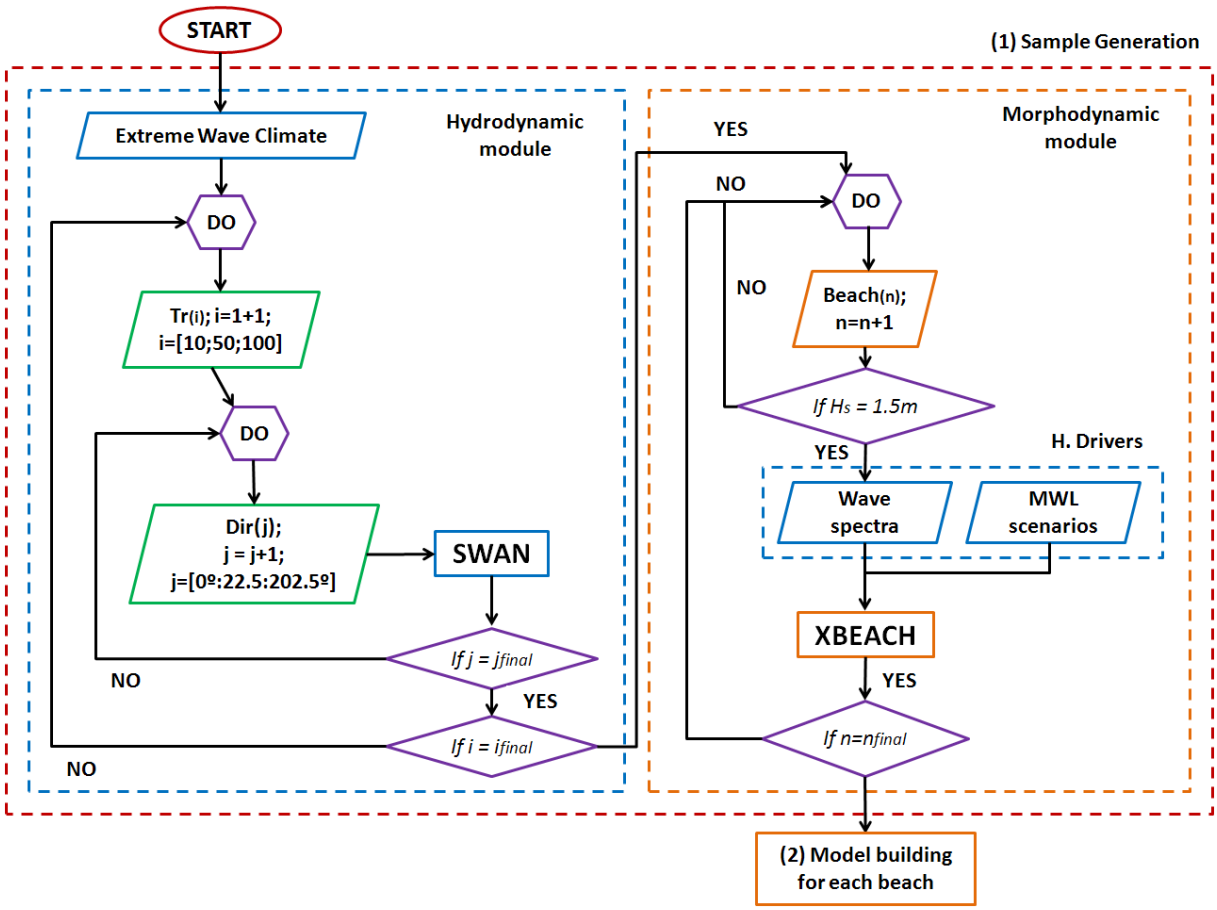

Figure 6.3.: Flowchart for the sample generation **(Step 1)** of the Risk module. ***Nomenclature:*** *Action or step (Rectangle); loop definition (Hexagon); conditional (Purple Rhomboid); data list (Rhomboid).*

6.2.2. Step 2: Model building for each beach

Once the dataset has been built, non-stationary multivariate models has been fitted for **each beach**. The **GAMLSS** (see Sec. 3.3.4.2) approach has been used for fitting the parameters of two non-stationary marginals Gumbel pdfs (Eqs. 6.2.1 and 6.2.2) and non-stationary Gumbel Archimedean copula (6.2.3).

$$f\left[\varepsilon_r \mid \mu_{\varepsilon_r}\left(H_{s,peak}, MWL, \theta_{w,peak}\right), \sigma_{\varepsilon_r}\left(H_{s,peak}, MWL\right)\right] = \frac{1}{\sigma_{\varepsilon_r}} exp\left\{\left(\frac{\varepsilon_r - \mu_{\varepsilon_r}}{\sigma_{\varepsilon_r}}\right) - exp\left(-\frac{\varepsilon_r - \mu_{\varepsilon_r}}{\sigma_{\varepsilon_r}}\right)\right\} \tag{6.2.1}$$

$$f\left[\varphi_r \mid \mu_{\varphi_r}\left(H_{s,peak}, MWL, \theta_{w,peak}\right), \sigma_{\varphi_r}\left(H_{s,peak}, MWL\right)\right] = \\ = \frac{1}{\sigma_{\varphi_r}} exp\left\{\left(\frac{\varphi_r - \mu_{\varphi_r}}{\sigma_{\varphi_r}}\right) - exp\left(-\frac{\varphi_r - \mu_{\varphi_r}}{\sigma_{\varphi_r}}\right)\right\} \tag{6.2.2}$$

$$\mathbf{C}\left(\varepsilon_r, \varphi_r \mid \theta_{\varepsilon_r,\varphi_r}\right) = exp\left[-\left\{\left(-log\ \varepsilon_r\right)^{\theta_{\varepsilon_r,\varphi_r}} + \left(-log\ \varphi_r\right)^{\theta_{\varepsilon_r,\varphi_r}}\right\}^{1/\theta_{\varepsilon_r,\varphi_r}}\right] \tag{6.2.3}$$

Where $\varepsilon_r \sim$ Eroded volume divided by surface(m^3/m^2) and $\varphi_r \sim$ Flood cost divided by surface $(euros/m^2)$.

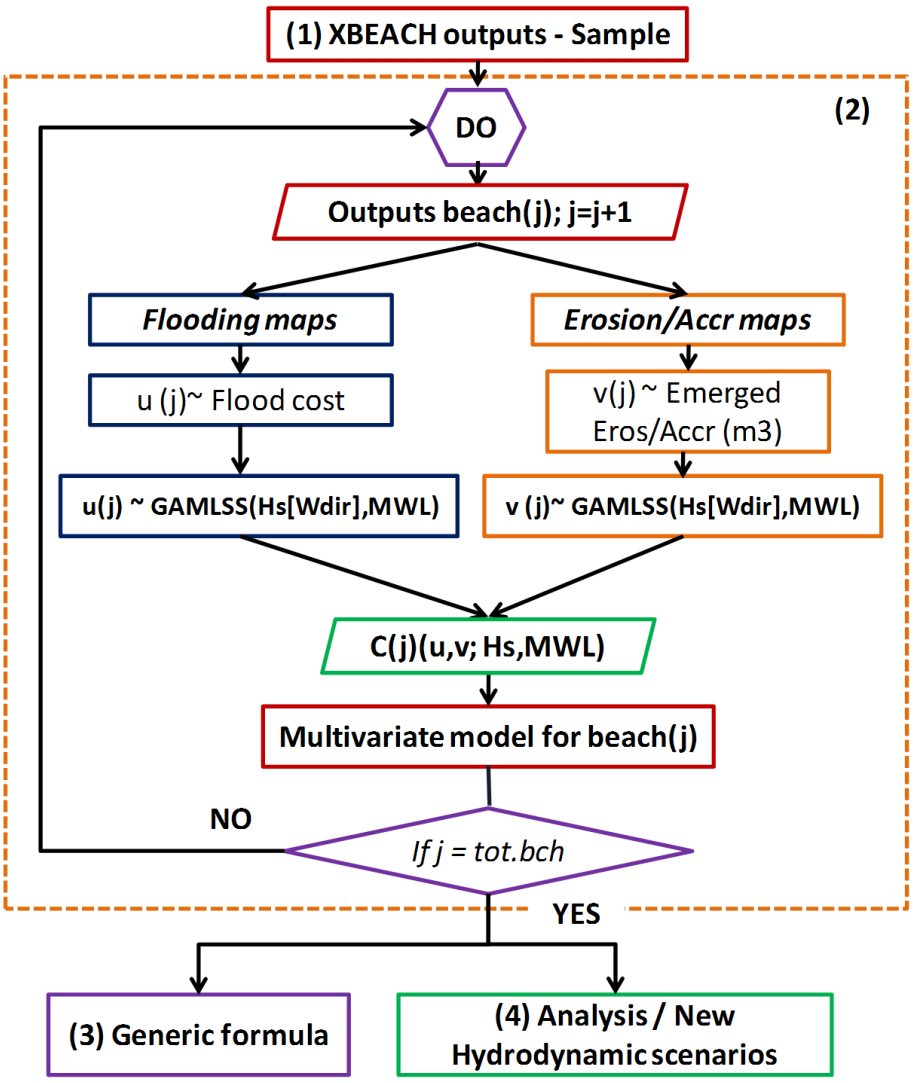

Figure 6.4.: Flowchart of the **multivariate model building for each beach (Step 2)** of the Risk module. ***Nomenclature:*** *Action or step (Rectangle); loop definition (Hexagon); conditional (Purple Rhomboid); data list (Rhomboid).*

The marginals and the copula depend on the marine drivers: (i) significant wave height at the storm peak $H_{s,peak}$, (ii) mean wave direction at the storm peak ($\theta_{w,peak}$, as a categorical variable) and the (iii) MWL (storm surge). Different interactions and number of degrees of freedom for covariate were tested. The information criteria (AIC and BIC, see Sec. 3.4), tests of significance and the principle of parsimony were the reference for selecting the appropriate models. AIC and BIC highlight how the model represents the dataset; interpretation represented how the model represented real-world conditions. A trade-off was carried out; always focusing on the principle of parsimony.

One of the relevant issues in this step is the **normalization** and **uniformity** of the dataset via the covariates. Despite each beach had different drivers, an essential task for the generic risk formula (see Step 3) was to quantify how a certain value of wave height and sea level will affect the location and scale parameters of the marginal distribution. For instance, the probability of a certain fixed erosion cost will be directly proportional to high $H_{s,peak}$ values.

6.2.3. Step 3: Generic risk formula

The main drawback of Step 2 is that a certain sample of storms modelled with the Morphodynamic module needs to be performed. These simulations have a set-up and computational cost that hampers the applicability of this methodology at an elevated number of beaches. After analysing a relevant number of beaches, there were observed a set of commonalities and possible relations among themselves. The covariate coefficients among the non-stationary location ($\mu_{\varepsilon_r}, \mu_{\varphi_r}$), scale ($\mu_{\varepsilon_r}, \mu_{\varphi_r}$) and association parameter ($\theta_{\varepsilon_r,\varphi_r}$) showed similarities among groups of beaches. It was hypothesized that the shortcoming of applicability to other beaches could be overcome via a generic definition of these five parameters (Fig. 6.5). Each parameter depends on a set of regression coefficients (Eqs. 6.2.4 to 6.2.8) that can be estimated from a set of morphodynamic features. The relationship has been modelled with Generalised Linear Models (GLMs), a particular case of the GAMLSS theory exposed in Sec 3.3.4.2.

$$\mu_{\varepsilon_r} = \beta_{(0,\mu_{\varepsilon_r})} + \alpha_{(H_s,\mu_{\varepsilon_r})}\beta_{(H_s,\mu_{\varepsilon_r})}H_{s,peak} + \beta_{(MWL,\mu_{\varepsilon_r})}MWL \tag{6.2.4}$$

$$\sigma_{\varepsilon_r} = \beta_{(0,\sigma_{\varepsilon_r})} + \beta_{(MWL,\sigma_{\varepsilon_r})}MWL \tag{6.2.5}$$

$$\mu_{\varphi_r} = \beta_{(0,\mu_{\varphi_r})} + \alpha_{(H_s,\mu_{\varphi_r})}\beta_{(H_s,\mu_{\varphi_r})}H_{s,peak} + \beta_{(MWL,\mu_{\varphi_r})}MWL \tag{6.2.6}$$

$$\sigma_{\varphi_r} = \beta_{(0,\sigma_{\varphi_r})} + \beta_{(MWL,\sigma_{\varphi_r})} MWL \tag{6.2.7}$$

$$\theta_{\varepsilon_r,\varphi_r} = \beta_{(H_s,\theta_{cp})} H_{s,peak} + \beta_{(MWL,\theta_{cp})} MWL \tag{6.2.8}$$

The 54 beaches already presented in previous sections have been termed as the Calibration Dataset. Prior to the GLMs fitting, a filtering process has been carried out. Those beaches whose episodic erosion and flooding are mainly influenced by local constraints have been discarded. There are three type of regression coefficients: (i) Intercept, (ii) Waves ($H_{s,peak}$) and (iii) MWL. Wave coefficients are corrected with an additional factor ($\alpha_{(H_s,\mu_{\varepsilon_r})}$ for erosion and $\alpha_{(H_s,\mu_{\varphi_r})}$ for flooding) that considers the wave direction at the storm peak $\theta_{w,peak}$. Ignoring the effect of $\theta_{w,peak}$ (i.e. a scalar approach) would lead to strange forecasts, as some waves for certain directional sectors would not hit the coast but they would predict important erosion and flooding.

The **directional coefficients** $\alpha_{(H_s,\mu_{\varepsilon_r})}$ and $\alpha_{(H_s,\mu_{\varphi_r})}$ work as reduction coefficients for the wave influence. They will be close to unity when the direction perpendicular to the shoreline and the $K_{\alpha(\cdot)}$ (wave directional coefficient following the ROM 3-91 method) coincide. A_{dean} acts as a refraction coefficient: the transition among directional sectors will be smoother at dissipative beaches (i.e. low values of A_{dean}), because the submerged beach slope is gentle and the results do not vary significantly regardless of the direction. However, **wave direction** is more important at **intermediate** and **reflective beaches**. The following set of GLMs have been proposed (Eqs. 6.2.9 and 6.2.10):

$$\alpha_{(H_s,\mu_{\varepsilon_r})} = \begin{cases} f_{(\varepsilon_r,cs-3)}\left(A_{dean}, K_{\alpha,cs_d-67.5}\right) & if\ \theta_{w,peak} = cs_{dir} - 67.5^\circ \\ f_{(\varepsilon_r,cs-2)}\left(A_{dean}, K_{\alpha,cs_d-45}\right) & if\ \theta_{w,peak} = cs_{dir} - 45^\circ \\ f_{(\varepsilon_r,cs-1)}\left(A_{dean}, K_{\alpha,cs_d-22.5}\right) & if\ \theta_{w,peak} = cs_{dir} - 22.5^\circ \\ f_{(\varepsilon_r,cs)}\left(A_{dean}, K_{\alpha,cs_d}\right) & if\ \theta_{w,peak} = cs_{dir} \\ f_{(\varepsilon_r,cs+1)}\left(A_{dean}, K_{\alpha,cs_d+22.5}\right) & if\ \theta_{w,peak} = cs_{dir} + 22.5^\circ \\ f_{(\varepsilon_r,cs+2)}\left(A_{dean}, K_{\alpha,cs_d+45}\right) & if\ \theta_{w,peak} = cs_{dir} + 45^\circ \\ f_{(\varepsilon_r,cs+3)}\left(A_{dean}, K_{\alpha,cs_d+67.5}\right) & if\ \theta_{w,peak} = cs_{dir} + 67.5^\circ \end{cases} \tag{6.2.9}$$

$$\alpha_{(H_s,\mu_{\varphi_r})} = \begin{cases} f_{(\varphi_r,cs-3)}\left(A_{dean}, K_{\alpha,cs_d-67.5}\right) & if\ \theta_{w,peak} = cs_d - 67.5° \\ f_{(\varphi_r,cs-2)}\left(A_{dean}, K_{\alpha,cs_d-45}\right) & if\ \theta_{w,peak} = cs_d - 45° \\ f_{(\varphi_r,cs-1)}\left(A_{dean}, K_{\alpha,cs_d-22.5}\right) & if\ \theta_{w,peak} = cs_d - 22.5° \\ f_{(\varphi_r,cs)}\left(A_{dean}, K_{\alpha,cs_d}\right) & if\ \theta_{w,peak} = cs_d \\ f_{(\varphi_r,cs+1)}\left(A_{dean}, K_{\alpha,cs_d+22.5}\right) & if\ \theta_{w,peak} = cs_d + 22.5° \\ f_{(\varphi_r,cs+2)}\left(A_{dean}, K_{\alpha,cs_d+45}\right) & if\ \theta_{w,peak} = cs_d + 45° \\ f_{(\varphi_r,cs+3)}\left(A_{dean}, K_{\alpha,cs_d+67.5}\right) & if\ \theta_{w,peak} = cs_d + 67.5° \end{cases} \quad (6.2.10)$$

Where cs_d refers to the directional sector that is perpendicular to the shoreline (maximum cross-shore transport, the reference direction in this formula, see Fig. 6.2). Each $f_{(\cdot,\cdot)}$ represents a GLM for a particular hazard (erosion (ε_r), flooding (φ_r)) and directional sector (that spans from the cs_d directional sector minus 67.5° to cs_d plus 67.5°). In summary, as higher $K_{\alpha(\cdot)}$ and finer sediment, the lower the reduction will be. In case the wave front is perpendicular to the shoreline (i.e. maximum cross-shore transport), then the reduction is almost nil. Oblique waves will have an important reduction.

Once estimated the directional coefficient, the regression coefficients can be modelled with Eqs. 6.2.11-6.2.22. Each $f_{(\cdot)}$ represents a GLM (see Sec. 3.3.4.2). The terms blue and orange refers to the colour of the GLMs that appear in the Results Section (see Figs. 6.7 , 6.8 and 6.9). The different coefficients has been clustered in three groups: (i) Intercept; (ii) Waves and (iii) MWL.

(i) Intercept (4 coefficients)

$$\beta_{(0,\mu_{\varepsilon_r})} = \begin{cases} f_{blue}\left(A_{dean}\right) & if\ beach = pocket \\ f_{orange}\left(A_{dean}\right) & if\ beach = open \end{cases} \quad (6.2.11)$$

$$\beta_{(0,\sigma_{\varepsilon_r})} = \begin{cases} f_{blue}\left(slp_{em}\right) & if\ A_{dean} \leq 0.4 \\ f_{orange}\left(slp_{em}\right) & if\ A_{dean} > 0.4 \end{cases} \quad (6.2.12)$$

$$\beta_{(0,\mu_{\varphi_r})} = \begin{cases} f_{blue}\left(slp_{em}\right) & if\ A_{dean} \leq 0.4 \\ f_{orange}\left(slp_{em}\right) & if\ A_{dean} > 0.4 \end{cases} \quad (6.2.13)$$

$$\beta_{(0,\sigma_{\varphi_r})} = \begin{cases} f_{blue}\left(slp_{em}\right) & if\ A_{dean} \leq 0.4 \\ f_{orange}\left(slp_{em}\right) & if\ A_{dean} > 0.4 \end{cases} \quad (6.2.14)$$

(ii) Waves (3 coefficients)

$$\beta_{(H_s,\mu_{\varepsilon_r})} = \begin{cases} f_{blue}\left(Brm_{bch}\right) & if\ A_{dean} \leq 0.4 \\ f_{orange}\left(Brm_{bch}\right) & if\ A_{dean} > 0.4 \end{cases} \tag{6.2.15}$$

$$\beta_{(H_s,\mu_{\varphi_r})} = \begin{cases} f_{blue}\left(W_{bch}\right) & if\ beach = open\ \&\ A_{dean} > 0.4 \\ f_{orange}\left(W_{bch}\right) & if\ beach = open\ \&\ A_{dean} \leq 0.4 \\ f_{green}\left(W_{bch}\right) & if\ beach = pocket \end{cases} \tag{6.2.16}$$

$$\beta_{(H_s,\theta_{cp})} = \begin{cases} f_{blue}\left(W_{bch}\right) & if\ beach = pocket \\ f_{orange}\left(W_{bch}\right) & if\ beach = open \end{cases} \tag{6.2.17}$$

(iii) Mean Water Level (5 coefficients)

$$\beta_{(MWL,\mu_{\varepsilon_r})} = \begin{cases} f_{blue}\left(A_{dean}\right) & if\ beach = pocket \\ f_{orange}\left(A_{dean}\right) & if\ beach = open \end{cases} \tag{6.2.18}$$

$$\beta_{(MWL,\sigma_{\varepsilon_r})} = \begin{cases} f_{blue}\left(A_{dean}\right) & if\ beach = pocket \\ f_{orange}\left(A_{dean}\right) & if\ beach = open \end{cases} \tag{6.2.19}$$

$$\beta_{(MWL,\mu_{\varphi_r})} = \begin{cases} f_{blue}\left(A_{dean}\right) & if\ beach = pocket \\ f_{orange}\left(A_{dean}\right) & if\ beach = open \end{cases} \tag{6.2.20}$$

$$\beta_{(MWL,\sigma_{\varphi_r})} = \begin{cases} f_{blue}\left(Brm_{bch}\right) & if\ beach = pocket \\ f_{orange}\left(Brm_{bch}\right) & if\ beach = open \end{cases} \tag{6.2.21}$$

$$\beta_{(MWL,\theta_{cp})} = \begin{cases} f_{blue}\left(Brm_{bch}\right) & if\ beach = pocket \\ f_{orange}\left(Brm_{bch}\right) & if\ beach = open \end{cases} \tag{6.2.22}$$

Where the morphodynamic features are (see Fig. 6.2): (i) the type of the beach (open or pocket), (ii) Dean parameter (A_{dean}), (iii) beach width (W_{bch}), (iv) emerged beach slope (slp_{em}), (v) berm height (Brm_{bch}). Several configurations have been tested with qualitative (interpretation of the formula parameters, Sub-Step 1) and quantitative methods (AIC and BIC for goodness-of-fit, Sub-Step 2, see Sec. B).

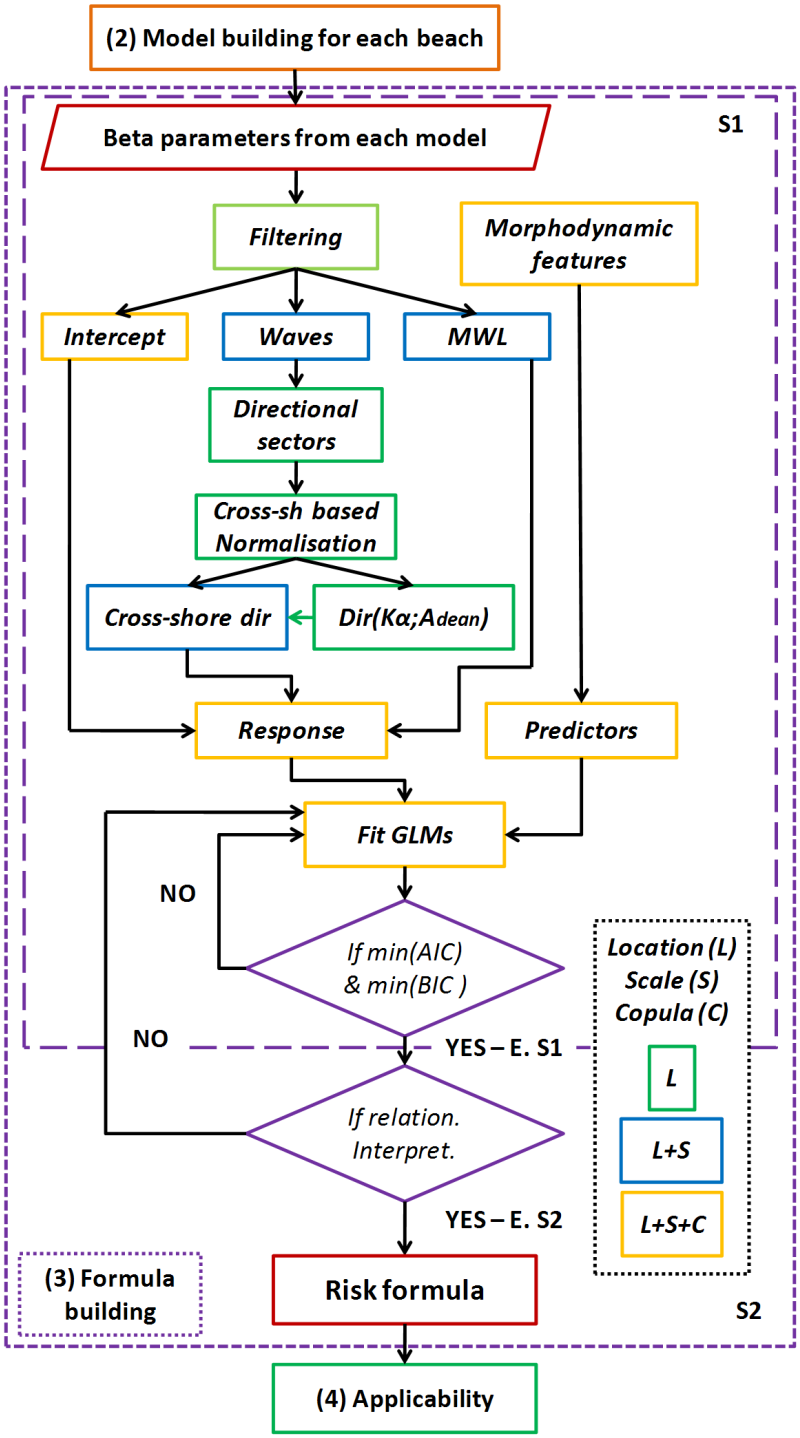

Figure 6.5.: Flowchart of the **integration of the individual models into a single formula (Step 3)** of the Risk module. ***Nomenclature:*** *Action or step (Rectangle); loop definition (Hexagon); conditional (Purple Rhomboid); data list (Rhomboid). Colours inside Step-3: Green (Actions that only affect the location parameter); Blue (Actions that affect Location and Scale parameter); Yellow (Actions that affect both the marginals and the copula parameters).* ***Legend:*** *S1 (sub-task 1) and S2 (sub-task 2).*

Fitness represented how the model was representing the data (as lower AIC and BIC, the better); interpretation represented how the model represented real-world conditions. A trade-off was carried out; always focusing on the principle of parsimony.

The erosion and flooding cost is extended to the whole sample.

The scope of the risk formula depends on the Calibration Dataset. Then, the proposed method holds valid for:

1. **Beaches that have an urban area at the rearside**. Only the flood costs from infrastructure damage have been considered. In natural environments, the quantification is more complicated, because it is necessary to valuate the natural ecosystem (Costanza et al., 1997) and that is out of the scope of this thesis. Despite the parameter p_{buil} controls the urban area, this one has to be distributed as homogeneous as possible. For instance, if the northern part of the littoral cell have camping areas, but the southern one is heavily urbanised, it will be hard to compute the real flooding costs. In a case in which the flooding happens at the north but rarely at the south, the costs will be lower than accounted in the formula. It is assumed that the whole littoral cell is flooded homogeneously. Nevertheless, at an important number of beaches in our study area, this behaviour can be considered as acceptable.
2. All the beaches from the training dataset are **wave-dominated microtidal** sandy beaches (Wright and Short, 1984; Davies, 1964).
3. The aim of this tool is not to substitute process based modelling, but to provide a **quick scan** of how two of the main coastal hazards (episodic flooding and erosion) happen at an urban coastal stretch. Local phenomena cannot be modelled with this approach. This is a generic formula that tries to capture homogeneous patterns.

6.2.4. Step 4: Applicability

The last step in the Risk module consists of the **application** of the risk formula to a certain set of beaches (Fig. 6.6). The inputs consist of Morphodynamic features and Marine forcings that can come directly from (i) the Hydrodynamic module (see Ch.3) or (ii) an extreme wave climate analysis.

The **morphodynamic inputs** of the formula are (see Fig. 6.2): (i) the type of the beach (open or pocket), (ii) Dean parameter (A_{dean}), (iii) beach length (L_{bch}), (iv) beach width (W_{bch}), (v) emerged beach slope (slp_{em}), (vi) directional coefficient following the ROM 3.91 method $\left(K_{\alpha,(\cdot)}\right)$, (vii) berm height ($Brm_{bch}$), (viii) building percentage ($buil_{\%}$). The **marine forcings** are (i) $H_{s,peak}$, (ii) $\theta_{w,peak}$ and (iii) MWL. The formula has been applied to the **Calibration** (**54** beaches) and **Validation** (**25** additional beaches) datasets.

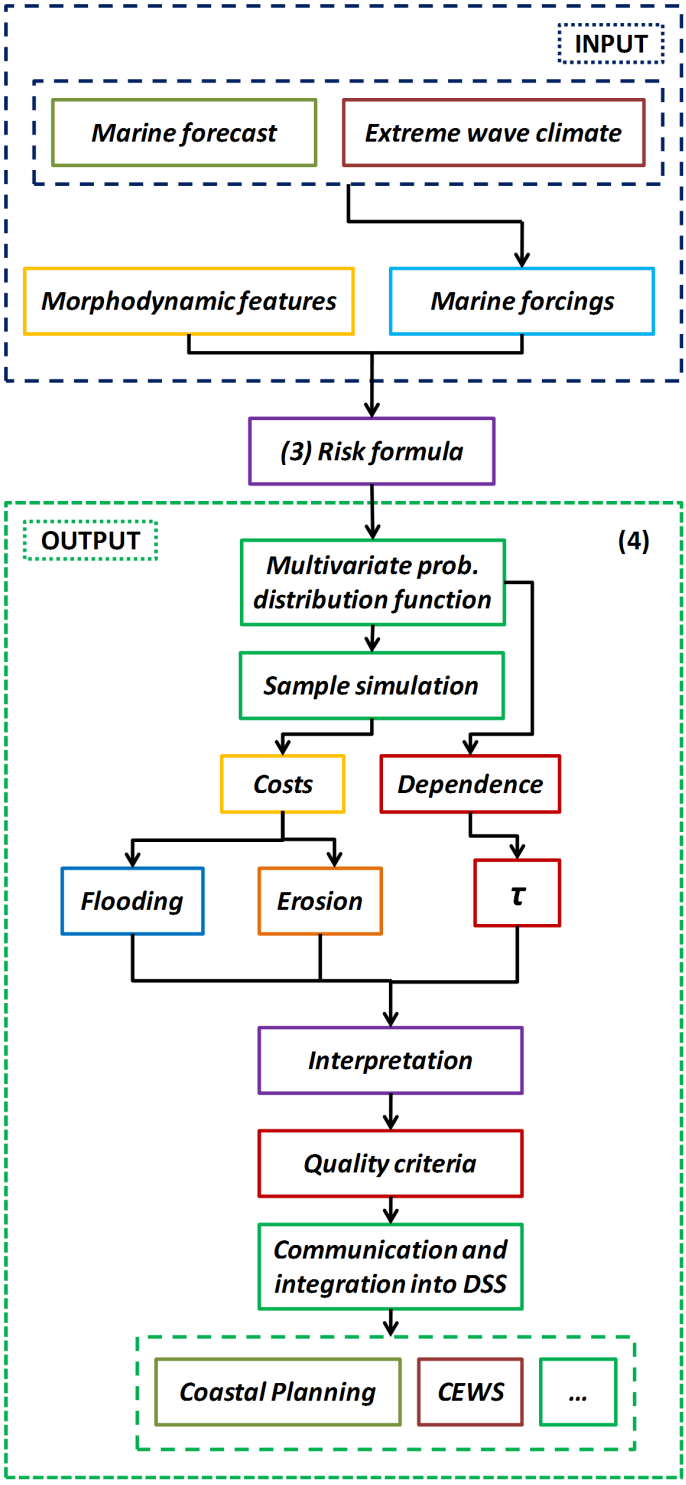

Figure 6.6.: Applicability (**Step 4**) of the Risk Module. The exogenous inputs (dark blue discontinuous box) are the forecasts from the hydrodynamic module (wave height and sea level). The output actions (green discontinuous box) embed the post-processing of the risk formula towards the communication phase. ***Nomenclature:*** *Action or dataset (coloured box).*

A multivariate probability distribution function is obtained. The **dependence** coefficient τ_K is estimated from the resulting θ_{cp}. Samples are simulated ranging from the 80 to the 99 percentile. This dissertation has considered 100*100 simulations (10000 samples per beach). This number of simulations showed convergence of the metrics that it had been used in this dissertation (convergence of the mean cost, maximum and minima). This restriction have had to be carried out because the sample simulation requires important demands of RAM memory.

This sampling reflects how the tail of the probability distribution should behave. It has been made a strong hypothesis (that the tail starts at 80 quantile). This criteria is subjective, but it was desired to consider the high quantiles (up to 75 quantile), in order to have a representative view of the worst case scenarios. The erosion and flood costs are derived from each element of the sample (i.e. it has been considered that the restoration cost of each m^3 of eroded sand is 6 euros). The information is interpreted and quality checked via qualitative methods. Once the information is considered clear and easy to be interpretable, it can be communicated to decision makers or to include it in Decision Support Systems (DSS), Coastal Planning management, etc.

The main outcomes that will be presented in this dissertation are **stress-tests** (i.e. behaviour of a beach under different marine forcings) and **risk forecasting** (results of the Ch. 5 storm hindcast). The representation of the forecasted total costs (erosion and flooding) have been discretized with the following categories (Tab. 6.1):

Category	**Cost (thousand of euros)**
1	<10
2	10 - 30
3	30 - 60
4	60 - 100
5	100 - 300
6	> 300

Table 6.1.: Categorization of the **sum** of the **costs** of episodic erosion and flooding.

6.3. Results

6.3.1. Database building

The results from the Morphodynamic module (Step 1, see Sec. 6.2.1) can be summarised in Tab. B.5 (erosion) and Tab.B.7 (flooding). A common pattern has been found among the different beaches: the **mean value of the erosion cost is higher than its variance**; but the **mean flooding cost is lower than its variance**. The relative difference between maximum and the third-quantile of the erosion is lower than the flooding. In the other hand, it can be noted that distance between the first and third quantile is inferior for erosion than for flooding. This trend shows that the flooding costs are more disperse than erosion.

In general, the training dataset beaches with higher berms and coarser sediment exhibit lower values of flooding and erosion (i.e. the higher berm protects against transient water discharges and coarser sand hampers mobility). In the following paragraphs, can be found summarised the behaviour of the beaches that would appear in the next sections (Sec. 6.3.3.2) of this Chapter.

For easing readability, the following definitions are needed: $\mathbf{n_s}$ is the total number of simulations at a particular beach*;* $\mathbf{E}(\boldsymbol{\varepsilon_{tot}}/\boldsymbol{\varphi_{tot}})$ is the expected value of the **total** erosion/flooding cost; $\mathbf{Var}\,(\boldsymbol{\varepsilon_{tot}}/\boldsymbol{\varphi_{tot}})$ is the variance of the total erosion/flooding cost**;** $\mathbf{Q_1}\,(\boldsymbol{\varepsilon_{tot}}/\boldsymbol{\varphi_{tot}})$ is the first-quantile of the total erosion/flooding cost; $\mathbf{Q_3}\,(\boldsymbol{\varepsilon_{tot}}/\boldsymbol{\varphi_{tot}})$ is the third-quantile of the total erosion/flooding cost; $\mathbf{Max}\,(\boldsymbol{\varepsilon_{tot}}/\boldsymbol{\varphi_{tot}})$ is the maximum value of the total erosion/flooding cost. The latter five variables are in **euros.** $\mathbf{E}\,(\boldsymbol{\varepsilon_c}/\varphi_\mathbf{r})$ is the **expected unitary value** of the erosion/flooding cost, in **euros/m^2**. A selected number of beaches representative of the Study Area are described in what follows:

Badalona beach is an intermediate beach with low unitary erosion costs ($\mathbf{E}\,(\boldsymbol{\varepsilon_c}) = 0.48$ euros$/m^2$). The mean cost of erosion ($\mathbf{E}(\boldsymbol{\varepsilon_{tot}}) = 4.80 \cdot 10^4$ euros) is slightly lower than the variance ($\mathbf{Var}\,(\boldsymbol{\varepsilon_{tot}}) = 6.44 \cdot 10^4$ euros). For the flooding cost, the mean value ($\mathbf{E}(\boldsymbol{\varphi_{tot}}) = 5.25 \cdot 10^5$ euros) is lower than the variance ($\mathbf{Var}\,(\boldsymbol{\varphi_{tot}}) = 8.54 \cdot 10^5$ euros).

At **Barcelona** beach, the total number of simulations $\mathbf{n_s} = 36$ is lower than Badalona, because the non-hydrostatic approach (i.e. higher computational cost) is required due to its local constraints (detached breakwater, Gas groin and Barcelona harbour). Barcelona also has a lower mean of the cost ($4.17 \cdot 10^5$ euros) of flooding than the variance ($7.08 \cdot 10^5$ euros). The erosion has a slightly lower variance ($\mathbf{Var}\,(\boldsymbol{\varepsilon_{tot}}) = 8.44 \cdot 10^4$ euros) than the mean ($\mathbf{E}(\boldsymbol{\varepsilon_{tot}}) = 8.36 \cdot 10^4$ euros).

Gavà is an open dissipative beach with low unitary erosion costs ($\mathbf{E}\,(\boldsymbol{\varepsilon_c})$=0.24 euros$/m^2$). However, the flooding cost at Gavà is somewhat high ($\mathbf{E}\,(\varphi_\mathbf{r}) = 8.19$ euros$/m^2$) because the percentage of building is high (0.53) and the berm is low (1.40 m). In fact, total flooding costs can surpass 10 million of euros in variance. This number is justified due to simulated extreme sea levels (MWL up to 1.7 m), whereas most of the simulations stop at MWL near 0.6 m. Gavà is one of the beaches

that has more sampling ($\mathbf{n_s} = 96$ simulations). The erosion cost is quite low (with maximum values of $\mathbf{Max}\,(\boldsymbol{\varepsilon_{tot}}) = 3.07 \cdot 10^5$ euros, two orders of magnitude inferior), if compared with the magnitude of flooding.

Premià de Mar is an intermediate beach with a reduced beach width that has an important shoreline retreat (-5.76 m/yr). The unitary erosion costs are high ($E(\boldsymbol{\varepsilon_c}) = 9.42$ euros/m^2). The erosion cost has higher mean ($\mathbf{E}(\boldsymbol{\varepsilon_{tot}}) = 1.17 \cdot 10^6$ euros) than the variance ($\mathbf{Var}\,(\boldsymbol{\varepsilon_{tot}}) = 4.41 \cdot 10^5$ euros). Flooding has slightly lower mean than the variance ($\mathbf{E}(\boldsymbol{\varphi_{tot}}) = 3.79 \cdot 10^5$ euros and $\mathbf{Var}\,(\boldsymbol{\varphi_{tot}}) = 4.80 \cdot 10^5$ euros, i.e. same magnitude).

Platja de la Rubina is a dissipative and wave-sheltered (due to Creus Cape) beach that exhibits a considerable value of unitary erosion cost ($\mathbf{E}(\boldsymbol{\varepsilon_c}) = 2.34$ euros/m^2). The mean erosion is $\mathbf{E}(\boldsymbol{\varepsilon_{tot}}) = 3.76 \cdot 10^5$ euros, that it is higher than the variance $\mathbf{Var}\,(\boldsymbol{\varepsilon_{tot}}) = 1.95 \cdot 10^5$ euros. The mean flooding is $\mathbf{E}(\boldsymbol{\varphi_{tot}}) = 3.01 \cdot 10^5$ euros, that is higher than the variance as well ($\mathbf{Var}\,(\boldsymbol{\varphi_{tot}}) = 2.46 \cdot 10^5$ euros).

Sant Pere Pescador is a long (9920 meters) fine sand ($D_{50} = 0.23$ mm) beach with high erosion cost: the mean total erosion cost is $\mathbf{E}(\boldsymbol{\varepsilon_{tot}}) = 9.88 \cdot 10^5$ euros and $\mathbf{Var}(\boldsymbol{\varepsilon_{tot}}) = 6.69 \cdot 10^5$ euros. The flooding cost is low ($\mathbf{E}(\boldsymbol{\varphi_{tot}}) = 1.53 \cdot 10^4$ euros and $\mathbf{Var}\,(\boldsymbol{\varphi_{tot}}) = 4.03 \cdot 10^4$ euros), because the emerged backshore area mainly covers wetlands.

Platja Santa Margarida (Roses municipality), though being well wave-sheltered, it does have fine sediment ($D_{50} = 0.31$ mm). Flooding costs can be superior ($\mathbf{Max}\,(\varphi_{\mathbf{tot}}) = 1.2 \cdot 10^6$ euros) versus the erosion ($\mathbf{Max}\,(\boldsymbol{\varepsilon_{tot}}) = 3.37 \cdot 10^5$ euros). The mean and variance flooding cost show similar values ($\mathbf{E}(\boldsymbol{\varphi_{tot}}) = 2.23 \cdot 10^5$ euros), but erosion exhibit a higher mean ($\mathbf{E}(\boldsymbol{\varepsilon_{tot}}) = 1.99 \cdot 10^5$ euros) than variance ($\mathbf{Var}\,(\boldsymbol{\varepsilon_{tot}}) = 6.97 \cdot 10^4$ euros).

Tossa de Mar is a short urban beach that suffers from high erosion rates: the mean value ($\mathbf{E}(\boldsymbol{\varepsilon_{tot}}) = 1.65 \cdot 10^5$ euros) is higher than the variance ($\mathbf{Var}(\boldsymbol{\varepsilon_{tot}}) = 7.42 \cdot 10^4$ euros); and the maximum value doubles the mean value ($\mathbf{Max}\,(\boldsymbol{\varepsilon_{tot}}) = 3.24 \cdot 10^5$ euros). The flooding costs show lower values of the mean ($\mathbf{E}(\boldsymbol{\varphi_{tot}}) = 1.92 \cdot 10^4$ euros) and the variance ($\mathbf{Var}\,(\boldsymbol{\varphi_{tot}}) = 6.70 \cdot 10^4$ euros), but the maximum is even superior ($\mathbf{Max}\,(\varphi_{\mathbf{tot}}) = 5.06 \cdot 10^5$ euros) than $\mathbf{Max}\,(\boldsymbol{\varepsilon_{tot}})$.

Lloret de Mar has lower erosion costs ($\mathbf{E}(\boldsymbol{\varepsilon_{tot}}) = 6.66 \cdot 10^4$ euros), compared with the mean value ($\mathbf{Var}(\boldsymbol{\varepsilon_{tot}}) = 1.85 \cdot 10^5$ euros). The flooding costs show the opposite trend (mean values lower than variance), but the sum of the costs are on the order of magnitude of less than $5 \cdot 10^4$ euros. The berm height and the sea promenade hampers high flooding costs.

Important eroded volumes are obtained at Estartit beach (8906 m), but it is such a long beach that the unitary erosion cost is low in comparison ($\mathbf{E}\,(\boldsymbol{\varepsilon_c}) = 1.62$ euros/m^2). The mean value of the total erosion ($\mathbf{E}(\boldsymbol{\varepsilon_{tot}}) = 1.14 \cdot 10^6$ euros) is higher than the variance ($\mathbf{Var}(\boldsymbol{\varepsilon_{tot}}) = 8.46 \cdot 10^5$ euros). That shows that the erosion provided by the model did not change strongly even with different storms and scenarios. On the contrary, flooding shows higher variance ($\mathbf{Var}\,(\boldsymbol{\varphi_{tot}}) = 7.61 \cdot 10^6$ euros) than the mean value ($\mathbf{E}(\boldsymbol{\varphi_{tot}}) = 2.08 \cdot 10^6$ euros).

Part of the sample was rejected because the erosion/flooding was lead by local processes. Once the data has been analysed, the following beaches has been discarded for the next steps: Palamos beach (24); St Feliu de Guixols (38); Cala Montgó (43); Platja Aiguablava (47); Platja Calau - Port Bo (50); Platja el Golfet (51); Cala del Cap de Planes (52).

6.3.2. Formula fitting

Once obtained the training dataset, the individual models are fitted in Step 2 (Sec. 6.2.2). The regression coefficients from these individuals models have served for building the risk formula (Step 3). As explained in Sec. 6.2.3, **12 coefficients** need to be found from a set of GLMs that uses morphodynamic features as input. In this section, it will be described the general behaviour of these GLMs. The behaviour of each coefficient can be checked at Figs. 6.7, 6.8 and 6.9.

The $\beta_{(0,\mu_{\varepsilon_r})}$-coefficient (Fig. 6.7) represents the intercept of the μ_{ε_r} at the Gumbel erosion pdf. This coefficient depend on the **type of the beach** (pocket (blue) or open (orange)). This coefficient acts as an offset, compared with the hydrodynamic drivers (waves and sea level). At pocket beaches, this value tends to get **higher values for dissipative beaches**, but values close to 0, in case the Dean parameter A_{dean} reaches 0.4. **Open beaches** show a **more stable behaviour** of the coefficient under different Dean parameters, because they tend to be more homogeneous. The physical interpretation is that pocket beaches with fine sediment would tend to have more mobility, because pocket beaches are confined places in which the water mass fluxes enter into the emerged beach (i.e. piling-up). However, the only mechanism for dissipating this extra water mass is essentially cross-shore transport that induces return flow. If this return flow leads to bed shear stresses that are superior to θ_{cr} (critical Shields), offshore transport will happen. Reaching critical Shield numbers is harder at coarse sediment beaches, because the fall velocity is directly proportional to the sediment size.

The $\beta_{(0,\sigma_{\varepsilon_r})}$-coefficient represents the intercept of the σ_{ε_r} at the Gumbel erosion pdf. The **emerged beach slope** is opted as a covariate, and the curves are classified as dissipative beaches (blue) and reflective beaches (orange). **Gentle emerged slopes and low** A_{dean} (hence, gentle submerged slopes), lead to an **efficient wave energy dissipation**. If the dissipation is greatly enforced, then the bed shear stresses will be low; and even with fine sediment, no transport will happen. If the emerged beach slope is increased, the run-down (and the return flow) increases in magnitude. Then the value increases negatively. The calibration dataset of $A_{dean} < 0.4$ (blue) covers a wide range of values and the heterocedascity suggests a flatten zone between 0.10 and 0.20. Once this slope is surpassed, the formula enters into a regime in which sample is not available (because steep beaches with fine sediment are a rarity in natural microtidal environments). Hence, slp_{em} from 0.05 - 0.10 shows divergence between emerged (gentle) and submerged slope (steep); slp_{em} from 0.10 - 0.20 presents stable values between gentle and steep slope.

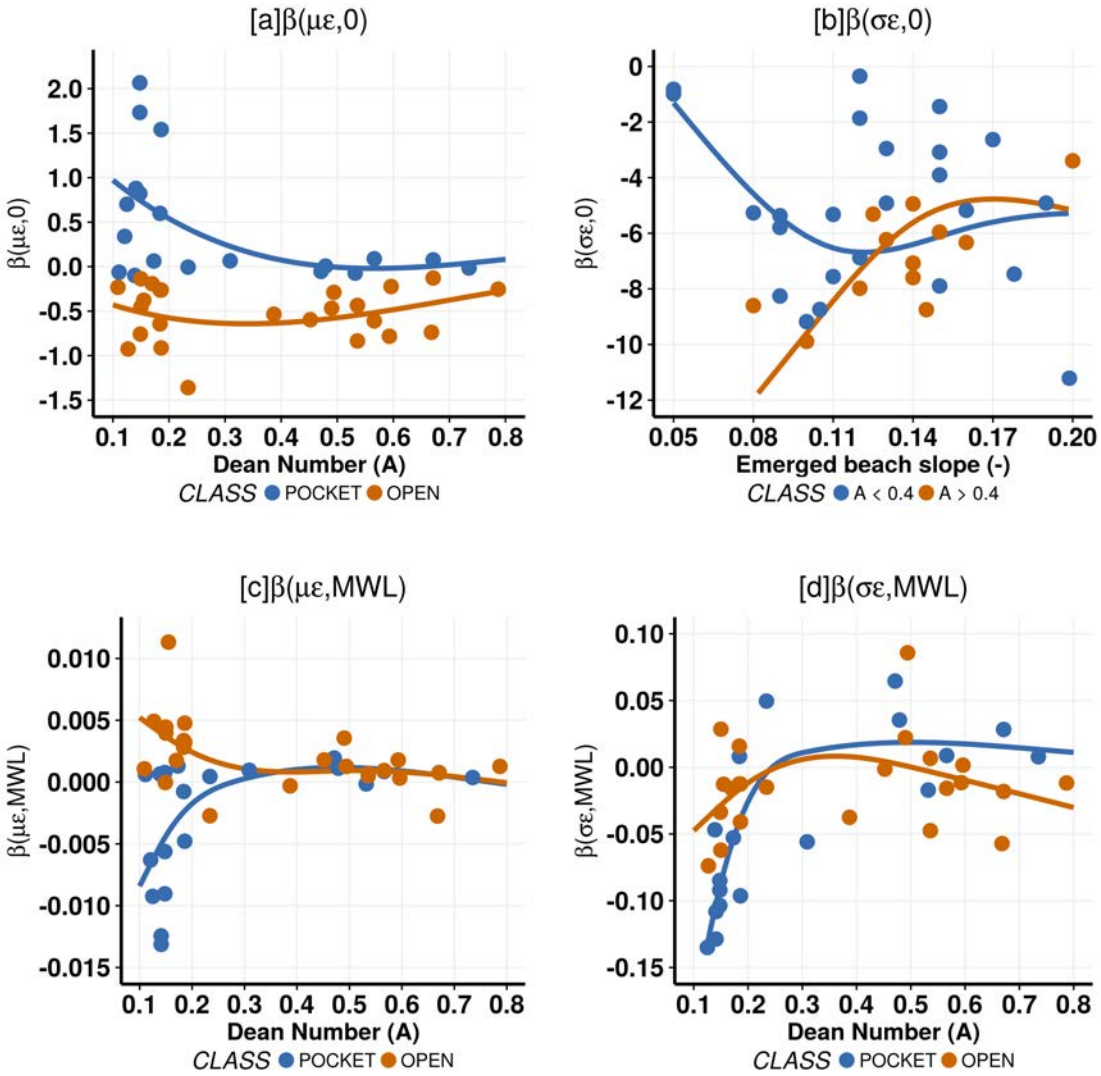

Figure 6.7.: [1-3] GLM fitting of the individual β obtained from **Step 2**. Each dot represent a beach from the Tab.B.1, once filtered for avoiding deviations from the trend. The solid continuous lines are the fitted GLMs at Step 3. **Legend:** (a,c,d): In **blue**, betas and GLM for pocket beaches; in **orange**, the same for open beaches. (b): In **blue**, betas and GLM for $A_{dean} < 0.4$ (dissipative beaches); in **orange**, the same for $A_{dean} > 0.4$ (reflective). *Individual description:* (a) Fitting of the intercept-$\beta_{(0,\mu_{\varepsilon_r})}$ for the **location** parameter of ε_r (Eq. 6.2.11); (b) the intercept-$\beta_{(0,\sigma_{\varepsilon_r})}$ for the **scale** parameter of ε_r (Eq. 6.2.12); (c) the $\beta_{(MWL,\mu_{\varepsilon_r})}$ MWL as covariate for the **location** parameter of ε_r (Eq. 6.2.18); (d) the $\beta_{(MWL,\sigma_{\varepsilon_r})}$ MWL as covariate for the **scale** parameter of ε_r (Eq. 6.2.19).

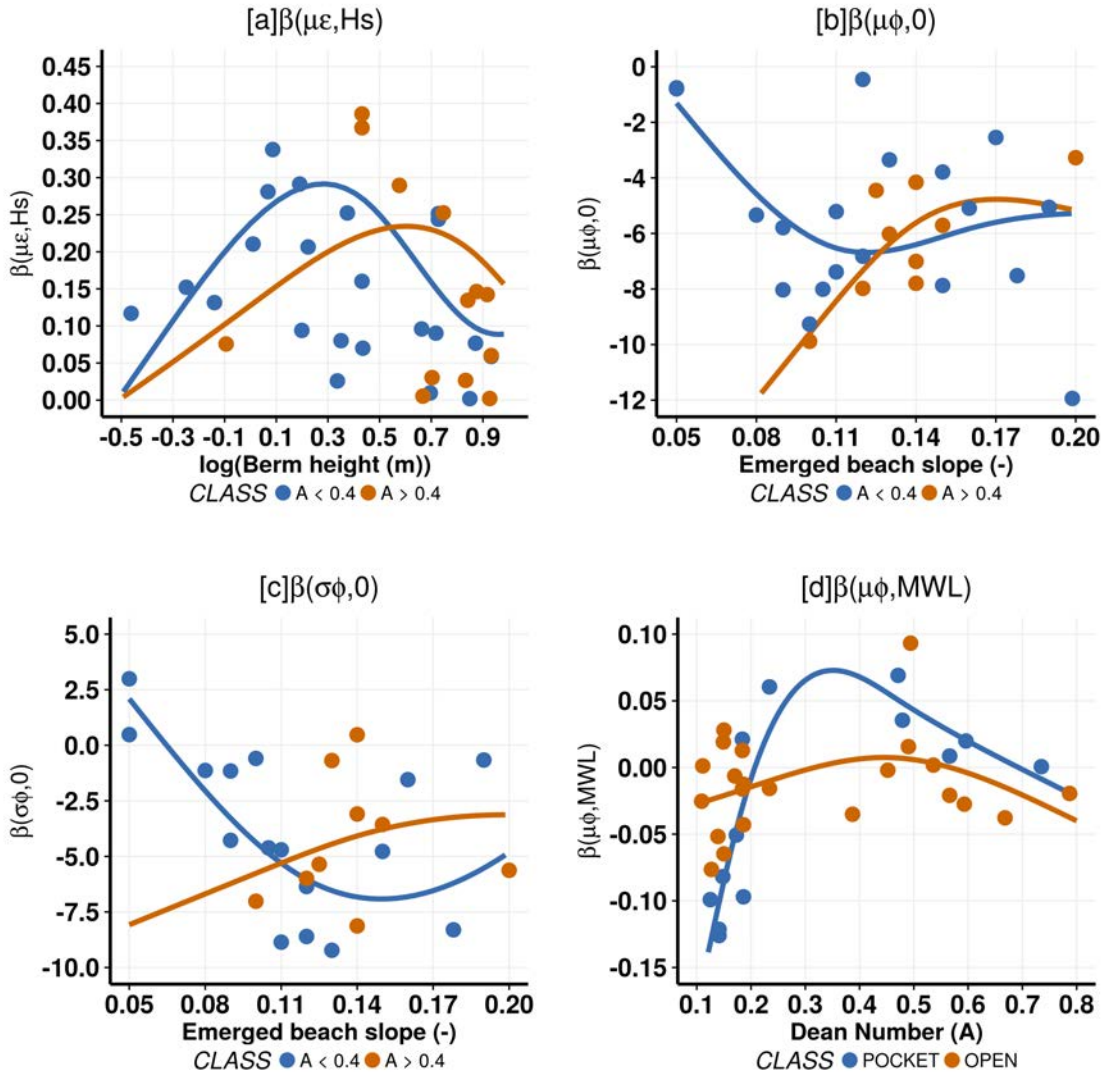

Figure 6.8.: [2-3] GLM fitting of the individual β obtained from **Step 2**. Each dot represent a beach from the Tab.B.1, once filtered for avoiding deviations from the trend. The solid continuous lines are the fitted GLMs at **Step 3**. **Legend:** (a,b,c): In **blue**, betas and GLM for $A_{dean} < 0.4$ (dissipative beaches); in **orange**, the same for $A_{dean} > 0.4$ (reflective). (d): In **blue**, betas and GLM for pocket beaches; in **orange**, the same for open beaches. *Individual description:* (a) Fitting of the intercept-$\beta_{(H_s,\mu_{\varepsilon_r})}$ $H_{s,peak}$ as covariate for the **location** parameter of ε_r (Eq. 6.2.15); (b) the intercept-$\beta_{(0,\mu_{\varphi_r})}$ for the **location** parameter of φ_r (Eq. 6.2.13); (c) the intercept-$\beta_{(0,\sigma_{\varphi_r})}$ for the **scale** parameter of φ_r (Eq. 6.2.14); (d) the $\beta_{(MWL,\mu_{\varphi_r})}$ MWL as covariate for the **location** parameter of φ_r (Eq. 6.2.20).

Reflective beaches (orange) face a similar issue. When the emerged slope is gentle, but not the submerged; waves are not so dissipated. Then, the run-up/down has

momentum and the return flow can advect sediment offshorewards. Values of slp_{em} from 0.15 - 0.20 presents stable values between gentle and steep.

The $\beta_{(MWL,\mu_{\varepsilon_r})}$-coefficient represents the weight of the MWL for the μ_{ε_r} at the Gumbel erosion pdf. For open beaches with low values of the Dean parameter, the lower the A_{dean}, the greater the coefficient. However, once reached 0.3 - 0.4 the coefficient takes low values. In pocket beaches, it happens the opposite. This coefficient **explains how the sand mobility will respond under high MWL**: open beaches (orange) have extension for sand transport (i.e. piling up does not happen here), then the water masses fluxes tend to be advected longshore or cross-shore, but the "water recirculation time" is low. The potential energy keeps low, but the kinetic energy increases. On the contrary, for pocket beaches (blue), the piling up acts as a reservoir. As MWL increases, the potential energy tends to increase, but not the kinetic one. If the kinetic energy diminishes, the return flow diminishes. The effect of MWL with coarse sand beaches will be close to zero.

The$\beta_{(MWL,\sigma_{\varepsilon_r})}$-coefficient is the weight of MWL for the σ_{ε_r}at the Gumbel erosion pdf. This parameter denotes that there will be more variability in the results according to MWL. **Pocket beaches** (blue) show **more sensibility than open beaches**, but both trends are similar. Because open beaches are not constrained, the values tend to be more stable under different ranges of the A_{dean} number. Pocket beaches show no sensibility from 0.3 to 0.8; but stronger with fine sediment. Note that the importance for MWL is higher for the scale parameter than the location. Hence, increases of MWL will affect the variance of the distribution (specially at beaches with fine sediment).

The $\beta_{(H_s,\mu_{\varepsilon_r})}$-coefficient (Fig. 6.8) represents the weight of the $H_{s,peak}$ for the μ_{ε_r} at the Gumbel erosion pdf. The **berm height** (Brm_{bch}) has been selected as predictor because it both presented the most plausible interpretation and the best goodness-of-fit. Both GLMs show that the influence of waves is minimal with low berm; the parameter grows until a maximum that is more restrictive in dissipative beaches (blue), because the sediment is finer (i.e. and the berm less stable under extreme waves); and it decays for high berm heights (i.e. the berm has enough sand volume to be reshaped into a gentle profile that dampens the erosion rate, if we compare it with "intermediate" berm heights). Note that $\beta_{(H_s,\mu_{\varepsilon_r})}$ presents higher values than $\beta_{(MWL,\sigma_{\varepsilon_r})}$: for instance, at a dissipative beach open, with $H_{s,peak} = 6$ m and a MWL =60 cm, then $\beta_{(H_s,\mu_{\varepsilon_r})} \approx 1.8$, whereas $\beta_{(MWL,\sigma_{\varepsilon_r})} \approx 0.3$.

Once found these 5 coefficients, it is needed to define $H_{s,peak}$, $\theta_{w,peak}$ and MWL. The final outcome is a Gumbel (Eq. 6.2.1) with a fixed location (μ_{ε_r}) and scale (σ_{ε_r}) defined. The simulation of the pdf can be done with state-of-the-art methods.

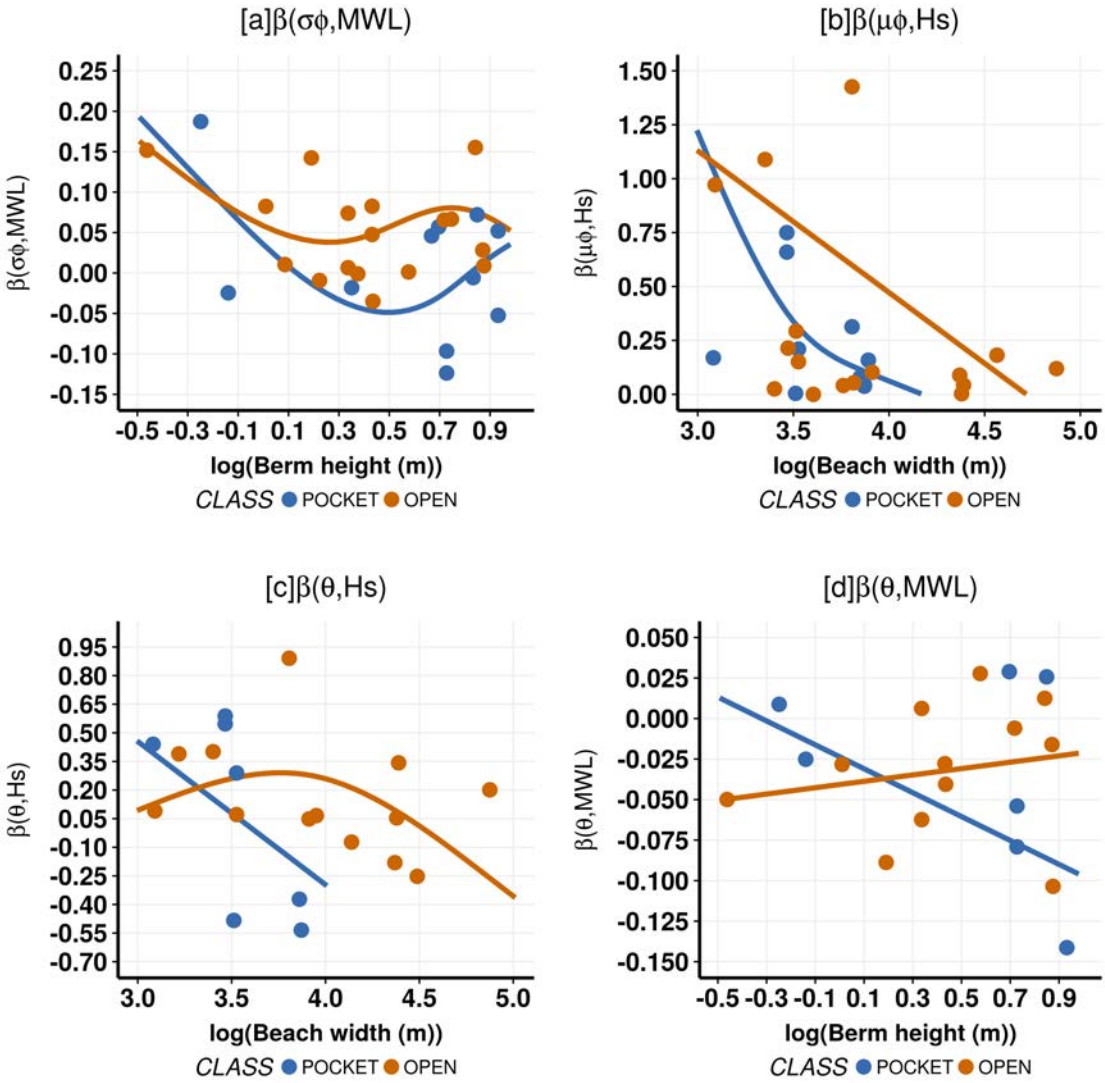

Figure 6.9.: [3-3] GLM fitting of the individual β obtained from **Step 2**. Each dot represent a beach from the Tab.B.1, once filtered for avoiding deviations from the trend. The solid continuous lines are the fitted GLMs at **Step 3**. **Legend:** In **blue**, betas and GLM for pocket beaches; in **orange**, the same for open beaches. *Individual descriptions:* (a) Fitting of the $\beta_{(MWL,\sigma_{\varphi_r})}$ MWL as covariate for the **scale** parameter of φ_r (Eq. 6.2.11); (b) the $\beta_{(H_s,\mu_{\varphi_r})}$ H_s as covariate for the **location** parameter of φ_r (Eq. 6.2.12); (c) the $\beta_{(H_s,\theta_{cp})}$ H_s as covariate for the **association** parameter of the copula (Eq. 6.2.18); (d) the $\beta_{(MWL,\theta_{cp})}$ MWL as covariate for the **association** parameter of the copula (Eq. 6.2.19).

The $\beta_{(0,\mu_{\varphi_r})}$-coefficient represents the intercept of the μ_{φ_r} at the Gumbel flooding pdf. Note that the behaviour is similar to $\beta_{(0,\sigma_{\varepsilon_r})}$: **steep** (0.10 to 0.20) **slopes**

(slp_{em}) **shows more stable values than gentle ones**. In case of dissipative beaches (blue), the gentle the slope, the worse (higher values of the intercept). Steeper beaches have a lower value of the intercept that counteracts $H_{s,peak}$ and MWL interaction. In addition, gentle beach slopes at dissipative beaches, such as Gavà, uses to imply low berm heights. The combination of gentle slopes and low elevation leads to wider floodplains. On the other hand, reflective beaches (orange) with gentle beaches dissipates more efficiently wave forces, due to the sudden change of slope (i.e. steep slope at submerged beach and gentle one at the emerged part).

The $\beta_{(0,\sigma_{\varphi r})}$-coefficient represents the intercept of the σ_{φ_r} at the Gumbel flooding pdf. The behaviour is analogous to $\beta_{(0,\mu_{\varphi r})}$, but they differ in magnitude. Steep slp_{em} leads to negative values that counterbalances the positive impact of MWL (see $\beta_{(MWL,\sigma_{\varphi r})}$). **Reflective beaches are more stable than dissipative beaches**, then showing less probability of high values of the scale parameter (i.e. the main actor in modelling variance).

The $\beta_{(MWL,\mu_{\varphi r})}$-coefficient is the weight of the MWL for the μ_{φ_r} at the Gumbel flooding pdf. Note that open beaches (orange) are more stable, regardless of the A_{dean} than pocket beaches (blue). This behaviour comes because pocket beaches suffer from piling-up (i.e. accumulation of wave-induced mass flux), whereas open beaches do not necessarily. Low values of the A_{dean} leads to dissipative beaches that dampens the wave energy and piling-up is attenuated. However, once the A_{dean} increases, the submerged profile cannot dissipative wave energy and the net inshoreward wave-induced mass flux enters into the pocket beach and increases flooding. Increases of MWL for both kind of beaches reduces wave breaking, then reinforcing piling-up.

The $\beta_{(MWL,\sigma_{\varphi r})}$-coefficient (Fig. 6.9) is the weight of the MWL for the σ_{φ_r} at the Gumbel flooding pdf. The general behaviour for both classes (open and pocket beaches) is that lower berm heights lead to higher values of $\beta_{(MWL,\sigma_{\varphi r})}$(i.e. more variance as MWL increases). Once reached a $log\,(Brm_{bch}) = 0.1$, the coefficients tends to stabilise for the case of open beaches (orange); but pocket beaches (blue) diminishes until reaching negative values. The latter, when $log\,(Brm_{bch}) = 0.5$ starts to converge to similar values than open beaches. This behaviour explains that **the variance at open beaches is more stable to changes in MWL**, once reached a certain berm height; but the pocket beaches are more heterogeneous.

The $\beta_{(H_s,\mu_{\varphi r})}$ -coefficient is the weight of the $H_{s,peak}$ for the μ_{φ_r} at the Gumbel flooding pdf. For both classes (open and pocket), **the wider the beach**, the **more distance** has to be reached and the more space for **dissipating wave energy** is available. Hence, $\beta_{(H_s,\mu_{\varphi r})}$ decreases as the beach width increases until reaching zero for exceptionally wider beaches. Pocket beaches (blue) tend to have shorter beach widths than open (orange), then the first ones should reach zero with lower W_{bch}. The nonlinear behaviour is due to the wide variety of coefficient ranges in the training dataset.

Once found the last 5 coefficients, it is needed to define $H_{s,peak}$, $\theta_{w,peak}$ and MWL. The final outcome is the second Gumbel (Eq. 6.2.2) with a fixed location (μ_{φ_r}) and

scale (σ_{φ_r}) defined. The last two coefficient refer to the association parameter of the copula (Eq. 6.2.3).

The $\beta_{(H_s,\theta_{cp})}$-coefficient is the weight of the $H_{s,peak}$ for the $\theta_{\varepsilon_r,\varphi_r}$ at the copula. Open and pocket beaches tend to have lower dependence as the beach width increases. This hypothesis asserts that **wider beaches will tend to have more erosion than flooding costs**. For pocket beaches (blue), this behaviour seems valid. The GLM stops at $log\,(W_{bch}) = 4.0$, because there are no more beaches beyond this value. But for open beaches (orange), prior to reaching this state, there is an increase of the dependence at the range $log\,(W_{bch}) = 3 - 3.75$; that is because the flooding and erosion costs tend to be balanced within this range (i.e. reaching a maximum agreement at $log\,(W_{bch}) = 3.75$), that makes sense in the training dataset. In the latter class, from $log\,(W_{bch}) = 3 - 3.75$, flooding seems to have a main role; whereas from $log\,(W_{bch}) = 3.75 - 5.00$, erosion costs are predominant.

The $\beta_{(MWL,\theta_{cp})}$-coefficient is the weight of the MWL for the $\theta_{\varepsilon_r,\varphi_r}$ at the copula. This factor at pocket beaches (blue) will always lead to a decrease of dependence, because the piling-up of the waves is reinforced with increases of MWL. Piling-up can be reduced with high berms that protect against flooding; but erosion rates are superior respect low berms, specially at the lower beach. Hence, dependence would be reduced. Note that with low berms, the parameter is positive (i.e. increases of MWL leads to more dependence). Open beaches (orange) show a more stable behaviour: dependence would slightly increase as the berm height increases. In this case, when the berm height increases, the flooding costs and the erosion are partially compensated and dependence increases. However, the parameter is always negative, then higher MWL would always lead to lower dependence.

6.3.3. Application

6.3.3.1. Wave module

The wave model has shown good accuracy at the study area (see Ch. 5). Here is shown what were the hindcasted hydrodynamic conditions at the offshore points of the calibration and validation beaches. In this Section, it will be briefly described the behaviour of the waves and sea level. More information about the wave generation and propagation can be found in Ch. 5 and Appendix D.

The wave conditions for the **O-15** storm (Fig. D.1) was east direction with $H_{s,peak} \approx$ 4 m at the Northern part of Catalonia, whereas at the Center part (Llobregat Delta), the values were slightly lower. The maximum sea level at the storm peak was about 50 cm.

N-15 storm (Fig. D.2) had similar magnitude of $H_{s,peak} \approx 4$ m than O-15, but the waves were coming from the SE(135°) with a more elevated sea level (60 cm).

J-16 storm waves (Fig. D.3) came from SSW (202.5°), and showed values near $H_{s,peak} \approx 4$ m at the Costa Brava, whereas at Creus Cape, Maresme and Barcelona

coast the storm peak was inferior ($H_{s,peak} \approx 3m$). The sea level was around 50 cm in average, but reaching peaks of 60 cm.

F-16 (Fig. D.4) had an elevated sea level (around 60 cm) at the storm peak, but its Eastern waves were the more moderated in the hindcast: the highest waves were found at the Offshore Creus Cape with $H_{s,peak} \approx 3.5$ m; and this storm-component decreases from North to South, reaching $H_{s,peak} \approx 2.5$ m at the Llobregat Delta.

D-16 (Fig. D.5) and **J-17** (Fig. D.6) showed elevated values of wave height, but lower sea levels (maximum sea levels of 50 cm (D-16) and 42 cm (J-17)). The synoptic conditions were similar (i.e. East waves generated by a stationary pressure centre at the North of Africa), but J-17 lasted for longer and the derived waves were superior than D-16. At both storms, the maximum $H_{s,peak} \approx 6$ m were reached at the offshore part of the Creus Cape and decreases the magnitude from North to South. However, the minimum at D-16 was $H_{s,peak} \approx 4$ m at the Llobregat Delta, whereas at J-17 was $H_{s,peak} \approx 5$ m. The total energy and the **storm duration** was **superior** at **J-17** (almost 7 days vs 3 days).

6.3.3.2. Cost-assessment at calibration beaches

The outcomes of the risk module can be summarised with two types: (i) via **stress-curves** and (ii) **forecast maps**.

The stress tests will be tested in calibration (see Tab. B.1) and validation beaches (see Tab. B.3). The chosen beaches will show a wide spectrum of the existing varieties in terms of forcings and morphodynamic features.

The stress curves consist of (i) a set of **curves** that shows the **averaged total cost** (erosion and flooding) in a beach for particular combinations of waves and sea level; (ii) a set of **curves** that show the **dependence** between **unitary flooding cost** (φ_r) and **erosion** (ε_r) for particular combinations of waves and sea level. Waves are characterized by their univariate return period of H_s (see the numbers that labels the curves). The range of T_r are the following: 1, 5, 10, 15, 20, 25, 50, 75 and 100 years. The MWL is characterized by increments of 10 cm: 0, 10, 20, 30, 40, 50 and 60 cm. The upper limits of both return periods and MWL have been assumed due to the available forcings scenarios tested in Step 1 (see Sec. 6.2.1).

The curves provide a quick glance of the behaviour of the beach. Hence, it is expected that waves will drive important changes of the total cost at reflective beaches; whereas MWL increases will drive changes at dissipative beaches.

Badalona beach (Fig.6.10) is an intermediate beach (Wright and Short, 1984) that has an intermediate berm height $Brm_{bch} = 2.34$ m and a steep slope $slp_{em} = 0.20$. The episodic losses are mainly due to flooding. With the above-mentioned features, when the sea level is low, high ESE storm return periods are required for triggering alarm (i.e. around $T_r = 50$ yr for MWL below 40 cm). Note that once reached MWL of 60 cm, economic losses can be reached with $T_r = 20$ yr. The dependence structure shows the common pattern: if H_s increases, correlation increases; when MWL increases, correlation decreases. Note also that the τ_K reaches 0.87 (i.e.

important correlation) with low sea levels (MWL = 0 cm) and $T_r = 100$ yrs. That means that with low sea levels and high wave return periods, the **values of the flooding** (φ_r) **and the erosion cost** (ε_r) **have similar magnitude.**

Premià de Mar (Fig.6.11) has a limited beach width, but a strong erosion gradient ($-5.76\ m/yr$, see Tab.B.1). This results in a decrease of losses from erosion, but an increase of the flooding costs. The heterogeneity of the results by the SLR effect decreases because the sediment budget is lower.

The moderate events will have a lower effect (O-15) (i.e. the moderate events lead erosion, but not flooding). The lack of sand budget and the decrease of the erosive gradient because the sheet-flow would be lower leads to that behaviour. The extreme events that would happen (D-16 and J-17) provide both flooding and erosion will provoke worse effects with SLR.

It has been chosen Premià de Mar as a beach for showing results with **5 years of shoreline retreat** (Fig.6.12), because it is one of the beaches of the sample that has an **acute** retreat. Despite the erosion costs diminishes due the lack of sand, the reduced beach width leads to an **increase of the flooding**. This misbalance leads to a shift in the dependence structure, in which as waves T_r increases, τ_K diminishes. The consequence in the forecast is that the total cost do not vary significantly when different MWL are considered. Thus, the future forecasts differ with the present state (Fig.6.11).

The **Rubina beach** (Fig.6.13) is a natural wave-sheltered coast due to the Creus Cape. The dependence (τ_K) is more moderated than in other sites such as Badalona. The erosion costs have a primary role in this open beach, because it consist of fine sand ($D_{50} = 0.32\ mm$) and has an important sediment budget to be eroded (i.e. a wide beach, $W_{bch} = 81\ m$). Then, wave action plays an active role, whereas that the accuracy of mean water level is not that important, except when dealing with moderate storms ($T_r = 1 - 5$ years).

Note that the cost with storms of $T_r = 1\ yr$ may vary between $40 \cdot 10^3$ (MWL = 0 cm) and $200 \cdot 10^3$ (MWL = 60 cm). **Hence, the importance of a proper forecasting is more important with moderate events (more usual) than extreme ones in which the level of damage is saturated.**

Santa Margerida beach (Fig.6.14) show moderate costs even with high wave return periods and MWL (note that the maximum costs reach $100 \cdot 10^3$ euros when considered a $T_r = 100$ yr and a MWL = 60 cm). The beach is well wave sheltered from almost all common storm directions (except from SSE). Hence, refracted/diffracted waves plus MWL are the main forcings.

The τ_K are high with low sea levels, but remarkably low with high sea levels. That leads to an increase of the uncertainty for MWL up to 60 cm, due to the misbalance between flooding and erosion costs. With such high values, the flooding cost becomes dominant and that is the reason for reaching maximum costs that differs from the mean value.

Lloret de Mar (Fig. 6.15) is a coarse sand beach that has an intermediate berm

height ($Brm_{bch} = 2.11$ m). Main morphodynamic changes are due to beach rotation (see Sec.2.3.1.1.1) and the erosion rate is quite stable (-0.48 m/yr). Hence, **flooding** is the **main hazard**. The figure shows similar trends regardless of the MWL predicted, but once reached MWL = 60 cm, the mean value and the maximum value increases significantly. The costs are moderate, with maximum mean costs of $100 \cdot 10^3$ euros under the most extreme scenarios. The τ_K coefficient is high with low MWL and moderate with high MWL. The storms within the Eastern directional sector have returns periods between $T_r = 1 - 5$ yrs.

Note that the whole Lloret de Mar beach can be flooded, but flooding can only enter into the village at the Southern part of the domain. That is due to a local lower elevation of the sea promenade (+3.5 m). Thus, Avinguda de Just Marlés Vilarodona, a former ephemeral stream, is one of the weak spots for coastal flooding.

Estartit beach stress curves for Eastern waves can be found in Fig.6.16. Note that the D-16 and J-17 show a wave return period of about 7 years. The losses are estimated about $100 \cdot 10^3$ euros. O-15 has a return period of around 1 year and no relevant loses reported.

Wave storms with 1 year return period does not lead to significant losses. When the sea level is high (60 cm), the costs tends to move from $400 \cdot 10^3$ to $800 \cdot 10^3$ euros. With a low sea level (0 cm), the minimum wave return period is 10 years. The losses range from $100 \cdot 10^3$ to $400 \cdot 10^3$ euros.

In all cases, **higher dependence can be achieved with lower sea levels**. As MWL increases, τ_K decreases.

This happens for two reasons. Firstly, (i) **extreme waves:** the erosion values reaches an asymptotic behaviour, but the flooding has room to be increased with higher waves; then dependence decreases. Secondly, (ii) **the behaviour of the sample:** as the sea level increases, the water depth increases and the bed shear stress diminishes for the same wave height (i.e. equilibrium between the velocity profile and the water pressure gradient); then the sand transport does not increase significantly, but the flooding costs increases dramatically (i.e. individual waves do not require high return periods for producing impact with a high sea level).

6.3.3.3. Cost-assessment at validation beaches

In the previous section it has been described the performance of the COPAS formula at beaches that were included for building the model. The main goal of the formula, though, is to be applied at the most possible places. The method has been **validated at 25 sites**. In this Section, it will be presented the stress-curves and correlation maps for Malgrat de Mar (Fig. 6.17), Callao beach (Fig. 6.18) and Ponent beach (Fig. 6.19). The rest of the validation dataset can be checked in Sec. 6.3.3.4.

Once reached Eastern wave storms with T_r =10 yrs ($H_s = 6$ m), even with low sea levels ($MWL = 0$ cm), **Malgrat de Mar** (Fig. 6.17) experiences important losses. These costs tend to be established within a range of $10 \cdot 10^3 - 200 \cdot 10^3$ euros. Until $MWL = 50$ cm, the sea level does not seem a decisive factor.

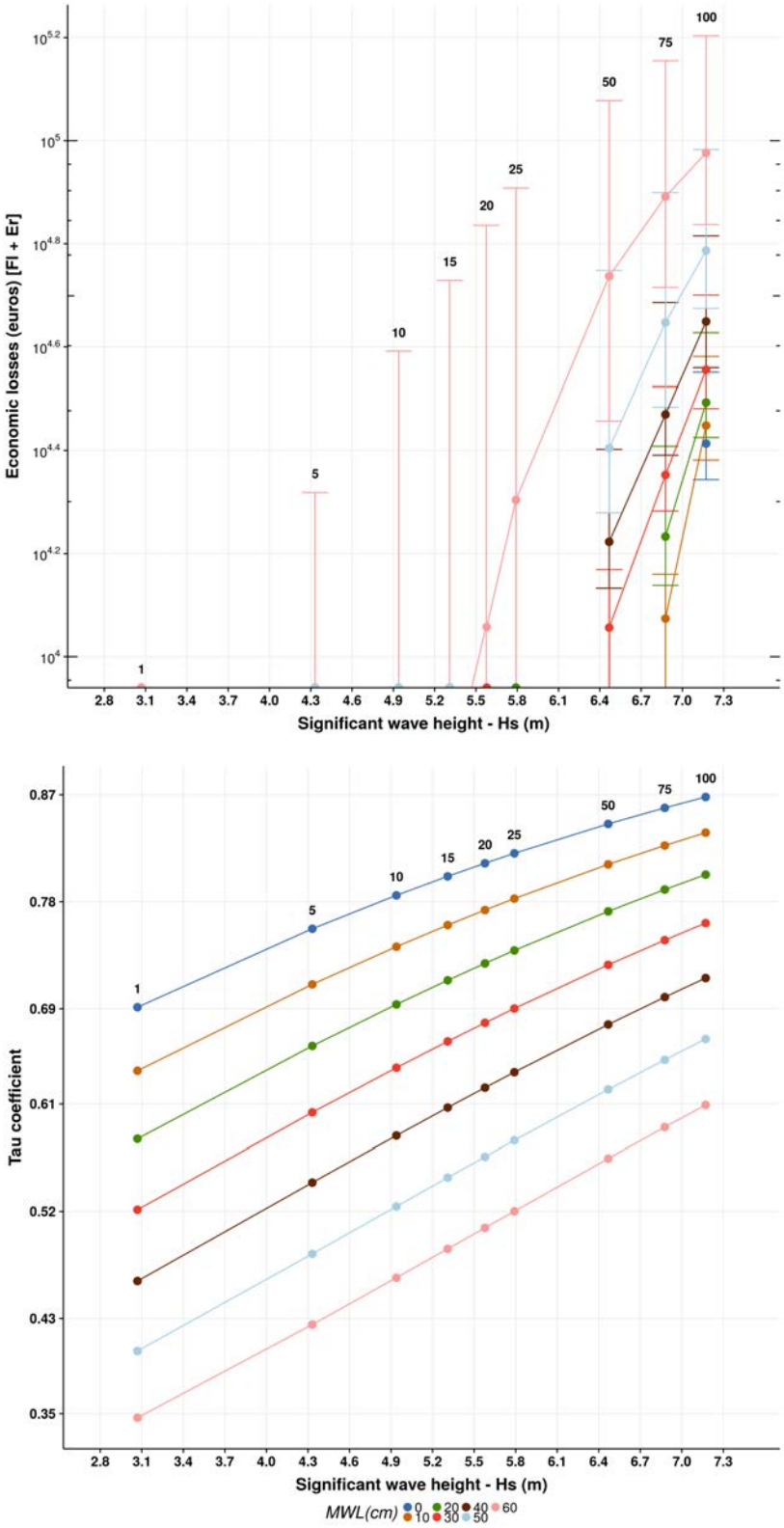

Figure 6.10.: Results from the Risk module at **Badalona** (see Fig. A.3). ESE wave direction. The colours represent different scenarios of extreme water level. (Up) Total Economic losses (erosion + flood) at the beach under different wave and sea level scenarios. The **green error bars** represent the predicted costs of the storms analysed in Chapter 4, using the hydrodynamic module outputs. (Down) Dependence coefficient (τ_K) between erosion and flooding. The numbers above the dots are the marginal H_s return period.

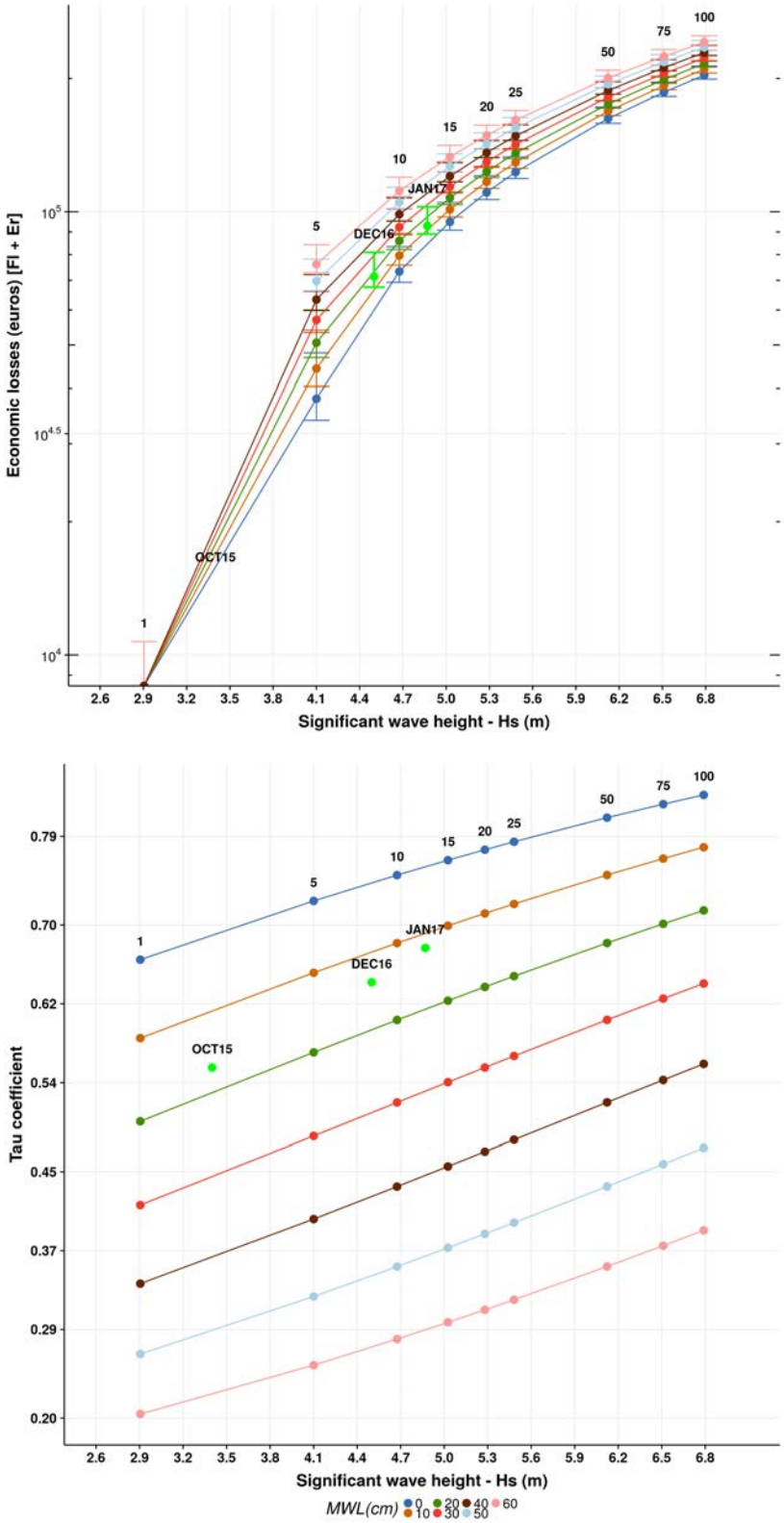

Figure 6.11.: Results from the Risk module at **Premià de Mar** (see Fig. A.2). East wave direction. The colours represent different scenarios of extreme water level. (Up) Total Economic losses (erosion + flood) at the beach under different wave and sea level scenarios. The **green error bars** represent the predicted costs of the storms analysed in Chapter 4, using the hydrodynamic module outputs. (Down) Dependence coefficient (τ_K) between erosion and flooding. The numbers above the dots are the marginal H_s return period.

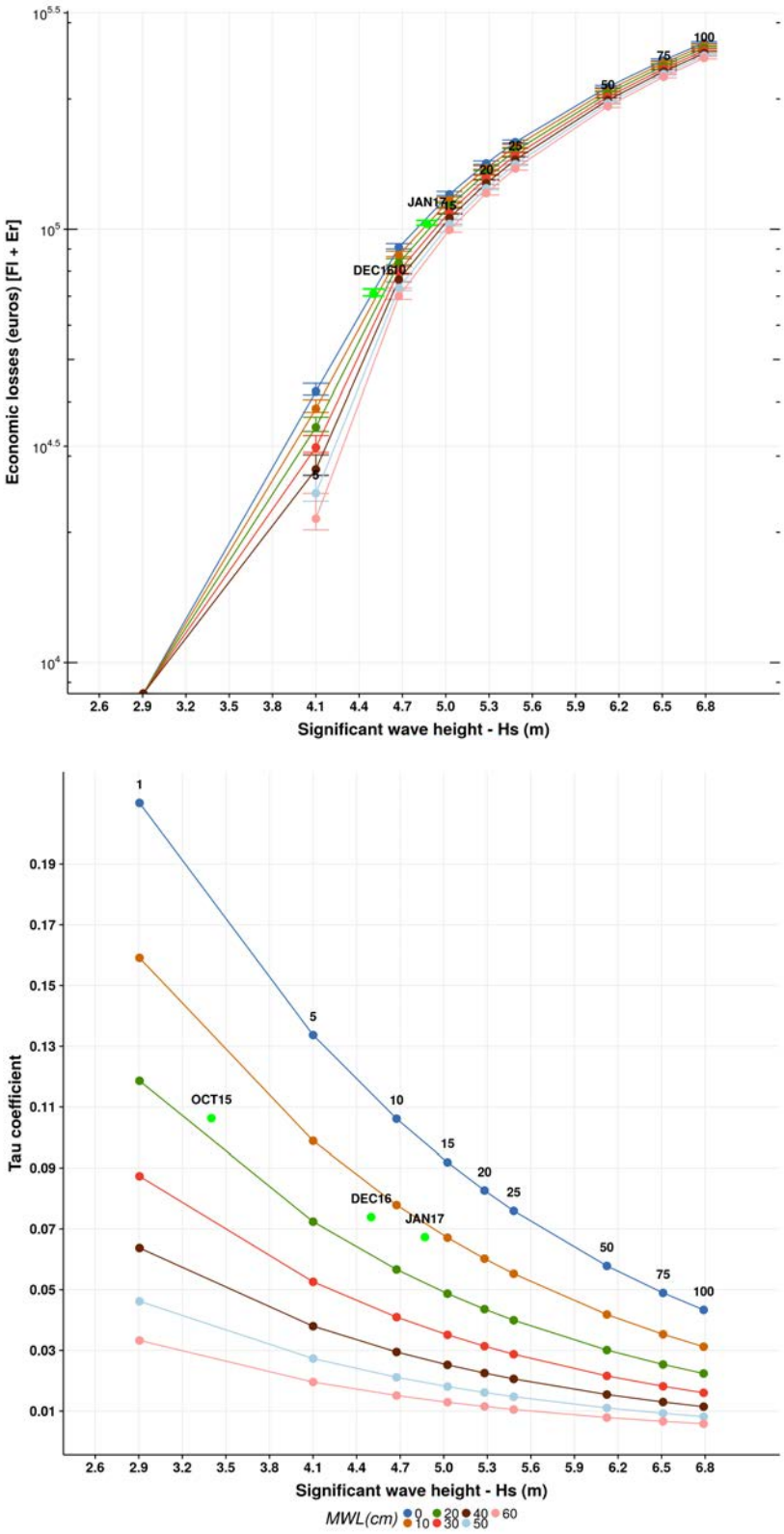

Figure 6.12.: Results from the Risk module at **Premià de Mar** (see Fig. A.2). East wave direction. W_{bch} is reduced with a cumulative ero_{rate} for the next 5 years. The colours represent different scenarios of extreme water level. (Up) Total Economic losses (erosion + flood) at the beach under different wave and sea level scenarios. The **green error bars** represent the predicted costs of the storms analysed in Chapter 4, using the hydrodynamic module outputs. (Down) Dependence coefficient (τ_K) between erosion and flooding. The numbers above the dots are the H_s return period.

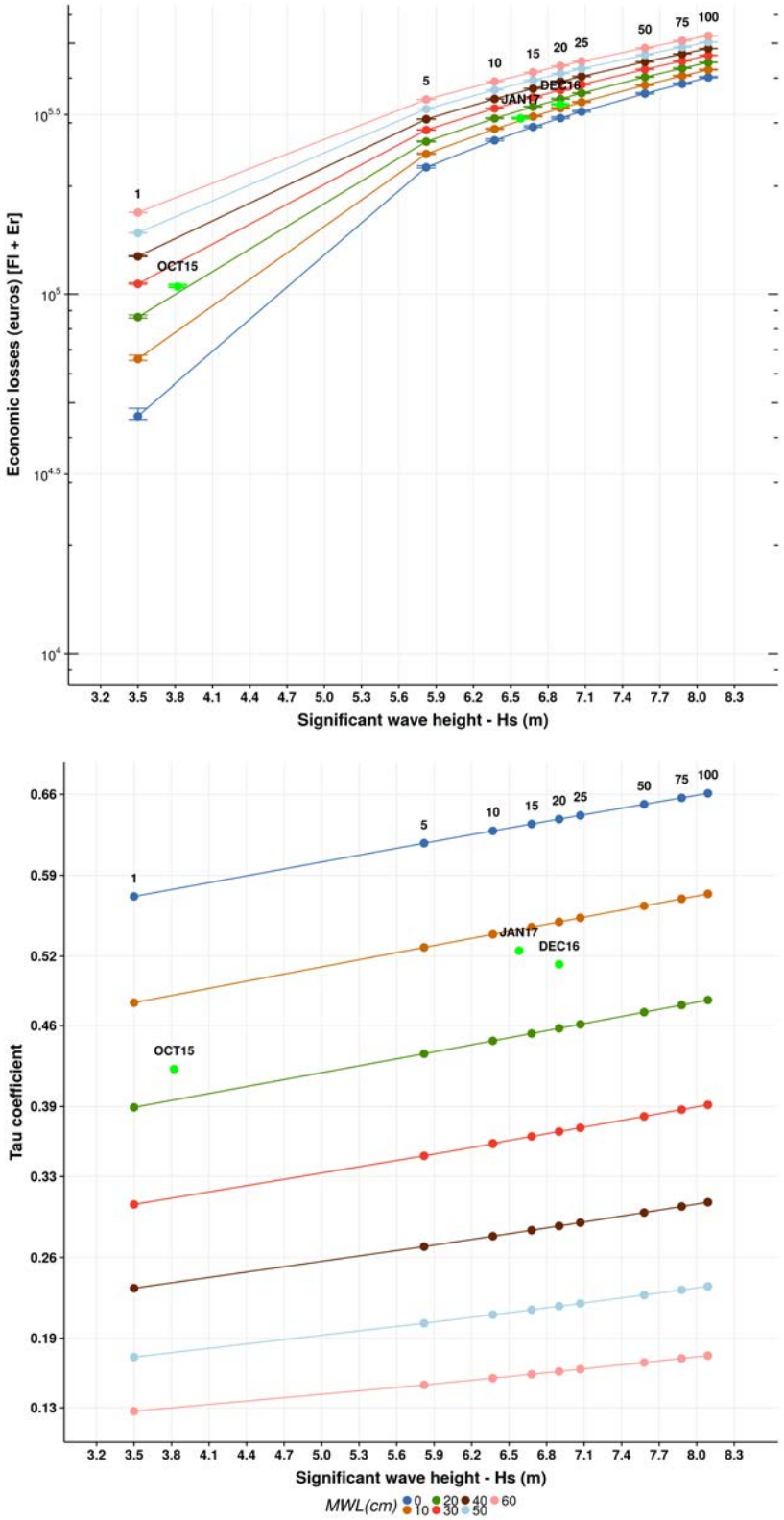

Figure 6.13.: Results from the COPAS formula at **Rubina beach** (see Fig. A.1). East wave direction. The colours represent different scenarios of extreme water level. (Up) Total Economic losses (erosion + flood) at the beach under different wave and sea level scenarios. The **green error bars** represent the predicted costs of the storms analysed in Chapter 4, using the hydrodynamic module outputs. (Down) Dependence coefficient (τ_K) between erosion and flooding. The numbers above the dots are the marginal H_s return period.

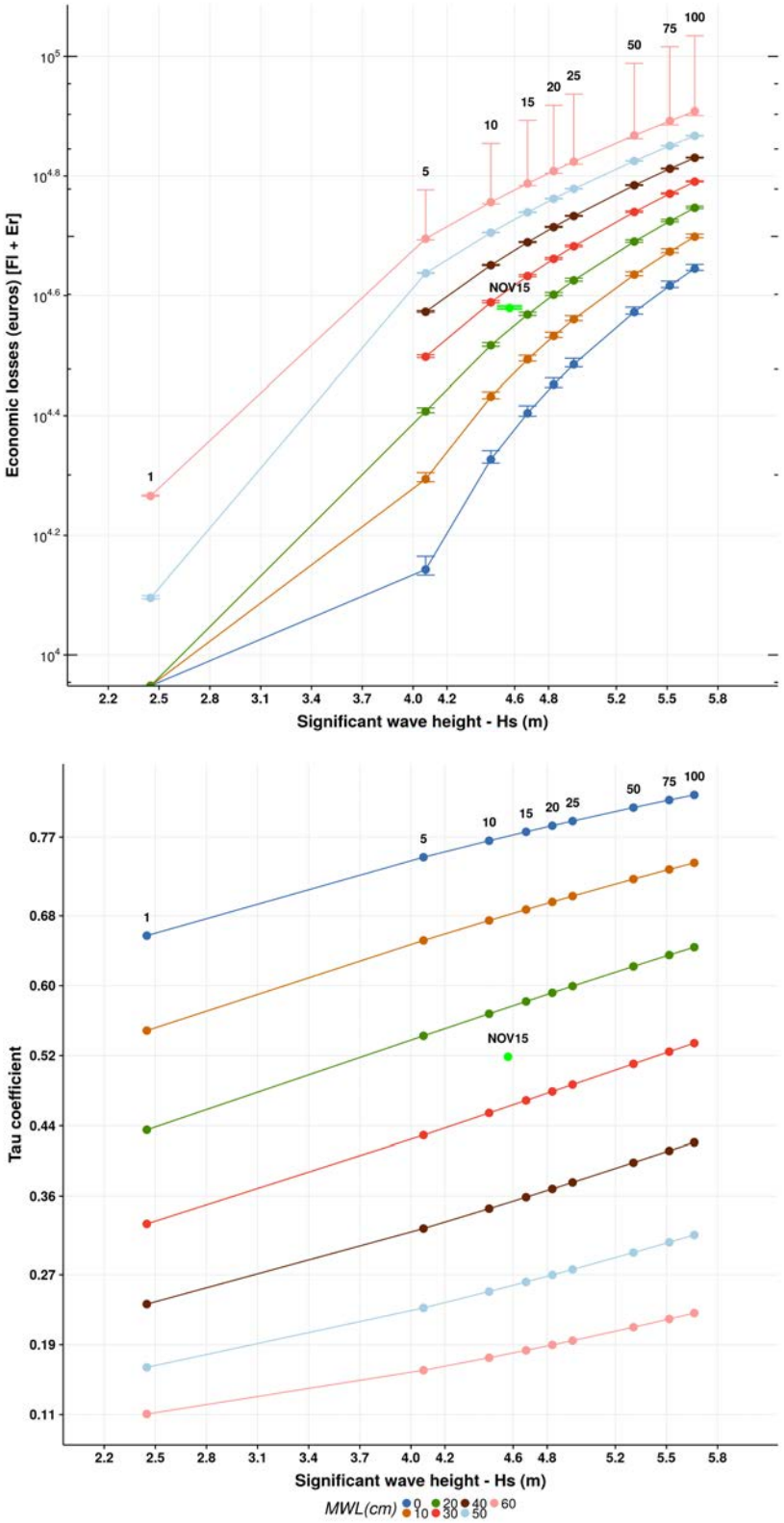

Figure 6.14.: Results from the Risk module at **Santa Margerida** (see Fig. A.3). SE wave direction. The colours represent different scenarios of extreme water level. (Up) Total Economic losses (erosion + flood) at the beach under different wave and sea level scenarios. The **green error bars** represent the predicted costs of the storms analysed in Chapter 4, using the hydrodynamic module outputs. (Down) Dependence coefficient (τ_K) between erosion and flooding. The numbers above the dots are the marginal H_s return period.

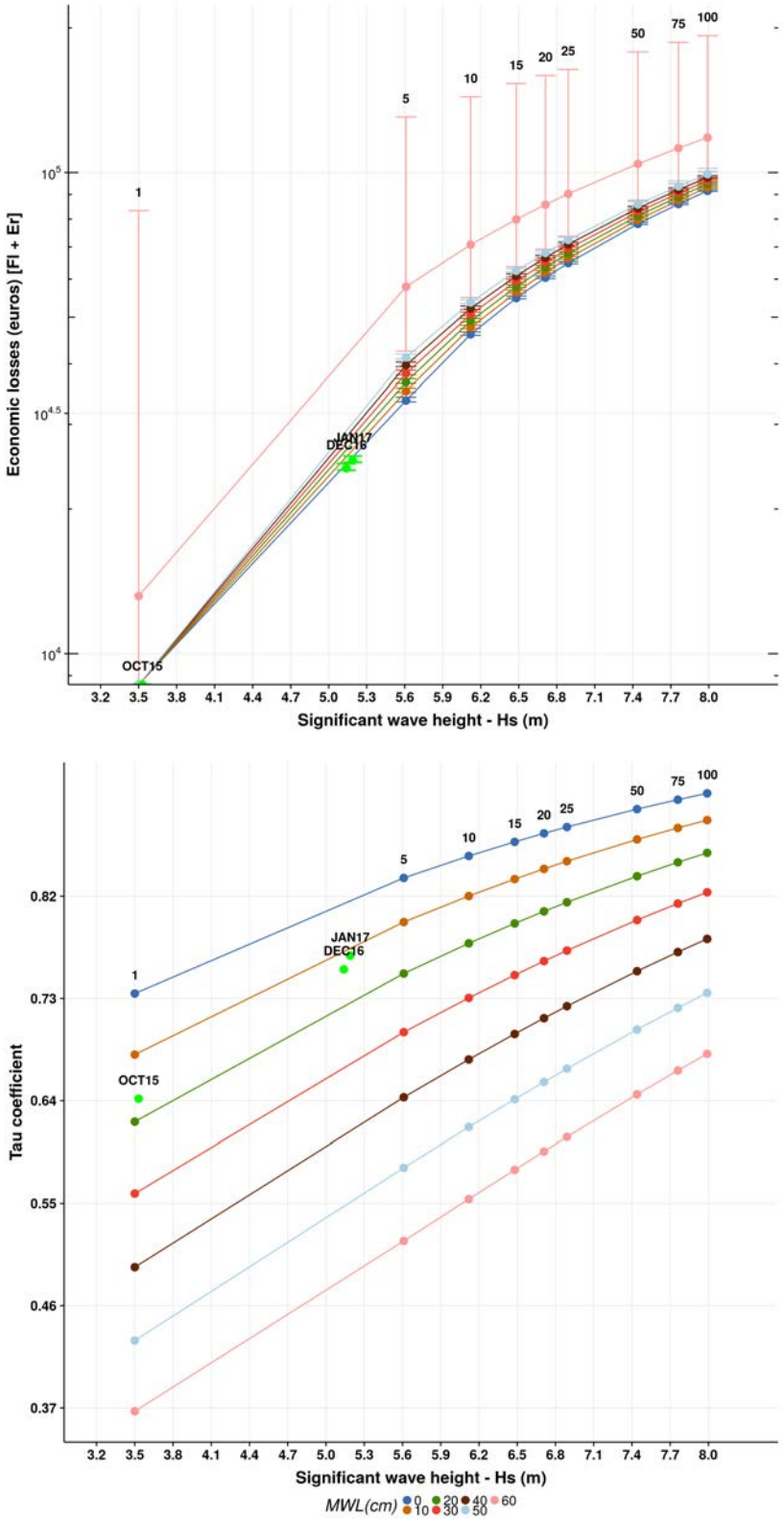

Figure 6.15.: Results from the Risk module at **Lloret de Mar** (see Fig. A.2). Eastern wave direction. The colours represent different scenarios of extreme water level. (Up) Total Economic losses (erosion + flood) at the beach under different wave and sea level scenarios. The **green error bars** represent the predicted costs of the storms analysed in Chapter 4, using the hydrodynamic module outputs. (Down) Dependence coefficient (τ_K) between erosion and flooding. The numbers above the dots are the marginal H_s return period.

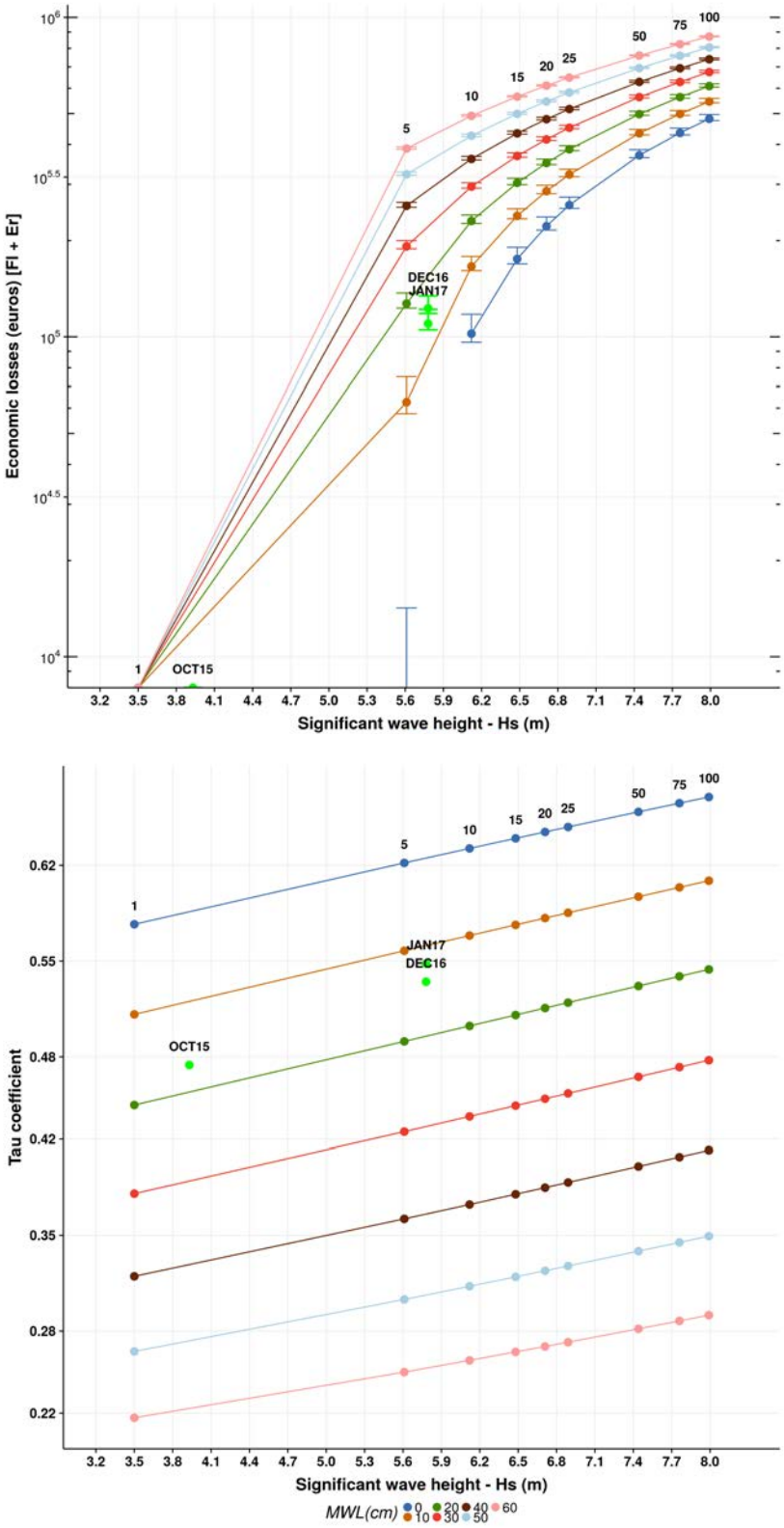

Figure 6.16.: Results from the Risk module at **Estartit** (see Fig. A.1). East wave direction. The colours represent different scenarios of extreme water level. (Up) Total Economic losses (erosion + flood) at the beach under different wave and sea level scenarios. The **green error bars** represent the predicted costs of the storms analysed in Chapter 4, using the hydrodynamic module outputs. (Down) Dependence coefficient (τ_K) between erosion and flooding. The numbers above the dots are the marginal H_s return period.

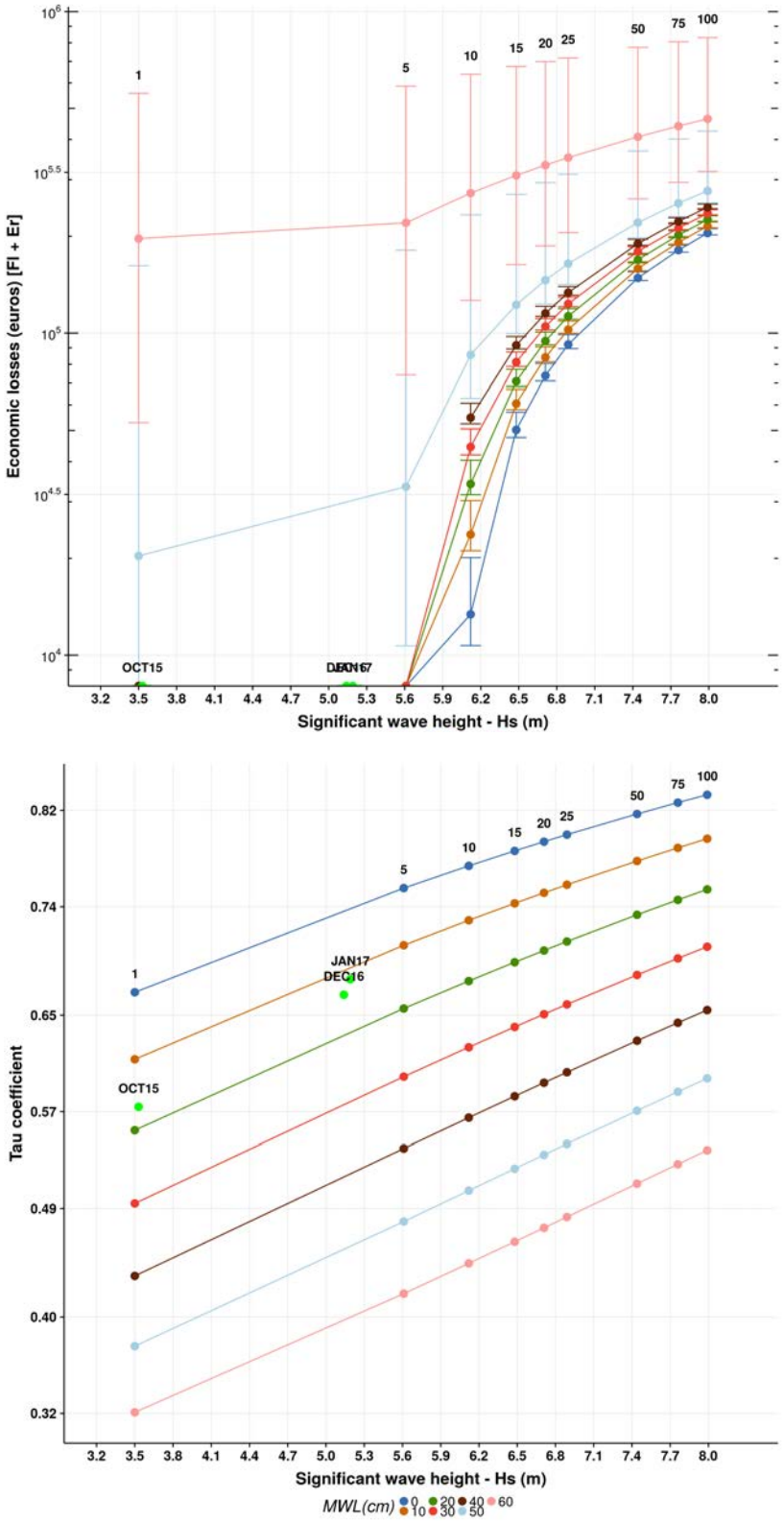

Figure 6.17.: Results from the Risk module at **Malgrat de Mar** (see Fig. A.2). East wave direction. The colours represent different scenarios of extreme water level. (Up) Total Economic losses (erosion + flood) at the beach under different wave and sea level scenarios. The **green error bars** represent the predicted costs of the storms analysed in Chapter 4, using the hydrodynamic module outputs. (Down) Dependence coefficient (τ_K) between erosion and flooding. The numbers above the dots are the marginal H_s return period.

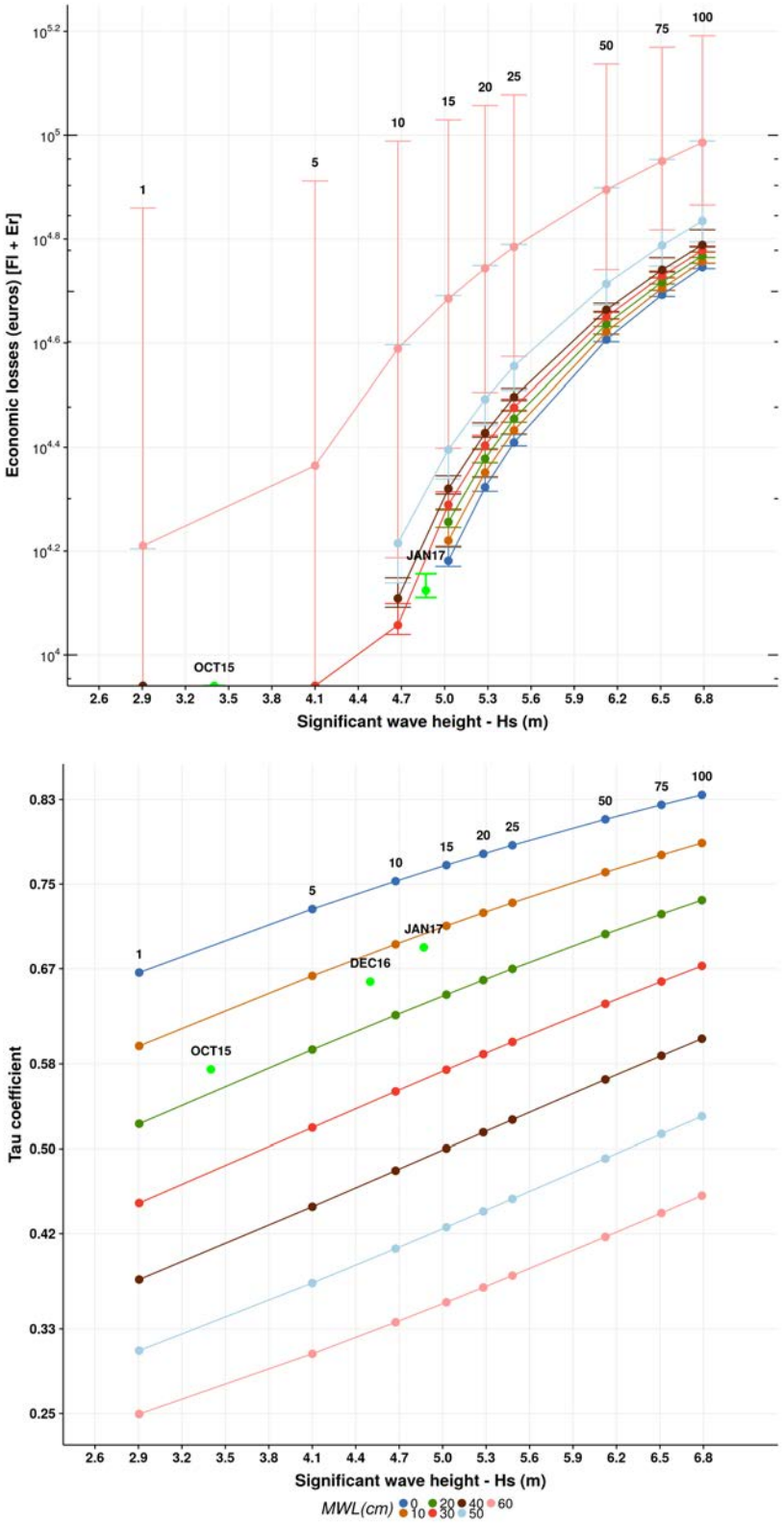

Figure 6.18.: Results from the Risk module at **Callao** (see Fig. A.2). East wave direction. The colours represent different scenarios of extreme water level. (Up) Total Economic losses (erosion + flood) at the beach under different wave and sea level scenarios. The **green error bars** represent the predicted costs of the storms analysed in Chapter 4, using the hydrodynamic module outputs. (Down) Dependence coefficient (τ_K) between erosion and flooding. The numbers above the dots are the marginal H_s return period.

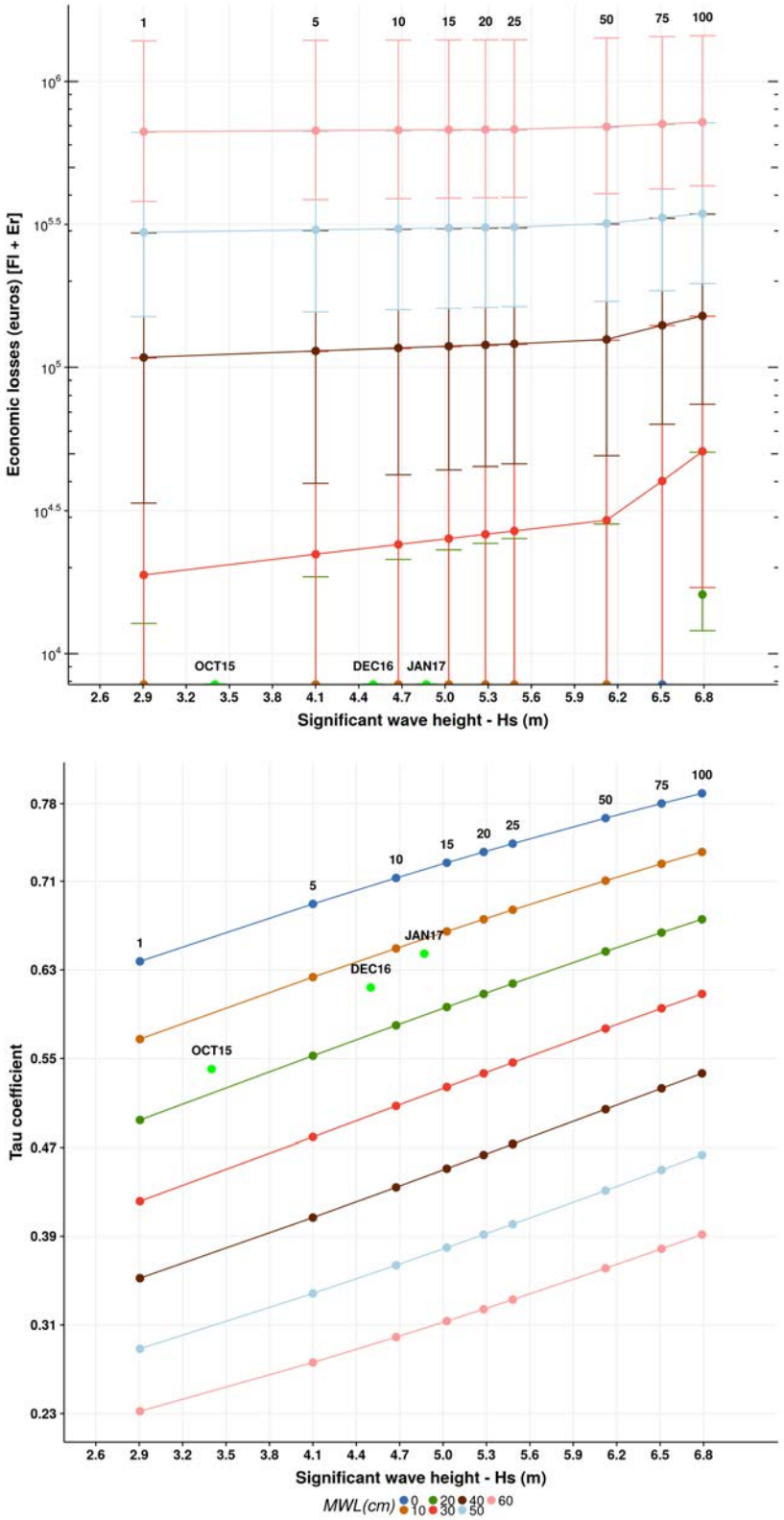

Figure 6.19.: Results from the Risk module at **Platja de Ponent** (see Fig. A.2). East wave direction. The colours represent different scenarios of extreme water level. *(Up)* Total Economic losses (erosion + flood) at the beach under different wave and sea level scenarios. The **green error bars** represent the predicted costs of the storms analysed in Chapter 4, using the hydrodynamic module outputs. *(Down)* Dependence coefficient (τ_K) between erosion and flooding.The numbers above the dots are the marginal H_s return period.

However, with sea levels up to 60 cm, the flooding costs become the main hazard. At these scenarios, MWL is the main driver. Wave directionality is another important factor. When storms come from ENE, waves play a minor role (i.e. the site is wave sheltered from this sector). Hence, there are no losses until MWL =50 cm of sea level is reached with the maximum cases. Regarding storms from the ESE sector, the formula predicts a similar behaviour than E, but with lower wave heights: T_r = 5 years may trigger important damages.

Once reached Eastern waves with H_s =4.7 m (T_r = 10 yr), damages start to be relevant at **Callao beach** (Fig. 6.18). Waves does not alter significantly the cost, growing from $10 \cdot 10^3 - 50 \cdot 10^3$ euros. Once it is reached $MWL = 60\ cm$, the beach shows losses, even with low return periods ($T_r = 1\ yr$). The dependence structure shows moderate dependence with low sea levels ($\tau_K = 0.67 - 0.83$). Dependence is higher with low sea levels and high waves. This behaviour is consistent, because it is expected that with high waves can co-exist erosion and flooding.

At **Ponent Beach** (Fig. 6.19) the sea level is the key driver. There exists important costs (around $40 \cdot 10^3$ euros) even with moderate sea levels ($MWL = 30\ cm$). The dependence is high ($\tau_K = 0.78 - 0.63$) with low values of the sea level. The dependence structure tends to decrease with higher sea levels. Until sea levels reach $MWL = 60\ cm$, the values are within a moderate dependence range ($\tau_K = 0.23 - 0.39$). When the waves increase, the dependence increase.

6.3.3.4. Forecasting maps

In the previous section it has been shown how specific beaches would be forecasted under a wide range of hydrodynamic forcings. In this section, it will be shown how the same formula would perform at all the calibration and validation beaches, under the storms analysed in Chapter 5.

Storm	Total cost from Risk module (K euros)	Post-storm repairing costs (K euros)
O-15	1970	1448
N-15	2510	
J-16	690	
F-16	1070	
D-16	2915	2764
J-17	3200	

Table 6.2.: Total **sum** of the **predicted costs** from the Risk module and the investment for post-storm repairing costs made by Ministerio de Agricultura y Pesca, Alimentación y Medio Ambiente (Spain). Cost in thousands of euros.

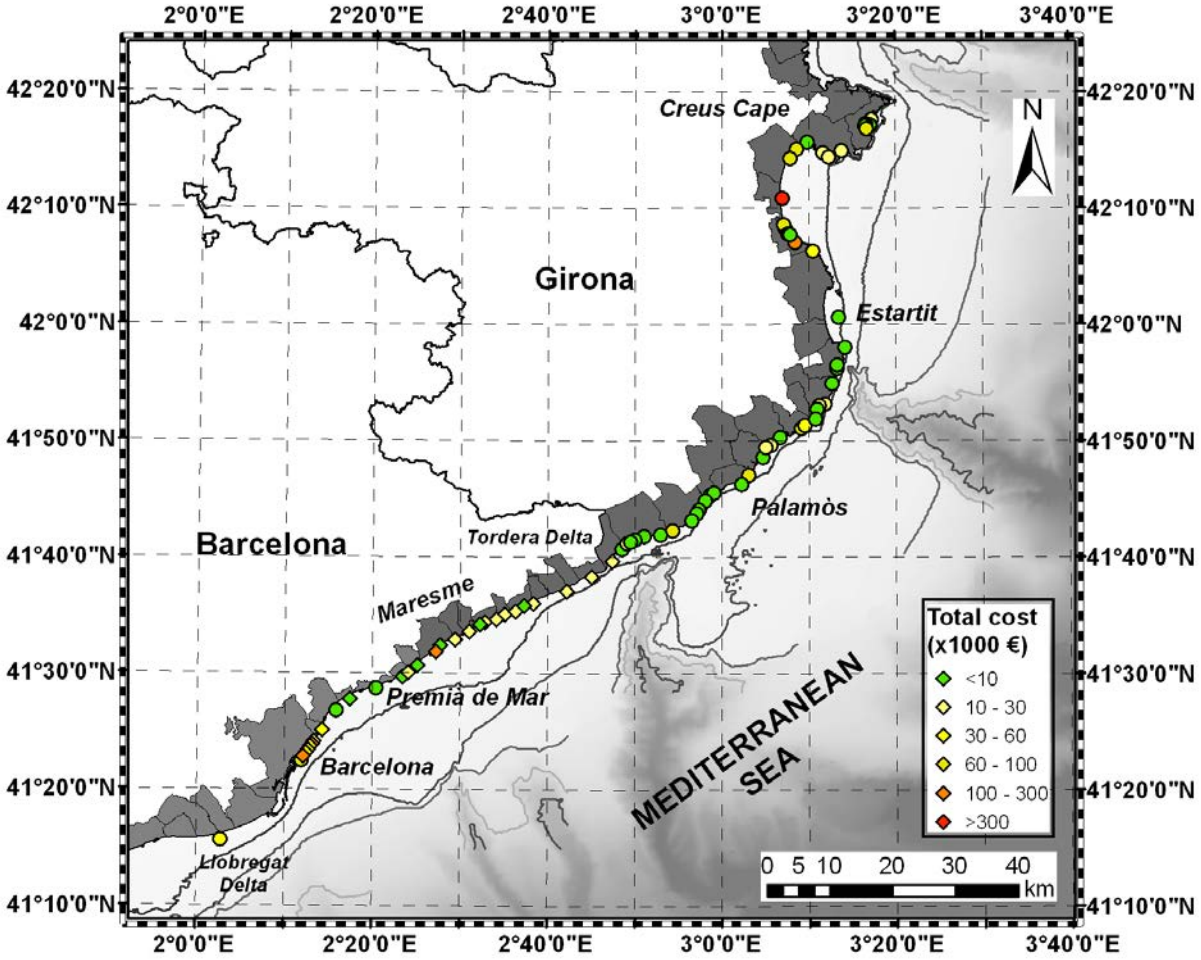

Figure 6.20.: . Risk estimation for the **October 2015** storm (see Ch. 5) at the Study Area. The dots are the calibration beaches and the rhomboids are the validation points. The colour scale belongs to the categories from Tab. 6.1.

O-15 (Fig. 6.20) consists of a storm event whose $H_{s,peak}$ has a $T_r = 1$ year (Fig. D.1) plus a moderate storm surge (almost 20 cm at the storm peak, Fig. 5.1). Though waves are not as extreme as D-16 or J-17, the storm surge enhances the risk category at dissipative and intermediate beaches. Creus Cape shows moderate risk, except at Sant Pere Pescador that present Category 6 (red colour). This behaviour is due to its low elevation and gentle slope ($slp_{em} = 0.11$, see Tab. B.1) and its alongshore length ($L_{bch} = 9920m$).

Barcelona city shows important risk (categories 4 and 5) and Maresme moderate risks (Categories 2 and 3). The overall expected cost is near 2M euros (Tab. 6.2). Results highlight the importance of a joint characterization of the main storm drivers: the joint action of moderate surges and moderate waves can lead to important damages that in global can have a relevant cost.

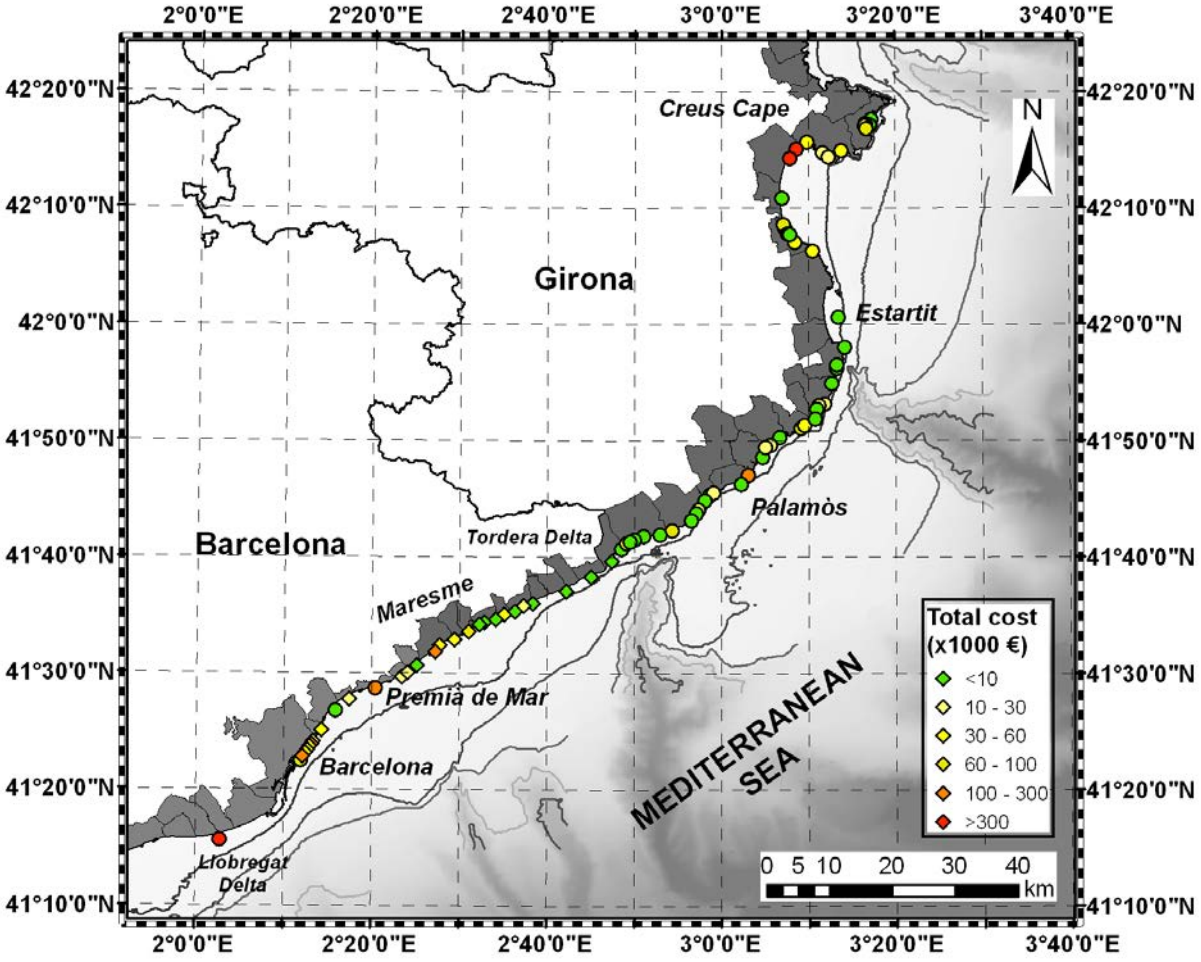

Figure 6.21.: Risk estimation for the **November 2015** storm (see Ch. 5) at the Study Area. The dots are the calibration beaches and the rhomboids are the validation points. The colour scale belongs to the categories from Tab. 6.1.

N-15 (Fig. 6.21) storm shows an important global cost (2.5M euros), despite an important part of the coast shows no risk. As showed in Ch. 5. This event is the one with the higher sea level. Then, dissipative beaches shows higher cost (Gavà, Empuriabrava, Rubina). Note that the Southern Maresme is in moderate risk, mainly due to the lack of beach width. A prominent case would be Premià de Mar that shows important losses (Category 5). Beaches that integrates Barcelona city has an overall cost of around (0.5M euros). The Northern Maresme shows no apparent risk. The Palamòs and Estartit area show low risk at the reflective beaches. Waves have a marginal return period of around 1 year, hence, beaches with enough beach width and a coarse sand would suffer low erosion and almost no flooding.

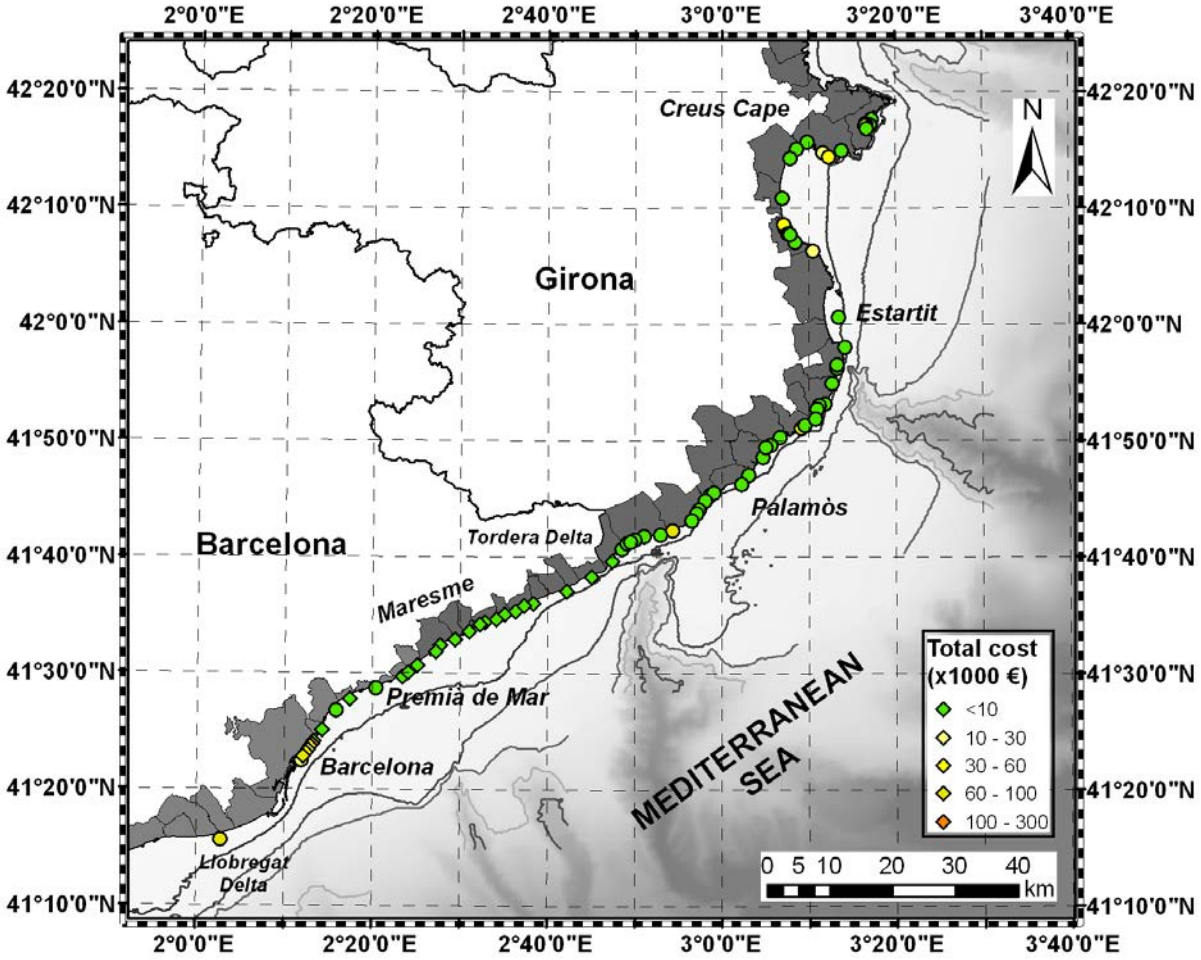

Figure 6.22.: Risk estimation for the **January 2016** storm (see Ch. 5) at the Study Area. The dots are the calibration beaches and the rhomboids are the validation points. The colour scale belongs to the categories from Tab. 6.1.

J-16 (Fig. 6.22) was constituted by moderate SSW waves (Fig. D.3) and a low sea level (Fig. 5.5). Despite the magnitude was slightly superior to F-16, the shoreline orientation of most part of the calibration and validation points are sheltered against this directional sector. Hence, this event checks the feasibility of the directional coefficients.

The risk module shows that the risk is very low (Category 1) at almost the whole Study Area, except from Llobregat Delta, Malgrat de Mar (both shorelines orientation are not sheltered against SSW waves) and Barcelona city (whose assets have the highest value, then showing moderate risk). The total cost of this event was the lowest (690K euros), mainly based on the abovementioned sites.

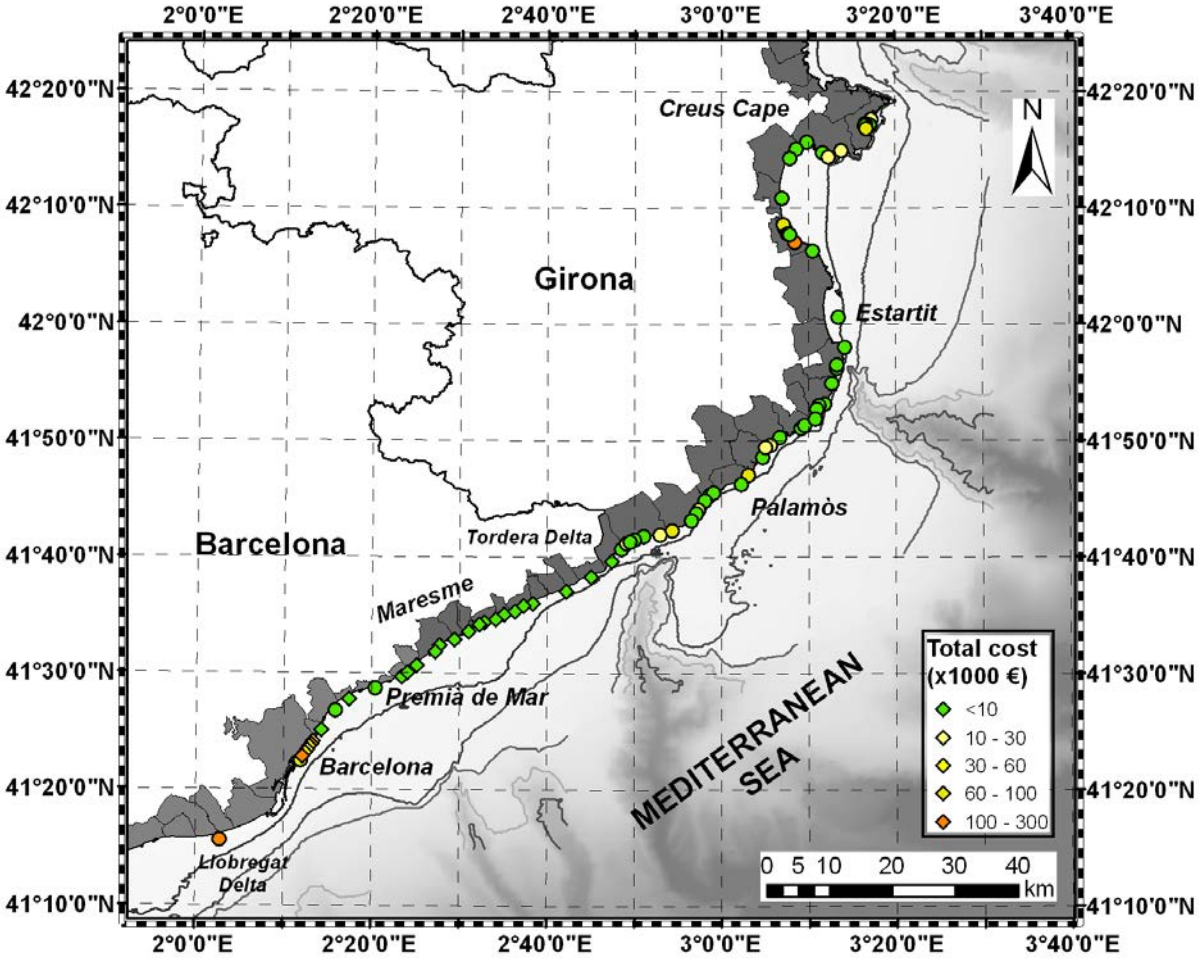

Figure 6.23.: Risk estimation for the **February 2016** storm (see Ch. 5) at the Study Area. The dots are the calibration beaches and the rhomboids are the validation points. The colour scale belongs to the categories from Tab. 6.1.

F-16 (Fig. 6.23) is a **moderate storm** ($H_{s,peak}$ hardly exceeds 3 meters at Creus Cape, Fig. D.3) that shows no-risk at almost the whole study area. Moderate risk (yellow) can be found at Barcelona city, Gavà and Blanes, where valuable assets can be found at the backshore. The expected cost slightly surpasses 1M euros, essentially at the abovementioned sites. Results coincide with the recorded information, because newspapers did not paid too much attention to this event. These outcomes also shows that the risk module has enough sensitivity to the inputs, without over-predicting high costs when the drivers are moderate.

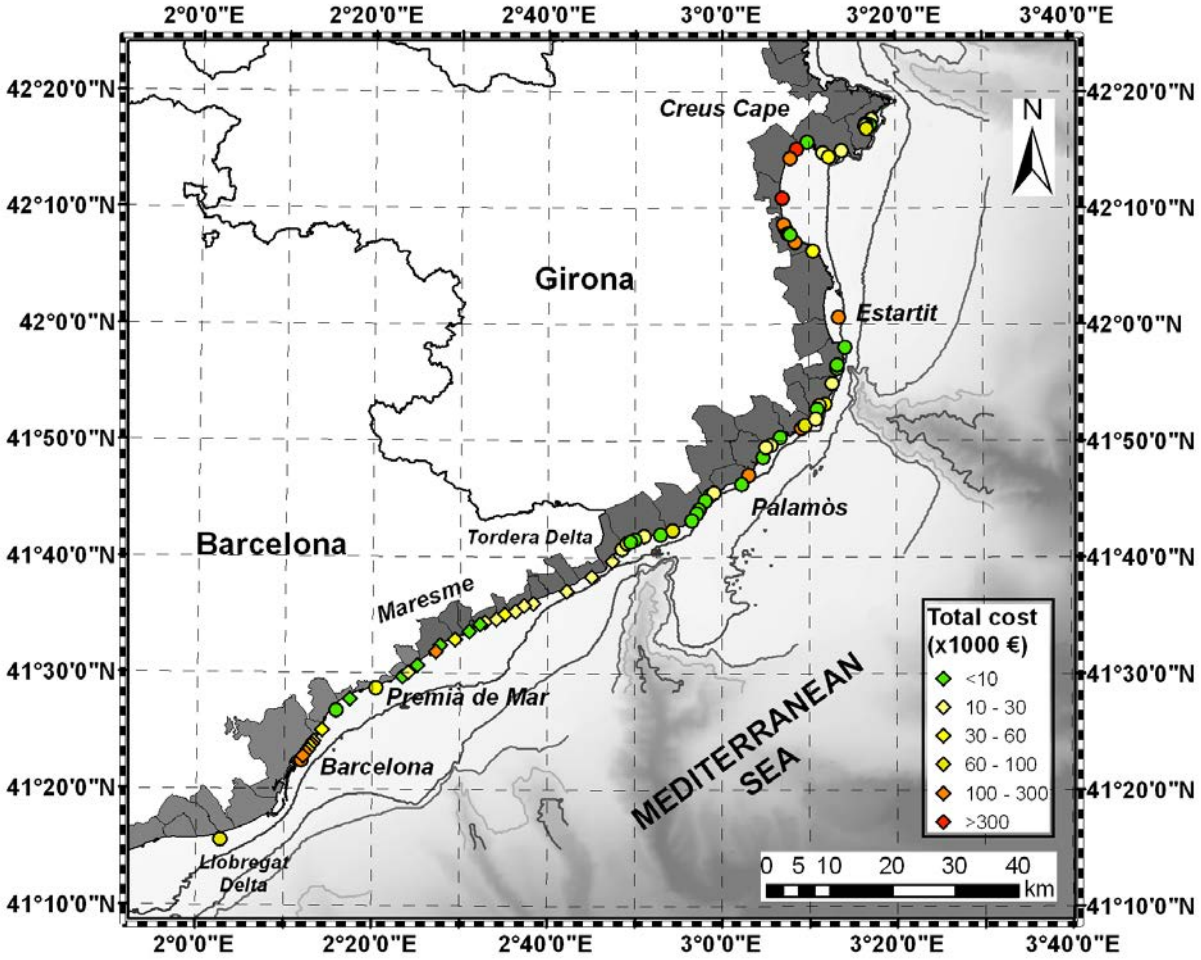

Figure 6.24.: Risk estimation for the **December 2016** storm (see Ch. 5) at the Study Area. The dots are the calibration beaches and the rhomboids are the validation points. The colour scale belongs to the categories from Tab. 6.1.

D-16 had $H_{s,peak}$ slightly inferior (Fig. D.5) than the J-17 event (Fig. 6.25) at the Southern part of the study area (Maresme, Barcelona and Llobregat Delta). However, $H_{s,peak}$ at the Northern part (Costa Brava) was significantly higher at D-16 than in J-17. Hence, the risk forecast is similar (Fig. 6.24), but with a lower total cost (2.9M euros vs. 3.2M euros), because more valuable assets (flood cost) are at the Southern part. Note that the Estartit, Sant Pere Pescador, Empuriabrava and Rubina have important costs. Barcelona city also presents important costs and the Maresme present moderate costs.

Despite the $H_{s,peak}$ were similar, the storm duration and the total energy at J-17 (Fig. D.6) was considerably higher than D-16 (Fig. D.5). Such storm components, not yet implemented in the risk module, are dependent with the $H_{s,peak}$ and the peak period $T_{p,peak}$ (Lin-Ye et al., 2016).

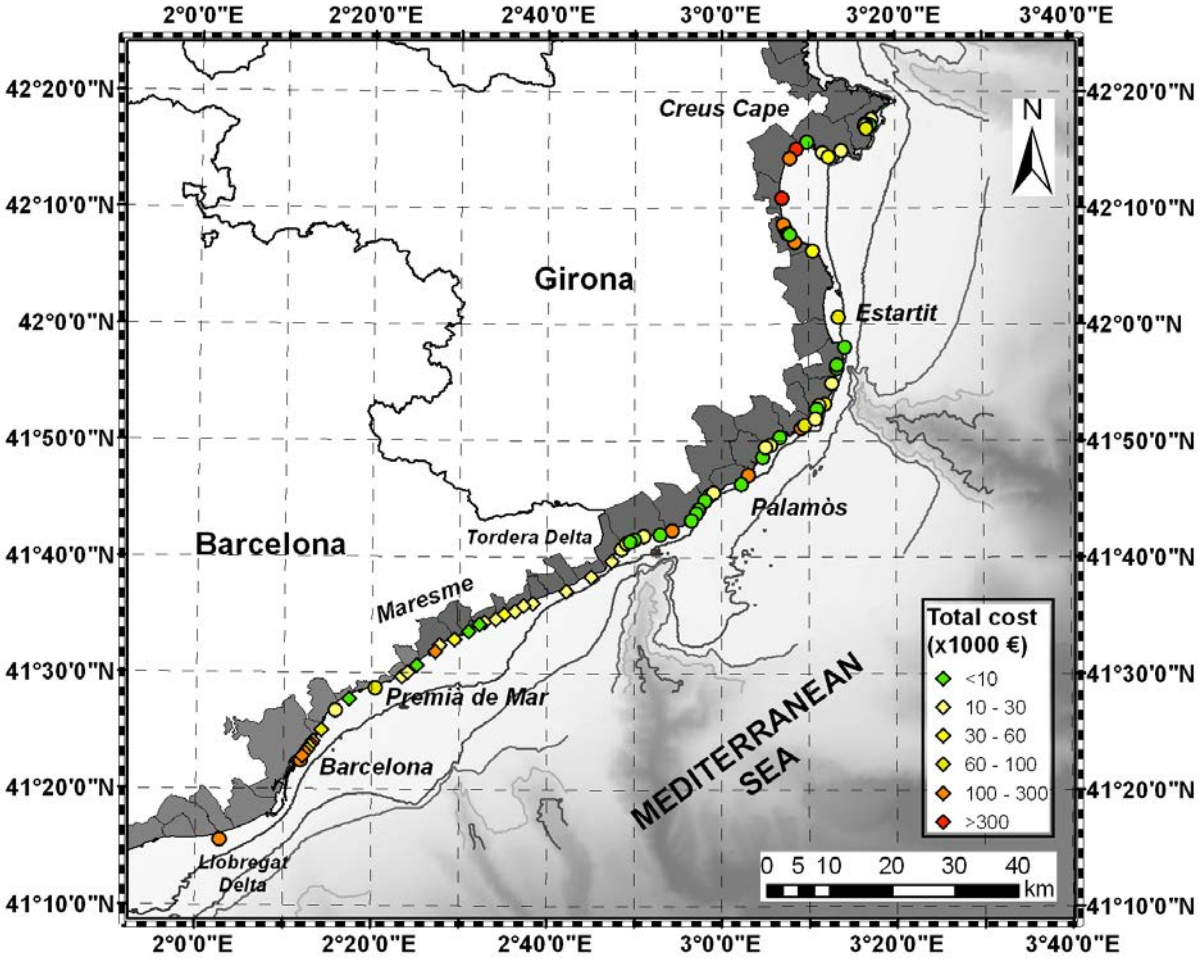

Figure 6.25.: Risk estimation for the **January 2017** storm (see Ch. 5) at the Study Area. The dots are the calibration beaches and the rhomboids are the validation points. The colour scale belongs to the categories from Tab. 6.1.

J-17 (Fig. 6.25) had the higher wave return period of the whole sample presented in this dissertation. Hence, it was expected higher costs (3.2M euros) than the other ones. Except for wave sheltered areas such as pocket beaches or St. Margerida beach (Creus Cape), the rest of the beaches exhibit moderate to high risk. The ones with higher costs are Sant Pere Pescador and Empuriabrava, because of the conjunction of: (i) extreme waves ($H_{s,peak} > 6m$, Fig. D.6) that impact almost perpendicular to their shorelines and (ii) fine sediment size and low-lying elevation. Barcelona city presents important losses (due to the squeezed beach width and the high value of the backshore). The whole Maresme and Gavà present moderate risk, because $H_{s,peak}$ is lower ($H_{s,peak} < 5m$, Fig. D.6).

The total cost that has been estimated with the Risk Module can be found in Tab. 6.2. J-17 and D-16 show the higher cost, whereas J-16 determined losses around

$690 \cdot 10^3$ euros. The other column show the invested cost for each storm-season. The **invested cost** only considers the investment made from *Ministerio de Agricultura y Pesca, Alimentación y Medio Ambiente* (Spanish Government). Damages paid by the Regional Government (Generalitat de Catalunya) and municipalities are not included. Note that the detailed costs for each storm cannot be quantified as well, due to the lack of data.

6.4. Discussion

In the previous sections, the four steps for building the COPAS formula have been described (Sec. 6.2); and Results (Sec. 6.3) have been shown via stress-curves, correlation curves and forecasting maps. This discussion will address the following points: (i) Hypothesis behind the formula building (i.e. how it was built); (ii) Results of the COPAS formula (i.e. what was found after building it); (iii) Practical implications for the COPAS implementation (i.e. how to implement and improve the current state of this Risk module).

6.4.1. Hypothesis behind the formula building

A multivariate non-stationary statistical model that forecasts the cost of episodic coastal hazards (erosion and flooding) has been proposed. The **calibration dataset**, derived from process-based modelling, exhibits the following features:

1. **Erosion is a bounded cost** (i.e. both maximum and minimum can be estimated). Sand is a limited resource and it is present in the exposed part of the beach. Sand dynamics tends to be present at all the calibration beaches, regardless of their morphodynamic features.
2. **Flooding** (specially at dense urban areas) **shows higher upside costs** than erosion. Despite that moderate forcings leads to almost nil costs; once waves and MWL surpass site-dependent thresholds, the trend shifts.
3. The mean value of the flooding cost tends to be lower than the erosion cost, because the flooding depends on impulsive action (i.e. overtopping grows non-linearly when forcings increases).

One of the strong points of the statistical model is its non-stationary dependence structure. That provides an interesting flexibility when predicting; but at the same time, imposes rigidity (the upper tail dependence shape is pre-defined as a Gumbel). This trade-off requires a previous explanatory analysis of the calibration dataset that corroborates such hypothesis. Nonetheless, this approximation may be considered as valid in this case, because the **dependence** structure is based on the **high quantiles**, that are the most interesting from an early-warning system point of view.

High values of τ_K show that the erosion and flooding costs share the same proportionality in the total cost. When there exist a mismatch between these individual

costs, τ_K tend to be lower. It has been found that low sea levels and high return period of waves lead to higher values of τ_K. That is because this combination of waves and sea level produces both erosion and overtopping. On the contrary, high water levels but low waves leads to prominent flooding but low erosion rates.

Note that a flooding and erosion cost copula may be unnecessary at those beaches in which these hazards are uncorrelated (they are almost independent) and/or there may be relevant differences in their magnitudes. For instance, the cost of flooding is almost nil at some Catalan beaches, unless high sea levels are reached. In these cases, the formula could be simplified to a non-stationary univariate distributions for the erosion cost (that would usually happen, because the erosion is a dynamic process that happens once the Shields number has been surpassed). Flooding is more related with impulsive conditions (i.e. overtopping) and requires specific forcing combinations.

From an **operational** point of view, **wave direction is** almost as **important** as the significant wave height, both for dissipative and reflective beaches. At dissipative beaches, although waves have more time for refracting and their direction is not the usual main problem, local flooding can be enhanced within specific directional sectors due to local emerged constraints. At reflective beaches, though, refraction processes are not fully developed and certain directional sectors may lead to combined cross-shore and long-shore gradients that exacerbate erosion. Hence, errors in wave direction would not affect the erosion at dissipative beaches, but they will affect the flooding, specially in those cases that have local lower elevations (river mouths, etc.).

Proper wave direction forecasting plus an **updated initial state of the coast** (see next subsection) would help to address beach rotation in pocket beaches, that is a highly related hazard with episodic scales. Fenals and Lloret beaches, for instance, suffer historical rotations (Sec.2.3.1.1.1): then, a combination of a SE storm (displacing the emerged sand southwards, reducing the beach width at the northern area) and a subsequent S storm, can cause significant flooding damage. The current formula does not consider the interaction of heterogeneous local emerged constraints.

The effects produced by wave period forecasting requires further sampling. Such sampling requires a dependence structure with the other storm components (Lin-Ye et al., 2016). Additionally, it should span a wide range of realistic wave steepness values (Vanem, 2016). Note that the forcings of the cost database (Step-1) have been built with the following constraints: (i) the type of storm is triangular with the same growth and decay rates; (ii) the time duration of the storm has been set to 24 hours, that is typical in the Mediterranean (Bolaños et al., 2009); (iii) the MWL has been considered as stationary, with a maximum level of $MWL = 60\ cm$ for almost all cases (some beaches such as Barcelona, Gavà or Estartit have been modelled with even higher MWLs scenarios).

The wave return period shown in the stress-curves was univariate ($H_{s,peak}$). This assumption has been held for the sake of simplicity, because storm-components

such as storm-duration, wave growth and decay have been considered as constant. Multivariate return periods would be more appropriated when applying different combinations of storm-components. Hence, future updates of the database may include storm-components that would follow a dependence structure such as the one proposed in (Lin-Ye et al., 2016, 2017).

The regression coefficients in the Step-3 tend to depend on just one covariable. With additional beach sites sample, it would be possible to find relationships of the regression coefficients with more than one covariable. The principle of parsimony, information criterion (minimisation of AIC/BIC) joint with the physical reasoning have been the cornerstone for building the general formula.

For instance, when we have low beach width, flooding may happen more frequently (thus, $\beta_{(H_s,\mu_{\varphi r})}$ has to be higher as stated in Fig. 6.9). In case of the pocket beaches, the reduction is quadratic because the effect of waves are lower (pocket beaches are more sheltered from wave action). Wave action for open beaches are defined as linear because the consequences from waves are more long lasting.

6.4.2. Results of the COPAS formula

The proposed multivariate formula handles the main features of the dataset. This formula relates commonalities among beaches and helps to extrapolate coastal risk to other sites in which sample is not available. The non-stationary parametrization implies that increases/decreases of hydrodynamic forcings leads to more/less damage at the system.

Erosion results tend to be more accurate than flooding because the former are derived directly from the model and the behaviour tends to be more homogeneous. Flooding is a transient phenomenon that relies on a set of local constraints that are somewhat hard to be included in a generalist model. It has been preferred to use the cost rather than the discharge/overtopping because this information can hardly be translated into risk managers. However, both erosion and flooding can be translated into an economic cost. Heterogeneity in flooding has been addressed by the building percentage ($buil_{\%}$). For instance, Sant Pere Pescador (Creus Cape) has a low degree compared with Sant Sebastià or Premià de Mar (Barcelona).

Dissipative beaches tend to exhibit **higher costs** than reflective beaches **under high MWL**. That is because most of the dissipative beaches in the calibration database have low berm height. In these cases, erosion is the main coastal hazard under low sea levels; but once reached a site-specific MWL threshold, flooding becomes the main hazard.

Reflective beaches have coarse sand and the erosion costs tend to be lower (i.e. due to lower sand mobility). Despite that erosion is the main hazard under low sea levels, the transport magnitude is somewhat lower than dissipative beaches. At these low sea levels, flooding costs tend to be significantly lower than in dissipative beaches, as well. Once surpassed a site-specific MWL threshold, flooding cost proportion

increases. This threshold tends to be higher than in dissipative coasts, partly because the berm height tends to be higher. Note also that an important part of coarse sand coasts in the sample are wave-sheltered pocket beaches with relatively low erosion problems.

It is not clear how will be the balance of the flooding and erosion costs in the future. The flooding costs would become more important in the near future if: (i) the assets increase in value or (ii) due to Sea Level Rise (SLR) (i.e. the overtopping will be more frequent). In the other hand, in the future, erosion will decrease as the sand budget becomes scarce (Sierra and Casas-Prat, 2014). Erosion costs, however, may be stabilised or even increase in case that sand prices rise sharply. A regional assessment of the COPAS formula may shed some light on what would be an optimum sand by-pass along the Catalan Coast.

The evolution of the dependence (τ_K) may be understood as well as an **indicator of the beach health**. Note that dependence is a consequence of the flood-erosion rate interaction.

There may be different **causes** for **low dependence**:

1. Low flooding rates because there are less valuable assets in the rearside.
2. Low erosion rates because the sediment size is coarse.
3. Low flooding rates because the beach width and the berm height is large.
4. Low availability of sand (low beach width) and valuable assets at the rearside. In this case, a low tau will be the symptom of a low beach health.

Once analysed the dependence diagram, it may be possible to trace back the causes. But without this diagram, it would not be straightforward to discern the possible causes for the dependence structure.

The forecasts tend to be more accurate with open, free from obstacles beaches (Sánchez-Arcilla et al., 2014). That is because the XBEACH model performs better at homogeneous domains (see Ch. 4, Gràcia et al. (2013b)). Fine sand beaches tend to have high values of erosion, that is somewhat hard to predict with the present sample. Notwithstanding, the results are smoothed, because the betas tend to be smoother than the ones obtained in the second step of the methodology. Increased performance at dissipative beaches would be expected with more beach samples from the Southern part of the Catalan coast. The present sample hinders to extrapolate to all the Catalan coast particularities, but shows considerably good skill for the Northern part.

Moderate events (i.e. moderate wave return periods ($T_r = 1 - 5\ yr$) joint with moderate storm-surges) can lead to significant total costs for the whole Northern coastal fringe. At the moderate **N-15** event there were estimated losses of $2510 \cdot 10^3$ euros that do not differ excessively from the extremal **J-17** ($3200 \cdot 10^3$ euros). Although they differ relevantly in wave magnitude, J-17 has a lower sea level; whilst the joint action of waves and MWL leads to hazardous rates in N-15. In these cases, prone to flooding beaches would be affected by the sea level and erosive sites will be aggravated due to waves. The cumulative costs at a wide coastal fringe such as the

Northern Catalan Coast can be significant. This justifies the need for accurate hydrodynamic forcings not only for extreme episodes, but also for moderate conditions (see Ch. 5).

6.4.3. Practical implications for the COPAS implementation

Risk communication with probabilistic forecasts is more complex than with deterministic ones (Gigerenzer et al., 2005). The aim of risk communication is to foster action towards preparedness. The transition between recommendation and intervention requires to build confidence in CEWS. Hence, these systems need to be **accurate**, **robust**, **updated-frequently** and **easily interpretable**. The implications for achieving such objectives can be found below.

6.4.3.1. Implications for improving the pre-forecasting phase: building robustness with better datasets and observations

Accuracy and robustness in COPAS can be addressed through two approaches: (i) upgrading the Step-1 database with a set of new hot-spots that would reinforce the **statistical characterization** of specific flooding and erosion physical processes; (ii) modifying the model with more covariates and/or degrees of freedom. More degrees of freedom means that the covariates would handle higher nonlinear effects (i.e. enhanced adaptability to different patterns). However, adding additional covariates without increasing the number of beach sites would lead to the danger of overfitting and/or overparameterization (Jakeman et al., 2006; Marra and Wood, 2011). In Sec. 6.4.1 has been highlighted a set of recommendations for improving the calibration dataset.

The forecasts can be **easily updated** with new observations, then paving the way for near-real-time quick scan forecasting (Bell et al., 2000; Tang et al., 2009). In-situ and remote sensing (i.e. SENTINEL missions) monitoring networks may benefit from this situation. If measurements are available, the forecast can be updated and be more accurate with the present state. Such incremental analysis updates (Leyton and Fritsch, 2004; Bishop et al., 2001) not only improve the forecast skill, but also leads to quantify how much a previous forecast diverges from the last observations available. That provides a good benchmark about the sensibility and accuracy of the CEWS (Baart et al., 2016).

This approach also requires a detailed description of the impacts at the coast. Such characterization needs to be frequently updated. In the Catalan coast, a storm impact database has been built recently, in the framework of the iCoast project (CIIRC, 2015). Additionally, the same database is constantly updated with an on-line form that can be found in the ICGC website[1].

[1] http://www.igc.cat/web/ca/icoast_form_icgc.html

6.4.3.2. Implications for interpretation at the post-forecast phase: how to tackle uncertainty and apply the CEWS for diminishing risk

As stated in the previous Sec. 6.4.2, coastal flooding has more uncertainty than erosion. The error bars shown in the stress-curves (please refer to Figs. 6.11 or 6.16) has been obtained through **thousands of computationally cheap simulations**. These simulations are estimated in seconds, rather than waiting hours, as in usual process-based modelling. These errors bars provide a fast assessment on how uncertain are specific hydrodynamic conditions. Probabilistic forecasting is usual in other atmospheric variables such as rainfall, wind-fields or temperatures (Cloke and Pappenberger, 2009; Zhang et al., 2014; Kruizinga and Murphy, 1983), but they are still in their infancy in coastal morphodynamics.

Uncertainties may arise from different factors: (i) **initial states** (proper state of the bathymetry and the inicial forcings); (ii) **boundary conditions** (forcings and sediment fluxes outside the domain); (iii) **simplifications** assumed by physical parametrizations; and (iv) **discretization methods** for solving the mathematical model. The first two affect relevantly to the forecast and must be specifically addressed; the third one involves increasing the body of knowledge of the physical processes embedded into the forecasting model, but it is harder to obtain results; the last one may provide better solutions once addressed the first three points above.

Uncertainty in bathymetry affects remarkably the sensibility of the forecast. Hence, a forecasting system should address different initial configurations and layouts. Changes in the initial state can alter the balance of the consequences. For instance, some post-storm profiles tend to homogenise the beach, but others tend to enhance heterogeneous patterns.

The sensibility of the CEWS to different layouts is not just to accurately forecast how the present state of the coast would evolve after an extreme event. Pro-active interventions (i.e. hypothetical transient alterations of the emerged and submerged bathymetry) may diminish coastal hazards in a timely and cost affordable manner. Hence, the same CEWS can become a powerful designing tool. One of the main design concerns is what factors are aiming to minimise: (i) dissipate wave energy (the driver) or (ii) reduce the wave run up (the impact). Deploying a submerged breakwater means to attenuate energy. Building a dune means to accept this energy and try to reduce the impact (protect). As will be analysed in Ch. 7, pro-active interventions for dissipative beaches would aim to reduce the impact (i.e. coastal dunes), whereas reflective beaches would aim to reduce the forcings (i.e. transient detached breakwaters).

6.5. Conclusions

The aim of this chapter was to develop COPAS, a non-stationary multivariate statistical model that can estimate the flooding and erosion costs in microtidal beaches.

COPAS is a quick-scan risk forecasting module that can estimate the episodic coastal flooding and erosion at a wide range of beaches and hydrodynamic scenarios. 54 beaches have been served as calibration dataset and 25 comprised the validation dataset. The methodology comprises four steps:

1. Generation of the flooding and erosion cost database for each calibration beach through process-based modelling (hydrodynamic and morphodynamic module, see Ch.3,4,5). A wide range of wave storms and sea level scenarios have been considered.
2. Building of individual GAMLSS models for each calibration site, in which the response variables are the flooding and erosion and the covariates are the hydrodynamic forcings (storm waves and MWL).
3. Finding relationships between the coefficients of the GAMLSS models and morphodynamics features (beach width, beach slope, berm height, etc.).
4. Application of the COPAS risk formula derived from the relationships obtained in the previous step. The results discussed in this Chapter are stress-curves, correlation-curves and forecast maps.

From the calibration dataset (Step-1) it has been found that erosion is a bounded cost and flooding shows high upside costs. Erosion results tend to be more accurate than flooding, because the former are derived directly from the process-based model outputs and the behaviour tends to be more homogeneous. The non-stationary parametrization (Step-2) implies that increases/decreases of hydrodynamic forcings leads to more/less damage at the system.

Dissipative beaches tend to exhibit higher costs than reflective beaches under high MWL (Step-3). That is because most of the dissipative beaches in the calibration database have low berm height. At reflective beaches, costs tend to be lower than dissipative ones, partly because the sand is coarser and berm heights tends to be higher.

Moderate events (i.e. moderate wave return periods ($T_r \leq 5\ yr$) joint with moderate storm-surges) can lead to significant total costs. At the moderate N-15 event there were estimated losses of $2510 \cdot 10^3$ euros that do not differ excessively from the extremal J-17 ($3200 \cdot 10^3$ euros). This justifies the need for accurate hydrodynamic forcings not only for extreme episodes, but also for moderate conditions (see Ch. 5).

The dependence coefficient between flooding and erosion (τ_K) may be a good indicator of the beach health, because it provides a quantitative assessment of the proportion of each coastal hazard in the total cost. This proportion may change in the future due to morphodynamic changes (i.e. reduced beach width) or Climatic Change consequences (i.e. Sea Level Rise).

A CEWS has to be accurate, robust, updated-frequently and easily interpretable; in order to foster action towards preparedness. Accuracy and robustness in COPAS can be addressed through two approaches: (i) upgrading the Step-1 database with new hot-spots that would reinforce the statistical characterization of specific flooding and erosion physical processes; (ii) modifying the model with more covariates and/or

degrees of freedom. The forecast can be updated frequently with near-real time observations from in-situ and remote sensing monitoring networks.

Probabilistic forecasting can provide fast assessments on how uncertain are specific hydrodynamic conditions. Important uncertainties may also arise from the bathymetry. The sensibility of the CEWS to different layouts would be paramount for designing pro-active interventions, such as the ones proposed in the next Chapter 7.

7. Evaluation of Proactive Interventions

7.1. Introduction

In the last three Chapters, it has been shown that LIM-COPAS can assess coastal risk at the Catalan Coast. Ch.4 shown that models were able to reproduce the post-storm response of two urban beaches, reaching BSS around 0.36-0.4, that be considered as acceptable (van Rijn et al., 2003). In Ch. 5, high return period wave storms ($T_{r,waves} \geq 10\ yrs$) were properly hindcasted ($COE = 0.58 \pm 0.11$ for the H_s at Barcelona). These hydrodynamic conditions were translated into coastal risk (Ch. 6), discerning the most vulnerable areas at the Northern and Central coastal fringe. The system predicted losses of around 3 million euros for a single event (J-17 and D-16). Urban beaches (Barcelona, Gavà, Maresme strait) were the most threatened ones, because they face two constraints: (i) sand scarcity and (ii) valuable assets in their rearside (sea promenades, buildings, transport infrastructures, etc).

This chronic problem has been addressed in Ch. 2. Reactive coastal management has been the mainstream response in Europe (EuropeanCommission, 2004). In the last decades, coastal managers have tried to control the coastline through **hard infrastructures** (Hamm et al., 2002; i.e. revetments and breakwaters) and beach nourishment (Hanson et al., 2002). Unfortunately, several of these measures have modified the sediment natural fluxes in an unexpected manner which has lead to exacerbated erosion and accretion patterns. Moreover, these solutions present other two disadvantages: (i) hard works induce a steady hydrodynamic behaviour and (ii) they require periodic beach nourishment. These factors have been the root cause of several coastal conflicts along the European coastline. As a result, policy makers are demanding to the scientific community another kind of solutions (Sánchez-Arcilla et al., 2011b), more in line with the natural dynamics.

The aim of CEWS forecasting is to provide a **time buffer** for fostering pro-active interventions that diminish coastal risk. This **local-based** information constitutes the standpoint for short-term works that protect the coast against extreme waves and sea levels. The specific features of each site, the availability of resources and the desired protection level hamper a generic solution; but a set of principles can be adopted as a basis. These principles are enclosed in the termed Quick Defence Measures (QDM) and Quick Accommodation Measures (QAM) (Fig. 7.1). The difference between QDM and QAM is that the QDM **enhance actively** the **protective**

function of the beach (i.e. transient dunes, detached breakwaters, sandbags, etc.), whilst the QAM **reduce passively** the **coastal impact** (i.e. prevent beach access, geotextile covers at the emerged area, etc.). Note that a single specific intervention can incorporate different shades of QDM/QAM.

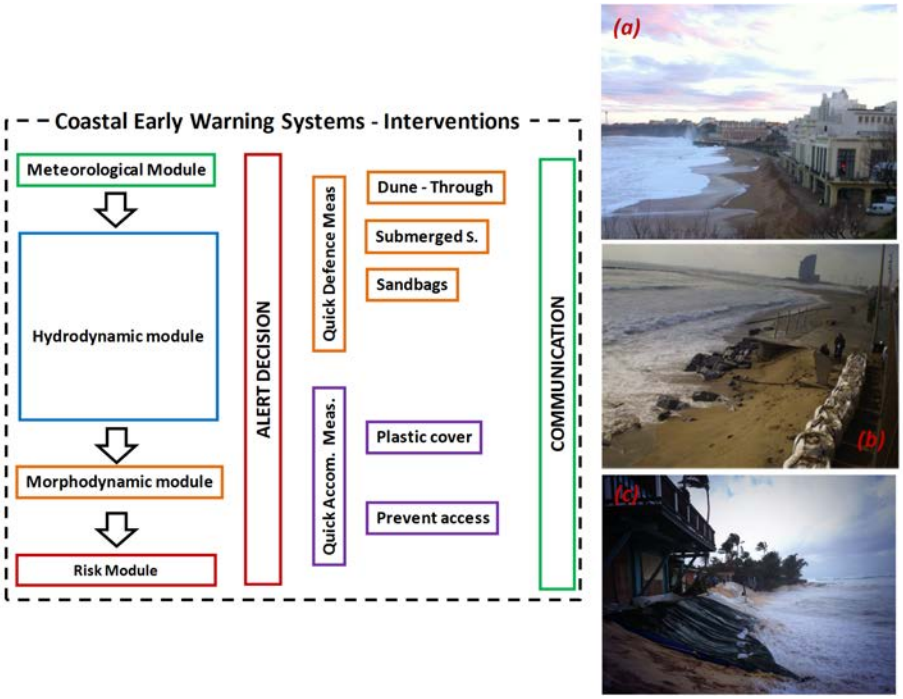

Figure 7.1.: List of intervention measures within a CEWS. Starting from a CEWS, the managers can adopt and evaluate the feasibility of a set of decisions for reducing coastal risk (Quick Defence Measures and Quick Accommodation measures). The decision will be communicated to the intervention group 24 hours prior to the storm event. (Right) Examples of QDM: (a) transient dune system at Biarritz beach (Spain) during Hercules storm (January 2014); (b) sand bags at Barcelona beach (March 2010); (c) Geotextile covering at Oahu Island (January 2014).

This Chapter will strongly focus on QDM. They consist of **transient, timely, local interventions** whose objective is to **minimise the coastal damages under extreme events**. The principles beneath their design are: (i) to be local-based and in tune with the littoral cell, (ii) to be cost-effective, (iii) to have short construction/demolition time, (iv) to be based on endogeneous resources, (v) to have a limited life-time, (vi) to increase compatibility with the natural, economic and protection functions. These principles are generic enough to span a wide range of solutions. In this dissertation, though, two specific cases will be analysed: (i) transient dunes and (ii) geotextile detached breakwaters.

These interventions, though, may a have a set of limitations: (i) their efficiency is bound to the accuracy of the forecast; (ii) local physics are complicated to be

forecasted (the whole modelling chain can significantly affect the response, as exposed in Ch. 4); (iii) the general morphodynamic behaviour needs to be known; (iv) resources have to be available (trained staff, raw material, machinery) and (v) monitoring is needed for assessing and/or readjusting the QDM performance.

Being in tune with the littoral cell requires to **predict** the **future** coastal state. Local perturbations can strongly affect the coastal response under extreme regimes. However, extreme events are uncertain and hard to be included in long-term plans. Hence, without the high spatio-temporal resolution forecasts from a CEWS, it is difficult to set-up an optimum design. In that sense, the forecast horizons are important constraints for complex solutions. Note that CEWS can predict the state of the coast **3 days ahead** (Baart et al., 2016). These just 72 hours are the time window for deploying action. Then, the intervention protocol has to be as precise as possible.

The aim of this **Chapter is to assess numerically whether Quick Defence Measures (QDM) can reduce episodic coastal risk** at the Catalan Coast. These results will be tested at two beaches that suffer chronic coastal hazards and are representative of the urban beaches that can be found at the Catalan Coast: Barceloneta (Sant Sebastià beach) and Gavà beach. Two kinds of QDM will be addressed: (i) dune systems and (ii) detached breakwaters.

The morphodynamic module will be the core diagnosis tool in this Chapter. The high resolution information (gridsizes of an order of few metres) are deemed indispensable to evaluate QDM performance. Note that the risk formulation proposed in Chapter 6 cannot model local behaviours, because the beach-local constraints interaction is not included yet. The modelled post-storm response of these two beaches will be compared with simulations with identical hydrodynamic forcings, but including QDM at their digital elevation models. The hydrodynamic forcings will span a set of synthetic yet plausible storm events (combinations of extreme waves and sea level).

This Chapter is structured as follows: Sec. 7.2 defines the two types of QDM that will be tested (transient dunes and detached breakwaters); Sec. 7.3 addresses the methodology; Sec. 7.4 presents the characterization of hazard and risk under the different QDM; these results will be discussed in Sec. 7.5 and concluded in Sec. 7.6.

7.2. QDM definition

QDM can be defined as a **transient, timely, local interventions** whose objective is to **minimise the coastal damages under extreme events**. These measures aim to find equilibrium between the actuation cost and the savings due to the reduction of human and material losses. They aim to be more environmental friendly than hard structures, becoming an ephemeral barrier to the dynamic fluxes.

Therefore, there is required a set of intervention protocols involving (i) thresholds of activation, (ii) typology of the solution and (iii) the required time for their de-

ployment/withdrawal. One of the primary assumptions is that the proposed actions **must be taken within 24 hours** (or less) prior to the forecasted storm episode. The defence strategies include the physical intervention on the beach by **building transient dunes** and **trenches** or by placing **sand bags** filled in-situ at the beach backside among others (Fig.7.2). Interventions are associated to a range of wave and water levels in which they are **functional**. Results obtained from coastal hazard and risk mapping will help managers to identify thresholds (storm intensities) and their consequences will be evaluated with the modelling framework presented below.

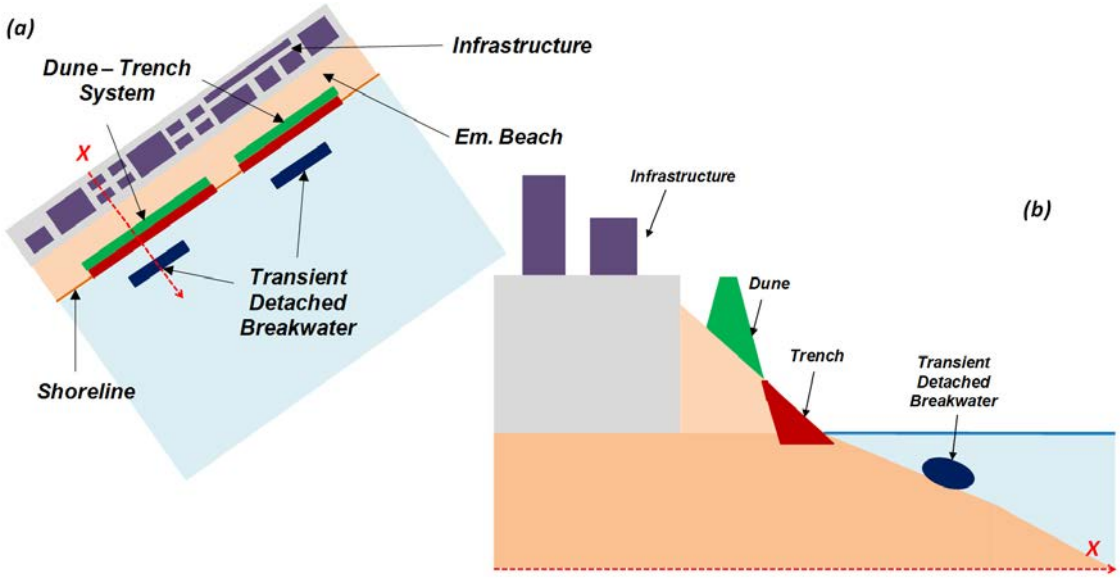

Figure 7.2.: Sketch of the **Quick Defence Measures (QDM)** that will be tested in this Chapter: a **Dune-Trench** system and a **detached breakwater**. Legend: (a) planview; (b) cross-section. In **green**, position of a transient **dune**; in **red**, position of a **trench**; in **dark blue**, **detached breakwater**.

The QDM aims to regulate the three hazardous episodic coastal risks (see Sec. 2.3): (i) erosion, (ii) accumulation and (iii) flooding. The specific details of the QDM tested in this Chapter can be described as follows. In the Discussion section (Sec. 7.5), once analysed the performance of QDM, the lesson-learns will be highlighted.

7.2.1. QDM-1: Dune-trench system

The QDM-1 consists of a **dune-trench system** at the emerged beach zone. It is aimed to provide temporal defence (dune) against flooding with the available material in the beach (sand) and to reduce the offshoreward erosive fluxes, due to return flow and sheet-flow that advect sand from the emerged part with fluxes with low water depth but high velocities and high sand concentrations.

The trench aims to dampen the hydraulic discharge and to trap bed-load transported sand. In theoretical terms, when the dune would be overtopped due the joint action

of waves and sea level, the trench would gradually store the offshoreward advected sand masses until the trench is filled.

In this Chapter, a dune has been designed with a trench at the offshore side. It must be remarked that it is not the only possible layout and there exists on-going work for the evaluation of other typologies of sand redistribution at the emerged zone.

7.2.2. QDM-2: Low-crested detached breakwater

The QDM-2 consists of a set of geotextile bags, filled with sand, that are moored at the sea bottom. The aim of this QDM is to exacerbate wave-breaking dissipation. Consequently, the hydrodynamic forcings will be reduced at the surf zone, swash zone and emerged zone. The flooding affectation level will be diminished and the structure will act as an artificial sediment transport barrier (especially offshoreward bed-load transport). In this Chapter the detached breakwater that are deployed at the Sant Sebastià beach are located at 2 meters water depth.

7.3. Methodology

The assessment of the efficiency of the QDM has been carried out with the XBEACH model (see Sec. 3.3.3), the morphodynamic module in LIM-COPAS. In this section, it will be described how was carried out this analysis. Sec. 7.3.1 presents the two study sites (Sant Sebastià and Gavà); Sec. 7.3.2 details the hydrodynamic forcings via synthetic storms; and Sec. 7.3.3 determines the coastal hazards indices and their translation into risk.

7.3.1. Pilot sites

The feasibility of such measures have been tested numerically at two urban beaches, representatives of the overall Catalan landscape: (i) a low-lying dissipative beach (Gavà, Gavà municipality) and (ii) an intermediate one (Sant Sebastià, Barcelona municipality), according to the morphodynamic classification by Wright and Short (1984).

For the sake of completeness a brief description of the pilot sites will be given. More information about the beaches analysed in this dissertation can be found in Sec. 2.4 and App. B.

Sant Sebastià beach is an **urban sandy low-lying beach** along the NW Mediterranean coast which as valuable assets in its rearside. The beach length is 1360 m, the beach width is 45 m, with maximums of 72 m and minimums of 16 m. The berm height is 2.4 m and the emerged slope is 0.14. The bathymetry can be seen in Fig. 7.3.

In morphodynamic terms, the zone is a **semi-pocket beach** with lateral obstacles (Espigó del Gas groin at the Northern part and the Barcelona harbour at the South).

In 2008, a detached breakwater was built with a length of 157 m and a width of 23 m. Ten years later (2018), a salient has been generated. The northern part of the beach has a **shorter beach width** and it is more prone to erosion due to the storm directionality. Despite the breakwater was designed to act as a shadow zone, the problem has not ceased. Present erosion rate is $-1.3\ m/yr$.

The sediment is coarse sand ($D_{50} = 870\ \mu m$; CIIRC, 2010). The beach profile exhibits an **intermediate behaviour**, with a depth of closure of 6.35 m (Hallermeier, 1981), and a morphodynamic modal state less than one (Dean, 1973). The shoreline presents a classical logarithmic equilibrium shape, in which the salient has divided the shore into two partitions: hereafter, the North and the South. At the central part of each partition, it can be found the narrowest emerged area.

Gavà beach is an **urban dissipative beach** with an alongshore length of 3580 m, backed by a seafront promenade and buildings. Due to its shoreline orientation, the area is **sheltered** from **Eastern waves** but exposed to Southern ones. The coastline can be divided into two zones: the North one (1950 m), that has a N76E orientation; whereas the South (1630 m) is oriented towards N83E. The sediment is **fine sand** ($D_{50} = 200 - 350\ \mu m$; CIIRC, 2010), the beach width is 60 m, with a maximum of 100 m and a minimum of 34 m. The berm height is 1.4 m and the emerged slope is 0.25. Present erosion rate is $-0.4\ m/yr$ (see the mid term erosion rates in Fig. 2.10 in Ch. 2).

The emerged beach profile highlights a **well developed dune** in its rear-side. The existing dune system has the following features: (i) an average dune height of 2 m above sea level; (ii) a base of 20 m and (iii) be located around $30 - 70\ m$ from the shoreline.

7.3.1.1. Model set-up

Sant Sebastià is an urban beach with obstacles (Espigó del Gas, detached breakwater). Additionally, transient detached breakwaters need to handle diffraction and proper wave breaking. Then, a phase-solving version of XBEACH has been used (non-hydrostatic version). Note that this implies a significant increase of the computational time (three times more that in the phase-averaged version). Additionally, more spatial resolution is needed, because a phase-solving model needs more resolution for modelling the water surface elevation. In this case, from the emerged beach to $-4\ m$, the gridsize is 3 m; from the $-4\ m$ to the $-7\ m$ isobath (depth of closure), a grid transition from 3 to 7 m; from the $-7\ m$ to the offshore boundary (around $-30\ m$), the grid ranges from 7 to 20 m. In the alongshore axis, the gridsize is 10 m.

Gavà is a dissipative open beach that has been modelled with a phase-averaged version. Wave breaking is parametrised, but there is further interest in the emerged beach performance due to the nourishment and dune system. The spatial resolution has followed the same criteria that was highlighted in Sec. 3.1. The grid is irregular at the cross-shore axis: from the emerged part to $-2\ m$, the gridsize was 4 m; at the transition zone to the depth of closure (from $-2\ m$ to $-7\ m$), the gridsize varies

from 5 to 20 m; from the depth of closure to the offshore boundary (around -15 m), the resolution is 20 m. The alongshore axis has a constant gridsize of 13.5 m.

This discretization ensures that the local constraints imposed by QDM and the nearshore processes can be assessed. A sensibility analysis with a finer mesh was conducted, but the results were not significantly better, and the computational time substantially increased.

7.3.2. Hydrodynamic scenarios

QDM feasibility has been assessed with synthetic representative storms. It is the same kind of methodology that was held in the previous Ch.6 for building the database (see Sec. 6.2.1 and Fig. 6.3). Three wave return periods (1,5 and 50 years) have been combined with three sea level return periods (no sea level, 1 year and 300 years) and with the directional sectors which impact at the local targets with a significant cross-shore component.

7.3.2.1. Wave climate and triangular distribution

The QDM works under extreme conditions (more than $H_s > 2$ m). Both beaches are located near the Llobregat Delta. Therefore, due to the shoreline orientation, the directional sectors in which are driven more wave-induced mass fluxes are ENE, E, ESE and SSW (see wave roses in Fig. 2.3 and coastline orientation in Fig. A.3). Note that the more severe waves are found at the East sector (the direction that heavily affects Sant Sebastià), but also must be remarked the SSW (the direction that heavily affects Gavà beach).

The morphodynamic characteristics of the beaches require the definition of the offshore boundary conditions in terms of evolution in time. For waves, in this impact assessment, a storm is defined with duration of 24 hours. The trend follows a triangular distribution of the significant wave height where the maximum is at the end of 12 hours.

The mean sea level and the wave direction are considered to be constant during the whole storm. The wave period is given by an exponential fit with the significant wave height (CIIRC, 2010).

7.3.2.2. Sea level climate

The joint action of high sea level with waves triggers levels of flooding/erosion in a non-linear manner. Differences up to 10 cm in sea level can shift a collision regime into overwash (Sallenger, 2000). That is the reason because apart from different wave regimes, they must be combined with different sea levels.

An extreme sea level climate has been used from the Barcelona harbour tidal gauge (Fig. 2.2). The recorded sea level is representative of the two analysed beaches,

so it can be extrapolated as offshore boundary conditions in the morphodynamic module. The return period of the maximum sea level has been computed and the outcomes span from 1 to 300 years. Note that the sea level sharply grows from 1 to 50 years, but the gradient decreases from that interval, and the difference is just 10 cm from 50 to 300 years.

			Sea level		
			No sea level	**T_r = 1 yr**	**T_r = 300 yr**
Waves	**T_r = 1 yr**	*BCN*	E,ESE,SE	E,ESE,SE	E,ESE,SE
		GAVÀ	SE,SSE,S,SW	SE,SSE,S,SW	SE,SSE,S,SW
	T_r = 5 yr	*BCN*	E,ESE,SE	E,ESE,SE	E,ESE,SE
		GAVÀ	SE,SSE,S,SW	SE,SSE,S,SW	SE,SSE,S,SW
	T_r = 50 yr	*BCN*	E,ESE,SE	E,ESE,SE	E,ESE,SE
		GAVÀ	SE,SSE,S,SW	SE,SSE,S,SW	SE,SSE,S,SW

Table 7.1.: Waves and sea levels combinations for assessing numerically QDM at the Sant Sebastià (BCN) and Gavà beaches. The elements of the case matrix denote the directional sectors.

Then, **three return periods** have been selected:

- Present mean water level (no storm surge contribution).
- Moderate sea level (1 year return period, around 53 cm).
- Extreme one (300 year return period, around 86 cm).

It has been opted to use these values because they cover the range the applicability of this solution. It must be remarked that **only 33 cm** differ from a return period of 1 to 300 years. These differences are comparable to the wave-induced mass fluxes from waves with a return period of 5 years and a return period of 50 years. Henceforth, the considered scenarios can be stated as consistent and realistic. Higher sea levels and higher waves would imply a kind of QDM that will be out of the scope of its definition, because the required cost and time for withstanding these upper limit conditions may decrease the efficiency of the proposed QDM.

On Tab. 7.1, the effective wave directions are presented (the effective wave directions are those that directly impact on the coastal targets). Therefore, for the Sant Sebastià beach, 27 cases have been analysed, whereas 36 runs have been needed at Gavà.

7.3.3. Flooding and erosion indicators

In order to evaluate the efficiency of such QDM strategies versus the impact of no-action, two indexes have been determined:

1. For the **flooding**, the **percentage** of the **flooded area** (in %) both for the diagnosis situations and the interventions. This means that the lower the coefficient, the more protection capacity against flooding has the emerged area.
2. For the **erosion/sedimentation**, the post-storm available volume has been determined individually for all the scenarios (diagnosis situation and strategies of adaptation/mitigation). Therefore, each final volumes obtained in the adaptation strategies has been compared to the corresponding diagnosis situation. Consequently, as higher the coefficient, more sand volume remains at the post-storm profile for a given QDM strategy. If this number is **over 1**, the **intervention keeps more volume of sand** than the **diagnosis** scenario; on the contrary, if it is under 1, a lower volume remains.

In the Sec. 7.4.3, the flooding costs would be estimated with the same methodology that was used in Ch. 6 (see Sec. 6.2.1). The reference price for the sand availability has been around 17 $euros/m^3$, that includes extraction, transport and deposition at the emerged area.

7.4. Results

In this section it will be shown the results from the Morphodynamic module. Each case study has been analysed separately: firstly, Sant Sebastià (Sec. 7.4.1); secondly, Gavà (Sec. 7.4.2). At each case study, the reference scenario (no intervention) is shown at the beginning and later the QDM implementation. Finally, the estimation of cost reductions is shown in Sec. 7.4.3.

7.4.1. Hazard characterization at Sant Sebastià (Barcelona)

7.4.1.1. Baseline scenario (no intervention)

Erosion and **flooding** has been assessed at 3 different sectors: E, ESE and SE, in accordance with the effective wave directions. Each directional sector is modelled through 3 categories of return period: 1, 5, and 50 years; and 3 categories of sea level return period: no sea level (0cm), 1 and 300 years. These cases span the **range of applicability** of these solutions.

This zone has coarser sediment than the Gavà beach, so the behaviour of the beach is not so dissipative. The three existing structures (Gas Groin in the northern part, detached breakwater in the central part and the breakwater of the Barcelona harbour) enclose the littoral cell. The **red line**, present in all the figures limits the emerged zone of the beach.

The shoreline orientation is such that the selected components (E, ESE and SE) are the ones that affect with significant cross-shore component. From these three directional ranges, the one with a major percentage of extreme waves is the Eastern condition, which, albeit losing frequency in the mean wave regime (0 to $< 2\ m$) of the significant wave height (H_s), does not behave in the same manner in extreme conditions ($H_s > 2\ m$). Henceforth, the directional sector where flooding and erosion cause the greatest impairment is the **Eastern sector**, followed by the ESE sector. The SE sector, apart from reporting waves of lower magnitude, belongs to a sector in which the **protection function** of the infrastructure acts more efficiently .

Three main patterns can be described:

1. The **northern** part of the beach presents a **limited width** at the **most eroded track**, and it is also the most vulnerable one to the extreme agents. In a scenario with **no sea level**, but with a **high return period**, the post-storm **beach width** would be **inadequate**. The eroded material at the emerged part is relocated in areas of over $4 - 5$ meters water depth.
2. At the **shadow area** of the detached breakwater, the sediment of the emerged part and a fraction of the eroded material from the sides are accumulated in shallow waters (between -1 and $-4\ m$), contributing to the **tombolo generation**. See the importance of accumulations (in **red**) at the inshore side of the detached breakwater (Fig. 7.4).
3. The **southern part** of the beach has its weakest spot at the **central** part, where there is a **narrower beach width**. This spot is the most affected by the wave action. Similarly to the other two areas, the eroded sand at the emerged part is accumulated at depths between 0 and $-3\ m$.

The most **unfavourable diagnosis** condition is the one with waves of **50 years** of return period (Fig. 7.3,c). Therefore, it will be specially stressed, due to its importance as an upper limit condition to determine impacts and to design management strategies.

Given a **non-sea level scenario** (baseline scenario), the central part of the tombolo is the most sheltered part from the marine flooding . Greater erosions (over 1 meter) are concentrated at the most sensible points of the northern and southern subzones. The southern zone, being much wider and open, enables an increased entry of flux of hydrodynamic mass and for this reason the water depths are greater next to the seashore.

With a **sea level return period of 1 year**, it can be appreciated that in the case of the Eastern waves, the flood-layer reaches to the same distance inland than at the northern part, but the water level is notably higher (i.e. increase of the flooding magnitude, but not the affected area). The **central part** features important affected areas, which are also associated to remarkable water levels. On the contrary, at the **southern part**, given the **higher sea levels**, the hydrodynamic flux goes into landward, accompanied by water level rises of the order of 20-40 cm near the limit zone. The waves from the ESE and SE sectors show a reduced flooding in comparison

to the eastern case, and the erosion-sedimentation patterns behave in a proportional manner.

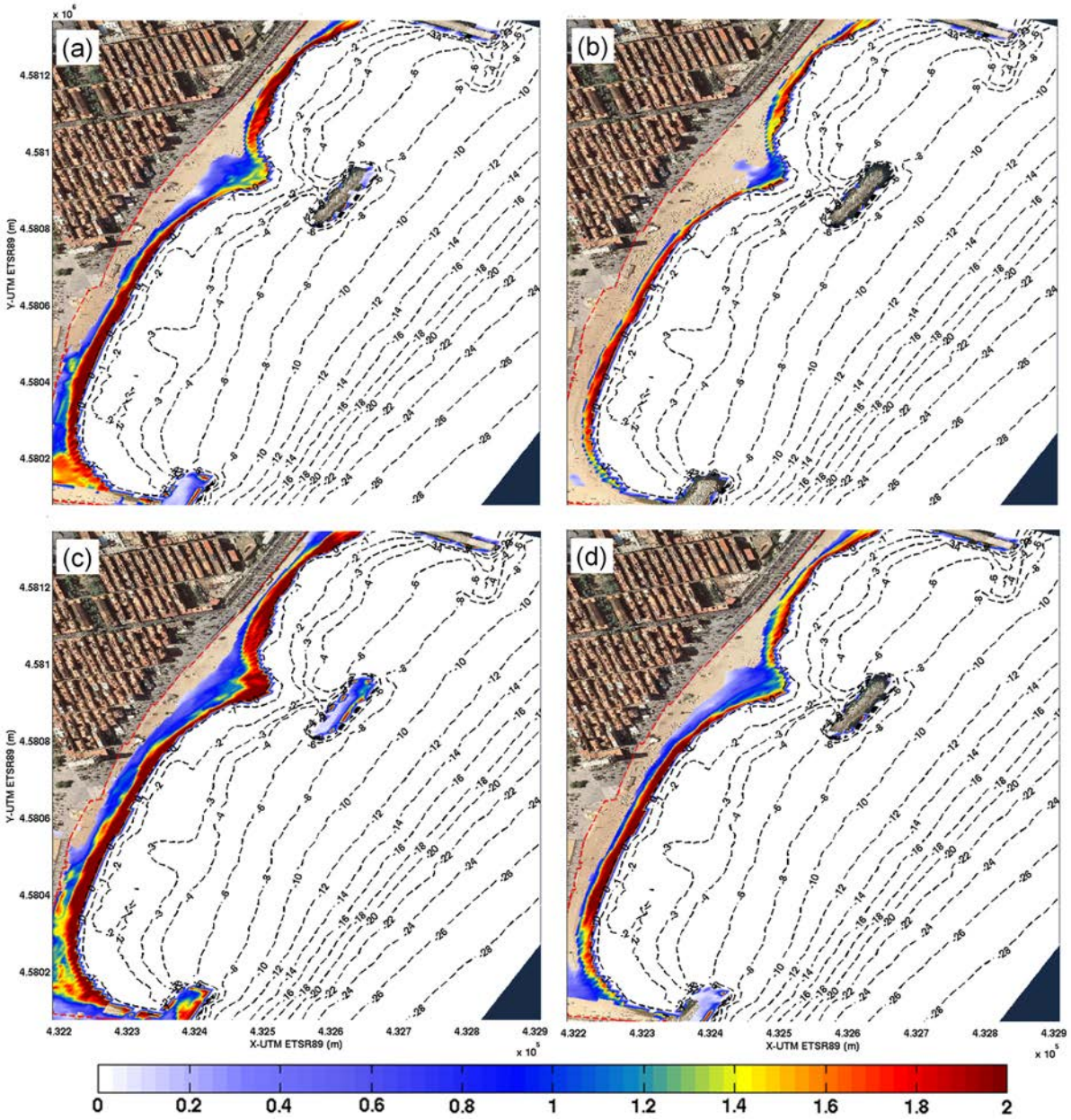

Figure 7.3.: Maximum **flooded** area at the **Sant Sebastià beach** for the **baseline** lay-out. The coloured areas represent the maximum water depth in meters. The discontinuous red line delimits the last line of defence. The four panels have a **sea level** with a $\mathbf{T_r}$ **=300 years**. *(a) Waves with T_r =5 years, with an E direction (90°); (b) Waves with T_r =5 years, with an ESE direction (112.5°); (c) Waves with T_r =50 years, with an E direction (90°); (d) Waves with T_r =50 years, with an ESE direction (112.5°).*

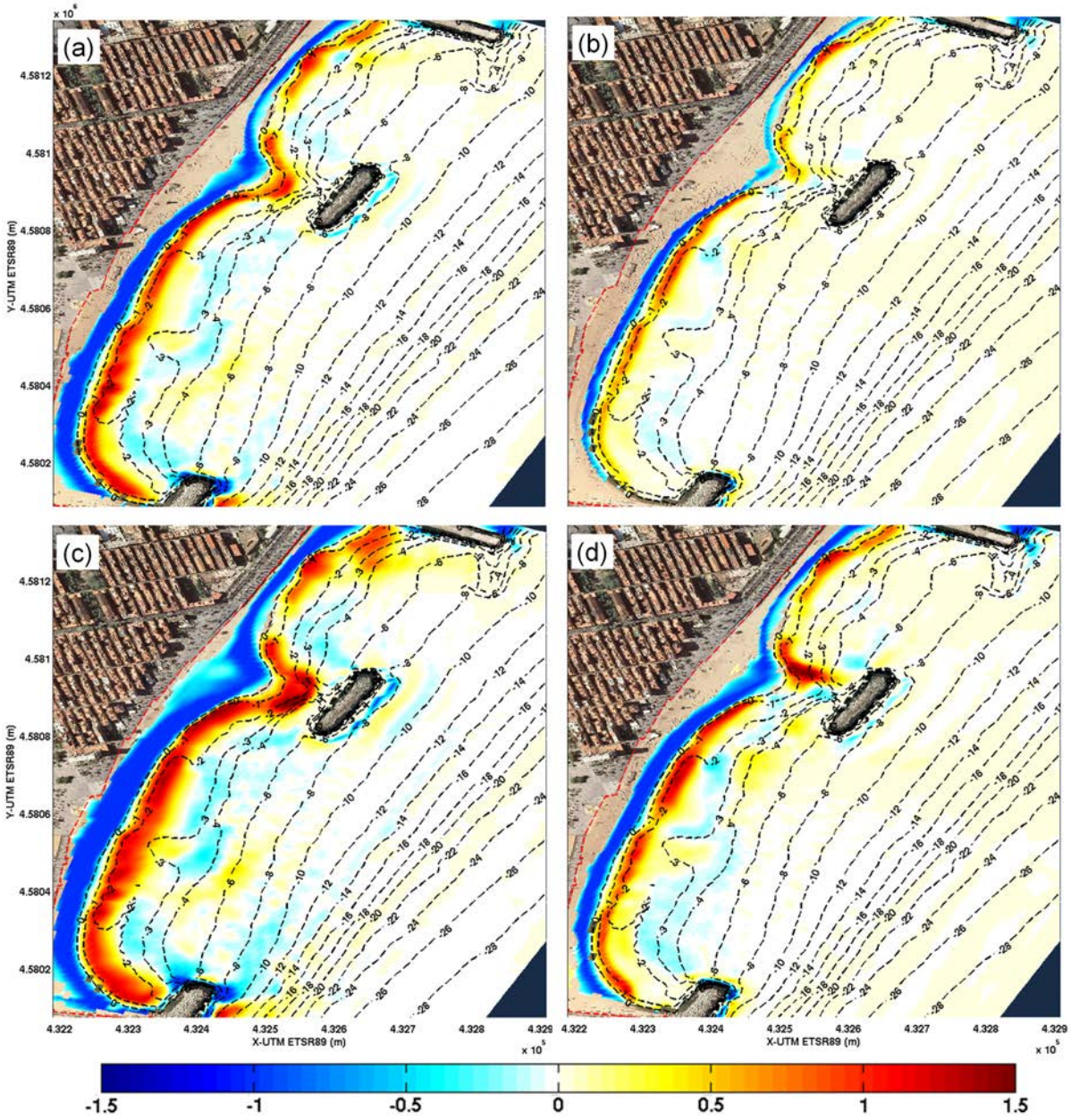

Figure 7.4.: Erosion and sedimentation patterns at the **Sant Sebastià beach** for the **baseline** lay-out. The coloured areas represent, in meters, **erosion** (negative values, **blue**) or **sedimentation** (positive values, **red**). The discontinuous red line delimits the last line of defence. The four panels have a **sea level** with a $\mathbf{T_r}$ **=300 years**. *(a) Waves with T_r =5 years, with an E direction (90°); (b) Waves with T_r =5 years, with an ESE direction (112.5°); (c) Waves with T_r =50 years, with an E direction (90°); (d) Waves with T_r =50 years, with an ESE direction (112.5°).*

The **sea level return period of 300 years** (Fig. 7.3) implies that the area flooded

by the Llevant (eastern) storms gains in magnitude, and that most of the emerged area has a water depth of over 1.5 m. The northern subzone has an almost nil beach width and the southern subzone shoreline retreats significantly. The eroded material remains at similar depths than the cases with lower sea levels (at 0 to $-3\ m$), although remarkable sand transport is modelled.

Nevertheless, at the southern part, the water layer does not surpass the limit of the emerged beach. Even with such high sea levels, the percentage of flooded area in the case of SE waves is in an intermediate situation between the Eastern storms without sea level return period of 1 year.

The results obtained from the simulations indicate that, in the case of the Sant Sebastià beach, the **waves** are the **main hydrodynamic agent**. The high sea levels boost the flooding/erosion but the behaviour of the beach profile implies that the **bed-load transport** has greater **significance** than in Gavà. This statement is based on the sediment dynamics at the swash and surf zone: although the differences in magnitude of the hydraulic offshore forcings for each simulation, the sediment tends to be accumulated between the coastline and the isobath $-3\ m$, rather than being homogeneously advected across the entire active cell (from 0 to $-6.5\ m$ water depth).

In the **no sea level scenario**, two associated issues have been determined for the Sant Sebastià beach: at the **northern** part, the lack of **beach width** leads to enhanced flooding at the emerged zone, thus causing the **flooding layer** to reach the promenade. The subpartition has a **highly erosive behaviour**, apart from being partially decoupled from the general littoral dynamics, given the presence of the Gas breakwater, and the semi-tombolo originated at the Sant Sebastià beach. Consequently, the sea storms mobilize seaward the sediment from the emerged part, so harnessing the recovery of such material.

The southern part has a similar behaviour, with a critical point at its midpoint where the width is the narrowest. This area tends to suffer erosion from the joint action of (i) the wave diffraction caused by the Barcelona Harbour breakwater and (ii) the detached breakwater. In these transects, the cross-shore component becomes the main morphodynamic driver. At both sites, the effect of the sea level reinforce this pattern due two factors: (i) a loss of the existing emerged (defence) area (Fig. 7.4); and, (ii) as the water level increases, the **waves break inlandwards**. This can induce lower dissipation in breaking, thus increasing the contribution of the wave radiation tensor in the momentum balance equations (see Sec. 3.3.3.2). The higher the radiation tensor, the higher the sediment fluxes and, consequently, the lower the area resilience.

7.4.1.2. Evaluation of QDM strategies

The diagnosis situation has served to assess numerically the possible interventions under extreme events (high waves plus high sea levels).

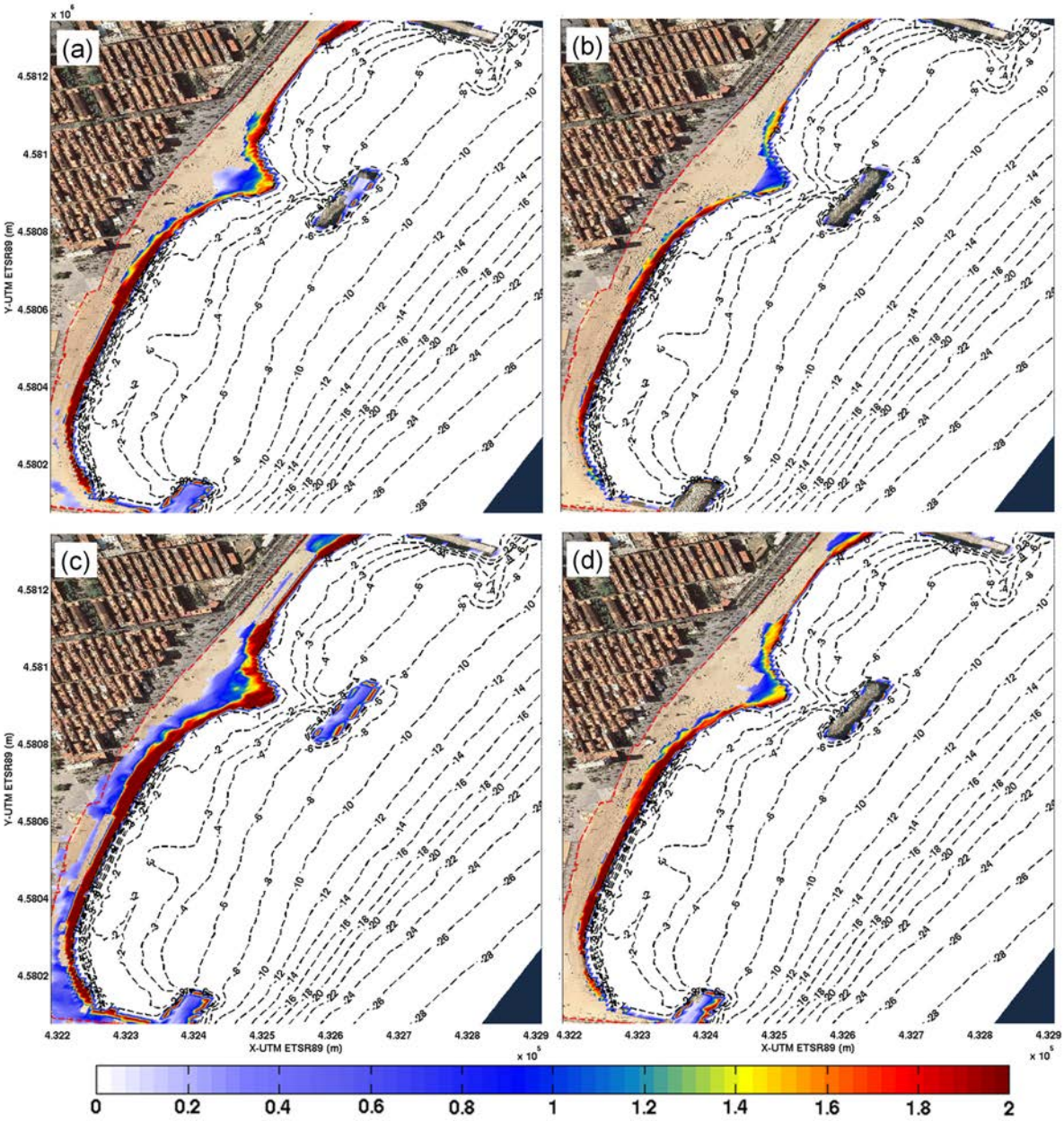

Figure 7.5.: Maximum **flooded** area at the **Sant Sebastià beach** for the **transient dune** lay-out. The coloured areas represent the maximum water depth in meters. The discontinuous red line delimits the last line of defence. The four panels have a **sea level** with a $\mathbf{T_{r,MWL}}$ **=300 years**. *(a) Waves with T_r =5 years, with an E direction (90°); (b) Waves with T_r =5 years, with an ESE direction (112.5°); (c) Waves with T_r =50 years, with an E direction (90°); (d) Waves with T_r =50 years, with an ESE direction (112.5°).*

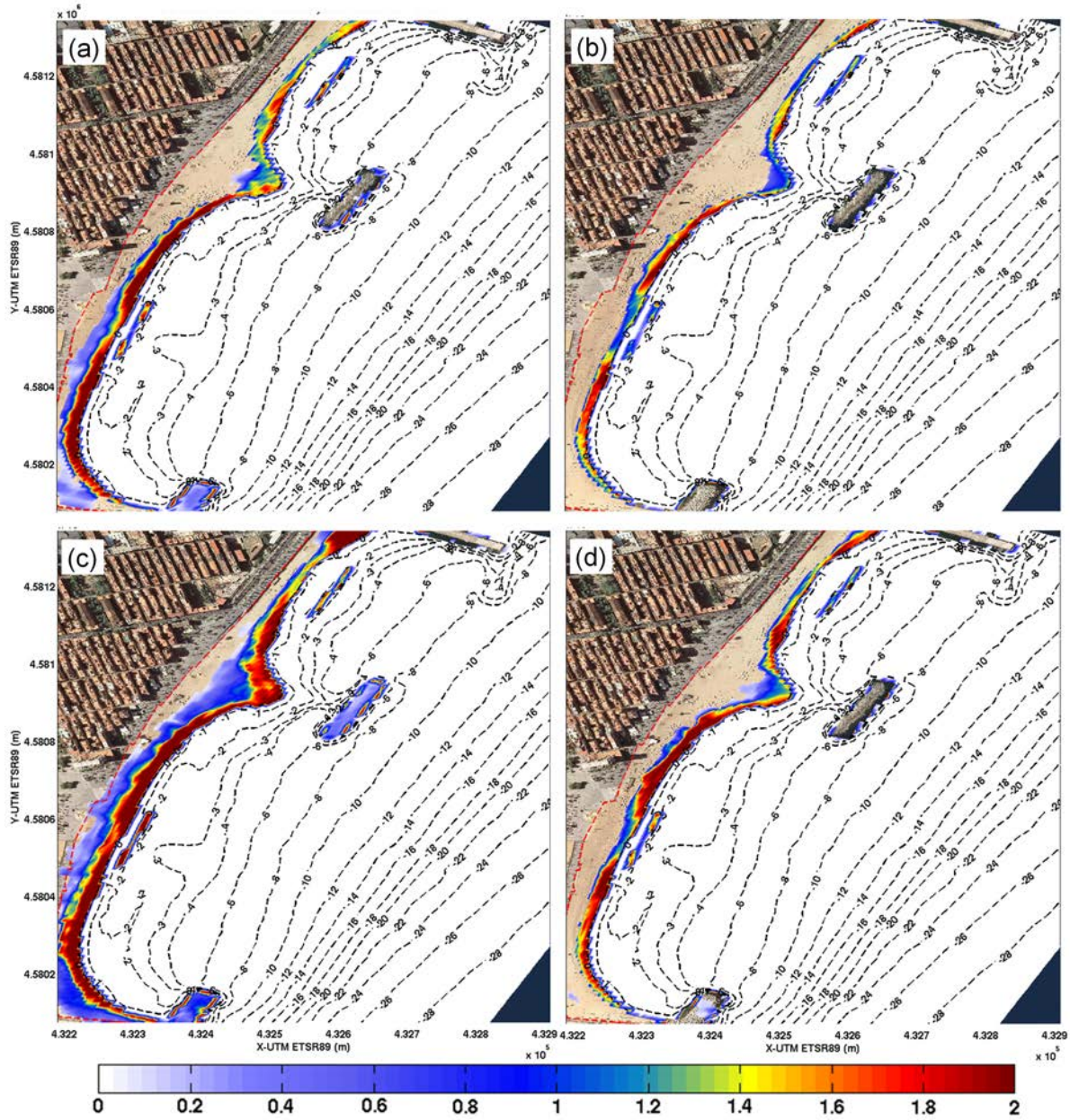

Figure 7.6.: Maximum **flooded** area at the **Sant Sebastià beach** for the **detached breakwater** lay-out. The coloured areas represent the maximum water depth in meters. The discontinuous red line delimits the last line of defence. The four panels have a **sea level** with a $\mathbf{T_{r,MWL}}$ **=300 years**. *(a) Waves with T_r =5 years, with an E direction (90°); (b) Waves with T_r =5 years, with an ESE direction (112.5°); (c) Waves with T_r =50 years, with an E direction (90°); (d) Waves with T_r =50 years, with an ESE direction (112.5°).*

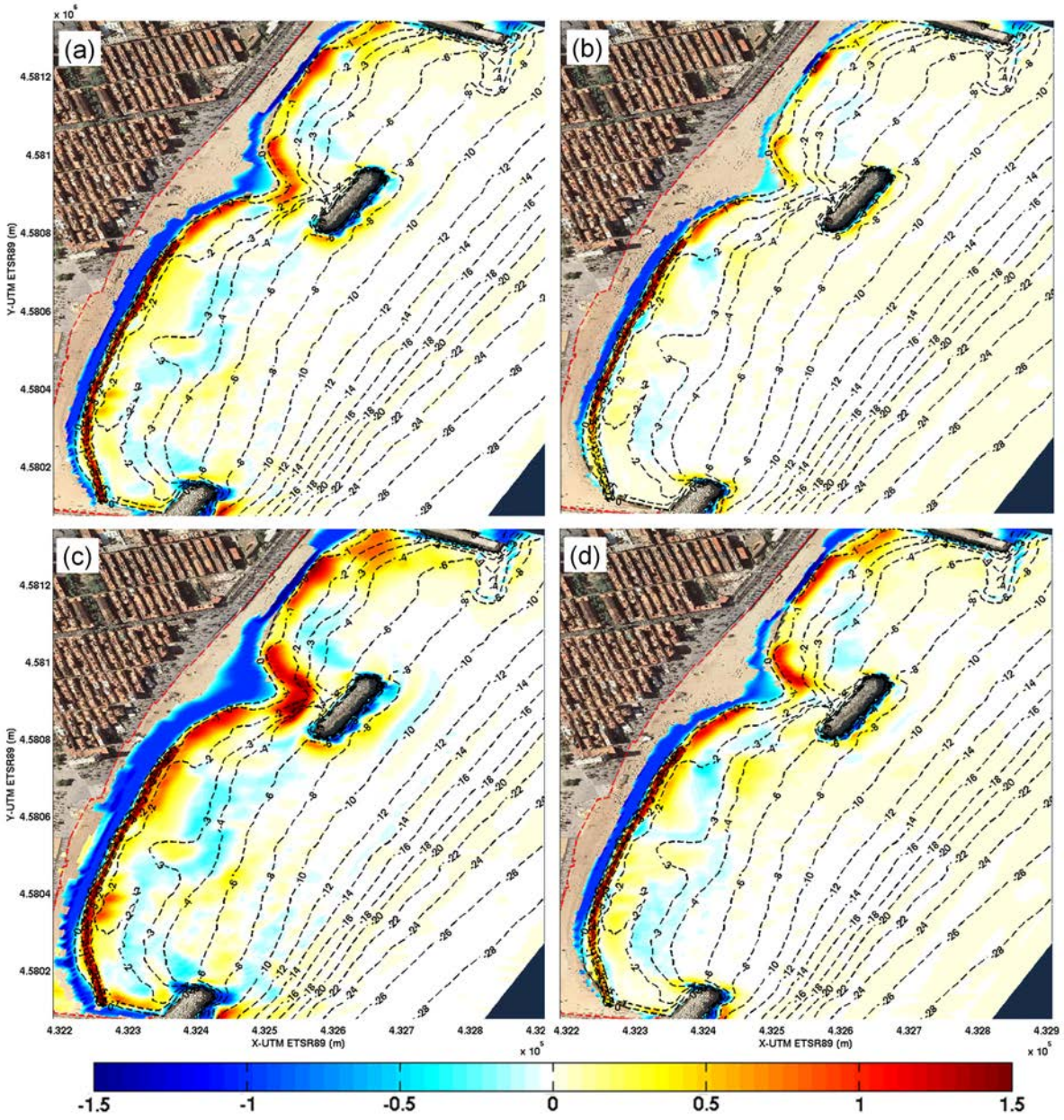

Figure 7.7.: Erosion and sedimentation patterns at the **Sant Sebastià beach** for the **transient dune** lay-out. The coloured areas represent, in meters, **erosion** (negative values, **blue**) or **sedimentation** (positive values, **red**). The discontinuous red line delimits the last line of defence. The four panels have a **sea level** with a $\mathbf{T_{r,MWL}}$ **=300 years**. *(a) Waves with T_r =5 years, with an E direction (90°); (b) Waves with T_r =5 years, with an ESE direction (112.5°); (c) Waves with T_r =50 years, with an E direction (90°); (d) Waves with T_r =50 years, with an ESE direction (112.5°).*

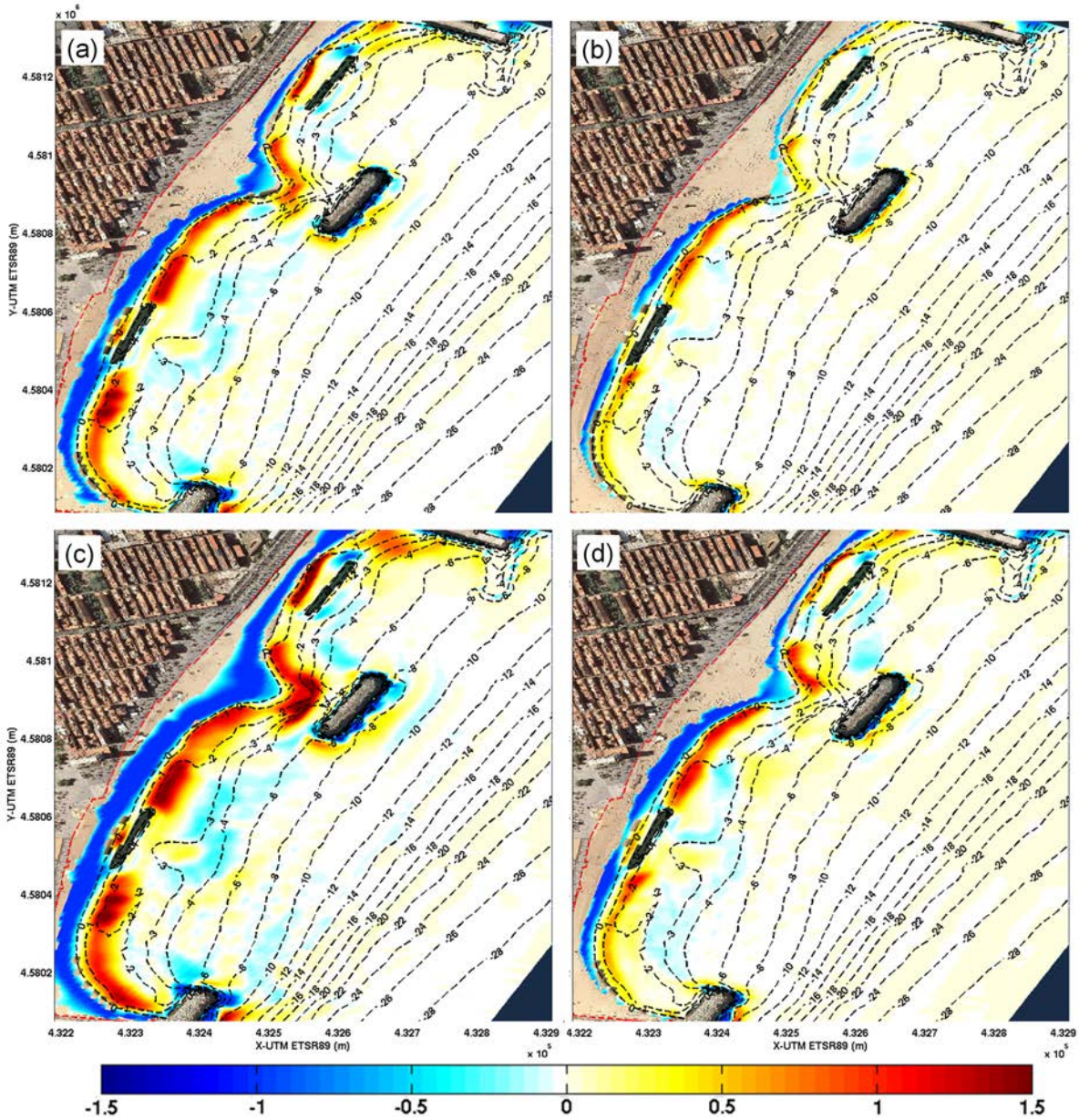

Figure 7.8.: Erosion and sedimentation patterns at the **Sant Sebastià beach** for the **detached breakwater** lay-out. The coloured areas represent, in meters, **erosion** (negative values, **blue**) or **sedimentation** (positive values, **red**). The discontinuous red line delimits the last line of defence. The four panels have a **sea level** with a $\mathbf{T_{r,MWL}}$ **=300 years**. *(a) Waves with T_r =5 years, with an E direction (90°); (b) Waves with T_r =5 years, with an ESE direction (112.5°); (c) Waves with T_r =50 years, with an E direction (90°); (d) Waves with T_r =50 years, with an ESE direction (112.5°).*

Two QDM strategies have been developed for the Sant Sebastià beach in its most conservative configuration, which is the storm season. Both aim to minimize/mitigate

episodic coastal risk, but, at the same time, they consider a future situation of optimizing natural, energy and economic resources, by focusing on endogenous sources. Two alternatives have been proposed (i) a transient dune system and (ii) two transient detached dams.

The dune system, parallel to the shoreline, is based on the following:

A **dune system** with the following dimensions for the northern part (140 m alongshore, trapezoidal cross-section and mean height of 1.5 m, 3 m wide at the crest) and the southern part (400 m long, trapezoidal cross-section and mean height of 1.5 m and 2 m wide at the crest). The dune slope is the same for the offshore and onshore sides. Note that the dune crest varies between a maximum of 1.8 m at the most unfavourable part (middle point of the southern part) and a minimum of 1.2 m at the part where a greater beach width is present. In total, the necessary sand volume is about $7.5 \mathring{u} 10^3$ m^3.

It serves as a mitigation strategy against **floods**, locating a greater crest height at the spots where greater wave incidence is expected (Fig. 7.5).

The sediment of the dune system comes from the submerged part (0 to -2 m deep), generating a submerged trench at the southern part of the beach. The material does **not come** from **dredging** neither from **extraction areas** at **great distances**, thus reducing the costs and the emissions related to extraction and transport. The objective of the trench, in its turn, is to act as a sand trap, in a way that once the dune system collapses, the material mobilizes seaward and fills the levelled site (Fig. 7.7). Hence, the sediment of the dune stays at more accessible depths that enable sand recovery at the periodical replenishment of such defence system. It provides additional material for the emerged part in an erosive area (CIIRC, 2010).

On the other hand, the two transient detached low-crested breakwaters are based on:

Two detached breakwaters, parallel to the shoreline, with individual dimensions of 140 m alongshore and a semi-ellipsoidal section (major semi-axis of 7 m, and minor semi-axis of 1.7 m). Such detached breakwater can be constituted by a group of geotextile bags full of sand, water or other types of fluid.

They aim to attenuate the wave-action at their shadow zone (Fig. 7.6). Hence, there is lower mobility. Furthermore, they act as sediment retention barriers at water depths between the detached breakwater and the emerged zone. Consequently, the post-storm sand recovery of the emerged part is more feasible.

Even under high sea level, certain extreme waves would start to break offshore (at crest height of the structure). This behaviour does not happen at the diagnosis situation.

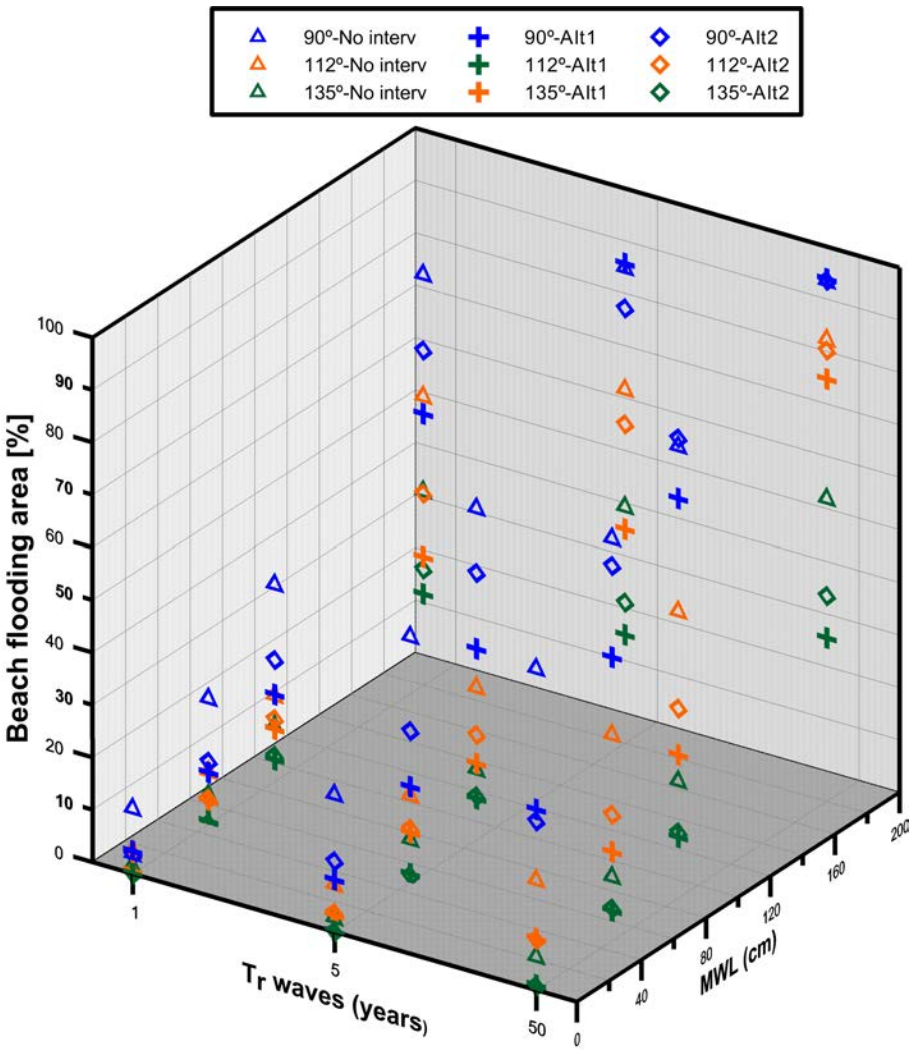

Figure 7.9.: Percentage of beach to be **flooded** (vertical axis) for the different **QDM**, regarding the marine drivers: **waves** (return period,$T_{r,waves}$, in years) and sea level (**MWL**). **Symbols:** the triangles represent the no-intervention option; the crosses are for the alternatives with dune system and the diamonds represent the solution with transient detached dams. The colour for each symbol stands for each wave direction.

This system can also store sand within the detached breakwaters (Fig. 7.8). Thus, once the storm season finishes, the filling material can be redistributed on the emerged part, just in time to be prepared for the bathing season.

Fig. 7.9 summarises all the simulations that were conducted at Sant Sebastià. It can be clearly seen that the **flooded volumes** are much **higher** in the **diagnosis** situation (triangles) **than** in the **QDM** alternatives. Therefore, in case of flooding, the **transient dune** is the option that presents the **lowest flood risk**, whereas the **detached breakwater** presents a **subtly better** result than the do-nothing

scenario. This trend is confirmed with the different directional sectors. The efficiency regarding floods (vertical distance between comparable scenarios) gains importance from sea levels and wave return periods greater or equal to 0.53m and 5 years, respectively. QDM strategies are feasible with lower hydro-dynamical conditions, but their performance lowly differs with the reference scenario.

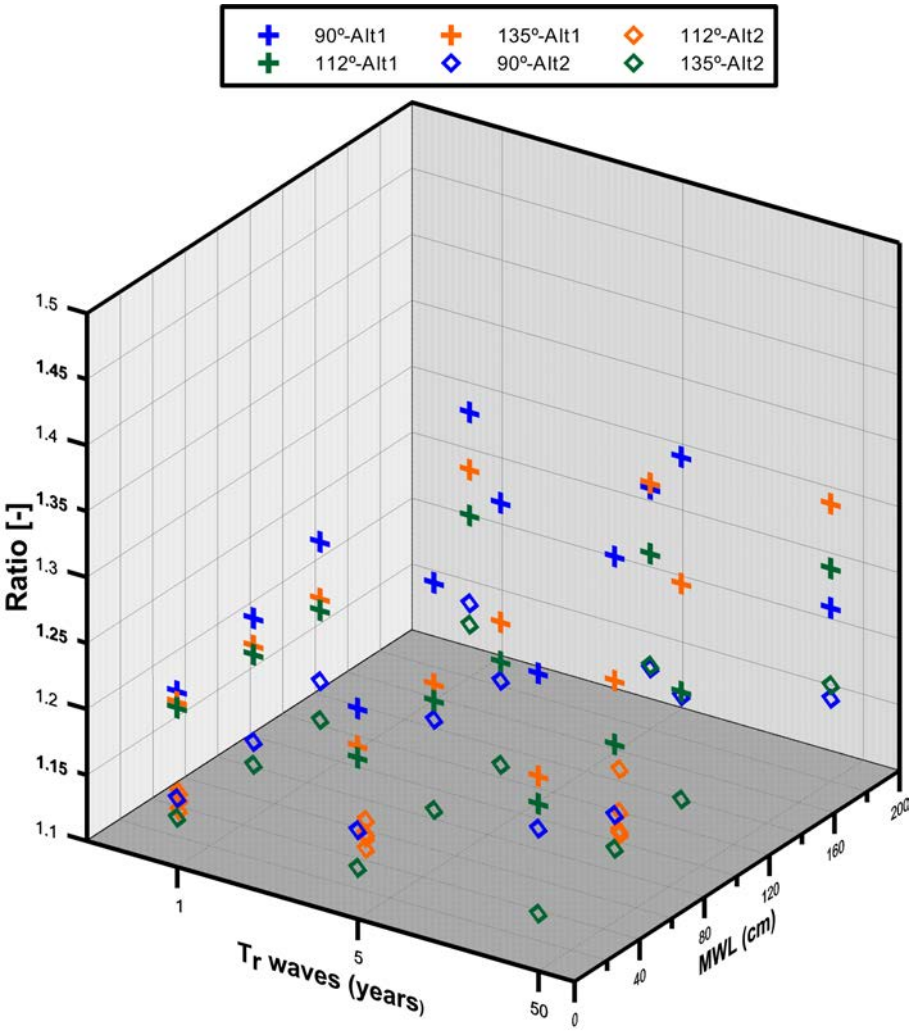

Figure 7.10.: Conservation ratio of the **final volume** of the beach (vertical axis) for the different **QDM**, regarding the marine drivers: **waves** (return period,$T_{r,waves}$, in years) and sea level (**MWL**). **Symbols:** the crosses represent the ratio between the volume kept with a dune system and the no-intervention scenario, the diamonds represent the same ratio between the solution with transient detached breakwaters and the diagnosis scenario. The colour for each symbol stands for each wave direction.

7.4.2. Hazard characterization at Gavà

7.4.2.1. Baseline scenario (no intervention)

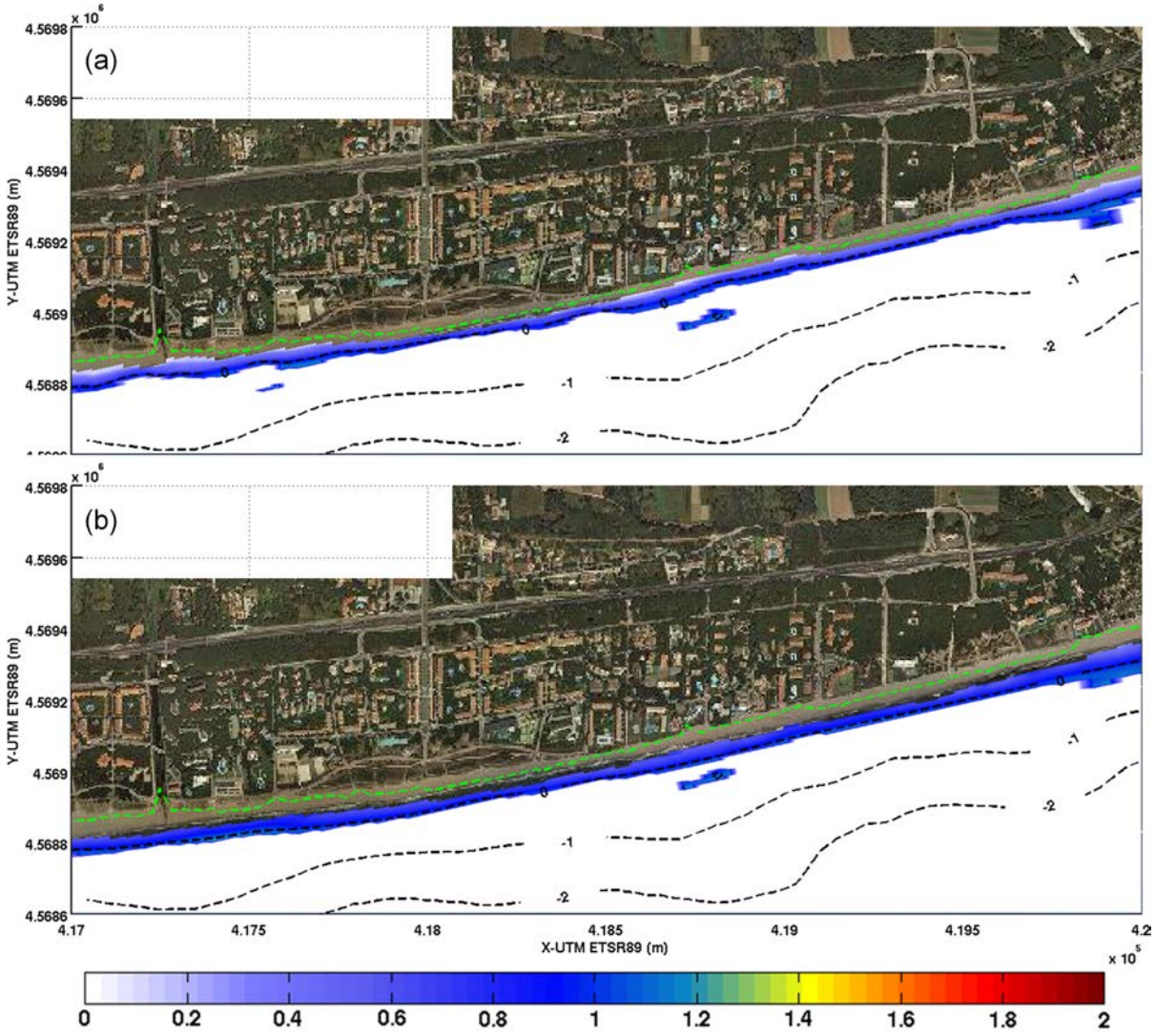

Figure 7.11.: Maximum **flooded** area at the **Gavà beach** for the **baseline** lay-out (a) and the **transient dune** lay-out (b). The coloured areas represent the maximum water depth in meters. The discontinuous green line delimits the last line of defence. The two panels have a $\mathbf{T_{r,MWL}}$ **=1 year** and a $\mathbf{T_{r,waves}}$ **= 5 years**, with an SSE direction (157.5°).

The analysis of the erosion and flooding has been addressed at 4 directional sectors: SE, SSE, S and SSW, in accordance with the effective wave directions. Each directional sector has been modelled with 3 categories of $T_{r,waves}$: 1, 5 and 50 years; and 3 categories of $T_{r,MWL}$: 0cm, 1 and 300 years.

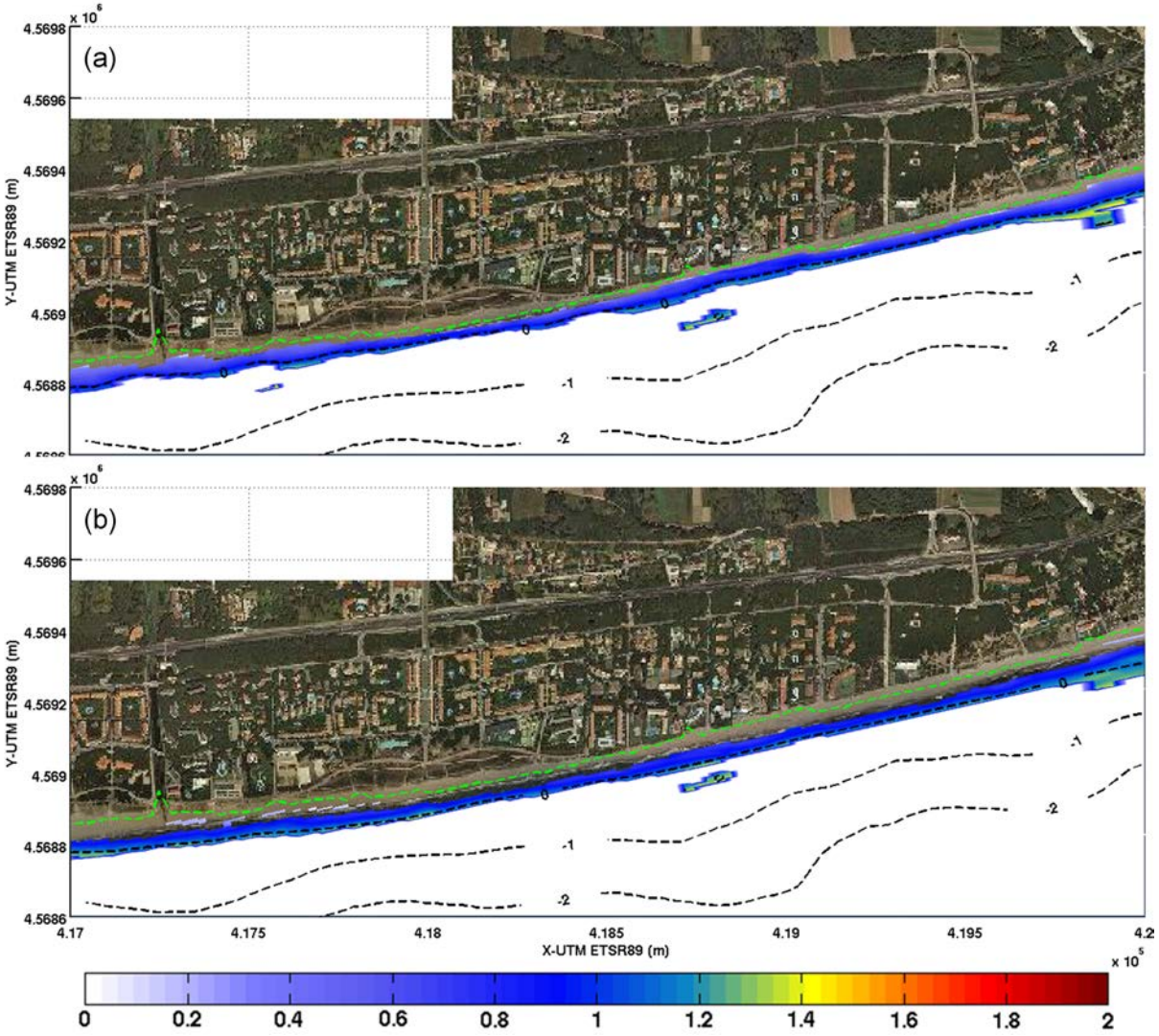

Figure 7.12.: Maximum **flooded** area at the **Gavà beach** for the **baseline** (a) and the **transient dune** lay-outs (b). The coloured areas represent the maximum water depth in meters. The discontinuous green line delimits the last line of defence. The two panels have a **sea level** with a $\mathbf{T_r}$ **=1 year**. Waves with $T_r = 50$ years, with an SSE direction (157.5°).

In case of low (or no) sea level , given that the SSW directional sector is the most frequent (Fig. 2.3), there is significantly more flooding and erosion in this sector than the other ones. In contrast, the sector SE is the one with fewer consequences regarding wave extremes. This statement is reinforced by the fact that the magnitude of the erosion/flooding pattern, even for wave high return periods (i.e. 50 years), is subtly lower than in other directional sectors.

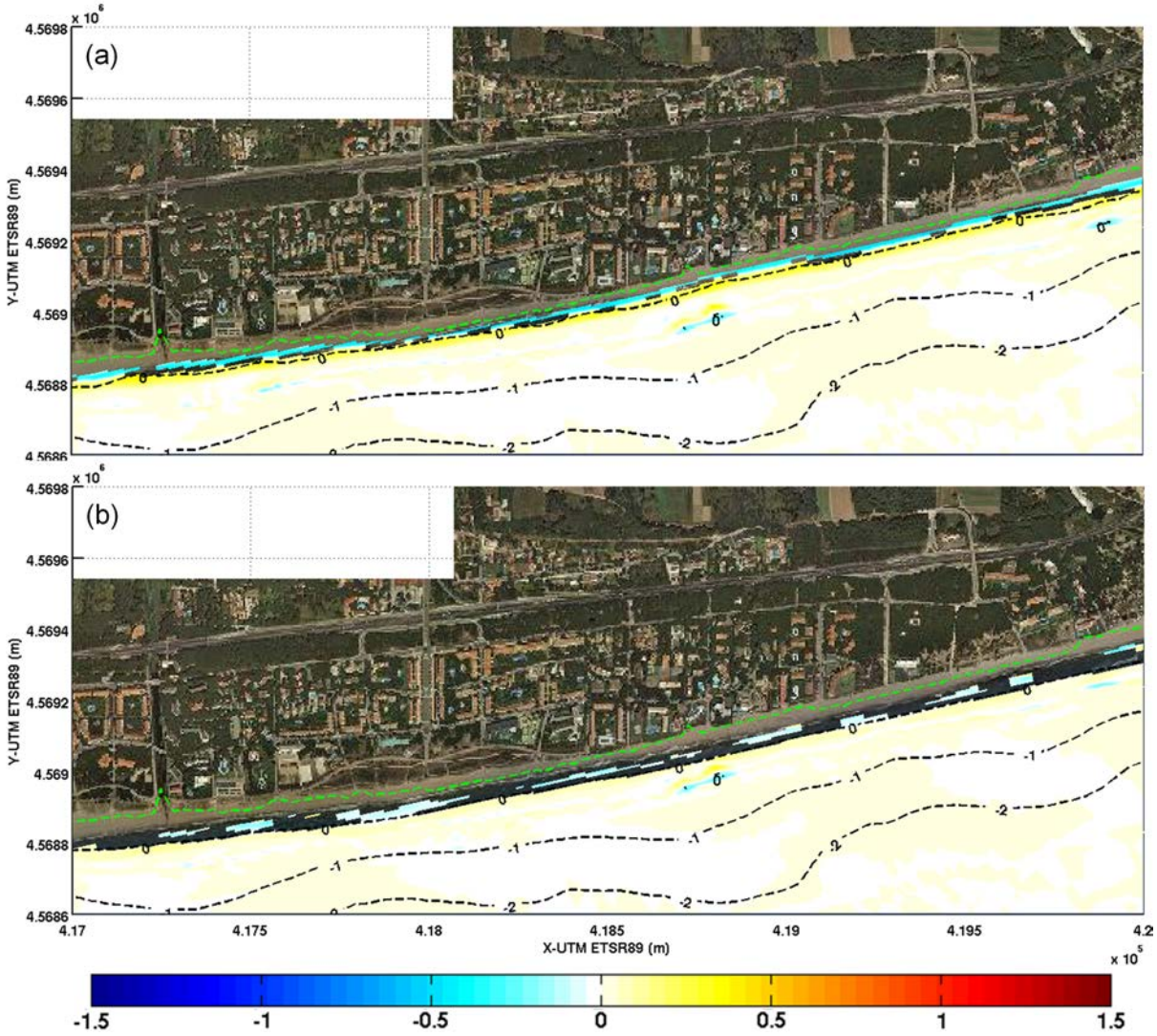

Figure 7.13.: Erosion and sedimentation patterns at the **Gavà beach** for the **baseline** (a) and the **transient dune** lay-outs (b). The coloured areas represent, in meters, **erosion** (negative values, **blue**) or **sedimentation** (positive values, **red**). The discontinuous green line delimits the last line of defence. The two panels have a **sea level** with a $\mathbf{T_r}$ **=1 year**. Waves with $\mathbf{T_r}$ **= 5** years, with an SSE direction (157.5°).

However, once reached a return period of 1 year, the sea level becomes a relevant factor for both flooding and erosion (Fig. 7.11). The wave directionality influence is diminished once the sea level gains importance. This trend is given by the **dissipative behaviour** of this beach: wave energy is significantly dissipated through wave breaking, thus its sand transport capacity have lowered prior to reach the emerged part (Fig. 7.13). Additionally, a high sea level implies that the beach profiles become submerged once adapted to the emerged zone, due to the reconfiguration by

the incident waves. The shallower depths at the flooded area are balanced with high velocity modulus, which can mobilise material. However, as stated earlier, sand is transported due to the joint action of (i) the emerged beach slope (with steeper slopes), (ii) overtopping driven by high sea level and waves, and (iii) wave-induced currents. Hence, the post-storm profile tends to a classical Vellinga (1986) profile (Fig. 7.14).

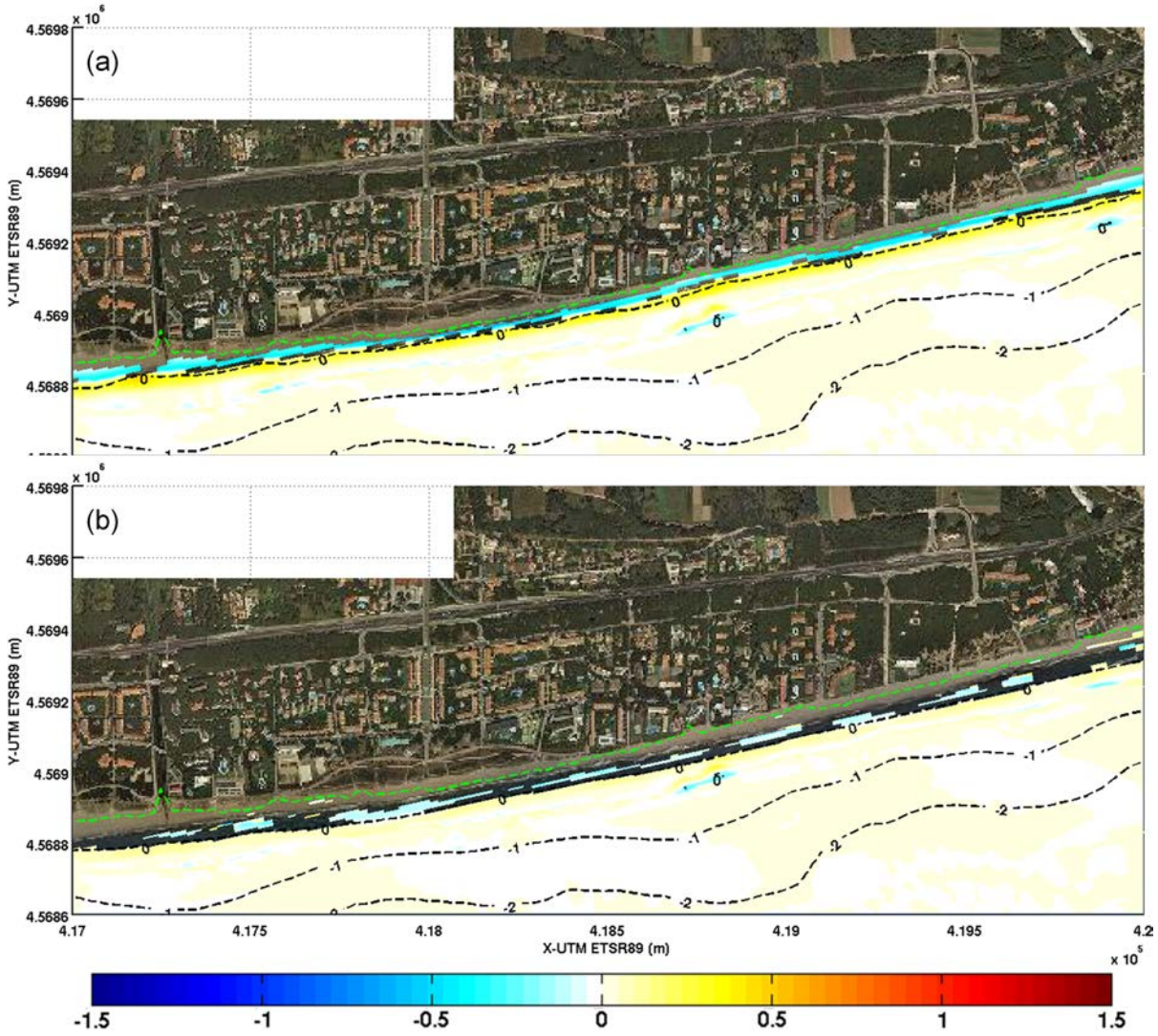

Figure 7.14.: Erosion and sedimentation patterns at the **Gavà beach** for the **baseline** (a) and the **transient dune** lay-outs (b). The coloured areas represent, in meters, **erosion** (negative values, **blue**) or **sedimentation** (positive values, **red**). The discontinuous green line delimits the last line of defence. The two panels have a **sea level** with a $\mathbf{T_r}$ **=1 year**. Waves with T_r = 50 years, with an SSE direction (157.5°).

Note that the main defence line of the beach, the existing dune system (green line

in all the figures) is not surpassed even with high wave return periods (50 years). Consequently, the existing dune system seems to resist/withstand water levels of up to 53 cm (1 year return period). According to the Sallenger (2000) scale, in these cases, the emerged profile would be in **collision** morphodynamic state.

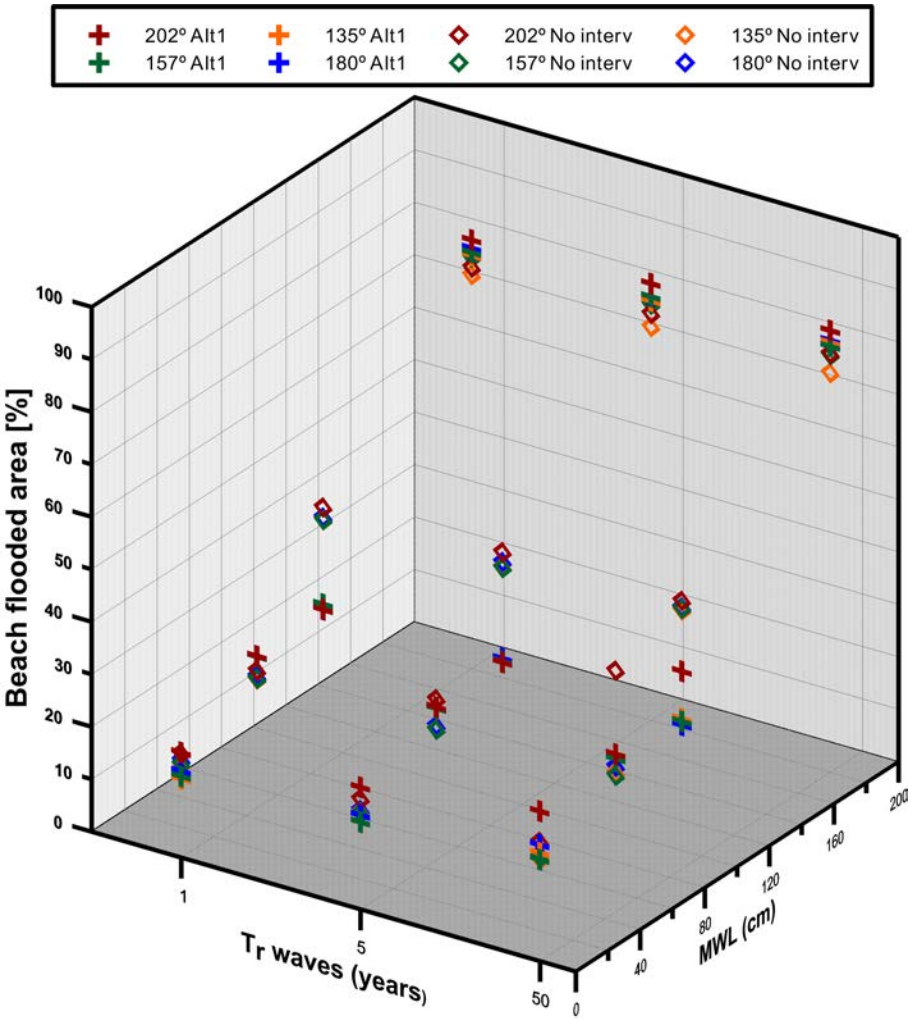

Figure 7.15.: Percentage of beach to be **flooded** (vertical axis) for the diagnosis situation and the QDM strategy proposed for **Gavà**, regarding the hydrodynamical agents: waves (return period,$T_{r,waves}$, in years) and sea level (return period, $T_{r,MWL}$, in years). **Symbols:** the diamonds represent the no-action option; the crosses are for the alternatives with transient dune plus beach nourishment. The colour for each symbol stands for each wave direction.

Nonetheless, for a sea level return period of 300 years and when SSW waves have a return period of 50 years, this defence line is surpassed at the northern part (from Llançà street to Premià de Mar street) and at the central part (Gavà Mar) of the beach. In this particular case, the high sea level plus the run-up and the wave set-

up, does it causes sea surface elevation enough as to overtop the dune. With these hydrodynamic conditions, the defence can be partially (overwash regime in Sallenger (2000)) or totally collapsed (inundation regime) in certain areas. Nevertheless, as it can be observed at other wave conditions (either from other sectors or with lower magnitudes), the post-storm profile with the present dune zone would still be able to protect the hinterland (Fig. 7.12). At those cases, though, the post-storm beach width would be insufficient for recreational uses.

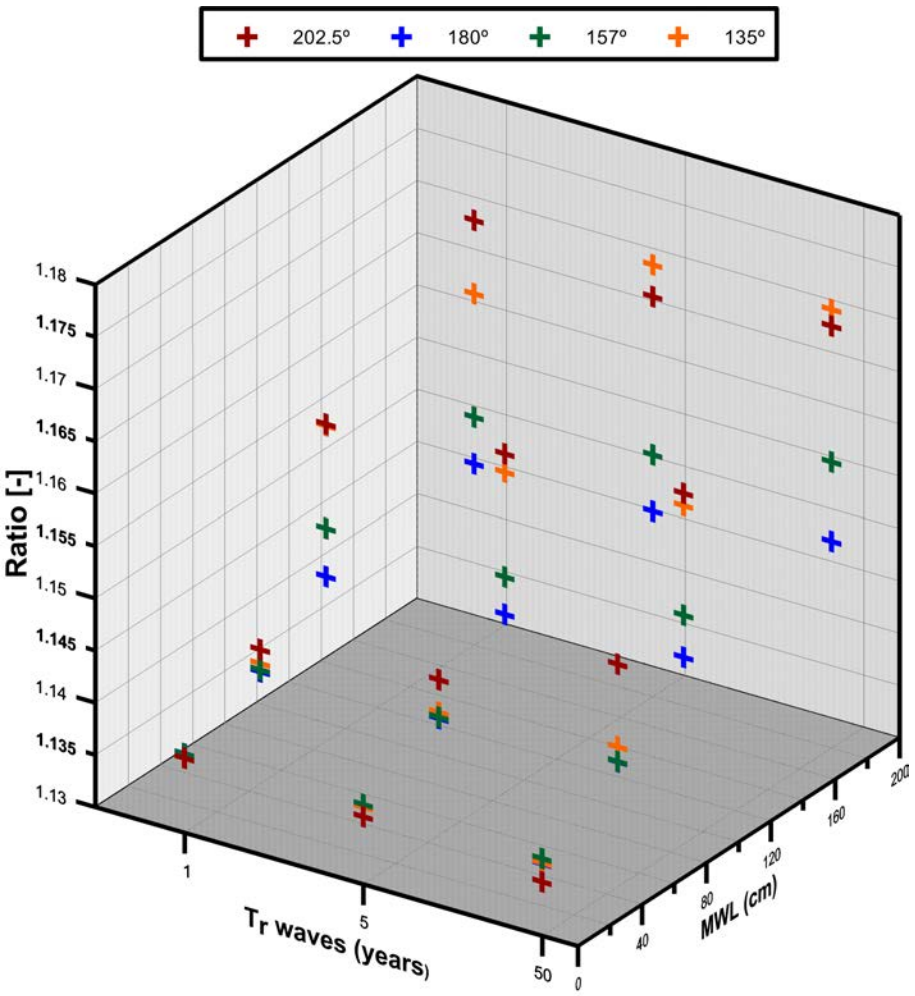

Figure 7.16.: Ratio of conservation of the **final beach volume** (vertical axis) for the QDM strategy proposed for **Gavà**, regarding the hydrodynamical agents: waves (return period,$T_{r,waves}$, in years) and sea level (return period, $T_{r,MWL}$, in years). **Symbols:** the diamonds represent the no-action option; the crosses are for the alternatives with transient dune plus beach nourishment. The colour for each symbol stands for each wave direction.

7.4.2.2. Evaluation of QDM strategies

The Gavà beach is a low-lying dissipative beach in which sea level has a primary role (joint with storm waves) for flooding and erosion. The different directional sectors drives flooding/erosion patterns of similar orders of magnitude, except in the case of the **SSW** direction, which shows an **increase** of the **flooded** area at the **northern** part of the domain. The tract is already in an erosive state which will be boosted by Climate Change (see Sec. 2.4.4.2). With the aim of maintaining enough beach width for protection against extreme sea regimes, the combination of two interventions is proposed:

1. A beach nourishment of $50 \cdot 10^3$ m^3 that increases beach width, to ensure a minimum of 30 m. The lifetime has been estimated in 15 years. Additionally, this material has to be deployed in a way that generates a smoother coastline in which the alongshore gradients are minimized.
2. A transient dune belt of $45 \cdot 10^3$ m^3, located as a defence line, parallel to the current dune system. Such transient dune would contribute to a coastal defence with a limited lifetime, besides of acting as an additional sand buffer for maintaining the minimal width of the emerged beach. Such intervention would have an alongshore length of 3.4 km and its cross-shore section (transect) would consist in a trapezoid; its mean height and crest width are 1.5 and 3 m, respectively.

In contrast to Sant Sebastià beach, in which the QDM interventions tend to show a better behaviour than in Gavà, the dune plus nourishment solution shows a better performance under high sea level (return period of 300 years). This is because the emerged beach area in the intervention is greater than in the diagnosis case, as the $50 \cdot 10^3$ m^3 nourishment homogenises the minimum width of 30 m. Consequently, its performance is lower than in Sant Sebastià beach (i.e. because the emerged area at Sant Sebastià remains constant).

However, the noteworthy difference in the high sea level case (return period of 300 years) demonstrates that the transient dune contributes to the protection of the emerged zone, thus reinforcing the present defence line (Fig. 7.15). It should be added that the **wave directionality** is not clearly discriminatory, then showing similar indexes for the whole range of analysed directions; except at the SSW direction, in which the highest flood-risk values are present in all the scenarios.

Despite that directionality does not lead to important differences in flood-risk, it does so for the post-storm volumes. More efficiency is found at the SSW sector, in which the waves are more extreme. This means that the transient dune and the nourishment are able to reduce the sediment flux more efficiently than the no-action layout. The differences (in the vertical axis) between directional sectors increase as the sea level increases. When the levels are relatively low period (0.53 m, 1 year return period), it is observed that the greater return periods (50 years, Fig. 7.14) exhibit better performance than the lower return period waves (Fig. 7.13).

Nevertheless, in all these cases the erosion ratio stays positive and, thus, the management strategies are able to reduce the erosive flux that the combination of extreme waves plus sea levels can cause to the Gavà beach (Fig. 7.16).

7.4.3. Risk reduction quantification

In the previous section has been shown that QDM can diminish coastal hazards at two beaches. Once the performance has been bounded, the economical feasibility needs to be assessed. With that aim, it has been estimated the cost of the implementation.

QDM type	Construction proceedings	Cost (K euros)
BCN - Dune	7.5 K m^3 Terrestrial	65
	7.5 K m^3 Maritime	130
BCN - Detached	(28 elements)	200
Gavà - Dune and nourishment	95 K m^3 Terrestrial	1330
	95 K m^3 Maritime	1530

Table 7.2.: Estimation of the implementation of the QDM proposed in this Chapter. **Legend:** BCN (Sant Sebastià) and Gavà. Cost in thousands of euros.

Two modes of construction proceedings have been considered: terrestrial and maritime. Extraction (via quarry or dredging), transport, building, human resources, machinery and material have been included in the price.

At Barcelona has been considered that the $7.5 \cdot 10^3$ m^3 of sand would be extracted from the submerged beach (trench at the swash zone). At Gavà, however, $95 \cdot 10^3$ m^3 need to be exported from other sites. That is the reason for the significant price difference: almost 15 $euros/m^3$ in Gavà, whereas at Barcelona is around 9.3 $euros/m^3$. For the latter case, it has been considered that the nourished sand would be equivalent to the native one ($D_{50} = 300$ μm).

In the case of the two detached breakwaters, each breakwater will be composed by 14 elements with the following properties: cylindrical geotextile non woven heavy-duty polyester, with dimensions $3\,m\,\emptyset \times 20\,m$ long. Material, sand filling and installation costs are included. The **order of magnitude** of the prices **matches** with **former international initiatives** (Restall et al., 2002; Hornsey et al., 2011).

The total estimation of the costs is summarised in Tab. 7.2. Prices were obtained from the ITeC (The Catalonia Institute of Construction Technology) database, construction projects and product catalogues. In those cases in which the reference price was outdated, it has been corrected with the inflation trend.

7.4.3.1. Barcelona

The joint action of extreme waves and sea levels can drive important flood losses (Fig. 7.17). The higher the wave and sea level return period, the higher the losses. Wave directionality also influences notably. The East direction with high return period is the one that leads to higher damages. Maximum losses are $320 \cdot 10^3$ *euros*. However, lower costs are predicted for the SE sector (less than $150 \cdot 10^3$ *euros*).

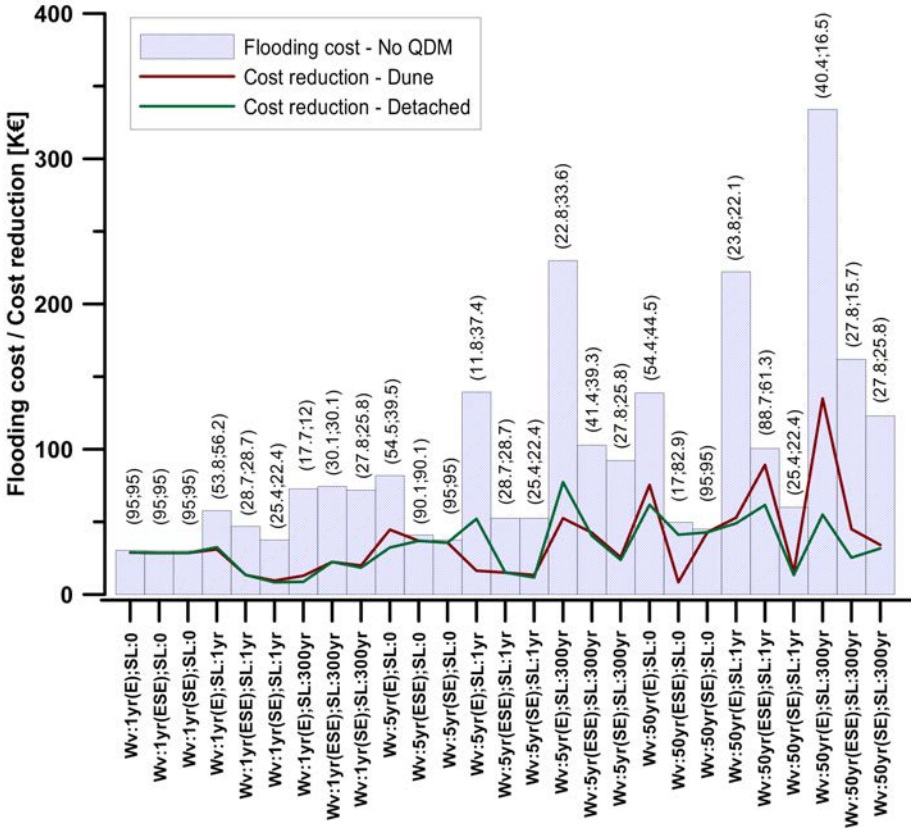

Figure 7.17.: Flooding costs versus reductions associated to particular QDM in **Barcelona** beach. The **blue bar** charts represent the flooding cost (in thousands of euros). The number at the top of the bar represent the percentage of the total flooding cost that can be reduced with the QDM. **Legend:** (dune reduction; detached breakwater reduction). The solid lines represent the reduction of the flooding costs due to the implementation of QDM. The dark red line refers to the Dune QDM and the dark green to the detached breakwaters. The x-axis labels the hydrodynamic conditions for each case. **Symbols:** *"Wv (return period in yr; wave direction); SL (return period in yr)".*

The detached breakwater performs equal or slightly better than the dune under **low sea levels**. The cost reduction due to the detached breakwater remains fairly stable, regardless of the hydrodynamic conditions (the average cost reduction is

50ů10^3 *euros*, with deviations of $\pm 30 \cdot 10^3$ *euros*). However, the dune shows a similar mean trend, but it is more efficient against **high sea levels** (reaching reductions of $125 \cdot 10^3$ *euros* for $T_{r,waves} = 50\ yr$ and $T_{r,MWL} = 300\ yr$). The detached breakwater breaks the waves and diminishes the hydrodynamic loads (run-up and overtopping) that enters into the emerged area. As the sea level increases, freeboard increases and wave damping attenuates. The dunes, though, protect the rearside assets until they collapse.

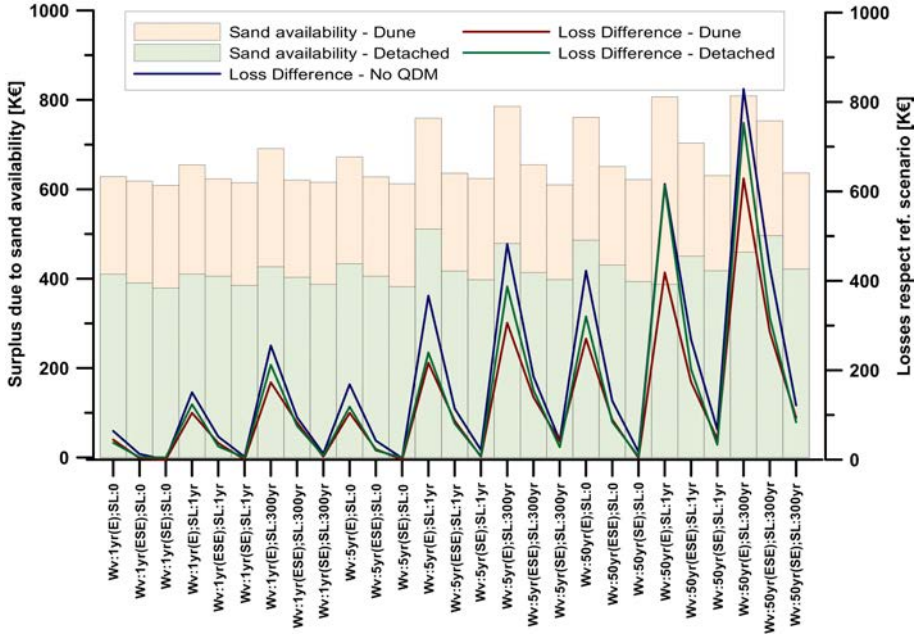

Figure 7.18.: Surplus due to **sand availability** associated to particular QDM in **Barcelona** beach. *Left axis:* The orange bar charts represent the surplus due to sand availability (in thousands of euros) for the **Dune** QDM, whereas the green bars represent the **Detached** QDM. *Right axis:* In solid lines, loss difference respect to a **reference** scenario **(Wv:1yr(SE);SL:0cm)** for the cases without QDM (**blue**), the Dune QDM (**dark red**) and the Detached QDM (**dark green**). The x-axis labels the hydrodynamic conditions for each case. **Symbols:** *"Wv (return period in yr; wave direction); SL (return period in yr)".*

Fig. 7.18 shows that **both QDM are able to maintain more sand volume at the emerged area than the reference case**. Note that the dune QDM systematically provides a higher surplus, because $7.5 \cdot 10^3\ m^3$ would be extracted from the swash zone. The volume differences between these two QDM, though, remain similar (around $200 \cdot 10^3$ *euros*). As shown in Fig. 7.8, two salients are formed at the shadow zone of the detached breakwaters, enabling the recovery of the sand.

Note that a higher surplus is found for high wave and sea level return period (around $800 \cdot 10^3$ *euros*). The losses respect to a reference scenario ($T_{r,wv} = 1\ yr$ and

$MWL = 0\ cm$) are attenuated for both cases (red and green solid lines vs. blue line), but the differences are more notable for Eastern storm waves. At these cases, the dune outperforms the detached breakwater.

7.4.3.2. Gavà

Fig. 7.19 shows that as the flooding losses increases, the magnitude of the cost reduction also increases, but it is not enough to cover the expenses. In this case, the sea level is the main driver for flooding. This behaviour, typical in dissipative environments, coincides with the results in Ch. 6.

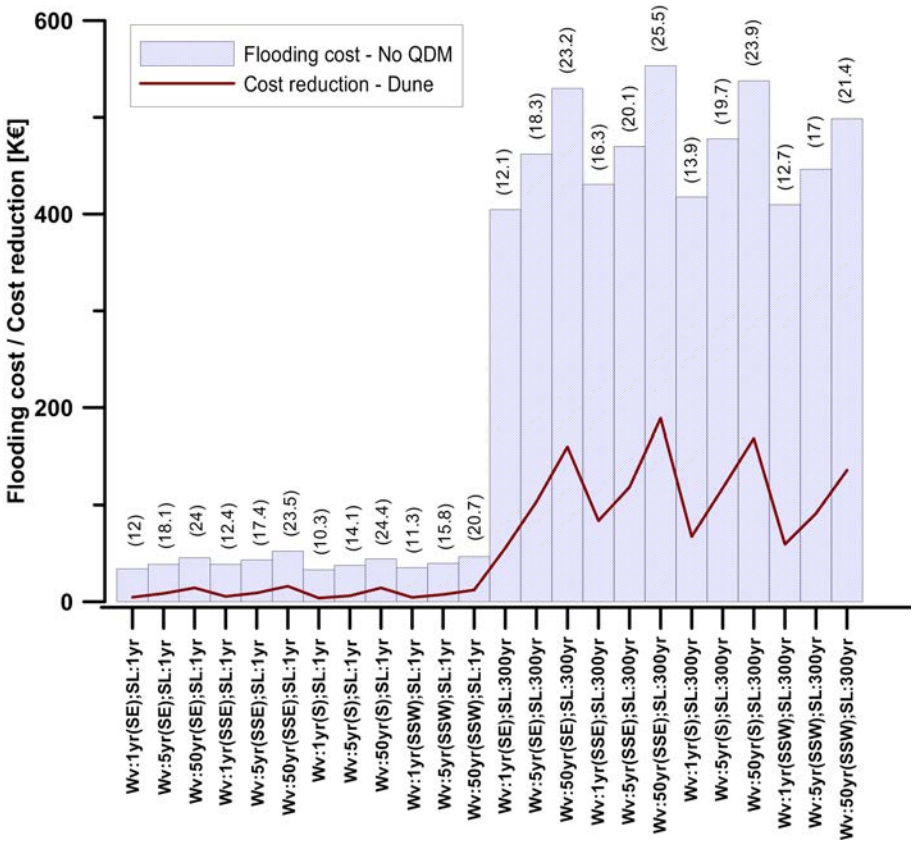

Figure 7.19.: Flooding costs versus reductions associated to particular QDM in **Gavà** beach. The blue bar charts represent the flooding cost (in thousands of euros). The number at the top of the bar represent the percentage of the total flooding cost that can be reduced with the dune. The solid lines represent the reduction of the flooding costs due to the implementation of QDM. The dark red line refers to the reduction of the flooding costs due to the implementation of the Dune. The x-axis labels the hydrodynamic conditions for each case. **Symbols:** *"Wv (return period in yr; wave direction); SL (return period in yr)".*

There are two clear regimes, that can be clustered by the sea level return period

(1 *yr* and 300 *yr*). The dune tends to harmonise the total flooding costs: when the wave return period increases, the cost reduction increases and reaches maximums of around 25%.

Note that there is **no flooding** when the sea level is **low** (not included in the graph because the value was zero). Wave directionality is not as decisive as in the Sant Sebastià case, although the highest costs are found for the SSE sector (maximum cost of around 550ů10^3 *euros*), and the lowest for the SSW (same as around 500ů10^3 *euros*).

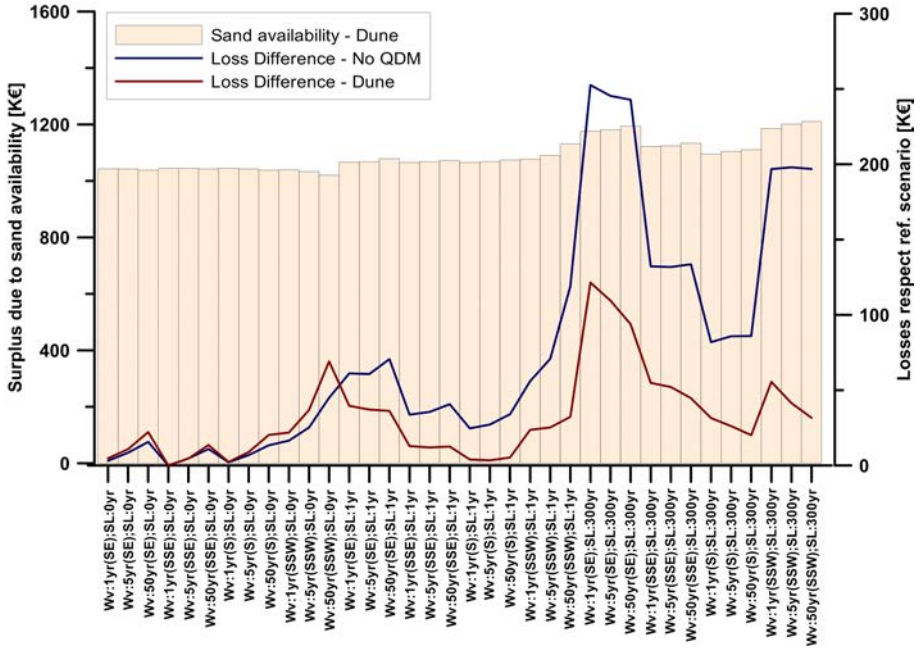

Figure 7.20.: Surplus due to **sand availability** associated to particular QDM in **Gavà** beach. *Left axis:* The orange bar charts represent the surplus due to sand availability (in thousands of euros) for the Dune QDM. *Right axis:* In solid lines, loss difference respect to a **reference** scenario **(Wv:1yr(SSE);SL:0cm)** for the cases **without QDM** (blue) and the **Dune QDM** (dark red). The x-axis labels the hydrodynamic conditions for each case. **Symbols:** *"Wv (return period in yr; wave direction); SL (return period in yr)".*

The efficiency of the dune is manifest with increases of the sea level (Fig. 7.20): at low sea level (0 *cm*), the loss difference of the QDM (red line) and the reference (blue line) is similar; but as the $T_{r,MWL}$ increases, the differences tend to be further noticed. The losses respect reference scenario are lower than in Sant Sebastià, that reinforces the concept that erosive fluxes are milder in Gavà. Note also that the main eroded sediment comes from the nourishment. The dune withstands partially in almost all scenarios, except specific ones with $T_{r,MWL} = 300\ yrs$.

The surplus due to sand availability remains fairly stable (orange bar charts), regardless of the hydrodynamic conditions. Therefore, the nourishment plus dune

reduces the sediment fluxes with similar efficiency. The savings due to sand availability do not exceed the total cost of the intervention (between 1330ů10^3 *euros* and 1530ů10^3 *euros*). As stated above, part of the nourishment is eroded, but the dune resists (costs that range between 625ů10^3 *euros* and 720ů10^3 *euros*).

7.5. Discussion

Once described the performance of the morphodynamic module for assessing coastal risk reduction (flooding and erosion) due to the use of QDM, the following points will be addressed in this Discussion: (i) **set-up of the modelling system** (Sec. 7.5.1), that addresses specific points of the implementation; (ii) **technical feasibility of the solutions** (Sec. 7.5.2), that discusses the different factors for QDM implementation; and (iii) **integration of QDM within long-term sustainable pathways** (Sec. 7.5.3), one of the main objectives of this dissertation, as exposed in Ch. 2.

7.5.1. Set-up of the modelling system

The XBEACH model **has been able to reproduce the main morphodynamic features and their interaction with the QDM**. The calibration coefficients obtained in Gràcia et al. (2013b) (dissipative beaches) and Ch. 4 (intermediate beaches) have provided a consistent post-storm response. Both pilot sites have shown sensibility to the forcings (waves and sea level), as expected due to its modal state (Wright and Short, 1984).

Sant Sebastià domain includes breakwaters, groins, obstacles, etc. that cannot be solved with the wave action balance equation. The phase-solving version has been able to deal with these wave scale processes (such as reflection and diffraction), joint with local consequences as the tombolo growth.

The main drawback of the phase-solving approach is the additional computational burden. In an operational chain, the simulation time of Sant Sebastià can be somewhat prohibitive: 14 hours for a synthetic storm of 24 hours. That sharply contrasts with the 1 hour and a half that requires Gavà, with just 3 cores. The main issue with the former is that the Poisson equation (see Sec. 3.3.3.5) is solved in a non-parallel implicit scheme. This problem could be alleviated in future versions by linking the source code with parallel solvers libraries.

The **spatial resolution** has ensured that the local features (dunes, detached breakwaters, etc.) and the local processes (wave propagation, flooding, etc.) at the pilot sites are properly represented. A sensibility analysis with a finer mesh was conducted, but the results were not significantly better. Additionally, the computational time substantially increased.

The 2DH (depth-averaged) hypothesis, despite its hindrances for addressing the velocity at the vertical profile, has proved to be an accurate approximation. The

interaction of cross-shore and long-shore processes was essential to capture the local behaviour of the areas. In Gavà, the Northern part has a lower elevation and tends to be flooded (Fig. 7.12). The longshore current advected sediment westwards, reinforcing the need for the nourishment at the Northern area. The erosion/accretion patterns with QDM show more heterogeneity than the reference scenario (Fig. 7.14); that result would have not been possible with a cross-shore model.

This assumption gains further relevance at Sant Sebastià. A cross-shore approach would not have been able to reproduce: (i) the sand filling of the trench (dune case, Fig. 7.7); (ii) the salient growth (detached breakwater case, Fig. 7.8) and (iii) the systematic flooding at the Southern part of the domain, that has lower elevation than at the North (Fig. 7.3).

The **sensitivity of the model** to these local factors has been the **standpoint** for assessing the **feasibility** of QDM for reducing coastal risk. From a design point of view, it is indispensable to discern where are the **active** and **non-active areas**. That can help us to determine the optimum places to set-up a QDM. For instance, if the detached breakwaters would be grounded in an erosive area, local scouring would trigger instabilities that could lead to structural collapse.[1]

7.5.2. Technical feasibility of the solutions

The previous paragraphs highlighted that the XBEACH results have been accurate enough for assessing coastal risk reduction with QDM. This section will further develop this point. The following topics will be addressed: (i) estimated risk reduction for each pilot site; (ii) general performance of QDM according to these results; (iii) construction elements and proceedings; (iv) QDM efficiency and lifetime; (v) recommendations for enhancing QDM robustness.

Tab. 7.3 summarises the flooding costs and their reductions, being clustered by their $T_{r,MWL}$. Systematically, as the **sea level increases**, the **efficiency** of the dune and the detached **decreases** (see $\%\mathbf{Red_{dune}}$ and $\%\mathbf{Red_{det}}$). At moderate $T_{r,MWL}$ (1 year or less), the detached breakwater performs better than the dune. This is due to the low freeboard that enhances wave breaking. At high sea levels, though, the dune tends to perform better (29.3 ± 7.6 vs. 25.0 ± 8.9, both in %). Note that the standard deviation for the dune and the detached tends to be lower for high sea levels. That means that the protection function tends to be saturated (no more assets can be protected). Remarkably, at high return periods for sea levels, the flood costs reductions are almost enough to cover the dune expenses (43.3 ± 36.7 vs. 65, both in thousands of euros).

[1] The last statement may sound obvious; but the personal experience of the PhD candidate and the state-of-the-art confirm that is not so uncommon to relegate bed stability at placing geotextile sandbags. Case studies reviews can be found in Hornsey et al., 2011; Restall et al., 2002.

Table 7.3.: Integrated **flooding costs** at Sant Sebastià. The costs are clustered according $T_{r,MWL}$. The first value is the mean value and the second one, the standard deviation. ***Legend: Cost*** *(flooding cost with no QDM);* $\mathbf{Red_{dune}}$ *(cost reduction due to dunes);* $\mathbf{Red_{det}}$ *(cost reduction due to detached breakwaters);* $\%\mathbf{Red_{dune}}$ *(same as* Red_{dune} *but as a percentage of the flooding cost);* $\%\mathbf{Red_{det}}$ *(same as* Red_{det} *but as a percentage of the flooding cost).*

$\mathbf{T_{r,MWL}}$	**Cost**	$\mathbf{Red_{dune}}$	$\mathbf{Red_{det}}$	$\%\mathbf{Red_{dune}}$	$\%\mathbf{Red_{det}}$
0 *cm*	53.8 ± 35.7	36.7 ± 18.0	37.4 ± 10.6	76.8 ± 28.3	81.3 ± 22.7
1 *yr*	85.5 ± 60.4	28.5 ± 26.5	28.6 ± 20.6	34.6 ± 23.1	33.5 ± 15.2
300 *yr*	140.3 ± 89.2	43.3 ± 36.7	33.7 ± 21.1	29.3 ± 7.6	25.0 ± 8.9

Erosion at Sant Sebastià show more sensitivity to waves than to the sea level. That is the reason that the values were clustered in this way (Tab. 7.4).

The surplus is the difference between the sediment that was available in the post-storm profile with no QDM minus the sediment available in the post-storm profile with QDM. Note that this unit is the **difference** between the two scenarios.

Table 7.4.: Integrated **erosion costs** at Sant Sebastià for the different QDM. The costs are clustered according $T_{r,waves}$. The first value is the mean value and the second one, the standard deviation. ***Legend:*** $\mathbf{Sav_{dune}}$ *(surplus due to sand availability - dune);* $\mathbf{Sav_{det}}$ *(surplus due to sand availability - detached);* $\mathbf{Flux_{act}}$ *(loss difference respect to a reference scenario - No QDM);* $\mathbf{Flux_{dune}}$ *(same as* $Flux_{act}$*, but for the dune); and* $\mathbf{Flux_{det}}$ *(same as* $Flux_{act}$*, but for the detached breakwaters). Units in thousands of euros.*

$\mathbf{T_{r,waves}}$	$\mathbf{Sav_{dune}}$	$\mathbf{Sav_{det}}$	$\mathbf{Flux_{act}}$	$\mathbf{Flux_{dune}}$	$\mathbf{Flux_{det}}$
1 *yr*	630.6 ± 26.2	399.7 ± 15.3	72.1 ± 84.5	50.3 ± 59.6	51.2 ± 71.0
5 *yr*	664.7 ± 64.3	426.3 ± 42.1	158.7 ± 166.1	102.8 ± 103.6	111.1 ± 128.7
50 *yr*	708.1 ± 76.2	438.0 ± 38.0	322.8 ± 274.4	223.5 ± 201.7	263.5 ± 263.3

There is a 40% difference in the sand surplus between the dune and the detached breakwater. In the dune, sand from the submerged part (trench) was distributed at the emerged part. In the detached case, the sand from the emerged part tends to be stored at the rearside of the detached breakwater, then generating salients. That implies that the minimum beach width area would be moved to the adjacent areas of the detached breakwaters.

Sand fluxes are also more attenuated at the dune case than at the detached one. The mean value of the fluxes does not deviate excessively between dune and detached

breakwater; however, the standard deviation for the detached breakwaters is higher. Note, as well, that the difference of surplus of available sand is significantly lower than in Gavà, because in this case, it has not been added extra nourishment.

Table 7.5.: Integrated **flooding costs** at Gavà. The costs are clustered according $T_{r,MWL}$. The first value is the mean value and the second one, the standard deviation. ***Legend: Legend: Cost*** *(flooding cost with no QDM);* $\mathbf{Red_{dune}}$ *(cost reduction due to dunes);* $\%\mathbf{Red_{dune}}$ *(same as* Red_{dune} *but as a percentage of the flooding cost).*

$\mathbf{T_{r,MWL}}$	**Cost**	$\mathbf{Red_{dune}}$	$\%\mathbf{Red_{dune}}$
0 *cm*	–	–	–
1 *yr*	40.7 ± 5.7	8.9 ± 4.3	17.0 ± 5.2
300 *yr*	469.9 ± 51.2	112.5 ± 51.2	18.7 ± 4.4

At Gavà, Tab. 7.5 highlights that the cost differences among the three sea level scenarios are important, but the **flooding cost reduction is similar** (around 18%). That is because the model has shown a homogeneous behaviour, because MWL is the main driver for flooding. The sea level value is more stationary than waves, then, the standard deviation does not deviate excessively.

The implementation of the dune system is around $625-720 \cdot 10^3$ *euros*. The flooding costs fairly exceed this value. Only under high sea levels ($T_{r,MWL} = 300$ *yr*), this cost reduction is considerable (112.5 ± 51.2 thousands of euros).

Table 7.6.: Integrated **erosion costs** at Gavà. The costs are clustered according $T_{r,MWL}$. The first value is the mean value and the second one, the standard deviation. ***Legend:*** $\mathbf{Sav_{dune}}$ *(surplus due to sand availability - dune);* $\mathbf{Flux_{act}}$ *(loss difference respect to a reference scenario - No QDM);* $\mathbf{Flux_{dune}}$ *(same as* $Flux_{act}$*, but for the dune plus nourishment). Units in thousands of euros.*

$\mathbf{T_{r,MWL}}$	$\mathbf{Sav_{dune}}$	$\mathbf{Flux_{act}}$	$\mathbf{Flux_{dune}}$
0 *cm*	1039.6 ± 6.9	12.7 ± 12.4	17.9 ± 19.3
1 *yr*	1077.4 ± 18.5	52.8 ± 26.6	20.4 ± 13.7
300 *yr*	1153.3 ± 41.9	165.3 ± 64.6	56.9 ± 33.4

Tab. 7.6 integrates the erosion costs at Gavà. The sand fluxes are consistently lowered with the dune (from 165 to 57, both in thousands of euros). That means that the proposed beach profile is more stable to extreme hydrodynamic behaviour than the reference. The difference is more noteworthy as the sea level increases. The

beach profile and the dune that was proposed is thought for moderate to relatively high sea levels. The beach nourishment was designed with a gentle slope, promoting run-up attenuation.

The surpluses ($\mathbf{Sav_{dune}}$) are consistent: a fraction from the nourishment has been lost, but the post-storm profile has still available around $1000 \cdot 10^3$ *euros* worthy of sand. The total investment ranges $(1330 - 1530) \cdot 10^3$ *euros*, but the estimated losses can be considered in the correct order of magnitude. The eroded volumes are in line with the lifetime of the nourishment (15 years) and the high return periods considered ($T_{r,waves} = 50\ yr$, see Fig. 7.14).

In general, it has been found that the benefits from **maintaining the sand volumes outperform** the **flooding cost reduction**. That is in line with the results from the Risk Module (see Ch. 6), but with a level of detail hard to be obtained without process-based modelling. Erosion is a more steady coastal hazard (i.e. the shoreline is eroded once a critical Shield is surpassed). Flooding, however, is more transient in nature, and harder to be simulated.

These solutions tend to produce higher costs reduction with high return period events. That is important, because in order to be cost-effective, the cost reduction must be superior to the construction cost. Those QDM that outperform against erosion would need to be firstly promoted. Three reasons are essential: (i) erosion happens more frequently than flooding; (ii) some QDM, such as dunes, depend on sediment; (iii) the sand budget is linked to the overall health of the beach (more on this on the next paragraphs). Hence, maintaining the sand budget would be a top priority.

The results has shown that the **MWL** is the **main driver** both for **flooding** and **erosion** at Gavà. At Sant Sebastià, **flooding** is more sensible to **MWL**, whilst extreme **waves** are more important **for erosion** (Tab. 7.7). This classification coincides with the risk module proposed in Ch. 6: dissipative beaches (such as Gavà) are more sensible to MWL variations; whereas intermediate and reflective beaches, depend further on ocean waves.

Table 7.7.: Classification of the sensibility of the hydrodynamic forcings by hazard and pilot site. **Legend:** (Main/Secondary) hazard.

Site	**Hazard**	
	Flood	**Erosion**
Sant Sebastià	MWL / Waves	Waves / MWL
Gavà	MWL / Waves	MWL / Waves

In general terms, the **detached breakwater** can be a **suitable option at intermediate beaches** against **low to moderate sea levels** and **high wave return periods**. Under these conditions, they perform better than dunes. As higher the

waves, further wave breaking is enhanced. At dissipative beaches, the intrinsic submerged profile is dissipative by nature.

The dunes perform better at high sea levels than the detached breakwaters. They can be suitable both for dissipative and intermediate beaches. However, their lifetime depends on the overall beach state.

In one hand, the **advantages** of **dunes** can be summarised as follow:

- Under **high sea levels**, they have **better performance** against flooding than detached breakwater.
- **Additional sand buffer** at the emerged area.
- Can be coupled with **Nature Based Solutions** (see Sec. 7.5.3); specially when a dune system used to exist at the area (dune restoration).

And the **hindrances** would be:

- Dunes require a **minimum beach width**: otherwise they will be located too offshorewards and will be easily eroded. In these cases, beach nourishment is recommended (as in Gavà).
- Dunes require **good quality sand**. Fine sand would be easily eroded by wind (aeolian transport) and/or occasional water mass fluxes.
- In case that vegetation is planted, extra maintenance effort is needed. Additionally, as exposed in Silvester and Hsu (1997) (Sec. 5.2), *"the root systems incorporated in the sand mass will hold the slope vertically, resulting in more efficient reflection of storm waves."*[2]

In the other hand, the **advantages** of **detached breakwaters** would be:

- Good for **intermediate beaches**, specially under low to moderate sea levels.
- The **lifetime** can be longer than the dune.
- They do not need a minimum beach width. However, without a minimum sand budget, they will not tend to form a salient/tombolo.
- Good solution for **sand starving beaches**, in which nourishment is not an option (or unavailable).
- **Less restrictive** than the dunes regarding the **sand quality**. In case that only fine sediment is available, it can still be used as filling material. In order to minimise the dredging environmental impact, a jet-pump system may be used.

And the **inconveniences** can be summarised as:

- **Lower** risk **reduction** against **high sea levels** than the dune.
- **Not convenient** for **dissipative beaches** due to their intrinsic gentle submerged profile.

[2]The same paragraph continues: *" This increases wave heights at the face and orbital motions of water particles, which aids removal to the offshore bar. Thus, in an erosive situation, vegetation will exacerbate the problem of dune removal".*

Both solutions present a series of challenges in design, mainly due to the uncertainty associated to the hydrodynamic drivers.

Cost-effectiveness is strongly connected with the **construction proceedings**. QDM aim to small volumes and endogenous sources. Terrestrial works are generally cheaper than maritime, specially with this kind of local interventions. The dune at Sant Sebastià costs about the double with maritime works. The lack of offshore sand deposits at the area is one of the factors that affects to this difference. Note, however, that sand transportation from a quarry to the beach, can signify an important proportion of the costs. That is one of the reasons for using the material from the trench.

At Gavà, the sediment may come from the **western end of the Llobregat littoral cell**. In that boundary, there exists accretion due to the joint action of (i) the littoral drift and (ii) the barrier effect created by a small craft harbour (Port Ginesta). The sediment can be bypassed to the North (i.e. Gavà beach) with terrestrial methods. There is not enough sand volume ($95 \cdot 10^3\ m^3$) and the deficit has to come from offshore sand deposits or from quarries. That is the reason for the elevated price (Tab. 7.2).

The Gavà dune withstands hydrodynamic scenarios up to $T_{r,waves} = 5\ yr$ and $T_{r,MWL} = 1\ yr$. However, when the sea level increases to a $T_{r,MWL} = 300\ yr$, the dune collapses at the storm peak (12 hours after the simulation starts), even with low return period waves $T_{r,waves} = 1\,yr$. Maximum run-up is highly dependent of the MWL: it can reach $1.2\,m$ for a $T_{r,MWL} = 1\,yr$, with deviations of $20\,cm$ that depend of the wave return period. But, in case that $T_{r,MWL} = 300\,yr$, the maximum run-up rises to $1.9\,m$ (with deviations of $30\,cm$). This run-up surpasses to the dune crest height. **Overwash** regime (Sallenger, 2000) unleashes and the dune is eroded until collapse.

Once the dune collapses, a fraction of the sediment will be advected (i) offshorewards (i.e. due to return-flow), and the other one (ii) will follow the littoral drift. The sand quality of the latter fraction tends to be better than the offshore one. Offshore sediment is usually harder to be recovered (via dredging) and tends to be mixed with the fine sediment (clay and silt), from the inner shelf (Grifoll et al., 2014).

The same offshore **fine material** can serve for **filling geotextile sandbags**. The size of the element matters: bigger elements perform better for local interventions (Hornsey et al., 2011; Restall et al., 2002). They have a set of advantages: (i) they have a weight that hampers to be drifted, (ii) extended contact surface, that increases friction (be it among the different elements or the seabed) (iii) lower implementation / dismantling time than smaller elements. For instance, the Limeburners breakwater (built in 2004, Australia) was filled with low quality material. With the aim of preventing wave transmission, two elements $40\,m$ long $\times$ $5.5\ m$ high were placed at $4\ m$ water depth. Around $8\,h$ were needed for filling each geotextile with a suction cutter dredge. Seven years later their deployment, the soil settlement was $< 300mm$, even though the poor quality of the soil.

Offshore dikes that uses geotextiles mats filled with low plasticity clays have been

also used at Tianjin Port (China), see Yan and Chu (2010). A 100 m long and 4.8 m high dike was built in 2001, and remained relatively stable nine years later. The settlement and the compressibility of the dike were 84.1 cm and 14.0 cm, respectively. These case studies demonstrate that former work, under even more restrictive conditions than the ones in Sant Sebastià, has been already been successfully applied in real conditions.

According to the state-of-the-art, the proposed dimensions ($3m\emptyset \times 20m$ long) for the elements of the detached breakwater are plausible. At other Mediterranean beaches, such as Emilia Romagna (Italy), the mean volume of the elements is significantly lower (2 m^3, approx. $3\times1.7\times0.4\ m$). In 1995, a 3 km alongshore barrier at 3 m water depth was built using this kind of woven HDPE[3] element (Martinelli et al., 2011), coupled with a $180\cdot10^3\ m^3$ nourishment. Barrier integrity was proven in 2006 by multi-beam survey. In this case, the high number of elements ensures enough friction (among the elements) and flow reduction to ensure stability and element drifting. However, such an intensive intervention, despite being more environmental friendly than hard engineering, cannot be classified as QDM.

The **efficiency** of the **dune** is bound to the **beach health state**. Beach width, that is correlated with the available emerged sand budget is a proxy health indicator. If a dune is located too offshoreward due to lack of beach width, the foredune would be promptly eroded by collision regime. Its lifetime substantially decreases. In García-León et al. (2015), other dune layouts were tested in Sant Sebastià, but those at offshoreward positions provided the lower skill. In a previous technical report, LIM/UPC (2014), a similar analysis was held for Gavà, with analogous conclusions. These results are compatible with the state of the art (Nordstrom and Jackson, 2003; Silvester and Hsu, 1997). That is why the dune system in Gavà includes a nourishment. The estimated dune resistance reported a few paragraphs above would not be reached. Note, as well, than in those cases in which the main goal is to obtain a tombolo, detached breakwaters also require a certain sand budget.

Hence, it can be concluded that the QDM functionality can be enhanced with the combination of the proper long-term actions (nourishments, sand bypasses, beach scraping, submerged vegetation, etc.). In the next part of the discussion, this issue will be readdressed.

Lastly, there are **nine tenets** that can enhance **QDM robustness**: (i) clear problem definition; (ii) clarity on the main physical processes at the area; (iii) interaction with long-term measures that maximise the efficiency of the QDM; (iv) simplicity in design; (v) simplicity in building; (vi) good forecast skill (timing); (vii) redundancy and willingness to adopt it (if the forecast misses, the QDM is useful); (viii) clear intervention protocols; (ix) continuous reassessment of the previous eight tenets. Some of these points will be addressed next.

[3](HDPE) High Density Polyethylene

7.5.3. Integration of QDM into sustainable coastal management

The above paragraphs have discussed the **internal constraints** to be considered for QDM implementation (i.e. performance, construction proceedings, lifetime, etc.). This last part will address the **external framework** of QDM: (i) the role that CEWS forecasting has in QDM efficiency; (ii) what to do when the forecast is wrong (i.e. reactive interventions); and (iii) Nature Based Solutions, as a way to promote beach and self-healing.

LIM-COPAS has systematically shown better performance under high return periods storms (D-08, D-16 and J-17, see Ch. 4 and 5) than under moderate ones (O-15, F-16). Additionally, the QDM risk reduction tends to be higher with this kind of events (see Sec. 7.5.2). Then, paradoxically, these pilot QDM interventions should address high energetic conditions first. The possible success of these pilot interventions would build trust and boost research on QDM suited for moderate events. It is expected that the ocean forecast skill will improve in the next years (Kourafalou et al., 2015), then handling better the uncertainty for a forecast horizon beyond 72 hours.

False alarms and missed hits can affect negatively the QDM implementation. These forecast mismatches are still common under storms with return period lower than $T_r \leq 5 - 10\, yrs$. Risk-averse municipalities may be against proactive interventions, specially under uncertain occurrence probabilities.

Such a high resolution forecast system requires a constant monitoring of the coastal state. The emerged area and the bathymetry need to be updated in the CEWS, with a site-specific frequency. For instance, Premià de Mar[4] ($ero_{rate} = -5.76\, m/yr$) would need to be updated more frequently than St. Feliu de Guíxols ($ero_{rate} = -0.22\, m/yr$). Data assimilation algorithms would need to be embedded into the CEWS architecture. The initial set-up of these data assimilation is not straightforward and QDM that slow-down the natural fluxes are preferable.

Hence, this research suggests than in the early stages of a CEWS, QDM with a higher lifetime (i.e. detached breakwater at intermediate beaches) may be more adequate than more ephemeral ones (i.e. dunes). In case that the total costs does not increase significantly, conservative QDM building should be prioritised. QDM that warrant a **redundant protection function** are a better choice to more optimal ones that are strongly attached to the forecast skill.

Redundancy is a way to solve forecast inaccuracies, but at some cases, it is not even enough. In these extreme cases, **reactive interventions** (i.e. traditional coastal engineering) have to be considered as an option. CEWS limitations need to be acknowledged and **post-storm works** can be the only option for avoiding permanent turning points. For instance, a post-storm beach nourishment joint with groin building can be the only short-term pathway towards a certain beach state. However, long-term planning should be a top priority and these kind of hard works

[4]See App. B.

would need to be keep exceptionally minimum. This minimisation goal can be reached with a **healthy beach state**.

Any long-term plan needs to foster beach health. Narrow and heavily constrained beaches with a strong erosive rate, such as Premià de Mar, are signs of poor health. Such health requires a **high-quality sand budget and local constraints** compatible with the meteo-oceanographic forcings. Usually, as fewer hard barriers for the fluxes (breakwaters, groins, revetments), the better. These natural fluxes enhance self-healing of the beach and further compatibility with the ecosystemic function (Nesshover et al., 2017). There are long-term works, termed Nature Based Solutions (NBS), that aims to find this equilibrium among the different coastal uses. Examples of NBS would be habitat restoration (coral reefs, foredunes, mangroves, saltmarshes, seagrass meadows, etc.). They provide as benefits: (i) hydrodynamic attenuation; (ii) carbon sequestration; (iii) nutrient cycling and water purification; (iv) fisheries provision and raw material; and (v) maintenance of wildlife.

NBS are particularly suitable for low-energy conditions (Morris et al., 2018; Borsje et al., 2011), such as in the Study Area. At urban Mediterranean beaches, the restoration of submerged vegetated areas, such as Posidonia Oceanica meadows could be a potential long-term coastal protection measure (Sánchez-Arcilla et al., 2015a). Submerged vegetation (i) breaks incoming waves, (ii) reduces wave length and velocity and (iii) dissipates wave energy (Horstman et al., 2014; Vuik et al., 2016). Note the commonalities with QDM.

In cases where ephemeral just-in-time rigidity is needed, QDM can provide extra protection for a limited lifetime. For instance, submerged geotextile bags at the offshore side of the meadow can provide a shelter area for diminishing biota stress in its early phases. In that sense, QDM can ease the transition towards a low carbon society, by maintaining acceptable risk levels whilst the NBS realign with the ecosystem.

Green solutions require periodic evaluations of their performance. Their flexibility adds a new layer in uncertainty, not only in their implementation phase, but also in the maintenance one. In-situ and remote sensing monitoring can help to measure relevant indicators such as the biota stress and growth, meteoceanographic drivers, water quality, turbidity, etc. This timely information can serve to redefine these interventions. CEWS forecast can also highlight whether further additional measures can be required. In short, *working with nature* demands long-term planning, but a proactive and adaptive vision is paramount.

7.6. Conclusions

In this Chapter, it has been assessed numerically the feasibility of Quick Defense Measures for mitigating episodic coastal risk at the Catalan Coast. The morphodynamic module has been tested at two urban beaches that suffer chronic coastal hazards: (i) Sant Sebastià and (ii) Gavà beach. Two types of QDM has been ad-

dressed: (i) dune systems and (ii) detached breakwaters.

At Sant Sebastià the QDM consist of: (i) two dunes with an overall height of 1.5 m and 140 m alongshore; (ii) two detached breakwaters, deployed at $-2\,m$, with a ellipsoidal cross-section (1.7 m height and 7 m width) and 140 metres alongshore. At Gavà has been proposed the joint action of a $50 \cdot 10^3\ m^3$ beach nourishment, with a transient dune belt of $45 \cdot 10^3\ m^3$ (1.5 m height and 3.4 km of alongshore length).

A set of hydrodynamic scenarios have been analysed, that spans the applicability range of QDM: (i) 24-hr storm waves with $T_{r,waves} = 1, 5, 50\,yrs$ and (ii) mean water levels with $T_{r,MWL} = 0\,cm, 1\,yr, 300\ yr$. The model has been able to reproduce the main morphodynamic features and their interaction with the QDM.

MWL is the main driver both for flooding and erosion at Gavà. At Sant Sebastià, flooding is more sensible to MWL, whilst waves are more important for erosion. These results coincide with the state-of-the-art and the results obtained in Ch. 6.

At Sant Sebastià, the efficiency of flood costs reduction decreases under high sea levels. At $T_{r,MWL} \leq 1\ yr$, the detached breakwater performs better than the dune; whereas at $T_{r,MWL} \geq 1\ yr$, the dune reduces the costs more efficiently (29.3 ± 7.6 (dune) vs. 25.0 ± 8.9 (detached), both in %). The saved costs are almost enough for covering the dune expenses.

Additionally, sand fluxes are more attenuated at the dune case. The mean value of these fluxes does not deviate excessively between the two QDM options; however, the standard deviation for the detached breakwaters is higher.

At Gavà, the flooding cost reduction is stable, regardless of the scenario (around 18%). Under high sea levels ($T_{r,MWL} = 300\ yr$), the cost reduction is considerable (112.5 ± 51.2 thousands of euros). The sand fluxes are consistently lowered with the dune (from 165 to 57, both in thousands of euros), implying that the proposed beach profile is more stable than the reference.

The benefits from maintaining the sand volumes outperform the flooding cost reduction. As exposed in Ch. 6, at both sites, erosion is a bounded cost, whereas flooding may have important upsides. QDM tend to produce higher costs reduction with high return period events. Note that LIM-COPAS is able to reproduce accurately this kind of extreme events (see Ch. 4 and 5).

In general terms, the detached breakwater can be a suitable option at intermediate beaches against low to moderate sea levels and high wave return periods. At dissipative beaches, dunes are the best option, but they require a minimum beach width (around $30\,m$) that ensures their lifetime.

QDM functionality can be enhanced with the joint action of compatible long-term actions (nourishments, sand bypasses, submerged vegetation, etc.). A healthy beach state is paramount for the QDM effectiveness. Coastal Risk Forecasting, Proactive Interventions and Long-term Planning are feasible elements for achieving high sustainability under present and future climate.

Summary and Conclusions

Summary of the Thesis

This thesis has assessed present coastal risk at the Catalan Coast through **a Coastal Early Warning System (CEWS), LIM-COPAS (LIM-COastal Processes Assessment System)**, that forecasts the more relevant episodic coastal hazards at the area. With this aim, this dissertation has made strong emphasis on the **simulation and analysis of the coastal response in terms of flooding/erosion against storm impacts.**

The main objective of this thesis can be partitioned into the following three clusters: *(i) Conceptualization of the problem; (ii) Architecture of the CEWS (i.e. design of the solution); (iii) Performance evaluation of the system under hindcasted events and synthetic scenarios (i.e. feasibility of the solution).* Each cluster has covered a set of steps. This summary section will provide a broad summary of the main findings in this dissertation:

Conceptualization of the problem

(Obj. 1A) Identification of the main coastal hazards at the Cat. Coast

The Catalan Coast faces the same endemic problems than most of the urban Mediterranean beaches (EUROSION, 2004): the rearside is occupied with infrastructure and the beaches are losing protection capacity. The shortage of sediment budget due to the regularisation of the rivers has led than 70% of the Catalan beaches are facing erosion (CIIRC, 2010).

Episodic coastal hazards (flooding and erosion) are increasing at an approximate rate of 40% per decade, due to this high urbanisation rate (Jiménez et al., 2012). Storm-waves and surges are the main hydrodynamic forcings at this time scale, but their predictability is limited to a time horizon of a few days. Consequently, it is hard to envisage the consequences of such extreme events and to embed them into a long-term plan.

Reactive interventions (i.e. post-storm action) have been the norm in the Spanish Coastal Management strategy. Only in the Catalan region, more than 50 million euros have been invested for the development and maintenance of coastal protection works and promenades (CEDEX, 2013). More than 10 millions m^3 of sand have been spent in beach nourishment alone (Gràcia et al., 2013c). Moreover, some

of these solutions demand hard engineering (i.e. revetments, groins, breakwaters) that imposes a permanent constraint against natural fluxes. At some cases, these blockages can even exacerbate coastal hazards, such as erosion.

However, these kind of interventions are not feasible in the current slow-growth paradigm. Then, this **dissertation has proposed a pro-active (pre-storm) management**, based on an early warning with smart interventions. Such measures aim to promote cost-effective measures, that are more eco-compatible with the existing coastal uses. This compatibility would avoid to reach tipping points and regime shifts, that once surpassed, can be cost-prohibitive to revert back.

Pre-storm intervention requires to forecast future post-storm coastal states. Hence, **this dissertation has proposed** a Coastal Early Warning Systems, termed LIM-COPAS, **as a forecast system for assessing episodic coastal risk**. CEWS particularly aims to short-range forecasts (time scale of 3-6 days) at local scales (littoral cell scale), with high resolution models (Baart et al., 2016).

The results from this dissertation highlights that **episodic erosion** is **more frequent** than **flooding**; but **erosion** has a **bounded cost**, whilst **flooding** has a **higher upside**. The predominance of a particular hazard depends on the intrinsic beach characteristics and the magnitude of the forcings: at dissipative beaches, MWL is the main driver both for flooding and erosion; however, at intermediate and reflective ones, extreme-waves can be determinant for erosion (see Ch. 6-7). Note that long-term Sea Level Rise (see Sec. 2.4.3) or a degenerative beach state (i.e. beach width decrease or a lower sand budget) may also imply regime shifting.

In short, the proposed high sustainability pathway combines: (i) CEWS (as the forecasting tool); (ii) pro-active interventions (for mitigating storm-impact); (iii) long-term interventions such as Nature Based Solutions (for enforcing beach health).

Architecture of the LIM-COPAS system

(Obj. 2A) The LIM-COPAS modelling chain

Episodic coastal risk has been assessed with LIM-COPAS. The flowchart of this system can be found in Fig. 3.1, defined by the following four sequential modules:

1. **Meteorological module** (Sec.3.3.1): The mesoscale WRF model (Skamarock et al., 2005), that solves the compressible, nonhydrostatic Euler equations, provides the wind fields that are the input for the hydrodynamic module.
2. **Hydrodynamic module** (Sec.3.3.2): Consists of the SWAN (Booij et al., 1999) spectral wave generation and propagation model, that solves a wave action balance equation. The wind from WRF and circulation fields from IBI-MFC (Sotillo et al., 2015) are introduced as an input. Two types of data are extracted: 2D wave spectra, that are used as input for the morphodynamic model (XBEACH); and integrated parameters (H_s,wave direction, etc.) that are used for the risk module.

3. **Morphodynamic module** (Sec.3.3.3): This module provides high resolution characterization of episodic coastal hazards (flooding and erosion). The XBEACH model (Roelvink et al., 2009) is the core of this module. The code solves nearshore wave propagation and circulation through a wave action balance equation, coupled to a 2DH Navier Stokes shallow-water solver. This coupling provides circulation which are used to feed an advection–diffusion equation that allow the estimation of sediment fluxes, and consequently erosion/accretion patterns. This dissertation is the first attempt to include a morphodynamic model in an oceanographic operational system at the Catalan Coast.
4. **Risk assessment module** (Sec.3.3.4 and Sec.6.2): This last module estimates coastal risk (flooding and erosion costs). A multivariate, non-stationary probabilistic function, fitted from the morphodynamic solver outputs, estimates the probability that a given cost will be surpassed. Other European initiatives have opted for another kind of risk assessment tools such as Bayesian networks (Jager et al., 2018) or Coastal State Indicators (van Koningsveld et al., 2005). This module has been newly developed in this dissertation, and it is the first attempt to build a multivariate non-stationary probabilistic model within a CEWS.

(Obj. 2B) Set-up of the LIM-COPAS system

Meteorological module

The meteorological module has consisted in three two-way nested grids: (i) the first grid spans Europe, has a spatial resolution of 27×27 km; (ii) the second one is located at the Western Mediterranean Sea and the last one (iii) represents the Balearic Sea, with a resolution of 3×3 km.

The area limitations for each grid can be found in Fig.3.2. The time step for the last nesting is around $\Delta t_{WRF} \approx 10\ s$. The meteorological outputs are stored each 20 minutes. The performance of such scheme has been assessed in Ch. 5 and will be summarised in Obj. 3A-3B.

The spatiotemporal resolution is enough for solving the expected gradients in time and space. The proposed set-up was due to the experiences with the wind fields used in Ch. 4: the spatiotemporal resolution was probably one of the causes for some of the mismatches.

In order to perform the hindcast analysis, the ERA-INTERIM global reanalysis (see Sec. 3.2.1), has been used as boundary conditions.

Hydrodynamic module

The SWAN model set-up consists of two one-way nested grids: (i) a regional one that spans the NW Mediterranean Sea, with a resolution of 5×5 km; and (ii) a second one that covers the Balearic Sea, with a resolution of 2×2 km.

The spectral model is run as non-stationary with a time step of $\Delta t_{SWN} \approx 10\ min$, in order to avoid numerical instabilities and diffusion.

This one has been the scheme that has been tested in Ch. 5 and 6.

Morphodynamic module

The proposed numerical scheme is 2DH, involving depth-averaged cross-shore and long-shore circulation. This assumption is essential to estimate the coastal response, specially at a local scale. 54 beaches have been set-up for the assessment (see Calibration beaches, denoted as green dots, in App.A; and their morphodynamic features in App.B).

Despite that the set-up is case specific, a set of common settings have been followed: (i) the computational grids are curvilinear and irregular (the cross-shore dimension has different different gridsizes); (ii) the cross-shore gridsize is around 5 m, from the emerged to the surf zone; but, (iii) from the surf zone to the offshore boundary, the gridsize transitions from 5 to 20 m; (iv) the alongshore dimension is kept as constant (around 10-20 m for beaches with an alongshore length inferior than 1 km; whilst those ones longer than 1 km have an approximate resolution of 20-30 m).

In those beaches in which wave diffraction, reflection and transmission have a minor role (i.e. open beaches), the model has been solved at wave group scale (phase-averaged approach, Fig. 3.3). However, in those zones with small islands, revetments, groins, detached breakwaters, etc., a phase-solving approach has been used (see Sec. 3.3.3.5). The latter, though, is more computationally expensive and requires a finer grid (around 3 m from the emerged to the surf zone) for handling the water surface elevation, specially under broken waves.

(Obj. 2C) Development of a risk module

The quantification of flooding and erosion can be misleading for policymaking. In order to boost a more proactive and knowledge-based management, coastal hazards need to be translated into risk. Economic losses due to extreme events can be compared with the intervention costs, then providing a clear message whether such investment should be made.

With this aim, a risk model, COPAS, has been conceptualized in this Thesis and the methodology and results can be checked in Ch. 6. COPAS is a non-stationary multivariate statistical model that can estimate flooding and erosion costs in microtidal beaches. The module development has consisted of four steps (Fig. 6.1):

1. **Generation of the sample** (Sec. 6.2.1): A database of **54 beaches**, considering flooding and erosion hazards, has been built with the morphodynamic module. Around **2300 simulations** have been run (see Tab.B.1), under a wide range of wave storm and MWL scenarios (see Obj.2F). The process is summarised in Fig. 6.3.

2. **GAMLSS model building for each calibration beach** (Sec. 6.2.2): Once the database was built, each beach has been fitted with a non-stationary multivariate GAMLSS model. In these GAMLSS models, the co-variates have been the hydrodynamic forcings (storm-waves and MWL), whereas the response variables has been the flooding and erosion cost (see Fig.6.4).
3. **Integration of the individual models into a risk formula** (Sec. 6.2.3): Each calibration beach has been fitted with an individual GAMLSS model. Each GAMLSS covariates have associated a set of coefficients. The coefficients of each individual model are related with its intrinsic morphodynamic features (beach width, berm height, beach slope, etc.). Hence, a set of beach properties (input) can determine coefficients (output) for building non-stationary multivariate probability distribution functions (see Fig. 6.5).
4. **Application** (Sec. 6.2.4) **of the risk formula** at both the calibration and validation beaches (25, Tab.B.3). The main outcomes have been (Fig. 6.6): (i) stress-curves, (ii) correlation-curves and (iii) forecast maps.

The Principle of Parsimony has been adopted for developing this module. An increase of the number of the parameters could have led to overfitting and/or over-parametrization. The hypothesis that the flooding and erosion are correlated is valid at a wide range of scenarios. However, due to the non-stationary nature of the copula, the dependence parameter can range from almost 0 (no correlation) to near 0.9. Despite being a probabilistic model, the computational cost is affordable: several minutes with a conventional desktop computer for the 79 beaches.

(Obj. 2D) Proposed error metrics and skill

The performance of LIM-COPAS has been contrasted with observations (see Sec. 3.2.2,3.2.4). The system veracity has been performed with qualitative and quantitative tools (Bennet et al., 2013). Each module has had specific metrics:

- **Meteorological and hydrodynamic module.** Most of these metrics are point-based (Hernández et al., 2015) and have been used in Ch. 4-5: (i) Mean Bias (MB); (ii) Root Mean Squared Error (RMSE); (iii) Normalised Root mean Squared Error (NRMSE); (iv) Pearson correlation coefficient; (v) Coefficient of Efficiency (COE) (Legates and McCabe, 1999); (vi) cost function (Holt et al., 2005).
- **Morphodynamic module.** In this case, it has been opted for the Brier Skill Score (BSS) index. This integrative coefficient compares the measured pre and post-storm LIDAR data with the modelled post-storm grid. An acceptable reproduction ranges around 0.4 (van Rijn et al., 2003), that has been the order of magnitude at the Study area (see Gràcia et al. (2013b) and Ch.4).
- **Risk module.** Quantitative criteria has been used in the fitting of the GAMLSS for each beach (Step 2, see Sec. 6.2.2), and the GLMs between the

coefficients and the morphodynamic features (Step 3, see Sec. 6.2.3). Concretely, two common information criterion have served for testing the goodness-of-fit of the sample with the risk model: (i) Akaike Information Criterion (AIC, Akaike (1973)) and Bayesian Information Criterion (BIC, Schwarz (1978)). For both cases, the lower the metric gets, more information from the sample describes the fitted model. The cornerstones for building the module have been (i) a physical reasoning of the suitability of each covariate, (ii) the principle of parsimony and (iii) minimisation of AIC/BIC.

(Obj. 2E) Design of proactive interventions

As noted in Obj.1A, this dissertation has proposed pro-active interventions with the aim of enhancing coastal protection against extreme events, but in a more compatible way with the other coastal uses (natural and socio-economic). This is the first time that has been tried to merge coastal forecasts with pro-active interventions at the Catalan Coast.

These solutions have been termed Quick Defense Measures (QDM, see Ch. 7). They consist of transient, timely, local interventions whose objective is to minimise coastal damages under extreme events. The principles beneath their design are: (i) to be local-based and tuned to the littoral cell; (ii) to be cost-effective; (iii) to have short construction time; (iv) to be based on endogeneous resources; (v) to have a limited life-time; (vi) to increase compatibility with the natural, economic and protection functions. Two specific cases has been analysed: transient dunes and geotextile detached breakwaters.

QDM has been designed for two urban beaches in Barcelona that suffer chronic coastal hazards: (i) Sant Sebastià (an intermediate beach) and (ii) Gavà (a dissipative one).

At Sant Sebastià the QDM consist of: (i) two dunes with an overall height of 1.5 m and 140 m alongshore; (ii) two detached breakwaters, deployed at $-2\,m$, with a ellipsoidal cross-section (1.7 m height and 7 m width) and 140 metres alongshore. At Gavà the proposed joint action consisted of a $50 \cdot 10^3\ m^3$ beach nourishment, with a transient dune belt of $45 \cdot 10^3\ m^3$ (1.5 m height and 3.4 km of alongshore length). The design lifetime of the nourishment has been set to 15 years.

The feasibility has been assessed in Obj.3G. However, the general behaviour of the two pilot sites has been evaluated at the designing phase (see Sec.7.4.1.1 and 7.4.2.1). The morphodynamic module has been used as a reference. For instance, the model outputs have discerned erosive/accretive and neutral areas. Active areas, from a sedimentary point of view, have been avoided to reduce possible stability problems.

Finally, **nine tenets** have been proposed to enhance **QDM robustness**: (i) clear problem definition; (ii) clarity on the main physical processes at the area; (iii) interaction with long-term measures that maximise the efficiency of the QDM; (iv) simplicity in design; (v) simplicity in building; (vi) good forecast skill (timing); (vii)

redundancy and willingness to adopt it (if the forecast misses, the QDM is useful); (viii) clear intervention protocols; (ix) continuous reassessment of the previous eight tenets.

(Obj. 2F) Selection of scenarios for testing the performance of LIM-COPAS

The performance of LIM-COPAS has been tested with (i) hindcast events (the whole modelling chain) and (ii) synthetic storm conditions (only the morphodynamic and risk modules).

The criteria for selecting the real events has been the following: (i) they needed to be representative of the extreme wave climate at the Study Area; (ii) observations needed to be available; (iii) they needed to be recent, because previous wave storms have been already analysed in the State-of-the-art (see Bolaños (2004); Alomar (2012); Pallarés (2016)).

The following storms were selected:

- **December 2008** [D-08, hereafter] (26/12/2008 - 29/12/2008), was a storm with a return period about $T_{r,waves} = 5\ yrs$ at the Northern part; $T_{r,waves} = 10\ yrs$ at the Central part; and at the Southern part was $T_{r,waves} = 1\ yrs$. The mean wave direction was East. The storm surge at the wave-storm peak was 15 cm at Barcelona.
- **October 2015** [O-15] (29/09/2015 - 01/10/2015) was an Eastern storm with a return period about $T_{r,waves} = 1-2\ yrs$, at the Central and Northern part of Catalonia. At the Southern part, the return period was near $T_{r,waves} = 1\ yrs$. The storm surge was around 14 cm for the whole episode at Barcelona.
- **November 2015** [N-15] (01/11/2015 - 04/11/2015) was a South-Eastern storm with a $T_{r,waves} = 1-2\ yrs$, at the Northern and Central part. The storm surge at the storm-peak was particularly important: 25 cm at Tarragona.
- **January 2016** [J-16] (10/01/2016 - 12/01/2016) was a SSW event with a $T_{r,waves} = 1\ yrs$ at the Northern part. At the Barcelona buoy, the return period was around $T_{r,waves} < 1\ yr$, due to the wave sheltering due to the shoreline orientation. The storm surge was 17 cm at the storm peak.
- **February 2016** [F-16] (27/02/2016 - 28/02/2016) was the mildest event in this dissertation. It consisted of an Eastern storm with a $T_{r,waves} < 1\ yr$ at the Northern part, and $T_{r,waves} = 1-2\ yrs$ at the Central part. The storm surge was 20 cm at Barcelona and 25 cm in Tarragona. Note that this high storm value was reached sharply: (15 cm in just 12 hours in 27/02/16).
- **December 2016** [D-16] (17/12/2016 - 23/12/2016) was a Eastern storm with a $T_{r,waves} = 8-10\ yrs$ at the Central part; $T_{r,waves} = 5-7\ yrs$ at the North. At the Southern part $T_{r,waves} = 2-4\ yrs$. The surge at the storm-peak was 15 cm.

- **January 2017** [J-17] (16/01/2017 - 24/01/2017) was the strongest event analysed in this thesis. The wave direction was East. $T_{r,waves} = 10 - 12\ yrs$ at the Central part; $T_{r,waves} = 5 - 7\ yrs$ at the North. At the Southern area, the $T_{r,waves}$ was $15 - 25\ years$. The surge at the storm-peak was higher at Tarragona (25 cm) than at Barcelona (10 cm).

The synthetic storm conditions have followed a set of references/guidelines.

- The initial and final wave height is set to $H_s = 2\,m$. The wave storm duration has been set-up at 24 hours, with equal growth and decay phases. These hypothesis are plausible and common at the Study Area, as stated in Lin-Ye et al. (2016).
- The database for building the risk module spans, as a minimum, wave return periods of 10, 50 and 100 years (Ch. 6). QDM (Ch. 7) has been assessed with another wave return periods (1,5 and 50 years). The wave directions were case-specific, focused on those that drove significant cross-shore fluxes.
- In Ch. 6, sea level scenarios that range from 0 to 60 cm has been tested, as a minimum. In Ch. 7, though, three sea level conditions has been tested: (i) no storm-surge contribution; (ii) $T_{r,MWL} = 1\ yr$ (around 53 cm); (iii) $T_{r,MWL} = 300\ yrs$ (around 86 cm). For the sake of simplicity, the sea level has been considered as stationary throughout the 24 hours of simulation.

The differences in the forcings between Ch. 6 - 7, can be justified as follows:

- In Ch. 6, the synthetic storms were the boundary conditions for generating a risk database. It was needed to span a wide range of extreme (but plausible) conditions at the Study Area (i.e. $T_{r,waves}$ =10 - 100 yrs; $MWL = 0 - 60\ cm$).
- In Ch. 7, these scenarios needed to assess the feasibility of QDM. So, the forcing spans the applicability range of QDM. The wave return period range is lower than the risk database (i.e. $T_{r,waves}$ =1 - 50 yrs); but the sea level was higher, for testing (i) the lifetime of the dune and (ii) the performance of the detached breakwater.

Performance of LIM-COPAS

The previous Section has summarised the proposed solution (LIM-COPAS) set-up and the testing scenarios. This part would summarise the system performance.

(Obj. 3A) Testing of the different modules with recent events and storm scenarios

In Obj. 2F, a set of (i) recent hindcast events and (ii) synthetic storm conditions have been summarised. The performance of the different modules can be found in the next paragraphs.

Meteorological module

Wind fields were systematically overestimated in all storms except D-08 (Ch. 5). The integrated mean bias was $-1.52 \pm 0.78\ m/s$. The modelled standard deviation was higher than the observed. Tarragona ($COE = 0.27 \pm 0.13$) and Begur ($COE = 0.29 \pm 0.17$) had metrics above the average value ($COE = 0.24 \pm 0.14$); but lower agreement was found at Mahón ($COE = 0.13 \pm 0.16$) and Dragonera. Note that a similar trend under the Klaus storm (January 2009) was reported by Bertotti et al. (2012).

LIM-COPAS has shown good accuracy with the most severe events of the database (i.e. D-16 and J-17). Note, though, that lower agreement was found for the moderate events (O-15 and F-16). That is probably due to the importance than local scale phenomena may have under moderate events; whilst the high return ones are strongly influenced by large-scale processes that usually exhibit better skill.

In the O-15 case, the pressure anomaly track was not properly modelled, then the spatial resolution of the wind fields were not accurate. The F-16 event experienced (i) a sea level pressure drop in its centre (around 10 hPa in 6 hours); (ii) heavy rains and (iii) a probable mismatch of the pressure anomaly track.

Hydrodynamic module

Wave metrics were higher than for the wind fields. Significant wave height (H_s) reported better performance than T_{m02}: the integrated H_s COE was 0.52 ± 0.12 and T_{m02} COE was 0.36 ± 0.14. The metrics for high return period events ($T_{r,waves} \geq 10\ yrs$; i.e. D-16 and J-17) show higher standard deviation than the observed. The moderate events (i.e. F-16, N-15 and J-16) tend to present lower standard deviation.

In Ch.4, D-08 hindcast was compared with altimeter data (Fig.4.5). Wave heights were accurately reproduced with NRMSE ranging from 0.2 to 0.6; but at coastal areas the model performance was more limited (NRMSE near 1.0).

At Barcelona, H_s has presented good metrics: low MB ($-0.06 \pm 0.08\ m$), low RMSE ($0.36 \pm 0.08\ m$), high correlation (0.92 ± 0.03) and high COE (0.58 ± 0.11). Begur metrics were the most stable: the standard deviation of the COE, both for H_s and T_{m02} was the lowest (± 0.05). This outcome is relevant, because both buoys show the LIM-COPAS performance at the Northern-Central part of the Catalan Coast, that is where coastal risk has been estimated (Ch. 6).

Morphodynamic module

The XBEACH model has been able to reproduce the main morphodynamic features. The calibration coefficients obtained in Gràcia et al. (2013b) (dissipative beaches) and Ch.4 (intermediate beaches) have provided a consistent post-storm response. The joint action of cross-shore and long-shore hydrodynamics was essential for capturing the coastal response. Alongshore processes gain importance in beaches with spatial heterogeneities, obstacles to the flow, etc.

For the event of **D-08**, in which a post-storm LIDAR was available, the BSS was

0.36 at Badalona and 0.38 at Mataró. These values can be considered as acceptable (van Rijn et al., 2003).

Risk module

The proposed risk model (Ch. 6) has been able to predict the same order of magnitude of total losses in comparison with the investment made from the Spanish competent ministry (Ministerio de Agricultura y Pesca, Alimentación y Medio Ambiente).

Erosion has been estimated as a bounded cost (i.e. both maximum and minimum can be estimated), whereas flooding (specially at dense urban areas) as a high upside cost. Erosion tends to be more accurate than flooding, because the former tends to be more time-homogeneous and the results are derived directly from the morphodynamic module outputs.

Dissipative beaches tend to exhibit higher costs than reflective beaches under high MWL, specially due to higher flooding damages. That is because most of the dissipative beaches in the calibration database have low berm heights. At reflective beaches, costs tend to be lower than dissipative ones, partly because the sand is coarser and berm heights tend to higher.

Moderate storm wave events (i.e. $T_{r,waves} \leq 10\,yrs$) joint with storm-surges can lead to significant damage costs. The estimated losses for the N-15 event ($2510 \cdot 10^3 euros$) do not differ excessively from the J-17 event ($3200 \cdot 10^3$ euros). The selected events (Obj. 2F) has shown spatial patterns that have lead to identify hot-spot areas, such as the Maresme strait, the Barcelona urban area and the Llobregat and Tordera deltas.

High values of dependence parameter(τ_K) show that the erosion and flooding costs share the same proportionality in the total coast. It has been found that low sea levels and high return periods of waves lead to higher values of τ_K.

(Obj. 3B) Comparison of hindcasted storms with in-situ and remote observations

The high resolution hindcasts have provided spatio-temporal gapless data on complex physical processes. They have been used as benchmark scenarios for the forecasting chain, but they have also helped to identify climatic patterns.

Note that the temporal scale has been the duration of a storm event (i.e. several days). Usually, analyses held in these temporal constraints (i.e. short-term under sharp gradients forcings) tend to have lower data agreement than at long-term scales (i.e. years). The detailed spatial scales plus the physical processes embedded in the different modules (see Obj. 2B) have strongly influenced the general performance of LIM-COPAS.

As highlighted in Obj.3A, the errors have been larger at the coastal zone. Errors in nearshore spectral wave parameters have been about twice what has been found in

the offshore Mediterranean basin. In Ch. 4, the D-08 error was 20% in hydrodynamics and 50% in morphodynamics. Systematically, when the meteorological module has exhibited good performance, good agreement has also been shown at SWAN. The next paragraphs will summarise the main findings for each specific storm.

The low agreement with the measurements in **O-15** was probably due to a non-properly modelled pressure anomaly track, then affecting the spatial distribution of the wind fields. It is hypothesized that the wave generation area was offshoreward than the computed one. The mismatches with the growth phase of the storm at Valencia buoy and the underestimation of the mean wave period reinforce this statement. However, the H_s metrics were accurate enough at Barcelona ($COE = 0.66$ and $RMSE = 0.3\,m$) and at Begur ($COE = 0.51$ and $RMSE = 0.57\,m$).

N-15 presented better metrics in wind speed and T_{m02} than O-15. The mean wave period at the storm-peak shows overestimations of $1.5\,s$ at Barcelona, Tarragona and Begur. At the same storm-interval, the wind speed had an overestimation of $6\ m/s$ at Begur; whilst at Tarragona has reached $3\ m/s$. The H_s metrics were similar to the ones in O-15.

J-16 was featured by a strong SSW wind jet that entered into the Mediterranean Basin via the Gibraltar Strait. The orographic effects of this strait were well captured with the WRF spatial resolution. The jet was properly modelled in intensity and direction, because the wind speed shown good agreement at Valencia, Tarragona and the Balearic island stations.

Although **F-16** was the mildest event, the wind speed COE was low at all in-situ points. Modelled H_s and T_{m02} had the same magnitude than the measurements, except from Valencia that shown an overestimation of $H_s \approx 1\,m$ at the storm peak. The wave storm-peak presented a lag of almost 1 day. As happened in O-15, a mismatch of the pressure anomaly track may be the cause. Wave direction errors at Tarragona (Fig. C.33) and Begur (Fig. C.35) reinforce this statement. Note also that heavy rains and a sharp pressure drop (10 hPa in 6 hours) were recorded in this episode.

D-16 and **J-17** had similar synoptic conditions, with the difference of the lifetime of the pressure centre: J-17 lasted 4 days, while D-16 only 2 days. In J-17, good wind speed metrics were achieved: (i) correlation coefficients higher than 0.75; (ii) $COE = 0.52$ in Begur; COE near 0.4 in Tarragona; and $COE = 0.40$ in Valencia.

In **D-16**, the H_s storm-peak was overestimated $0.5\,m$ in Barcelona and $1.5\,m$ at Tarragona (i.e. same order of magnitude than D-08 in Ch. 4). In **J-17** storm-peak, even better agreement was achieved: 30 cm of H_s error at Barcelona (measured $H_s = 5.3\,m$, Fig. C.42); and less than 10 cm at Tarragona (measured $H_s = 6.2\,m$, Fig. C.46).

(Obj. 3C) Testing of different configurations of the modelling chain

Meteorological and Hydrodynamic module

The hydrodynamic module has been tested with two different configurations:

- In the D-08 (Ch.4), the winds comprised operational ECMWF winds blended with remote-sensing observations (Bentamy et al., 2007) with a spatio-temporal resolution of 25×25 km and 6 h. The sea level and currents were daily-averaged with a resolution of circa 7 km from MyOcean (Tonani et al. (2009)). The SWAN model used three one-way regular grids (Fig. 4.1), that ranges from 9 to 1 km.
- For the rest of the hindcasted events (Ch. 5), the wind fields have been obtained from the downscaling of ERA-INTERIM reanalysis (Dee et al., 2011) with WRF (Skamarock et al., 2005) to a maximum spatio-temporal resolution of 3×3 km and 20 min. The sea level and current, from IBI-MFC Sotillo et al. (2015) were hourly-averaged with a resolution of circa 3 km. The SWAN model used two one-way regular grids (Fig. 3.2), that ranges from 5 to 2 km.

D-08 (Ch.4) and the high return period events in Ch.5 (D-16 and J-17) shared commonalities in the synoptic conditions (i.e. Eastern storm) and the model performance. Despite the differences in the origin of the inputs, both approaches provided good skill.

Offline coupling of wave-current fields increased the performance of the storm-peak modelling, specially in those cases in which strong wind-induced currents are within the inner shelf. Wind-induced currents at J-16, D-16 and J-17 reached important modulus that dampened ocean waves. In these cases, offline coupling improved the performance in a range of 20-50 cm the H_s at the storm-peaks. The inclusion of these consistent physical processes, instead of relying of overparametrization of wave dissipation mechanisms, proved to be essential to achieve better skills.

Morphodynamic module

The depth-averaged hypothesis has proved to be an accurate approximation. The interaction of cross-shore and and long-shore processes were necessary to capture these local behaviour. Note that two approaches of the XBEACH model has been used: (i) a phase-averaged version (Fig.3.3) aimed to obstacle-free open beaches; and (ii) a phase-solving mode (Sec.3.3.3.5) that can deal with individual wave scale processes (such as reflection and diffraction). The latter mode has an additional computational burden: the spatial gridsize needs to be finer (around $3\,m$ at Sant Sebastià case) and the time step lower, as well (i.e. to reach Courant numbers that ensures stability).

This phase-solving approach has been use in those beaches that exhibits local features such as detached breakwaters, groins or islands. In this dissertation, case studies such as Sant Sebastià beach, L'Estartit, Tossa de Mar, Premià de Mar, required this method (Tab. B.1). This non-hydrostatic hypothesis has proved to be valuable for assessing the QDM performance at Sant Sebastià, joint with local consequences as the tombolo growth (see Ch. 7 and Obj.3G).

(Obj. 3D) Establishing the sensibility to the inputs

LIM-COPAS has shown a relevant sensitivity to the inputs. Errors in the first steps of the modelling chain affect severely the whole forecast. For instance, in D-08 (Ch. 4), the wind modulus were perturbed in a ±20%, for the sake of coherence with the former statement (see Obj.3B) that the hydrodynamics errors ranged around 20%.

The reference COEs (i.e. no perturbation) for the wave parameters were (see Sec. 4.5): at Blanes, the H_s was 0.74 and the T_p was 0.51; at Llobregat, the same metrics were 0.68 and 0.59; and at Cape Tortosa, 0.73 and 0.49, respectively. However, once the wind speed was decreased a 20%, the COEs drop dramatically to low levels: at Blanes, H_s COE was 0.26 and T_p COE was 0.18; at Llobregat, COE decreased to -0.12 and 0.22; and at Cape Tortosa to -0.15 and 0.22, respectively.

The morphodynamic performance was also affected by these wind perturbations (Sec.4.6): in Mataró, the model improves substantially with +5% wind increases (BSS from 0.38 (base) to 0.44); in Badalona, the BSS increases from 0.36 to 0.40, when the wind decreases −5%. Badalona shown more wind sensitivity than Mataró: under heavier wind perturbations (±20%), Badalona BSS decreased to 0.2.

The initial state of the forecast can affect severely the error. At the Blanes buoy, in D-08, despite that the SWAN model and the buoys shared a similar growth slope, their offsets differ by about 1 m (Fig.4.2). Possible ways to overcome these hurdles may be: (i) the initial state has to be as coherent as possible with in-situ and remote observations; (ii) the forecast need to have enough spin-up time for dampening initial instabilities.

Cost estimation (Ch. 6) is significantly sensible to the wave height at reflective beaches, whereas similar sensibility is due to the sea level at dissipative beaches. The reason for this sensibility pattern may be that erosion losses are higher at reflective beaches, but flooding damages prevail at dissipative ones. Fortunately, LIM-COPAS has shown better wave skill at the Northern Area (Ch. 5), that is where most of the reflective beaches can be found.

The results of Ch. 6 and 7 have remarked the importance of wave direction. Errors in wave direction would not affect severely the erosion at dissipative beaches; but, they can drive flooding costs differences, specially in those case with low-lying features.

In general, sensibility can be understood as a double razor edge: (i) on the one hand, the LIM-COPAS system is flexible enough to reproduce slight changes; (ii) on the other hand, at some cases, specially under moderate events, slight perturbations may lead to raise/halt alarm. In the latter particular cases, an experience forecaster is paramount for avoiding false alarms and missed hits, then warranting CEWS rigidity and robustness.

(Obj. 3E) Identification of uncertainty in the modelling chain

Uncertainties in a CEWS may arise from different factors: (i) initial states (inicial forcings and morphodynamic features); (ii) boundary conditions (forcings and fluxes from outside the computational domain); (iii) simplifications assumed by physical parameterizations; and (iv) discretization methods for solving the mathematical model. The first two, affect relevantly to the forecast and must be specially addressed; the third one involves increasing the body of knowledge about the physical processes, but it is harder to obtain results; the last one may provide better solutions once addressed the first three points above.

In the meteorological module (Ch. 5), the spatial resolution of the last nesting ($3 \times 3\ km$) was enough for reproducing the most important orographic features (i.e. Pyrenees, Alps, Gibraltar strait). However, it may prove to be too coarse for modelling local phenomena (cloud fraction, precipitation, moisture levels, heat fluxes, land-sea processes) and surface processes that are heavily parametrized. Slight inconsistencies among variables can drive further errors. These inconsistencies may arise due to inaccurate surface physics or non-proper boundary conditions.

Run-off processes and river discharges would also provide local changes in flooding, sea salinity and temperature. The inclusion of the Ebro river discharge may affect the Tarragona buoy area and the Llobregat river, the one in Barcelona. Note that, in D-08, precipitation had daily mean values of 20 mm. In that event, the land discharge (i.e. sewer outfall in Badalona and the river stream in Mataró) was not included due to the lack of quantitative observations.

Another important source of uncertainty is the ceaseless variability of the swash zone and the sand budget at the littoral cell. Periodic monitoring of the emerged and submerged area can serve for bounding the uncertainty.

In the risk module (Ch. 6), the flooding costs would become more important in the near future if: (i) the assets increase in value or (ii) due to Sea Level Rise (SLR) (i.e. the overtopping will be more frequent). In the other hand, in the future, erosion will decrease as the sand budget becomes scarce (i.e. reduced beach width). One indicator for assessing how this ratio flooding/erosion costs change is via the dependence coefficient (τ_K). Additionally, the same coefficient may also serve for assessing the beach health.

Probabilistic forecasting can provide fast assessments on how uncertain are specific hydrodynamic conditions. The error bars shown in the stress-curves (Figs. 6.10-6.19) were obtained through thousands of cheap simulations. Despite that process-based modelling provides more detailed information, decision makers can benefit from this bounding; specially under low return period events in which intervention may be not so clear/justifiable.

(Obj. 3F) Quantification of the forecasting limits with the proposed tools

As stated in Obj.3B, the D-08 error was 20% in hydrodynamics and 50% in morphodynamics (Ch.4). Such error may be unacceptable under low return period events, because it can be the source of false alarms and missed hits. Additionally, forecast models rely on a set of parameterizations that may lead to lower prediction skills in the next decades. Climate Change will probably affect extremes (Trenberth and Shepherd, 2015; Emanuel, 2017). The hypothesis and the balances beneath these tools may change.

Monitoring networks constitute the basis for uncertainty reduction, thus providing robustness in the decision making. Long time series such as the Puertos del Estado and XIOM networks verify model projections and assess physical processes that the models cannot reproduce (Ch. 2.6).

Inconsistency among the interaction of the atmospheric variables was probably the main source of errors in the WRF model (Ch. 5). Such inconsistency can be due to: (i) difficulties for achieving the same quality for all the forcings; (ii) lack of input-data for variables that may have impact under extreme regimes; (iii) model simplifications and hypothesis, such as sub-grid scale processes and local phenomena; (iv) overparametrization of certain interactions among physical processes; (v) errors derived from the numerical scheme.

These errors boost wind speed overestimation, then leading to the following behaviour in the SWAN model:

- Overestimation of the significant wave height (H_s), partially alleviated because H_s is an integrated value of the bi-dimensional wave spectra (Eq. 3.4.7).
- Errors in wave period, when overestimated winds are located at the coastal zone, the high-frequency partition of the wave spectra tends to be overestimated; however, when the winds are located a the offshore part, then the low-frequency partition may be overestimated (see O-15 and F-16 in Sec. 5.4.2).
- Mismatches in the wave direction, specially in cases in which the wind veers towards a different sector at the decay-phase (see N-15 and F-16 in Sec. 5.4.2).

The XBEACH model tend to be more accurate with open, free from obstacle beaches (Ch. 4). The main constraints for improving morphodynamic forecasts are: (i) local phenomena implementation and (ii) digital elevation model update. The emerged area and the bathymetry need to be updated in the CEWS, with a site-specific frequency. For instance, Premià de Mar ($ero_{rate} = -5.76\, m/yr$) would need to be updated more frequently than St. Feliu de Guíxols ($ero_{rate} = -0.22\, m/yr$), see Tab. B.1.

In short, a CEWS has to be accurate, robust, updated-frequently and easily interpretable; in order to foster action towards preparedness (Obj. 3G).

(Obj. 3G) Determination of the feasibility of proactive interventions for diminishing coastal risk

In Obj.2E two pilot sites were proposed for assessing numerically the feasibility of QDM for mitigating episodic coastal risk. The following results has been found:

At Sant Sebastià, the efficiency of flood costs reduction decreases under high sea levels. At $T_{r,MWL} \leq 1\ yr$, the detached breakwater performs better than the dune; whereas at $T_{r,MWL} \geq 1\ yr$, the dune performs better (29.3 ± 7.6 (dune) vs. 25.0 ± 8.9 (detached), both in %). The saved costs are almost enough for covering the dune expenses.

Additionally, sand fluxes are more attenuated at the dune case. The mean value of the fluxes does not deviate excessively between the two QDM options; however, the standard deviation for the detached breakwaters is higher.

The proposed dimensions for the elements of the detached breakwater are plausible (Hornsey et al., 2011). The offshore fine material from the inner-shelf (Grifoll et al., 2014) can serve for filling geotextile sandbags. The transident dune at Sant Sebastià costs about the double with maritime works. The lack of offshore sand deposits at the area is one of the factors that affects to this difference. That is why has been proposed to extract the sand from a trench at the lower water depths (0 to $-2\ m$ deep).

The Gavà dune withstands hydrodynamic scenarios up to $T_{r,waves} = 5\ yr$ and $T_{r,MWL} = 1\ yr$. However, when the sea level increases to a $T_{r,MWL} = 300\ yr$, the dune collapses at the storm peak (12 hours after the simulation starts), even with low return period waves $T_{r,waves} = 1\ yr$.

At Gavà, the flooding cost reduction is stable, regardless of the scenario (around 18%). Under high sea levels ($T_{r,MWL} = 300\ yr$), the cost reduction is considerable (112.5 ± 51.2 thousands of euros). The sand fluxes are consistently lowered with the dune (from 165 to 57, both in thousands of euros), implying that the proposed beach profile is more stable than the reference.

The sediment may come from the western end of the Llobregat littoral cell. In that boundary, there exists accretion due to the joint action of (i) the littoral drift and (ii) the barrier effect created by a small craft harbour (Port Ginesta). The sediment can be bypassed to the North (i.e. Gavà beach) with terrestrial methods.

The total investment ranges $(1330 - 1530) \cdot 10^3\ euros$, but the estimated losses can be considered in the correct order of magnitude. The eroded volumes are in line with the lifetime of the nourishment (15 years) and the high return periods considered ($T_{r,waves} = 50\ yr$, see Fig. 7.14).

The benefits from maintaining the sand volumes outperform the flooding cost reduction. As exposed in Ch. 6, at both sites, erosion is a bounded cost, whereas flooding may have important upsides. QDM tend to produce higher costs reduction with high return period events. Note that LIM-COPAS is able to reproduce accurately this kind of extreme events (see Ch. 4 and 5).

In general terms, the detached breakwater can be a suitable option at intermediate beaches against low to moderate sea levels and high wave return periods. At dissipative beaches, dunes are the best option, but they require a minimum beach width (around 30 m) that ensures their lifetime.

QDM functionality can be enhanced with the joint action of compatible long-term actions (nourishments, sand bypasses, submerged vegetation, etc.), see Sec. 7.5.3. A healthy beach state is paramount for the QDM effectiveness. Coastal Risk Forecasting, Proactive Interventions and Long-term Planning are feasible elements for achieving high sustainability under present and future climate.

Conclusions of the Thesis

This thesis has assessed present coastal risks at the Catalan Coast through **a Coastal Early Warning System (CEWS), LIM-COPAS (LIM-COastal Processes Assessment System)**, that forecasts the more relevant episodic coastal hazards at the area. With this aim, this dissertation has made strong emphasis on the **reproduction/simulation and analysis of the coastal response in terms of flooding/erosion against storm impacts**.

LIM-COPAS is composed by four modules: (i) a meteorological model (WRF, Skamarock et al. (2005)); (ii) a hydrodynamic model (SWAN, Booij et al. (1999)); (iii) a morphodynamic module (XBEACH, Roelvink et al. (2009)) and (iv) a risk module based on a multivariate non-stationary model. The performance has been tested with (i) a set of hindcast events and (ii) synthetic storm conditions. The hindcasted events have been: December 2008 (D-08); October-2015 (O-15); November 2015 (N-15); January 2016 (J-16); February 2016 (F-16); December 2016 (D-16) and January 2017 (J-17). Different observational data has been used as reference: (i) Puertos del Estado and XIOM meteo-oceanographic networks; (ii) LIDAR data and (iii) altimeter data.

In D-08, errors in nearshore spectral wave parameters have been about twice what has been found in the offshore Mediterranean basin. The error was around 20% in hydrodynamics and 50% in morphodynamics. The post-storm response, compared with LIDAR, shown a Brier Skill Score (BSS) of 0.36 at Badalona and 0.40 at Mataró, that can be considered as acceptable (van Rijn et al., 2003).

The modelling chain has shown strong sensitivity to the inputs: once the wind speed decreased a 20% at Llobregat buoy, the H_s Coefficient of Efficiency (COE) decreased from 0.68 to -0.12; and the T_p COE from 0.59 to 0.22. Same wind reductions lead to BSS of 0.2 at Badalona and 0.32 at Mataró.

LIM-COPAS has shown good accuracy with the most severe events of the database (i.e. $T_{r,waves} \geq 10\,yrs$, D-16 and J-17). Note, though, that lower agreement was found for the moderate events (O-15 and F-16).

The meteorological module provided wind fields that were systematically overestimated. The integrated Mean Bias (MB) was $-1.52 \pm 0.78\ m/s$. The modelled standard deviation was higher than the observed. Tarragona ($COE = 0.27 \pm 0.13$) and Begur ($COE = 0.29 \pm 0.17$) had metrics above the average value ($COE = 0.24 \pm 0.14$); but lower agreement was found at Mahón ($COE = 0.13 \pm 0.16$) and Dragonera. Note that a similar trend under the Klaus storm (January 2009) was reported by Bertotti et al. (2012).

Wave metrics had better agreement with data than those for the wind fields. Significant wave height (H_s) reported better performance than T_{m02}: the integrated H_s COE was 0.52 ± 0.12 and T_{m02} COE was 0.36 ± 0.14. High return period events ($T_{r,waves} \geq 10\,yrs$; i.e. D-16 and J-17) show higher standard deviation than the observed; whereas the moderate ones (i.e. F-16, N-15 and J-16) tend to present lower standard deviation.

Offline coupling of wave-current increased the performance of the storm-peak modelling, specially in those cases in which strong wind-induced currents are within the inner shelf. In J-16, D-16 and J-17, the inclusion of IBI-MFC outputs (Sotillo et al., 2015), improved the performance in a range of 20-50 cm the H_s at the storm-peaks.

At Barcelona, H_s has presented good metrics: low MB ($-0.06 \pm 0.08\ m$), low RMSE ($0.36 \pm 0.08\ m$), high correlation (0.92 ± 0.03) and high COE (0.58 ± 0.11). Begur metrics were the most stable: the standard deviation of the COE, both for H_s and T_{m02} was the lowest (± 0.05). This outcome is relevant, because both buoys show the LIM-COPAS performance at the Northern-Central part of the Catalan Coast, that is where coastal risk has been estimated.

The newly developed risk module has been implemented at 79 beaches (54 calibration dataset and 25 validation). The calibration dataset comprises 2300 simulations from the morphodynamic module. The computational time for building this dataset is of the order of several months with parallel computing. Episodic erosion and flooding costs have been derived from the XBEACH outputs. Erosion has been estimated as a bounded cost, whereas flooding (specially at dense urban areas) as a high upside cost.

The LIM-COPAS system has been able to predict the same order of magnitude of total losses in comparison with the investment made from the Spanish competent ministry (Ministerio de Agricultura y Pesca, Alimentación y Medio Ambiente).

Dissipative beaches tend to exhibit higher costs than reflective beaches under high sea levels. That is because most of the dissipative beaches in the calibration database have low berm height and are, thus, more vulnerable to flooding. At reflective beaches, costs tend to be lower than dissipative ones, partly because the sand is coarser and berm heights tend to higher.

Moderate storm wave events (i.e. $T_{r,waves} \leq 10\,yrs$) joint with storm-surges can lead to significant damage costs. The estimated losses for the N-15 event ($2510 \cdot 10^3 euros$) do not differ excessively from the J-17 event ($3200 \cdot 10^3$ euros). Additionally, high values of dependence parameter(τ_K) show that the erosion and flooding costs share the same proportionality in the total coast. It has been found that low sea levels and high return periods of waves lead to higher values of τ_K.

After testing the LIM-COPAS system, this dissertation has proposed pro-active interventions with the aim of enhancing coastal protection against extreme events, but in a more eco-compatible way with the other coastal uses. These solutions have been termed Quick Defence Measures (QDM). QDM feasibility has been numerically tested in two urban beaches that suffer chronic coastal hazards: (i) Sant Sebastià (an intermediate beach, according to Wright and Short (1984)) and (ii) Gavà (a dissipative one).

At Sant Sebastià the QDM consist of: (i) two dunes with an overall height of 1.5 m and 140 m alongshore; (ii) two detached breakwaters, deployed at $-2\,m$, with a ellipsoidal cross-section (1.7 m height and 7 m width) and 140 metres alongshore. At Gavà has been proposed the joint action of a $50 \cdot 10^3\ m^3$ beach nourishment, with a transient dune belt of $45 \cdot 10^3\ m^3$ (1.5 m height and 3.4 km of alongshore length).

A set of hydrodynamic scenarios have been analysed, spanning the applicability range of QDM: (i) 24-hr storm waves with $T_{r,waves} = 1, 5, 50\,yrs$ and (ii) mean water levels with $T_{r,MWL} = 0\,cm, 1\,yr, 300\,yr$. LIM-COPAS has been able to reproduce the main morphodynamic features and their interaction with the QDM.

At Sant Sebastià, the efficiency of flood costs reduction decreases under high sea levels. At $T_{r,MWL} \leq 1\,yr$, the detached breakwater performs better than the dune; whereas at $T_{r,MWL} \geq 1\,yr$, the dune performs better (29.3 ± 7.6 (dune) vs. 25.0 ± 8.9 (detached), both in %). The saved costs are almost enough for covering the dune expenses.

Additionally, sand fluxes are more attenuated at the dune case. The mean value of the fluxes does not deviate excessively between the two QDM options; however, the standard deviation for the detached breakwaters is higher.

At Gavà, the flooding cost reduction is stable, regardless of the scenario (around 18%). Under high sea levels ($T_{r,MWL} = 300\,yr$), the cost reduction is considerable (112.5 ± 51.2 thousands of euros). The sand fluxes are consistently lowered with the dune (from 165 to 57, both in thousands of euros), implying that the proposed beach profile is more stable than the reference.

The benefits from maintaining the sand volumes outperform the flooding cost reduction. In general terms, the detached breakwater can be a suitable option at intermediate beaches against low to moderate sea levels and high wave return periods. At dissipative beaches, dunes are the best option, but they require a minimum beach width (around $30\,m$) that ensures their lifetime.

QDM functionality can be enhanced with the joint action of compatible long-term actions (nourishments, sand bypasses, submerged vegetation, etc.). A healthy beach state is paramount for the QDM effectiveness. Coastal Risk Forecasting, Proactive Interventions and Long-term Planning are feasible elements for achieving high sustainability under present and future climate.

Future research work

This dissertation has proposed LIM-COPAS as a forecasting system for assessing present coastal risk. This general idea paves the way for improvements that could be addressed in future works. Herein can be found a short proposal:

1. **Operational testing:** LIM-COPAS has been tested with a set of hindcast scenarios (Ch. 4-6). The next step would be to include LIM-COPAS within an operational framework to evaluate its feasibility.
2. **Pilot testing of Quick Defence Measures (QDM) in a hot-spot area:** The feasibility of QDM has been numerically analysed in Ch. 7. But the efficiency needs to be assessed with a real pilot intervention. This deployment would require to be heavily monitored.
3. **Testing the interaction of Nature Based Solutions with QDM:** The efficiency of the QDM depends on the beach health. Nature Based Solutions are long-term oriented interventions, but their interaction with the QDM would need to be further assessed with pilot testing. Such testing would quantify their eco-compatibility and to bound their applicability range.
4. **Promoting continuous monitoring at the CEWS Study Area, via in-situ and remote-sensing:** Observations are the only way to verify the model forecasts and to improve the body of knowledge of the different physical processes that happens in the Study area. Long-term monitoring is the only way to ensure that the parametrizations and the physical processes are updated with the current coastal state. Remote-sensing can provide observations at places in which conventional in-situ instrumentation would be complicated. In the same regard, data assimilation algorithms could improve the forecast skill, with strong emphasis on areas in which local processes have a primary role.
5. **Improving the forecast skill with moderate storms:** Moderate storms are more frequent that high return period ones. However, the present version of LIM-COPAS shows lower skill under low return period events. In order to build trust, research should emphasis in these moderate cases, specially under concomitant action of waves and surges. Several tasks needs to be conducted: (i) to improve the consistency of the inputs and forcings at the whole forecasting chain; (ii) to hindcast and analyse storm events, in order to find coherent patterns and rules; (iii) to conduct ensemble forecasting, for bounding the uncertainty.
6. **Improving the forecast skill for the wind fields:** The current version of the meteorological module has systematically overestimated the wind speed (Ch.5). Hence, the atmospheric circulation processes, both at mesoscale and local scale need to be further addressed. Further tests with other parameterizations could be used.
7. **Inclusion of a regional circulation model inside LIM-COPAS:** The inclusion of currents has been relevant for improving the wave metrics, specially

under strong wind-induced currents events (J-16, D-16 and J-17). The meteorological module can provide forcings for storm-surge and circulation forecasts. Note that there already exists successful initiatives in the Mediterranean Sea, such as NIVMAR (Álvarez-Fanjul et al., 2001). Additionally, a high resolution model, such as ROMS (Shchepetkin and McWilliams, 2005), could address local circulation at the continental and inner-shelf. For the sake of coherence between these local models and already implemented initiatives, NIVMAR or IBI-MFC (Sotillo et al., 2015) forecasts could be used as forcings.

8. **Incorporating river and run-off processes:** A coupled hydrological and hydraulic model forced with the precipitation forecasts from the meteorological module, could provide land water discharges. These discharges would lead to more accurate balances in heat fluxes, moisture, sea temperature and salinity.
9. **Two-way coupling of the met-ocean and sedimentary module:** This dissertation has considered one-way coupling among the different LIM-COPAS modules. This one-way coupling involves a set of hypothesis that could not be satisfied under certain combinations of factors. Overparametrization of certain couplings could be better handled with a dynamic exchange of information among models. Hence, it is proposed to test further two-way couplings. Note that important advances at the Study Area has already been conducted in previous research (Grifoll et al., 2016; Pallarés, 2016), but further testing, specially under extreme events is necessary. Two-way coupling could improve consistency among the inputs of the models, then leading to improve the metrics in complex events as O-15 and F-16.
10. **Unstructured grids testing:** The present version of LIM-COPAS relies on nesting procedures at the atmospheric and wave model (see Ch.3). The computational time could be reduced with unstructured grids, as Pallarés et al. (2017) shown with the SWAN model. In the same work, unstructured grids required half of the computational time than the structured ones, but without any significant difference of the error metrics.
11. **Improvement of the risk module database:** The current version of the risk database (Step 1 in Ch.6) requires further sampling at dissipative and open beaches, that are more usual at the Southern part of the Catalan Coast. Another important issue is the hypothesis of the storm duration (24 hours) with equal growth and decay phase. Despite that this hypothesis is plausible in the NW Mediterranean Sea, this may prove insufficient at other areas. Different storm combinations would need to be included. In case that the risk module would be implemented in macro-tidal environments, the morphodynamic simulations would need to consider such tidal ranges.
12. **Improvement of the risk module formula:** The principle of parsimony and minimisation of AIC/BIC have been important metrics for building the risk formula (Step 3 in Ch.6). However, further sampling may imply to add covariates and/or degrees of freedom to the GAMLSS and GLMs. These new covariates would aim to expand the applicability range of the risk module.

13. **Exporting LIM-COPAS to other environments:** The proposed CEWS strategy can be replicated at other coastal areas, be it another areas of the Spanish coastline or another countries. Microtidal areas, such as the Black Sea would be suitable candidates with the present model strategy. However, the proposed approach could be developed for tidal sites. In these cases, and as highlighted above, the implementation of the CEWS would require long-term monitoring for ensuring a robust standpoint towards reliable forecasts.

A. Detailed maps of the Study Area

This Appendix A presents the detailed maps of the Northern and Central Catalan Coast. These maps have been cited throughout this dissertation. They shows the exact position of the in-situ monitoring network (Puertos del Estado, XIOM) and the Calibration (green) and Validation (purple points). Note that this information complements Appendix B, that presents the morphodynamic features for the beaches that have been considered in this dissertation.

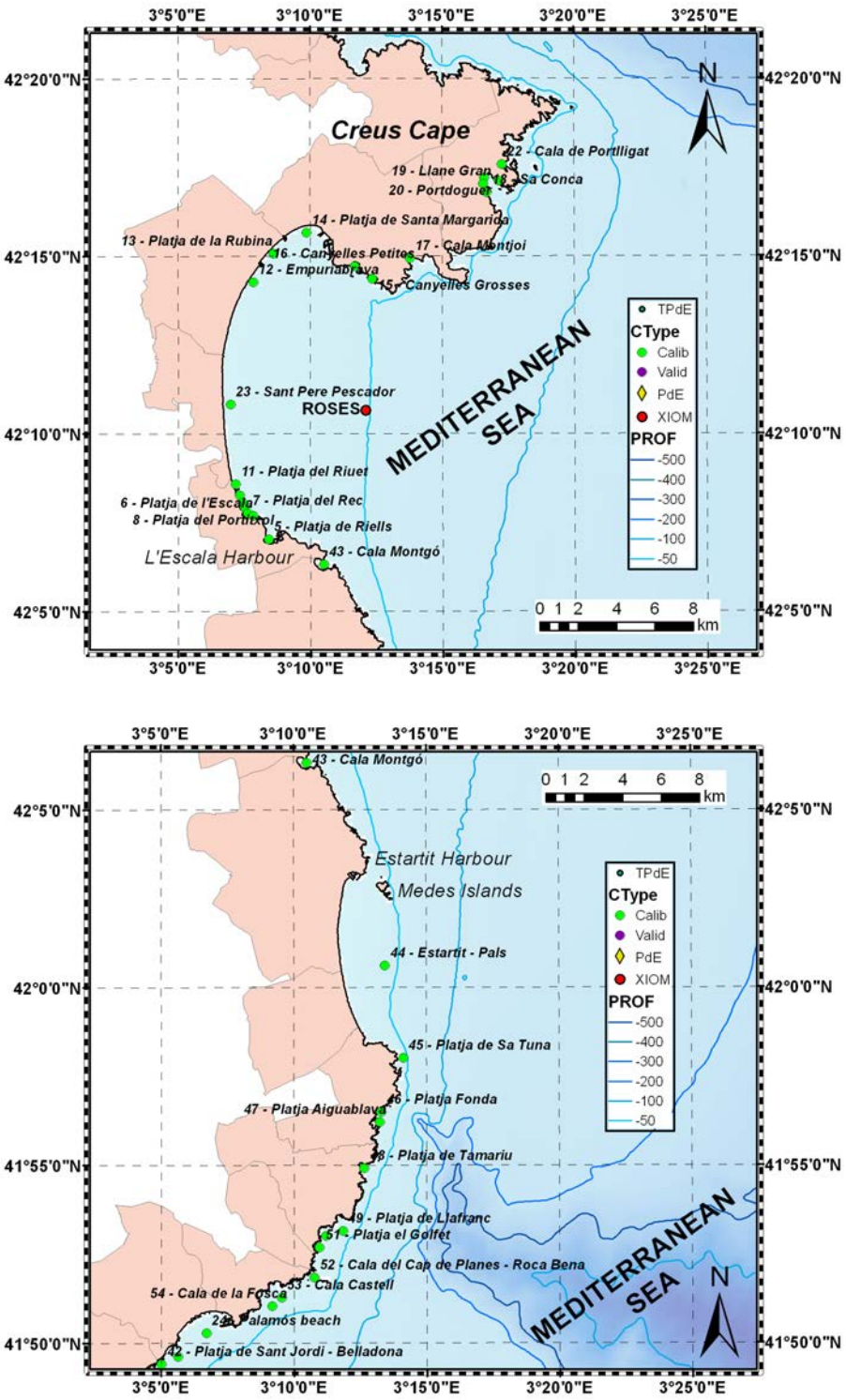

Figure A.1.: Subplot [1-2/5] of the study area, showing the position of the beaches that will be studied in this dissertation. The contour areas show the bathymetry. Yellow diamonds denote the position of the buoys of the PdE network. In red dots, it can be found the XIOM dataset. In green dots, the position of the calibration beaches (see Ch. 6).

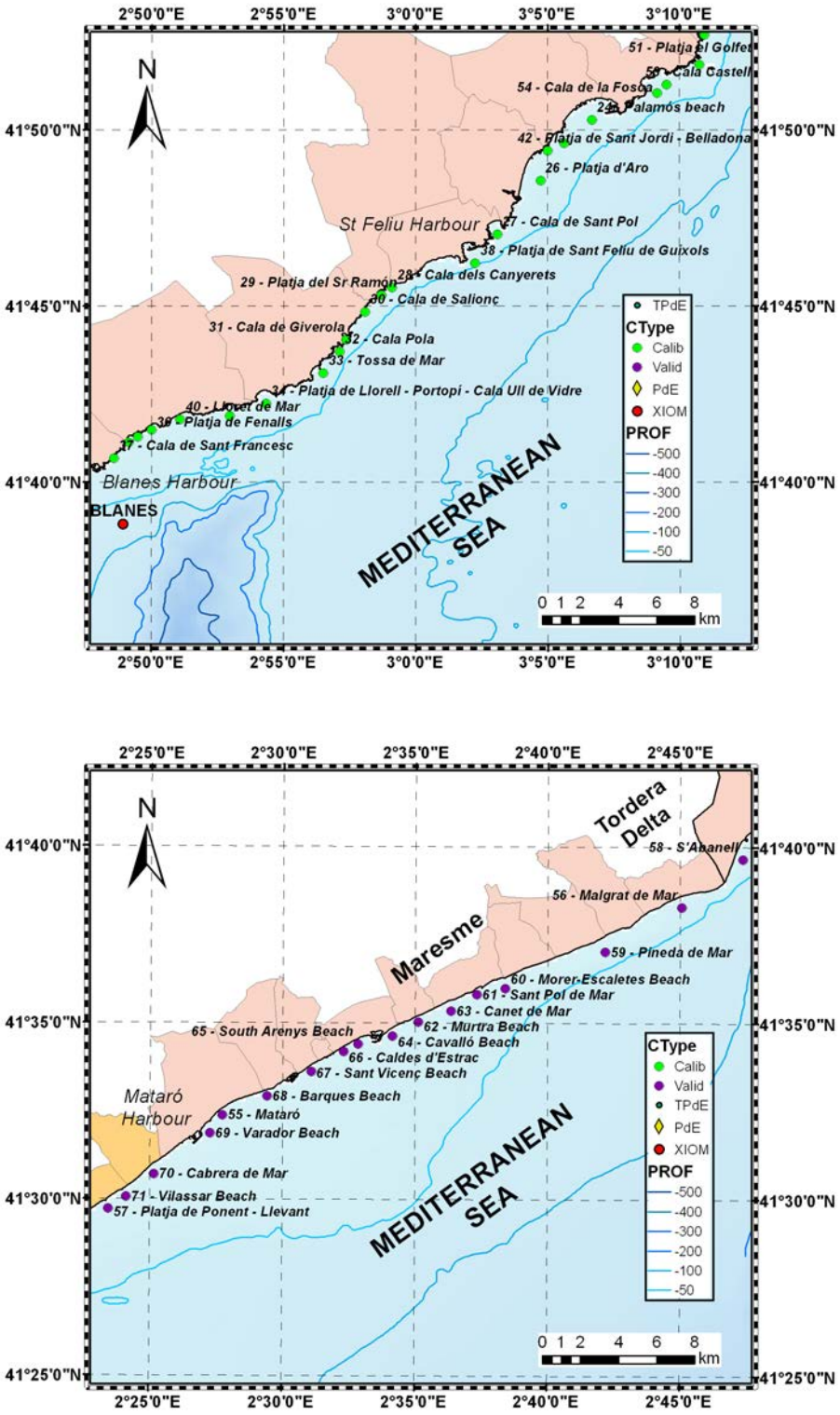

Figure A.2.: Subplot [3-4/5] of the study area, showing the position of the beaches that will be studied in this dissertation. The contour areas show the bathymetry. Yellow diamonds denote the position of the buoys of the PdE network. In red dots, it can be found the XIOM dataset. In green dots, the position of the calibration beaches, whereas the purple ones denote the validation beaches (see Ch. 6).

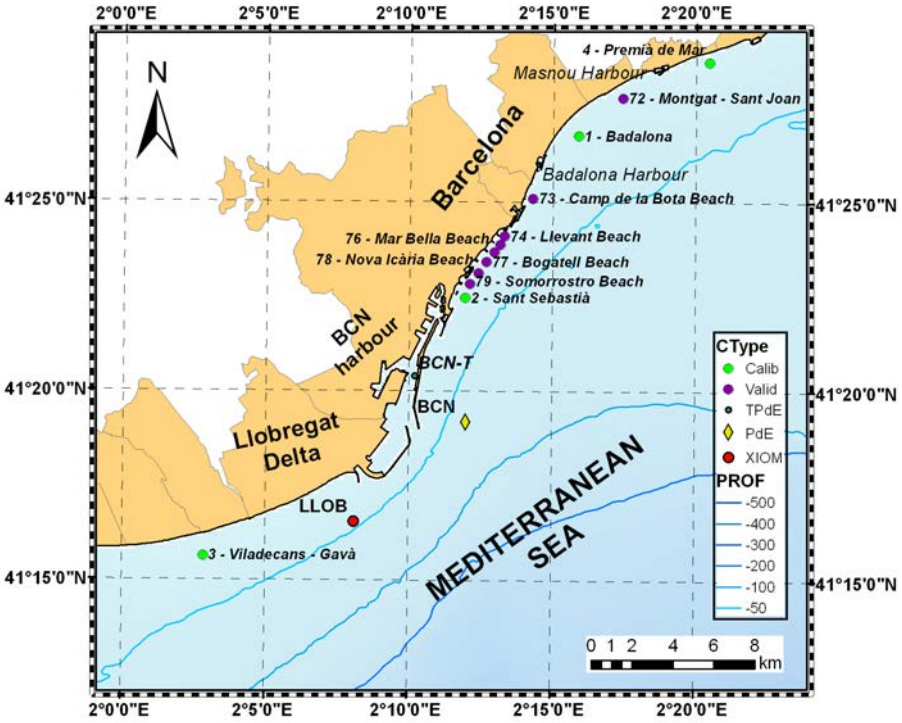

Figure A.3.: Subplot [5/5] of the study area, showing the position of the beaches that will be studied in this dissertation. The contour areas show the bathymetry. Yellow diamonds denote the position of the buoys of the PdE network. In red dots, it can be found the XIOM dataset. In green dots, the position of the calibration beaches, whereas the purple ones denote the validation beaches (see Ch. 6).

B. Morphological features and risk dataset description

This Appendix B presents the **morphological features** of the different beaches that have been analysed in this dissertation. Additionally, it is summarised the main **statistics** of the **erosion** and **flooding costs** associated to the **Calibration** dataset in the risk module (Ch. 6).

B.1. Morphological features and dataset description

Table B.1.: Morphological features of the simulated beaches with the Morphodynamic module (**calibration** dataset for the Risk module, see Ch. 6). **Legend:** ***ID*** *(identification number that matches with the ones at the* ***green*** *dots at Fig. A.1,A.2 and A.3);* ***Name*** *(name of the beach);* ***Type*** *(beach type: Open (O) or Pocket (P));* $\mathbf{L_{bch}}$*(beach alongshore length in m);*$\mathbf{W_{bch}}$*(beach width in m);*$\mathbf{A_{dean}}$*(Dean Number);*$\mathbf{Brm_{bch}}$*(berm height in m);*$\mathbf{slp_{em}}$*(beach slope);*$\mathbf{D_{50}}$*(mean sediment size in mm);*$\mathbf{ero_{rate}}$*(erosion rate in m/yr);* $\mathbf{buil_{\%}}$*(percentage of building area at the backshore).*

ID	Name (Type)	L_{bch}	W_{bch}	A_{dean}	Brm_{bch}	slp_{em}	D_{50}	ero_{rate}	$buil_{\%}$
1	Badalona (O)	3096	34	0.23	2.34	0.20	0.55	-1.92	0.55
2	Barcelona (P)	1360	45	0.79	2.40	0.14	0.87	-1.30	0.72
3	Gavà (O)	3580	89	0.12	1.40	0.25	0.25	-0.40	0.53
4	Premià de Mar (O)	4130	30	0.23	1.40	0.17	0.55	-5.76	0.46
5	Platja de Riells (P)	507	54	0.12	1.22	0.12	0.29	-0.17	0.72
6	La Platja (Creus) (P)	105	19	0.49	1.54	0.15	1.21	-0.17	0.71
7	Platja del Rec (P)	321	23	0.15	1.54	0.15	0.43	-0.17	0.30
8	Platja del Portitxol (P)	184	22	0.15	2.74	0.15	0.43	-0.64	0.33

ID	Name (Type)	L_{bch}	W_{bch}	A_{dean}	Brm_{bch}	slp_{em}	D_{50}	ero_{rate}	$buil_{\%}$
9	Les Muscleres (P)	417	22	0.15	2.54	0.19	0.43	-1.49	0.33
10	Muscleres Grosses (P)	233	54	0.16	1.07	0.13	0.47	-1.83	0.10
11	Platja del Riuet (P)	685	37	0.15	1.94	0.15	0.44	-0.91	0.07
12	Empuriabrava (O)	1283	96	0.15	1.25	0.15	0.44	-1.27	0.58
13	Platja de la Rubina (O)	1969	81	0.13	1.21	0.11	0.32	-0.86	0.18
14	Pl. Sta Margarida (O)	1330	34	0.13	0.78	0.12	0.31	-0.63	0.56
15	Canyelles Grosses (P)	461	32	0.14	2.07	0.12	0.39	-0.11	0.59
16	Canyelles Petites (P)	350	32	0.14	2.07	0.12	0.39	-0.11	0.57
17	Cala Montjoi (P)	299	32	0.19	1.09	0.09	0.72	-0.12	0.16
18	Sa Conca (P)	91	19	0.19	1.10	0.28	0.72	-0.12	0.25
19	Llane Gran (P)	94	25	0.19	3.58	0.16	0.72	-0.21	0.60
20	Portdoguer (P)	211	22	0.18	1.01	0.09	0.7	-0.10	0.57
21	Platja Ses Oliveres (P)	76	18	0.18	1.42	0.10	0.7	-0.10	0.54
22	Platja de Port Lligat (P)	188	34	0.18	0.63	0.11	0.7	-1.02	0.39
23	Sant Pere Pescador (O)	9920	131	0.40	1.55	0.11	0.23	-3.51	0.03
24	Palamos beach (O)	3300	52	0.49	2.32	0.14	1.22	-0.33	0.58
25	Can Cristos (P)	440	55	0.67	2.53	0.15	1.69	-0.68	0.30
26	Platja d'Aro (O)	3175	48	0.6	5.66	0.40	1.49	-0.75	0.38
27	Platja de Sant Pol (P)	700	50	0.14	2.39	0.12	0.38	0.16	0.55
28	Cala dels Canyerets (P)	194	32	0.31	2.79	0.09	0.74	-0.33	0.07
29	Platja del Sr Ramon (P)	320	31	0.67	0.91	0.16	1.69	-0.56	0.09
30	Cala de Salionc (P)	97	49	0.74	3.04	0.33	1.86	-0.05	0.24
31	Cala de Giverola (P)	160	62	0.53	2.02	0.08	1.32	-0.19	0.12
32	Cala Pola (P)	70	52	0.62	2.11	0.08	1.56	-0.05	0.07
33	Tossa de Mar (O)	507	79	0.59	2.73	0.13	1.48	-0.86	0.50
34	Platja de Llorell (P)	730	48	0.17	2.01	0.18	0.61	-0.81	0.19

ID	Name (Type)	L_{bch}	W_{bch}	A_{dean}	Brm_{bch}	slp_{em}	D_{50}	ero_{rate}	$buil_{\%}$
35	Platja de Canyelles (P)	377	47	0.47	2.54	0.10	1.16	-0.76	0.23
36	Platja de Fenalls (O)	720	45	0.57	3.10	0.26	1.41	-0.31	0.29
37	Cala de St Francesc (P)	133	48	0.57	1.95	0.12	1.41	-0.06	0.37
38	St Feliu de Guixols (P)	611	63	0.20	3.14	0.14	0.83	-0.22	0.48
39	Platja de Treumal (P)	432	45	0.48	2.30	0.29	1.33	-0.17	0.13
40	Lloret de Mar (O)	1322	43	0.45	2.11	0.14	1.23	-0.48	0.48
41	Cala de sa Cova (P)	200	41	0.54	2.50	0.23	1.33	-0.04	0.02
42	Platja de Sant Jordi (P)	313	26	0.20	2.61	0.14	0.93	-0.08	0.34
43	Cala Montgó (P)	155	52	0.18	1.40	0.15	0.41	-2.59	0.14
44	Estartit Bch / Pals (O)	8906	80	0.17	2.05	0.13	0.39	-1.36	0.12
45	Platja de sa Tuna (P)	68	23	0.26	1.41	0.18	0.61	-0.15	0.18
46	Platja Fonda (P)	131	18	0.67	1.54	0.20	1.68	-0.15	0.21
47	Platja Aiguablava (P)	70	24	0.31	1.50	0.12	0.73	-0.15	0.19
48	Platja de Tamariu (P)	209	25	0.74	2.27	0.08	2.27	-0.33	0.28
49	Platja de Llafranc (P)	347	29	0.39	2.83	0.08	2.83	-0.42	0.46
50	Calau bch – Port Bo (P)	462	16	0.63	1.43	0.17	1.43	-0.30	0.54
51	Platja el Golfet (P)	75	17	0.59	2.40	0.21	2.4	-0.34	0.19
52	Cala Cap de Planes (P)	481	13	0.59	0.95	0.13	0.95	-0.60	0.07
53	Platja de Castell (P)	339	63	0.54	1.78	0.13	1.78	-1.03	0.08
54	Platja de la Fosca (P)	514	34	0.15	1.46	0.21	1.45	-1.08	0.47

Table B.3.: Morphological features of the of the **validation** dataset for the **Risk** module, see Ch. 6). **Legend:** ***ID*** *(identification number that matches with the ones at the* ***purple*** *dots Fig. A.1,A.2 and A.3);* ***Name*** *(name of the beach);* ***Type*** *(beach type: Open (O) or Pocket (P));* $\mathbf{L_{bch}}$*(beach alongshore length in m);*$\mathbf{W_{bch}}$*(beach width in m);*$\mathbf{A_{dean}}$*(Dean Number);*$\mathbf{Brm_{bch}}$*(berm height in m);*$\mathbf{slp_{em}}$*(beach slope);*$\mathbf{D_{50}}$*(mean sediment size in mm);*$\mathbf{ero_{rate}}$*(erosion rate in m/yr);* $\mathbf{buil_{\%}}$*(percentage of building area at the backshore).*

ID	Name (Type)	$\mathbf{L_{bch}}$	$\mathbf{W_{bch}}$	$\mathbf{A_{dean}}$	$\mathbf{Brm_{bch}}$	$\mathbf{slp_{em}}$	$\mathbf{D_{50}}$	$\mathbf{ero_{rate}}$	$\mathbf{buil_{\%}}$
55	Mataró bch (O)	1785	30	0.42	1.73	0.19	1.02	-1.25	0.29
56	Malgrat de Mar (O)	5862	64	0.53	2.31	0.19	1.32	-1.29	0.26
57	Ponent - Llevant bch (O)	1920	65	0.27	1.78	0.24	0.65	0.66	0.38
58	S'Abanell (O)	2990	34	0.54	2.88	0.18	1.35	-0.87	0.45
59	Pineda de Mar (O)	5510	56	0.51	2.91	0.18	1.26	-1.26	0.45
60	Platja del Morer (O)	1145	61	0.71	2.90	0.16	1.78	0.84	0.22
61	Sant Pol de Mar (P)	725	19	0.71	2.64	0.19	1.80	-1.44	0.48
62	Murtra beach (P)	869	28	0.63	2.36	0.18	1.58	-0.38	0.10
63	Canet de Mar (O)	3806	44	0.56	3.58	0.19	1.38	0.01	0.49
64	Cavalló beach (O)	1558	82	0.72	3.10	0.19	1.81	0.20	0.25
65	Arenys harbour S (P)	595	68	0.38	1.80	0.18	0.92	-4.10	0.51
66	Musclera bch (O)	1169	59	0.31	2.18	0.22	0.75	-4.42	0.32
67	St Vicenç bch (O)	1838	79	0.34	2.04	0.24	0.82	-1.79	0.40
68	Barques bch (P)	365	30	0.29	1.21	0.12	0.69	-0.21	0.46
69	Varador bch (P)	780	105	0.26	2.00	0.18	0.62	-2.90	0.59
70	Cabrera de Mar bch (O)	1457	36	0.23	2.20	0.10	0.54	-3.55	0.35
71	Vilassar bch (P)	981	19	0.39	2.40	0.14	0.95	-2.00	0.79
72	Montgat - St. Joan (O)	2715	36	0.25	1.71	0.18	0.58	-5.00	0.31
73	Camp de la Bota bch (P)	1285	45	0.61	2.65	0.14	1.51	2.10	0.30
74	Llevant bch (P)	218	30	0.20	1.90	0.15	0.52	-3.60	0.05

ID	Name (Type)	L_{bch}	W_{bch}	A_{dean}	Brm_{bch}	slp_{em}	D_{50}	ero_{rate}	$buil_{\%}$
75	Nova Mar Bella bch (P)	265	45	0.24	2.20	0.30	0.57	-2.50	0.08
76	Mar Bella bch (P)	515	43	0.20	2.10	0.10	0.47	-2.50	0.13
77	Bogatell bch (P)	625	32	0.20	2.50	0.10	0.47	-2.40	0.12
78	Nova Icària bch (P)	410	54	0.20	1.40	0.15	0.46	-1.40	0.26
79	Somorrostro bch (P)	520	74	0.12	2.60	0.09	0.27	-1.20	0.45

Table B.5.: Summary of the **erosion cost** ε_r obtained from the morphodynamic module simulations (**Step 1** of the Risk module). **Legend:** $\mathbf{n_s}$ *(total number of simulations at that beach)* $\mathbf{E}(\boldsymbol{\varepsilon_{tot}})$ *(expected value of the* ***total*** *erosion cost)* **,Var** $(\boldsymbol{\varepsilon_{tot}})$ *(variance of the total erosion cost),*$\mathbf{Q_1}(\boldsymbol{\varepsilon_{tot}})$*(first-quantile of the total erosion cost)* **,**$\mathbf{Q_3}(\boldsymbol{\varepsilon_{tot}})$ *(third-quantile of the total erosion cost),***Max** $(\boldsymbol{\varepsilon_{tot}})$ *(maximum value of the total erosion cost). The latter five variables in* ***euros.*** $\mathbf{E}(\boldsymbol{\varepsilon_c})$ *is the* ***expected unitary value*** *of the erosion cost, in* $\mathbf{euros/m^2}$.

ID	Name	n_s	$\mathbf{E}(\varepsilon_{tot})$	$\mathbf{Var}(\varepsilon_{tot})$	$\mathbf{Q_1}(\varepsilon_{tot})$	$\mathbf{Q_3}(\varepsilon_{tot})$	$\mathbf{Max}(\varepsilon_{tot})$	$\mathbf{E}(\varepsilon_c)$
1	Badalona	144	4.80E+4	6.44E+4	3.01E+2	7.95E+4	2.86E+5	0.48
2	Barcelona	36	8.36E+4	8.44E+4	1.81E+4	1.35E+5	3.08E+5	1.38
3	Gavà	96	8.04E+4	8.19E+4	2.07E+4	9.98E+4	3.07E+5	0.24
4	Premià de Mar	59	1.17E+6	4.41E+5	8.24E+5	1.45E+6	2.20E+6	9.42
5	Platja de Riells	24	8.91E+4	1.93E+4	7.32E+4	1.00E+5	1.33E+5	3.3
6	La Platja (Creus)	45	1.50E+4	8.71E+3	6.93E+3	2.33E+4	2.84E+4	7.38
7	Platja del Rec	42	9.49E+4	1.76E+4	8.17E+4	1.09E+5	1.20E+5	13.14
8	Platja del Portitxol	42	4.26E+4	3.97E+3	3.98E+4	4.56E+4	4.92E+4	10.5
9	Les Muscleres	56	5.92E+4	6.39E+3	5.58E+4	6.48E+4	6.93E+4	6.54
10	Muscleres Grosses	56	1.09E+5	3.32E+4	8.21E+4	1.29E+5	1.84E+5	8.7

ID	Name	n_s	$\mathbf{E}(\varepsilon_{tot})$	$\mathbf{Var}(\varepsilon_{tot})$	$\mathbf{Q_1}(\varepsilon_{tot})$	$\mathbf{Q_3}(\varepsilon_{tot})$	$\mathbf{Max}(\varepsilon_{tot})$	$\mathbf{E}(\varepsilon_c)$
11	Platja del Riuet	42	7.42E+4	2.44E+4	5.84E+4	8.57E+4	1.16E+5	2.94
12	Empuriabrava	39	4.67E+5	2.33E+5	2.79E+5	6.56E+5	9.14E+5	3.78
13	Platja de la Rubina	33	3.76E+5	1.95E+5	2.26E+5	5.28E+5	7.59E+5	2.34
14	Pl. de Sta Margarida	21	1.99E+5	6.97E+4	1.55E+5	2.45E+5	3.37E+5	4.38
15	Canyelles Grosses	33	8.25E+4	1.91E+4	6.91E+4	9.17E+4	1.38E+5	5.58
16	Canyelles Petites	30	6.68E+4	1.39E+4	5.76E+4	7.54E+4	1.01E+5	5.94
17	Cala Montjoi	24	3.19E+4	1.24E+4	2.39E+4	3.70E+4	5.80E+4	3.3
18	Sa Conca	36	2.04E+4	1.40E+3	1.97E+4	2.15E+4	2.31E+4	11.82
19	Llane Gran	52	1.53E+4	3.87E+3	1.20E+4	1.88E+4	2.15E+4	6.54
20	Portdoguer	36	1.13E+4	4.07E+3	8.85E+3	1.40E+4	1.96E+4	2.46
21	Platja de Ses Oliveres	45	7.54E+3	6.82E+2	7.15E+3	7.93E+3	8.72E+3	5.64
22	Platja de Port Lligat	45	1.21E+4	4.75E+3	8.91E+3	1.63E+4	2.14E+4	1.86
23	Sant Pere Pescador	80	9.88E+5	6.69E+5	4.47E+5	1.29E+6	3.00E+6	0.78
25	Can Cristos	42	8.59E+3	6.62E+3	3.41E+3	1.26E+4	2.33E+4	0.36
26	Platja d'Aro	92	8.64E+4	8.86E+4	2.48E+4	1.16E+5	3.42E+5	0.54
27	Platja de Sant Pol	46	2.78E+4	1.19E+4	2.09E+4	3.59E+4	5.49E+4	0.78
28	Cala dels Canyerets	42	6.05E+3	4.83E+3	2.58E+3	9.41E+3	1.49E+4	0.96
29	Platja del Sr Ramon	42	1.04E+4	8.86E+3	3.11E+3	1.90E+4	2.89E+4	1.08
30	Cala de Salionc	42	8.95E+2	1.42E+3	1.88E+2	1.82E+3	3.53E+3	0.18
31	Cala de Giverola	46	3.82E+1	2.64E+3	4.51E+2	1.67E+3	7.52E+3	0.18
32	Cala Pola	38	9.98E+2	9.37E+2	1.78E+2	1.67E+3	2.82E+3	0.3
33	Tossa de Mar	81	1.65E+5	7.42E+4	1.09E+5	2.41E+5	3.24E+5	4.14
34	Platja de Llorell	42	1.98E+4	1.09E+4	1.15E+4	2.90E+4	3.86E+4	0.54
35	Platja de Canyelles	42	2.11E+4	9.94E+3	1.43E+4	2.73E+4	4.44E+4	1.2
36	Platja de Fenalls	42	3.99E+4	3.42E+4	1.68E+4	4.78E+4	1.48E+5	1.2
37	Cala de St Francesc	42	3.56E+3	1.71E+3	2.41E+3	4.74E+3	7.51E+3	0.54

ID	Name	n_s	$\mathbf{E}(\varepsilon_{\mathbf{tot}})$	$\mathbf{Var}(\varepsilon_{\mathbf{tot}})$	$\mathbf{Q_1}(\varepsilon_{\mathbf{tot}})$	$\mathbf{Q_3}(\varepsilon_{\mathbf{tot}})$	$\mathbf{Max}(\varepsilon_{\mathbf{tot}})$	$\mathbf{E}(\varepsilon_{\mathbf{c}})$
39	Platja de Treumal	42	1.47E+4	5.22E+3	1.11E+4	1.82E+4	2.48E+4	0.78
40	Lloret de Mar	84	1.85E+5	6.66E+4	1.37E+5	2.24E+5	3.46E+5	3.24
41	Cala de sa Cova	42	8.38E+3	4.80E+3	4.63E+3	1.13E+4	1.72E+4	1.02
42	Platja de Sant Jordi	44	8.23E+3	2.81E+3	6.18E+3	1.03E+4	1.44E+4	1.02
44	Platja Estartit – Pals	154	1.14E+6	8.46E+5	4.38E+5	1.71E+6	3.20E+6	1.62
45	Platja de sa Tuna	48	2.83E+4	2.22E+4	6.46E+3	4.57E+4	7.65E+4	18
46	Platja Fonda	28	1.56E+4	9.28E+3	7.49E+3	2.04E+4	3.73E+4	6.48
48	Platja de Tamariu	36	2.23E+4	2.27E+4	2.75E+3	3.54E+4	8.16E+4	4.26
49	Platja de Llafranc	36	2.52E+4	2.19E+4	6.78E+3	4.18E+4	7.70E+4	2.52
53	Platja de Castell	28	7.08E+4	5.47E+4	2.76E+4	9.38E+4	1.96E+5	3.3
54	Platja de la Fosca	26	5.98E+4	3.84E+4	2.76E+4	8.04E+4	1.44E+5	3.48

Table B.7.: Summary of the **flooding cost** φ_r obtained from the morphodynamic module simulations (**Step 1** of the Risk module). **Legend:** $\mathbf{n_s}$ *(total number of simulations at that beach)* $\mathbf{E}(\varphi_{\mathbf{tot}})$ *(expected value of the* ***total*** *flooding cost)* **,**$\mathbf{Var}(\varphi_{\mathbf{tot}})$ *(variance of the total flooding cost)***,**$\mathbf{Q_1}(\varphi_{\mathbf{tot}})$*(first-quantile of the total flooding cost)* **,**$\mathbf{Q_3}(\varphi_{\mathbf{tot}})$ *(third-quantile of the total flooding cost)***,**$\mathbf{Max}(\varphi_{\mathbf{tot}})$ *(maximum value of the total flooding cost). The latter five variables in* ***euros.*** $\mathbf{E}(\varphi_{\mathbf{r}})$ *is the* ***expected unitary value*** *of the flooding cost, in* $\mathbf{euros/m^2}$.

ID	Name	n_s	$\mathbf{E}(\varphi_{\mathbf{tot}})$	$\mathbf{Var}(\varphi_{\mathbf{tot}})$	$\mathbf{Q_1}(\varphi_{\mathbf{tot}})$	$\mathbf{Q_3}(\varphi_{\mathbf{tot}})$	$\mathbf{Max}(\varphi_{\mathbf{tot}})$	$\mathbf{E}(\varphi_{\mathbf{r}})$
1	Badalona	144	5.25E+5	8.54E+5	1.64E+4	6.44E+5	4.86E+6	0.37
2	Barcelona	36	4.17E+5	7.08E+5	1.62E+4	5.54E+5	3.80E+6	3.66
3	Gavà	96	1.33E+6	2.36E+7	1.70E+4	1.07E+7	7.97E+7	8.19
4	Premià de Mar	59	3.79E+5	4.80E+5	6.60E+4	4.61E+5	2.35E+6	0.44

ID	Name	n_s	$\mathbf{E}(\varphi_{tot})$	$\mathbf{Var}(\varphi_{tot})$	$\mathbf{Q_1}(\varphi_{tot})$	$\mathbf{Q_3}(\varphi_{tot})$	$\mathbf{Max}(\varphi_{tot})$	$\mathbf{E}(\varphi_r)$
5	Platja de Riells	24	5.78E+2	0.00E+0	5.78E+2	5.78E+2	5.78E+2	0.01
6	La Platja (Creus)	45	7.33E+4	3.69E+4	4.07E+4	1.01E+5	1.48E+5	5.07
7	Platja del Rec	42	1.97E+2	0.00E+0	1.97E+2	1.97E+2	1.97E+2	0.01
8	Platja del Portitxol	42	5.69E+1	0.00E+0	5.69E+1	5.69E+1	5.69E+1	0.01
9	Les Muscleres	56	6.34E+4	1.81E+4	5.14E+4	7.56E+4	9.10E+4	3.55
10	Muscleres Grosses	56	1.45E+2	6.91E+2	5.22E+1	5.22E+1	5.22E+3	0.01
11	Platja del Riuet	42	4.88E+2	7.60E+2	2.87E+2	2.87E+2	4.70E+3	0.01
12	Empuriabrava	39	1.09E+5	1.47E+5	1.88E+4	1.24E+5	7.75E+5	0.12
13	Platja de la Rubina	33	3.01E+5	2.46E+5	5.03E+4	4.55E+5	1.09E+6	0.77
14	Pl. de Sta Margarida	21	2.23E+5	3.22E+5	2.84E+4	2.63E+5	1.20E+6	1.45
15	Canyelles Grosses	33	5.08E+4	4.91E+4	1.41E+4	7.46E+4	2.10E+5	1.38
16	Canyelles Petites	30	4.19E+4	1.93E+4	2.18E+4	5.40E+4	7.61E+4	1.59
17	Cala Montjoi	24	4.44E+4	1.69E+4	3.45E+4	5.90E+4	6.57E+4	1.99
18	Sa Conca	36	8.90E+3	2.81E+3	7.22E+3	1.14E+4	1.31E+4	7.97
19	Llane Gran	52	2.83E+4	1.52E+4	1.62E+4	3.97E+4	6.70E+4	4.10
20	Portdoguer	36	1.89E+4	2.18E+4	3.27E+3	3.46E+4	7.80E+4	4.28
21	Platja de Ses Oliveres	45	3.51E+3	1.15E+3	3.04E+3	4.20E+3	5.80E+3	6.13
22	Platja de Port Lligat	45	1.35E+4	1.45E+4	2.72E+2	2.56E+4	4.71E+4	3.92
23	Sant Pere Pescador	80	1.53E+4	4.03E+4	1.09E+3	1.20E+4	3.04E+5	0.07
25	Can Cristos	42	8.52E+2	1.86E+3	1.07E+2	6.39E+2	9.87E+3	0.04
26	Platja d'Aro	92	4.81E+4	5.31E+4	1.74E+4	5.60E+4	3.61E+5	0.15
27	Platja de Sant Pol	46	1.25E+4	1.29E+4	2.54E+3	1.69E+4	5.66E+4	0.11
28	Cala dels Canyerets	42	1.54E+3	6.37E+3	1.48E+1	1.48E+1	3.95E+4	0.59
29	Platja del Sr Ramon	42	2.87E+1	0.00E+0	2.87E+1	2.87E+1	2.87E+1	0.01
30	Cala de Salionc	42	7.45E+2	1.40E+3	1.10E+1	1.00E+3	6.39E+3	0.35
31	Cala de Giverola	46	5.35E+1	0.00E+0	5.35E+1	5.35E+1	5.35E+1	0.01

ID	Name	n_s	$\mathbf{E}(\varphi_{\mathbf{tot}})$	$\mathbf{Var}(\varphi_{\mathbf{tot}})$	$\mathbf{Q_1}(\varphi_{\mathbf{tot}})$	$\mathbf{Q_3}(\varphi_{\mathbf{tot}})$	$\mathbf{Max}(\varphi_{\mathbf{tot}})$	$\mathbf{E}(\varphi_{\mathbf{r}})$
32	Cala Pola	38	1.41E+1	0.00E+0	1.41E+1	1.41E+1	1.41E+1	0.01
33	Tossa de Mar	81	1.92E+4	6.70E+4	6.78E+2	3.58E+3	5.06E+5	0.15
34	Platja de Llorell	42	7.41E+3	8.51E+3	4.00E+2	1.36E+4	3.05E+4	0.10
35	Platja de Canyelles	42	7.27E+3	4.23E+3	3.42E+3	8.06E+3	2.20E+4	0.29
36	Platja de Fenalls	42	2.52E+3	8.26E+3	3.75E+2	3.75E+2	5.01E+4	0.03
37	Cala de St Francesc	42	3.11E+3	3.75E+3	1.07E+2	4.53E+3	1.48E+4	0.16
39	Platja de Treumal	42	3.51E+3	8.05E+3	8.91E+1	8.73E+2	3.26E+4	0.21
40	Lloret de Mar	84	1.75E+4	4.41E+4	2.57E+3	1.66E+4	3.76E+5	0.13
41	Cala de sa Cova	42	2.44E+2	1.22E+3	2.00E+0	2.00E+0	7.63E+3	0.81
42	Platja de Sant Jordi	44	1.55E+2	0.00E+0	1.55E+2	1.55E+2	1.55E+2	0.01
44	Platja Estartit – Pals	154	2.08E+6	7.61E+6	5.66E+4	1.66E+6	9.03E+7	0.93
45	Platja de sa Tuna	48	1.53E+4	4.35E+4	3.29E+2	8.46E+3	2.89E+5	0.49
46	Platja Fonda	28	6.64E+4	2.87E+4	4.66E+4	9.27E+4	1.28E+5	4.90
48	Platja de Tamariu	36	4.05E+4	5.36E+4	2.24E+3	6.00E+4	2.21E+5	0.90
49	Platja de Llafranc	36	1.91E+5	2.25E+5	2.67E+4	2.56E+5	7.43E+5	1.29
53	Platja de Castell	28	1.48E+5	1.29E+5	5.32E+4	2.13E+5	4.62E+5	4.17
54	Platja de la Fosca	26	2.80E+4	4.54E+4	6.69E+2	3.56E+4	1.65E+5	0.21

C. Time series from the Meteo-Hydro module

In this Appendix can be found the time series of the modules compared with observations. The error metrics and discussion can be found at the main text of the dissertation. This information has not been included in the main text due to its extension, and for easing readability. This information is complementary with the text and Figures present in Ch. 5.

The information is classified in two levels: the first levels belongs to the module (Meteorological (Sec. C.1) and Hydrodynamic (Sec. C.2)), and secondly, for each module can be found the results for each storm event considered in Ch. 5: *O-15, N-15, J-16, F-16, D-16 and J-17*. For the meteorological module, modelled and observed wind time series are presented; whereas that significant wave height, mean wave period and wave direction can be found for the hydrodynamic module. The observational series belong to Puertos del Estado monitoring network (REDEXT and REDCOS).

C.1. Meteorological module

C.1.1. October 2015

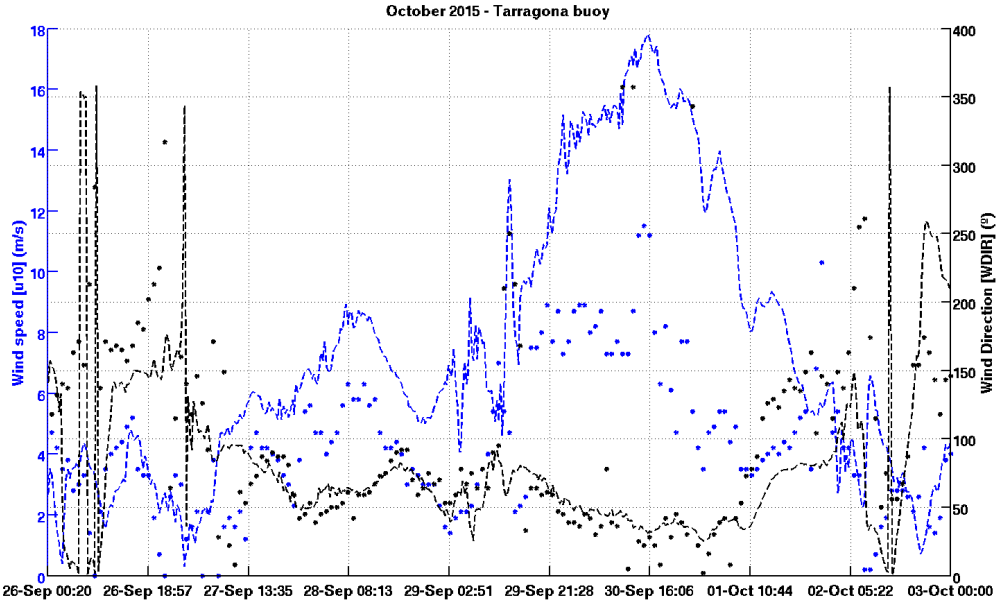

Figure C.1.: Time series of the wind speed (left axis, units in m/s, in **blue**) and wind direction (right axis, units in degrees, in **black**) at the **Tarragona buoy** for the **October 2015** storm. For both cases, the contour **lines** correspond to the **meteorological** module and the **dots** are **buoy** observations.

C.1.2. November 2015

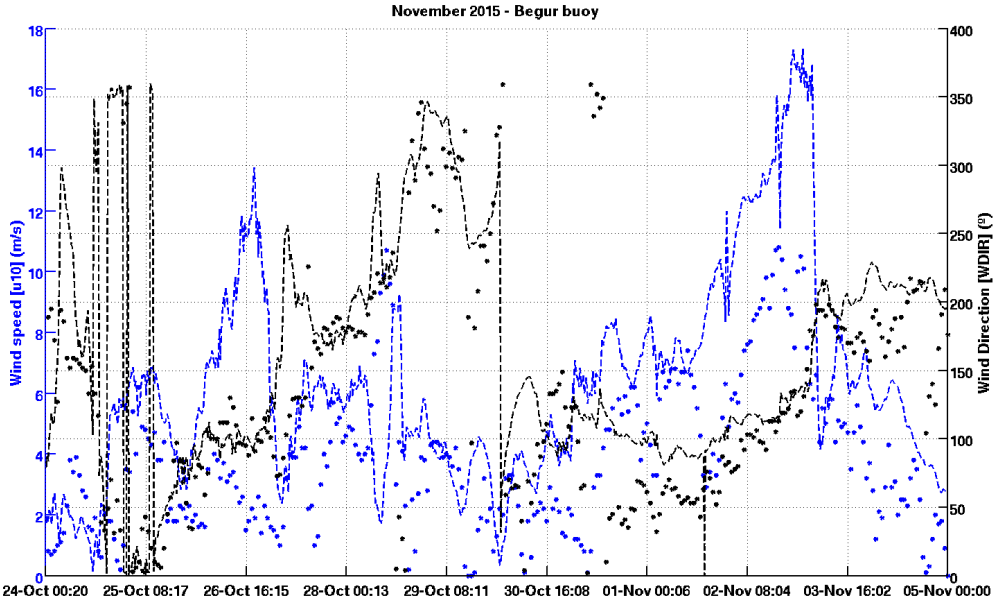

Figure C.2.: Time series of the wind speed (left axis, units in m/s, in **blue**) and wind direction (right axis, units in degrees, in **black**) at the **Begur buoy** for the **November 2015** storm. For both cases, the contour **lines** correspond to the **meteorological** module and the **dots** are **buoy** observations.

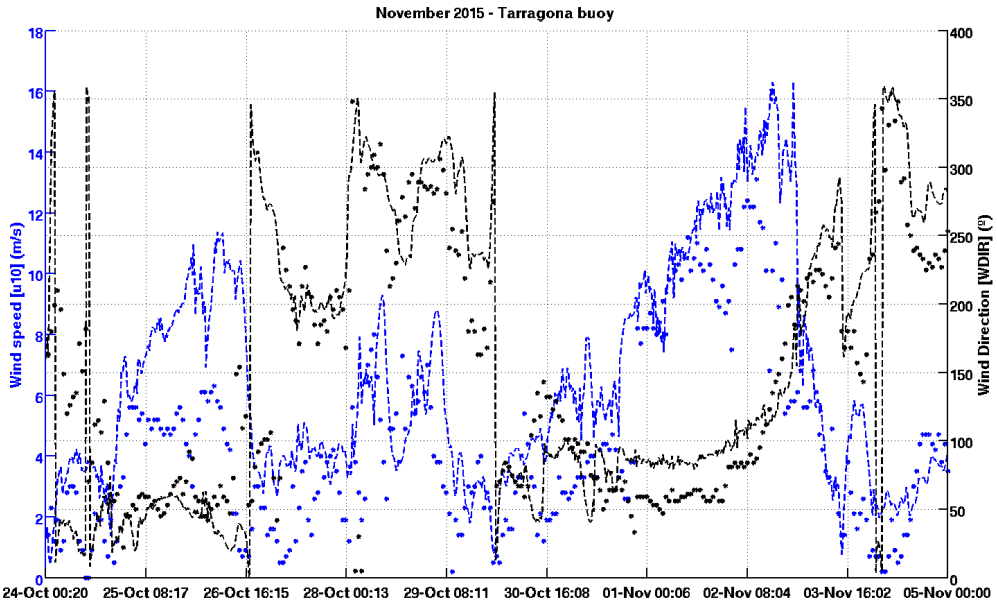

Figure C.3.: Time series of the wind speed (left axis, units in m/s, in **blue**) and wind direction (right axis, units in degrees, in **black**) at the **Tarragona buoy** for the **November 2015** storm. For both cases, the contour **lines** correspond to the **meteorological** module and the **dots** are **buoy** observations.

C.1.3. January 2016

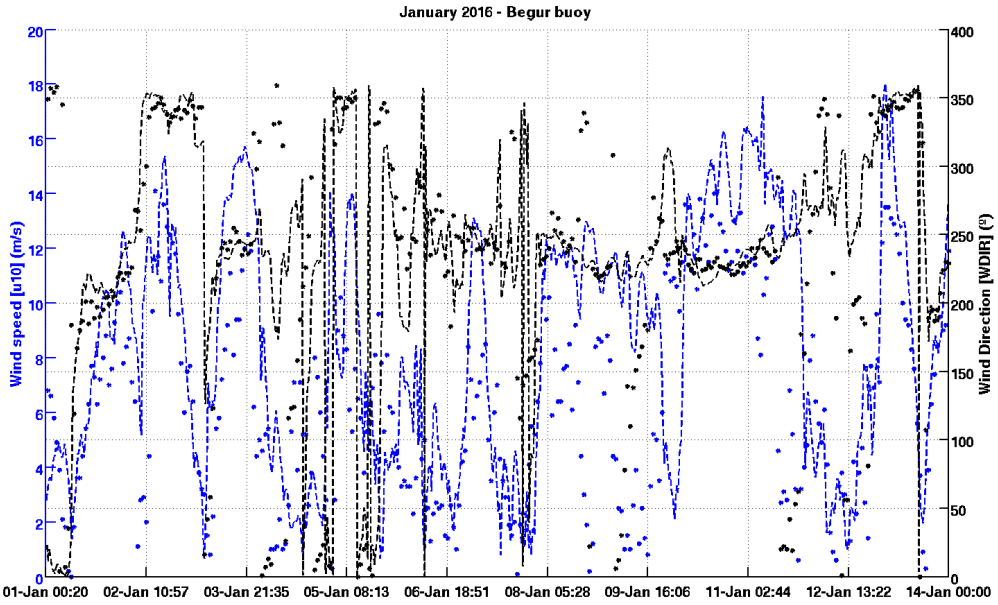

Figure C.4.: Time series of the wind speed (left axis, units in m/s, in **blue**) and wind direction (right axis, units in degrees, in **black**) at the **Begur buoy** for the **January 2016** storm. For both cases, the contour **lines** correspond to the **meteorological** module and the **dots** are **buoy** observations.

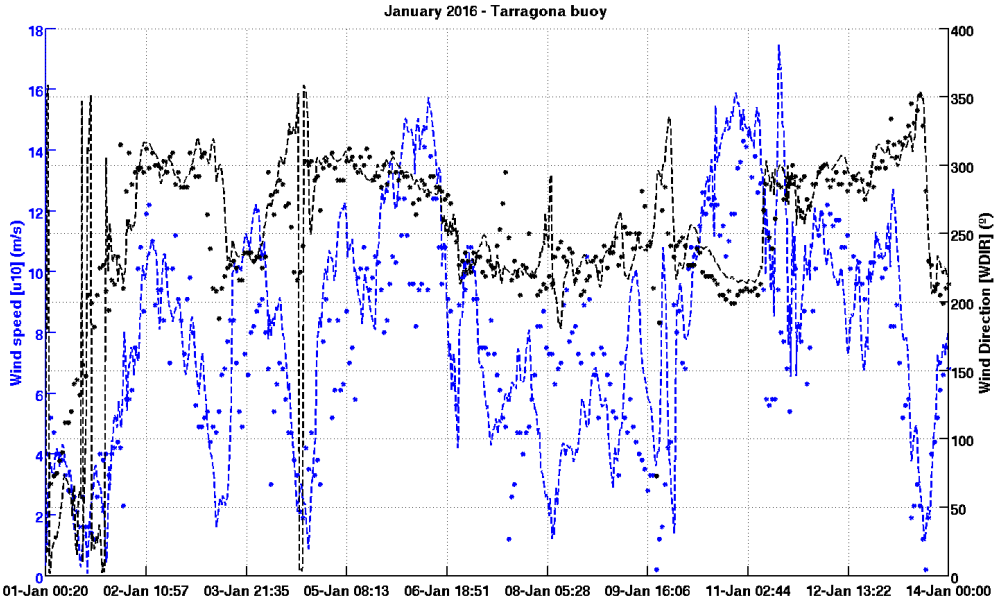

Figure C.5.: Time series of the wind speed (left axis, units in m/s, in **blue**) and wind direction (right axis, units in degrees, in **black**) at the **Tarragona buoy** for the **January 2016** storm. For both cases, the contour **lines** correspond to the **meteorological** module and the **dots** are **buoy** observations.

C.1.4. February 2016

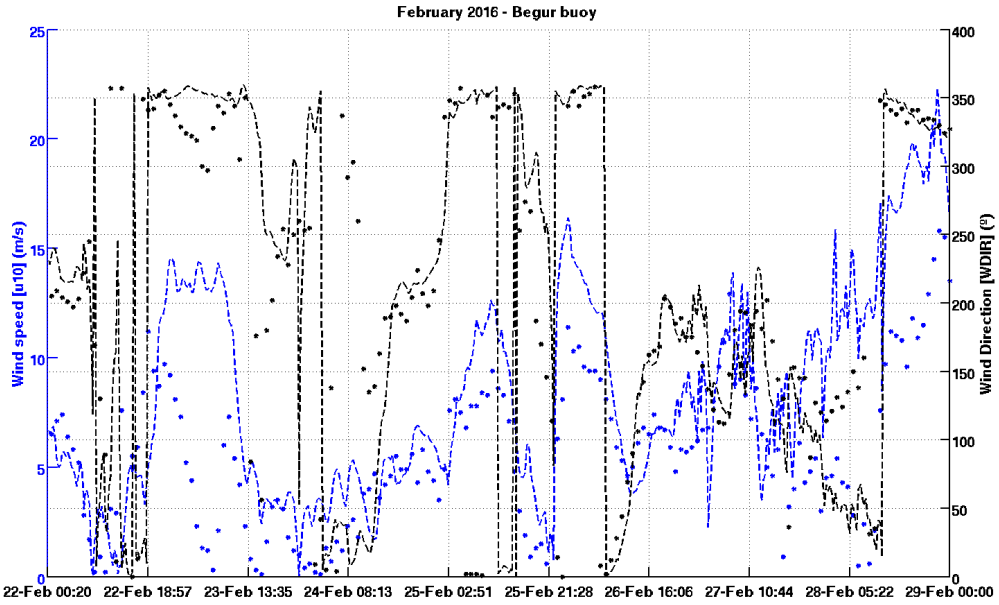

Figure C.6.: Time series of the wind speed (left axis, units in m/s, in **blue**) and wind direction (right axis, units in degrees, in **black**) at the **Begur buoy** for the **February 2016** storm. For both cases, the contour **lines** correspond to the **meteorological** module and the **dots** are **buoy** observations.

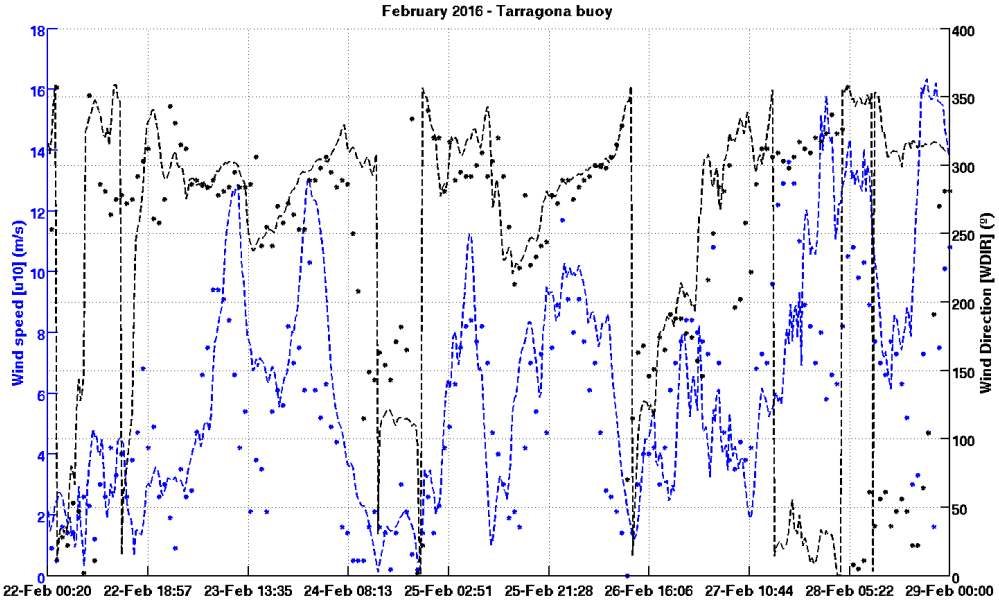

Figure C.7.: Time series of the wind speed (left axis, units in m/s, in **blue**) and wind direction (right axis, units in degrees, in **black**) at the **Tarragona buoy** for the **February 2016** storm. For both cases, the contour **lines** correspond to the **meteorological** module and the **dots** are **buoy** observations.

C.1.5. December 2016

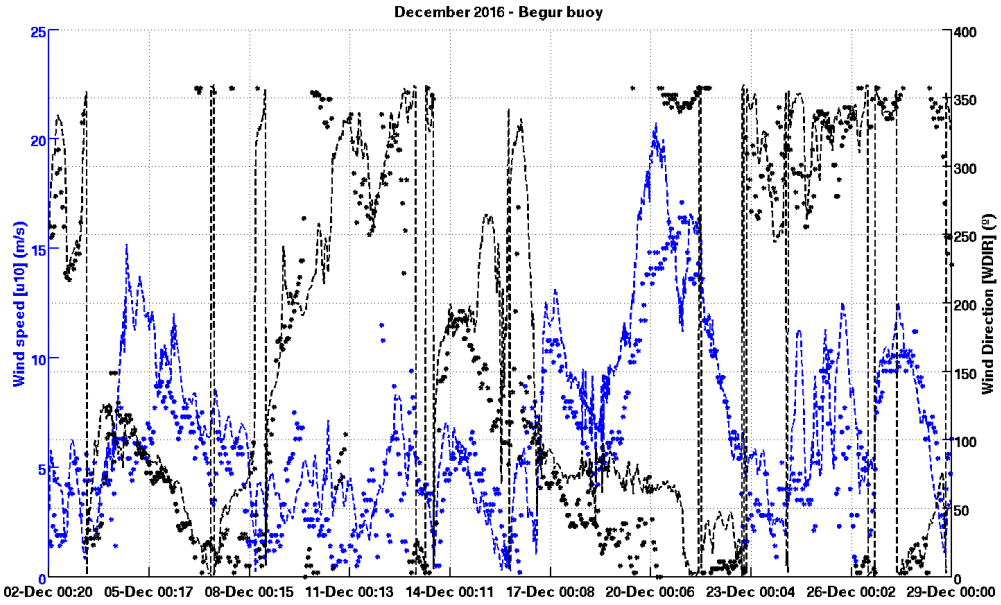

Figure C.8.: Time series of the wind speed (left axis, units in m/s, in **blue**) and wind direction (right axis, units in degrees, in **black**) at the **Begur buoy** for the **December 2016** storm. For both cases, the contour **lines** correspond to the **meteorological** module and the **dots** are **buoy** observations.

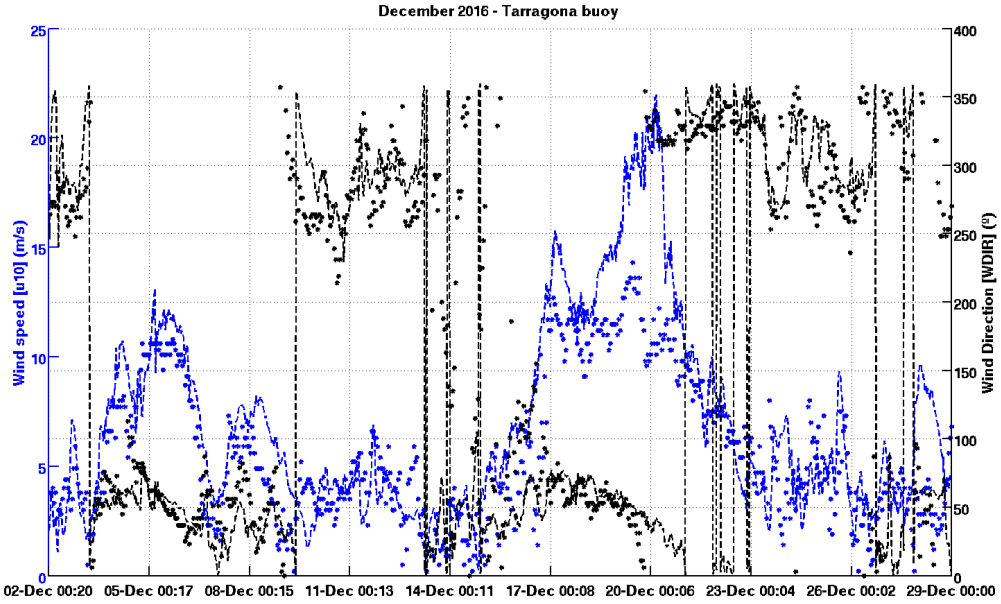

Figure C.9.: Time series of the wind speed (left axis, units in m/s, in **blue**) and wind direction (right axis, units in degrees, in **black**) at the **Tarragona buoy** for the **December 2016** storm. For both cases, the contour **lines** correspond to the **meteorological** module and the **dots** are **buoy** observations.

C.1.6. January 2017

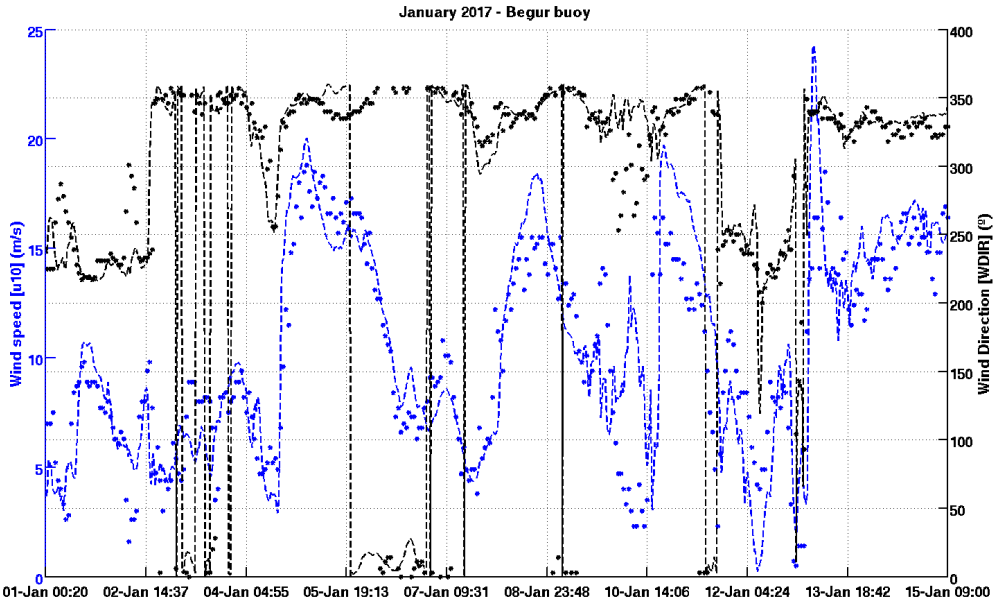

Figure C.10.: Time series of the wind speed (left axis, units in m/s, in **blue**) and wind direction (right axis, units in degrees, in **black**) at the **Begur buoy** for the **January 2017** storm. For both cases, the contour **lines** correspond to the **meteorological** module and the **dots** are **buoy** observations.

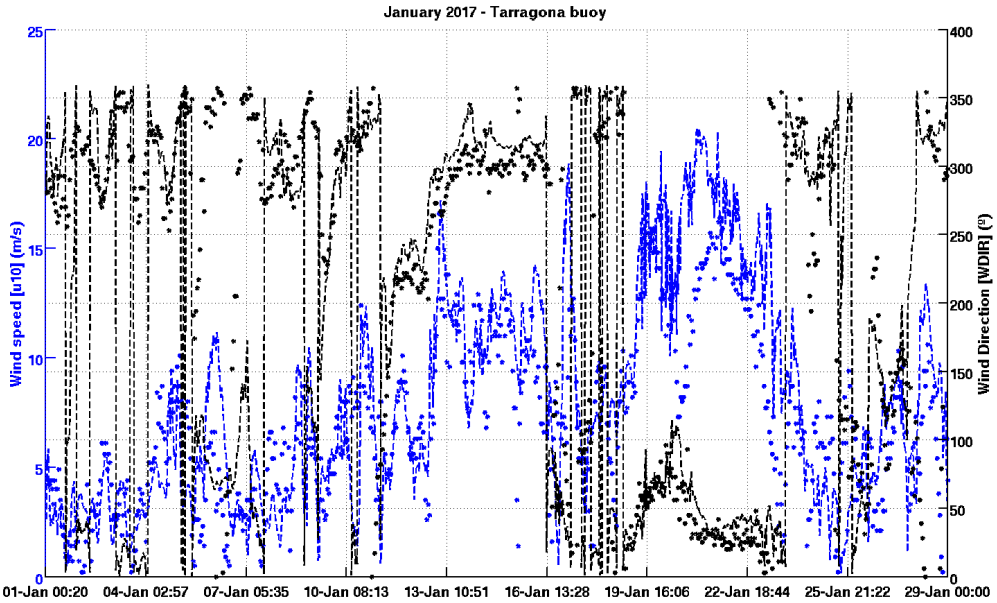

Figure C.11.: Time series of the wind speed (left axis, units in m/s, in **blue**) and wind direction (right axis, units in degrees, in **black**) at the **Tarragona buoy** for the **January 2017** storm. For both cases, the contour **lines** correspond to the **meteorological** module and the **dots** are **buoy** observations.

C.2. Hydrodynamic module

C.2.1. October 2015

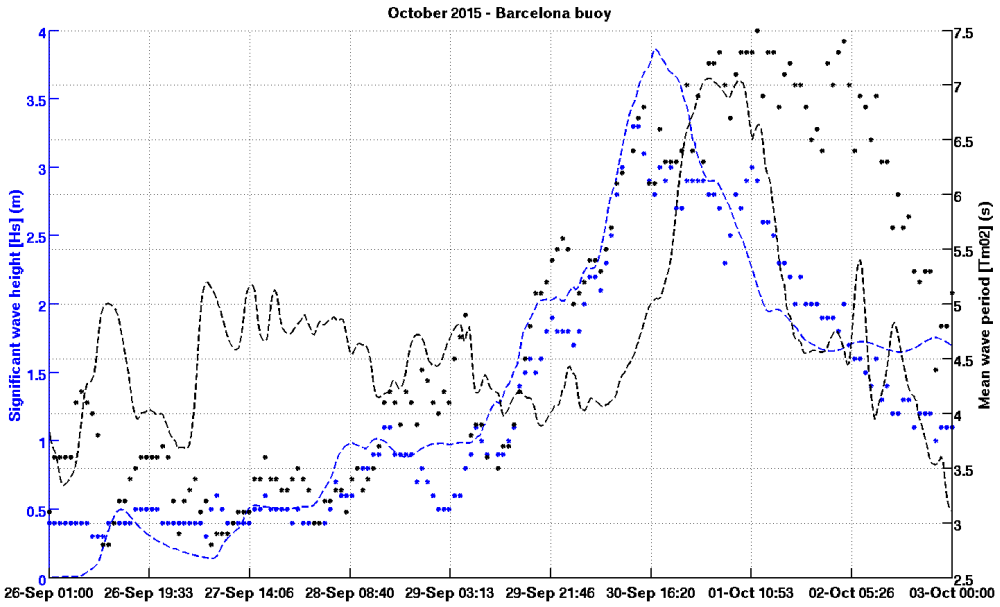

Figure C.12.: Time series of the significant wave height H_s (left axis, units in meters, in **blue**) and mean wave period Tm_{02}(right axis, units in seconds, in **black**) at the **Barcelona buoy** for the **October 2015** storm. For both cases, the contour **lines** correspond to the **SWAN** model and the **dots** are **buoy** observations.

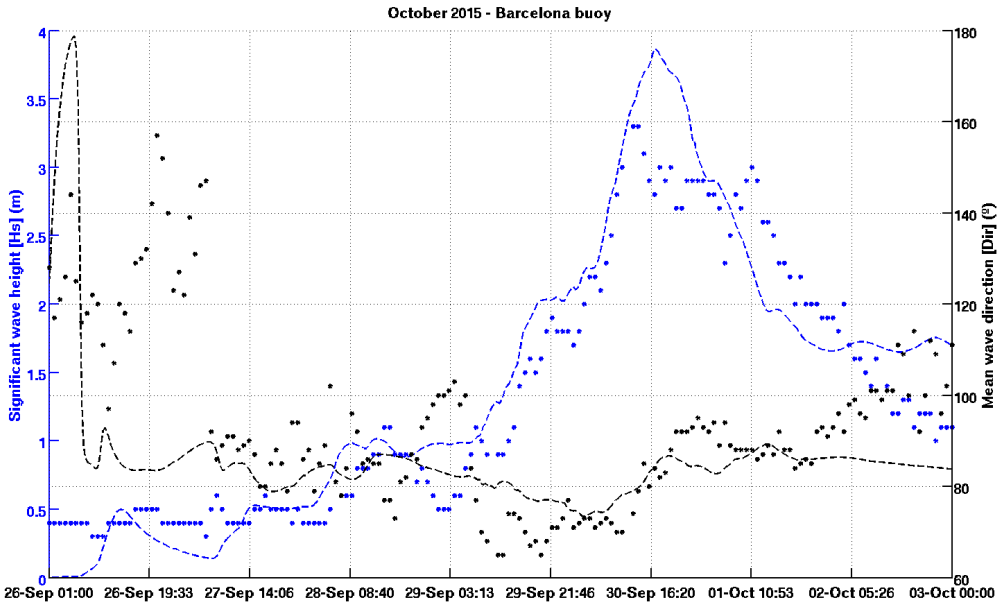

Figure C.13.: Time series of the significant wave height H_s (left axis, units in meters, in **blue**) and mean wave direction (right axis, units in degrees, in **black**) at the **Barcelona buoy** for the **October 2015** storm. For both cases, the contour **lines** correspond to the **SWAN** model and the **dots** are **buoy** observations.

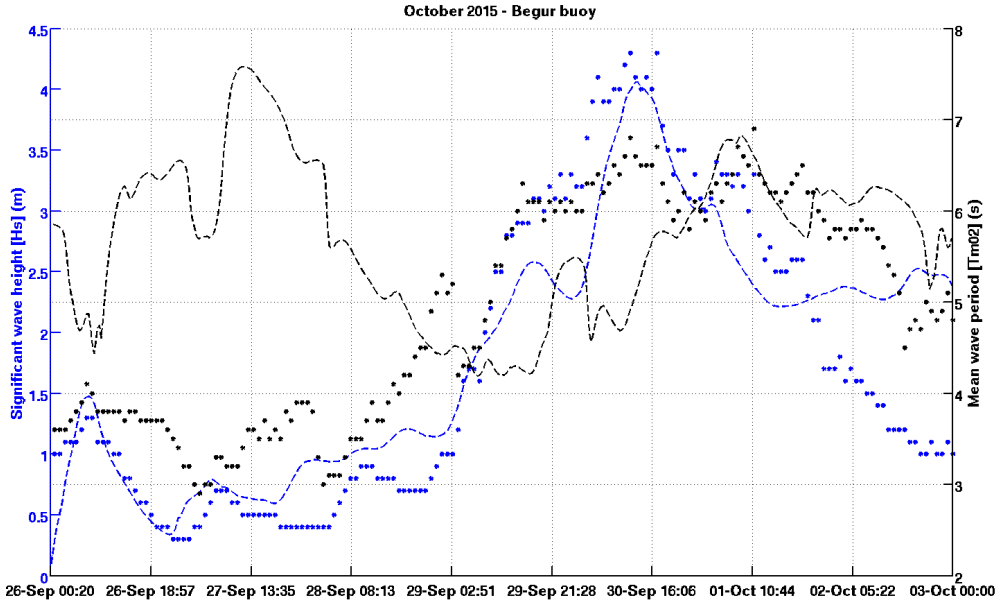

Figure C.14.: Time series of the significant wave height H_s (left axis, units in meters, in **blue**) and mean wave period Tm_{02}(right axis, units in seconds, in **black**) at the **Begur buoy** for the **October 2015** storm. For both cases, the contour **lines** correspond to the **SWAN** model and the **dots** are **buoy** observations.

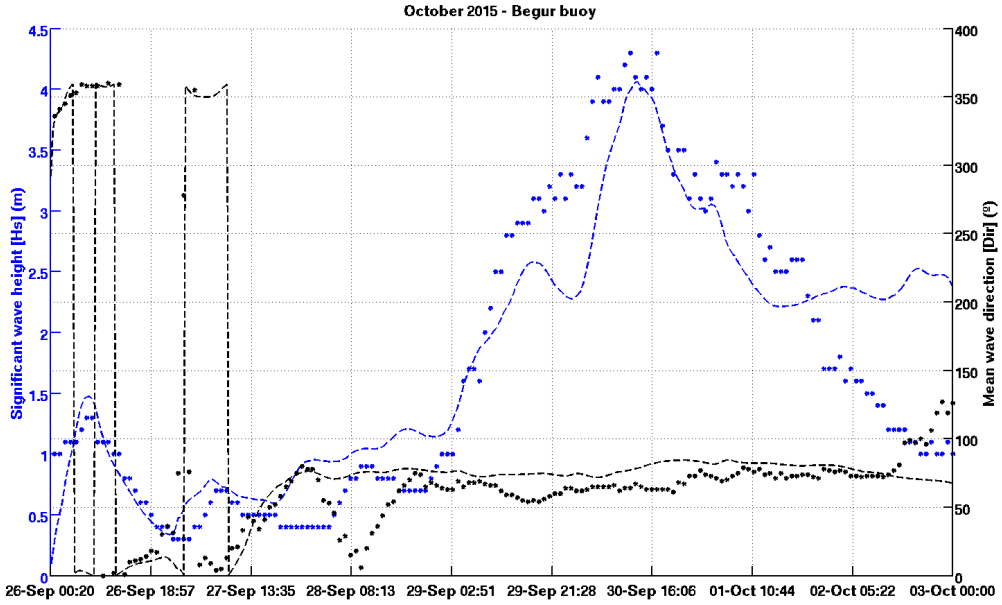

Figure C.15.: Time series of the significant wave height H_s (left axis, units in meters, in **blue**) and mean wave direction (right axis, units in degrees, in **black**) at the **Begur buoy** for the **October 2015** storm. For both cases, the contour **lines** correspond to the **SWAN** model and the **dots** are **buoy** observations.

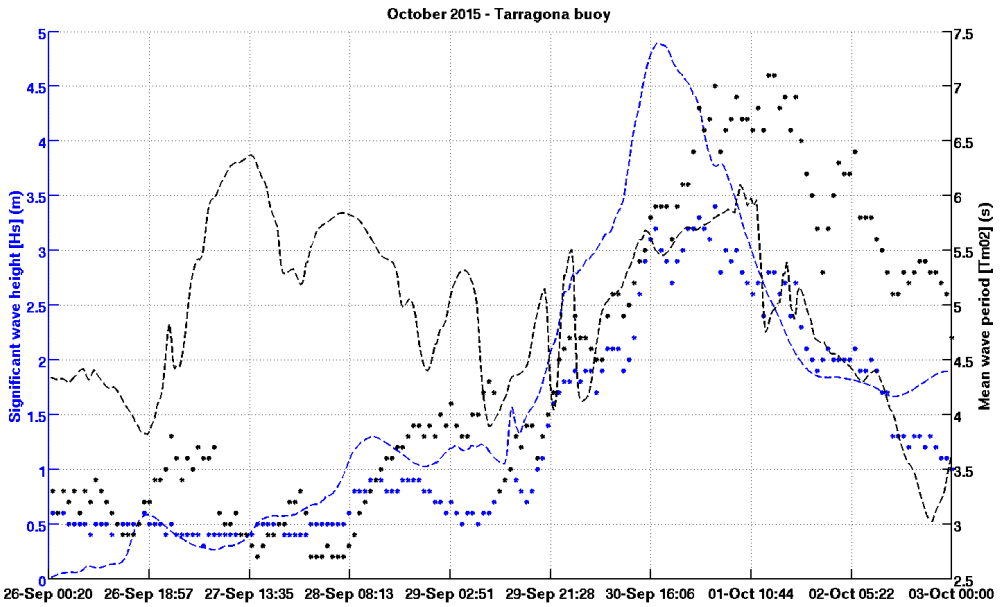

Figure C.16.: Time series of the significant wave height H_s (left axis, units in meters, in **blue**) and mean wave direction Tm_{02}(right axis, units in seconds, in **black**) at the **Tarragona buoy** for the **October 2015** storm. For both cases, the contour **lines** correspond to the **SWAN** model and the **dots** are **buoy** observations.

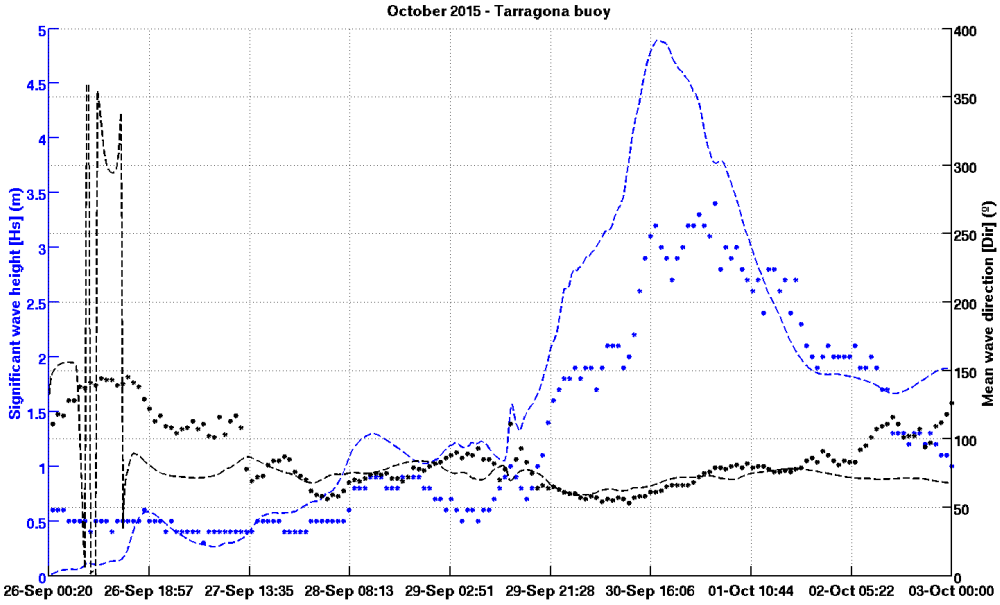

Figure C.17.: Time series of the significant wave height H_s (left axis, units in meters, in **blue**) and mean wave direction (right axis, units in degrees, in **black**) at the **Tarragona buoy** for the **October 2015** storm. For both cases, the contour **lines** correspond to the **SWAN** model and the **dots** are **buoy** observations.

C.2.2. November 2015

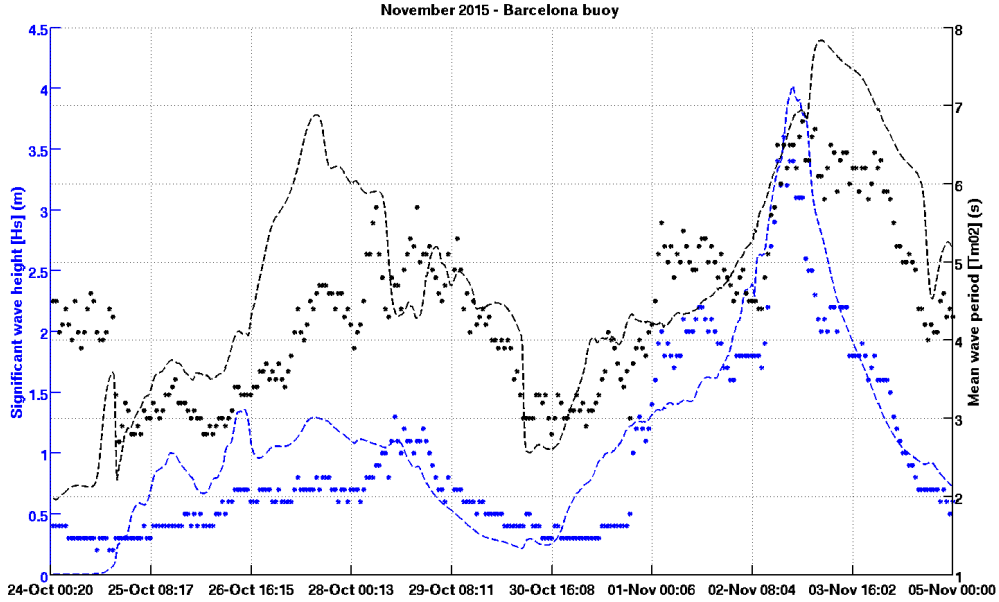

Figure C.18.: Time series of the significant wave height H_s (left axis, units in meters, in **blue**) and mean wave direction Tm_{02}(right axis, units in seconds, in **black**) at the **Barcelona buoy** for the **November 2015** storm. For both cases, the contour **lines** correspond to the **SWAN** model and the **dots** are **buoy** observations.

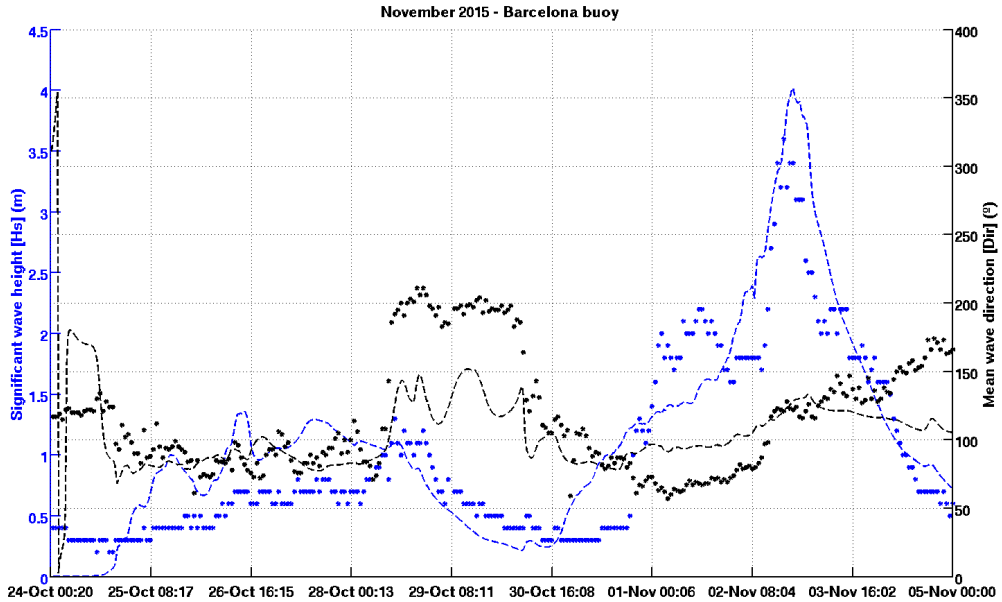

Figure C.19.: Time series of the significant wave height H_s (left axis, units in meters, in **blue**) and mean wave direction (right axis, units in degrees, in **black**) at the **Barcelona buoy** for the **November 2015** storm. For both cases, the contour **lines** correspond to the **SWAN** model and the **dots** are **buoy** observations.

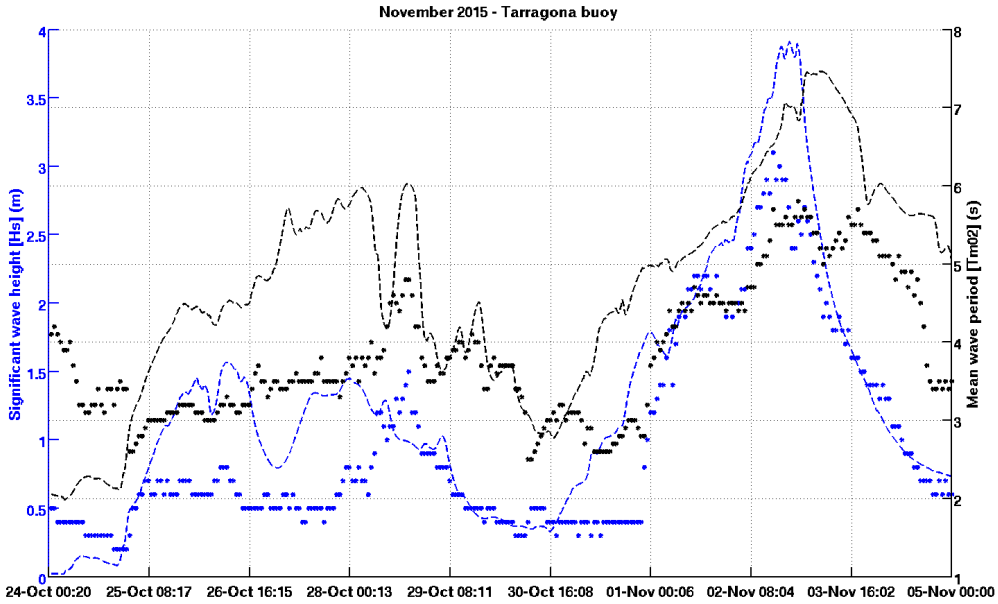

Figure C.20.: Time series of the significant wave height H_s (left axis, units in meters, in **blue**) and mean wave period Tm_{02}(right axis, units in seconds, in **black**) at the **Tarragona buoy** for the **November 2015** storm. For both cases, the contour **lines** correspond to the **SWAN** model and the **dots** are **buoy** observations.

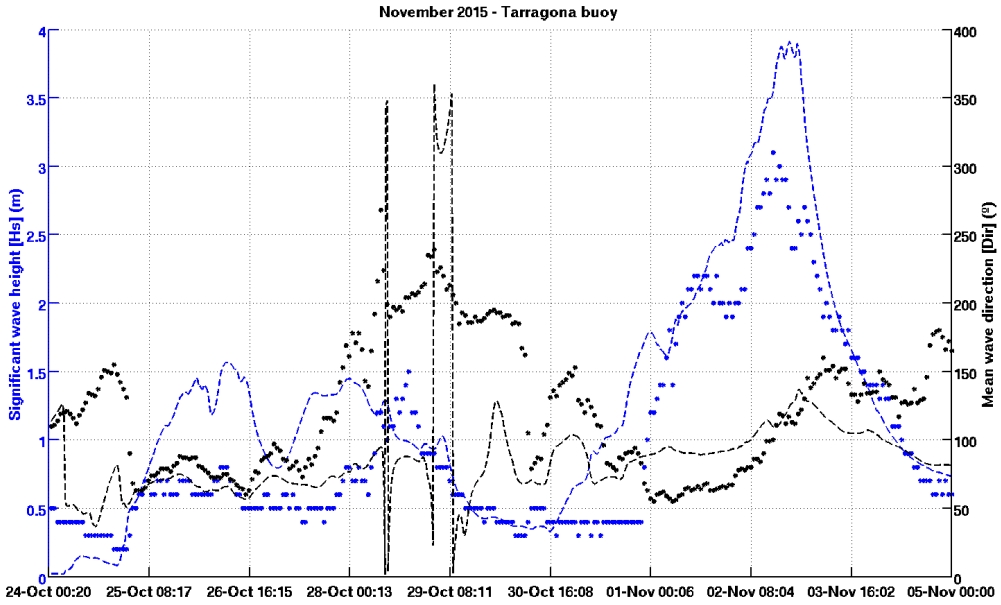

Figure C.21.: Time series of the significant wave height H_s (left axis, units in meters, in **blue**) and mean wave direction (right axis, units in degrees, in **black**) at the **Tarragona buoy** for the **November 2015** storm. For both cases, the contour **lines** correspond to the **SWAN** model and the **dots** are **buoy** observations.

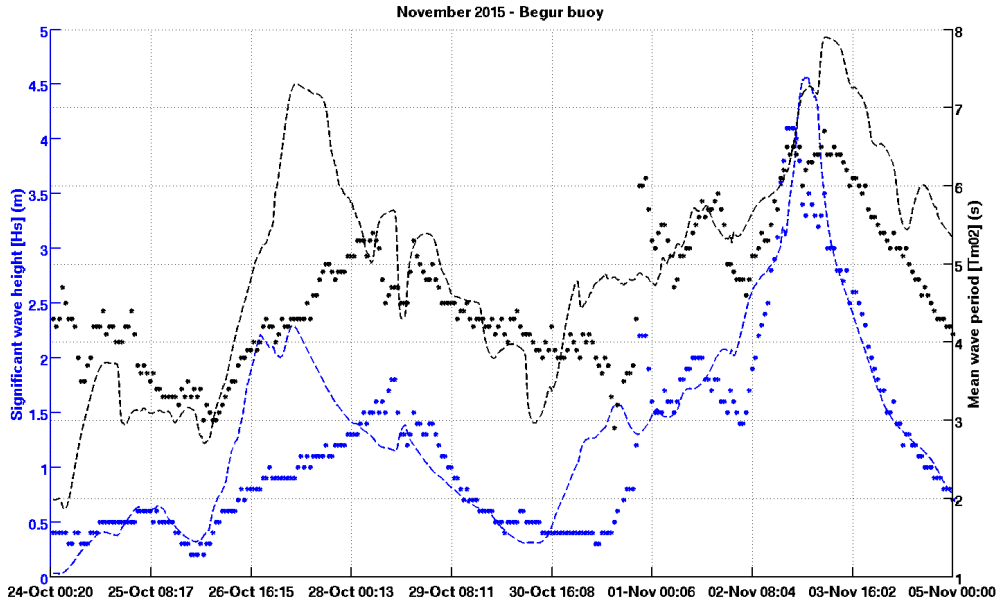

Figure C.22.: Time series of the significant wave height H_s (left axis, units in meters, in **blue**) and mean wave period Tm_{02}(right axis, units in seconds, in **black**) at the **Begur buoy** for the **November 2015** storm. For both cases, the contour **lines** correspond to the **SWAN** model and the **dots** are **buoy** observations.

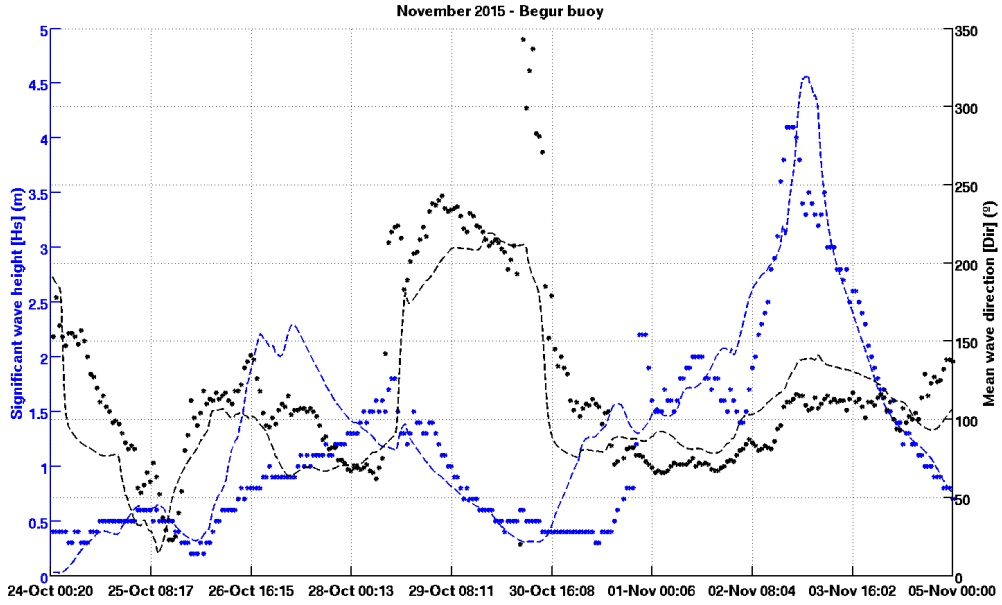

Figure C.23.: Time series of the significant wave height H_s (left axis, units in meters, in **blue**) and mean wave direction (right axis, units in degrees, in **black**) at the **Begur buoy** for the **November 2015** storm. For both cases, the contour **lines** correspond to the **SWAN** model and the **dots** are **buoy** observations.

C.2.3. January 2016

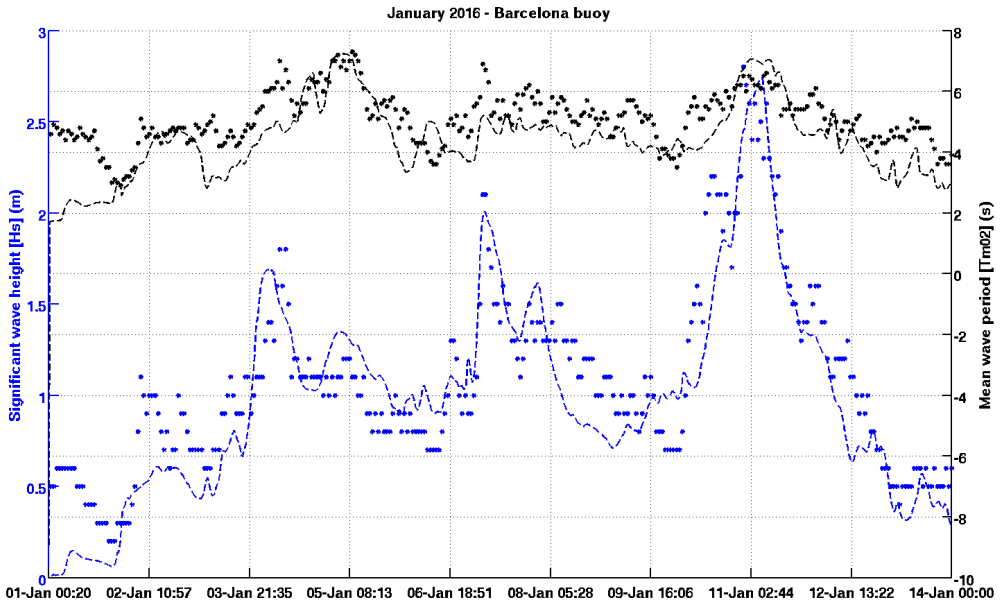

Figure C.24.: Time series of the significant wave height H_s (left axis, units in meters, in **blue**) and mean wave direction Tm_{02}(right axis, units in seconds, in **black**) at the **Barcelona buoy** for the **January 2016** storm. For both cases, the contour **lines** correspond to the **SWAN** model and the **dots** are **buoy** observations.

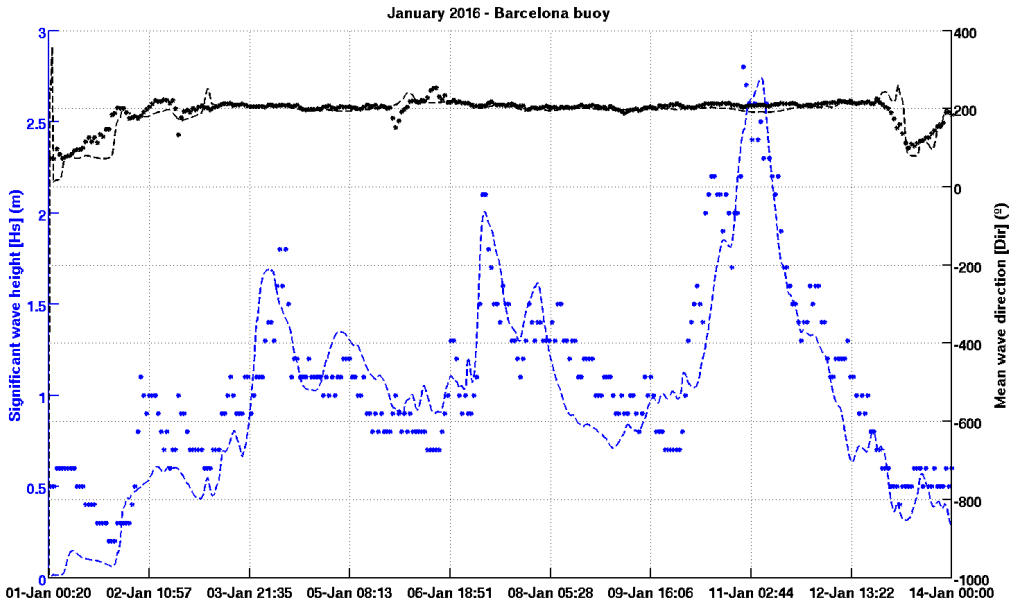

Figure C.25.: Time series of the significant wave height H_s (left axis, units in meters, in **blue**) and mean wave direction (right axis, units in degrees, in **black**) at the **Barcelona buoy** for the **January 2016** storm. For both cases, the contour **lines** correspond to the **SWAN** model and the **dots** are **buoy** observations.

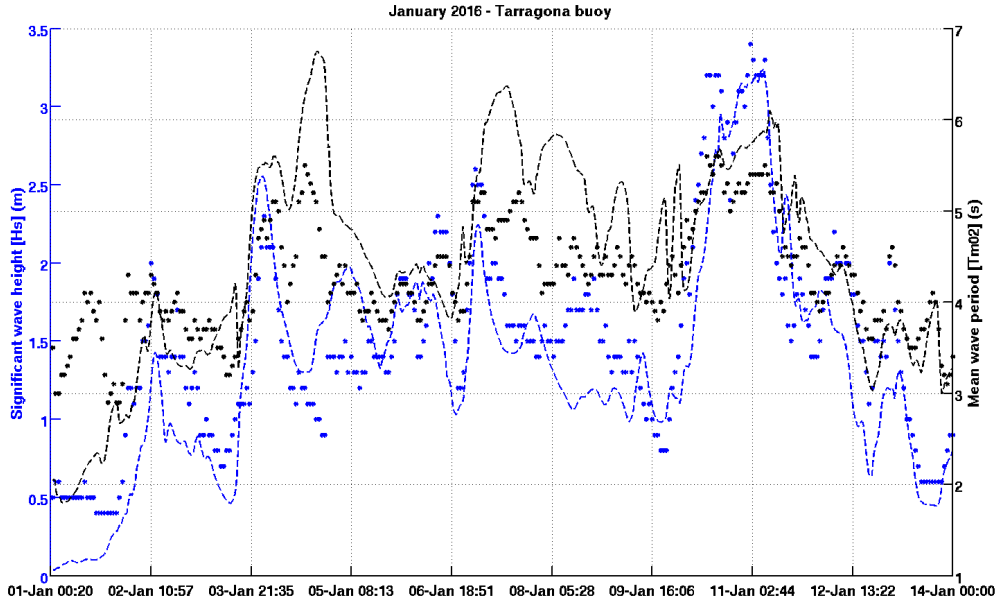

Figure C.26.: Time series of the significant wave height H_s (left axis, units in meters, in **blue**) and mean wave direction Tm_{02}(right axis, units in seconds, in **black**) at the **Tarragona buoy** for the **January 2016** storm. For both cases, the contour **lines** correspond to the **SWAN** model and the **dots** are **buoy** observations.

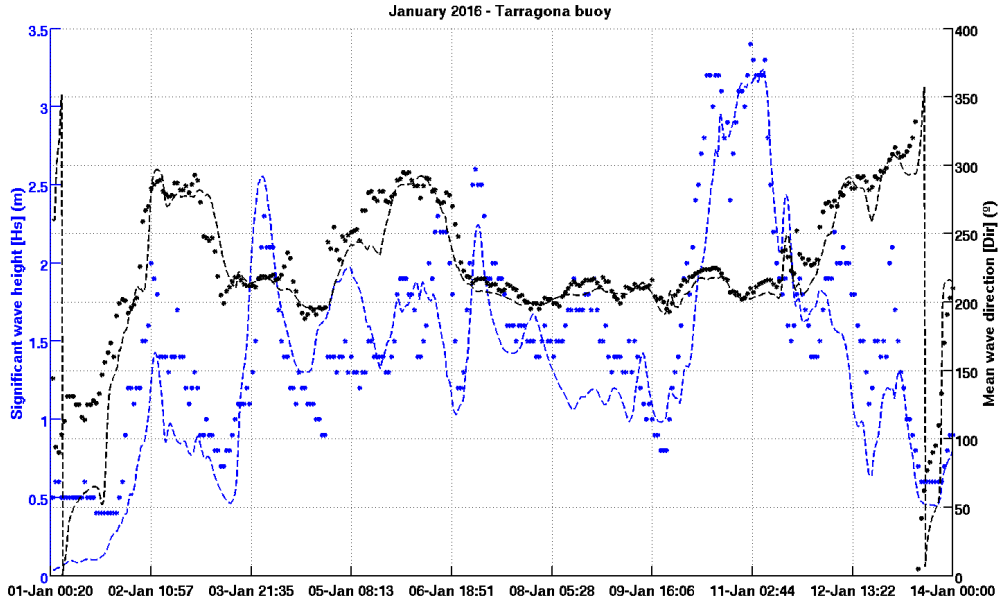

Figure C.27.: Time series of the significant wave height H_s (left axis, units in meters, in **blue**) and mean wave direction (right axis, units in degrees, in **black**) at the **Tarragona buoy** for the **January 2016** storm. For both cases, the contour **lines** correspond to the **SWAN** model and the **dots** are **buoy** observations.

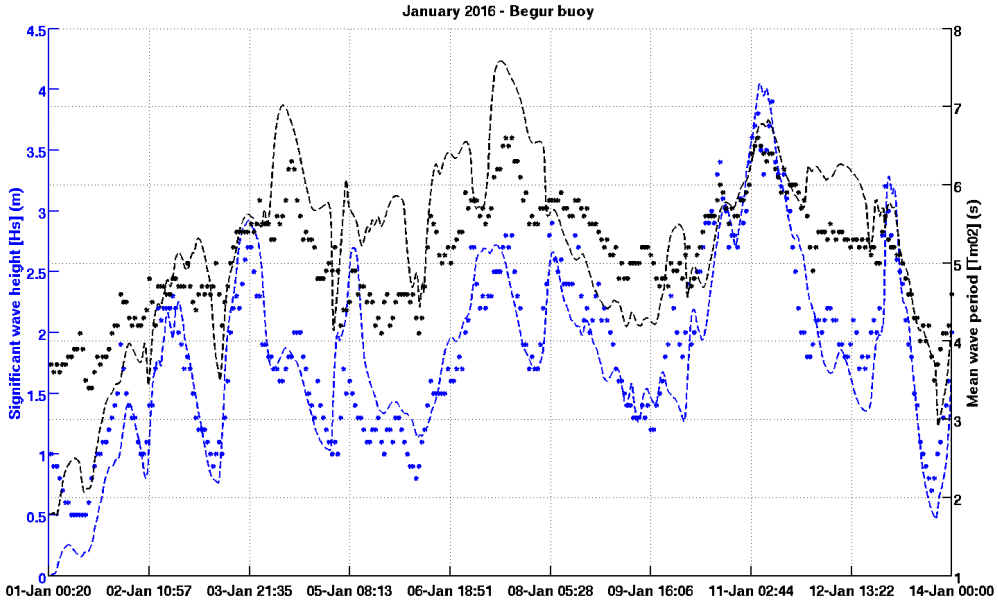

Figure C.28.: Time series of the significant wave height H_s (left axis, units in meters, in **blue**) and mean wave direction Tm_{02}(right axis, units in seconds, in **black**) at the **Tarragona buoy** for the **January 2016** storm. For both cases, the contour **lines** correspond to the **SWAN** model and the **dots** are **buoy** observations.

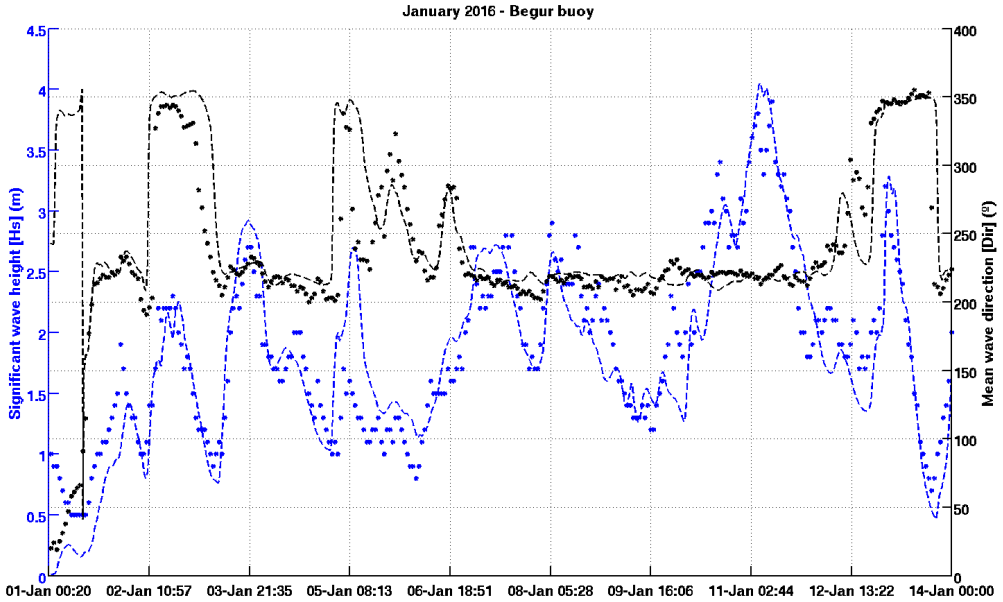

Figure C.29.: Time series of the significant wave height H_s (left axis, units in meters, in **blue**) and mean wave direction (right axis, units in degrees, in **black**) at the **Begur buoy** for the **January 2016** storm. For both cases, the contour **lines** correspond to the **SWAN** model and the **dots** are **buoy** observations.

C.2.4. February 2016

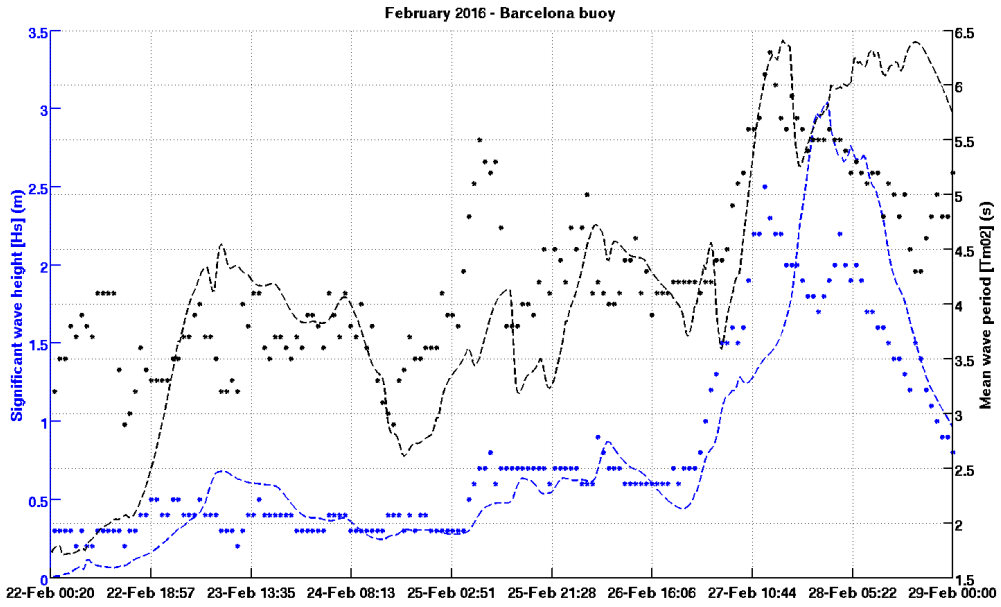

Figure C.30.: Time series of the significant wave height H_s (left axis, units in meters, in **blue**) and mean wave direction Tm_{02}(right axis, units in seconds, in **black**) at the **Barcelona buoy** for the **February 2016** storm. For both cases, the contour **lines** correspond to the **SWAN** model and the **dots** are **buoy** observations.

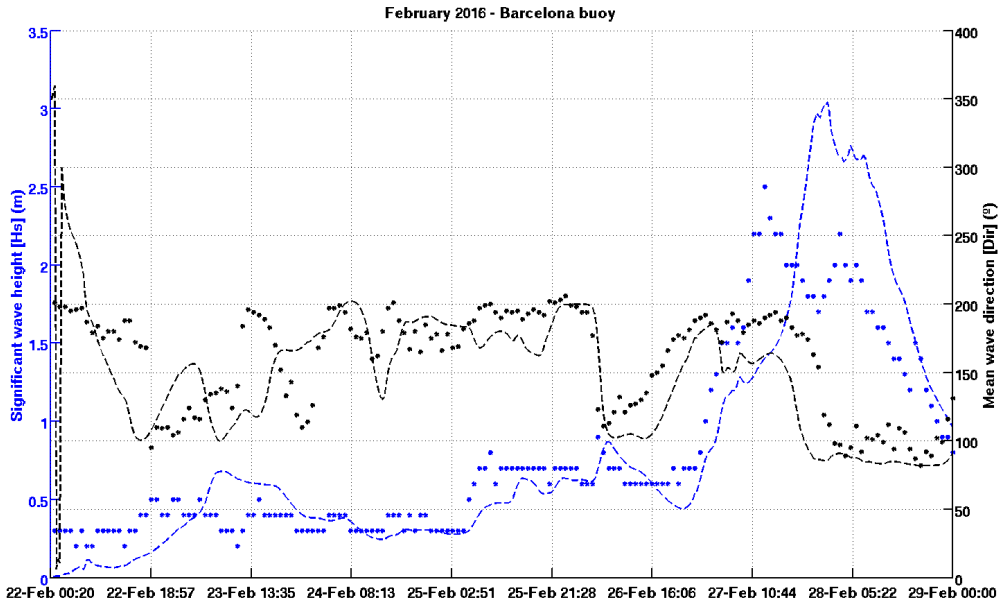

Figure C.31.: Time series of the significant wave height H_s (left axis, units in meters, in **blue**) and mean wave direction (right axis, units in degrees, in **black**) at the **Barcelona buoy** for the **January 2016** storm. For both cases, the contour **lines** correspond to the **SWAN** model and the **dots** are **buoy** observations.

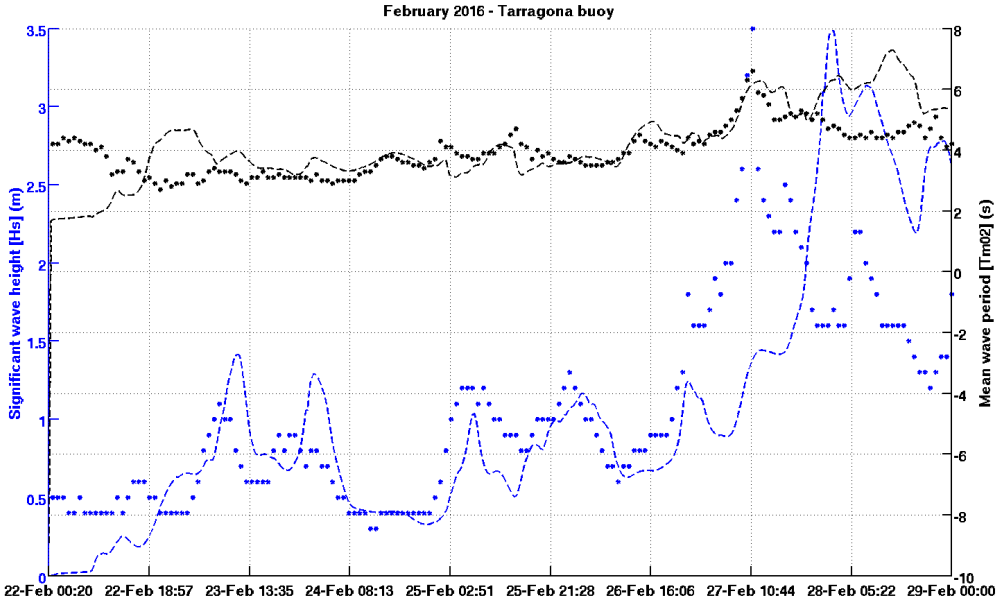

Figure C.32.: Time series of the significant wave height H_s (left axis, units in meters, in **blue**) and mean wave direction Tm_{02}(right axis, units in seconds, in **black**) at the **Tarragona buoy** for the **February 2016** storm. For both cases, the contour **lines** correspond to the **SWAN** model and the **dots** are **buoy** observations.

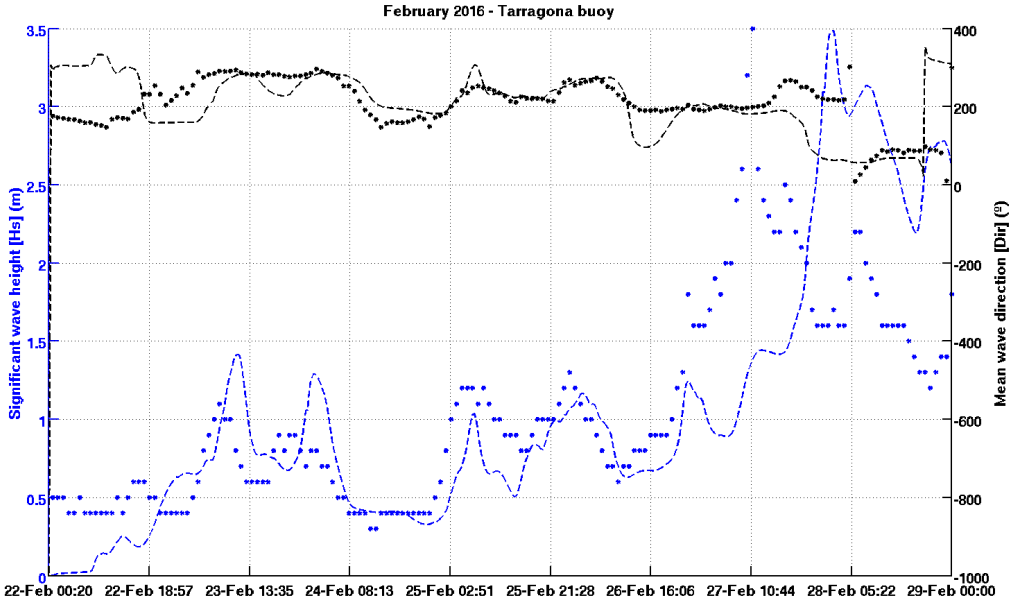

Figure C.33.: Time series of the significant wave height H_s (left axis, units in meters, in **blue**) and mean wave direction (right axis, units in degrees, in **black**) at the **Tarragona buoy** for the **February 2016** storm. For both cases, the contour **lines** correspond to the **SWAN** model and the **dots** are **buoy** observations.

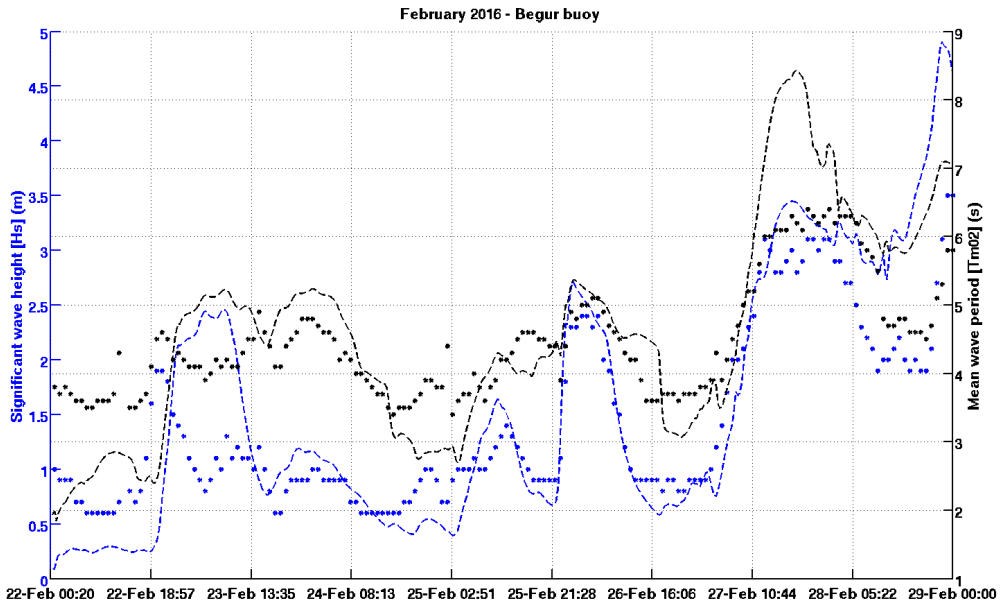

Figure C.34.: Time series of the significant wave height H_s (left axis, units in meters, in **blue**) and mean wave direction Tm_{02}(right axis, units in seconds, in **black**) at the **Begur buoy** for the **February 2016** storm. For both cases, the contour lines correspond to the SWAN model and the dots are buoy observations.

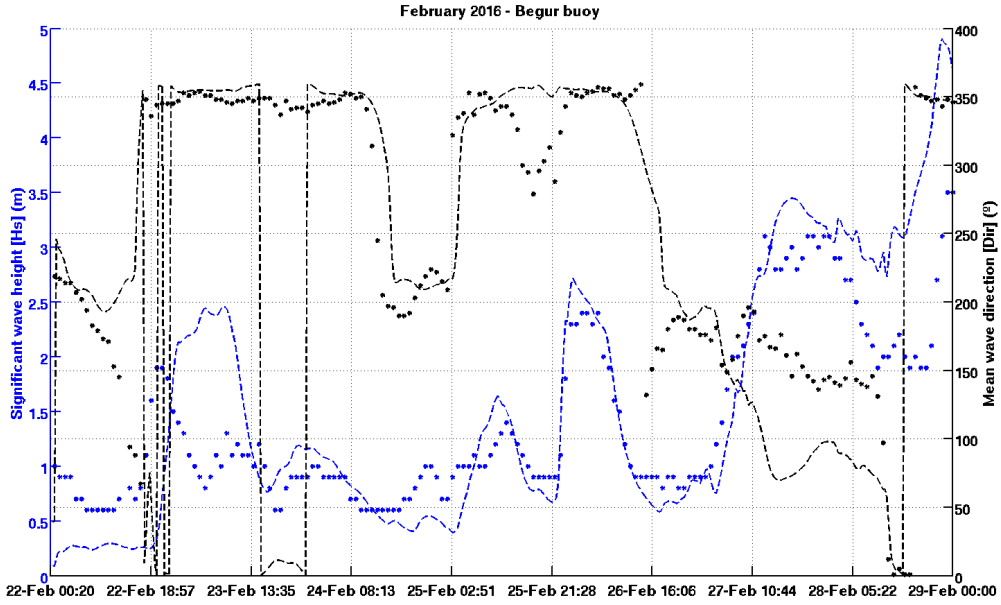

Figure C.35.: Time series of the significant wave height H_s (left axis, units in meters, in **blue**) and mean wave direction (right axis, units in degrees, in **black**) at the **Begur buoy** for the **February 2016** storm. For both cases, the contour **lines** correspond to the **SWAN** model and the **dots** are **buoy** observations.

C.2.5. December 2016

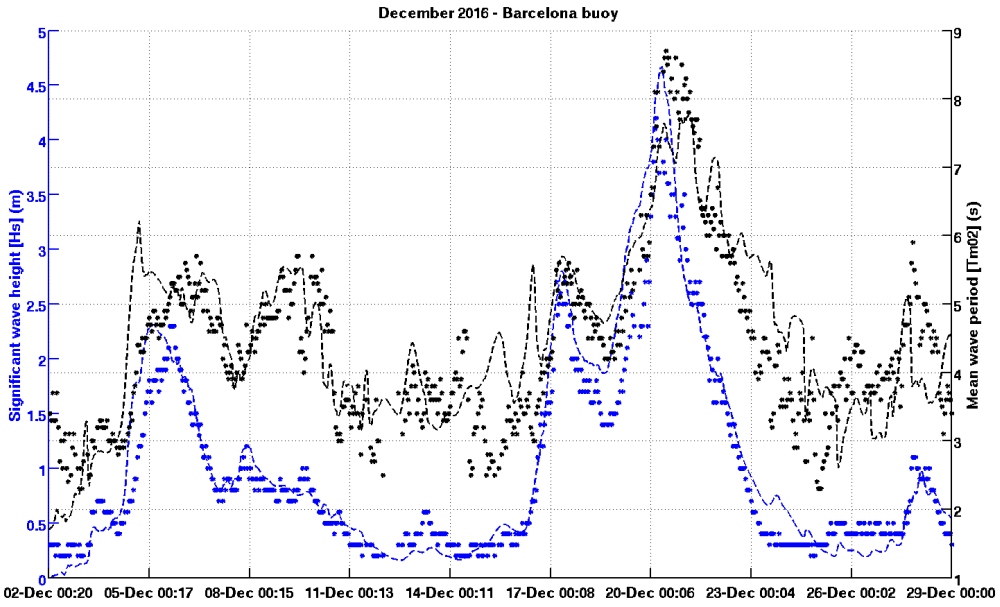

Figure C.36.: Time series of the significant wave height H_s (left axis, units in meters, in **blue**) and mean wave direction Tm_{02}(right axis, units in seconds, in **black**) at the **Barcelona buoy** for the **December 2016** storm. For both cases, the contour lines correspond to the SWAN model and the dots are buoy observations.

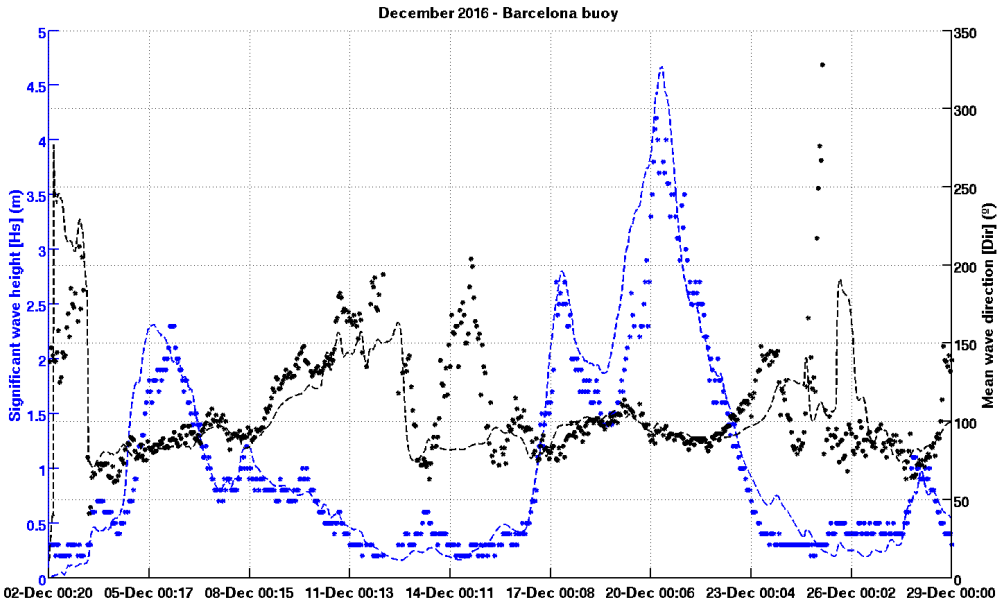

Figure C.37.: Time series of the significant wave height H_s (left axis, units in meters, in **blue**) and mean wave direction (right axis, units in degrees, in **black**) at the **Barcelona buoy** for the **December 2016** storm. For both cases, the contour **lines** correspond to the **SWAN** model and the **dots** are **buoy** observations.

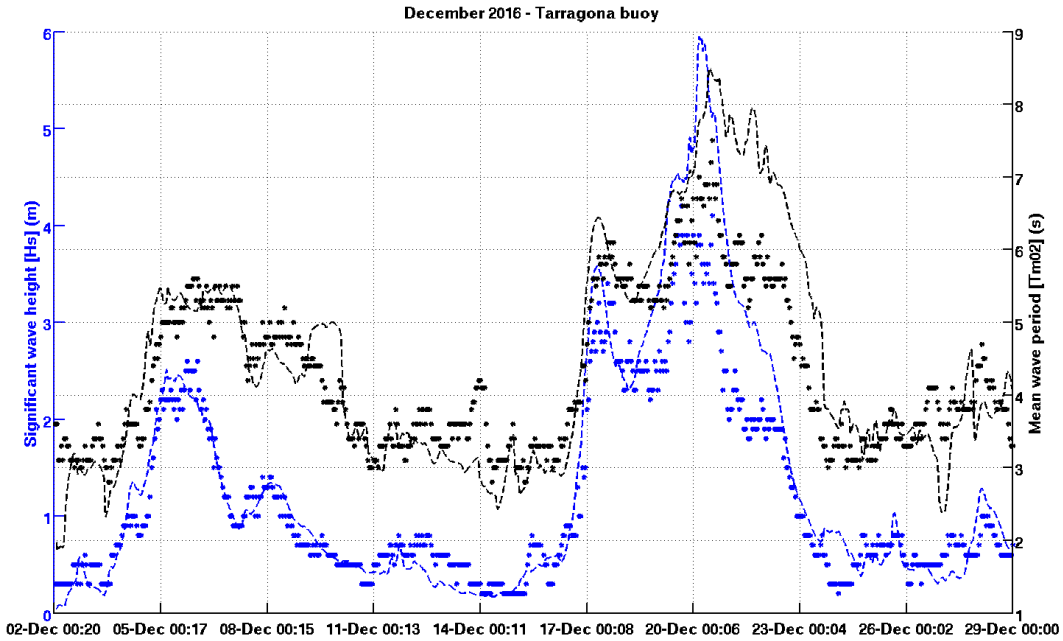

Figure C.38.: Time series of the significant wave height H_s (left axis, units in meters, in **blue**) and mean wave direction Tm_{02}(right axis, units in seconds, in **black**) at the **Tarragona buoy** for the **December 2016** storm. For both cases, the contour **lines** correspond to the **SWAN** model and the **dots** are **buoy** observations.

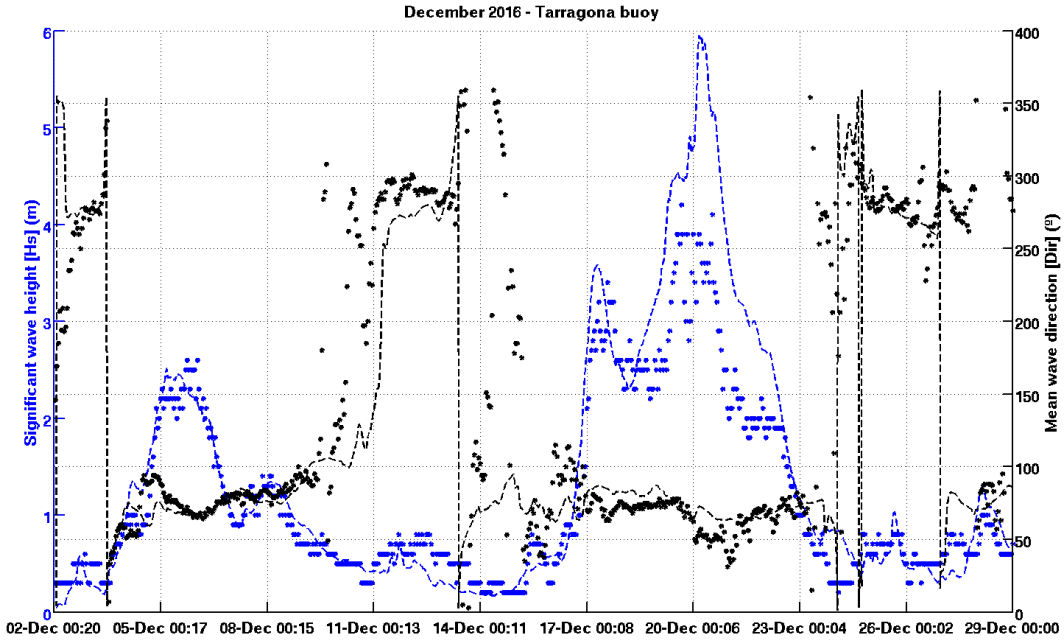

Figure C.39.: Time series of the significant wave height H_s (left axis, units in meters, in **blue**) and mean wave direction (right axis, units in degrees, in **black**) at the **Tarragona buoy** for the **December 2016** storm. For both cases, the contour **lines** correspond to the **SWAN** model and the **dots** are **buoy** observations.

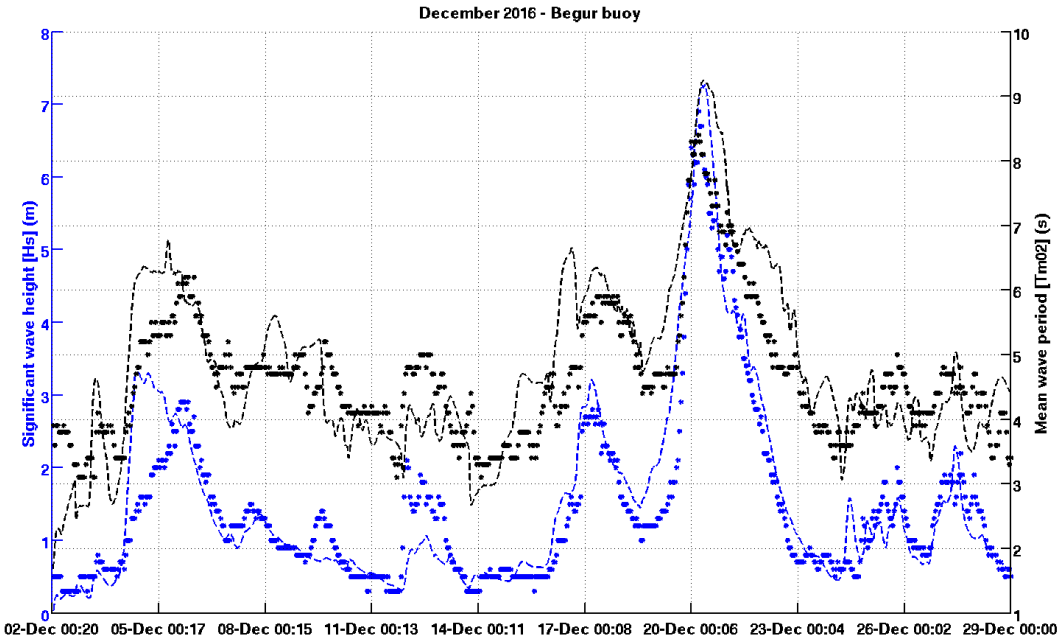

Figure C.40.: Time series of the significant wave height H_s (left axis, units in meters, in **blue**) and mean wave direction Tm_{02}(right axis, units in seconds, in **black**) at the **Begur buoy** for the **December 2016** storm. For both cases, the contour **lines** correspond to the **SWAN** model and the **dots** are **buoy** observations.

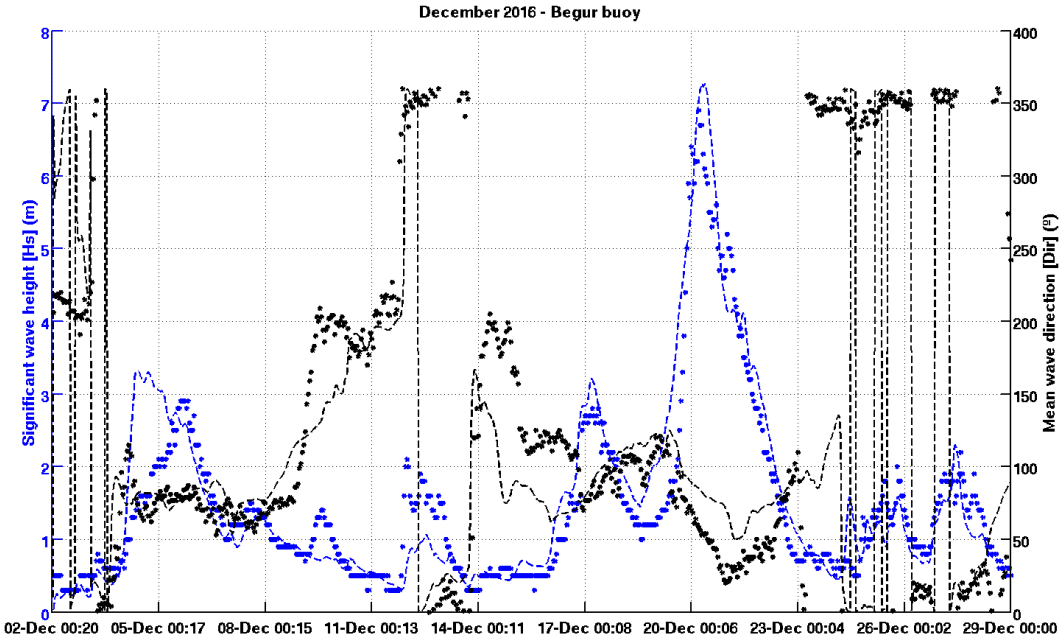

Figure C.41.: Time series of the significant wave height H_s (left axis, units in meters, in **blue**) and mean wave direction (right axis, units in degrees, in **black**) at the **Begur buoy** for the **December 2016** storm. For both cases, the contour **lines** correspond to the **SWAN** model and the **dots** are **buoy** observations.

C.2.6. January 2017

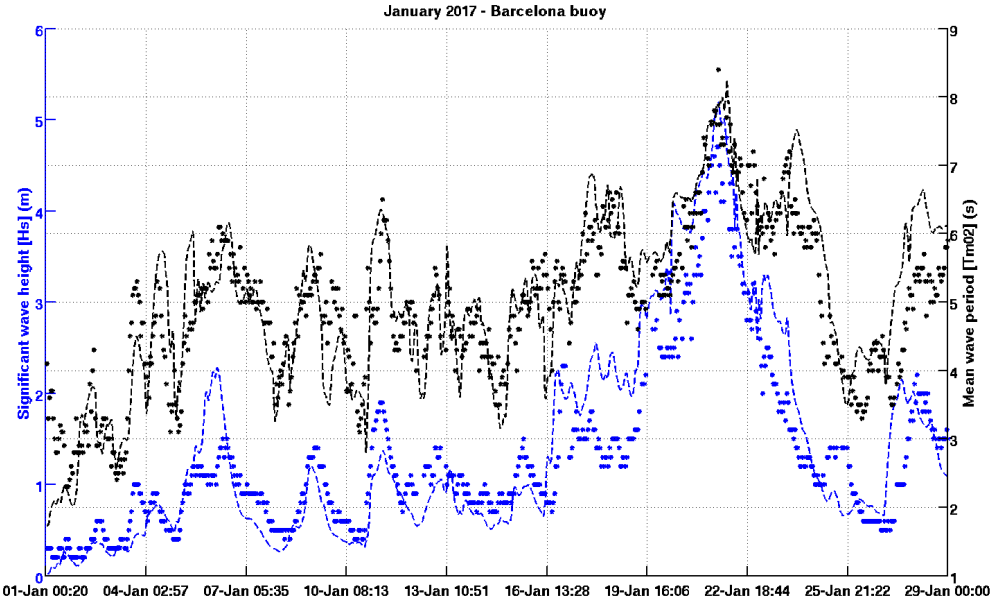

Figure C.42.: Time series of the significant wave height H_s (left axis, units in meters, in **blue**) and mean wave direction Tm_{02}(right axis, units in seconds, in **black**) at the **Barcelona buoy** for the **January 2017** storm. For both cases, the contour lines correspond to the SWAN model and the dots are buoy observations.

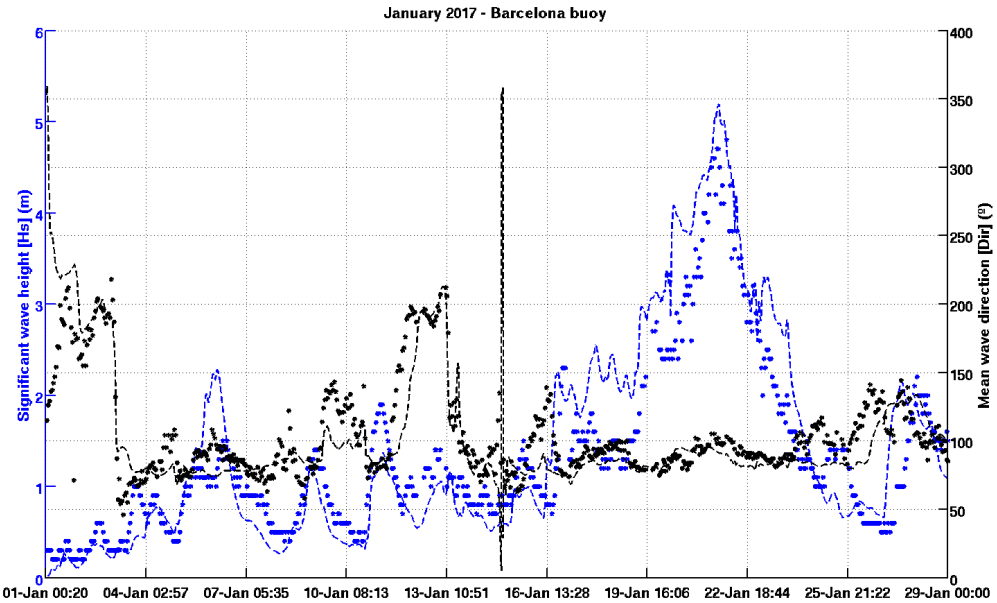

Figure C.43.: Time series of the significant wave height H_s (left axis, units in meters, in **blue**) and mean wave direction (right axis, units in degrees, in **black**) at the **Barcelona buoy** for the **January 2017** storm. For both cases, the contour **lines** correspond to the **SWAN** model and the **dots** are **buoy** observations.

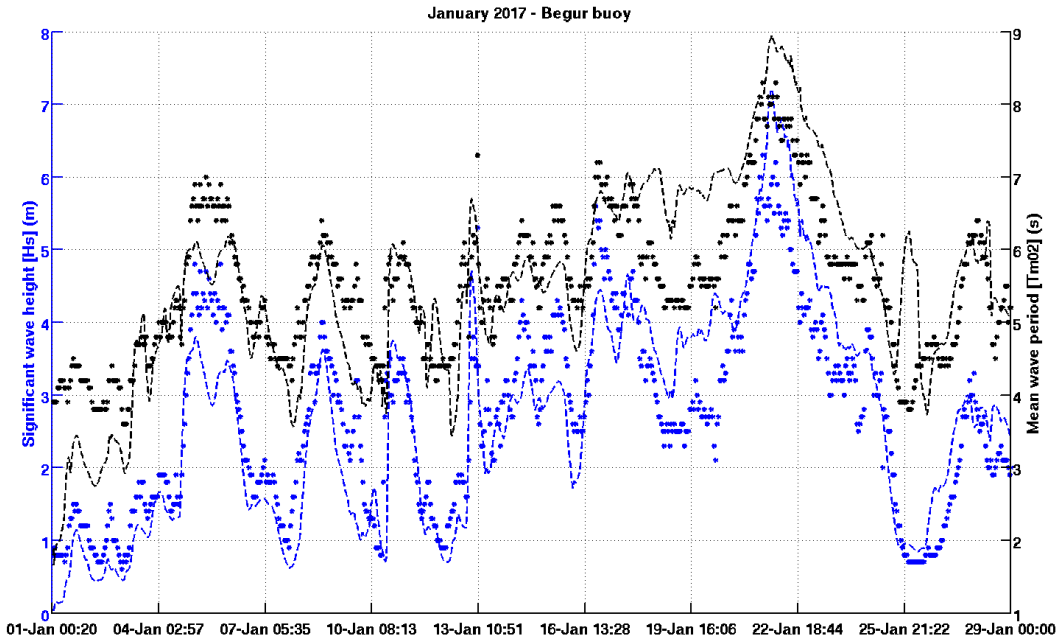

Figure C.44.: Time series of the significant wave height H_s (left axis, units in meters, in **blue**) and mean wave direction Tm_{02}(right axis, units in seconds, in **black**) at the **Begur buoy** for the **January 2017** storm. For both cases, the contour **lines** correspond to the **SWAN** model and the **dots** are **buoy** observations.

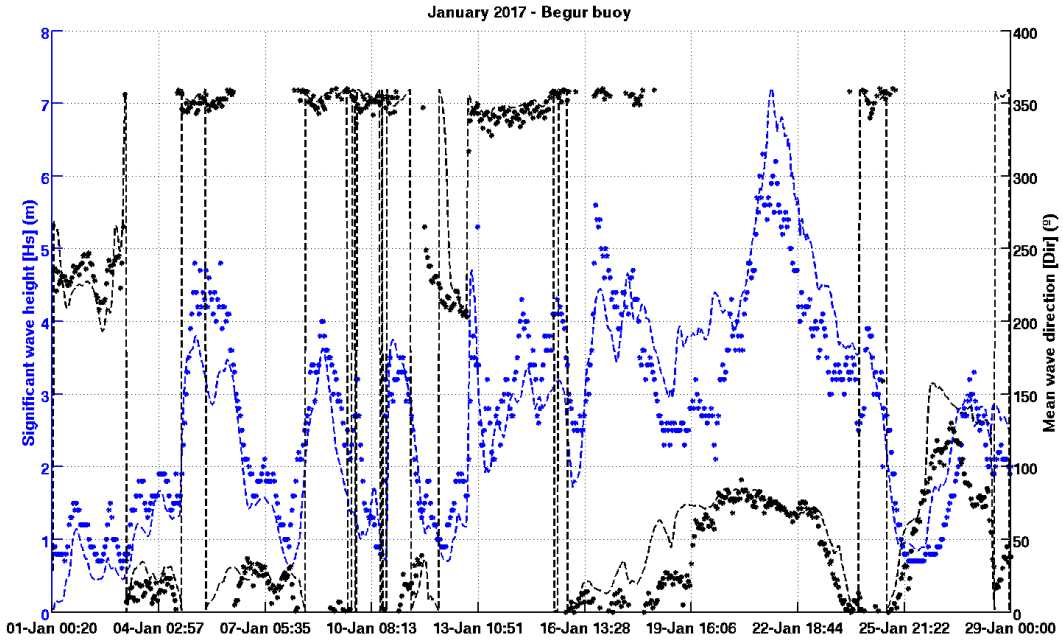

Figure C.45.: Time series of the significant wave height H_s (left axis, units in meters, in **blue**) and mean wave direction (right axis, units in degrees, in **black**) at the **Begur buoy** for the **January 2017** storm. For both cases, the contour **lines** correspond to the **SWAN** model and the **dots** are **buoy** observations.

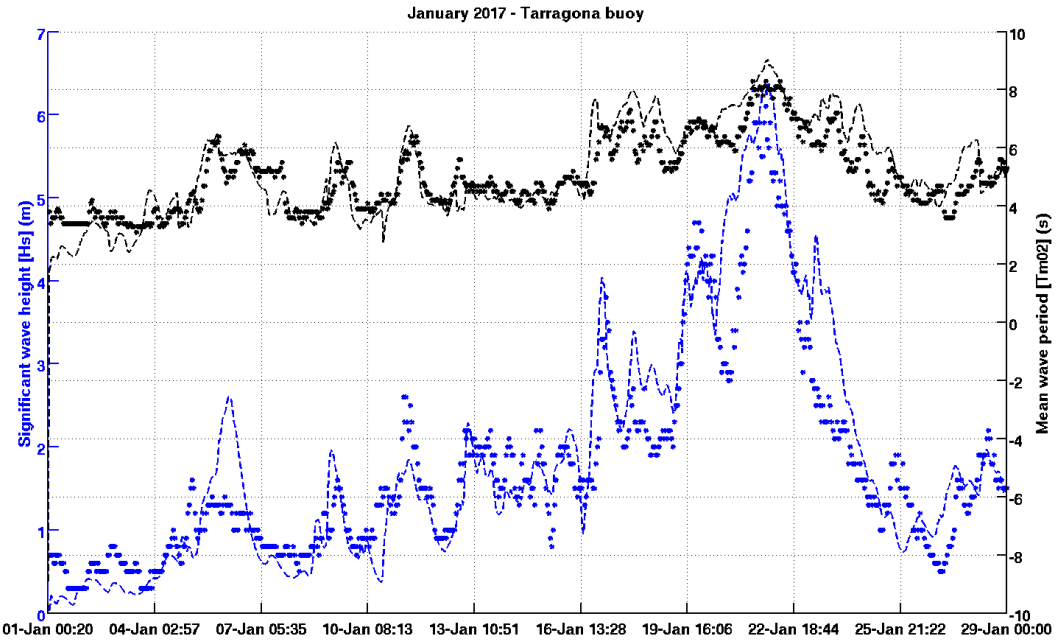

Figure C.46.: Time series of the significant wave height H_s (left axis, units in meters, in **blue**) and mean wave direction Tm_{02}(right axis, units in seconds, in **black**) at the **Tarragona buoy** for the **January 2017** storm. For both cases, the contour **lines** correspond to the **SWAN** model and the **dots** are **buoy** observations.

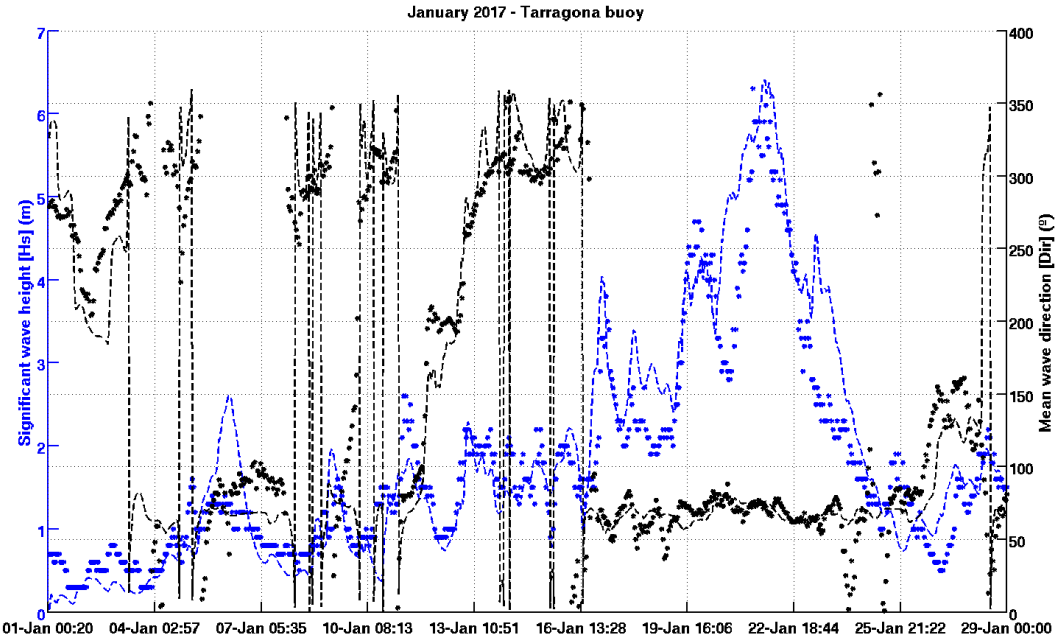

Figure C.47.: Time series of the significant wave height H_s (left axis, units in meters, in **blue**) and mean wave direction (right axis, units in degrees, in **black**) at the **Tarragona buoy** for the **January 2017** storm. For both cases, the contour **lines** correspond to the **SWAN** model and the **dots** are **buoy** observations.

D. Wave hindcasts for the Risk module

This Appendix D presents additional results of the wave hindcast performed in Ch. 5. These consist of time series of offshore points representative of the Calibration and Validation beaches that have been tested in the risk module (Ch. 6). For each storm event, time series of the significant wave height and mean wave period are shown at six representative areas of the Northern and Central Catalan coast (from North to South): (i) Creus Cape, (ii) Costa Brava (Center), (iii) Costa Brava (South), (iv) Maresme zone, (v) Barcelona area, (vi) Llobregat Delta.

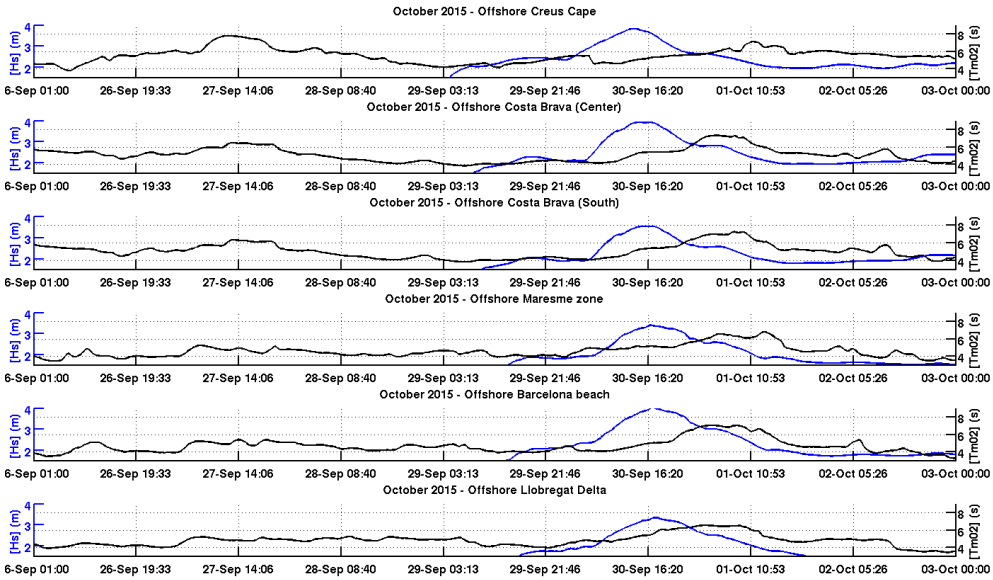

Figure D.1.: Results from the hydrodynamic module (presented in Ch. 5) for the selected offshore points at **October 2015** storm. The time series are shown from North (Creus Cape, upper figure) to South (Llobregat Delta, the lower one). The **blue series** represents the significant wave height H_s (in meters, left axis) , whereas the **black series** represents the mean wave period Tm_{02} (in seconds, right axis). The mean wave direction at the storm peak was mainly 90° (East).

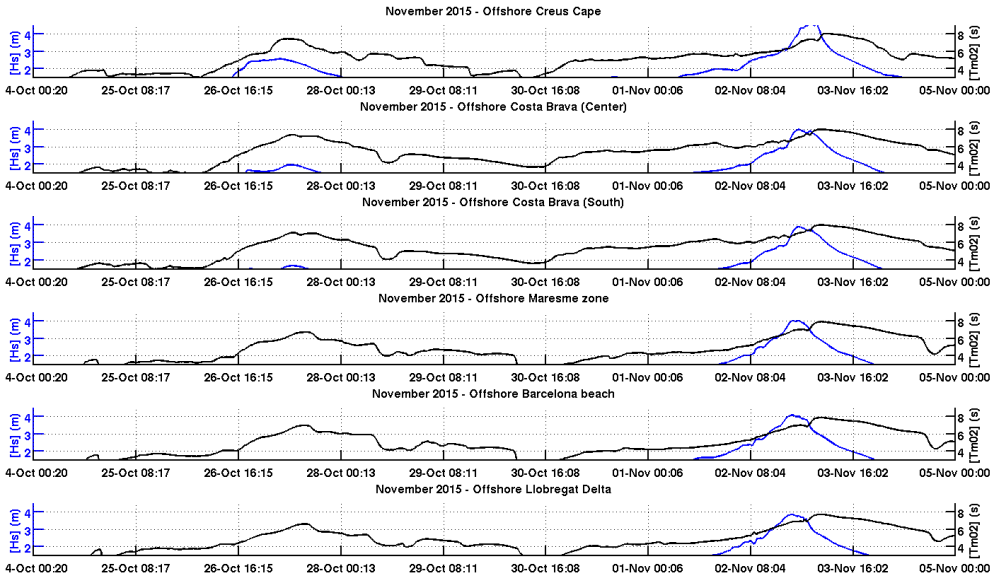

Figure D.2.: Results from the hydrodynamic module (presented in Ch. 5) for the selected offshore points at **November 2015** storm. The time series are shown from North (Creus Cape, upper figure) to South (Llobregat Delta, the lower one). The **blue series** represents the significant wave height (in meters, left axis) , whereas the **black series** represents the mean wave period (in seconds, right axis). The mean wave direction at the storm peak was mainly 135° (South-East).

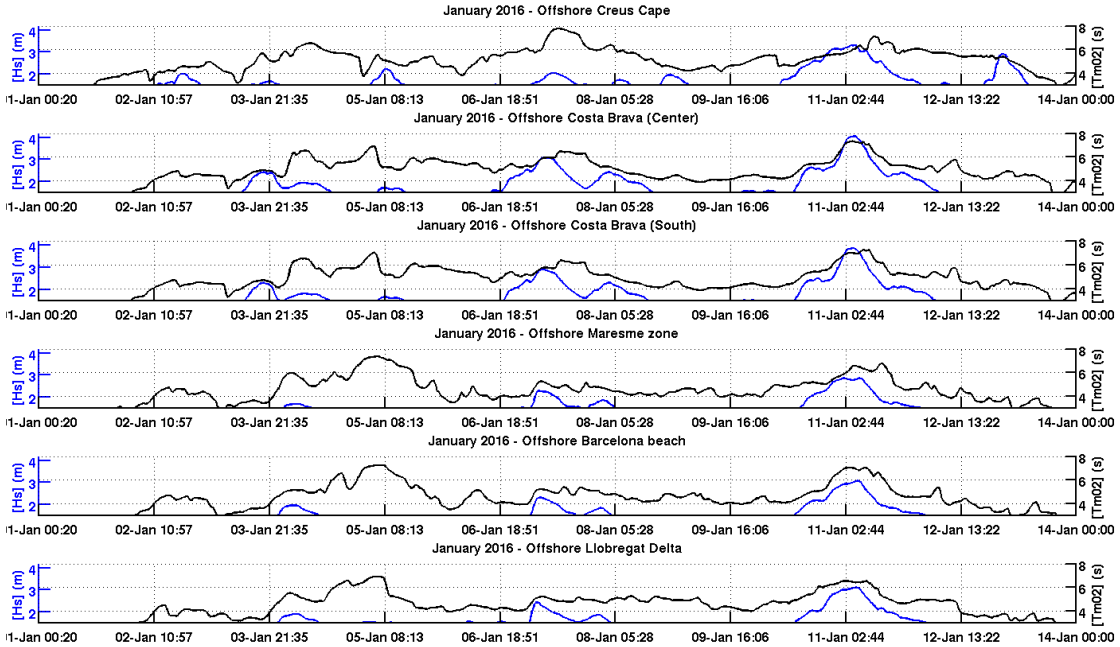

Figure D.3.: Results from the hydrodynamic module (presented in Ch. 5) for the selected offshore points at **January 2016** storm. The time series are shown from North (Creus Cape, upper figure) to South (Llobregat Delta, the lower one). The **blue series** represents the significant wave height (in meters, left axis) , whereas the **black series** represents the mean wave period (in seconds, right axis). The mean wave direction at the storm peak was mainly 202.5° (SSW).

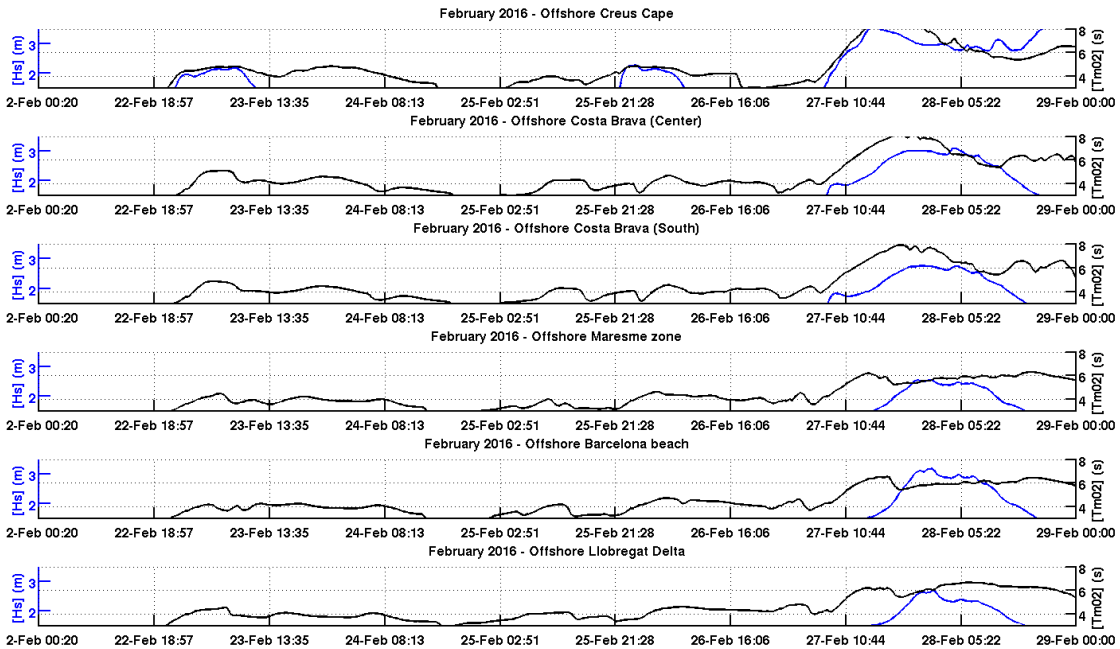

Figure D.4.: Results from the hydrodynamic module (presented in Ch. 5) for the selected offshore points at **February 2016** storm. The time series are shown from North (Creus Cape, upper figure) to South (Llobregat Delta, the lower one). The **blue series** represents the significant wave height (in meters, left axis) , whereas the **black series** represents the mean wave period (in seconds, right axis). The mean wave direction at the storm peak was mainly 90° (East).

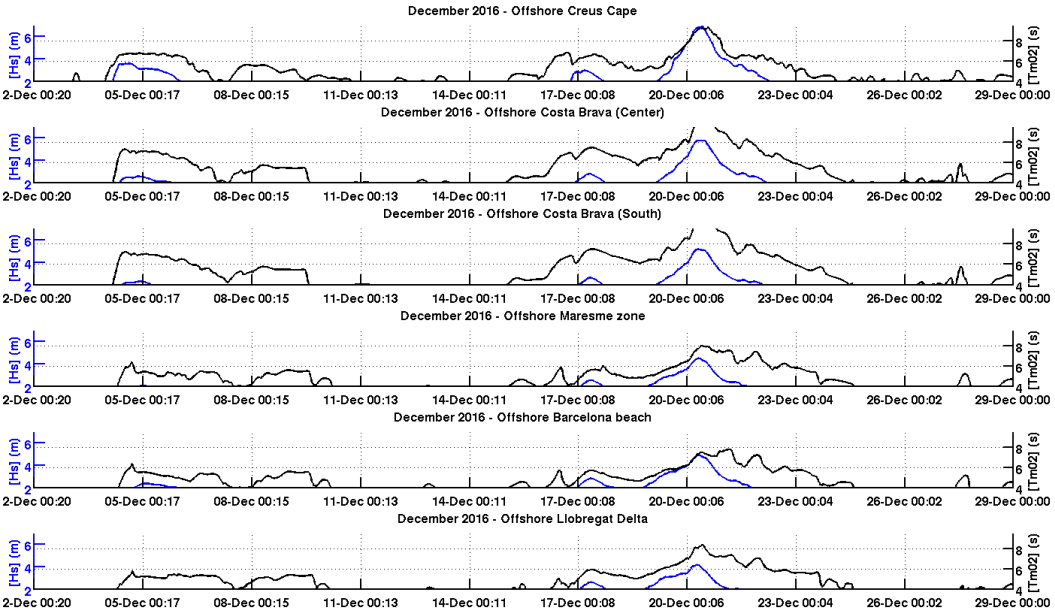

Figure D.5.: Results from the hydrodynamic module (presented in Ch. 5) for the selected offshore points at **December 2016** storm. The time series are shown from North (Creus Cape, upper figure) to South (Llobregat Delta, the lower one). The **blue series** represents the significant wave height (in meters, left axis) , whereas the **black series** represents the mean wave period (in seconds, right axis). The mean wave direction at the storm peak was mainly 90° (East).

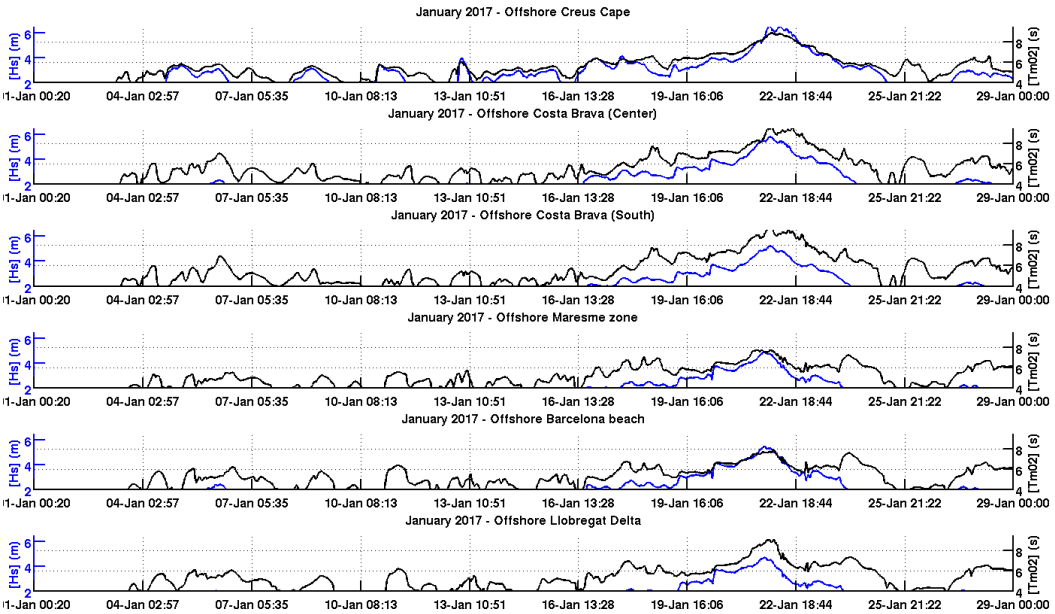

Figure D.6.: Results from the hydrodynamic module (presented in Ch. 5) for the selected offshore points at **January 2017** storm. The time series are shown from North (Creus Cape, upper figure) to South (Llobregat Delta, the lower one). The **blue series** represents the significant wave height (in meters, left axis) , whereas the **black series** represents the mean wave period (in seconds, right axis). The mean wave direction at the storm peak was mainly 90° (East).

Bibliography

Abadie, L. M., I. Galarraga, and E. S. de Murieta: 2017, 'Understanding risks in the light of uncertainty: low-probability, high-impact coastal events in cities'. *Environmental Research Letters* **12**(1), 014017. 1

ACA: 2006, 'La Directiva Marc de l' Aigua'. Agència Catalana de l'Aigua. 2.5

Akaike, H.: 1973, 'Information theory and an extension of the maximum Likelihood Principle'. In: B. Petrov and F. Csáki (eds.): *Second International Symposium on Information Theory*. pp. 267–281, Budapest: Akadémiai Kaidó. 3.4.3, 7.6

Alomar, M.: 2012, 'Improving Wave Forecasting in variable wind conditions. The effect of Resolution and Growth rate for the Catalan Coast'. Ph.D. thesis, Polytechnic University of Catalonia. 3.3.2, 5.1, 5.2, 5.4.1, 7.6

Alomar, M., R. Bolaños, A. Sánchez-Arcilla, and A. Sairouni: 2010, 'Wave growth under variable wind conditions'. In: *32rd International Conference in Coastal Engineering (2010)*. 4.5

Alomar, M., R. Bolaños, A. Sánchez-Arcilla, A. Sairouni, and F. Ocampo-Torres: 2009, 'Uncertainties in wave modeling for fetch-limited growth conditions'. In: *33rd IAHR Congress, Hyatt Regency Vancouver*. pp. 2846–2853. 4.5

Alomar, M., A. Sánchez-Arcilla, R. Bolaños, and A. Sairouni: 2014, 'Wave growth and forecasting in variable, semi-inclosed domains'. *Continental Shelf Research* **87(1)**, 28–40. 4.2, 4.3, 4.5

Alsina, J. and I. Cáceres: 2011, 'Sediment suspension events in the inner surf and swash zone. Measurements in large-scale and high-energy wave conditions'. *Coastal Engineering* **58(8)**, 657–670. 4.6

Álvarez-Fanjul, E., B. Pérez, and I. Rodríguez: 2001, 'NIVMAR: a storm-surge forecasting system for Spanish waters'. *Scientia Marina* **60**, 145–154. 5.4.4, 7

Ardhuin, F. and A. Roland: 2012, 'Coastal wave reflection, directional spread, and seismoacoustic noise sources'. *Journal of Geophysical Research: Oceans* **117**(C11). 5.4.3

Baart, F., T. van der Kaaij, M. van Ormondt, A. van Dongeren, M. van Koningsveld, and J. Roelvink: 2009, 'Real-time forecasting of morphological storm impact: a case study in the Netherlands'. *Journal of Coastal Research* **56**, 1617–1621. 1, 1.1

Baart, F., M. van Ormondt, J. van Thiel de Vries, and M. van Koningsveld: 2016, 'Morphological impact of a storm can be predicted three days ahead'. *Computers & Geosciences* **90**(Part B), 17 – 23. Uncertainty and Sensitivity in Surface Dynamics Modeling. 1, 1.1, 6.4.3.1, 7.1, 7.6

Battjes, J.: 1975, 'Modelling of turbulence in the surfzone'. In: *Symposium on Modelling Techniques*. San Francisco, pp. 1050–1061. 3.3.3.2

Battjes, J. and J. Janssen: 1978, 'Energy loss and set-up due to breaking of random waves'. In: ASCE (ed.): *Proc. 16th Int. Conf. Coastal Engineering*. pp. 569–587. 3.3.2

Beljaars, A.: 1995, *The parametrization of surface fluxes in large scale models under free convection*. Shinfield Park, Reading. 5.4.3

Bell, M. J., R. M. Forbes, and A. Hines: 2000, 'Assessment of the FOAM global data assimilation system for real-time operational ocean forecasting'. *Journal of Marine Systems* **25**(1), 1–22. 6.4.3.1

Bennet, N., B. F. Croke, G. Guariso, J. H. Guillaume, S. H. Hamilton, A. Jakeman, S. Marsili-Libelli, L. T. Newham, J. Norton, C. Perrin, S. Pierce, B. Robson, R. Seppelt, A. Voinov, B. Fath, and V. Andreassian: 2013, 'Characterising performance of environmental models'. *Environmental Modelling and Software* **40**, 1–20. 3.4, 7.6

Bentamy, A., H. Ayina, P. Queffeulou, D. Croize-Fillon, and V. Kerbaol: 2007, 'Improved near real time surface wind resolution over the Mediterranean Sea'. *Ocean Science* **3**, 259–271. 4.2, 5.1, 5.4.3, 7.6

Berrisford, P., D. Dee, P. Poli, R. Brugge, K. Fielding, M. Fuentes, P. Kållberg, S. Kobayashi, S. Uppala, and A. Simmons: 2011, *The ERA-Interim archive Version 2.0*. Shinfield Park, Reading. 3.2.1

Bertotti, L., J. Bidlot, C. Bunney, L. Cavaleri, L. D. Passeri, M. Gomez, J. Lefèvre, T. Paccagnella, L. Torrisi, A. Valentini, and A. Vocino: 2012, 'Performance of different forecast systems in an exceptional storm in the Western Mediterranean Sea'. *Quarterly Journal of the Royal Meteorological Society* **138**(662), 34–55. 5.4.3, 7.6, 7.6

Bertotti, L. and L. Cavaleri: 2011, 'The predictability of meteo-oceanographic events'. *Ocean Dynamics* **61**, 1391–1402. 4.5

Bishop, C. H., B. J. Etherton, and S. J. Majumdar: 2001, 'Adaptive Sampling with the Ensemble Transform Kalman Filter. Part I: Theoretical Aspects'. *Monthly Weather Review* **129**(3), 420–436. 6.4.3.1

Bolaños, R.: 2004, 'Tormentas de oleaje en el Mediterraneo: Fisica y prediccion'. Ph.D. thesis, Polytechnic University of Catalonia. 5.1, 5.2, 5.4.1, 7.6

Bolaños, R., G. Jorda, J. Cateura, J. Lopez, J. Puigdefabregas, J. Gomez, and M. Espino: 2009, 'The XIOM: 20 years of a regional coastal observatory in the Spanish Catalan coast'. *Journal of Marine Systems* **77**, 237–260. 2.4.1, 3.2.2, 3.3.1, 4.1, 4.2, 6.4.1

Booij, N., R. Ris, and L. Holthuijsen: 1999, 'A third-generation wave model for coastal regions, Part I, Model description and validation'. *Journal of Geophysical Research* **104 (C4)**, 7649–7666. 3.1, 2, 7.6

Borsje, B. W., B. K. van Wesenbeeck, F. Dekker, P. Paalvast, T. J. Bouma, M. M.

van Katwijk, and M. B. de Vries: 2011, 'How ecological engineering can serve in coastal protection'. *Ecological Engineering* **37**, 113–122. 7.5.3

Botts, M., G. Percivall, C. Reed, and J. Davidson: 2008, 'OGC sensor web enablement: Overview and high level architecture'. *GeoSensor Networks* **1**, 175–190. 2.5.1.2

Brown, S., R. Nicholls, J. Lowe, and J. Hinkel: 2013, 'Spatial variations of sea-level rise and impacts: An application of DIVA'. *Climatic Change* pp. 1–14. 2.6

Bruneau, N., R. Toumi, and S. Wang: 2018, 'Impact of wave whitecapping on land falling tropical cyclones'. *Scientific reports* **8**(1), 652. 5.4.3

Bruun, P. F.: 1962, 'Sea level rise as a cause of shore erosion'. *Journal of Waterways and Harbors Division* **88(1)**, 117–130. 2.3.1.3

Campins, J., A. Genovés, M. A. Picornell, and A. Jansà: 2011, 'Climatology of Mediterranean cyclones using the ERA-40 dataset'. *International Journal of Climatology* **31**(11), 1596–1614. 5.4.4

Casas-Prat, M. and J. Sierra: 2013, 'Projected Future Wave Climate in the NW Mediterranean Sea'. *Journal of Geophysical Research: Oceans* **118**, 3548–3568. 2.4.3

Cavaleri, L.: 2009, 'Wave modeling - missing the peaks'. *Journal of Physical Oceanography* pp. 2757–2778. 4.5, 5.3.2, 5.4.1

Cavaleri, L., L. Bertotti, R. Buizza, A. Buzzi, V. Masato, G. Umgiesser, and M. Zampieri: 2010, 'Predictability of extreme meteo-oceanographic events in the Adriatic Sea'. *Q. J. R. Meteorol. Soc.* **136**, 400–413. 4.5

Cavaleri, L., B. Fox-Kemper, and M. Hemer: 2012, 'Wind Waves in the Coupled Climate System'. *Bulletin of the American Meteorological Society* **93**(11), 1651–1661. 5.4.3

Cavaleri, L. and P. Malanotte-Rizzoli: 1981, 'Wind wave prediction in shallow water: Theory and applications'. *Journal of Geophysical Research* **86, No. C11**, 10, 961–10,973. 3.3.2

CEDEX: 2013, 'Estudio de la dinámica litoral, defensa y propuesta de mejora en las playas con problemas: Estrategia de actuación en el Maresme'. Technical report, Centro de Estudios y Experimentación de Obras Públicas. 1, 1.1, 2.4.1, 2.4.4.1, 7.6

Chen, G., L. Zhao, and A. Mochida: 2016, 'Urban Heat Island Simulations in Guangzhou, China, Using the Coupled WRF/UCM Model with a Land Use Map Extracted from Remote Sensing Data'. *Sustainability* **8**(7(628)), 1–14. 5.4.3

Church, J., P. Clark, A. Cazenave, J. Gregory, S. Jevrejeva, A. Levermann, M. Merrifield, G. Milne, R. Nerem, P. Nunn, A. Payne, W. Pfeffer, D. Stammer, and A. Unnikrishnan: 2013, *Sea Level Change*, book section 13, p. 1137Ű1216. Cambridge, United Kingdom and New York, NY, USA: Cambridge University Press. 2.4.3, 2.4.3

CIIRC: 2010, 'Estat de la zona costanera a Catalunya'. (Departament de Política

Territorial i Obres Públiques) Generalitat de Catalunya. 2.3.2, 2.4.1, 4.4, 5.3.2, 6.2.1, 7.3.1, 7.3.2.1, 7.4.1.2, 7.6

CIIRC: 2015, 'Deliverable C1-C2-C4: Inventory of contemporary coastal disasters related to storms. Restricted document from the iCoast project (ECHO/SUB/2013/661009)'. Technical report, CIIRC - ICGC. 6.4.3.1

Cloke, H. and F. Pappenberger: 2009, 'Ensemble flood forecasting: a review'. *Journal of Hydrology* **375**(3), 613–626. 6.4.3.2

Collins, J.: 1972, 'Prediction of shallow water spectra'. *Journal of Geophysical Research* **77, No. 15**, 2693–2707. 3.3.2

Conte, D. and P. Lionello: 2013, 'Characteristics of large positive and negative surges in the Mediterranean Sea and their attenuation in future climate scenarios'. *Global and Planetary Change* **111**, 159–173. 1.1, 2.4.3, 4.1

Cooper, J. and O. Pilkey: 2012, *Pitfalls of Shoreline Stabilization: Selected Case Studies*, Vol. 333 pp. London: Springer. 2.4.3

Costanza, R., R. d'Arge, R. De Groot, S. Farber, M. Grasso, B. Hannon, K. Limburg, S. Naeem, R. V. O Neill, J. Paruelo, et al.: 1997, 'The value of the world's ecosystem services and natural capital'. *Nature* **387**(6630), 253–260. 1

Dan, S., M. J. Stive, D.-J. R. Walstra, and N. Panin: 2009, 'Wave climate, coastal sediment budget and shoreline changes for the Danube Delta'. *Marine Geology* **262**(1-4), 39 – 49. 2.4.3

Davies, S.: 1964, 'A morphogenic approach to world shorelines'. *Zeitschrift für Geomorphology* **8**, 127–142. 2

Dean, R. G.: 1973, 'Heuristic models of sand transport in the surf zone'. *Proc. Conf. Engineering Dynamics in the Surf Zone* (208-214). 7.3.1

Dee, D. P., S. M. Uppala, A. J. Simmons, P. Berrisford, P. Poli, S. Kobayashi, U. Andrae, M. A. Balmaseda, G. Balsamo, P. Bauer, P. Bechtold, A. C. M. Beljaars, L. van de Berg, J. Bidlot, N. Bormann, C. Delsol, R. Dragani, M. Fuentes, A. J. Geer, L. Haimberger, S. B. Healy, H. Hersbach, E. V. Hólm, L. Isaksen, P. Kållberg, M. Köhler, M. Matricardi, A. P. McNally, B. M. Monge-Sanz, J.-J. Morcrette, B.-K. Park, C. Peubey, P. de Rosnay, C. Tavolato, J.-N. Thépaut, and F. Vitart: 2011, 'The ERA-Interim reanalysis: configuration and performance of the data assimilation system'. *Quarterly Journal of the Royal Meteorological Society* **137**(656), 553–597. 3.2.1, 7.6

Devoy, R.: 1987, *Sea surface studies: A global view*. London: Croom Held and Chapman Hall. 2.4.3

Devoy, R.: 2015, 'Sea-level Rise: Causes, Impacts and Scenarios for Change'. In: D. Sherman and J. Ellis (eds.): *Coastal and Marine Hazards, Risks and Disasters*. Amsterdam: Elsevier, pp. 197–242. 2.4.3

DHI: 2017, '(LITPACK) https://www.mikepoweredbydhi.com/products/litpack (Last access: 28th August 2017)'. 2.5.2.1

DPTOP: 2005, 'Pla de Ports de Catalunya'. (Departament de Política Territorial i Obres Públiques) Generalitat de Catalunya. 2.4

Duro, J. and D. Rodríguez: 2011, 'Estimació del PIB turístic per Catalunya, en comarques'. Technical report, Direcció General de Turisme. Generalitat de Catalunya. 1

EEA: 2014, 'European Environmental Agency Report, Global and European Sea-level Rise (CLIM 012) - Assessment Published Sept. 2014 "http://www.eea.europa.eu/data-and-maps/indicators/sea-level-rise-2/assessment"'. 2.4.3, 2.4.3

El-Samra, R., E. Bou-Zeid, and M. El-Fadel: 2018, 'What model resolution is required in climatological downscaling over complex terrain?'. *Atmospheric Research* **203**, 68 – 82. 5.4.3

Eldeberky, Y. and J. Battjes: 1995, 'Parametrization of triad interactions in wave energy models.'. In: *Proceedings of Coastal Dynamics Conference 1995*. Gdansk, Poland, pp. 140–148. 3.3.2

Emanuel, K.: 2017, 'Will Global Warming Make Hurricane Forecasting More Difficult?'. *Bulletin of the American Meteorological Society* **98**(3), 495–501. 5.4.4, 7.6

EuropeanCommission: 2004, 'Living with Coastal Erosion in Europe: Sediment and Space for Sustainability. Part I: Major findings and Policy Recommendations of the EUROSION project'. Office for Official Publications of the European Communities, Luxembourg. 7.1

EUROSION: 2004, 'Living with coastal erosion in Europe: sediment and space for sustainability. Coastal erosion - Evaluation of the need for action'. Technical report, Directorate General Environment European Commission. 1, 2.4.4.1, 7.6

Evensen, G.: 2001, 'Sequential Data Assimilation for Nonlinear Dynamics: The Ensemble Kalman Filter'. In: N. Pinardi and J. Woods (eds.): *Ocean Forecasting. Conceptual basis and Applications*. Springer, pp. 97–116. 2

Fan, Y., S.-J. Lin, I. M. Held, Z. Yu, and H. L. Tolman: 2012, 'Global Ocean Surface Wave Simulation Using a Coupled AtmosphereŰWave Model'. *Journal of Climate* **25**(18), 6233–6252. 5.4.3

FLOODSite: 2005, 'Integrated Flood Risk Analysis and Management Methodologies'. Language of Risk. Project Definitions. T32-04-01, Co-ordinator HR Wallingford UK. 2.2

Galapatti, R.: 1983, 'A depth integrated model for suspended transport. Report 83-7, Communications on Hydraulics'. Technical report, Delft University of Technology, Department of Civil Engineering. 3.3.3, 3.3.3.3

García-León, M., V. Gràcia, L. Robichaux, A. Kroger, J. Gault, and A. Sánchez-Arcilla: 2015, *Evaluation of Transient Defence Measures against storms*, Chapt. 166. World Scientific. 2.4.4.2, 2.6, 7.5.2

Gault, J., A. O. Hagan, V. Cummins, J. Murphy, and T. Vial: 2011, 'Erosion management in Inch beach, South West Ireland'. *Ocean and Coastal Management* **54**(12), 930 – 942. Concepts and Science for Coastal Erosion Management (Conscience). 2.6

Gigerenzer, G., R. Hertwig, E. Van Den Broek, B. Fasolo, and K. V. Katsikopoulos: 2005, 'A 30% chance of rain tomorrow: How does the public understand probabilistic weather forecasts?'. *Risk analysis* **25**(3), 623–629. 6.4.3

Gómez, M. and J. Carretero: 2005, 'Wave forecasting at the Spanish coasts'. *Journal of Atmospheric and Ocean Science* **10**(4), 389–405. 1.1

Gràcia, V., D. Alvarado-Aguilar, M. Hernández, and A. Sánchez-Arcilla: 2013a, 'Coastal flooding assessment using numerical modeling'. In: Klijn and Schweckendiek (eds.): *Comprehensive Flood Risk Management*. Taylor and Francis Group. 4.3

Gràcia, V., M. García-León, M. Grifoll, and A. Sánchez-Arcilla: 2013b, 'Breaching of a barrier under extreme events. The role of morphodynamic simulations'. *Journal of Coastal Research* **65**, 951–956. 2.3.1.1.2, 2.4.4.2, 4.4, 4.5, 6.4.2, 7.5.1, 7.6, 7.6

Gràcia, V., A. Sánchez-Arcilla, and G. Anfuso: 2013c, 'Spain'. In: E. Pranzini and A. WIlliams (eds.): *Coastal Erosion and Protection in Europe*, Coastal erosion and protection in Europe. Oxon: Routledge, pp. 254–274. 1, 1.1, 2.3.1, 2.4.1, 2.4.4.1, 7.6

Gràcia, V., A. Sánchez-Arcilla, M. García-León, J. Gault, P. Oller, J. Fernández, A. Sairouni, E. Cristofiori, and R. Toldrà: 2014, 'A new generation of early warning systems for coastal risk. The iCoast Project'. *Proceedings of the 34th International Conference on Coastal Engineering*. 2, 2.6

Grasso, V. F. and A. Singh: 2007, 'Global Environmental Alert Service (GEAS)'. *Advances in Space Research* **42**, 1836–1852. 2.5.1.2

Grifoll, M., A. L. Aretxabaleta, and M. Espino: 2015, 'Shelf response to intense offshore wind'. *Journal of Geophysical Research: Oceans* **120**(9), 6564–6580. 3.3.1

Grifoll, M., V. Gràcia, A. Aretxabaleta, J. Guillén, M. Espino, and J. Warner: 2014, 'Formation of fine sediment deposit from a flash flood river in the Mediterranean Sea'. *Journal of Geophysical Research: Oceans* **119**(9), 5837–5853. 5.4.3, 7.5.2, 7.6

Grifoll, M., J. Navarro, E. Pallarés, L. Ràfols, M. Espino, and A. Palomares: 2016, 'Ocean–atmosphere–wave characterisation of a wind jet (Ebro shelf, NW Mediterranean Sea)'. *Nonlinear Processes in Geophysics* **23**(3), 143–158. 3.2.3, 5.4.3, 9

Grinsted, A., S. Jevrejeva, R. E. Riva, and D. Dahl-Jensen: 2015, 'Sea level rise projections for northern Europe under RCP8.5'. *Climate Research* **64**(1), 15–23. 2.3.1.3

Guillén, J.: 1992, 'Dinámica y balance de sedimentos en los ambientes fluvial y litoral del Delta del Ebro'. Ph.D. thesis, Universitat Politécnica de Catalunya. 2.3.2

Guillén, J.: 2008, 'Els Riscos Litorals a Catalunya (RISKCAT)'. Technical report, CSIC. 1

Gumbel, E. J.: 1935, 'Les valeurs extrêmes des distributions statistiques'. *Ann. Inst. Henri Poincaré* **5**(2), 115–158. 3.3.4

Haasnoot, M., H. Middelkoop, A. Offermans, E. Beek, and W. Deursen: 2012, 'Exploring pathways for sustainable water management in river deltas in a changing environment'. *Climatic Change* **115**(3-4), 795–819. 2.6

Haerens, P., P. Ciavola, O. Ferreira, A. van Dongeren, M. van Koningsveld, and A. Bolle: 2012, 'Online Operational Early Warning System Prototypes to forecast Coastal Storm Impacts (CEWS)'. In: *33rd International Conference in Coastal Engineering (2012)*. 2.5.2

Hahmann, A. N., C. L. Vincent, A. Peña, J. Lange, and C. B. Hasager: 2015, 'Wind climate estimation using WRF model output: method and model sensitivities over the sea'. *International Journal of Climatology* **35**(12), 3422–3439. 5.4.2

Hallermeier, R.: 1981, 'A profile zonation for seasonal sand beaches from wave climate'. *Coastal Engineering* **4**(253-277). 7.3.1

Hamm, L., M. Capobianco, H. Dette, A. Lechuga, R. Spanhoff, and M. Stive: 2002, 'A summary of European experience with shore nourishment'. *Coastal Engineering* **47**(2), 237 – 264. Shore Nourishment in Europe. 2.4.1, 7.1

Hanson, H., A. Brampton, M. Capobianco, H. Dette, L. Hamm, A. Laustrup, A. Lechuga, and R. Spanhoff: 2002, 'Beach nourishment project, practices and objectives: An European overview'. *Coastal Engineering* **47**(81-111). 7.1

Harley, M. D. and P. Ciavola: 2013, 'Managing local coastal inundation risk using real-time forecasts and artificial dune placements'. *Coastal Engineering* **77**, 77 – 90. 2.4.4.2

Hasselmann, K.: 1974, 'On the spectral dissipation of ocean waves due to whitecapping'. *Boundary Layer Meteorology* **6, 1-2**, 107–127. 3.3.2

Hasselmann, K., T. Barnett, E. Bouws, H. Carlson, D. Cartwright, K. Enke, J. Ewing, H. Gienapp, D. Hasselmann, P. Kruseman, A. Meerburg, P. Müller, D. Olbers, K. Richter, W. Seññ, and H. Walden: 1973, 'Measurements Of Wind-wave Growth And Swell Decay During The Joint North Sea Wave Project (JONSWAP)'. *Dtsch. Hydrogr. Z.* **A 8(12)**. 3.3.2

Hasselmann, S., K. Hasselmann, J. Allender, and T. Barnett: 1985, 'Computations and parametrizations of the nonlinear energy transfer in a gravity wave spectrum. Part II: Parametrizations of the nonlinear transfer for application in wave models'. *Journal of Physical Oceanography* **15,11**, 1378–1391. 3.3.2

Hernández, F., E. Blockley, G. B. Brassington, F. Davidson, P. Divakaran, M. Drévillon, S. Ishizaki, M. Garcia-Sotillo, P. J. Hogan, P. Lagemaa, B. Levier, M. Martin, A. Mehra, C. Mooers, N. Ferry, A. Ryan, C. Regnier, A. Sellar, G. C. Smith, S. Sofianos, T. Spindler, G. Volpe, J. Wilkin, E. D. Zaron, and A. Zhang: 2015, 'Recent progress in performance evaluations and near real-time assessment of operational ocean products'. *Journal of Operational Oceanography* **8**(sup2), 221–238. 1.1, 7.6

Hinkel, J., D. Lincke, A. T. Vafeidis, M. Perrette, R. J. Nicholls, R. S. J. Tol, B. Marzeion, X. Fettweis, C. Ionescu, and A. Levermann: 2014, 'Coastal flood

damage and adaptation costs under 21st century sea-level rise'. *Proceedings of the National Academy of Sciences* **111**(9), 3292–3297. 1, 2.6

Hinkel, J., R. Nicholls, R. Tol, Z. Wang, J. Hamilton, G. Boot, A. Vafeidis, L. McFadden, A. Ganopolski, and R. Klein: 2013, 'A global analysis of erosion of sandy beaches and sea-level rise: An application of DIVA'. *Global and Planetary Change* **111**, 150–158. 2.3.1.3

Holman, R. A. and J. Stanley: 2007, 'The history and technical capabilities of Argus'. *Coastal Engineering* **54(6-7)**, 447–491. 2.5.2.1

Holt, J., J. Allen, R. Proctor, and F. Gilbert: 2005, 'Error quantification of a high-resolution coupled hydrodynamic-ecosystem coastal-ocean model: Part 1 Model overview and assessment of the hydrodynamics'. *Journal of Marine Systems* **57**, 167–188. 3.4.1, 4.3, 7.6

Holthuijsen, L., N. Booij, and R. Ris: 1993, 'A spectral wave model for the coastal zone'. In: *Proc., 2nd Int. Symp. on Ocean Wave Measurement and Analysis, New Orleans, 630-641.* 3.3.2, 3.3.3

Hornsey, W., J. Carley, I. Coghlan, and R. Cox: 2011, 'Geotextile sand container shoreline protection systems: Design and application'. *Geotextiles and Geomembranes* **29**(4), 425–439. 7.4.3, 1, 7.5.2, 7.6

Horstman, E., C. Dohmen-Janssen, P. Narra, N. van den Berg, M. Siemerink, and S. Hulscher: 2014, 'Wave attenuation in mangroves: A quantitative approach to field observations'. *Coastal Engineering* **94**, 47 – 62. 7.5.3

Ibáñez, C., J. W. Day, and E. Reyes: 2014, 'The response of deltas to sea-level rise: Natural mechanisms and management options to adapt to high-end scenarios'. *Ecological Engineering* **65**, 122 – 130. Sustainable Restoration. 2.3.1.3, 2.4.4.2

Ibáñez, C., P. Sharpe, J. Day, J. Day, and N. Prat: 2010, 'Vertical Accretion and Relative Sea Level Rise in the Ebro Delta Wetlands (Catalonia, Spain)'. *Wetlands* (30), 979–988. 2.3.1.3

IDESCAT: 2018, 'Anuari Estadístic de Catalunya, 2017. Institut d'Estadística de Catalunya. Generalitat de Catalunya. URL: http://www.idescat.cat/pub/?id=aec ((Accessed 15-03-2018'. 2.4

IH-Cantabria: 2009, '(SMC) http://www.smc.ihcantabria.com/ (Last access: 28th August 2017)'. 2.5.2.1

IIASA: 2012, 'IIASA (International Institute for Applied Systems Analysis) 2012 SSP Database (version 0.93) (https://secure.iiasa.ac.at/web-apps/ene/SspDb/dsd?Action=htmlpage&page=about)'. (document), 2.8, 2.4.3

IPCC: 2014, *Climate Change 2014: Impacts, Adaptation, and Vulnerability. Part A: Global and Sectoral Aspects. Contribution of Working Group II to the Fifth Assessment Report of the Intergovernmental Panel on Climate Change [Field, C.B., V.R. Barros, D.J. Dokken, K.J. Mach, M.D. Mastrandrea, T.E. Bilir, M. Chatterjee, K.L. Ebi, Y.O. Estrada, R.C. Genova, B. Girma, E.S. Kissel, A.N. Levy, S. MacCracken, P.R. Mastrandrea, and L.L. White (eds.)].* Cambridge, United Kingdom and New York, NY, USA: Cambridge University Press. 2.4.3

Jager, W., E. Christie, A. Hanea, C. den Heijer, and T. Spencer: 2018, 'A Bayesian network approach for coastal risk analysis and decision making'. *Coastal Engineering* **134**, 48 – 61. 4

Jakeman, A., R. Letcher, and J. Norton: 2006, 'Ten iterative steps in development and evaluation of environmental models'. *Environmental Modelling and Software* **21**, 602–614. 2.5.1.2, 6.4.3.1

Janssen, P.: 1991, 'Quasi-linear theory of wind-wave generation applied to wave forecasting'. *Journal of Physical Oceanography* **21**, 1631–1642. 3.3.2

Jevrejeva, S., J. Moore, A. Grinsted, A. Matthews, and G. Spada: 2014, 'Trends and acceleration in global and regional sea levels since 1807'. *Global and Planetary Change* **113**, 11–22. 1.1, 2.3.1.3, 2.4.3, 2.6

Jiménez, J., V. Gràcia, H. Valdemoro, E. Mendoza, and A. Sánchez-Arcilla: 2011, 'Managing erosion-induced problems in NW Mediterranean urban beaches'. *Ocean and Coastal Management* **54**, 907–918. 2.4.4.1

Jiménez, J., A. Sancho-García, E. Bosom, H. Valdemoro, and J. Guillén: 2012, 'Storm-induced damages along the Catalan coast (NW Mediterranean) during the period 1958-2008'. *Geomorphology* **143-144**, 24–33. 1.1, 2.3.1, 2.3.1.1, 2.3.3, 7.6

Jiménez-Esteve, B., M. Udina, M. Soler, N. Pepin, and J. Miró: 2018, 'Land use and topography influence in a complex terrain area: A high resolution mesoscale modelling study over the Eastern Pyrenees using the WRF model'. *Atmospheric Research* **202**, 49 – 62. 5.4.3

Jordá, G., R. Bolaños, M. Espino, and A. Sánchez-Arcilla: 2007, 'Assessment of the importance of the current-wave coupling in the shelf ocean forecasts'. *Ocean Science* **3**(3), 345–362. 3.1, 3.2.3

Klein, N., T. Kneib, S. Klasen, and S. Lang: 2015, 'Bayesian structured additive distributional regression for multivariate responses'. *Journal of the Royal Statistical Society: Series C (Applied Statistics)* **64**(4), 569–591. 3.3.4.2

Kolev, N. and D. Paiva: 2009, 'Copula-based regression models: A survey'. *Journal of Statistical Planning and Inference* **139**(11), 3847 – 3856. Special Issue: The 8th Tartu Conference on Multivariate Statistics & The 6th Conference on Multivariate Distributions with Fixed Marginals. 3.4.3

Komen, G., S. Hasselmann, and K. Hasselmann: 1984, 'On the existence of a fully developed wind-sea spectrum'. *Journal of Physical Oceanography* **14**, 1271–1285. 3.3.2

Kourafalou, V., P. D. Mey, J. Staneva, N. Ayoub, A. Barth, Y. Chao, M. Cirano, J. Fiechter, M. Herzfeld, A. Kurapov, A. Moore, P. Oddo, J. Pullen, A. van der Westhuysen, and R. Weisberg: 2015, 'Coastal Ocean Forecasting: science foundation and user benefits'. *Journal of Operational Oceanography* **8**(sup1), 147–167. 7.5.3

Kruizinga, S. and A. H. Murphy: 1983, 'Use of an analogue procedure to formulate

objective probabilistic temperature forecasts in the Netherlands'. *Monthly Weather Review* **111**(11), 2244–2254. 6.4.3.2

Lam, D. and R. Simpson: 1976, 'Centered differencing and the box scheme for diffusion convection problems'. *Journal of Computational Physics* **22**, 486–500. 3.3.3.5

Larsén, X. G., J. Du, R. Bolaños, and S. Larsen: 2017, 'On the impact of wind on the development of wave field during storm Britta'. *Ocean Dynamics* **67**(11), 1407–1427. 5.4.3

Larson, M., N. Kraus, and M. Byrnes: 1990, 'SBeach: Numerical model for simulating storm-induced beach change. Report 2: Numerical formulation and model tests'. Technical report, U.S. Army Engineer Waterways Experiment Station, Coasta Engineering Research Center, Vicksburg, MS. 2.3.1.1, 2.5.2.1

Legates, D. R. and G. J. McCabe: 1999, 'Evaluating the use of Şgoodness-of-fitŤ Measures in hydrologic and hydroclimatic model validation'. *Water Resources Research* **35**(1), 233–241. 3.4.1, 7.6

Legates, D. R. and G. J. McCabe: 2013, 'A refined index of model performance: a rejoinder'. *International Journal of Climatology* **33**(4), 1053–1056. 3.4.1

Lellouche, J.-M., O. Le Galloudec, M. Drévillon, C. Régnier, E. Greiner, G. Garric, N. Ferry, C. Desportes, C.-E. Testut, C. Bricaud, R. Bourdallé-Badie, B. Tranchant, M. Benkiran, Y. Drillet, A. Daudin, and C. De Nicola: 2013, 'Evaluation of global monitoring and forecasting systems at Mercator Océan'. *Ocean Science* **9**(1), 57–81. 3.2.3

Lesser, G., J. Roelvink, J. van Kester, and G. Stelling: 2004, 'Development and validation of a three-dimensional morphological model'. *Coastal Engineering* **51**(8-9), 883 – 915. Coastal Morphodynamic Modeling. 2.3.1.1

Leyton, S. M. and J. M. Fritsch: 2004, 'The Impact of High-Frequency Surface Weather Observations on Short-Term Probabilistic Forecasts of Ceiling and Visibility'. *Journal of Applied Meteorology* **43**(1), 145–156. 6.4.3.1

LIM/UPC: 2014, 'Proposal for the predesign of solutions for coastal stabilisation at the Gava Beaches'. Technical report, LIM/UPC (Maritime Engineering Laboratory - Polytechnic University of Catalonia). ASA VG XG MGL. 2.4.4.2, 7.5.2

Lin, N. and K. Emanuel: 2016, 'Grey swan tropical cyclones'. *Nature Climate Change* **6**(1), 106–111. 1.1

Lin-Ye, J., M. García-León, V. Gràcia, M. Ortego, P. Lionello, and A. Sánchez-Arcilla: 2017, 'Multivariate statistical modelling of future marine storms'. *Applied Ocean Research* **65**, 192 – 205. 1.1, 2.4.3, 5.4.4, 6.1, 6.4.1

Lin-Ye, J., M. García-León, V. Gràcia, M. Ortego, A. Stanica, and A. Sánchez-Arcilla: 2018, 'Multivariate Hybrid Modelling of Future Wave-Storms at the Northwestern Black Sea'. *Water* **10**(2(221)). 5.4.4

Lin-Ye, J., M. García-León, V. Gràcia, and A. Sánchez-Arcilla: 2016, 'A multivariate statistical model of extreme events: An application to the Catalan coast'. *Coastal Engineering* **117**, 138 – 156. 2.6, 6.1, 6.2.1, 6.3.3.4, 6.4.1, 7.6

Lionello, P., U. Boldrin, and F. Giorgi: 2008, 'Future changes in cyclone climatology over Europe as inferred from a regional climate simulation'. *Climate Dynamics* **30**, 657–671. 2.4.3

Liste, M., M. Grifoll, and J. Monbaliu: 2014, 'River plume dispersion in response to flash flood events. Application to the Catalan shelf'. *Continental Shelf Research* **87**, 96 – 108. Oceanography at coastal scales. 5.4.3

Lowe, J. A., P. L. Woodworth, T. Knutson, R. E. McDonald, K. L. McInnes, K. Woth, H. von Storch, J. Wolf, V. Swail, N. B. Bernier, S. Gulev, K. J. Horsburgh, A. S. Unnikrishnan, J. R. Hunter, and R. Weisse: 2010, *Past and Future Changes in Extreme Sea Levels and Waves*, pp. 326–375. Wiley-Blackwell. 2.4.3

Madec, G.: 2008, 'NEMO ocean general circulation model reference manuel'. In: *Internal Report*. LODYC/IPSL Paris. 3.2.3

Madsen, O., Y. Poon, and H. Graber: 1988, 'Spectral wave attenuation by bottom friction: Theory'. In: ASCE (ed.): *Proceedings of 21th International Conference in Coastal Engineering*. pp. 492–504. 3.3.2

Malvarez, G., J. Pollard, and R. Dominguez: 2000, 'Origins, management and measurement of stress on the coast of Southern Spain'. *Coastal Management* (28), 215–234. 2.4.4.1

Marchand, M., A. Sanchez-Arcilla, M. Ferreira, J. Gault, J. Jimenez, M. Markovic, and J. Mulder: 2011, 'Concepts and science for coastal erosion management - An introduction to the CONSCIENCE framework'. *Ocean and Coastal Management* **12**(54), 859–866. 2.4.4.1

Marra, G. and S. N. Wood: 2011, 'Practical variable selection for generalized additive models'. *Computational Statistics & Data Analysis* **55**(7), 2372 – 2387. 6.4.3.1

Martinelli, L., B. Zanuttigh, N. D. Nigris, and M. Preti: 2011, 'Sand bag barriers for coastal protection along the Emilia Romagna littoral, Northern Adriatic Sea, Italy'. *Geotextiles and Geomembranes* **29**(4), 370–380. Geosynthetics in Hydraulic Applications. 7.5.2

Martínez, M., A. Intralawan, G. Vázquez, O. Pérez-Maqueo, P. Sutton, and R. Langrave: 2007, 'The coasts in our world: Ecological, economic and social importance'. *Ecological Economics* **63**(2-3), 254–272. 1.1

Mendoza, E., J. Jiménez, and J. Mateo: 2011, 'A coastal storms intensity scale for the Catalan sea: NW Mediterranean'. *Natural Hazards and Earth System Sciences* **11**, 2453–2462. 1

Menéndez, M., M. García-Díez, L. Fita, J. Fernández, F. J. Méndez, and J. M. Gutiérrez: 2014, 'High-resolution sea wind hindcasts over the Mediterranean area'. *Climate Dynamics* **42**(7), 1857–1872. 5.4.1

Menéndez, M. and P. L. Woodworth: 2010, 'Changes in extreme high water levels based on a quasi-global tide-gauge data set'. *Journal of Geophysical Research: Oceans* **115**(C10), n/a–n/a. 2.4.3

Merkens, J.-L., L. Reimann, J. Hinkel, and A. T. Vafeidis: 2016, 'Gridded population projections for the coastal zone under the Shared Socioeconomic Pathways'. *Global and Planetary Change* **145**, 57 – 66. 1.1, 2.4.3

Miles, J.: 1957, 'On the generation of surface waves by shear flows'. *Journal of Fluid Mechanics* **3**, 185–204. 3.3.2

Milliff, R. F., A. Bonazzi, C. K. Wikle, N. Pinardi, and L. M. Berliner: 2011, 'Ocean ensemble forecasting. Part I: Ensemble Mediterranean winds from a Bayesian hierarchical model'. *Quarterly Journal of the Royal Meteorological Society* **137**(657), 858–878. 5.4.4

Morris, R. L., T. M. Konlechner, M. Ghisalberti, and S. Swearer: 2018, 'From grey to green: Efficacy of eco-engineering solutions for nature-based coastal defence'. *Global Change Biology* **24**(5), 1827–1842. 1, 7.5.3

Muis, S., B. Güneralp, B. Jongman, J. C. Aerts, and P. J. Ward: 2015, 'Flood risk and adaptation strategies under climate change and urban expansion: A probabilistic analysis using global data'. *Science of The Total Environment* **538**, 445 – 457. 2.6

Nelder, J. A. and R. W. M. Wedderburn: 1972, 'Generalized Linear Models'. *Journal of the Royal Statistical Society. Series A (General)* **135**(3), 370–384. 3.3.4.2

Nesshover, C., T. Assmuth, K. N. Irvine, G. M. Rusch, K. A. Waylen, B. Delbaere, D. Haase, L. Jones-Walters, H. Keune, E. Kovacs, K. Krauze, M. Kulvik, F. Rey, J. van Dijk, O. I. Vistad, M. E. Wilkinson, and H. Wittmer: 2017, 'The science, policy and practice of nature-based solutions: An interdisciplinary perspective'. *Science of The Total Environment* **579**, 1215–1227. 7.5.3

Neumann, B., A. Vafeidis, J. Zimmermann, and R. Nicholls: 2015, 'Future Coastal Population Growth and Exposure to Sea-Level Rise and Coastal Flooding - A Global Assessment'. *PLoS ONE* **10**(3), e0118571. 1.1, 2.4.3

Ninyerola, M., X. Pons, J. Roure, J. Martín-Vide, J. Raso, and P. Clavero: 2003, 'Atles Climàtics de Catalunya'. CD-ROM. 2.6

Nissen, K., G. Leckebusch, J. Pinto, and U. Ulbrich: 2014, 'Mediterranean cyclones and windstorms in a changing climate'. *Regional Environmental Change* **14**(5), 1873–1890. 2.4.3

Nordhaus, W.: 2006, 'Geography and macroeconomics: new data and new findings'. *Proceedings of the National Academy of Sciences* **103**, 3510–3517. 1.1

Nordstrom, K. F. and N. L. Jackson: 2003, 'Alternative restoration outcomes for dunes on intensively developed coasts'. In: E. A. Ozhan (ed.): *MEDCOAST' 03.* MEDCOAST Secretariat, pp. 1469–1478. 7.5.2

O Neill, B., E. Kriegler, K. Riahi, K. Ebi, S. Hallegatte, T. Carter, R. Mathur, and D. van Vuuren: 2014, 'A new scenario framework for climate change research: the concept of shared socioeconomic pathways'. *Climatic Change* **122**(3), 387–400. 2.4.3

Pallarés, E.: 2016, 'High-resolution wave forecasting. The Catalan coast case. Mod-

elling, coupling and validation'. Ph.D. thesis, Polytechnic University of Catalonia. 5.1, 5.2, 5.4.1, 7.6, 9

Pallarés, E., J. López, M. Espino, and A. Sánchez-Arcilla: 2017, 'Comparison between nested grids and unstructured grids for a high-resolution wave forecasting system in the western Mediterranean sea'. *Journal of Operational Oceanography* **10**(1), 45–58. 5.4.3, 10

Pallarés, E., A. Sánchez-Arcilla, and M. Espino: 2014, 'Wave energy balance in wave models (SWAN) for semi-enclosed domains. Application to the Catalan coast'. *Continental Shelf Research* **87**, 41–53. 3.3.2, 4.2, 5.3.2, 5.4.3

Phillips, O.: 1957, 'On the generation of waves by turbulent wind'. *Journal of Fluid Mechanics* **2**, 417–445. 3.3.2

Pinardi, N., A. Bonazzi, S. Dobricic, R. F. Milliff, C. K. Wikle, and L. M. Berliner: 2011, 'Ocean ensemble forecasting. Part II: Mediterranean forecast system response'. *Quarterly Journal of the Royal Meteorological Society* **137**(657), 879–893. 5.4.4

PROCICAT: 2013, 'Pla Territorial de Protecció Civil de Catalunya'. (Departament d'Interior) Generalitat de Catalunya. 2.5.1.1

Queffeulou, P.: 2004, 'Long term validation of wave height measurements from altimeters'. *Marine Geodesy* **27**, 495–510. 4.2

Reniers, A., J. Roelvink, and E. Thorton: 2004a, 'Morphodynamic modelling of an embayed beach under wave group forcing'. *Journal of Geophysical Research* **109**. 3.3.3.3

Reniers, A., E. Thorton, T.Stanton, and J. Roelvink: 2004b, 'Vertical flow structure during Sandy Duck: Observations and Modeling'. *Coastal Engineering* **51**, 237–260. 3.3.3.1

Restall, S., L. Jackson, G. Heerten, and W. Hornsey: 2002, 'Case studies showing the growth and development of geotextile sand containers: an Australian perspective'. *Geotextiles and Geomembranes* **20**(5), 321–342. Geosynthetic Containers. 7.4.3, 1, 7.5.2

Rigby, R. A. and D. M. Stasinopoulos: 2005, 'Generalized additive models for location, scale and shape'. *Journal of the Royal Statistical Society: Series C (Applied Statistics)* **54**(3), 507–554. 3.3.4.2

Roelvink, J. A.: 1993, 'Dissipation in random wave groups incident on a beach'. *Coastal Engineering* **19**, 127–150. 3.3.3.1

Roelvink, J. A., A. Reniers, A. V. Dongeren, J. van Thiel de Vries, R. McCall, and J. Lescinski: 2009, 'Modeling storm impacts on beaches, dunes and barrier islands'. *Coastal Engineering* **56**(11-12), 1133–1152. 2.3.1.1, 2.4.4.2, 2.5.2.1, 3.1, 3.3.3, 3.3.3.1, 3, 7.6

Rogers, W. E., P. A. Hwang, and D. W. Wang: 2003, 'Investigation of wave growth and decay in the SWAN model: three regional-scale applications'. *Journal of Physical Oceanography* **33**(2), 366–389. 5.1

Rovira, A., R. Ballinger, C. Ibáñez, P. Parker, M. Dominguez, X. Simon, A. Lewandowski, B. Hochfeld, M. Tudor, and L. Vernaeve: 2014, 'Sediment imbalances and flooding risk in European deltas and estuaries'. *Journal of Soils and Sediments* **14**(8), 1493–1512. 2.4.4.2

Sabeti, A., M. Wei, and R. V. Craiu: 2014, 'Additive models for conditional copulas'. *Stat* **3**(1), 300–312. 3.3.4.2

Sallenger, A.: 2000, 'Storm Impact Scale for Barrier Islands'. *Journal of Coastal Research* **16(3)**, 890–895. 2.3.1.1.2, 3, 7.3.2.2, 7.4.2.1, 7.4.2.1, 7.5.2

Sánchez-Arcilla, A., I. Cáceres, L. van Rijn, and J. Grüne: 2011a, 'Revisiting mobile bed tests for beach profile dynamics'. *Coastal Engineering* **58(7)**, 583–593. 4.6

Sánchez-Arcilla, A., M. García-León, and V. Gràcia: 2014, 'Hydro-morphodynamic modelling in Mediterranean storms - errors and uncertainties under sharp gradients'. *Nat. Hazards Earth Syst. Sci.* **14**, 2993–3004. 1.2, 2.4.4.1, 2.6, 4, 6.4.2

Sánchez-Arcilla, A., M. García-León, and V. Gràcia: 2015a, 'Sustainability of artificial coasts: the Barcelona coast case'. In: *Coastal zones: solutions for the 21st Century*. Elsevier, pp. 163–182. 2.4.4.1, 2.6, 7.5.3

Sánchez-Arcilla, A., M. García-León, V. Gràcia, R. Devoy, A. Stanica, and J. Gault: 2016a, 'Managing coastal environments under climate change: Pathways to adaptation'. *Science of The Total Environment* **572**, 1336 – 1352. 2.1, 2.4.3

Sánchez-Arcilla, A., M. García-León, V. Gràcia, and J. P. Sierra: 2017, 'Assessment of green measures as coastal defences using numerical models'. In: *Proceedings of Coastal Dynamics 2017*. pp. 727–738. 2.6

Sánchez-Arcilla, A., D. González-Marco, and R. Bolaños: 2008, 'A review of wave climate and prediction along the Spanish Mediterranean coast'. *Nat. Hazard. Earth Sys.* **8(6)**, 1217–1228. 4.1, 5.4.1

Sánchez-Arcilla, A., V. Gràcia, M. García-León, J. A. Jiménez, I. Cáceres, and H. I. Valdemoro: 2015b, *Natural Accretion Mechanisms. The role in future coastal sustainability*, Chapt. 159. World Scientific. 2.4.4.2

Sánchez-Arcilla, A., V. Gràcia, M. Grifoll, M. García, and E. Pallarés: 2012, 'Operational Forecast of Beach Morphodynamics. Reability and Predictions Limits'. In: *33rd International Conference in Coastal Engineering (2012)*. 2.4, 2

Sánchez-Arcilla, A., V. Gràcia, J. Solé, M. García-León, and A. Sairouni: 2013, 'Forecasting beach morphodynamics: The shoreline border as a control for flooding risks'. In: Klijn and Schweckendiek (eds.): *Comprehensive Flood Risk Management*. Taylor and Francis Group. 2.3.3, 4.3, 4.4

Sánchez-Arcilla, A., J. Jiménez, and M. Marchand: 2011b, 'Managing coastal evolution in a more sustainable manner. The Conscience approach'. *Ocean and Coastal Management* **54**(951-955). 7.1

Sánchez-Arcilla, A., C. Mosso, J. P. Sierra, M. Mestres, A. Harzallah, M. Senouci, and M. E. Raey: 2011c, 'Climatic drivers of potential hazards in Mediterranean coasts'. *Regional Environmental Change* **11**, 617–636. 4.3

Sánchez-Arcilla, A., J. P. Sierra, S. Brown, M. Casas-Prat, R. J. Nicholls, P. Lionello, and D. Conte: 2016b, 'A review of potential physical impacts on harbours in the Mediterranean Sea under climate change'. *Regional Environmental Change* pp. 1–14. 1.1, 5.4.4

Sancho-García, A., J. Guillén, G. Simarro, R. Medina, and V. Cánovas: 2012, 'Beach Inundation Prediction during Storms using Differents Wave Heights as Inputs'. In: *33rd International Conference in Coastal Engineering (2012)*. 2.3.3

Sardà, R., C. Avila, and J. Mora: 2005, 'A methodological approach to be used in integrated coastal zone management processes: the case of the Catalan Coast (Catalonia, Spain).'. *Estuarine, Coastal and Shelf Science* **62**(3), 427–439. 2.4

Schwarz, G.: 1978, 'Estimating the dimension of a model'. *The Annals of Statistics* **6**(2), 461–464. 3.4.3, 7.6

Shchepetkin, A. and J. McWilliams: 2005, 'The regional ocean modeling system (ROMS): a split - explicit, free - surface, topography - following - coordinates ocean model'. *Ocean Modelling* **9**, 347–404. 5.4.3, 7

Sierra, J. P. and M. Casas-Prat: 2014, 'Analysis of potential impacts on coastal areas due to changes in wave conditions'. *Climatic Change* **124**, 861–876. 1, 5.4.4, 6.4.2

Sierra, J. P., M. Casas-Prat, M. Virgili, C. Mösso, and A. Sánchez-Arcilla: 2015, 'Impacts on wave-driven harbour agitation due to climate change in Catalan ports'. *Natural Hazards and Earth System Sciences* **15**(8), 1695–1709. 5.4.4

Silvester, R. and J. R. Hsu: 1997, *Coastal Stabilization*. World Scientific Publishing Co. Pte. Ltd. 7.5.2

SIMO: 2015, 'Deliverable F.2. Report on the analysis of the test implementation. Restricted document from the iCoast project (ECHO/SUB/2013/661009)'. Technical report, SIMO - CIIRC - ITHACA. 3.1

Skamarock, W., J. Klemp, J. Dudhia, D. Gill, D. Barker, W. Wang, and J. Powers: 2005, 'A description of the Advanced Research WRF Version 2'. Technical report, National Center for Atmospheric Research (NCAR). 3.1, 3.3.1, 5.4.1, 1, 7.6, 7.6

Sklar, A.: 1959, *Fonctions dé repartition á n dimension et leurs marges*. Université Paris 8. 3.3.4.1

Sotillo, M. G., S. Cailleau, P. Lorente, B. Levier, R. Aznar, G. Reffray, A. Amo-Baladrón, J. Chanut, M. Benkiran, and E. Alvarez-Fanjul: 2015, 'The MyOcean IBI Ocean Forecast and Reanalysis Systems: operational products and roadmap to the future Copernicus Service'. *Journal of Operational Oceanography* **8**(1), 63–79. 1.1, 3.2.3, 2, 7.6, 7.6, 7

Stanica, A. and N. Panin: 2009, 'Present evolution and future predictions for the deltaic coastal zone between the Sulina and Sf. Gheorghe Danube river mouths (Romania)'. *Geomorphology* **107**(1), 41 – 46. Coastal vulnerability related to sea-level rise. 2.4.3

Stelling, G. and M. Zijlema: 2003, 'An accurate and efficient finite-difference algo-

rithm for non-hydrostatic free-surface flow with application to wave propagation'. *International Journal for Numerical Methods in Fluids* **43**, 1–23. 3.3.3.5

Stive, M. and M. Dingemans: 1984, 'Calibration and verification of a one-dimensional wave energy decay model'. Technical report, Delft Hydraulics, Delft, The Netherlands. 3.3.3

Stockdon, H. F., R. A. Holman, P. A. Howd, and A. H. Sallenger: 2006, 'Empirical parametrization of setup, swash and runup'. *Coastal Engineering* **53(7)**, 573–588. 2.3.3

Stocker, T., D. Qin, G.-K. Plattner, M. tignor, S. Allen, J. Boschung, A. Nauels, Y. Xia, V. Bex, and P. Midgley: 2013, 'IPCC, 2013: Summary for Policymakers'. In: *Climate Change 2013: The Physical Science Basis. Contribution of Working Group I to the Fifth Assessment Report of the Intergovernmental Panel on Climate Change*. Cambridge University Press, Cambridge, United Kingdom and New York, NY, USA. 2.3.3, 2.4.3, 2.7

Sullivan, P. P. and J. C. McWilliams: 2010, 'Dynamics of Winds and Currents Coupled to Surface Waves'. *Annual Review of Fluid Mechanics* **42**(1), 19–42. 5.4.3

Tang, L., V. Titov, and C. Chamberlin: 2009, 'Development, testing, and applications of site-specific tsunami inundation models for real-time forecasting'. *Journal of Geophysical Research: Oceans* **114**(C12). 6.4.3.1

Taylor, K.: 2001, 'Summarizing multiple aspects of model performance in a single diagram'. *Journal of Geophysical Research* **106**, 7183–7192. 3.4.1, 5.3

Thomalla, F. and R. Larsen: 2010, 'Resilience in the context of tsunami early warning systems and community disaster preparedness in the Indian Ocean Region'. *Environmental Hazards. Human and Policy Dimensions* **9**, 249–265. 2.5.1.1

Tonani, M., N. Pinardi, C. Fratianni, J. Pistoia, S.Dobricic, S.Pensieri, M. de Alfonso, and K. Nittis: 2009, 'Mediterranean Forecasting System: forecast and analysis assessment through skill scores'. *Ocean Science* **5**, 649–660. 4.2, 7.6

Trenberth, K.E., F. J. and T. Shepherd: 2015, 'Attribution of climate extreme events'. *Nature Climate Change*. 1.1, 5.4.4, 7.6

Trenberth, K. E.: 2007, 'Warmer Oceans, Stronger Hurricanes'. *Scientific American* **July**, 44–51. 1.1

Trigo, I. F., G. R. Bigg, and T. D. Davies: 2002, 'Climatology of cyclogenesis mechanisms in the Mediterranean'. *Monthly Weather Review* **130**(3), 549–569. 5.4.4

Tsimplis, M. N., S. A. Josey, M. Rixen, and E. V. Stanev: 2004, 'On the forcing of sea level in the Black Sea'. *Journal of Geophysical Research: Oceans* **109**(C8). 2.4.3

Turner, R., S. Subak, and W. Adger: 1996, 'Pressures, trends, and impacts in coastal zones: interactions between socioeconomic and natural systems'. *Environmental Management* **20**(2), 159–174. 1.1

UNISDR: 2010, 'Emerging challenges for Early Warning Systems in context of Climate Change and Urbanization'. Technical report, Platform for Promotion of Early Warning (UNISDR). 2.5.1.1, 2.5.1.1

Valchev, N. N., E. V. Trifonova, and N. K. Andreeva: 2012, 'Past and recent trends in the western Black Sea storminess'. *Natural Hazards and Earth System Science* **12**(4), 961–977. 2.4.3

Van der Meer, J. W., R. Briganti, B. Zanuttigh, and B. Wang: 2005, 'Wave transmission and reflection at low-crested structures: Design formulae, oblique wave attack and spectral change'. *Coastal Engineering* **52**(10), 915–929. 5.4.3

van Dongeren, A., A. Bolle, M. I. Vousdoukas, T. Plomaritis, P. Eftimova, J. Williams, C. Armaroli, D. Idier, P. V. Geer, J. V. T. de Vries, P. Haerens, R. Taborda, J. Benavente, E. Trifonova, P. Ciavola, Y. Balouin, and D. Roelvink: 2009, 'MICORE: Dune Erosion and Overwash Model Validation with Data from Nine European Field Sites'. *Coastal Dynamics*. 2.5.2.1

van Dongeren, A. and J. V. T. de Vries: 2011, 'Validation of dune impact models using European field data - Deliverable 4.1. and 4.2. (combined): validation of XBeach and off-the-shelf models'. Technical report, Deltares. 2.13

van Dongeren, A., N. Plant, A. Cohen, D. Roelvink, M. C. Haller, and P. Catalan: 2008, 'Beach Wizard: Nearshore bahymetry estimation through assimilation of model computations and remote observations'. *Coastal Engineering* **55**, 1016–1027. 2.5.2.1

van Koningsveld, M., M. Davidson, and D. Huntley: 2005, 'Matching Science with Coastal Management Needs: The Search for Appropiate Coastal State Indicators'. *Journal of Coastal Research* **21**, 399–411. 3, 4

van Rijn, L.: 2007, 'Unified view of sediment transport by current and waves, part I, II, III and IV'. *Journal of Hydraulic Engineering* **133(6,7)**, 649–689 (part I & part II), 761–793 (part III & part IV). 3.3.3, 3.3.3.3, 4.4, 4.6

van Rijn, L. C., D. J. R. Walstra, B. Grasmeijer, J. Sutherland, S. Pan, and J. P. Sierra: 2003, 'The predictability of cross-shore bed evolution of sandy beache at the time scale of storms and seasons using process-based Profile models'. *Coastal Engineering* **47(3)**, 295–327. 3.4.2, 7.1, 7.6, 7.6, 7.6

Vanem, E.: 2016, 'Joint statistical models for significant wave height and wave period in a changing climate'. *Marine Structures* **49**, 180–205. 6.4.1

Velasco, M., Àngels Cabello, and B. Russo: 2016, 'Flood damage assessment in urban areas. Application to the Raval district of Barcelona using synthetic depth damage curves'. *Urban Water Journal* **13**(4), 426–440. 3

Vellinga, P.: 1986, 'Beach and Dune Erosion during Storm Surges'. Ph.D. thesis, Delft University of Technology. 7.4.2.1

Voinov, A. and F. Bousquet: 2010, 'Modelling with stakeholders'. *Environmental Modelling and Software* **25**, 1268–1281. 2.5.1.1

Vuik, V., S. Jonkman, B. Borsje, and T. Suzuki: 2016, 'Nature-based flood pro-

tection: The efficiency of vegetated foreshores for reducing wave loads on coastal dikes'. *Coastal Engineering* **116**, 42 – 56. 7.5.3

Wang, X. L., Y. Feng, and V. R. Swail: 2015, 'Climate change signal and uncertainty in CMIP5-based projections of global ocean surface wave heights'. *Journal of Geophysical Research: Oceans* **120**(5), 3859–3871. 2.6

WISE Group: 2007, 'Wave modelling-the state of the art'. *Prog. Oceanogr.* **75**, 603–674. 5.3.2

WMO: 2010, 'Guidelines on Early Warning Systems and Applications of Nowcasting and Warning Operations, WMO/TD N1559'. Technical Report WMO/TD N1559, World Meteorological Organization. 2.5.1.3

Wright, L. and A. Short: 1984, 'Morphodynamic variability of surf zones and beaches: A synthesis'. *Marine Geology* **56 (1-4)**, 93–118. 4.4, 2, 6.3.3.2, 7.3.1, 7.5.1, 7.6

Yan, S. and J. Chu: 2010, 'Construction of an offshore dike using slurry filled geotextile mats'. *Geotextiles and Geomembranes* **28**(5), 422–433. 7.5.2

Yu, Y., X. Yang, W. Zhang, B. Duan, X. Cao, and H. Leng: 2017, 'Assimilation of Sentinel-1 Derived Sea Surface Winds for Typhoon Forecasting'. *Remote Sensing* **9**(8(845)), 1–17. 5.4.4

Zhang, Y., J. Wang, and X. Wang: 2014, 'Review on probabilistic forecasting of wind power generation'. *Renewable and Sustainable Energy Reviews* **32**, 255–270. 6.4.3.2